Composition and age of Cenozoic volcanism in Libya

by

ABDELMONIEM AHMED MOHAMED MASOUD

A thesis submitted to Glasgow University

in partial fulfilment for the degree of

DOCTOR OF PHILOSOPHY

Scottish Universities Environment Research Centre

(SUERC)

2014

Abstract

Libya has five major Cenozoic volcanic provinces (Garian, Jabal Al Haruj al Aswad, Jabal Al Hasawinah, Jabal as Sawda and Jabal Nuqay) that have a surface area of approximately 66,000 km^2. These volcanic provinces are dominated by alkali to mildly alkali basalts. The provinces are aligned NNW-SSE, typically occurring where NE-SW trending structural features intersect the main regional uplift structures. Small volumes of phonolites are associated with the basaltic volcanism at Garian and Jabal Al Hasawinah.

Despite their size and relative accessibility the Cenozoic volcanic provinces of Libya have been rarely studied. In the first part of this thesis I report a new study of the petrology, geochemistry (major and trace elements, REE, Sr-Nd isotopes) and geochronology ($^{40}Ar/^{39}Ar$) of basalts and phonolites from the Garian volcanic province in north Libya. These analyses indicate that the plateau and late basalts are not distinct basalt types produced from melting of different mantle regions at different times as proposed by earlier studies. They are the product of fractional crystallisation of a common parent. There is little indication of crustal contamination. Trace element and REE data support an origin in 2 to 12 % melts of heterogeneous sub-lithosphere mantle. Trace elements and Nd and Sr isotopic composition of the Garian basalts overlap values measured in metasomatised peridotite xenoliths in the GVP. They are compositionally similar to Cenozoic volcanism of northern Libya (e.g. Jabal Al Haruj) and southern Italy (e.g. Etna and Pantelleria; European asthenosphere mantle reservoir), and they lack the influence of enriched mantle present in other North African Cenozoic basalt provinces. Compositional variation in the Garian province phonolitic magmas is dominated by extensive fractional crystallisation (50-83%) of plagioclase and alkali feldspars combined with an unusual style of assimilation (2-45%) of old upper crust typical of Pan-African shield. The new high precision age determinations of the phonolites suggest that they were produced over a very short period at ~8.1 Ma. This contrasts strongly with previous age determinations that were 40-50 Ma.

In the second half of the thesis I report new Ar/Ar chronology measurements for extrusive and intrusive rocks all the major Cenozoic volcanic fields in Libya. The major pulse of basaltic volcanism in Garian in the north (from 6 to 2 Ma) overlaps in time in Jabal Al Haruj province in southern Libya. Jabal Al Hasawinah and Jabal as Sawda basalts were erupted significantly earlier (23-10 Ma). Dykes and plugs at all provinces imply basaltic volcanism started in Miocene, followed by periods of erosion. There is no systematic trend of time in Cenozoic basaltic volcanism of Libya. It appears to be related to reactivation of ancient structures during the passive rifting that has been produced in response to interaction of African and European plates since the late Mesozoic.

DEDICATION

TO THE MEMORY OF MY FATHER

TO MY MUM, MY WIFE, MY DAUGHTERS, MY BROTHERS AND SISTERS

THANKS YOU ALL FOR YOUR PRAYER, SUPPORT, LOVE AND SACRIFICE

Acknowledgements

I am grateful to Almighty Allah, who bestowed me with ability to successfully complete this research work and present my thesis.

The successful completion of my PhD thesis would not have been possible without the efficient assistance, support and cooperation of a great number of people and organization. I would like to express my sincere gratefulness for their contribution and support.

I wish to thank my First supervisor, Prof. Fin Stuart, who gave great support to this study. I thank him for the confidence he has shown in me, for the useful and valuable training and advice, and for his "to the point" comments. I gained a lot from him while working under his supervision.

I would like to thank my second supervisor, Dr. Darren Mark, a nice supervisor, for many things, clear guidance, critical vision, kindness and strong support in the different stages of the research.

My sincere thanks go to Prof. Ali Aboazom, who was always ready to consult me concerning the different aspects of this study.

I would also like to thank the support from fellow postgraduate students and the help I have received from several members of staff in the Scottish Universities Environment Research Centre (SUERC).

I wish to thanks my family in Libya, my mother, sisters and brothers, who suffered from my years of absence, for their patience and support.

Finally, I would like to express my deep gratitude to my wife for her encouragement, support and understanding during all these years of my study. To my daughters, Fatma, Raghed, Botena, Zianab and Rayyan, I am thankful for their understanding.

Contents

Contents

Appendices

LIST OF FIGURES

LIST OF TABLES

Chapter One

The Cenozoic volcanic rocks of Libya

1.1 Introduction

Libya has several major Cenozoic volcanic provinces (Figure 1.1) that cover more than 66,000 km^2. In order of decreasing size they are Jabal Al Haruj (~45,000 km^2), Jabal As Sawda (~10,000 km^2), Jabal Nugay (~8,000 km^2), Garian (3,000-4,000 km^2) and Jabal Al Hasawinah (~1,000 km^2) (Klitzsch, 1968; 1970; Goudarzi; Piccoli, 1970; Almond *et al*., 1974; Busrewil, 1974; Woller and Fediuk, 1980). Other smaller Cenozoic volcanic areas occur in Jabal Arkenu, Jabal Al Awaynat and the Wau an Namus. They form some of the largest volcanic provinces in North Africa. Despite their size, relative accessibility and importance in a region of major hydrocarbon exploitation, they have not been studied in detail. Consequently there is little agreement regarding why, when and how they formed (Ade-Hall *et al*., 1975 and Bausch, 1978).

1.2 Cenozoic volcanism in South Europe and North Africa

There has been abundant Cenozoic volcanic activity across Southern Europe (Figure 1.2) and North Africa (Figure 1.3). Volcanism in Southern Europe has developed from early Tertiary to Quaternary times in a complex tectonic environment (Magmatism is spatially and temporally associated with Alpine-Pyrenean collisional tectonics, the development of an extensive lithospheric rift system in the northern foreland of the Alps, and, locally, with uplift of Variscan basement massifs (Massif Central, Rhenish Massif, Bohemian Massif) that resulted from the collision of the African and European continental blocks (Wilson and Downes, 2006). It has produced a wide range of magma types in a range of tectonic regimes (Barberi *et al*., 1974). The most common primitive mafic magma types are sodic basanites and alkali basalts (e.g., Urach, Germany); potassic alkaline mafic magmatism (e.g the West Eifel, Germany);

sodic magma types (e.g., Linosa in the Sicily Channel) and felsic magmatic rocks occur in most of the volcanic fields (e.g., Pantelleria volcanic). Cenozoic volcanism in north-western Africa (Algeria, Tunisia and Morocco), although less abundant, is also likely to be related to plate collision of the African and European continental blocks (Frizon de Lamotte *et al*., 2000).

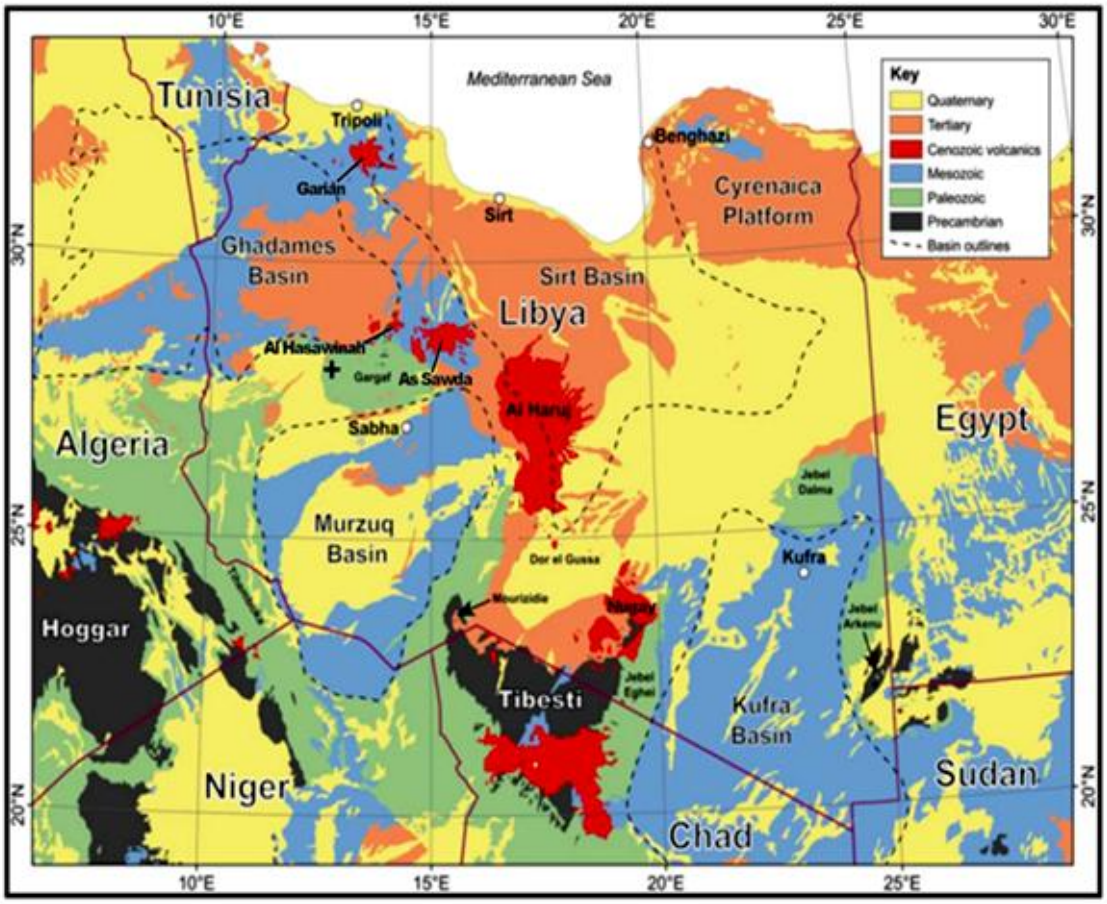

Figure 1.1: Geological map of central North Africa showing the Cenozoic volcanic fields of Libya, the Tibesti volcanic province in Chad and the Hoggar volcanic province in Algeria (after Meinhold *et al*., 2011).

The volcanic islands of Pantelleria and Linosa are sited along a NW-SE trending rift in the Sicily Channel, which separates the Sicilian platform from North Africa. They are the closest European volcanic systems to the volcanic province in northern Libya. The Pantelleria volcanic complex (5–300 ka) comprises weakly alkaline to transitional basalts but dominated by trachytes and rhyolites (Peccerillo, 2005). The volcanic rocks of Linosa are dominated by

Na-alkaline to slightly transitional basalts and hawaiites (0.53–1.06 Ma; Rossi *et al*., 1996).

With the exception of the tholeiitic volcanism in Ethiopia (Beccaluva *et al*., 2009) the origin of the major volcanic fields in North Africa are less clear. The Hoggar (or Ahaggar) volcanism, in the central Sahara, is Eocene to Quaternary in age (Aït-Hamou *et al*., 2000). The oldest Cenozoic volcanic rocks are represented by a thick pile of tholeiitic plateau basalts while the younger (Neogene–Quaternary) volcanic rocks have a generally alkaline affinity and include both basic lavas and a trachyte-phonolite series (Liégeois *et al*., 2005). Hoggar volcanism is considered to be a mantle plume product (Sleep, 1990) or response to stress applied by the Africa-Europe collision on pre-existing shear zones and fractures, within a semi-rigid block (Liégeois *et al*., 2005).

The Tertiary to Holocene Darfur volcanic provinces (Lucassen *et al*., 2008) have a generally alkaline affinity and include both basic lavas and trachyte–phonolites series (Franz *et al*., 1994). Its origin has been ascribed to a mantle plume (Franz *et al*., 1994) or located at a possible triple junction in the African lithosphere. Rifting occurs along the Abu Gabra Rift to the southeast of Jebel Marra, while the Ngaoundere lineament and the volcanic fields of Hoggar and Tibesti respectively represent the other arms of the postulated triple junction (Browne and Fairhead, 1983) which was probably reactivated as a rift structure in response to Lower Cretaceous opening of the Atlantic.

The Tibesti volcanism is believed to have started during the early Tertiary with the extrusion of mildly alkaline basalts from fissure eruption followed by evolved magmatism (trachytes and phonolites) after caldera collapse (Gourgaud and Vincent, 2004). Field investigations, Ar/Ar age determination, petrographical and geochemical data were used to describe the development of Emi Koussi shield volcano in Tibesti, an intraplate volcanic province. The regional uplift and nature of the magmatism indicate that a mantle plume is the most likely explanation for this volcanism, as proposed in Darfur Dome in Sudan (Franz et al., 1994). Liégeois *et al*. (2005) concluded that the Tibesti volcanism resulted as stress reaction by the Africa-Europe collision.

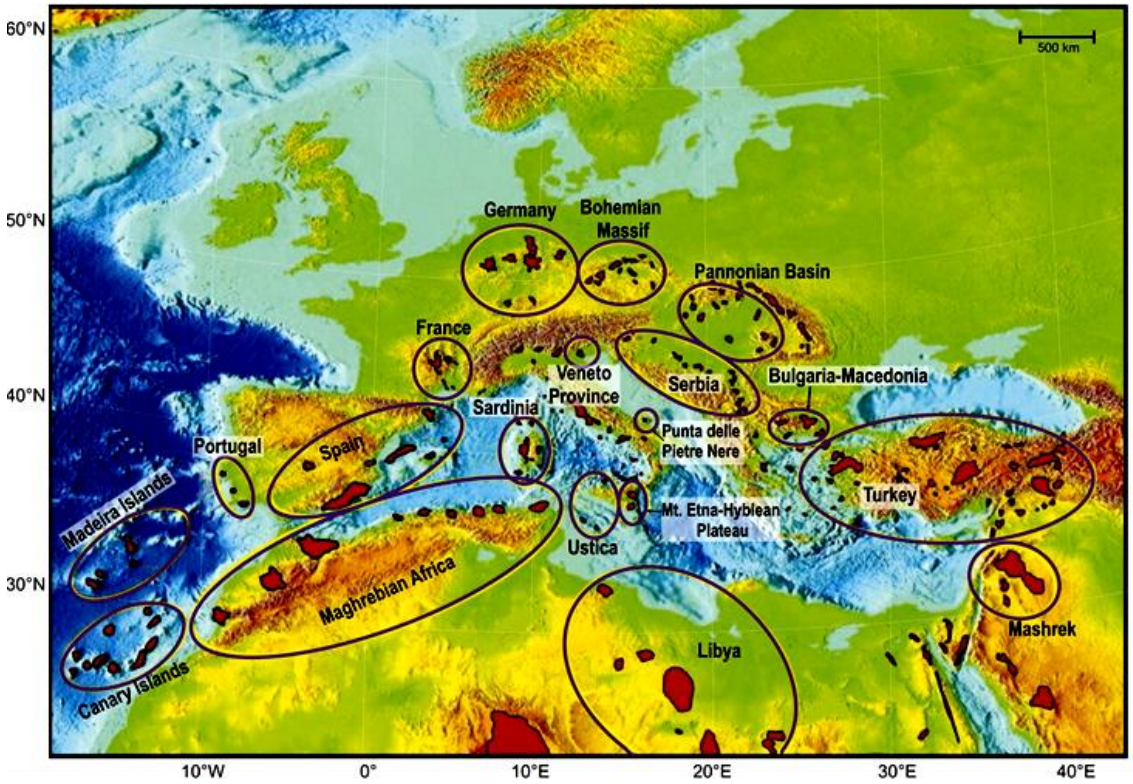

Figure 1.2: Topographic map of North Africa, Europe and the Mediterranean region showing the major Cenozoic volcanic fields (after Mjelde *et al*., 2010).

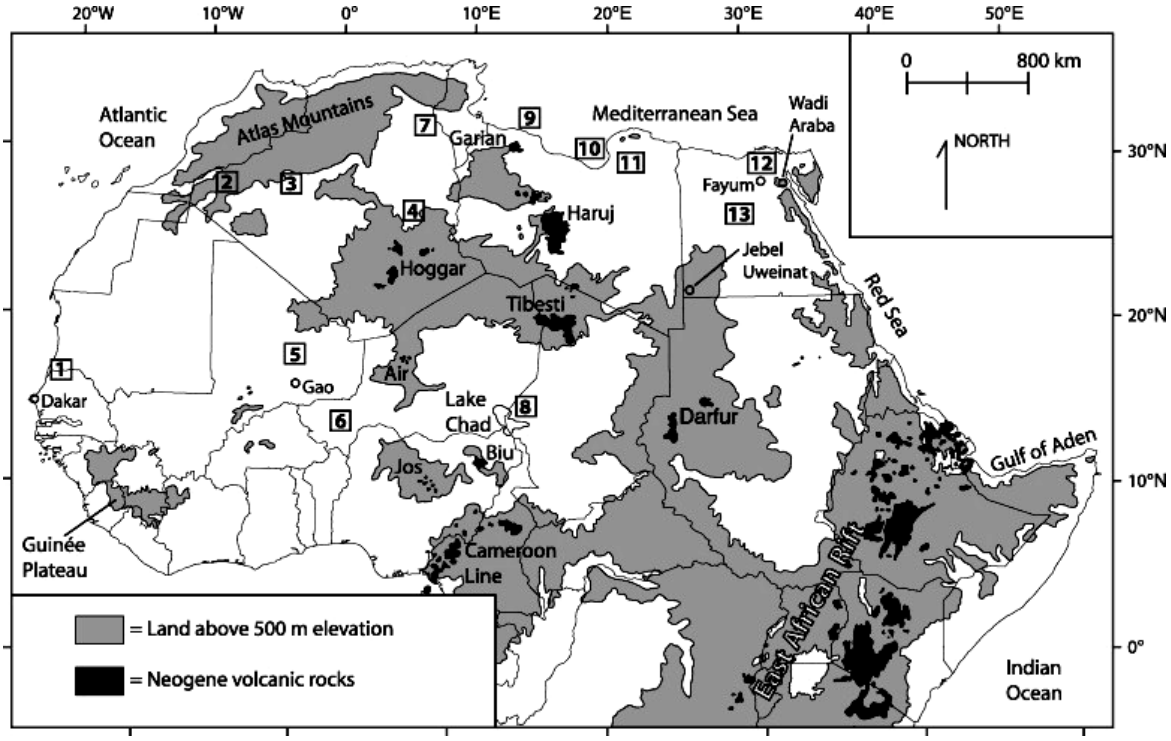

Figure 1.3: Map showing the distribution of Cenozoic volcanic fields in North Africa (after Swezey, 2009).

1.3 Cenozoic volcanism in Libya

1.3.1 History of study

Horneman (1802) was the first to identify the volcanic rocks of the Al Haruj field. Von Wervecke (1880) made the first study of the mineralogy and petrology of phonolites from Garian volcanic province (GVP). The first reports of volcanic rocks from the Jabal Al Hasawinah province were written by Freulon and Lefrance (1954) and Bordet *et al*. (1955). The first study of Jabal as Sawda volcanism was written by Dalloni (1931). Published studies of the petrology, geochemistry and chronology of the Cenozoic volcanic fields of Libya have been sporadic since the early discoveries (Klitzch, 1968; Goudarzi 1970; Piccoli 1971; Almond *et al*., 1974; Woller and Fediuk, 1980).

There has been a resurgence of interest in the Cenozoic Libyan volcanism in the last few years. This has largely concentrated on petrology, geochemistry and chronology of the Al Haruj and Wau an Namus fields in southern Libya (Nixon, 2011; Miller *et al*., 2012; Bardintzeff *et al*., 2012; Abdel-Karim *et al*., 2013). There have been two recent studies of the Garian volcanic province; one concentrated on petrology and geochemistry of mantle xenoliths (Beccaluva *et al*., 2008) and one that studied the mafic and felsic volcanic rocks from the NW sector of the province (Lustrino *et al*., 2012).

1.3.2 Cenozoic volcanism in Libya

The Cenozoic volcanic fields of Libya generally fall on a NNW-SSE trend extending from the Garian volcanic province in northwest Tripolitania, through Jabal Al Hasawinah, Jabal As Sawda and Jabal Al Haruj in central Libya, south to Jabal Nugay close to the Tibesti massif of northern Chad (Figure 1.1). Volcanism is dominated by alkaline basalts with the less common transitional and tholeiitic basalts (e.g., Almond *et al*., 1974; Busrewil and Wadsworth, 1980; Woller and Fediuk, 1980). Small volumes of more evolved rocks, such as trachytes and phonolites, are present in the Garian and Jabal Al Hasawinah fields (Almond *et al*., 1974).

The Cenozoic volcanic fields of Libya are located at the junction of major NW-SE trending features including the Tripoli-Tibesti uplift and Al Haruj uplift trends. These uplift structures that were probably formed during the Caledonian Orogeny in the early Palaeozoic. These structures are called The Tripoli-Tibesti and Al Haruj uplifts (Klitzsch, 1968; 1970; Goudarzi, 1980; Woller and Fediuk, 1980) and resulted from synsedimentary faulting which indicates that most of the faults are probably basement-controlled (Said, 1974). This trend is parallel to the large Afro-Arabian rift system that extends from Turkey to Mozambique, including the Dead Sea, Red Sea, Gulf of Aden and East African Rifts (Goudarzi, 1980). Most of the Cambro-Ordovician, Silurian, Devonian and Carboniferous sediments have a decreased thickness in the area of these uplifts (Al Festawi, 2001).

The Garian volcanic province is located at the intersection with the NNE-SSW trending Nafusha uplift (a function of a horst block uplift; Pizzi and Sartori, 1984) (Figure 1.4). Jabal al Hasawinah province appears to be related to the Tertiary reactivation of the ENE-WSW trending late Palaeozoic-early Mesozoic Al Qarqaf uplift (Pre-Carboniferous Hercynian fault systems) (Figure 1.4) (Jurak, 1978; Goudarzi, 1980; Busrewil and Oun, 1991; Al Festawi, 2001).

Jabal as Sawda is situated at the intersection of early Palaeozoic Al Haruj uplift with the late Palaeozoic-Mesozoic Al Qarqaf uplift (Goudarzi 1980; Woller and Fediuk, 1980; Al Festawi, 2001). The Al Haruj basalt field appears to coincide with intersection of three fault systems (Figure 1.4); the early Palaeozoic Al Haruj uplift (NNW-SSE), the late Palaeozoic-Mesozoic NE Libyan fault system (Dur al Qussah), and the extension of the Cretaceous-Tertiary Hun graben (NW-SE direction) (Woller and Fediuk, 1980; Busrewil and Suwesi, 1993).

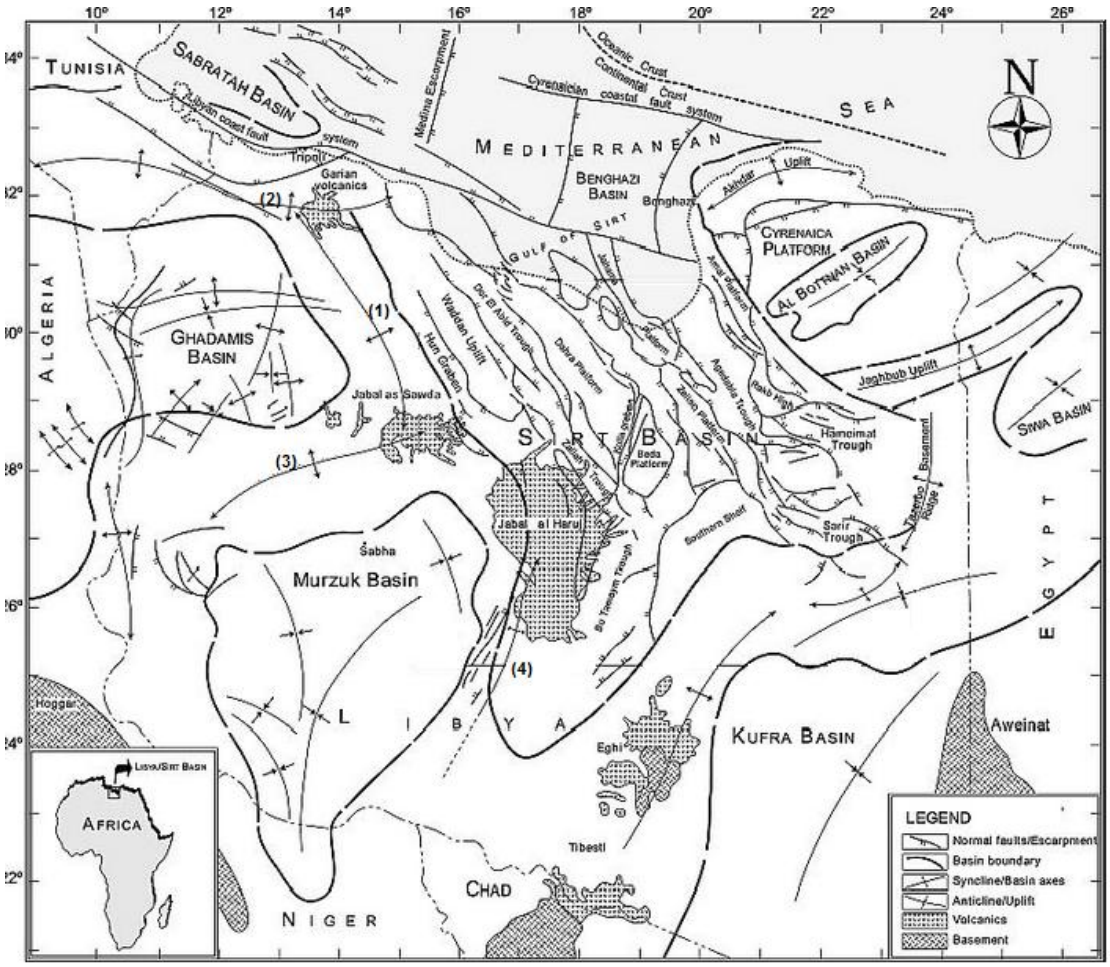

Figure 1.4: The major structural and tectonic features of Libya (modified from Abadi *et al*., 2008)**.** (1): Tripoli-Tibesti uplift; (2): Nafusha uplift; (3): Al Qarqaf uplift and (4): Dur al Qussah uplift.

Asran *et al*. (2004) and Farahat *et al*. (2006) have classified the Libyan volcanic rocks as a low-volcanicity rift type related to a large Afro-Arabian rift system that extends from Turkey to Mozambique, and includes the Dead Sea, Red Sea, Gulf of Aden and East African Rift. In this model the volcanism is related to propagating fractures caused by intra-plate stresses (formed as a deformation from the complex crustal structure that is composed of a series of basins and uplifts which resulted by the Eurasia-Africa continental collision). The low-volcanicity rift types is consistent with the low rates of crustal extension, the small volumes of volcanic rocks, and the discontinuous volcanic activity, the range of basaltic magma compositions and small volume of evolved magma types compared to high-volcanicity rift types (Barberi *et al*.,

1982). Beccaluva *et al*. (2008) proposed that the relatively low $^{3}He/^{4}He$ (5.3–6.5 R_a) of lherzolite xenoliths from Garian indicates that the basaltic volcanism originates within the upper mantle and is unrelated to the deep-seated mantle plume source of the Ethiopian–Yemen plateau basalts. A similar conclusion can be drawn from the low $^{3}He/^{4}He$ measured in olivines from Al Haruj (Nixon, 2011). Lustrino *et al*. (2012) concluded that the Garian province volcanism is linked to passive lithospheric thinning related to the development of continental rifts like those of Sicily Channel (e.g., Pantelleria and Linosa) and Sardinia. This conclusion supported by the NW-SE alignment of Garian emission centres and dykes testifies a strong structural control of volcanic activity on the lithospheric evolution of the area and to the low degree partial melting (3-9 %) of shallow mantle sources in the spinel/garnet facies and the typical OIB-like major and trace element composition as well as the Sr-Nd ratios.

Based on the apparent decrease in age from NNW to SSE, Fouad (1990) and Hegazy (1999) attributed the volcanism to movement of the African plate over a fixed hot-spot in the mantle. Nixon (2011) used the rare earth element inversion modelling of alkali and tholeiitic basalts to calculate the mantle temperature of ~1460-1480 °C for the Al Haruj basalts. She concluded that the melting begins at 145 km in a passively upwelling mantle plume, and continues to depths of 70 and 75 km for tholeiitic and alkali basalts, respectively. This depth of melting is in agreement with estimated of lithosphere thickness of < 80 km (Priestley and McKenzie, 2006; Fishwick, 2010). Farahat *et al*. (2006) proposed a mixed model involving both intra-plate stresses coupled with involvement of the Afar mantle plume.

1.4 Thesis structure

Despite the location of the Garian volcanic province close to major population centres in Libya, there has been few studies with modern analytical techniques and approaches. With the exception of recent studies by Beccaluva *et al*. (2008) and Lustrino *et al*. (2012), most studies were made in

1970s and 1980s (Piccoli, 1971; Schult and Soffel, 1973; Almond *et al*., 1974; Ade-Hall *et al*., 1975; Bausch, 1978; Busrewil and Wadsworth, 1980).

This thesis is composed of two main studies. The first study uses the petrology, geochemistry and geochronology of Garian volcanic province rocks to constrain the relationship between the main volcanic rock types and understand their origin and the processes that have shaped them. In the second study I present new geochronological data from basalts from all the main Libyan Cenozoic volcanic provinces in order to understand the regional volcanic history. The thesis is organised into the following chapters:

Chapter 2 provides an introduction to the geology of Garian region and the volcanic province.

Chapter 3 reports the petrography, geochemistry, isotopic composition and geochronology of basaltic rocks from the Garian volcanic province.

In Chapter 4 the petrogenesis of the basaltic rocks is discussed. It concentrates on crystal fractionation, partial melting and crustal contamination. The nature of the mantle source and melting conditions are also investigated.

Chapter 5 is a petrographic, geochemical and chronological study of the phonolitic rocks from Garian volcanic province. The petrogenesis of the rocks is discussed.

Chapter 6 presents the $^{40}Ar/^{39}Ar$ ages of Cenozoic volcanic rocks of Jabal al Hasawinah, Jabal as Sawda and Al Haruj al Aswad.

In Chapter 7 the relationship of Garian volcanism with the other Cenozoic volcanism of Libya is discussed, and put into regional context.

Chapter Two

The Garian volcanic province, Libya

2.1 Introduction

The Garian volcanic province is located approximately 100 km south of Tripoli between the towns of Garian, Beni Walid and Tarhunah (Figure 2.1). Volcanic rocks form a more or less continuous lava sheet over ~3,000 km^2, centred on 32°N, 13°30'E. In this chapter I review the geomorphology and regional geology, concentrating on previous studies of the Cenozoic volcanism in Garian region.

2.2 Geological setting of the Garian region

2.2.1 Landscape

The Garian region (Figure 2.2) can be separated into three main geomorphologic units: the Jeffara Plain, the escarpment (Jabal) and the plateau (Dahr). The Jeffara Plain is a flat-lying coastal area that is bounded by the Mediterranean Sea to the north and Jabal Nafusah (sometimes called Jebal Neffusah) to the southeast. The plain rises gently from sea level to around 200 meters at the foot of the escarpment.

The escarpment (Jabal Nafusah) rises sharply from the Jeffara Plain about 80 km south of Tripoli. Locally it is called Jabal Garian (between Garian and Yafrin) and Jabal Mesallatah (between Mesallatah and Tarhunah). Some 400 km long, extending from the coast in the east (near the town of Tarhunah) to the Tunisian border in the west (Figure 2.1) where it continues westward before turning sharply northward within Tunisia itself. It exposes Mesozoic limestone, sandstone, clays and dolomitic limestone. Zaccagna (1919) suggested that it represents an uplifted marine cliff. Lipparini (1940) and Miller

(1971) attributed the formation of the escarpment to pre-Miocene movement on the Al Aziziyah Fault (normal fault).

The flat-lying plateau above 700 metres is comprosed mainly of resistant Upper Cretaceous dolomitic limestone. The northern part of the plateau surface close to the escarpment is dissected by canyons and wadis. Conspicuous black hills of basalts and phonolites are present in the area between Garian and Sidi-as-Sid.

2.2.2 Geology

The Cenozoic volcanic rocks of the GVP sit on Mesozoic marine and continental sediments that were deposited in the northern Ghadamis basin (sometimes called Al Hamada al Hamra) and part of the Sirt Basin (Gray, 1971). A lithostratigraphic subdivision of the Mesozoic and Tertiary sequence of the Garian area is shown in Figures 2.4 and 2.5. These sediments sit on Devonian shales and Cambro-Ordovician sandstones that unconformably overlie crystalline Pan-African basement exposed ~400 km south of the region (Jurak, 1978).

The oldest exposed sedimentary rocks are Middle Triassic Kurrush Formation sandstones. These are overlain locally by the Middle to Upper Triassic limestones of Aziziyah Formation, Upper Triassic Abu Shaybah Formation sandstones and Bu Ghaylan Formation limestones. Jurassic sediments represent cycles of continental and shallow marine sediments (Figure 2.5).

The region was uplifted during the early Cretaceous (as a result of intra-plate deformation convergence of Africa and Europe) and extensively eroded. Cretaceous limestones and dolomites were deposited conformably on the Jurassic sediments. Quaternary sediment covers most of the region. Alluvial fans and cones of clastic material derived from the escarpment are present across the Jeffara plain, and patches of shelly sand and gravels derived mainly from Cretaceous sediments are formed on the plateau (Desio *et al*., 1963; El Hinnawy *et al*., 1975).

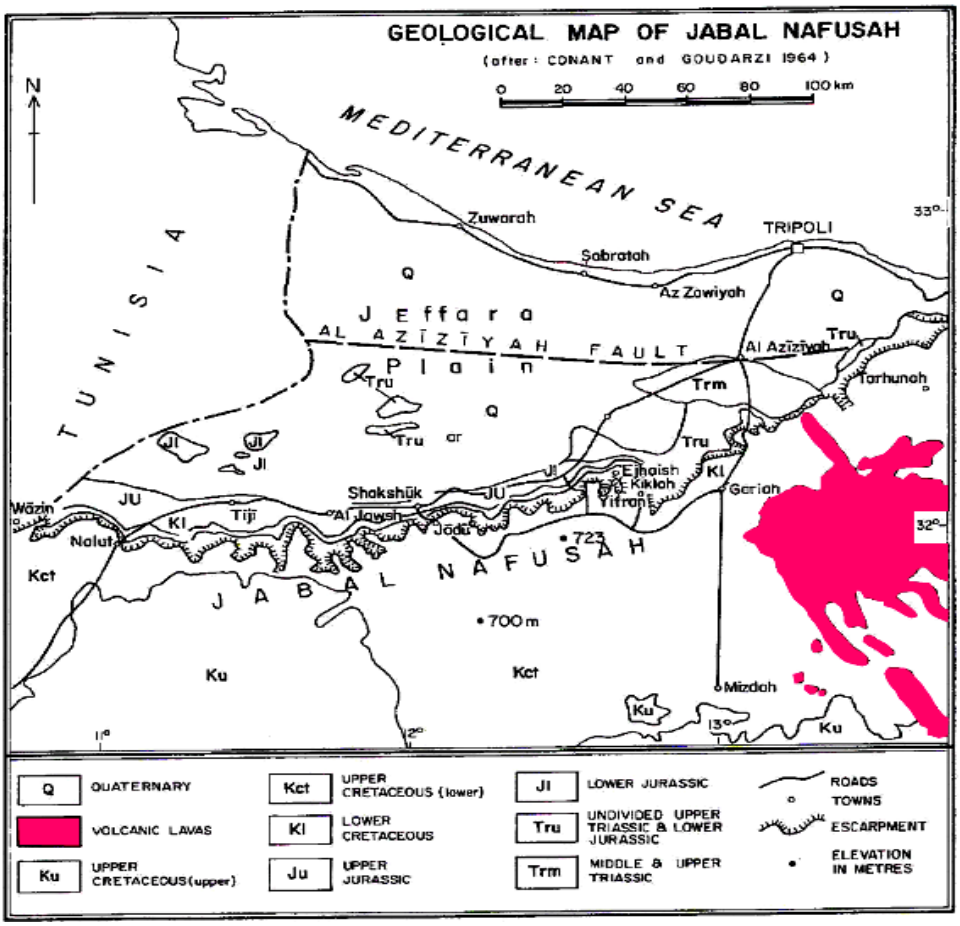

Figure 2.1: Geological map of Jabal Nafusah shows the Cenozoic volcanic fields and the geomorphologic units of Garian region (Jeffara Plain and Jabal Nafusah escarpment) (after Goudarzi, 1964).

Figure 2.2: Photograph looking north from the top of Kaf Abu Rashadah on the Jeffara Plain to Jabal Nafusah escarpment (1) a small phonolite plugs (2).

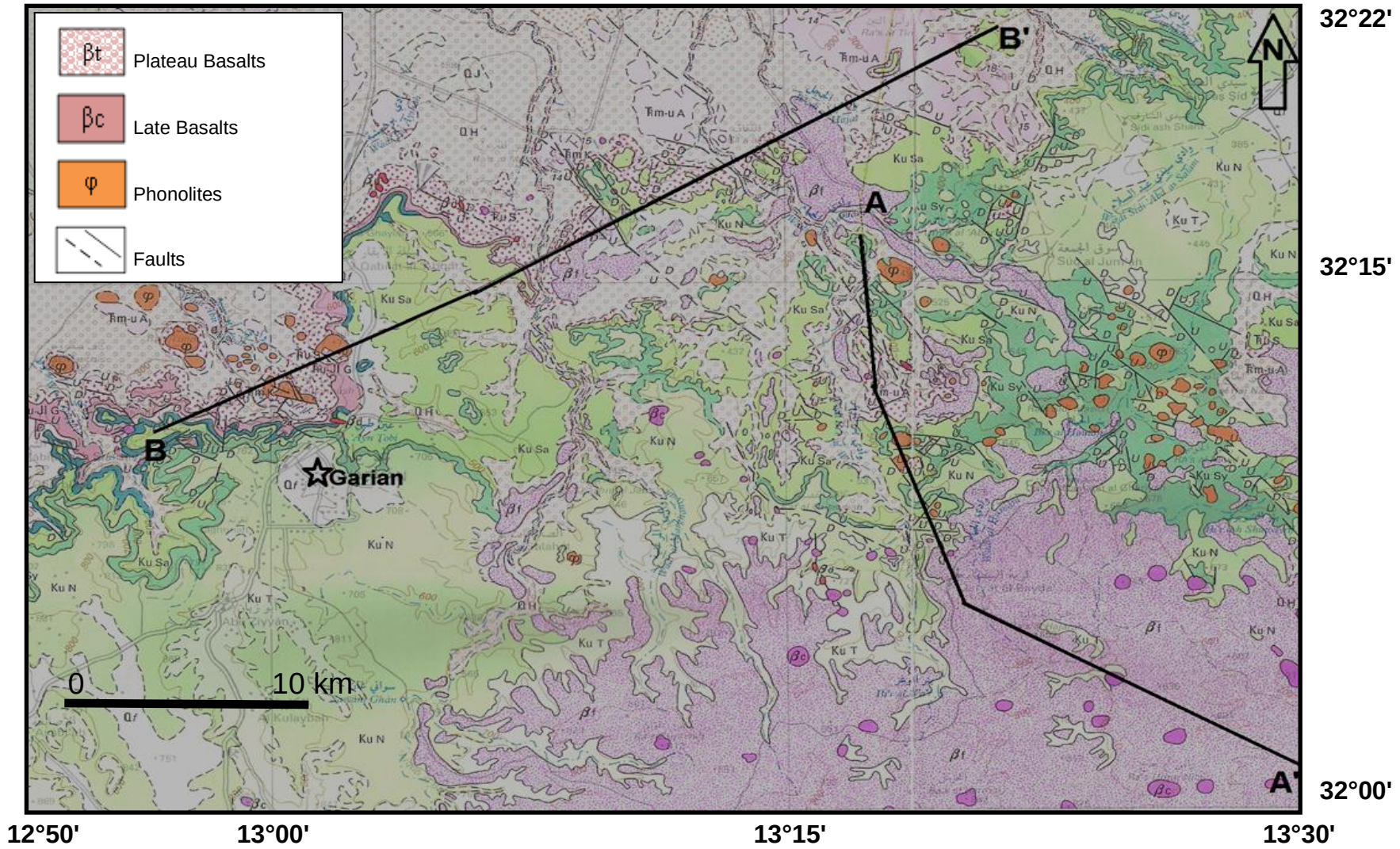

Figure 2.3: Geological map of the north part of Garian volcanic field, north-west Libya (after El Hinnawy and Cheshitev, 1975). The belts A-A' and B-B' are the directions of geological cross sections shown on Figure 2.4.

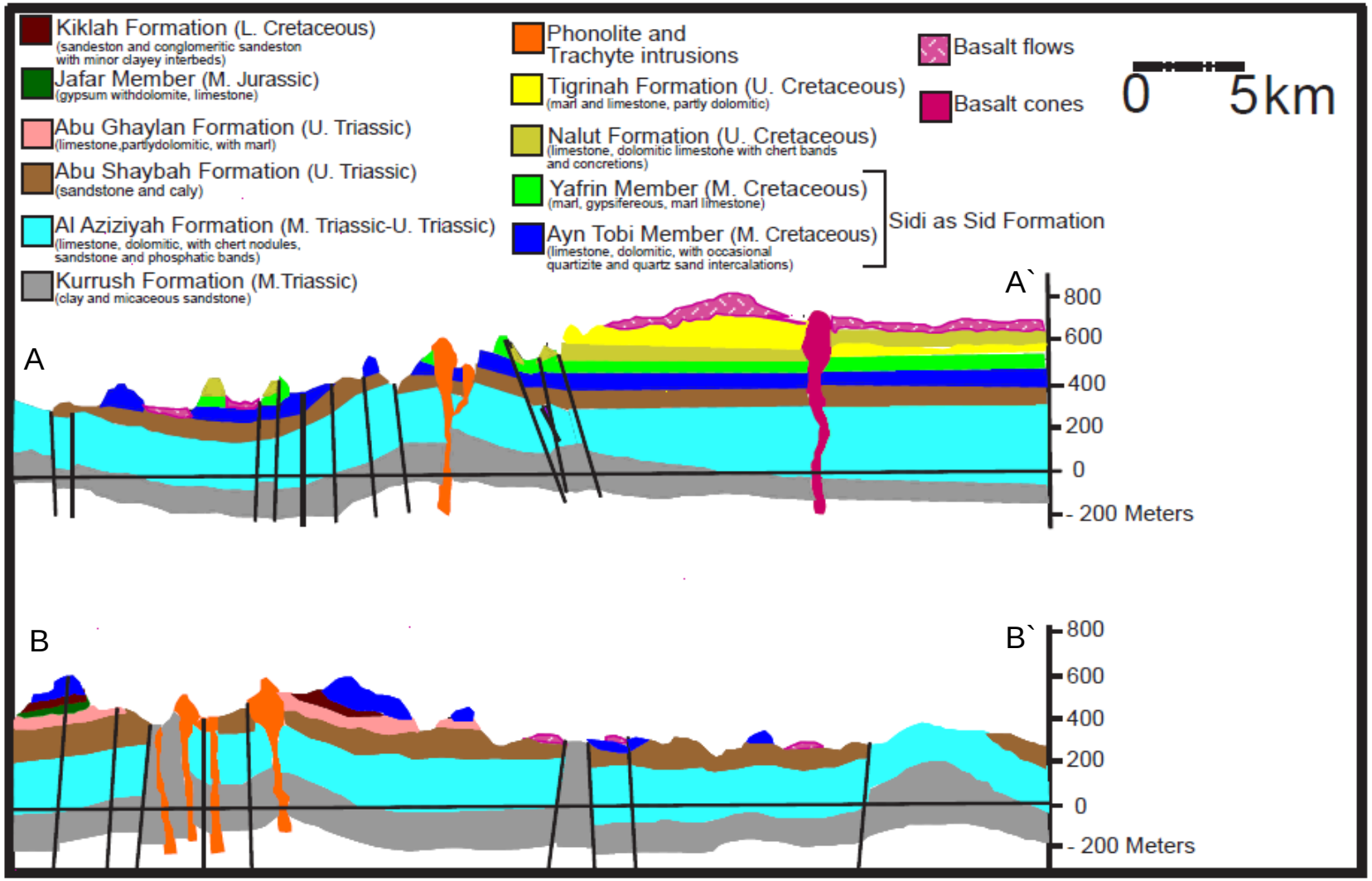

Figure 2.4: Geology of the Garian volcanic field showing the relationship between the three different episodes of volcanic rocks (after El Hinnawy *et al*., 1975). Sections A-A' and B-B' are shown on Figure 2.3.

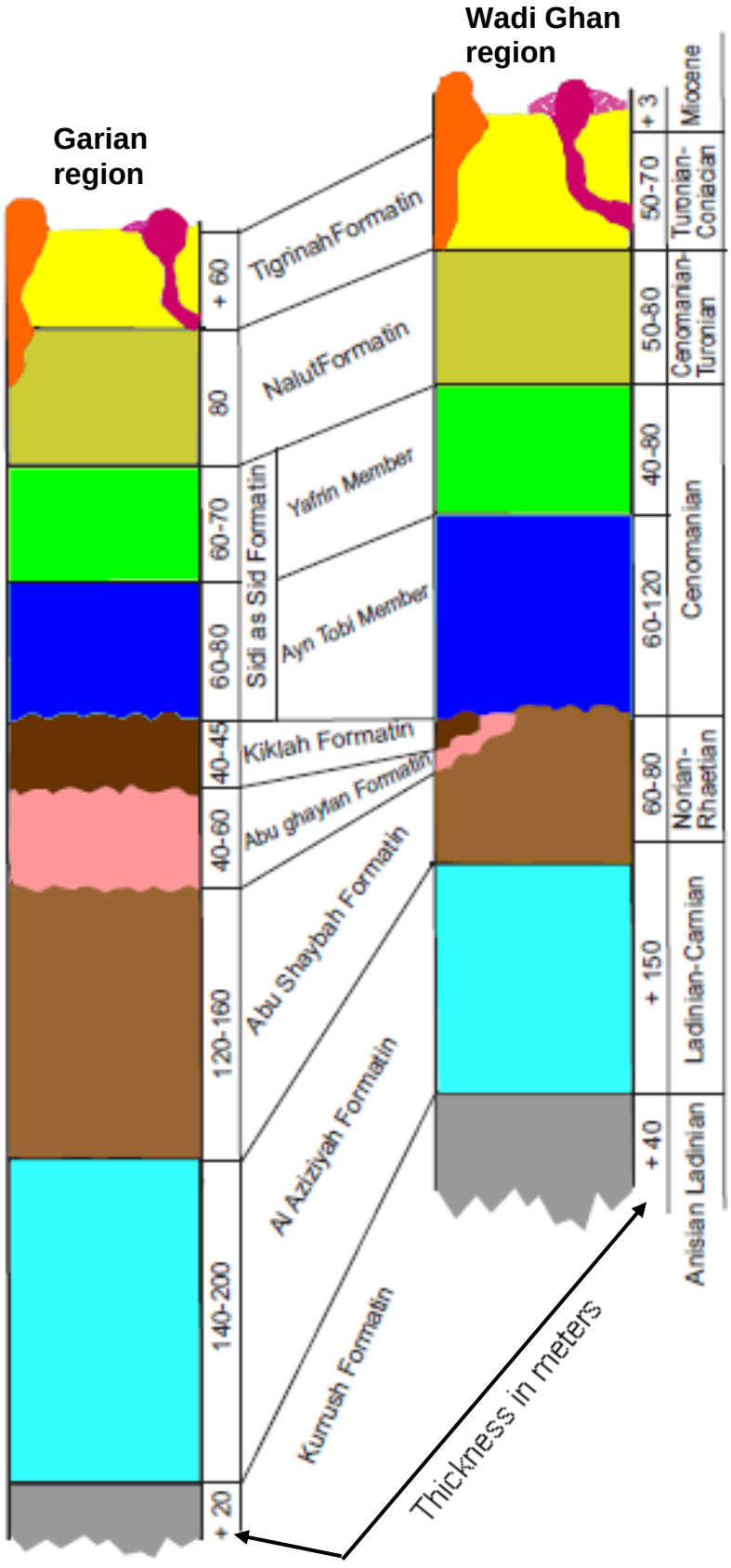

Figure 2.5: Stratigraphic sections through the Mesozoic-Cenozoic sequence beneath the Garian volcanic province (after El Hinnawy *et al*., 1975).

2.2.3 Tectonic setting

The origin and formation of intra-plate deformation zones have been debated as these are not directly included in the plate tectonics system. The Tripolitania region (NW Libya) is a 500 meter high plateau neighbouring the Sirt basin. Towards the east, the surface of the Tripolitania plateau deepens into Sirt basin. The Sirt basin has wide rift (500 km wide and 500 km long) consists of a series of NW–SE trending grabens separated by platforms active from the Late Cretaceous to the Paleogene (Figures 1.4 and 2.1). Previous studies proposed that this basin resulted by the interplay between the differential motions of the African plate during the opening of the Atlantic Ocean (Guiraud and Maurin, 1992). New study by Capitanio *et al*., (2009), proposed that Sirt rifting could have been driven by the pull exerted by the Hellenic subduction. The tectonic model of the Tripolitania area is so far poorly known. Capitanio *et al*., (2011) found evidence of Pliocene deformation along a belt stretching from the Jebel-Al Khums region to Jebel As Sawda, southern Hun Graben, where volcanism and reactivation of normal faults suggest a NE-directed extension. The age of the deformation and its orientation are compatible with the opening of the Sicily Channel rift zone, representing the southernmost culmination of a belt that propagates from the convergent margin for more than 1400 km.

In particular, the main structure of the Garian area formed as a NW–SE trending anticline whose axial trace lies west of Garian. In the same area a number of NW-SE major fault zones (Coastal fault zone, Al Aziziah fault zone and Wadi Ghan fault zone) are parallel to the main fold which formed the positions for volcanic intrusion and extrusion. These zones are controlled by two main trends, NW-SE and E-W. The component faults show dip-slip normal motion with the amount of throw varying from a few metres to some hundred metres. The origin of the faults was interpreted to be linked to African–European collision and to reactivation of the Jeffara uplift of Hercynian age (Lipparini, 1940; Desio *et al*., 1963; Christie, 1966 and Anketell and Ghellali, 1991).

The most recent study of Abadi *et al*. (2008) for the subsidence of the Hun Graben and Sirt Basin indicated that the E-W to SE-NW faulting was most active in the Lower Cretaceous (time of Africa-Europe collision) but continued sporadically in parts of the basin until Upper Cretaceous. During Upper Cretaceous and continuing into the Tertiary several rifting phases are identified with subsidence and normal faulting in a NW-SE orientation. Therefore, it is believed that the main NW trending of Hun Graben system faults and their associated folds correspond with the Jabal Nafusah fault system (Alfandi, 2012).

The geological map of the Garian area (El Hinnawy and Cheshitev, 1975) shows a broad NW trending zone of intrusions that lie between the Wadi Ghan fault zone and a line running NW-SE east of Garian itself (Figure 2.6A). This belt of intrusions can be subdivided into NW and NE trending linear chains whose intersection is the most common locus of the intrusions (Figure 2.6B). These could be corresponding with the Hun Graben fault system, which may control the regional ascent of the magma, while at a more localised scale the intersection of the Hun Graben structures with the Jebel Nafusah faults acts as a control on the locus for the emplacement of the intrusions.

2.3 Garian volcanic province

2.3.1 Introduction

The first geological observations of eruptive phenomena in the region were made by Von Wervecke (1880) and Artini (1914). Lipparini (1940) reported trachytic phonolite and alkaline trachytes between Garian and Mizda. Piccoli (1960) conducted a geological reconnaissance of the region in 1959 that resulted in a brief account of the field relations and confirmed their division into two petrological types: "basic" and "phonolitic". Christie (1966) described the extensive basalt flows southeast of Garian and "small cross-cutting intrusions of basalt, and larger intrusions of phonolite". This was followed by more detailed petrographic and geochemical studies by Piccoli and Spadae (1964), Almond *et al*. (1974), Busrewil (1974), Bausch (1978), Aboazom *et al*.

(2006) and most recently Lustrino *et al*. (2012). El Hinnawy and Cheshitev (1975) published 1:250,000 geological maps of the north-western part of Garian volcanic province (Figure 2.3). The age of the volcanic rocks has been determined by the K/Ar technique (Mobil Oil Company, 1967; Piccoli, 1971; Schult and Soffel, 1973; Ade Hall *et al*., 1975).

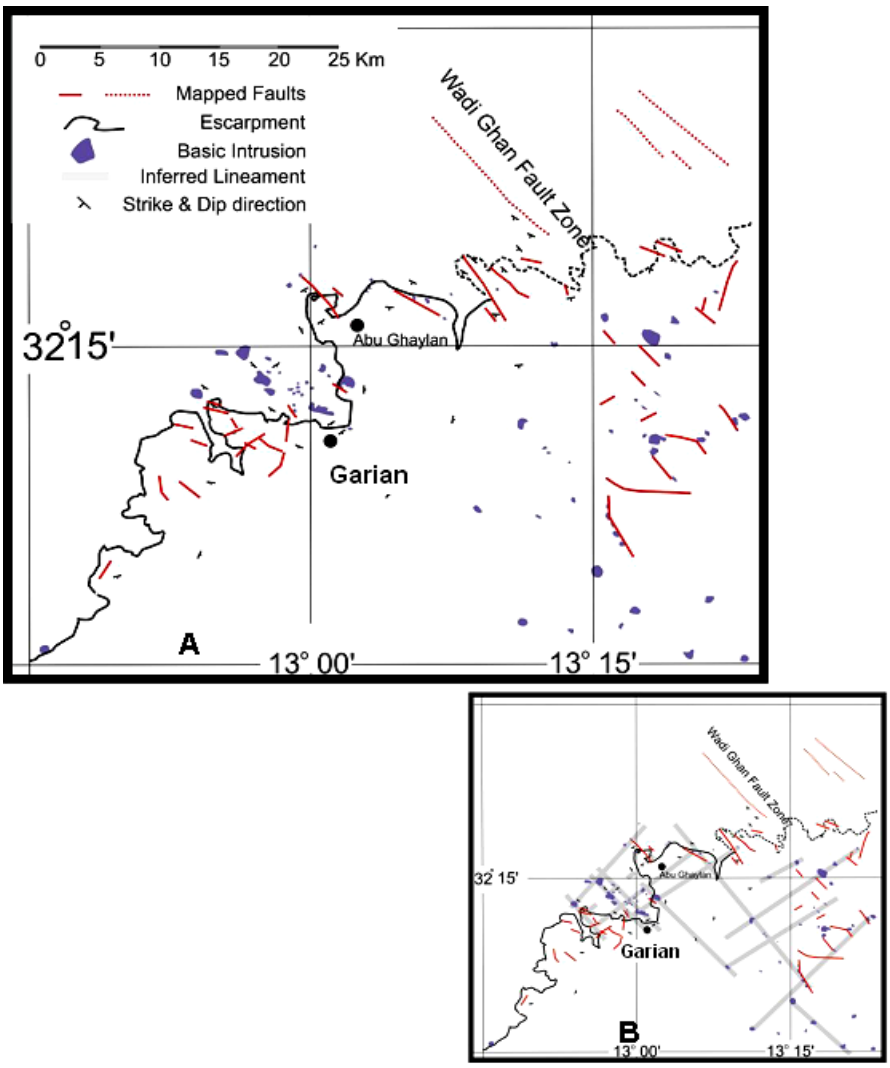

Figure 2.6: (A) Location of igneous intrusions around Garian area from the 1:25, 00 scale geological maps (Sheet NI 33.13R, Tarabulus, 1975). (B) Their interpretation as being located at the intersection of NW-SE Hun Graben faults and NW-SE Jabel Nafusah faults (after Alfandi, 2012).

The most thorough studies of the Garian volcanic province identified three principal manifestations of volcanic rocks. The first is a sequence of plateau basalts which cover most of the region (Piccoli, 1971; Busrewil, 1974). These are associated with basaltic dykes in the country rock around the basalt province and the general trends coincides with the direction of two major sets of faults; 315° (Christie, 1966) and 280-300° (Gray, 1971).

Numerous small cones sit on top of the plateau basalts and were proposed by Piccoli (1971) to be a significantly younger, distinctive volcanic phase (late basalts). Christie (1966) reported some significant NW trending faults in Wadi Ghan (up to 200 meters of displacement) and links these NW structures spatially to small igneous domes.

A suite of phonolite-trachyte intrusions occur as individual domes or clusters of domes northwest of Garian and along the northern limit of the plateau basalts (Figures 2.3). The relationship between the three main rock types has been questioned by Ade-Hall *et el*. (1975) and Bausch (1978) who, on petrological and volcanological grounds consider that the plateau basalts and late basalts were coeval.

2.3.2 Plateau basalts

In the nomenclature of the early workers the plateau basalts are a sequence of horizontal flows that cover approximately 3,000 km^2 (Piccoli, 1971; Almond *et al*., 1974; Bausch, 1978). They are associated with the tectonic axis from Wadi Ghan in the north to west of Beni Walid in the south and extend for approximately 100 km on either side of this axis. The lavas were erupted from both fissures and central volcanoes (Lipparini, 1940) but there is no obvious trace of the original source of most flows. The lava sequence rarely comprises more than four or five individual flows, reaching a maximum total thickness of only some tens of metres (Almond *et al*., 1974; Busrewil, 1974). In general, they are best exposed in the wadis. In the central part of the region, but at the east margins they form the cap of flat hills (Figures 2.7) (Piccoli, 1971).

In hand-specimen they are relatively coarse-grained, and often show a rather open texture. Pyroxene and olivine are the only phenocryst phases, and they are seldom abundant (Almond *et al*. 1974). They form a chemically consistent group lying close to the basalt-hawaiite boundary, transitional between tholeiitic and alkalic affinities (Busrewil and Wadsworth, 1980). Total alkalis range from 3 to 5 wt% ($Na_2O > K_2O$) and they plot between the alkaline and sub-alkaline fields on alkalis vs silica diagrams. MgO ranges from 6 to 9 wt%, major element trends indicate that the fractional crystallisation is the key factor to produce compositional variations in these rocks (Almond *et al*., 1974; Busrewil, 1974).

Piccoli (1971) determined K/Ar ages of 4 samples. They range from 3.5 ± 0.1 to 53.5 ± 1.9 Ma (maximum systematic error of 3.5%). Schult and Soffel (1973) reported a palaeomagnetic age of 42 ± 10 Ma for 20 plateau basalts. Four basalts dated by K/Ar range from 2.1 ± 0.8 to 6.1 ± 0.4 Ma (2σ) (Ade-Hall *et al*., 1975) (Table 2.1 and Figure 2.10).

2.3.3 Late Basalts

More than 50 shield volcanoes and scoria cones sit on the plateau basalts and the nearby Mesozoic sediments (Figure 2.8). They typically form small hills or clusters of hills. The flows from these volcanic centres are much less extensive than the plateau basalts, rarely being more than 100 meter long.

In hand-specimen the late basalts tend to be finer-grained and more compact, and are therefore considerably darker than the plateau basalts. They are characterised by the presence of abundant pyroxene and olivine phenocrysts and an absence of plagioclase phenocrysts (Busrewil and Wadsworth, 1980). They cover a much wider compositional range than the plateau basalts, but in most respects the two groups do not overlap. They are characterised by low silica, relatively high MgO and total alkali contents. In addition, they are strongly sodic with the $Na_2O/K_2O > 2$ and they plot between the alkaline and sub-alkaline fields on TAS diagrams. Most are basanitic, but locally they are trachybasalt compositions (Busrewil and Wadsworth, 1980).

.

Figure 2.7: Flat-lying plateau basalts capping Mesozoic sedimentary rocks (limestone) southwest of Garian.

K/Ar ages of 4 lava flows (olivine nephelenite and basanite) range from 1.3 ± 0.3 to 7.9 ± 1.5 Ma (Mobil Oil Company, 1967). Piccoli (1971) determined K/Ar ages of samples from Ras Tebra (volcanic neck) and Ras el Mohor (small shield volcano) that range are 8.5 ± 0.3 to 11.5 ± 0.4 Ma (Table 2.1 and Figure 2.10).

2.3.4 Phonolite-trachytes

Domes of phonolite-trachyte series rocks form an east-west belt along the northern edge of the plateau basalt field (Figure 2.3). They appear as prominent hills that rise from 370 to 725 meters above the Mesozoic limestone bedrock. They are organized as two different directions following the main fault trends, NW-SE (northwest of Garian) and NE-SW to ENE-WSW (east of Garian) (Figure 2.3).

The phonolites display a variety of contact relationships with the Mesozoic limestones. In some places (e.g., Kaf Abu Ghannush) they form laccolith

shapes that arch the overlying sediments while the underlying sediments are relatively undisturbed. In other cases they are represented by extrusive flow domes (e.g., Kaf Bu Rshadah and Kaf Mantrus) (Figure 2.9).

Figure 2.8: Photograph of the eroded remnants of the intrusive centres (10-20 m in diameter and 40 m in length) that sit on the Mesozoic limestone along Mizdah-Garian road of 33 km south of Garian (31°52'10"N 12°59'36"E).

They are fine- to medium-grained, mostly porphyritic. Flow textures are observed with the feldspathoid (e.g., nepheline) and alkali feldspar (e.g., sanidine), as well as small alkali pyroxene and amphiboles phenocrysts are oriented in a grey green groundmass. They display considerable variation in chemical composition. Generally, they are undersaturated and strongly peralkaline (normative nepheline 16.4–34.6% and acmite) with SiO_2 55.1–61.6 wt% (Busrewil and Wadsworth, 1980). Total alkalis range from 11.2–14.6 wt%. Trachytes are less undersaturated than the phonolites (normative nepheline 3.2–10.9%), with SiO_2 ranging from 57.1–64.4 wt%. They have low TiO_2, FeO, MgO (0.23 wt%), CaO, P_2O_5, V and Ni contents and are interpreted as fractional crystallisation of Fe-Ti oxides and/or olivine, clinopyroxene and apatite (Aboazom *et al*., 2006). Lustrino *et al*. (2012) identified two types based on petrographic, mineral chemical, major and trace element concentrations. They proposed that the Type-1 trachytes and phonolites are

formed by removal of clinopyroxene, plagioclase, alkali feldspar, amphibole, magnetite and titanite from benmoreitic magmas. The Type-2 might be the result of high fractional crystallisation starting from mafic alkaline magma, without removal of titanite (Lustrino *et al*., 2012).

The K/Ar age of phonolite from Ras Umm Al-ezz was determined to be 37.2 ± 0.7 Ma (Mobil Oil Company, 1967). Piccoli (1971) dated 3 phonolites by K/Ar; 37.7 ± 1.3 Ma (Kaf Tekut), 39.7 ± 1.4 Ma (Kaf Mantrus) and 40.7 ± 1.4 Ma (Kaf Abu Ghannush) (Table 2.1 and Figure 2.10).

Figure 2.9: The Kaf Mantrus phonolitic plug intrudes the Mesozoic limestone in Jeffara Plain about 12 km west of Garian (~32°12'48"N 12°53'55.17"E).

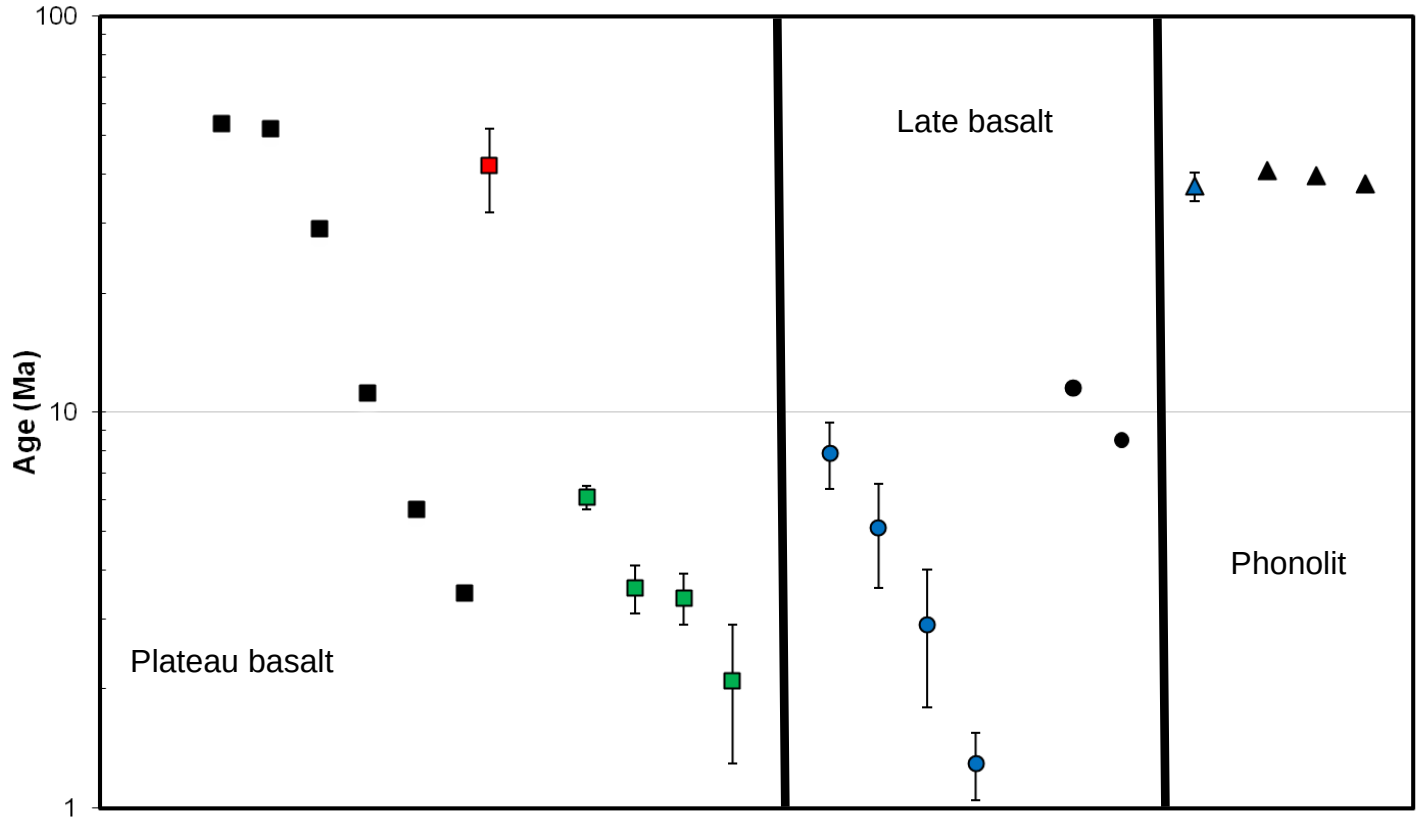

Figure 2.10: Age distribution of the Garian volcanic province rocks used K/Ar method. Squares: plateau basalt; circles: late basalt; triangles: phonolite. Blue: Mobil Oil Company (1967); black: Piccoli (1971); red: Schult and Soffel (1973), green: Ade-Hall *et al*. (1975).

Table 2.1: Summary of the previous age determinations of Garian volcanism.

Rock type and locality	Age (Ma)	Method	Rock unit	Source
Olivine nephelinite 13º 22' 30"E, 32º 10' 40"N Olivine basanite 13º 21' 10"E, 32º 03' 00"N Olivine basanite 13º 13' 42"E, 32º 12' 00"N Olivine nephelinite 12º 58' 04"E, 31º 51' 00"N	1.3 ± 0.3 2.9 ± 1.1 5.1 ± 1.5 7.9 ± 1.5	K–Ar	Late Basalt	Mobil Oil Company (1967)
Ras el Mohor, small shield volcano Ras Tebra, volcanic neck	11.5 ± 0.4 8.5 ± 0.3	K–Ar	Late basalt	Piccoli (1971)
Valley flow NE of Bir Tarsin Basalt flow in Wadi Guasem Flow in valley of Wadi Ghan Flow on Jebel as Soda near Mizda Flow at Beni walid	52 ± 1.2 53.5 ± 1.9 29 ± 1.0 11.2 ± 0.4 5.7 ± 0.2- 3.5 ± 0.1	K–Ar	Plateau Basalts (hawaiites)	Piccoli (1971)
13º 4'E, 32º 0.0'N	42 ± 10	Palaeomagnetic	Plateau Basalts	Schult and Soffel (1973)
C014 = 13º 7.2'E, 32º 9.8'N C015 = 13º 7.2'E, 32º 9.8'N C016 = 13º 7.2'E, 32º 9.8'N C034 = 13º 6.0'E, 32º 0.4'N	2.1 ± 0.8 3.4 ± 0.5 6.1 ± 0.4 3.6 ± 0.5	K–Ar and Palaeomagnetic	Unspecified basalt flow	Ade-Hall *et al*. (1975)
Ras Umm Al-ezz.	37.2 ± 0.7	K–Ar	Phonolites	Mobil Oil Company (1967)
Kaf Abu Ghannush Kaf Mantrus Kaf Tekut	40.7 ± 1.4 39.7 ± 1.4 37.7 ± 1.3	K–Ar	Phonolites	Piccoli (1971)

Chapter Three

Petrography, geochemistry and geochronology of the basaltic rocks from the Garian volcanic province

3.1 Introduction

In March 2010, ten samples (four late basalts, two plateau basalts and four phonolites) were collected from the Garian volcanic province (GVP) during a field trip that included visits to all the Cenozoic volcanic fields of Libya. The sample selection from the GVP aimed to cover the greatest spatial extent whilst also attempting the largest possible temporal variation according to the ages determined by Piccoli (1971).

The civil war in Libya that started in February 2011 forced a change in the focus of the PhD project as subsequent fieldwork was impossible. In June 2011 I was given access to samples of GVP rocks (one syenogabbro intrusion as late basalt, four plateau basalts and one phonolite) from the Manchester University collection that was originally sampled by Dr Mabruk Busrewil in 1971 for his PhD (Busrewil, 1974). The location of all samples is shown in Figure 3.1.

In this chapter I present the petrography, geochemistry and geochronology of the extrusive and intrusive mafic rocks from the GVP. As well as classifying the rocks, and making a preliminary assessment of the processes which shaped them, the data are used to distinguish the relationship between the two basaltic rock types proposed by Almond *et al*. (1974) and Busrewil (1974).

Thin-section descriptions and scanning electron microscope investigation of the phenocryst populations are presented. Detailed descriptions of hand specimens are presented in Appendix A. Mineral chemistry was determined by electron microprobe analysis at the University of Edinburgh. The details of these procedures are given in Appendix B.

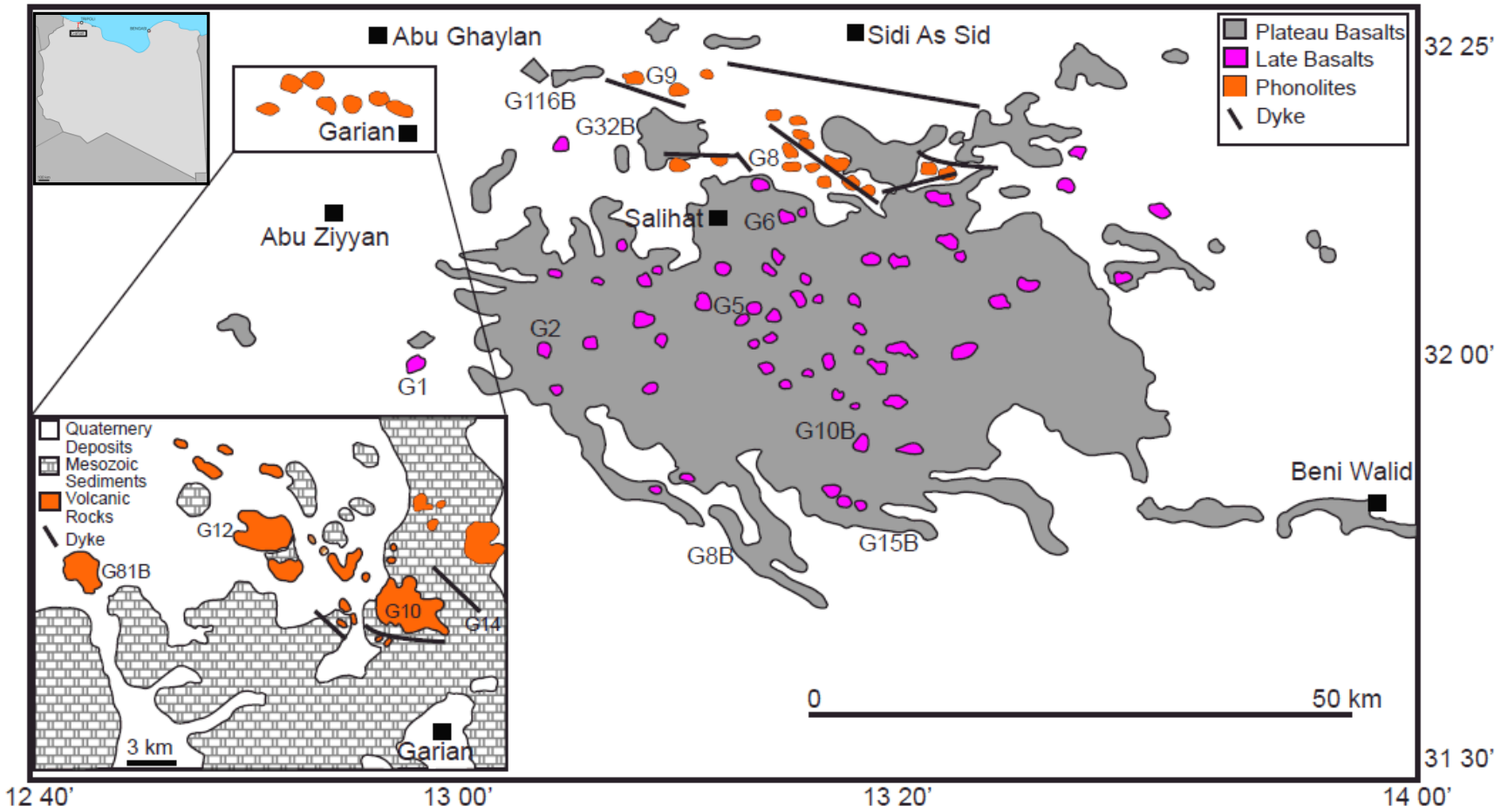

Figure 3.1: Geological map of the Garian volcanic province, NW Libya, showing the location of samples used in this study. This map is modified from geological sketch maps in Busrewil (1974) and Lustrino *et al*. (2011). Original 1:250.000 scale geological maps produced by the Libya Industrial Research Centre (Gray, 1971) are unavailable from all sources (IRC, Tripoli and Sebha University).

Table 3.1 Details of basalt samples from Garian volcanic province.

Sample	Rock type	Rock	Location	Latitude and longitude	Origin
Plateau Basalt sequence					
G9	Tholeiite olivine basalt	Lava	Flow from the top of Wadi Ghan sequence 26 km NE of Garian	32°17'00''N 13°17'30''E	February 2010
G14	Dolerite	Dyke	Kabdet El Gamel 6 km N of Garian	32°12'43.3''N 13°01'32.1''E	February 2010
G8B	Olivine basalt	Lava	Flow near the east side of Wadi Qidmu ~61 km SE of Garian	~31°40'6.1''N 13°18'6.2''E	MU collection
G15B	Tholeiite basalt	Lava	The lowest flow in Wadi Hashem (west side) ~71 km SE of Garian	~31°38'9.4''N 13°26'3.2''E	MU collection
G32B	Tholeiite olivine basalt	Lava	The lower part of Wadi al Waar section ~26 km NE of Garian	~32°12'28.1''N 13°17'30.2''E	MU collection
G116B	Tholeiite olivine basalt	Lava	Flow from the top of section in Wadi Ghan ~12.5 km NE of Garian	~32°15'26.9''N 13°8'5.8''E	MU collection
Late Basalt sequence					
G1	Basanite	Plug	33 km S of Garian	31°52'9.9''N 12°59'36.2''E	February 2010
G2	Basanite	Lava	19 km SE of Garian	32°01'2.2''N 13°06'20.7''E	February 2010
G5	Basanite	Lava	31.5 km E of Garian	32°01'49.2''N 13°18'1.2''E	February 2010
G6	Alkali olivine basalt	Lava	35 km NE of Garian	32°09'42''N 13°23'15.1''E	February 2010
G10B	Syenogabbro	Plug	From the Ras al Moher ~51 km SE of Garian	~31°47'20.6''N 13°19'35''E	MU collection

Major and trace element concentrations were determined by X-ray fluorescence at the Edinburgh University. Rare earth element concentrations were determined on all samples by inductively coupled plasma mass spectrometry (ICP-MS), and Sr and Nd isotopes were measured by thermal ionisation mass spectrometry at the SUERC. The details of the analytical procedures and data are given in Appendix C.

$^{40}Ar/^{39}Ar$ age determinations were made on the purified groundmass separates from all samples at SUERC. Sample preparation and analysis procedures are described in Appendix D along with the data tables.

3.2 Petrography

3.2.1 Plateau basalts

The plateau basalt samples (n = 6) appear to share similar petrographic characteristics. They are variably porphyritic (Figure 3.2), dominated by olivine phenocrysts with rarer clinopyroxene and plagioclase phenocrysts. These are set in a fine-grained groundmass dominated by plagioclase, pyroxene and Fe-Ti oxides. The dyke sample (G14, Kabdet El Gamel) displays doleritic texture. The phenocryst population is the same as basalts except for the absence of plagioclase.

Olivine phenocrysts typically represent 2 to 10 % of the basalts and range in size from 0.1 to 2 mm. They are often fractured and show evidence of iddingsite alteration. Three olivine phenocryst types are present in thin section: (1) large partially resorbed crystals up to 2 mm with irregular borders (Figure 3.2A), (2) euhedral crystals (0.5 - 1 mm) (Figure 3.2B) and (3) small (~0.1 mm) subhedral to euhedral crystals.

Euhedral pyroxene phenocrysts (0.5 to 0.8 mm) make up less than 5 % of most samples. Glomerocrysts of pyroxene, olivine and plagioclase are observed in many flows (Figure 3.2A and E). Occasionally euhedral pyroxene phenocrysts (e.g., G8B and G14) are corroded and stained brown. They

display a sieve-textured that surrounded by an extensive, fresh, uncorroded and unstained rim that comprises 25 – 50 % of the total crystal (Figure 3.2C & D).

Plagioclase phenocrysts are up to 2 mm in length but are generally rare. They are typically resorbed, appearing to be out of equilibrium with the basaltic liquid. They often occur as a glomerocrysts with pyroxene (Figure 3.2A & F). Plagioclase laths are the dominant groundmass phase in most basalt, making up 60 %. Clinopyroxene represents about 20 volume % in the groundmass.

3.2.2 Late basalts

The late basalts (n = 5) are typically olivine and pyroxene-phyric (Figure 3.3). Plagioclase phenocrysts are only present in the syenogabbro G10B (Figure 3.3A). The groundmass is fine-grained to glassy with lower plagioclase content than the plateau basalts and a higher proportion of Fe-Ti minerals and randomly oriented laths of plagioclase. Dyke G1 displays the same texture as the basalts but lacks plagioclase laths in the groundmass (Figure 3.3B).

Olivine is the dominant phenocryst phase, making up more than 10 %. The three olivine types recognized in the plateau basalts are present in most samples (Figures 3.3A to F). Iddingsite alteration of olivine rims is common.

Rare clinopyroxene phenocrysts (0.5-1.0 mm) are euhedral mostly appearing as glomerocrysts with olivine (Figure 3.3E and F). The altered and corroded pyroxenes with sieve-textured cores seen in plateau basalts are also present in samples G2 and G5 (Figures 3.3D and E).

Plagioclase phenocrysts in syenogabbro G10B are up to 2 mm and are often partially resorbed. They are associated with the megacrysts of olivine and pyroxene and Ti-Fe oxides with an interstitial network of alkali feldspar and apatite (Figure 3.3F).

Plagioclase laths are the dominant groundmass phase in most late basalts, making up 50 % (Figures 3.3C and F). They exhibit normal twinning. Clinopyroxene is common as microlites representing about 30 volume % in the groundmass. Olivine and Ti-Fe oxides make up ~20 % of the rock.

3.2.3 Scanning electron microscope observations

Back-scattered electron analyses of polished thin sections were used primarily to distinguish the differences between the different types of olivine and clinopyroxene phenocrysts. The major element compositions of the crystals selected for study were determined by electron microprobe (see Appendix B). Six samples (basalts, intrusions and dykes) were selected for microprobe analysis to represent both basalts types of the GVP.

3.2.3.1 Olivines

Three general types of olivine phenocrysts are distinguished in all basalts:

(1) The large partially resorbed olivine crystals often have thin Fe-rich rims and high Mg cores, typical of overgrowth zonation. The cores tend to have low CaO contents compared to the other olivine types (Figures 3.4 and 3.5). Small spinel and Fe-Ti oxides are present in the plateau basalt olivines (Figure 3.5A). High Ca (Figure 3.5A) and Fe-rich (Figure 3.5B) overgrowths are observed in several large olivines in late basalts.

(2) The large euhedral olivines tend to have consistent compositional variation of increasing Ca content from core to rim (normal zonation). They have higher CaO contents than the resorbed olivine crystals. Several large euhedral olivine crystals in sample G5 have low CaO contents and high Mg cores (Figure 3.5C).

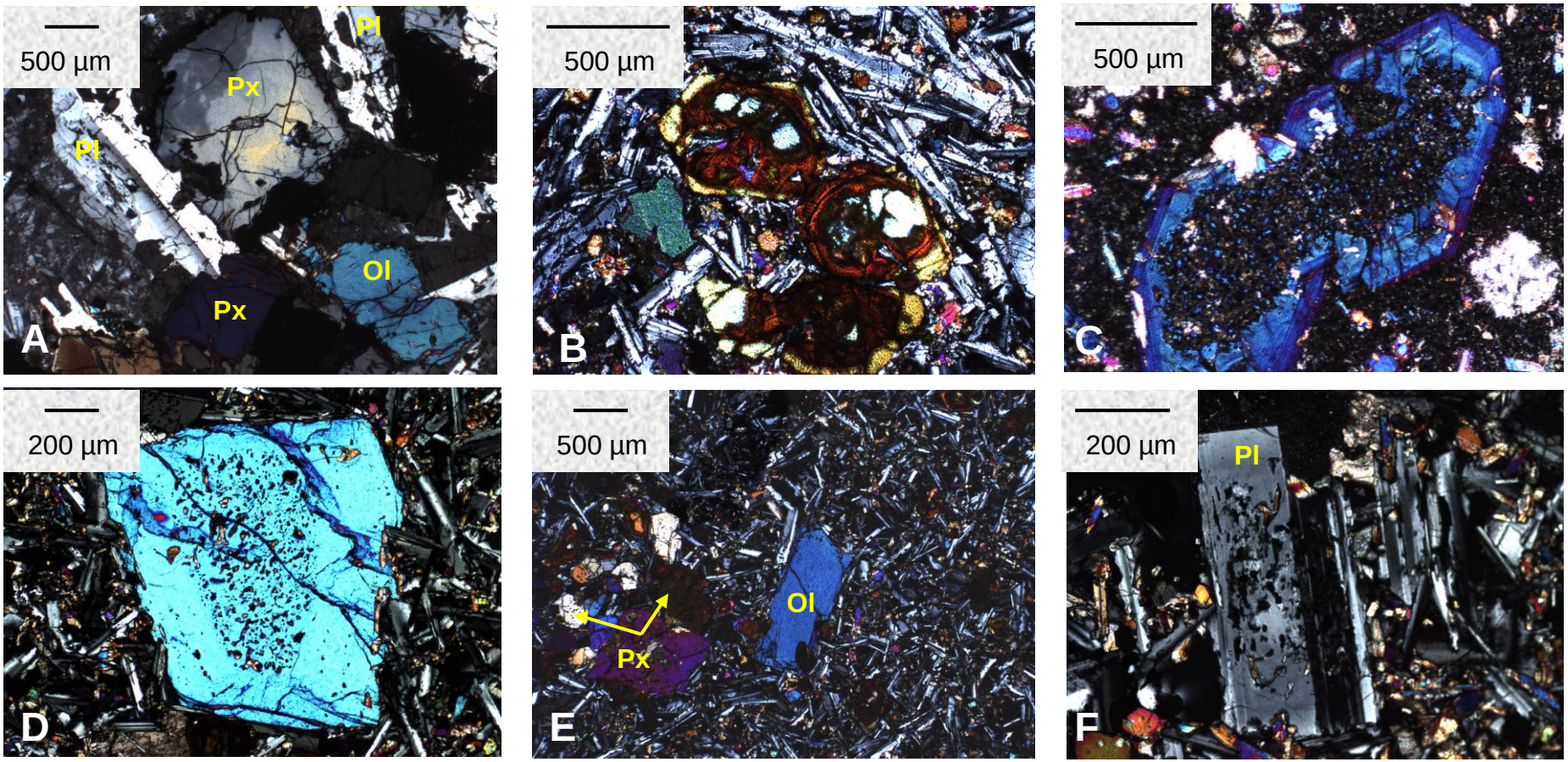

Figure 3.2: Photomicrograph, under crossed polarised of plateau basalts from GVP. (A) Irregular resorbed olivine (Ol), plagioclase (Pl) and pyroxene (Px) crystals (basalt G8B). (B) Large euhedral altered olivine phenocrysts (≥0.5 mm) (basalt G9). (C & D) euhedral pyroxene with sieve-textured core and an extensive fresh rim (basalts G14 & G8B respectively). (E) Glomerocryst of large olivine (Ol) phenocrysts with clinopyroxene (Px) phenocrysts in medium-grained of plagioclase laths (G8B). (F) Large resorbed plagioclase (Pl) xenocryst.

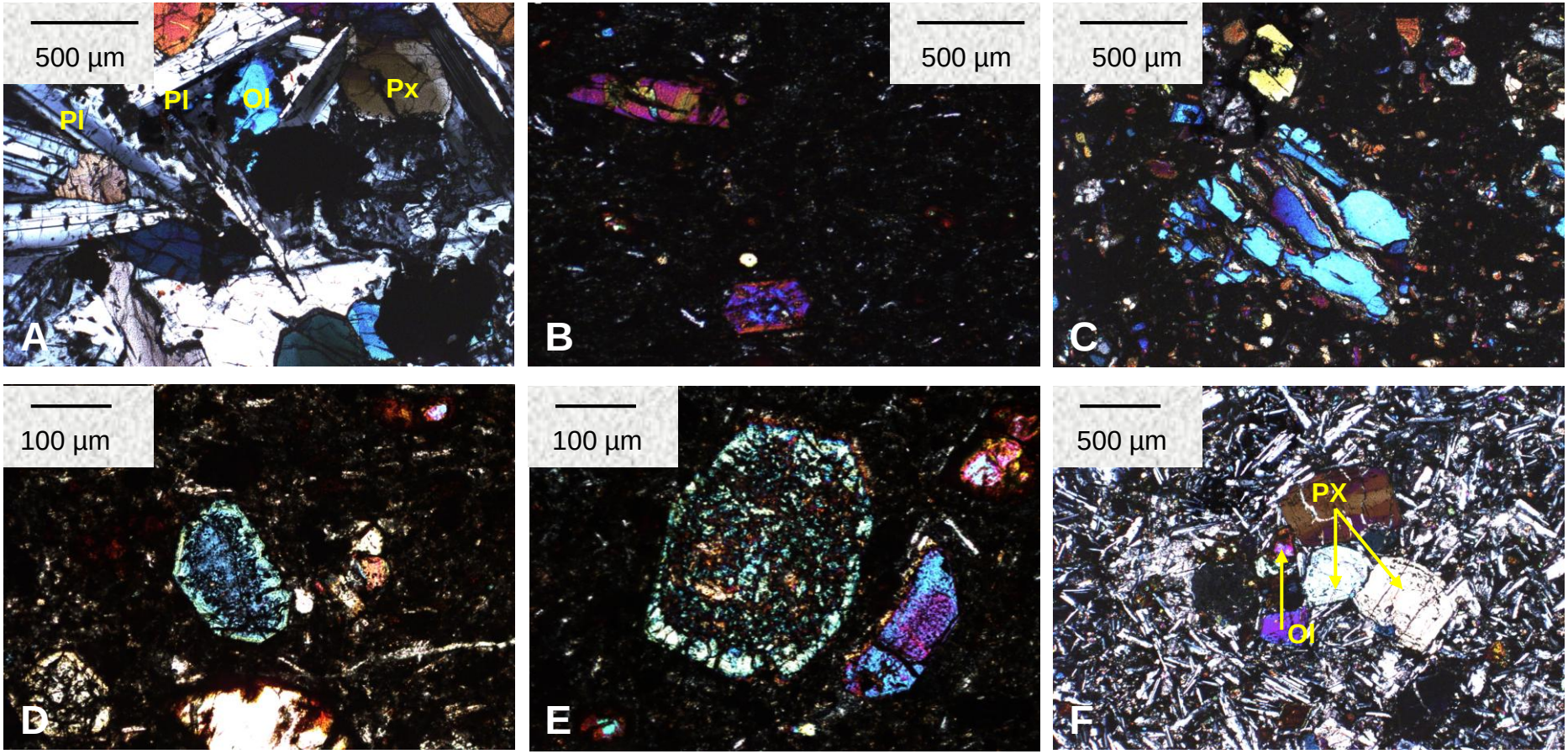

Figure 3.3: Photomicrograph, under crossed polarised of late basalt samples from GVP. (A) Glomerocrysts of large resorbed plagioclase (Pl), clinopyroxene (Px) and olivine (Ol) xenocrysts (syenogabbro G10B). (B) Short hexagonal euhedral olivine phenocrysts (≤ 0.4mm) set in fine-grained groundmass made up of the pyroxene with Fe-Ti oxides and glassy groundmass. (C) Resorbed olivine phenocrysts set in fine-grained groundmass interstitial pyroxene and Ti-Fe oxides. (D & E) Euhedral pyroxene with sieve-textured core and a fresh rim (basalt G5). (F) Glomerocrysts of clinopyroxene (Px) set in medium-grained groundmass of plagioclase laths and olivine (Ol) with Fe-Ti oxides.

(3) The cores of small euhedral olivines tend to be inclusion-free, compositionally homogeneous and have lower Mg/Fe than large euhedral olivines. CaO contents are similar. Fe enrichment is typically apparent in the rims of these olivines (Figure 3.5D).

3.2.3.2 Pyroxene

Large pyroxene phenocrysts (up to 3 mm) are present in most basalt rocks (Figures 3.2A and E and 3.3A and F). The resorbed pyroxenes are often strongly zoned and have sieve-textured cores similar to sieve textures described by Fodor *et al*. (1995). The cores are made up of small grains of olivine, glass, pyroxene and Fe oxides (Figure 3.4C) often comprising more than half of the crystal. The overgrowth has high Ca in comparison. The small euhedral pyroxene phenocrysts (≤ 1 mm) have similar Fe-Mg zoning patterns but with narrower Fe-rich rims (Figure 3.4D).

3.2.4 Mineral chemistry

The composition of the phenocrysts was determined using a Cameca SX-100 electron microbe at University of Edinburgh (Appendix B1.1). Six thin sections were selected for microprobe analysis to represent the mineral composition of two basalt types.

3.2.4.1 Olivine

The major element composition (Fe, Mg, Ca, Ni Si, Cr, Ti, Al and Mn) of cores (n = 107) and rims (n = 103) were measured in 93 olivine crystals. Forsterite (Fo) content of each spot was calculated from Fo = 100 * Mg/(Mg + Fe^{2+}) and is plotted in Figures 3.6 (plateau basalts) and 3.7 (late basalts).

The MgO content of mantle melts is proportional to the melt temperature. Consequently the Fo content of olivine that is in equilibrium with the melt reflects the melt temperature (Beattie, 1993; Putirka *et al*., 2007).

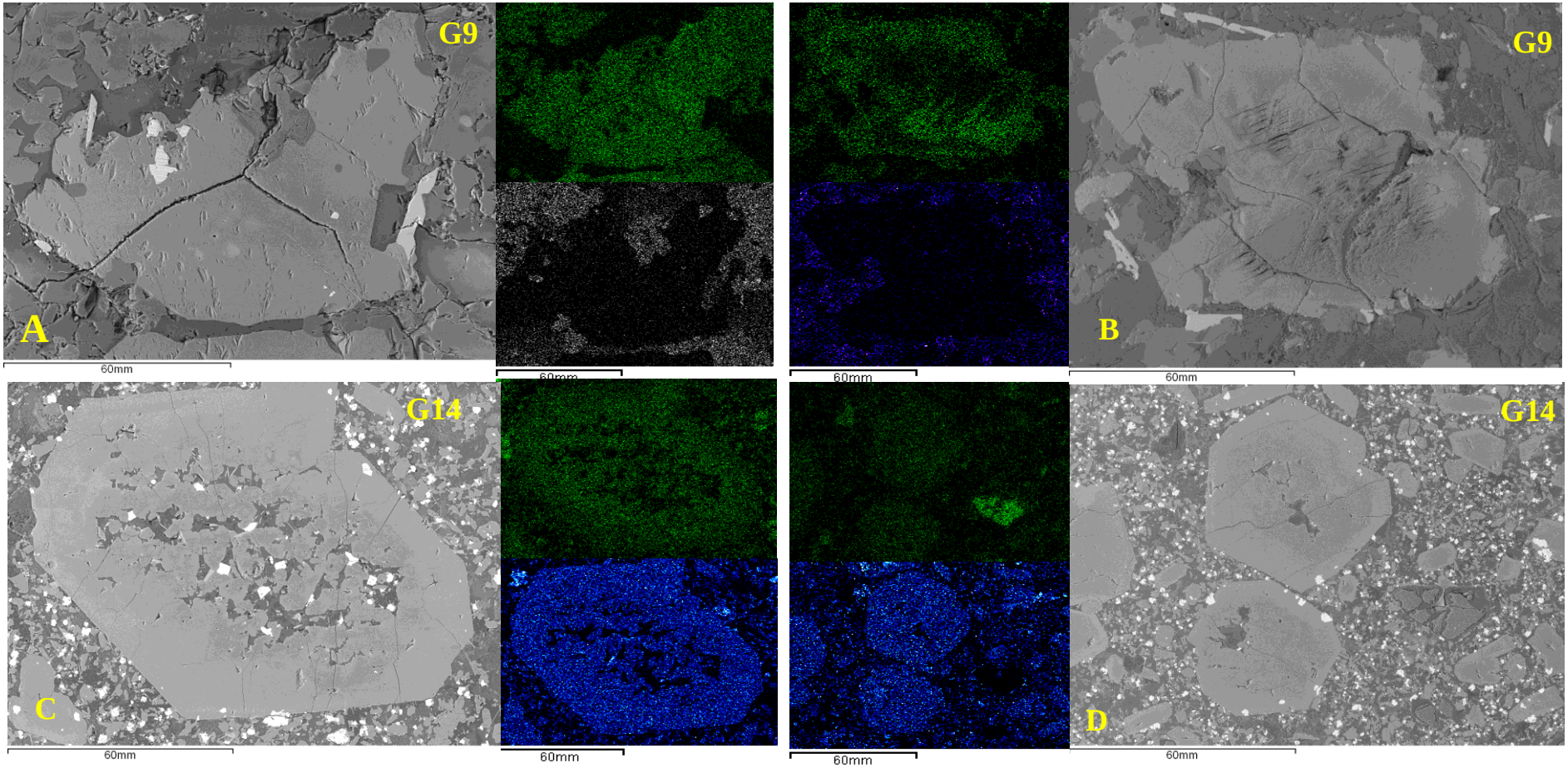

Figure 3.4: Backscattered SEM images and X-ray maps of plateau basalt samples from GVP. (A and B) Irregular resorbed olivine crystals with inclusions, high Ca and Fe-rich overgrowths respectively. (C) Large euhedral pyroxene phenocrysts with sieve-textured core (grains of olivine, glass, pyroxene and FeO) and fresh rim. (D) Two small euhedral subhedral pyroxene phenocrysts with narrow zoned. Green= Mg contents, blue and grey= Ca contents.

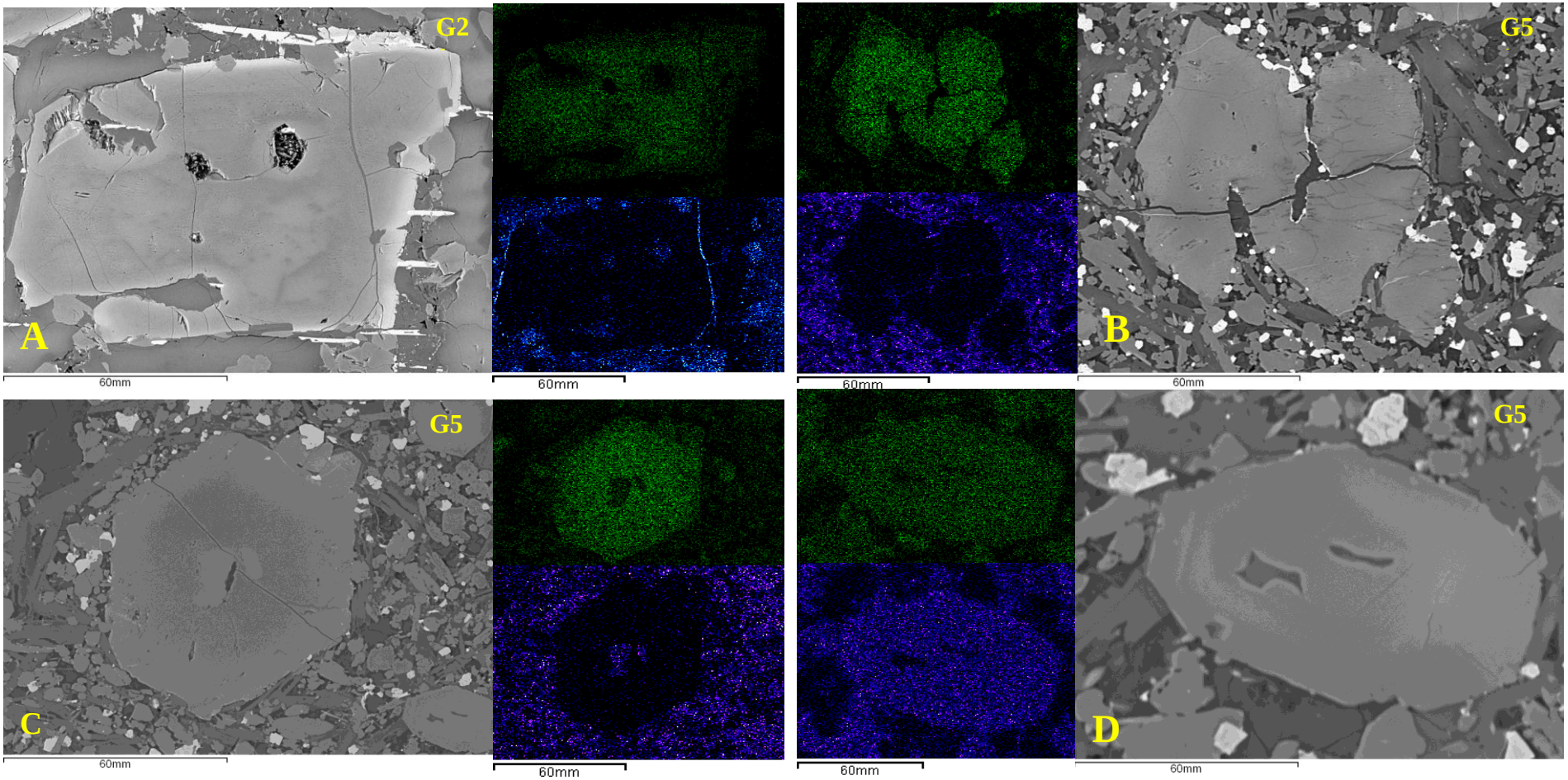

Figure 3.5: Backscattered SEM images and X-ray maps of late basalt samples from GVP. (A and B) Irregular resorbed olivine xenocrysts. The xenocrysts identified by their high Mg and low Ca. (C) Large euhedral antecryst olivine (low-CaO olivine). (D) Small euhedral olivine phenocrysts with narrow compositional (FeO) zonation. Green= Mg contents and blue= Ca contents.

The temperatures can be precisely calculated from experimentally established basalt phase equilibria by plotting the whole rock Mg# against the forsterite contents of olivine (e.g., Roeder and Emslie, 1970). The relationship between the two parameters is characterized by the Fe-Mg exchange relationship:

$$K_{D_{ol-melt}}^{Fe-Mg} = \left(\frac{X_{melt}^{Mg}}{X_{olivine}^{Mg}}\right)/\left(\frac{X_{melt}^{Fe^{2+}}}{X_{olivine}^{Fe^{2+}}}\right)$$

where K_D describes the partitioning of iron and magnesium between olivine and liquid. X is the mole fraction. Roeder and Emslie (1970) determined K_D for Fe-Mg to be 0.3 ± 0.03.

The chemistry of olivine can be used to determine if the minerals were in chemical equilibrium with their host magmas. This is done by calculating the range of mineral composition that would be in equilibrium with the magma using K_D = 0.3 ± 0.03 (Roeder and Emslie, 1970). Figure 3.8 shows the chemical composition of the three olivine types from six samples plotted against the composition in equilibrium with the host magma calculated from bulk-rock composition.

Simkin and Smith (1970) proposed that the Fo and CaO content of olivine discriminates mantle-derived olivine xenocrysts from phenocrysts. The CaO content of olivines from mantle peridotites are commonly less than 0.1 wt% and Fo is generally in the range 88 to 94 (Simkin and Smith, 1970; Embey-Isztin and Dobosi, 2007). Olivine that crystallized from magmas typically have CaO > 0.1 wt% and Fo = 57 to 90 (Simkin and Smith, 1970).

All analyses of the cores of the resorbed olivine crystals in the plateau basalts have Fo_{85-89}, with the exception of one core measurement (Fo_{79}) (Figure 3.6 A and B). The rims have lower and limited Fo values (Fo_{85-86}) compared to cores. In contrast, the cores of resorbed olivines in the late basalts are more variable. Core compositions are in the range Fo_{78-91} with a peak around Fo_{90} (Figure 3.7A). Rim compositions occur in two peaks, one peak around Fo_{90}

and a second peak with considerably lower values (Fo_{58-80}: Figure 3.7B). Most crystals display normal compositional zoning, with decrease of Fo content from core to rim. The highest Fo values in both basalt types are similar to those of olivine in mantle peridotites (e.g., Simkin & Smith, 1970). All resorbed olivine crystals from plateau basalts, and most from late basalts, have higher forsterite content than predicted from the whole rock basalt composition, consistent with a xenocryst origin (Figure 3.8).

The cores of the large euhedral olivine in the plateau basalts have lower Fo values (Fo_{48-83}) and larger variation compared to the resorbed crystals. There appears to be two peaks; Fo_{48-70} and Fo_{80-85} (Figure 3.6C). Rim compositions are Fo_{42-66} but concentrated about Fo_{55} (Figure 3.6D). All olivine cores overlap or are slightly below the olivine-liquid line (Figure 3.8) indicating that the most fosteritic olivine cores approach equilibrium with their bulk-rock compositions.

The cores and rims of olivines from the late basalts have slightly higher Fo content (63-85 and 55-85 respectively) than olivine of the plateau basalts (Figure 3.7C and 3.7D). Several cores of the large euhedral crystals in G5 and G10B appear to be more forsteritic with respect to their bulk-rock compositions (Figure 3.8).

Small olivine phenocrysts in the plateau basalts are more Fe-rich than the large euhedral olivine phenocrysts and tend to overlap the range measured in the rims of large euhedral olivine. The cores are Fo_{37-75} with a major peak at Fo_{45-55} (Figure 3.6E). Rims have a narrow compositional range (Fo_{41-50}) (Figure 3.6F). In general, most of the olivine cores plot below olivine-liquid line in Figure 3.8, suggesting these olivine phenocrysts may have accumulated from varying stages of fractional crystallisation.

The cores of the small olivines in the late basalts tend to have slightly higher Fo than the plateau basalts, with peaks at Fo_{59-65} and Fo_{78-85} (Figure 3.7E). The rims have a narrow compositional range (Fo_{53-76}) but with higher Fo than the small olivines of the plateau basalts (Figure 3.7F). Fo contents of cores in

sample G5 plot above and below the olivine-liquid equilibrium composition whereas the G2 olivine cores plot below the olivine-liquid line (Figure 3.8).

The low CaO (<0.1%) and generally high Fo of the cores of the resorbed olivines in the late basalts (Figure 3.9) are similar to pristine olivine from spinel lherzolite xenoliths from Garian (Beccaluva *et al*., 2008) indicating a xenocryst origin. However there is a group that trend to values as low as Fo_{78}. Lower Fo content (down to Fo_{78}) is recorded by olivine micro-crysts (secondary olivine) in reaction patches products in metasomatic assemblage (Beccaluva *et al*., 2007, 2008). The cores of resorbed olivine in plateau basalts have elevated CaO (up to 0.23%) despite a narrow forsterite range (~Fo_{87}) (Table B1.1 and Figure 3.9). High Ca contents have been measured in high Fo metasomatic olivine micro-crysts in Garian xenoliths (Beccaluva *et al*., 2008) and they may be the source.

CaO in the large euhedral olivines in both basalt types are > 0.2% with the exception of one (Fo_{64}) core (Figure 3.9). The rims have CaO contents ranging from 0.24 to 0.92% (Table B1.2 Appendix B). Small olivine phenocrysts in both basalt types have CaO contents (> 0.2%), (Figure 3.9). The rims have CaO contents ranging from 0.25 to 0.98% (Table B1.3 Appendix B).

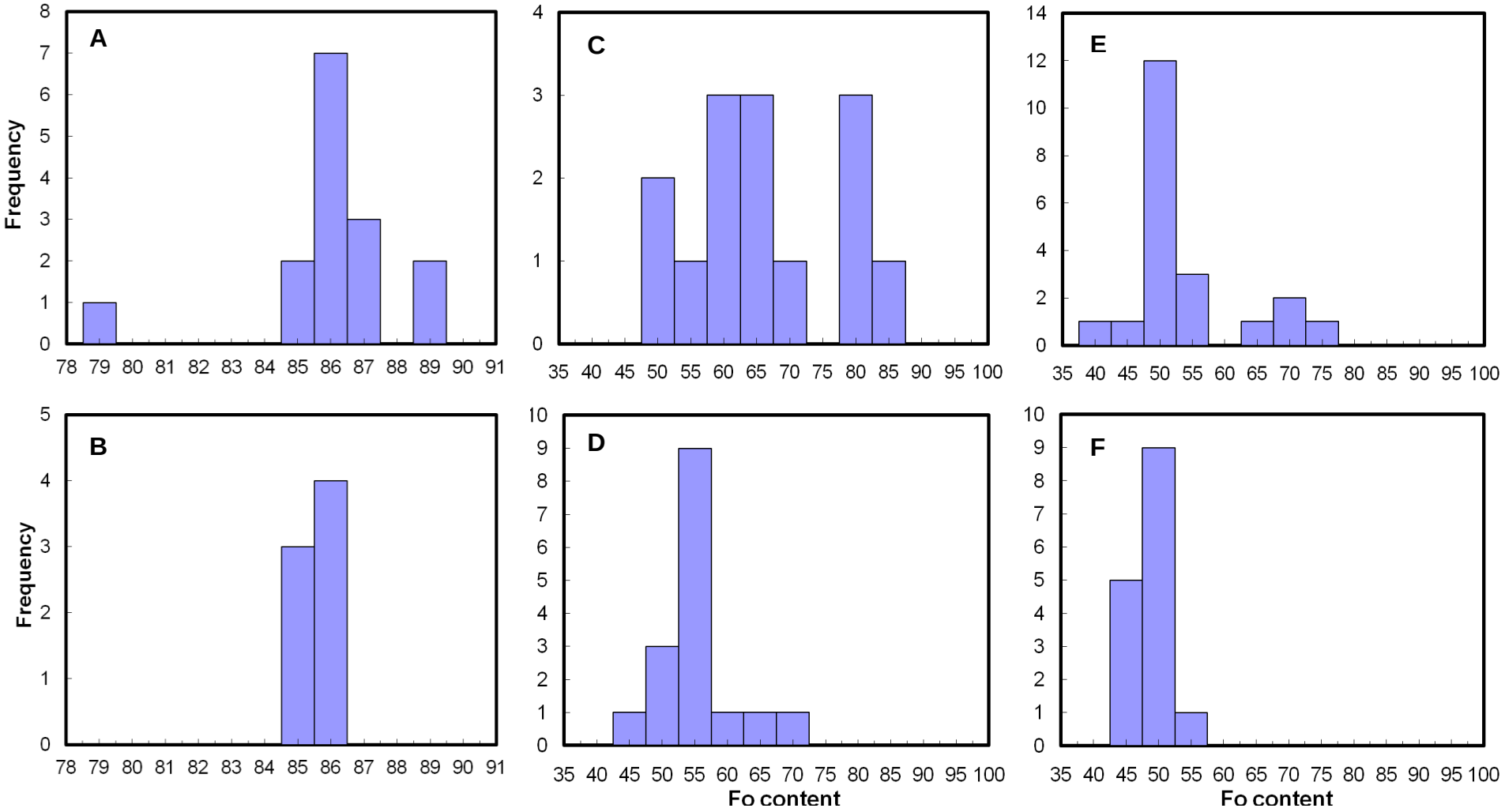

Figure 3.6: Histogram of olivine composition for plateau basalt samples show the frequency and variation of Fo content in cores and rims of different types of olivine. A: Resorbed crystal cores. B: Resorbed crystal rims. C: Euhedral crystal cores. D: Euhedral crystal rims. E: Small crystal cores. F: Small crystal rims.

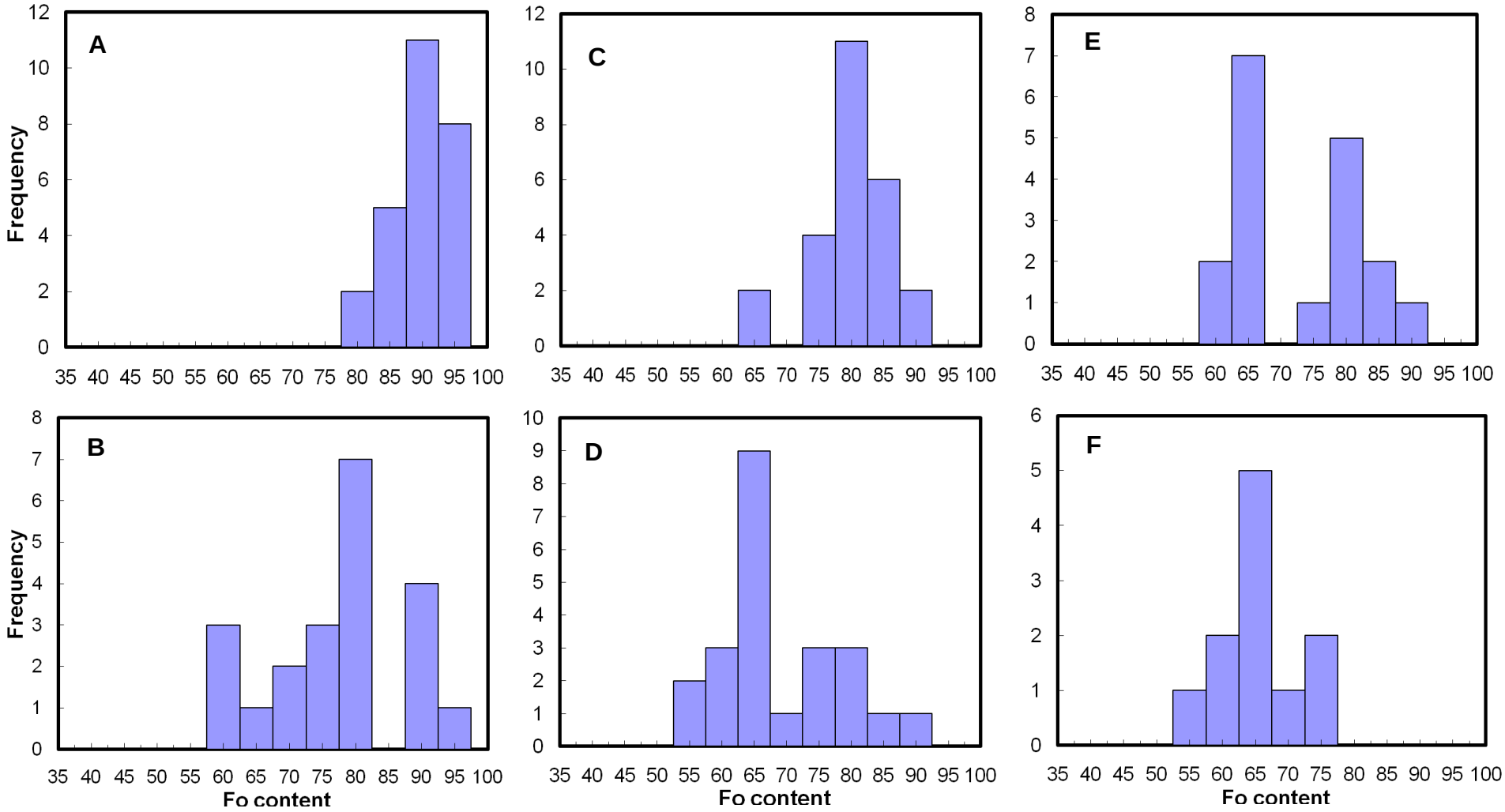

Figure 3.7: Histogram of olivine composition for late basalt samples show the frequency and variation of Fo content in cores and rims of different types of olivine. A: Resorbed crystal cores. B: Resorbed crystal rims. C: Euhedral crystal cores. D: Euhedral crystal rims. E: Small crystal cores. F: Small crystal rims.

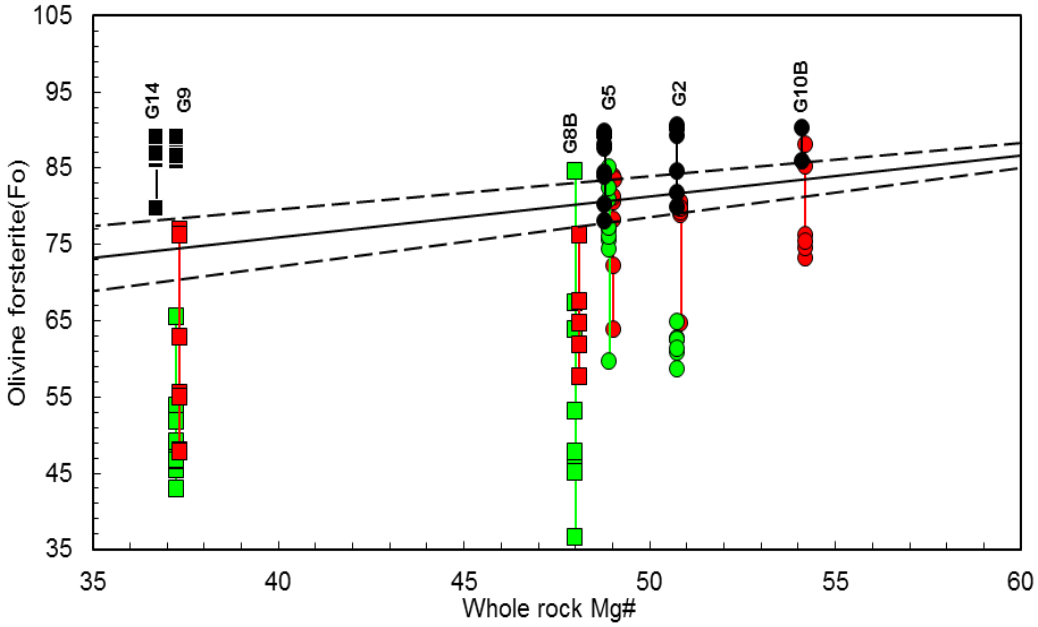

Figure 3.8 Forsterite content (Fo %) of olivine crystal cores plotted against the whole rock Mg# = [(Mg/Mg + Fe^{2+}) 100]. Bars show the range of Fo compositions whilst symbols represent the olivine types. The black line represents the olivine-liquid equilibrium composition of K_d = 0.3, the black dashed lines show K_d = 0.3 ± 0.03 (Roeder and Emslie, 1970; Ulmer 1989). late basalt olivines are circles; plateau basalt olivines are squares; Resorbed olivine is black, large euhedral olivine is red and small olivine is green.

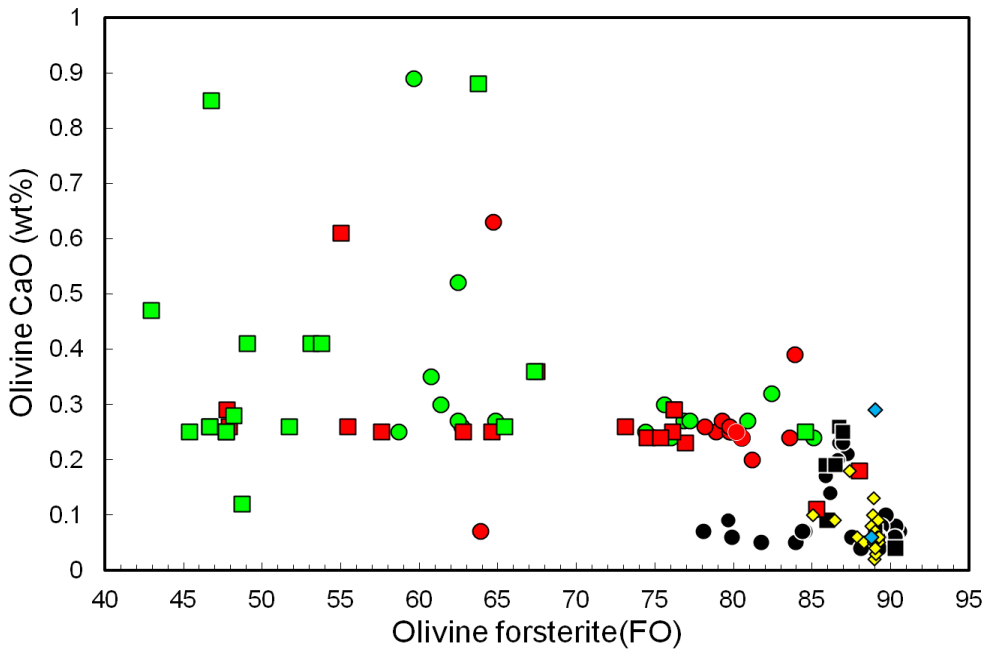

Figure 3.9: Forsterite content (Fo %) of olivine crystal cores plotted against CaO contents compared to peridotite xenoliths from same study area by Beccaluva *et al*. (2008) (yellow diamonds are primary olivine, blue diamonds are from metasomatic veins). Symbols are the same as Figure 3.8.

3.2.4.2 Pyroxene

The pyroxene phenocrysts of plateau basalt flows (cores and rims from 123 crystals) plot in the augite field of the En–Fs–Wo classification diagram of Morimoto (1988) in Figure 3.10. Most pyroxenes from dyke G14 plot in the diopside field but range from wollastonite to augite, with rims being slightly more Ca-rich than the cores. The cores are typically more Fe-rich than the rims of pyroxene in the dyke. The pyroxene compositions of the late basalts display similar trends. Pyroxene in the intrusion G10B plot on the boundary between wollastonite and diopside fields but most pyroxenes from the flows have more variation from wollastonite to augite with rim composition being more Fe-rich.

Generally, the pyroxene compositions of the two basalt types overlap. Clinopyroxene in the late basalts have a wider compositional range (Wo_{36} to Wo_{62}) than the plateau basalts (Wo_{41} to Wo_{53}).

The majority of the euhedral clinopyroxene crystals in both basalts are characterized by Mg# values of 64-84 and all samples, except sample G5 (given the same behaviour in olivine composition), contain equilibrium-composition clinopyroxene (Figure 3.11). The resorbed crystals in samples G9 and G14 are plotted above the clinopyroxene-liquid equilibrium composition, consistent with their origin as xenocrysts.

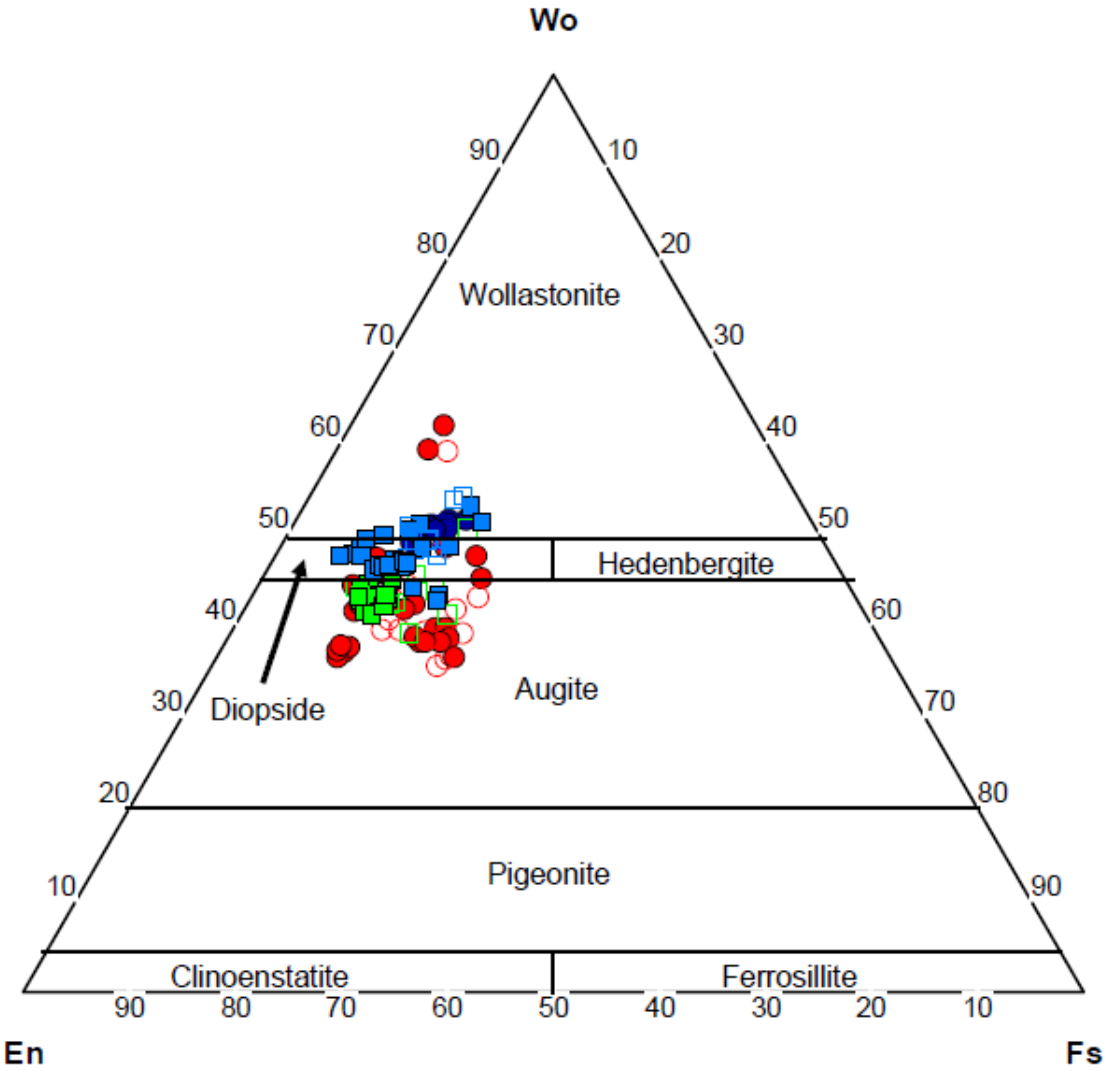

Figure 3.10: Compositional variation of clinopyroxene phenocrysts (cores and rims) projected onto the Wo-En-Fs quadrilateral for Ca-pyroxene (Morimoto, 1988). Circles are late basalts (cores): red (basalts) and dark blue (intrusions). Squares are plateau basalts (cores): green (basalts) and light blue (intrusions). Open symbols are rims.

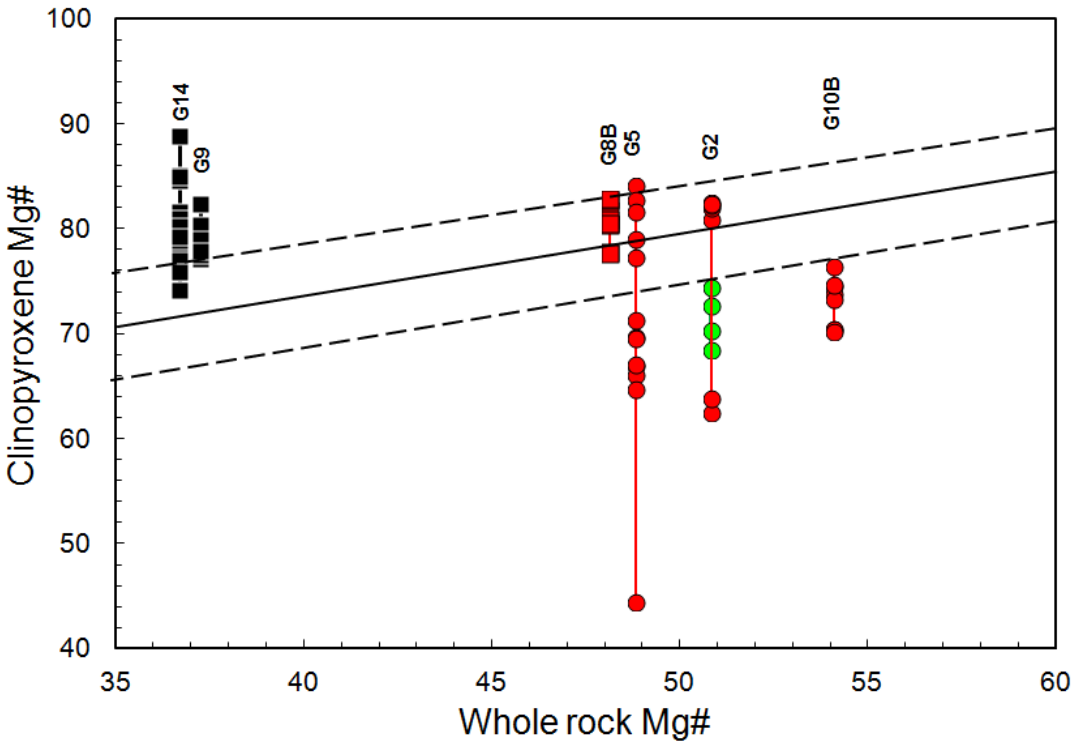

Figure 3.11: Mg-number of clinopyroxene crystal cores plotted against the whole rock Mg#. Bars show the range of Mg#, whilst symbols represent the clinopyroxene types. The black line represents a clinopyroxene-liquid equilibrium composition of K_d = 0.23, the black dashed lines show a value of ± 0.05 (Grove and Bryan, 1992; Toplis and Carroll, 1995). The same symbols are used in Figure 3.8.

3.2.4.3 Plagioclase

Plagioclase occurs as subhedral to euhedral laths in the groundmass of most samples, few phenocrysts of Plagioclase occurs in some samples and as large resorbed crystals in syenogabbro G10B. Ninety-four spots (cores and rims) have been analysed from four samples. Compositions were calculated on the basis of 4 oxygens. These are plotted on an Ab-An-Or diagram (Deer *et al*., 1966) (Figure 3.12).

The groundmass plagioclase crystal core compositions from plateau basalts typically are labradorite (An_{52} to An_{58}) with rims extending to more Na-rich

compositions ($An_{29–59}$) and some grains tend to be k-rich plagioclase (Figure 3.12). The groundmass of plagioclase core compositions in the late basalts are labradorite to andesine (An_{44} to An_{57}) with rim compositions being more sodic (An_{46} to An_{57}) (Figure 3.12). In contrast, the groundmass plagioclase cores of the dyke G10B has a wider range (An_{40} to An_{58}) with rim compositions found to be more Na-rich of andesine (An_{29}) and becoming more sodic towards the rims (Figure 3.12).

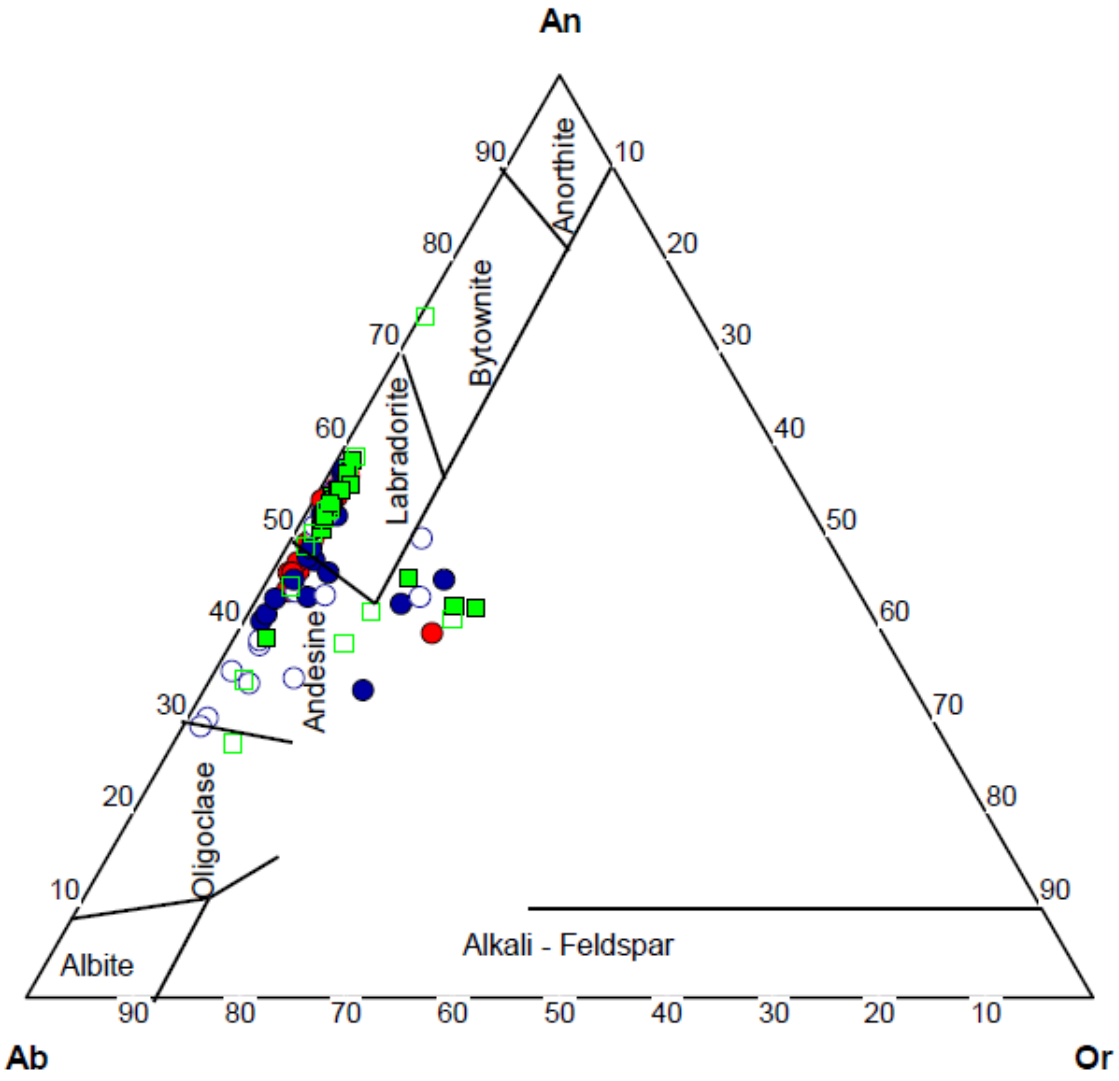

Figure 3.12: Plagioclase composition of laths and resorbed crystals (core and rims) projected into the ternary anorthite-albite-orthoclase (mol %). The same symbols used in Figure 3.10.

3.2.5 Implications

Several conclusions can be drawn from the study of the petrography and mineral chemistry.

1. The similarity of the plateau and late basalts suggest that they are not distinct basalt types produced from melting of different mantle regions at different times as proposed by earlier workers (Piccoli, 1971; Schult and Soffel, 1973; Almond *et al*., 1974; Busrewil, 1974; Ade-Hall *et al*., 1975). These similarities include:

(i) The presence of the same olivine populations in both basalt types (Figures 3.2 to 3.5).

(ii) The compositional similarity of olivines in both basalts (Figures 3.6 to 3.9).

(iii) The presence of the sieve-textured pyroxenes in both basalt types (Figures 3.2 C&D; 3.3 D&E and 3.4 C).

2. Fractional crystallisation was the main process in the evolution of the basaltic magmas. The key evidence to support this is:

(i) The plateau basalts are more evolved than the late basalts as they contain less olivine and pyroxene phenocrysts, and more plagioclase laths in the groundmass.

(ii) The cores of large olivine phenocrysts are typically more Fo-rich (80 to 85) than the rims (55 to 65) in both basalt types (Figure 3.6 and 3.7).

(iii) The small olivine phenocrysts are more Fe-rich than the large euhedral olivine phenocrysts.

3. The petrography and mineral chemistry reveal information about the mantle melting and magma storage history.

(i) The resorbed olivines and sieve-textured clinopyroxenes are fragments of lithospheric mantle that have been incorporated into the basaltic magma (Simkin and Smith, 1970; Embey-Isztin and Dobosi, 2007). Most grains are compositionally similar normal mantle. However the moderate Ca content of several olivines might indicate the incorporation of metasomatic olivine recorded in reaction patches in lherzolite xenoliths (Beccaluva *et al*., 2007, 2008).

(ii) The sieve-textured clinopyroxene may be explained by the breakdown of the mineral during high-temperature transport of the xenocrysts to the surface in their host magmas. However, they may also develop in response of interactions between the mantle mineral assemblage and transient metasomatic liquids and/or fluids (Carpenter *et al*., 2002). This texture of clinopyroxene may be the result of reactions between clinopyroxenes and a metasomatic agent as a primary type comparable to the field of primary xenoliths clinopyroxene from Garian area (Beccaluva *et al*., 2008).

3.3 Geochemistry

In this section I report the major and trace element, and rare earth element (REE) concentrations and Sr-Nd isotope composition of both basaltic rock units (plateau and late basalts). The description of these data is done to illustrate the compositional limits of the rock suite, classify the rocks and make preliminary assessment of the differentiation processes which will be addressed with more details in the next chapter.

3.3.1 Major elements

The plateau basalts have higher SiO_2 (48.5 - 52.7 wt %) than the late basalts (41.6 - 48.3 wt %), and plot between alkaline and sub-alkaline fields on TAS diagram (Figure 3.13 and Tables C.1 Appendix C). The late basalts are strongly undersaturated, with normative nepheline in excess of 5 % in most samples (Table C.2 Appendix C). They largely plot in tephrite-basanite fields in TAS diagram and are mostly alkaline (Figure 3.13). The syenogabbro G10B

falls in the trachy-basalt field. The new analyses of the GVP basic rocks plot in range recorded by previous studies (Figure 3.13) (Piccoli, 1970; Almond *et al*., 1974; Busrewil, 1974; Hegazy, 1999; Aboazom *et al*., 2006; Lustrino *et al*., 2012). The compositional ranges of the plateau and late basalts overlap and appear to be continuous, suggesting that they are related.

In Harker-type SiO_2 variation diagrams (Figure 3.14) the new data overlap previous studies. The plateau basalts are characterized by restricted range of MgO (6.4 to 7.3 wt %) compared to the late basalts (6.0 to 11.7 wt %). There is a positive correlation between SiO_2 and Al_2O_3, and negative correlations with MgO, CaO and FeO. There is no clear correlation with the alkali elements K and Na (Figures 3.14).

MgO, CaO and FeO are incorporated in the structure of mafic minerals (olivine and pyroxene) during fractional crystallisation process. The correlation with SiO_2 suggests that the addition or removal of mafic minerals from melt has been the most important process controlling the compositional variation (Figure 3.14). The lack of a clear relationship between SiO_2 and Na_2O (decreases in late basalts and increases in plateau basalts) and K_2O (increases in late basalts and decreases in plateau basalts) suggests that the loss or addition of felsic minerals (K-feldspar and sodic plagioclase) that crystallise during the later magmatic stages has been not as important as the mafic minerals in controlling the composition of the basalts.

The Na_2O/K_2O ratio decreases with SiO_2 content in the late basalts yet increases with SiO_2 for the plateau basalts (Figure 3.15A). This suggests that the variation in late basalts is controlled by olivine and clinopyroxene crystallisation but the composition of plateau basalts may be controlled by K-feldspar accumulated supported by the positive anomaly 1.00-1.03 (Figure 3.18) and peak at Sr in primitive mantle normalized spider diagrams (Figure 3.19). Figure 3.15B shows the variation of Sr with MgO. There is a clear difference in Sr concentration between the two basalt types. This figure indicates that the plateau basalt composition has been affected by plagioclase accumulated.

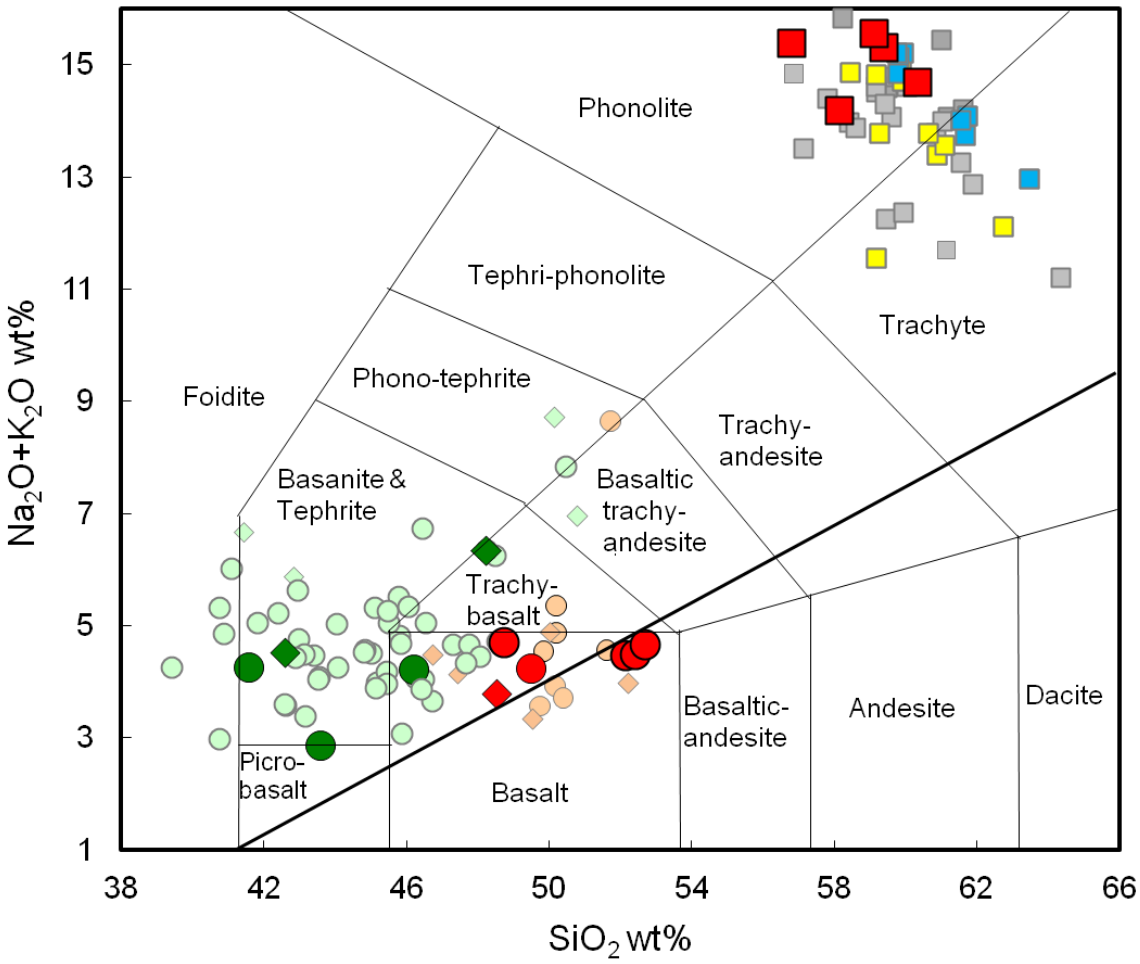

Figure 3.13 Total alkali plotted against SiO_2 for basalts and phonolites from the Garian volcanic province (after Le Bas *et al*., 1986). Red circles: plateau basalt flows; green circles: late basalt flows; diamonds: intrusions or dykes. Light colour: Published data, light green: late basalts; rose: plateau basalts and grey: phonolites from Piccoli (1970); Almond *et al*. (1974); Busrewil (1974); Hegazy (1999), Aboazom *et al*. (2006) and Lustrino *et al* (2012). Red squares: phonolites of this study; small grey squares: previous studies (Almond *et al*., 1974; Hegazy, 1999; Aboazom *et al*., 2006). Type-1 and type-2 phonolites (Lustrino *et al*., 2012) are yellow and blue squares. The subdivision of alkaline (above) and tholeiitic field (below) is distinguished by the heavy line (after Irvine and Baragar, 1971).

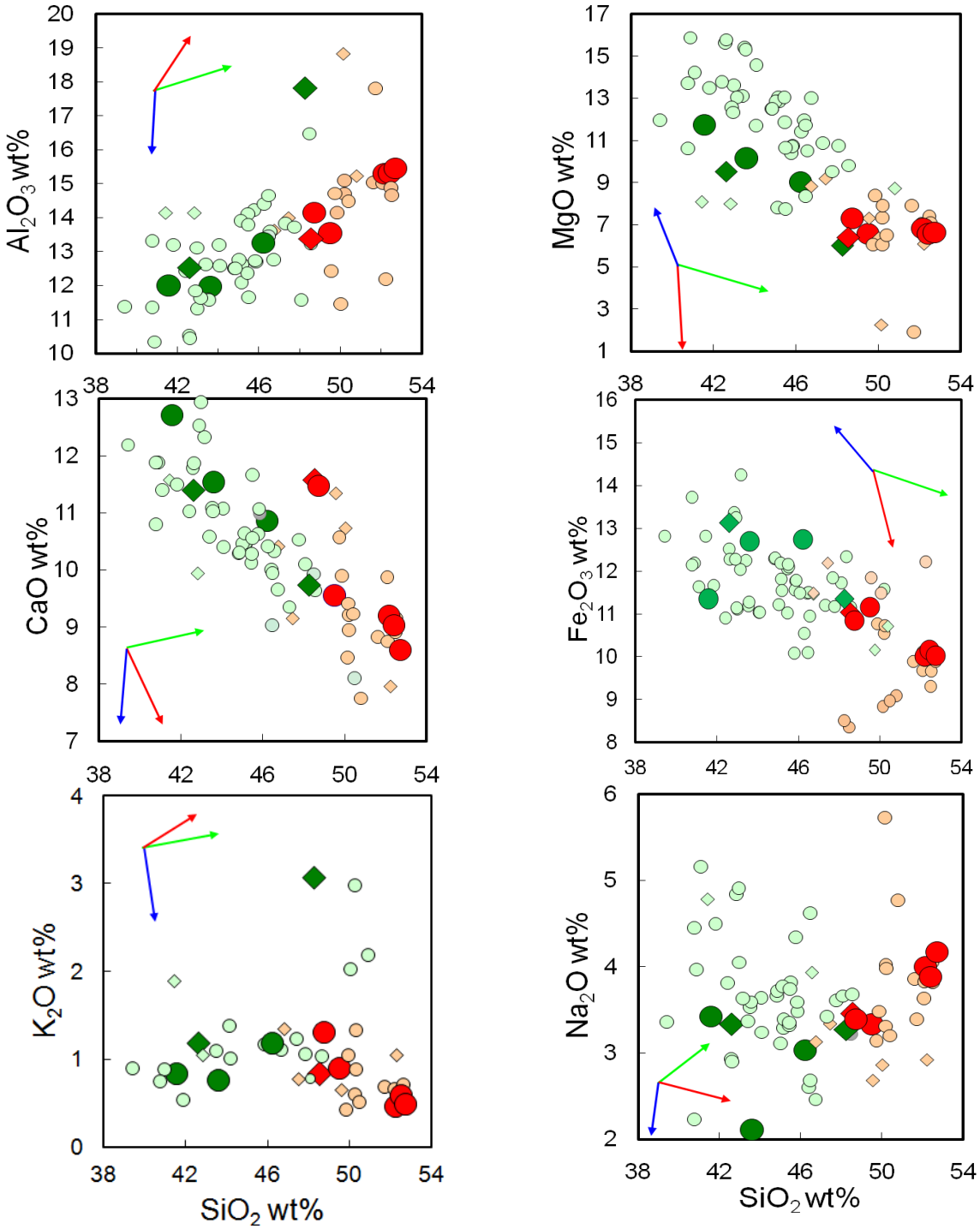

Figure 3.14: Harker diagrams of major element abundances plotted against SiO_2 wt% for basaltic rocks from the Garian volcanic province. Red: plateau basalts; green: late basalts, circles represent flows, and diamonds represent intrusions/dykes. Published data are shown as light small symbols, from Piccoli (1970); Almond *et al*. (1974); Busrewil (1974); Hegazy (1999), Aboazom *et al*. (2006) and Lustrino (2012). The arrows show the approximate effect of the removal of minerals from melts: olivine (green), clinopyroxene (red) and plagioclase (blue).

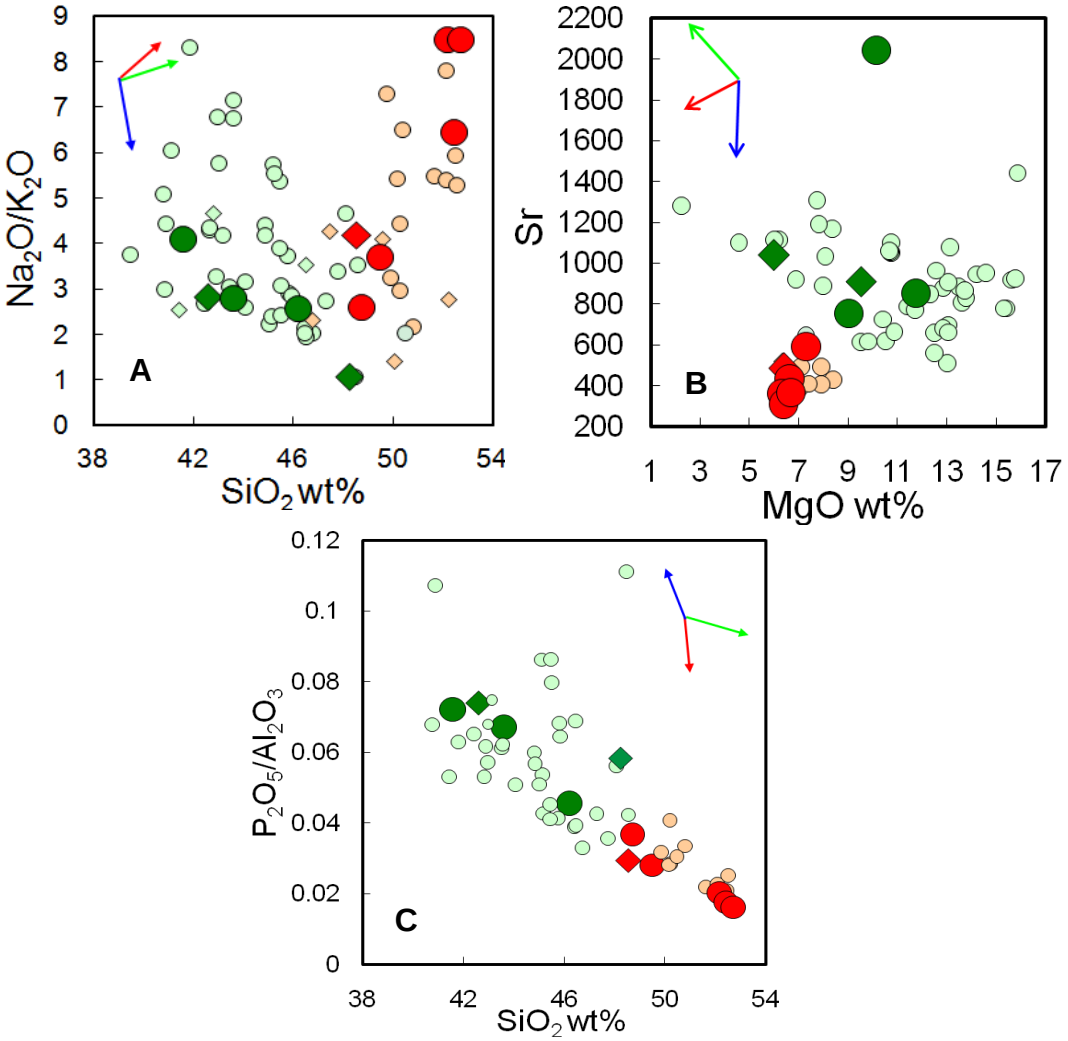

Figure 3.15: Diagrams showing major and trace element variation for basaltic rocks from the Garian volcanic province. The same symbols are used in Figure 3.14. (A): Na_2O/K_2O vs. silica; (B): Sr vs. MgO and (C): P_2O_5/Al_2O_3 ratio vs. silica.

3.3.2 Trace elements

In trace element variation diagrams (Figures 3.16 and 3.17; Tables C.3 and C.4 Appendix C) the late basalt rocks have consistently higher compatible and incompatible trace element concentrations than the plateau basalt rocks. Figure 3.16 shows trace element concentrations plotted against SiO_2. The new measurements overlap the range of previous measurements of GVP basalts, and in many cases form continuous trends (Figure 3.16) (Piccoli,

1970; Almond *et al*., 1974; Busrewil, 1974; Hegazy, 1999; Aboazom *et al*., 2006; Lustrino *et al*., 2012). Several observations can be made:
(1) The compatible elements, such as Cr, Sc and V, show a prominent negative correlation with SiO_2.

(2) High field strength elements (HFSE), such as Zr, Y and Nb, have a strong negative correlation with SiO_2.

(3) Large ion lithophile elements (LILE), such as Sr and Ba, demonstrate a significant negative correlation with SiO_2 in both plateau and late basalts.

The Figure 3.17 shows plots of several trace elements against La (an index of fractionation). In general the LILE and REE have positive correlation with La which increases from the plateau to the late basalts. This is consistent with the crystal fractionation trends identified from the variation in the major element concentrations.

3.3.3 Rare earth elements

Chondrite-normalized rare earth element patterns (Figure 3.18) show that the light rare earth elements (LREE) are enriched relative to the middle (MREE) and heavy rare earth elements (HREE). The plateau basalts and late basalts display similar but distinct trends that do not overlap. The REE content of the plateau basalt rocks range from 7 to 100 and 7 to 40 times the value of chondrite (Figure 3.17), whereas the late basalts rocks range from 8 to 160 and 11 to 240 times chondrite values (Figure 3.18).

The plateau basalts are moderately fractionated, with $(La/Yb)_N$ = 5.5 - 13.5, with no significant Eu anomaly [Eu/Eu* = 1.00-1.03; where Eu* = $Eu_N\sqrt{[(Sm_N)*(Gd_N)]}$. The late basalts display relatively smooth REE patterns with more LREE enrichment than the plateau basalts [$(La/Yb)_N$ = 20.4-17.6]. They appear to show small negative Eu-anomalies [Eu/Eu* = 0.98-0.94] that can be generated by removal of minor amounts of plagioclase.

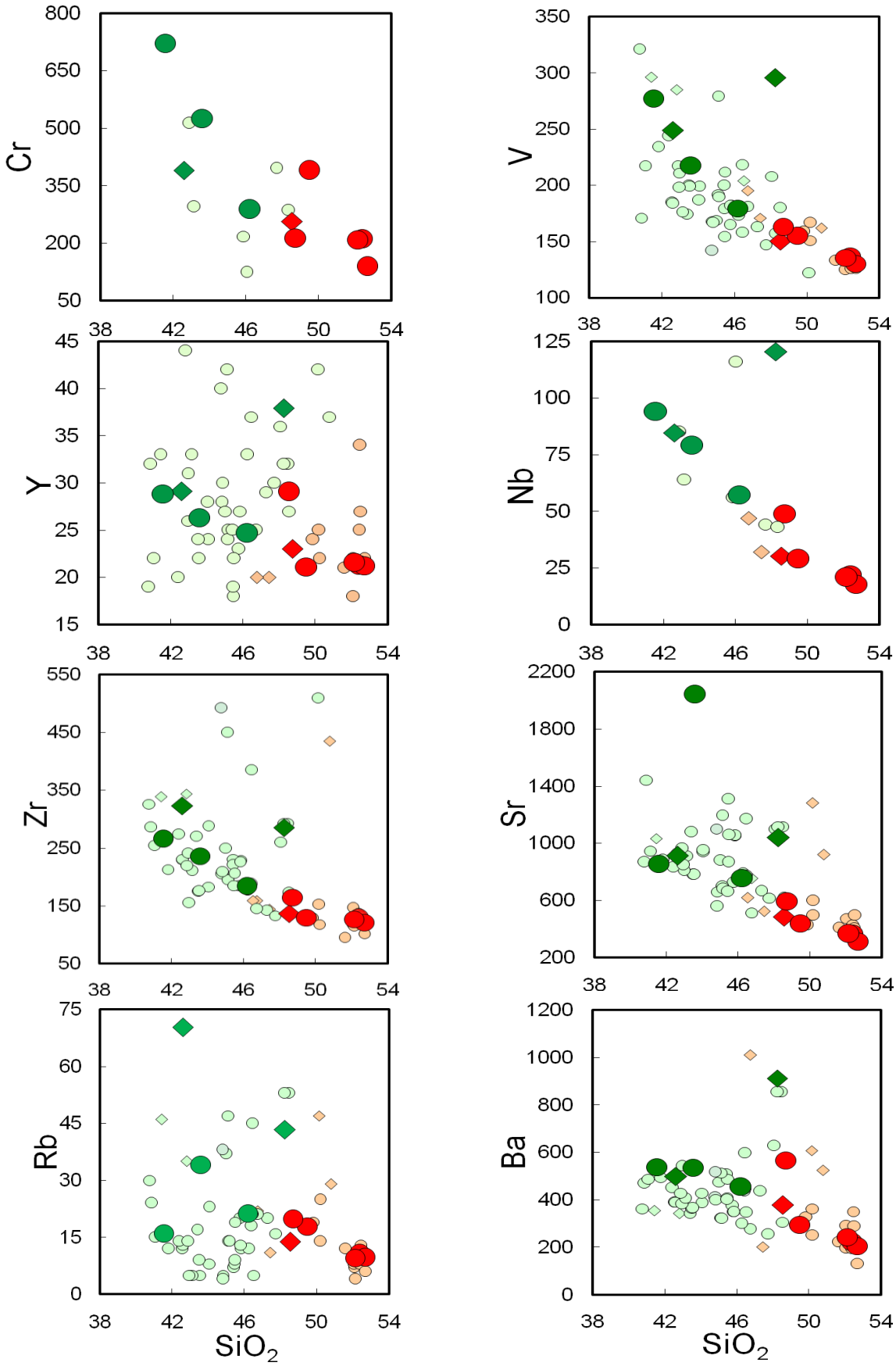

Figure 3.16: Harker diagrams of trace element abundances (ppm) against SiO_2 wt% for basaltic rocks from the Garian volcanic province. The same symbols are used in Figure 3.14.

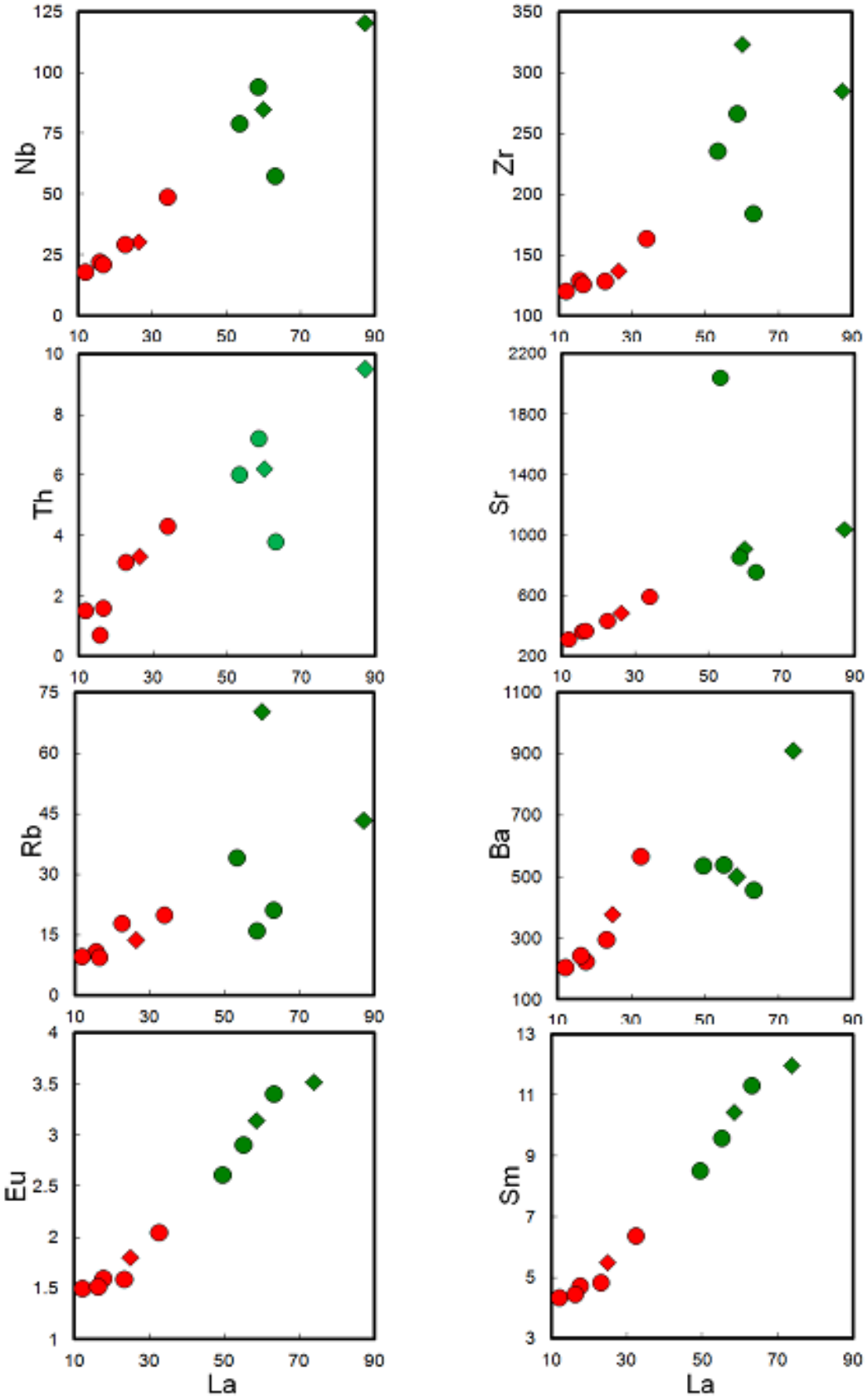

Figure 3.17: Trace element concentrations (ppm) plotted against La for basaltic rocks from the Garian volcanic province. The same symbols are used in Figure 3.14.

The rare earth element patterns of GVP basalts measured by Aboazom *et al*. (2006) and Lustrino *et al*. (2012) (5 samples) overlap these data, and fill the gap between the plateau and late basalts. This is consistent with the trace and major element data and appears to support the idea that the two basalt types are a continuous trend rather than compositionally discrete melts.

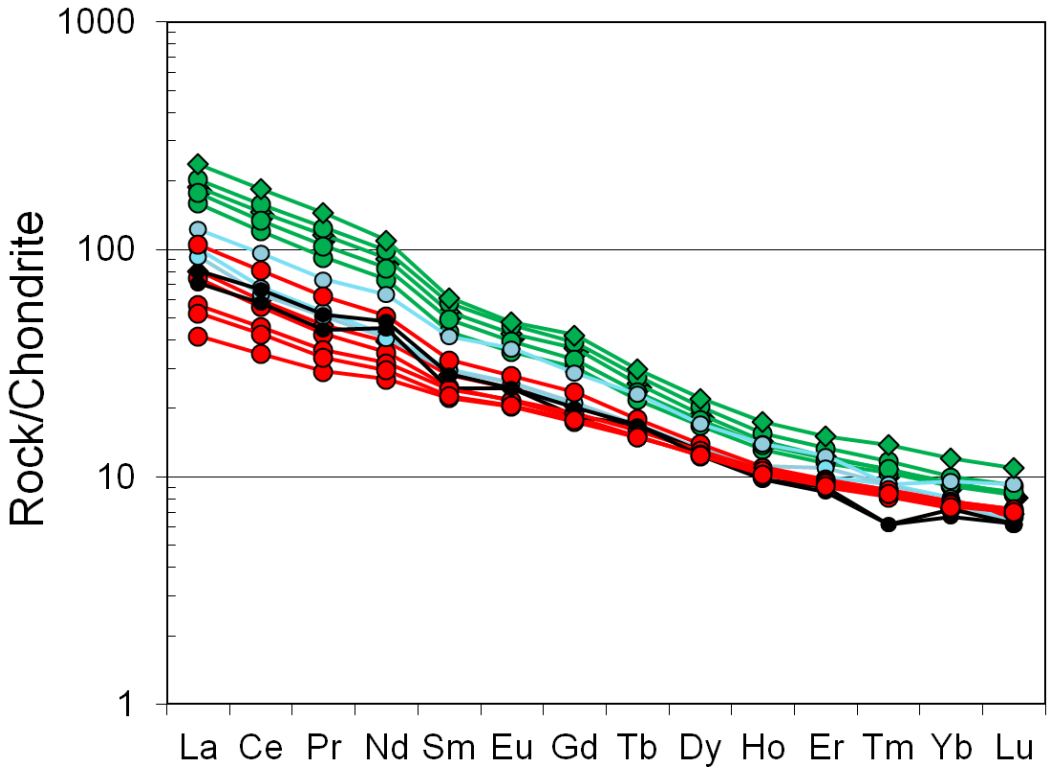

Figure 3.18: Chondrite-normalized REE patterns for basalt and phonolite rocks from the Garian volcanic province. Red circles: plateau basalt flows; green circles: late basalt flows; diamonds: intrusions or dykes. Published data are from Aboazom *et al*. (2006) (light blue) and Lustrino *et al*. (2012) (black). Chondrite values are from Nakamura (1974).

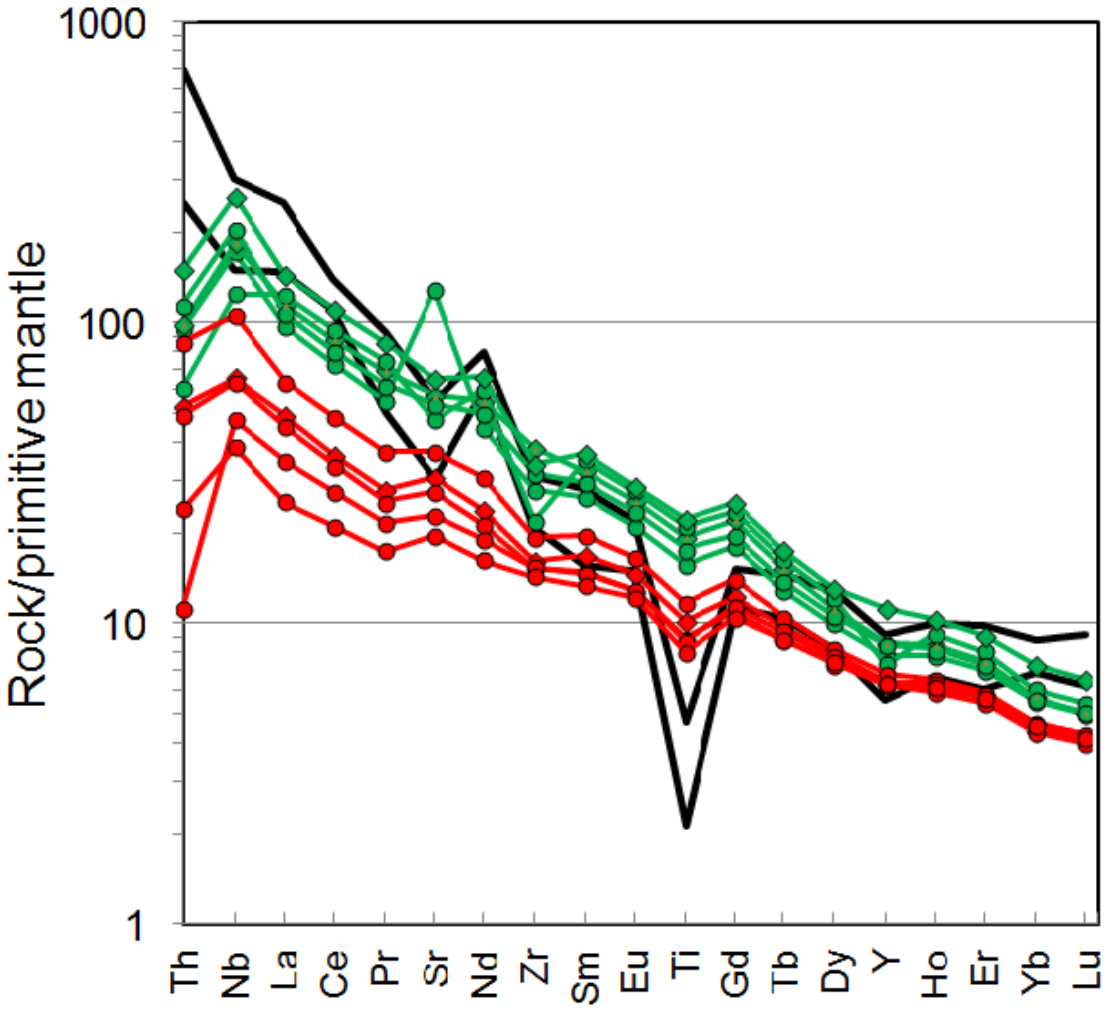

Figure 3.19: Primitive mantle normalized spider diagrams for late basalts (green lines) and plateau basalts (red lines) from the Garian volcanic province (normalization values after Lyubetskaya and Korenaga, 2007). Black lines show the compositional field of the metasomatic fluid that affected the GVP spinel lherzolite xenoliths on the basis of the composition of metasomatic clinopyroxene (Beccaluva *et al.,* 2008).

The multi-element diagram (spider diagrams) normalized against primitive mantle (Figure 3.19) can be used to constrain the source and melting characteristics of rocks (Pearce, 1983). The plateau and late basalts show relatively smooth patterns with similar trends. The deficiency of Ti in both basalt types is reflected in larger negative Ti anomalies in metasomatised lherzolites from GVP (Beccaluva *et al*., 2008).

3.3.4 Sr and Nd isotopes

The late basalts (Figure 3.20) have $^{87}Sr/^{86}Sr$ (0.70358-0.70563) that overlaps the range of plateau basalts (0.70334-0.70397). Sample G5 has a high value (0.70563) which could be generated from crustal contamination (consistent with the high Sr concentration Figure 3.16). They have $^{143}Nd/^{144}Nd$ (0.51287-0.51295) that overlap the plateau basalts (0.51281-0.51292). Dykes of both rock types have slightly more radiogenic $^{143}Nd/^{144}Nd$ and less radiogenic $^{87}Sr/^{86}Sr$ than the flows.

Lustrino *et al*. (2012) analysed five GVP basaltic rocks. $^{87}Sr/^{86}Sr$ (0.70327-0.7038) and $^{143}Nd/^{144}Nd$ (0.51283-0.51289) which overlap the measurements reported here. Beccaluva *et al*. (2008) reported Sr and Nd isotopes for seven peridotite xenoliths as well as two alkali basalts from GVP. The alkali basalts show slightly lower $^{87}Sr/^{86}Sr$ (0.70319-0.70320) and higher $^{143}Nd/^{144}Nd$ (0.51299-0.51295) than this study. Clinopyroxene from the metasomatised xenolith have lower $^{87}Sr/^{86}Sr$ (0.70227-0.70304) and higher $^{143}Nd/^{144}Nd$ (0.51387-0.51296) than the basalts. The xenolith and basalt fields do not overlap. However, the isotope composition of the basalts is closest to the most metasomatised mantle xenoliths based on their LREE enrichment (Beccaluva *et al*. 2008).

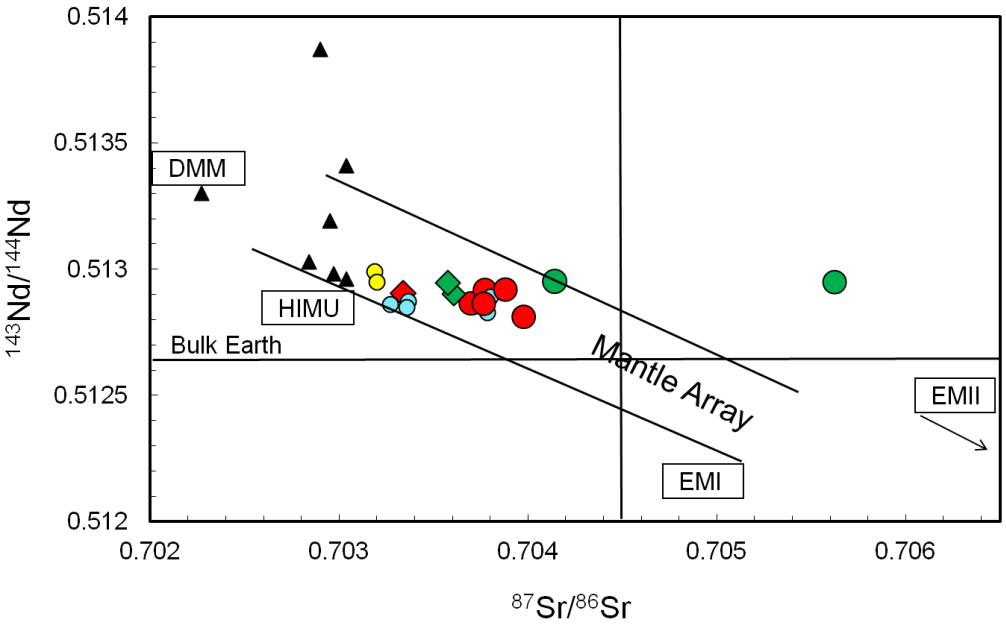

Figure 3.20: $^{143}Nd/^{144}Nd$ vs. $^{87}Sr/^{86}Sr$ composition of basalts from the Garian volcanic province. Red circles: plateau basalt flows; green circles: late basalt flows; diamonds: intrusions or dykes. Published data are from Beccaluva *et al*. (2008) (basaltic rocks, yellow circles and xenoliths, black triangles) and Lustrino *et al*. (2012) (light blue), and mantle end-member compositions (Zindler & Hart, 1986). DMM = depleted mantle; and EMII = enriched mantle type 2 and HIMU = mantle with high U/Pb ratio.

3.3.5 Implications of the basalt geochemistry

The geochemical observations reveal information about the magmatic differentiation history and source of the volcanism which will be discussed in the next chapter. The results are summarised as follows:

1. The overlap of $^{87}Sr/^{86}Sr$ and $^{143}Nd/^{144}Nd$, and the similarity of the REE patterns in both basalt types, indicates that they are derived from a similar mantle source.

2. The major, trace and rare earth element variations suggest that fractional crystallisation was a key process in the evolution of the basaltic magmas, and links the two basalt types.

3. The geochemistry places constraints on the source of the basalts:

(i) Garian basalts are enriched in LREE relative to HREE indicating equilibration of the basaltic melts with shallow mantle in the spinel-garnet transition facies (i.e. < 80–90 km) (Nickel, 1986; Adam and Green, 2006).

(ii) The prevalent HIMU fingerprint and trace element modelling (negative Ti anomalies) of basaltic rocks and associated mantle xenoliths, suggest that the origin of the basalts rock is linked to a common sub-lithospheric metasomatic event across the Garian region.

3.4 Geochronology

$^{40}Ar/^{39}Ar$ age determinations were made on the purified groundmass separates from all samples at SUERC. Sample preparation and analysis procedures are described in Appendix D along with the data tables.

3.4.1 $^{40}Ar/^{39}Ar$ age determinations

Samples of groundmass were subjected to incremental heating $^{40}Ar/^{39}Ar$ age determinations. Results for the 11 samples are shown in Tables 3.2 and 3.3. The results of step-heating analyses of the basalts are generally plotted as the cumulative percent of ^{39}Ar released (x axis) against apparent age (y axis) for each step. K/Ca ratios were calculated for each increment from the measured $^{39}Ar/^{37}Ar$ ratios. The $^{40}Ar/^{39}Ar$ data are reported as plateau ages, inverse isochron and integrated ages.

Three criteria were used to determine whether the data generated are geologically significant: (1) the plateau must represent > 50% of the ^{39}Ar released; (2) the plateau and isochron (slope that result by plotting the atmospheric related $^{36}Ar/^{40}Ar$ against the radiogenic $^{39}Ar/^{40}Ar$) ages must agree within uncertainty; and (3) the MSWD (mean square of weighted deviation) must be < 2 (Sarah, 2009). The plateau diagrams plot the data at 95% confidence level (2σ) and the result at 68% confidence level (1σ) while the isochrons data and results are presented at 68% confidence level (1σ).

3.4.1.1 Plateau basalts

3.4.1.1.1 G14 dolerite dyke, Kabdet El Gamel

The plateau age of 27.911 ± 0.046 Ma (1σ, presented at 68% confidence level with internal precision, the age of mineral standards and the unknown sample are irradiated at the same time) is determined from 86 % of the ^{39}Ar released (steps 2 to 10 from 12 age steps). K/Ca decrease from middle to high temperature, the last 3 steps correspond to the degassing of K-poor, Ca-rich mineral phases (plagioclase and/or pyroxene). The integrated age (27.900 ± 0.200 Ma) is indistinguishable from the plateau age. Slightly older ages in the lower temperature fraction (step 1) may be caused by excess of ^{40}Ar or recoil of ^{39}Ar gas. The inverse isochron yields an age that overlaps with the plateau and integrated age. It has an initial ^{40}Ar/^{36}Ar of 299 ± 2 (1σ) that is statistically equivalent to the atmospheric value (298.56 ± 0.31: Lee *et al*., 2006 and Mark *et al*., 2011b) (Figure 3.21 and Table 3.2). The absolute age relative to Renne *et al*. (2010, 2011) is 28.187 ± 0.050 Ma. Note that the Renne et al. (2010, 2011) optimization model outputs ages and uncertainties including full systematic errors (i.e., standard age and decay constant uncertainty).

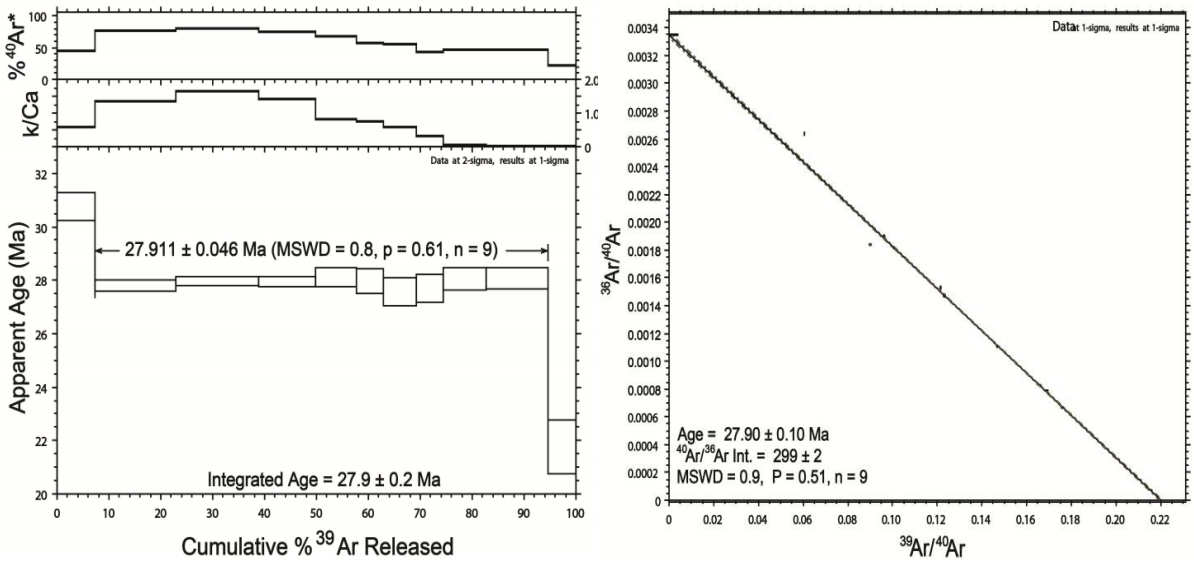

Figure 3.21: ^{40}Ar/^{39}Ar age spectra (left) and inverse isochron plot (right) for dolerite dyke (sample G14).

3.4.1.1.2 G32B tholeiitic olivine basalt, Wadi Al Waar

This sample yields a plateau age of 5.382 ± 0.035 Ma (MSWD = 1.000) for 87 % of the ^{39}Ar released (steps 1 to 8 from 12 age steps). The integrated age (5.340 ± 0.040 Ma) overlaps with the plateau age. The isochron age (5.360 ± 0.080 Ma) is indistinguishable from the plateau and integrated age. The trapped $^{40}Ar/^{36}Ar$ = 299 ± 1.0 with an acceptable MSWD of 1. This is indistinguishable from atmospheric composition and demonstrates the absence of detectable excess $^{40}Ar^*$ (Figure 3.22 and Table 3.2). The K/Ca systematically decreases with the increase of degassing temperatures. K/Ca shows the lowest value in the highest degassing temperature, probably reflecting the effect of degassing from Ca-rich minerals, such as clinopyroxene. The $^{40}Ar^*$ increase with the increase of degassing temperatures but decreases within the last four steps at highest temperatures as recoil of ^{39}Ar gas. The absolute age relative to Renne *et al*. (2010, 2011) is 5.435 ± 0.035 Ma.

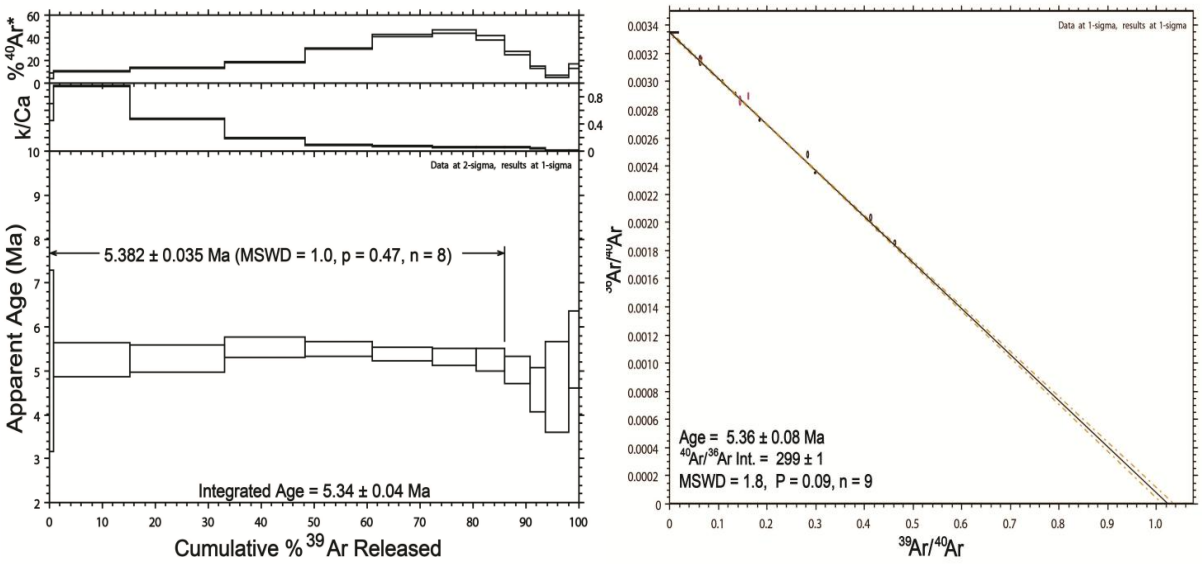

Figure 3.22: $^{40}Ar/^{39}Ar$ age spectra (left) and inverse isochron plot (right) for tholeiitic olivine basalt (sample G32B).

3.4.1.1.3 G8B olivine basalt from Wadi Qidmu

The plateau age of 4.703 ± 0.009 Ma recorded from all steps (1σ, internal precision) is comparable to the inverse isochron of 4.710 ± 0.010 Ma. The $^{40}Ar/^{36}Ar$ of 296 ± 2 is indistinguishable from the atmospheric value, with low MSWD = 1.00 and p (probability value) = 0.41 indicating generally good correspondence between expected errors and estimated errors. Further the inverse isochron analysis is indistinguishable from plateau ages showing the data to be robust. These ages are comparable with the integrated age of 4.700 ± 0.010 Ma, comprising step ages with the same systematically decreasing of high $^{40}Ar^*$ and low K/Ca ratios (Figure 3.23 and Table 3.2). The recalculated age relative to Renne *et al*. (2010, 2011) is 4.750 ± 0.010 Ma.

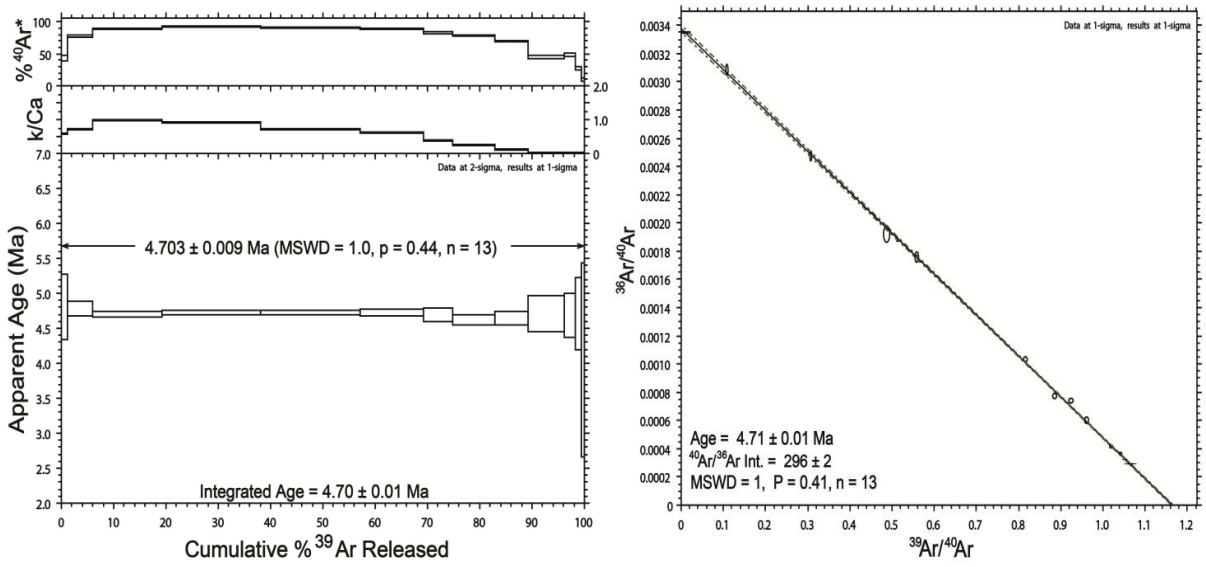

Figure 3.23: $^{40}Ar/^{39}Ar$ age spectra (left) and inverse isochron plot (right) for an olivine basalt (sample G8B).

3.4.1.1.4 G15B porphyritic tholeiitic basalt, Wadi Hashem

The plateau age of this sample is 4.430 ± 0.021 Ma (1σ, internal precision; MSWD = 1.40) for 90% of the ^{39}Ar released (steps 1 to 8 from 12 age steps). The integrated age is indistinguishable from the plateau of 4.440 ± 0.030 Ma. The higher temperature steps yielded slightly older ages than the plateau (steps 10 to 13) may be caused by recoil loss of ^{39}Ar. This step ages comprising with relatively low ^{40}Ar* and K/Ca ratios which may be caused by recoil of ^{37}Ar gas. An inverse isochron yields age of 4.460 ± 0.060 Ma (MSWD = 1.50, p = 0.16) with ^{40}Ar/^{36}Ar intercept (297 ± 2). The near-atmospheric initial ^{40}Ar/^{36}Ar ratio suggests that there is no significant excess argon in this sample (Figure 3.24 and Table 3.2). The recalculated age relative to Renne *et al*. (2010, 2011) is 4.474 ± 0.021 Ma.

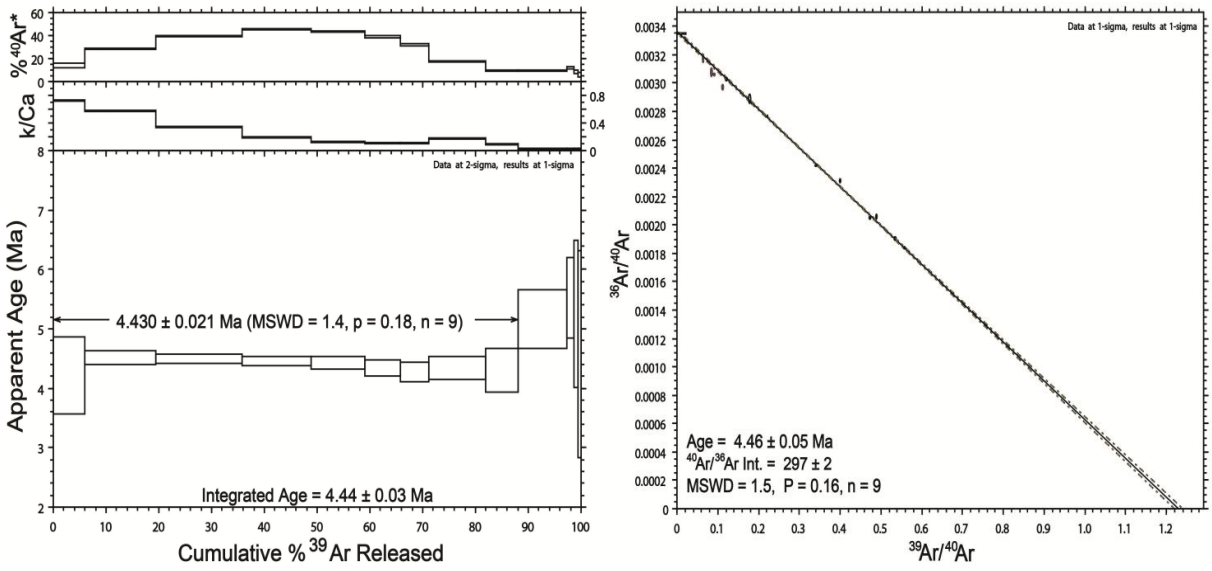

Figure 3.24: ^{40}Ar/^{39}Ar age spectra (left) and inverse isochron plot (right) for a tholeiitic basalt (sample G15B).

3.4.1.1.5 G116B tholeiitic olivine basalt, Wadi Ghan

G116B was the only plateau basalt sample that failed to produce a plateau age. It displays a classic saddle-shape pattern indicating excess or inherited argon (see inverse isochron diagram, higher than atmospheric composition) (Lanphere and Dalrymple, 1976). The youngest ages observed in the spectra are 2.500 to 3.600 Ma. The integrated age is 4.330 ± 0.090 Ma and can therefore only be interpreted as a maximum age (Integrated age ± uncertainty ×√MSWD is given the best summary age) (Figure 3.25 and Table 3.2). This sample exhibits decreasing K/Ca in the higher temperature fractions. The absolute maximum age relative to Renne *et al*. (2010, 2011) is 4.373 ± 0.091 Ma.

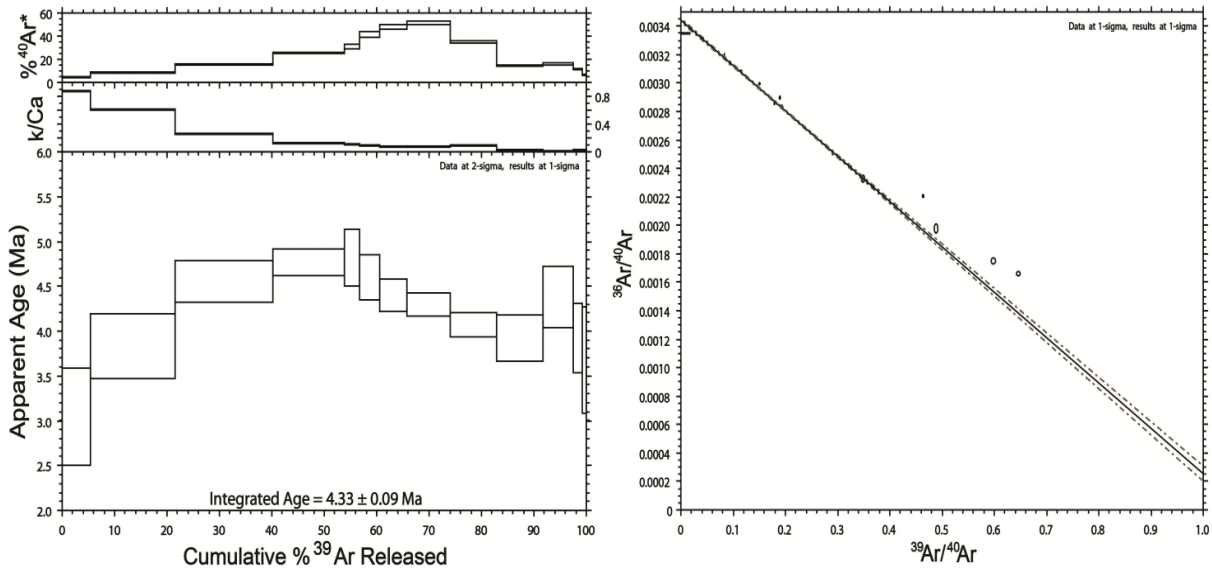

Figure 3.25: $^{40}Ar/^{39}Ar$ age spectra (left) and inverse isochron plot (right) for a tholeiitic olivine basalt (sample G116B).

3.4.1.1.6 G9 tholeiitic olivine basalt, Wadi Ghan

This sample produced data similar to that of G8B and similar interpretations apply. The plateau age 2.643 ± 0.010 Ma is from all steps. It is indistinguishable from the inverse isochron of 2.650 ± 0.010 Ma. The initial $^{40}Ar/^{36}Ar$ of 298 ± 1 (MSWD = 1.60; p = 0.10) is indistinguishable from air. Further the isochron and plateau ages overlap and show the data to be robust. These ages are comparable with the integrated age of 2.640 ± 0.010 Ma. These analyses have low K/Ca ratios and high $^{40}Ar^*$ more than 60 % an average (Figure 3.26 and Table 3.2) indicating a chemically homogenous population of minerals in the groundmass. The recalculated age relative to Renne *et al*. (2010, 2011) is 2.669 ± 0.010 Ma.

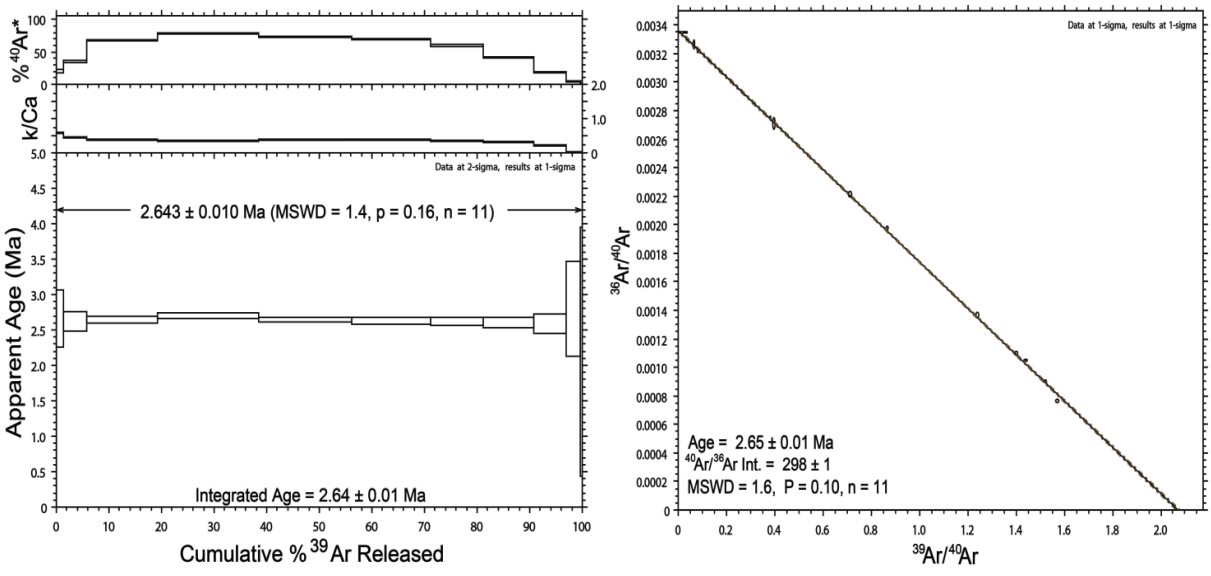

Figure 3.26: $^{40}Ar/^{39}Ar$ age spectra (left) and inverse isochron plot (right) for a tholeiitic olivine basalt (sample G9).

Table 3.2: $^{40}Ar/^{39}Ar$ data of the plateau basalt samples.

Decay constants of Steiger & Jager (1977), Fish Canyon sanidine at 28.02 ± 0.16 Ma (Renne *et al*., 1998), atmospheric argon isotope ratios of Lee *et al*. (2006) and Mark *et al*. (2011b) (298.56 ± 0.31).														Optimisation model (Renne *et al*., 2010, 2011) - full external precision (standard age, decay constant).	
ID	Sample type	Mass (mg)	Plateau age (Ma)	(1σ)	^{39}Ar (%)	MSWD	Isochron age (Ma)	(1σ)	$^{40}Ar/^{36}Ar$	(1σ)	MSWD	Integrated age (Ma)	(1σ)	Age (Ma)	(1σ)
G14	Dolerite (dyke)	285	27.911 (*n* = 9)	0.046	86	0.800	27.900 (*n* = 9)	0.100	299	2.000	0.900	27.900	0.200	28.187	0.050
G32B	Basalt	281	5.382 (*n* = 8)	0.035	87	1.000	5.360 (*n* = 9)	0.080	299	1.000	1.800	5.340	0.040	5.435	0.035
G8B	Basalt	262	4.703 (*n* = 13)	0.009	100	1.000	4.710 (*n* = 13)	0.010	296	2.000	1.000	4.700	0.010	4.750	0.010
G15B	Basalt	284	4.430 (*n* = 9)	0.021	90	1.400	4.460 (*n* = 9)	0.050	297	2.000	1.500	4.440	0.030	4.474	0.021
G116B	Basalt	289	- (*n* = 0)	-	-	-	- (*n* = 0)	-	-	-	-	4.330	0.090	4.373	0.091
G9	Basalt	301	2.643 (*n* = 11)	0.010	100	1.400	2.650 (*n* = 11)	0.010	298	1.000	1.600	2.640	0.010	2.669	0.010

3.4.1.2 Late basalt rocks

3.4.1.2.1 G10B syenogabbro plug, Ras al Moher

Sample G10B was the only late basalt rock that failed to produce a plateau age. It displays a classic saddle-shape pattern on the age spectrum diagram. The three oldest age fractions at middle temperature steps (3 to 5) contained only 25 % of total ^{39}Ar with high $^{40}Ar^*$ and low K/Ca ratios. This sample exhibits decreasing K/Ca within the first five steps then increasing with the last six steps (two phases) with high $^{40}Ar^*$. The high K/Ca ratios suggest that most of the argon was evolved from a K-rich phase (e.g., alkali feldspar). The integrated age = 16.000 ± 3.000 Ma (Figure 3.27 and Table 3.3) (Integrated age ± uncertainty ×√MSWD is given the best summary age). The absolute maximum age relative to Renne *et al*. (2010, 2011) is 16.231 ± 3.043 Ma. This intrusion was previously dated by K/Ar to be 11.5 ± 0.4 Ma (Piccoli, 1971). This age could be affected by excess Argon contamed in phenocrysts and/or xenocrysts.

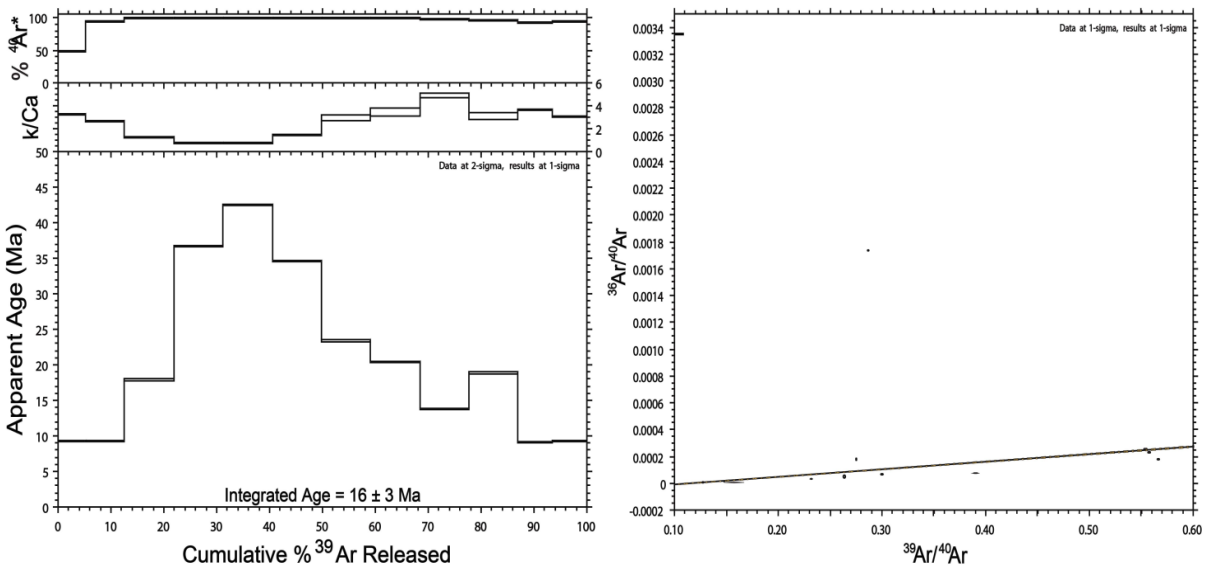

Figure 3.27: $^{40}Ar/^{39}Ar$ age spectra (left) and inverse isochron plot (right) for the syenogabbro G10B.

3.4.1.2.2 G1 basanite from 33 km south of Garian

The plateau age of 10.471 ± 0.160 Ma has a low MSWD of 0.5 for 92 % of the ^{39}Ar released (steps 1 to 7 from 10 age steps). The ^{40}Ar* decreases while K/Ca increases within the temperature. This sample gives an integrated age (10.430 ± 0.100 Ma) that is indistinguishable from the plateau age. Slightly younger ages occur in the higher temperature fractions (step 8 to 10) may be caused by recoil of ^{39}Ar. The isochron age (10.490 ± 0.040 Ma) overlaps with the plateau and integrated age. The initial ^{40}Ar/^{36}Ar of 297 ± 3 is statistically equivalent to modern day atmosphere (298.56 ± 0.31: Lee *et al*., 2006 and Mark *et al*., 2011b) (Figure 3.28 and Table 3.3). The absolute age relative to Renne *et al*. (2010, 2011) is 10.574 ± 0.017 Ma.

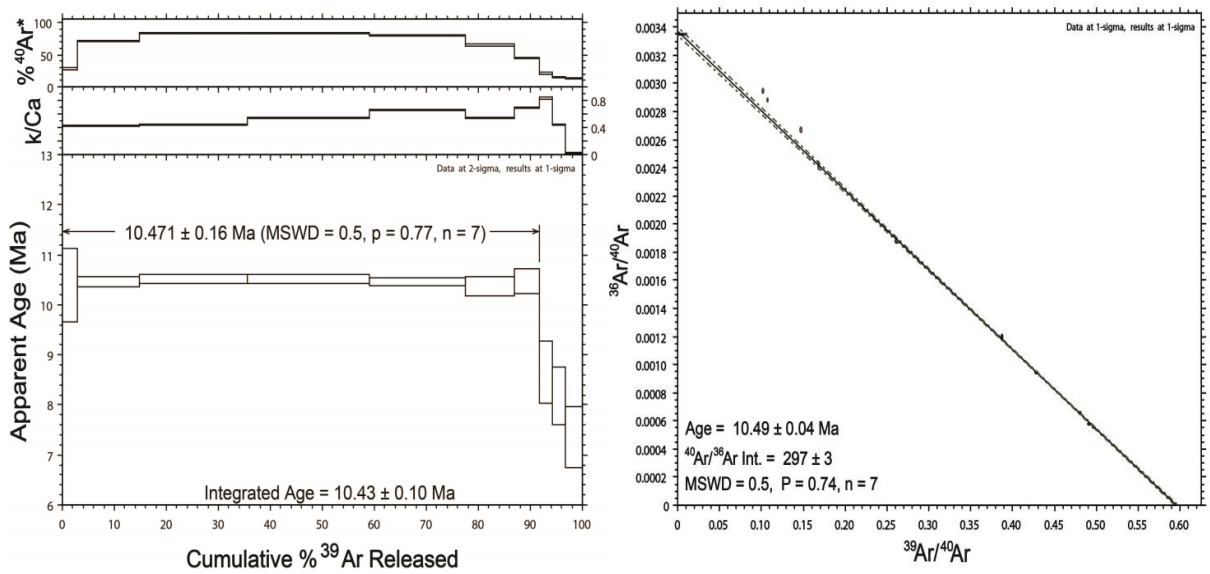

Figure 3.28: ^{40}Ar/^{39}Ar age spectra (left) and inverse isochron plot (right) for a basanite plug (sample G1).

3.4.1.2.3 G5 basanite lava from 31.5 km east of Garian

The plateau age of 4.271 ± 0.018 Ma is recorded from all steps (1σ, internal precision) and is comparable to the inverse isochron of 4.280 ± 0.030 Ma. The $^{40}Ar/^{36}Ar$ ratio at of 297 ± 3 is indistinguishable from atmospheric composition with low MSWD of 0.70 and p of 0.69. Further the inverse isochron and plateau ages are overlap and showing the data to be robust. These ages are comparable with the integrated age of 4.270 ± 0.020 Ma. This sample also has slight decreasing of low K/Ca ratios (≤ 0.8) and $^{40}Ar^*$ over more moderate and high temperature fractions, likely to be caused by degassing of pyroxene (Figure 3.29 and Table 3.3). The recalculated age relative to Renne *et al*. (2010, 2011) is 4.313 ± 0.018 Ma.

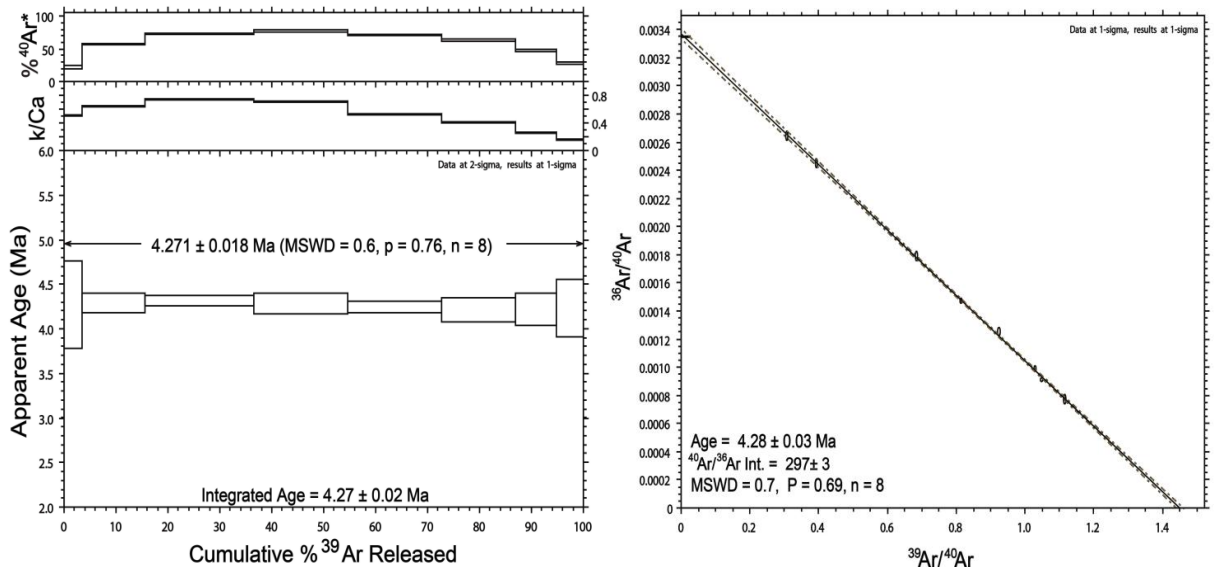

Figure 3.29: $^{40}Ar/^{39}Ar$ age spectra (left) and inverse isochron plot (right) for a basanite rock (sample G5).

3.4.1.2.4 G6 alkali olivine basalt from 35 km northeast of Garian

The plateau age of 4.133 ± 0.011 Ma (1σ, internal precision) with low MSWD of 1.00 is determined from 90 % of the ^{39}Ar released (steps 1 to 8 from 10 age steps). The ^{40}Ar* and K/Ca increases within the first three steps and constant at medium of temperatures than decreases within the high temperatures. It yields an integrated age (4.110 ± 0.040 Ma) that is indistinguishable from the plateau age. The high temperature (steps 9 and 10) yields lower ages due to recoil loss of irradiation produced ^{37}Ar (Koppers *et al*., 2000). The inverse isochron yields an age (4.130 ± 0.020 Ma) overlaps with the plateau and integrated age. The initial ^{40}Ar/^{36}Ar of 300 ± 3 is statistically equivalent to modern day atmosphere (298.56 ± 0.31: Lee *et al*., 2006 and Mark *et al*., 2011b) (Figure 3.30 and Table 3.3). The absolute age relative to Renne *et al*. (2010, 2011) is 4.174 ± 0.012 Ma.

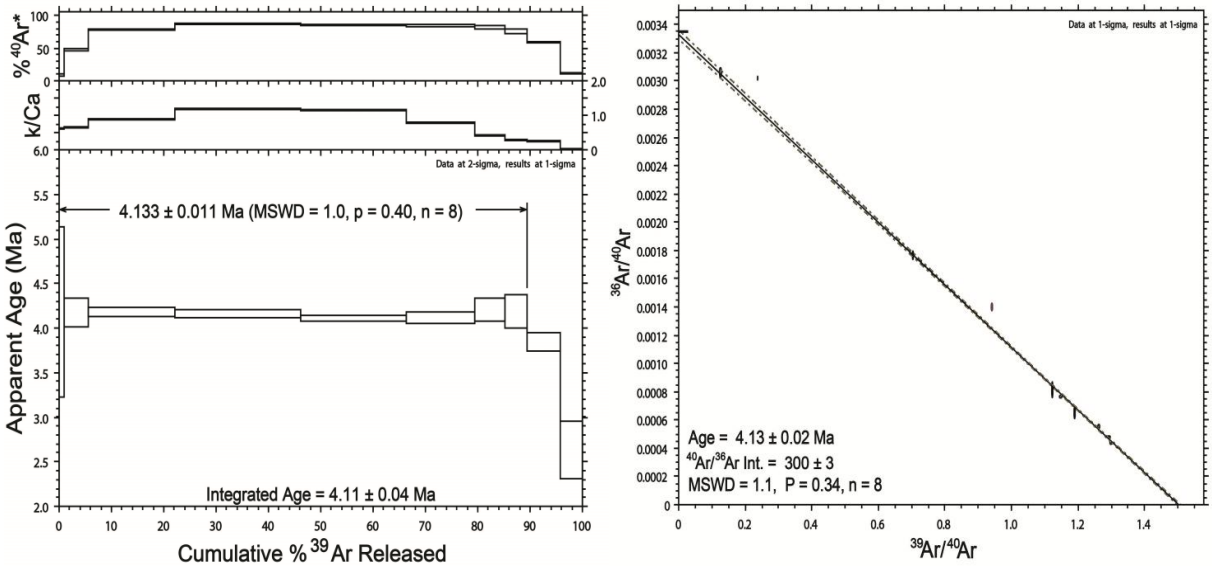

Figure 3.30: ^{40}Ar/^{39}Ar age spectra (left) and inverse isochron plot (right) for an alkali olivine basalt (sample G6).

3.4.1.2.5 G2 basanite lava from 19 km southeast of Garian

This sample produced data similar to that of G5 and similar interpretations apply. The statistically robust age use plateau age of 3.772 ± 0.011 Ma is from all steps. It is indistinguishable from the inverse isochron of 3.800 ± 0.020 Ma. The $^{40}Ar/^{36}Ar$ of 293 ± 3 with MSWD of 0.40 is slightly lower than the atmosphere ruling out excess ^{40}Ar. Further the inverse isochron and plateau ages are overlap with integrated age of 3.770 ± 0.010 Ma and show the data to be robust. The low K/Ca ratios (≤ 0.8) suggest that most of the argon was evolved from a K-poor phase (e.g., pyroxene) (Figure 3.31 and Table 3.3). The recalculated age relative to Renne *et al*. (2010, 2011) is 3.809 ± 0.011 Ma.

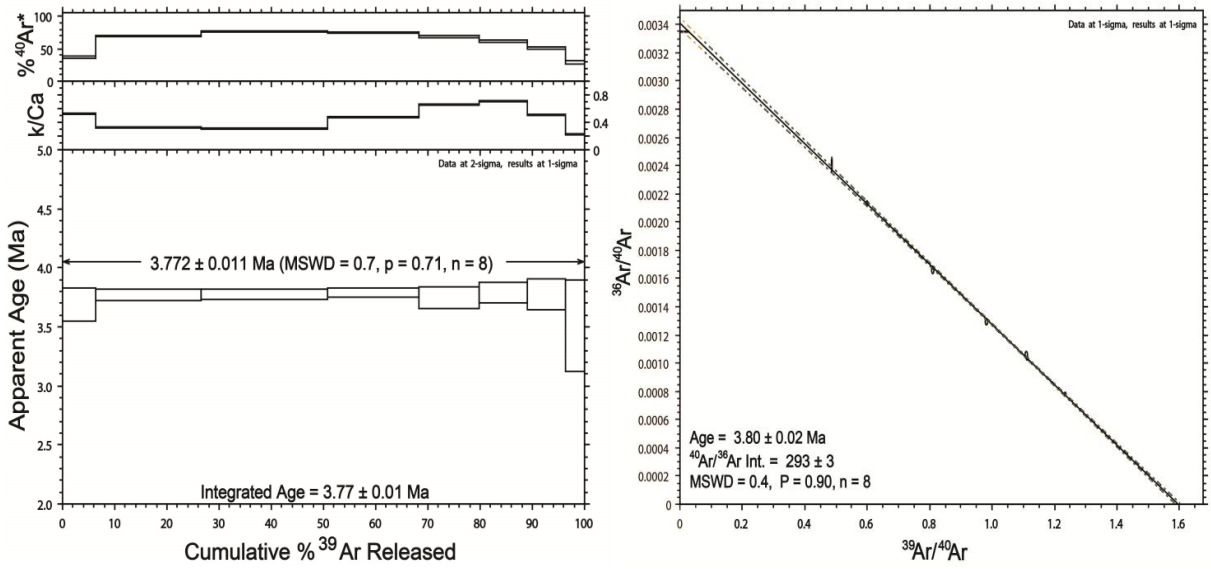

Figure 3.31: $^{40}Ar/^{39}Ar$ age spectra (left) and inverse isochron plot (right) for basanite rock (sample G2).

Table 3.3: $^{40}Ar/^{39}Ar$ data of the late basalt samples.

Decay constants of Steiger & Jager (1977), Fish Canyon sanidine at 28.02 ± 0.16 Ma (Renne *et al*., 1998), atmospheric argon isotope ratios of Lee *et al*. (2006) and Mark *et al*. (2011b) (298.56 ± 0.31).													Optimisation model (Renne *et al*., 2010, 2011) - full external precision (standard age, decay constant).	
ID	Sample type	Mass (mg)	Plateau age (Ma)	(1σ)	^{39}Ar (%)	MSWD	Isochron age (Ma)	(1σ)	$^{40}Ar/^{36}Ar$	(1σ)	MSWD	Integrated age (Ma)	(1σ)	Age(Ma)	(1σ)
G10B	Gabbro (intrusive)	268	- (*n* = 0)	-	-	-	- (*n* = 0)	-	-	-	-	16.000	3.000	16.231	3.043
G1	Dolerite (intrusive)	280	10.471 (*n* = 7)	0.016	92	0.500	10.490 (*n* = 7)	0.040	297	3.000	0.500	10.430	0.100	10.574	0.017
G5	Basalt	297	4.271 (*n* = 8)	0.018	100	0.600	4.280 (*n* = 8)	0.030	297	3.000	0.700	4.270	0.020	4.313	0.018
G6	Basalt	234	4.133 (*n* = 8)	0.011	90	1.000	4.130 (*n* = 8)	0.020	300	3.000	1.100	4.110	0.040	4.174	0.012
G2	Basalt	286	3.772 (*n* = 8)	0.011	100	0.700	3.800 (*n* = 8)	0.020	293	3.000	0.400	3.770	0.010	3.809	0.011

3.4.2 Implications of the basalt geochronology

High precision $^{40}Ar/^{39}Ar$ age determinations of the Garian province basalts reveal:

(1) The two basalt types have overlapping range of ages; 5.44 ± 0.04 to 2.67 ± 0.01 Ma (plateau basalts) and 4.31 ± 0.02 to 3.81 ± 0.01 Ma (late basalts). This confirms petrographic and geochemical evidence that they are not distinct basalt types produced at different times as proposed by earlier workers (Piccoli, 1971; Schult and Soffel, 1973; Almond *et al*., 1974; Busrewil, 1974; Ade-Hall *et al*., 1975).

(2) The plateau basalts erupted over a much shorter duration (from 5.44 ± 0.04 to 2.67 ± 0.01 Ma) (~ 3 Ma) than previously established (Figure 3.32). K/Ar ages (53.50 ± 1.90 to 3.5 ± 0.10) of the oldest plateau basalt were ~50 Ma (Piccoli, 1971). The old K/Ar ages probably reflect the presence of excess Ar in phenocrysts (McDougall *et al*., 1969).

(3) The intrusive rocks record the oldest ages determined here. A dolerite dyke (G14) from the plateau basalts is 28.19 ± 0.05 Ma. A syenogabbro (G10B) and basalt plug (G1) give ages of 16.23 ± 3.04 and 10.57 ± 0.02 Ma, respectively.

The lava ages confirm that the two basalt types erupted simultaneously. The absence of basaltic lavas associated with the old intrusives indicates that the region has been affected by erosion that may have removed most traces of lava erupted before 4-5 Ma.

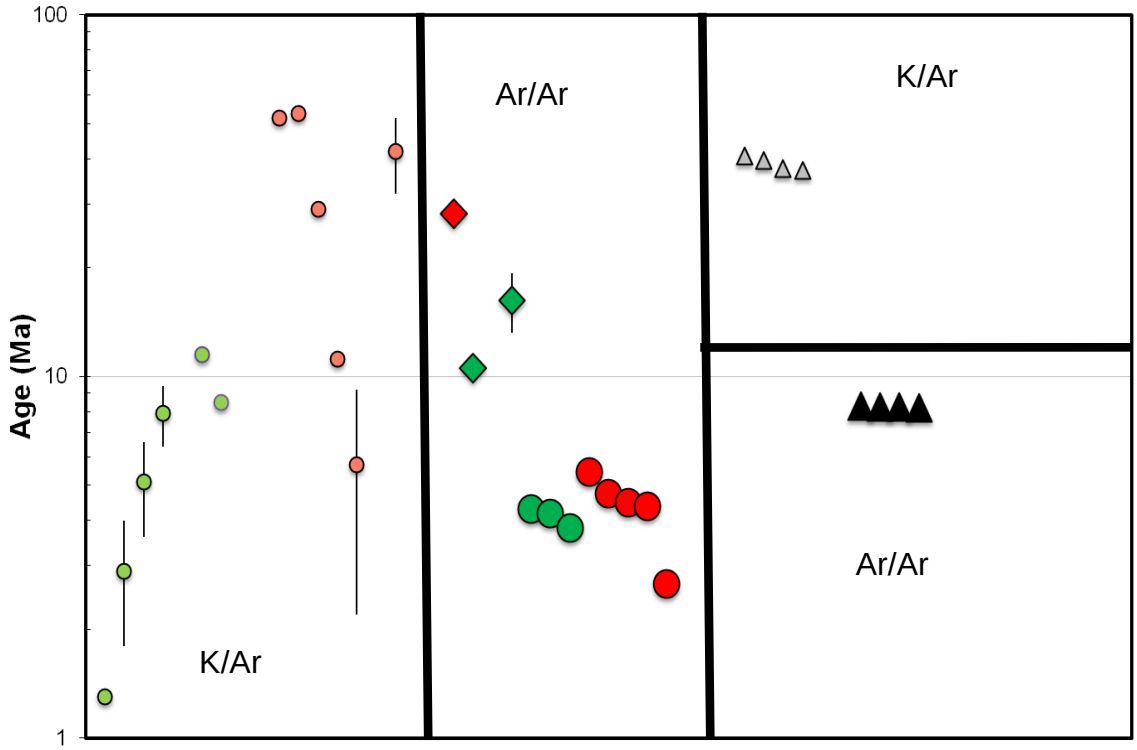

Figure 3.32: Comparison of new $^{40}Ar/^{39}Ar$ ages (relative to the Optimisation Model of Renne *et al*., 2010, 2011) to existing K/Ar ages of the Garian volcanic province. Red circles: plateau basalt flows; green circles: late basalt flows. Basaltic intrusions are shown as diamonds. Phonolites are black triangles. Small symbols (K/Ar and palaeomagnetic age) are previously published data (Mobil Oil Company, 1967; Piccoli, 1971; Schult and Soffel, 1973). Bars show the range of uncertainty.

Chapter Four

Petrogenesis of the Garian basaltic rocks

4.1 Introduction

The petrography and geochemistry of the GVP basalt provided in Chapter 3 indicates that they were produced by magmatic differentiation of basalt magma. In this chapter I use the data to place constraints on the genesis and evolution of the basaltic melts. Specifically, the aims of this chapter are:

1. To evaluate the role of crustal contamination/assimilation.
2. To determine the extent that the compositional variation can be explained by fractionation of the main phenocryst phases.
3. To estimate the degree of partial melting that generated the basalts.
4. To determine the mineral and chemical composition of the mantle source.

4.2 Crustal contamination

4.2.1 Introduction

The rocks of the continental crust are generally enriched in Ba, Rb, K, La, Ce and Sr relative to Th, Nb, REE, Y, Zr and Hf in comparison with mantle melts (Rudnick and Gao, 2003). Assimilation of crustal rocks by basaltic melts tends to increase the concentration of these elements. The continental crust is enriched in Rb relative to Sr and evolves radiogenic $^{87}Sr/^{86}Sr$ (Gast, 1960).

The combination of crustal assimilation and fractional crystallisation (AFC) has proved to be a common mechanism for modifying the composition of basaltic magmas in the continental crust. DePaolo (1981) developed a quantitative framework to examine the effects of AFC by combining trace element and radiogenic isotopic data that are sensitive to open system differentiation. Numerous studies of basaltic flows from continental areas have demonstrated the importance of crustal contamination (e.g. De Paolo, 1981; Watson, 1982;

Huppert and Sparks, 1985). Crustal contamination of Cenozoic basalts from North Africa and Arabia is evident from Sr and Nd isotopes, and trace element compositions (Davidson and Wilson, 1989; Baker et al., 1997; Franz et al., 1999; Lucassen et al., 2008).

It is essential to determine the magnitude of crustal contamination on the composition of GVP basalts in order to allow the degree of melting and fractional crystallisation to be determined, as well as constrain the source composition. In this section I identify evidence for crustal contamination and quantify the effect of bulk mixing and assimilation fractional crystallisation of potential contaminating rock types.

4.2.2 Qualitative observations

The Sr-Nd isotope composition of the GVP basalts (Figure 3.19) overlap the range of values measured in metasomatised lithosphere mantle measured in mantle xenoliths in several Cenozoic basalt fields in North Africa (Beccaluva *et al*., 2007; 2008). Several samples tend to have a more radiogenic $^{87}Sr/^{86}Sr$ composition, with no significant change in $^{143}Nd/^{144}Nd$. This may reflect the presence of variable contributions of enriched mantle in the source (for example EMII of Zindler and Hart, 1986), however it is also consistent with contamination of basalt melts by continental crust with radiogenic $^{87}Sr/^{86}Sr$ composition.

Plotting Sr isotopic composition against trace element ratios such as K/Nb is a simple test of the extent of crustal contamination (Weaver, 1991). In Figure 4.1 it seems there a weak relationship between K/Nb and $^{87}Sr/^{86}Sr$ for the GVP basalts. However K/Nb ratios are in the range of ocean island basalts (66 - 430, Taylor and McLennan, 1985; Weaver, 1991) and provide no clear support for crustal contamination being major influence on these rocks.

The scatter of some trace elements in the GVP basalts may also be produced by crustal contamination. For instance the syenogabbro G10 appears to be

significantly enriched in Ba and K that may also indicate incorporation of crustal rocks.

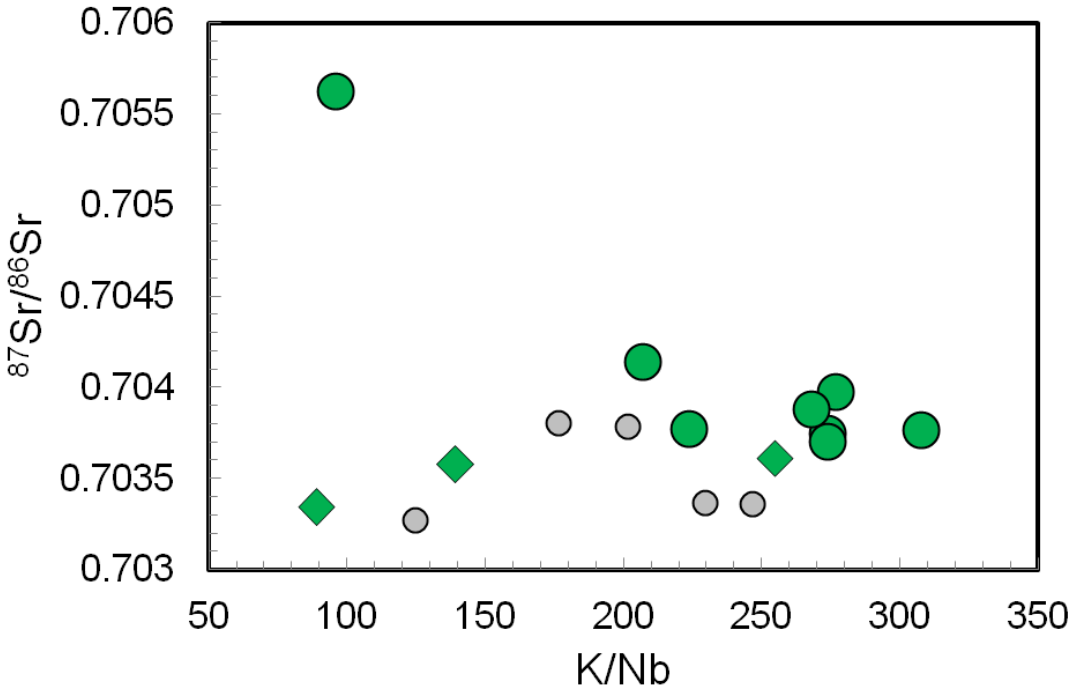

Figure 4.1: K/Nb ratios vs. $^{87}Sr/^{86}Sr$ for basalts (circles) and dykes (diamonds) at Garian volcanic province. Grey symbols are from Lustrino *et al*. (2012).

4.2.3 Quantifying the extent of crustal contamination

In order to determine the degree to which the GVP basalts have been affected by crustal contamination I have calculated the effect of bulk mixing and assimilation-crystal fractionation on the Sr and Nd isotope composition of basalts. The result of the modelling depends upon the composition of the contaminating crustal rocks and the composition of the basaltic melt, as well as the fractionating phases and solid/melt distribution co-efficient for AFC. There is lack of information regarding the composition of the crustal rocks beneath or close to the Garian volcanic province. The regional geology is dominated by Mesozoic marine and continental sediments although small mantle xenoliths are present in the Garian lavas no crustal xenoliths are reported (Beccaluva et al., 2008). The nearest exposure of upper crustal rocks is the Neoproterozoic granites in the Tibesti massif in

southern Libya (Suayah et al., 2006). The nearest exposure of likely deep crustal rocks is Pan-African basement from Jebel Marra, Sudan (Davidson and Wilson, 1989; Lucassen et al., 2008).

Figure 4.2 shows the effect of bulk mixing between two basalt end-members and three crustal components using equations from Langmuir *et al*. (1978). The two basaltic end-members span the full range of $^{143}Nd/^{144}Nd$ measured in GVP: (1) A2 basalt ($^{143}Nd/^{144}Nd$ = 0.51299; Beccaluva *et al*. 2008), and (2) alkali basalt LY 2A ($^{143}Nd/^{144}Nd$ = 0.51285; Lustrino *et al.* 2012). The three different crustal end-members include two examples of upper crustal rock, and one lower crust (see Figure 4.2 caption for explanation). The effect of assimilation fractional crystallisation is plotted in Figure 4.3, using the same end-members as in Figure 4.2. The AFC model equations of DePaolo (1981) are used.

4.2.4 Discussion

Basalt G5 has the highest $^{87}Sr/^{86}Sr$ (0.7056) and appears to require assimilation of 15 - 25% upper crustal rock. Note that the Pan-African granites used in this model have extremely high $^{87}Sr/^{86}Sr$ (0.7306) and if the contaminating rock had lower $^{87}Sr/^{86}Sr$, the degree of contamination required to explain the $^{87}Sr/^{86}Sr$ of G5 would be higher. It has lower SiO_2 (43.6 wt%) and incompatible element contents, and higher MgO (10.2 wt%) and Cr (524 ppm), than many of the other alkali basalts from GVP, and there is a vague indication from trace element ratios (e.g. K/Nb; Figure 4.1) for crustal contamination. The high Sr isotopic signature of G5 may also have been caused by the Mesozoic limestone that dominates the underlying sedimentary rocks (see section 2.2.2). Limestones typically have high Sr contents (up 400 ppm) and Mesozoic seawater $^{87}Sr/^{86}Sr$ is ~0.709 (e.g. Peterman et al., 1970). However, basalt G5 has the highest Sr concentration of all the GVP basalts (2042 ppm) that makes contamination by crustal rocks difficult. The presence of highly radiogenic Sr in the sample G5 could be as mantle-derived xenolith indicates that the host basaltic magma has risen rapidly from the mantle after entrainment of the xenoliths. Therefore subsequent fractionation has not

occurred and the duration of contact between magmas and crustal rocks has been minimal.

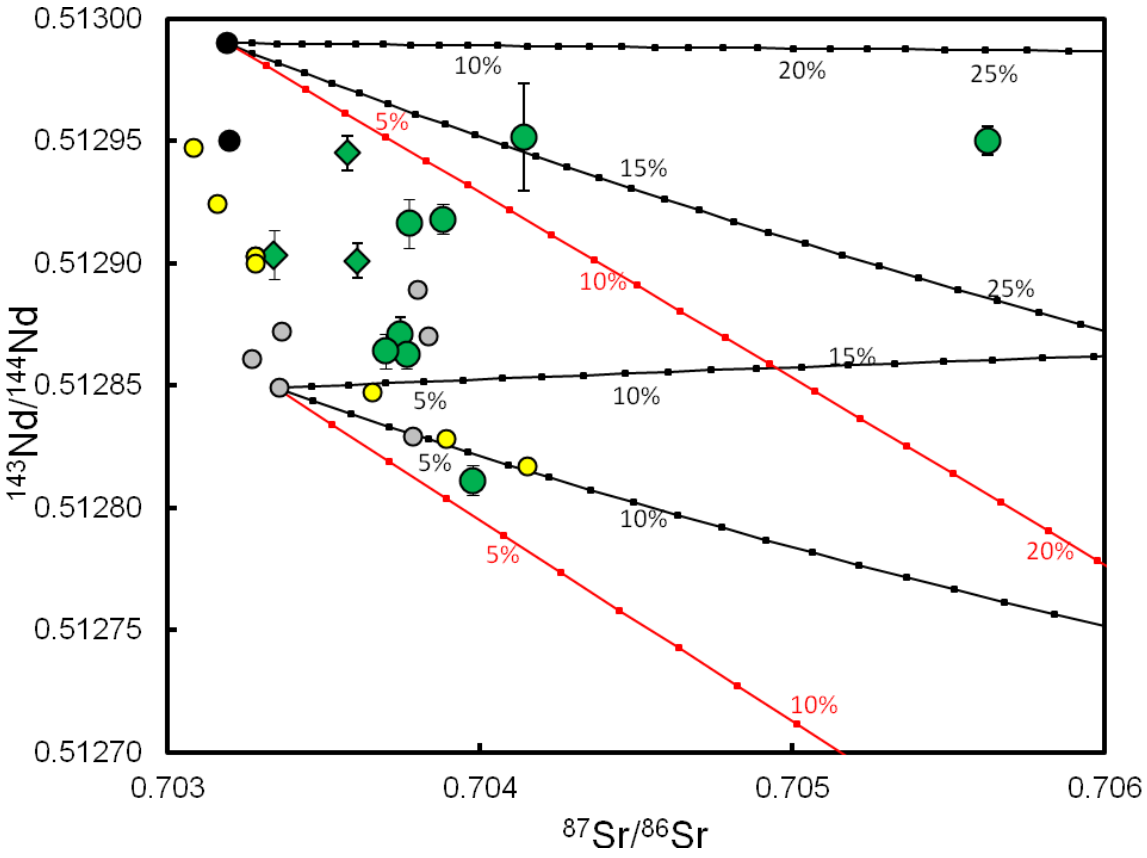

Figure 4.2: Bulk mixing calculations illustrating the possible effect of crustal contamination on Sr and Nd isotopic composition of basaltic rocks from the Garian volcanic province. The basaltic magma end-members are alkali basalt LY 2A which has $^{87}Sr/^{86}Sr$ = 0.70336, $^{143}Nd/^{144}Nd$ = 0.51285, Sr = 531 ppm, Nd = 24.5 ppm, and basalt A2 from Beccaluva *et al*. (2008) with $^{87}Sr/^{86}Sr$ = 0.70319, $^{143}Nd/^{144}Nd$ = 0.51299, Sr = 774 ppm, Nd = 41.7 ppm. The two upper crust compositional end-members chosen are biotite-hornblende granite and 2-mica granite (black mixing line) from Suayah et al. (2006) (Tibesti Massif). Lower crust compositional end-member is biotite-gneiss (red mixing line) from Davidson and Wilson (1989) (Darfur, X135). Compositions of the crustal end-member are shown in Table C.10, Appendix C. Basalts of this study are large and green. Published data are small symbols, from Beccaluva et al., 2008 (black), Lustrino *et al*., 2012 (grey). Al Haruj basalts of Nixon (2011) are also plotted (yellow). Flows are shown as circles, intrusions or dykes are shown as diamonds.

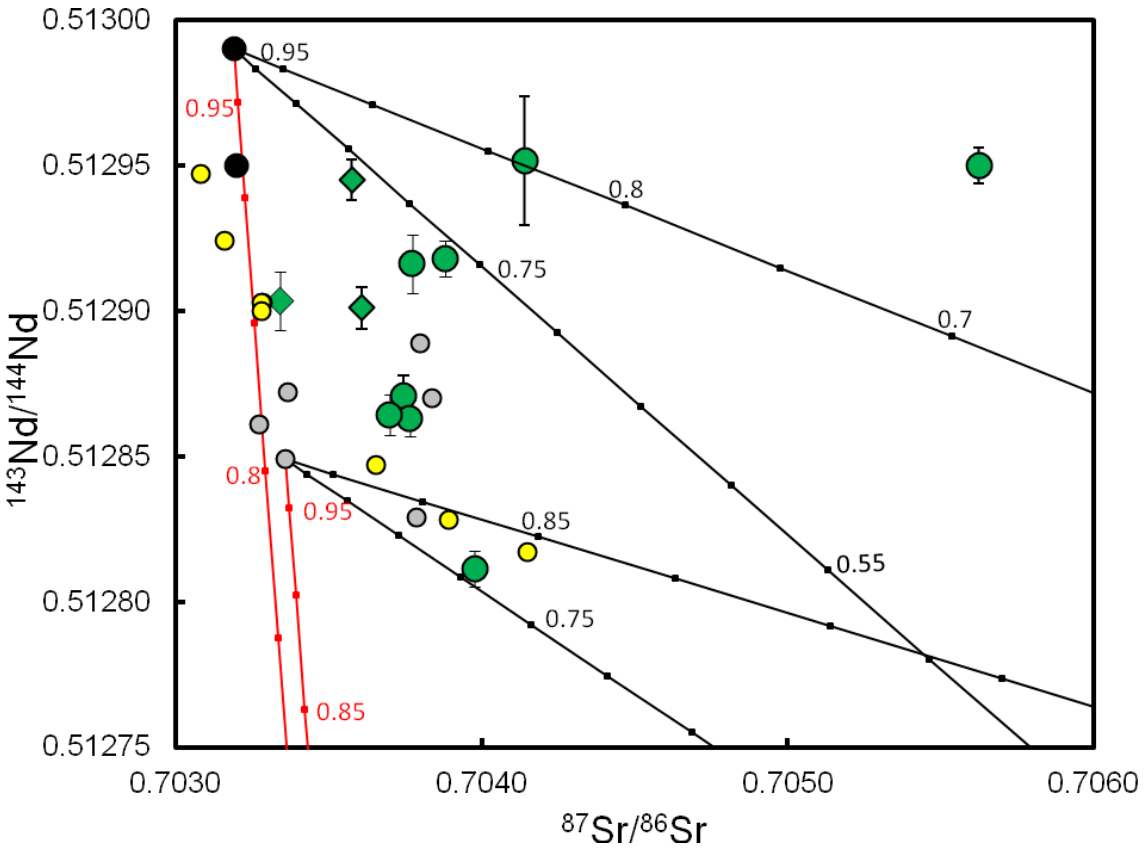

Figure 4.3: Plot illustrating the possible effect of assimilation fractional crystallisation on the Sr and Nd isotopic composition of basaltic rocks from the GVP. The end-members and symbols are the same used in Figure 4.1. The modeled mixing lines are calculated using the ratio (r) of mass assimilation rate to fractional crystallisation rate of 0.6, and the small squares indicate the amount of remaining melt (F) at 5% intervals using equations of DePaolo (1981).

Mixing of a small amount of crust into basalt magmas can account for the range of Sr and Nd isotopic compositions of most of the GVP basalts. The majority of the basalts can be explained by assimilation of up to 10% crust. The basalt data do not lie on a simple AFC-derived evolution line with lower crust rocks, suggesting that contamination by upper crust is more likely. Both the basalt end-members used in this modelling are at the low end of the range of $^{87}Sr/^{86}Sr$ measured in GVP basalts. Thus the degree of crustal contamination that is recorded in the mixing relationships must be considered a maximum.

4.3 Fractional crystallisation

4.3.1 Introduction

As minerals crystallise from a cooling melt, compatible elements tend to concentrate in early formed minerals, whereas incompatible elements remain in the residual liquids. Fractionation therefore occurs between compatible and incompatible elements and is represented by variations of abundance of certain elements and ratios of compatible/incompatible elements in igneous rocks. In this way trace elements can be used for unravelling the history of fractional crystallisation.

The crystallising mineral assemblage is also affected by pressure. Higher pressures favour clinopyroxene crystallisation over plagioclase. The relationship between elements that arises from crystallisation in a magma chamber is known as the liquid line of descent. Estimating the composition and proportions of minerals which are extracted from a primitive basaltic melt allows the control on a liquid line of descent by fractional crystallisation to be predicted. Providing the basaltic samples follow a single line of descent, compositional trends can be used to estimate the pressure of crystallisation. Variations in the abundance of elements and ratios of compatible to incompatible elements in igneous rocks can be represented by the fractionation processes.

In this section I use the petrography and geochemistry of the GVP basalts provided in Chapter 3 to investigate the role of fractional crystallisation in producing the range of basalts of the Garian volcanic province.

4.3.2 Qualitative observations

The presence of olivine and clinopyroxene phenocrysts in all GVP basalts is a strong indication that they have experienced fractional crystallisation. Both phases are chemically zoned and display consistent compositional variation

with size and rock type. Major and trace element trends reflect the removal of olivine and pyroxene from a basaltic melt composition (Figures 3.14 to 3.16).

Figure 3.14 show that MgO is negatively correlated with SiO_2 indicating that olivine was the main early crystallising phase. A negative correlation between Cr and MgO (Figures 3.14 and 3.16) and silica supported that the olivine crystallised during the early stages of fractional crystallisation. Fractionation of pyroxene as one of the main phases to crystallise at early stage of fractionation in these rocks is suggested from the negative correlation of CaO, MgO, Fe_2O_3, Sc, Y and Nd with SiO_2.

Sparse plagioclase phenocrysts occur in some of the transitional basalts. A clear positive correlation is observed between SiO_2 and Al_2O_3 and Na_2O (Figure 3.14); these oxides are incorporated in felsic minerals that crystallise during the later magmatic stages and decrease CaO activity in the melt could be explained as accumulation of plagioclase and consequence of crystal fractionation processes. The Sr against MgO content shows depletion in alkaline basalt samples could have been controlled by fractionation of olivine and/or clinopyroxene in the early stages. The transitional basalt samples can be explained by crystallization of the plagioclase in the later stage (Figure 3.15B). Also the positive peaks at Sr of transitional basalt samples seen in the mantle-normalised diagrams (Figure 3.19) are consistent with a metasomatized source.

Fractionation of oxides, the decreases in TiO_2, V, and Cr with increasing SiO_2 suggest that magnetite and ilmenite crystallised and could be segregated in the latest stages of fractional crystallisation (Rollinson, 1993). The correlation of P_2O_5/Al_2O_3 (Figure 3.15C) and TiO_2 with SiO_2 indicates the crystallisation of ilmenite and apatite in the silica under-saturated lavas.

In Figure 4.3 the relationship between the Nd/Ce with Nd is plotted. The effect of partial melting on the Nd/Ce ratio is much more significant than fractional crystallisation of mafic minerals from basaltic melt (Ahmad et al., 1999). Consequently fractionating basaltic melts evolve on horizontal lines in Figure

4.3 while partial melting moves compositions along a slope. The Garian basalts follow a trend that is parallel to the fractional crystallisation pathway, confirming that the fractional crystallisation was the dominant process to generate the Garian basalts. At the same time partial melting process cannot be completely ruled out. This figure shows small variation in Nd/Ce ratios that may reflect small variation in the amount of partial melting.

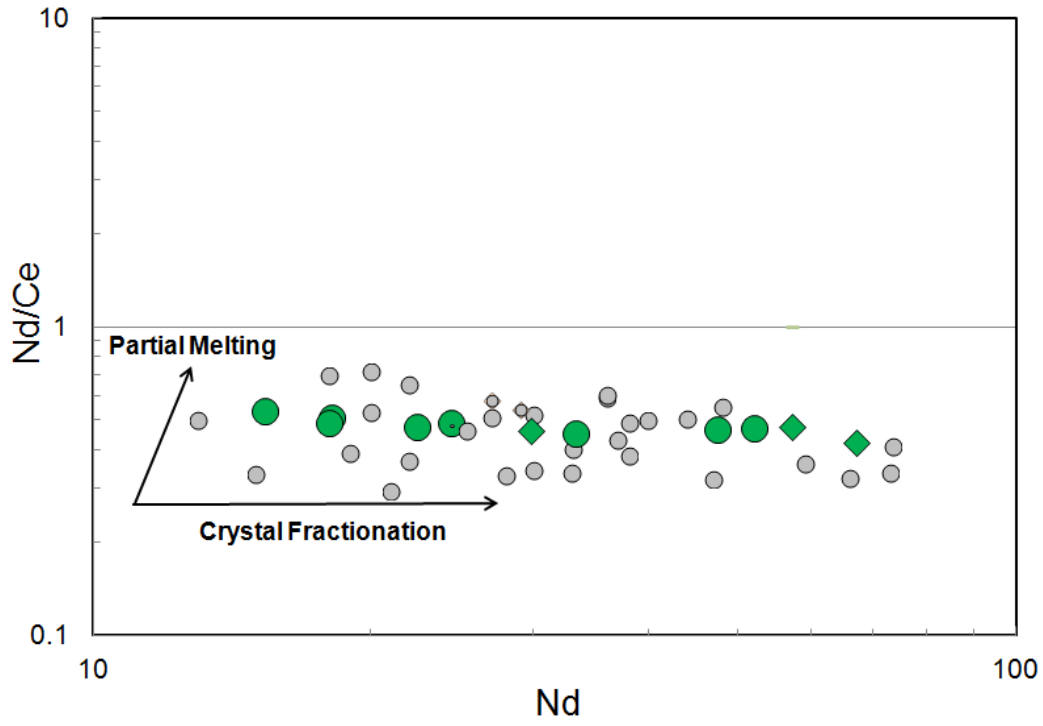

Figure 4.4: Nd/Ce versus Nd (Pearce, 1980) diagram showing fractional crystallisation and partial melting trends for basalts of this study (green) from the Garian volcanic province (Jung and Masberg, 1998). Circles: Basalt flow and diamonds: intrusions or dykes. Published data are grey circles (Busrewil 1974; Hegazy 1999, Aboazom et al. 2006, Lustrino et al. 2012).

4.3.3 Modelling fractional crystallisation of GVP basalts

The software Petrolog3 (Danyushevsky and Plechov, 2008) has been used to estimate the crystal fractionation trends and the amount of accumulated minerals that fit the major element composition of the Garian basalts. Figure 4.4 show the results of closed system fractional crystallisation modelling for

major element oxides plotted against SiO_2 of all analyses of GVP basalts (this work and previous studies). The amount of a mineral phase extracted from the melt on each increase of crystallisation is 1.0%. The parameters used in the modelling are shown in Table 4.1. The models for olivine and clinopyroxene crystallisation have been calibrated at pressure above 1 atm and incorporate a pressure function.

The model of Nielsen (1985) for spinel crystallisation does not allow for crystallisation at high pressures and a correction of 15°/kbar is applied. The initial bulk compositions correspond to most primitive alkaline basalt (sample G2). The liquid line of descent which most closely fits the Garian basalts is generated from starting composition by crystallising olivine, clinopyroxene and spinel at 10 kbar. Petrolog3 compares calculated pseudo-liquidus temperatures for a chosen number of minerals that may crystallise from a given melt composition.

The final composition at 10 kbar indicates that the starting composition initially fractionated olivine as the only liquidus phase at 41.55 wt% SiO_2 with the amount of accumulated of olivine about 2 wt%. Olivine fractionation dominantly removes MgO from the melt. Clinopyroxene begins to be fractionated at 51.97 wt% SiO_2 with amount cumulated about 12 wt%. Although spinel is not observed as a phenocryst phase in any of the basaltic rocks of this study, a small amount (~0.1 wt %) could be present as inclusions within olivine crystals.

The modelled fractional crystallisation paths generally fit well with the evolution of most major elements, especially Mg and Fe. The lack of perfect fit to the data probably reflects the assumption of open system evolution of magmas. The position of the inflection point in CaO concentrations is not evidenced in the data and reflects the control by plagioclase fractionation.

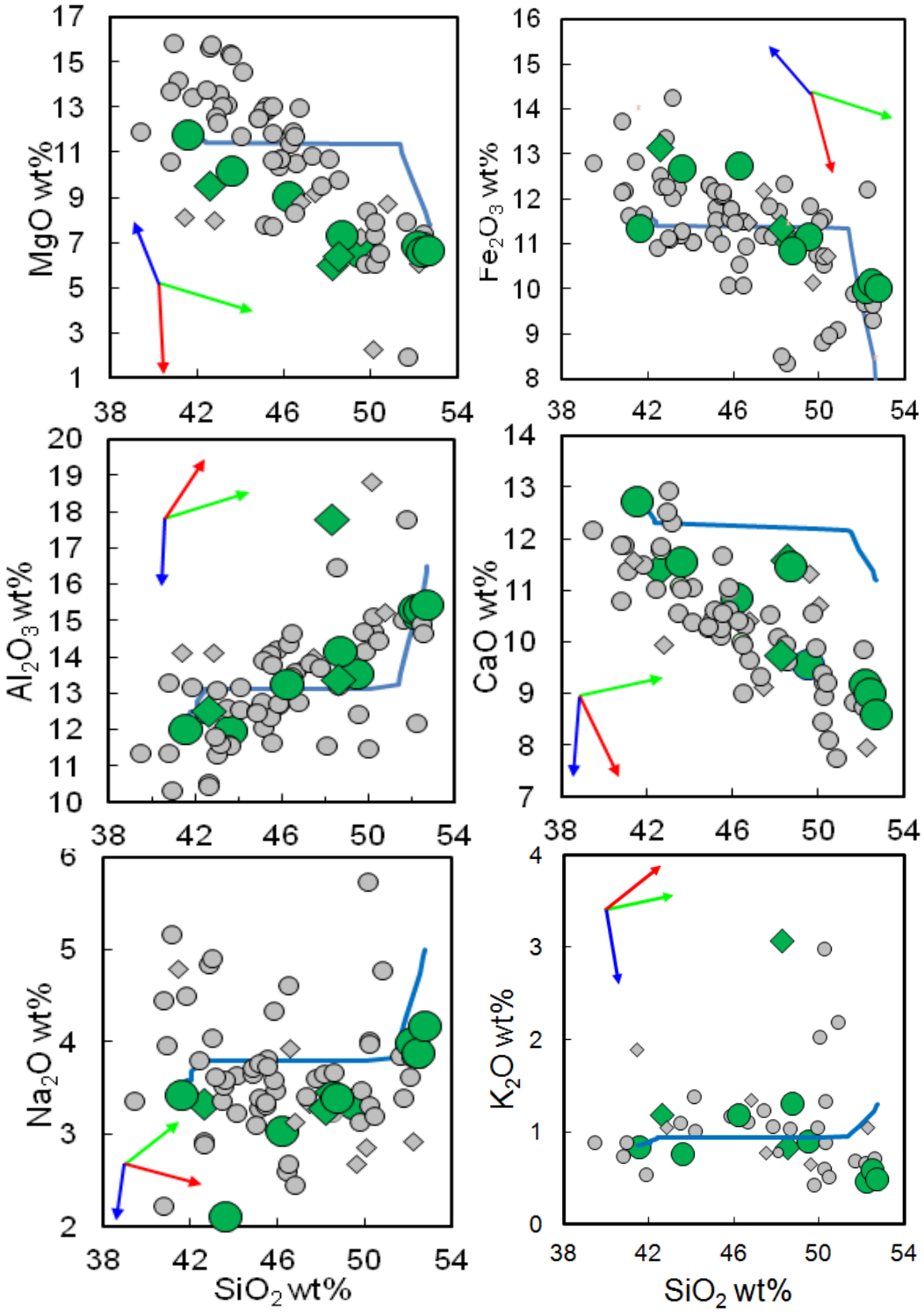

Figure 4.5: Harker diagrams of major element abundances plotted against SiO_2 wt% for basaltic rocks from the Garian volcanic province. The fractional crystallisation paths are shown as blue lines. The arrows show the approximate effect of the removal of minerals from melts: olivine (green), clinopyroxene (red) and feldspar (blue). The same symbols are used in Figure 4.4.

Table 4.1: Mineral-melt equilibrium models and physical parameters used in Petrolog3 to model fractional crystallisation paths.

Parameter	Model/Conditions
Olivine model	Beattie, 1993
Olivine composition K_d	Olivine composition is calculated using K_d(Fe-Mg) = 0.3
Clinopyroxene model	Langmuir et al. 1992
Spinel model	Nielsen, 1985
Spinel pressure correction	15°/kbar
$f(o_2)$	Kilinc et al. 1983
Fe_2O_3 in the melt	calculated using QFM buffer of oxygen fugacity
Melt density	Lange & Carmichael 1987
Melt viscosity	Bottinga & Weill 1972

The software Petrolog3 analyses of the major element composition of the Garian basalts estimated that fractionation appears to be occurred at temperatures between 1095°C and 1273°C as a result from Petrolog3 analyses in Excel. This is consistent with fractionation occurring in regions of magma storage at depths of 20 to 35 km. Based on the iron ratio and albite ratio can be considered as indicators of the extent of fractionation (Yoder and Tilly, 1962) of Garian basalts, Hegazy (1999) calculated that the crystallisation temperature of majority of the basalts of GVP lies near the 1200°C trend line.

4.4 Partial melting

4.4.1 Introduction

Partial melting of mantle rocks takes place over a range of temperatures as upwelling mantle passes through the liquidus temperature. The mineral components with the lowest melting temperatures melt first. Partial melts are

enriched in the chemical components of minerals with lower melt temperatures. There are two end-member types of melting. In *equilibrium* melting the melt remains in contact with the residual solid crystals continuously reacting with them. In this case the melt composition changes until the rock has completely melted. In *fractional* melting the melt is continuously extracted from the residual solid rock as it is produced. This leads to differentiation of chemical components in the melt, and to the creation of different rock types from the same mantle source.

Although it has been shown previously that fractional crystallisation is the dominant control on the major element differentiation trends of the GVP basalts, variation in the degree of partial melting may have affected the composition of the basalts to some extent. The objective of this section is to use the trace element composition to determine the degree of partial melting of the alkaline and transitional basalts at the Garian volcanic province.

4.4.2 Role of partial melting

In Figure 4.6 I report the variation of incompatible trace element ratios with respect to La. These ratios do not vary significantly during crystallisation but because this ratio do not fractionate substantially during moderate degrees of crystal fractionation of basaltic melts but are quite susceptible to variable degrees of partial melting of mantle sources, variations in the concentrations and ratios reveal the extent of partial melting. The extent of partial melting depends partly on the composition of the melting mantle. Melting trajectories are shown in Figures 4.6A and B for the average (spinel- and garnet-bearing) lithospheric mantle of McDonough (1990); modal composition of 57% olivine, 18% orthopyroxene, 12% clinopyroxene, 8% spinel/garnet and 5% amphibole, such a peridotitic source has been modelled to melt partially in a non-modal fashion, hypothesizing olivine formation after incongruent melting of enstatite. The amounts of minerals participating to the melt used in the model are as follows: 5% olivine, 25% orthopyroxene, 35% clinopyroxene, 25% amphibole and 10% spinel/garnet. The batch melting equation of Shaw (1970) is used to calculate the composition of the partial melts:

$C_l = C_0/(D + F*(1 - P))$

where C_l is the composition of the partial melt, C_0 is the composition of the source, D is the bulk partition coefficient of the source, F is the degree of partial melting, and P is the bulk partition coefficient of the eutectic. This model assumes that the trace element concentrations of the Garian basalts are similar to primitive unfractionated melts that are in equilibrium with the mantle sources.

Figure 4.6A shows a positive correlation between La and La/Y. This can be best explained by variation in the degree of partial melting. The alkali basalts were produced by partial melting of between 3 and 10%, while the transitional basalts cluster around ~12% melting of spinel/garnet facies.

Figure 4.6B shows the co-variation of Ba and La in the GVP basalts. They have similar distribution coefficients between spinel and garnet and thus are not sensitive to the mantle source, or depth of melting. The new Garian basalt data plot along a trend which is similar to the partial melting trend recognised in earlier study of GVP basalts (Lustrino et al. 2012). They indicate that Ba and La concentrations are a function of the variation in the degree of partial melting that are similar to those determined from La-La/Y relationship (Figure 4.6A).

A common approach to melt modelling is the use of plots of MREE/HREE versus LREE/HREE ratios, e.g., Dy/Yb versus La/Yb (Figure 4.5C). This plot is particularly useful as it distinguishes between melting in the spinel and garnet stability fields (e.g. Thirlwall et al., 1994). Garnet-facies melting produces little change in Dy/Yb ratios in melts compared with a large change in La/Yb ratios because garnet-facies melted in the source. Variable degrees of partial melting of a spinel/garnet-bearing peridotite can generate the La/Yb and Dy/Yb trends of the Garian alkali basalts. The data reveal melting between 0.5 and 2.5% for the alkali basalts, while the transitional basalts cluster around 5% melting.

The new measurements of the basaltic rocks from the Garian volcanic province appear to have been produced by between 2 and 12% partial melting of spinel/garnet facies. The alkali basalts require less melting than transitional basalts. This implies that the alkali and transitional basalts are controlled be slightly different of pressure and temperature. These results are generally similar to the earlier study of Lustrino et al. (2012) who determined partial melting of 3 to 9% of shallow mantle sources.

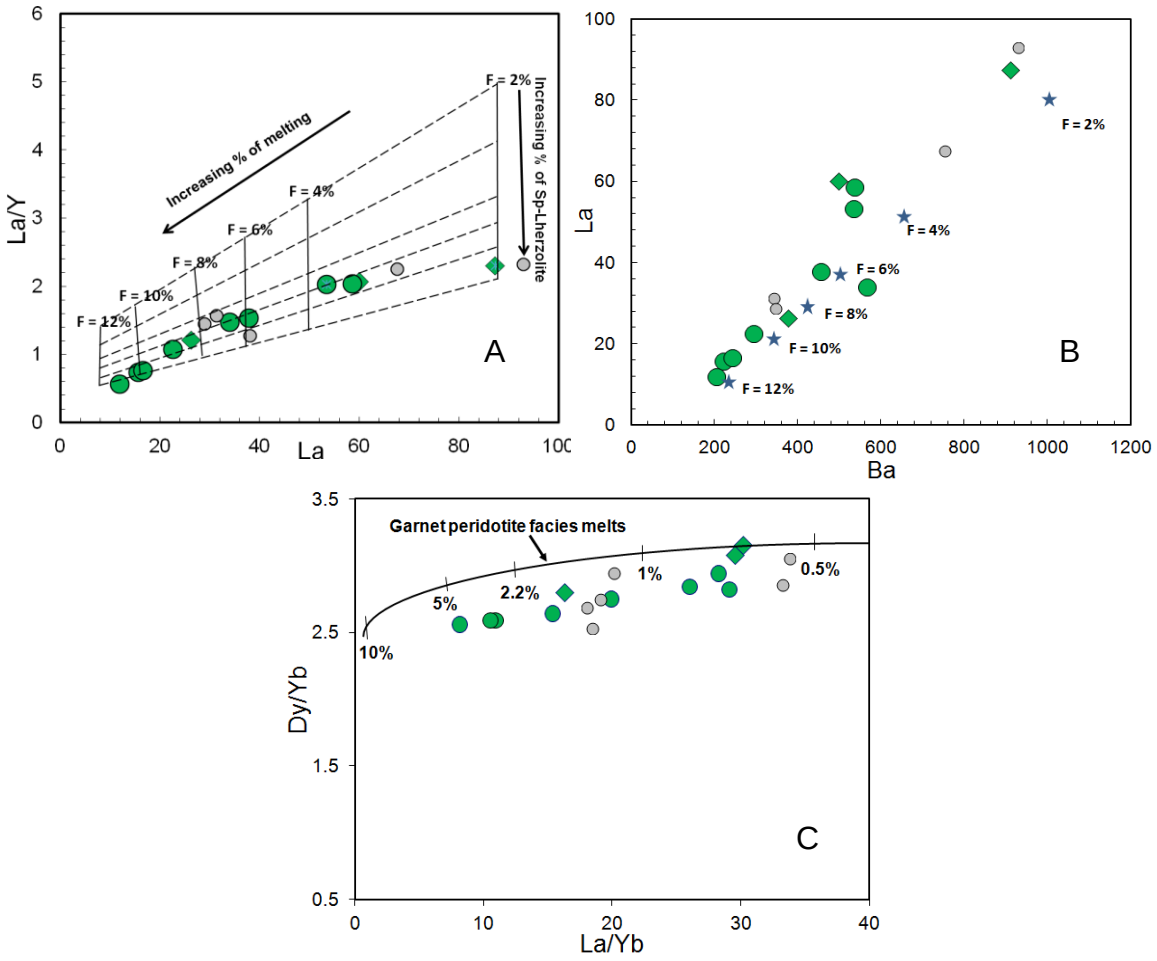

Figure 4.6: La/Y vs. La (A), La vs. Ba (B) (Lustrino et al., 2012) and Dy/Yb vs. La/Yb (C) (Thirlwall et al., 1994) for Garian volcanic province basalts of this study (green). The symbols are the same as used in Figure 4.4. Melt compositions are modelled in Lustrino et al (2012).

4.5 Nature of the source

4.5.1 Introduction

The incompatible trace elements are diagnostic in characterizing mantle source of volcanic rocks (e.g. Hart et al., 1997). Major and trace element evidence (e.g. high CaO/Al_2O_3, nearly constant Y and Yb concentrations, high La/Yb and Zr/Y) can be used to indicate that the basaltic magmas derived from a garnet-bearing mantle source (Frey et al., 1978; Brey et al., 1979). Multi-element diagrams (spider diagrams) normalized against primitive mantle can be used to constrain the source and melting characteristics of rocks (Pearce, 1983).

In this section, the geochemical and mineralogical information compiled in this study and presented by other authors who worked in the region will be discussed in order to try evaluating the nature and approximate depth of magma sourcing that originated the basalt magmas beneath the Garian volcanic province.

4.5.2 Melt generation

The high Mg (up to 11.7 MgO wt%), Ni (up to 828 ppm) and Cr concentrations (up to 721 ppm) of the least fractionated basalts indicate that they were probably in equilibrium with peridotite mineral assemblage. The shape of REE patterns is controlled by the occurrence of phases whose presence is in its turn controlled by pressure/depth, such as spinel and garnet (e.g. Ellam, 1992; Kerr, 1994). Garian basalts are enriched in LREE relative to HREE (Figure 3.18) considering to have been generated with mantle in the spinel-garnet transition facies at the depth of 80 to 90 km (Nickel, 1986; McKenzie & O'Nions, 1991; Adam and Green, 2006), indicating that magma generation should have occurred within the asthenosphere.

McKenzie & O'Nions (1991) and Ellam (1992) investigated the relationship between trace element compositions of basalts, variations in thickness of the

lithosphere and final depths of melt segregation. Thus Ellam (1992) formulated a method, using REE ratios such as Ce/Yb to estimate depths of extraction of final melts produced at depths shallower than 125 km near the lithosphere-asthenosphere interface. Since such ratios are sensitive indicators of changing lithospheric thickness, they will not be radically affected by fractional crystallisation. Based on Ellam (1992) formula, the Garian basalts have average Ce/Yb of 42 of the alkaline basalts and 20.8 for transitional basalts. This translates to final basaltic melt segregation depth of 120 km and 80 km, respectively. This interpretation is consistent with the composition of the REE in basaltic rocks (LREE enrichment over HREE).

The Nb/La versus La/Yb diagram (Figure 4.7) can be used to constrain the source. The high field strength elements such as Nb are depleted in the lithospheric mantle relative to the LREEs (e.g. La). High Nb/La ratios (> 1) indicate an OIB-like asthenospheric mantle source while values < 1 indicate a lithospheric mantle source (Bradshaw and Smith, 1994; Smith et al., 1999). The Garian basalt have Nb/La and La/Yb ratios (1.3 and 25) that overlap those of Lustrino *et al*. (2012) (1.5 and 30 respectively) and are consistent with an asthenospheric mantle source.

4.5.3 Evidence for involvement of metasomatised mantle in the GVP basalts

Metasomatic effects are indicated by the widespread pyrometamorphic textures represented by reaction patches with secondary mineral parageneses in spinel lherzolites in the GVP basalts (Beccaluva *et al.* 2008). The sieve-textured cores in the clinopyroxene crystals, the low CaO (<0.1%) and generally high Fo of the cores of the resorbed olivines in the Garian basalts (Figure 3.9) that similar to the pristine olivine from spinel lherzolite xenoliths from Garian. Lower Fo content (down to Fo_{78}) with high CaO (up to 0.23%) is recorded by olivine micro-crysts (secondary olivine) in reaction patches products in metasomatic assemblage (Beccaluva *et al*., 2007, 2008). Trace element modelling (deficiency of Ti anomalies) of basaltic rocks and

associated mantle xenoliths affected by metasomatic agent across the Garian region.

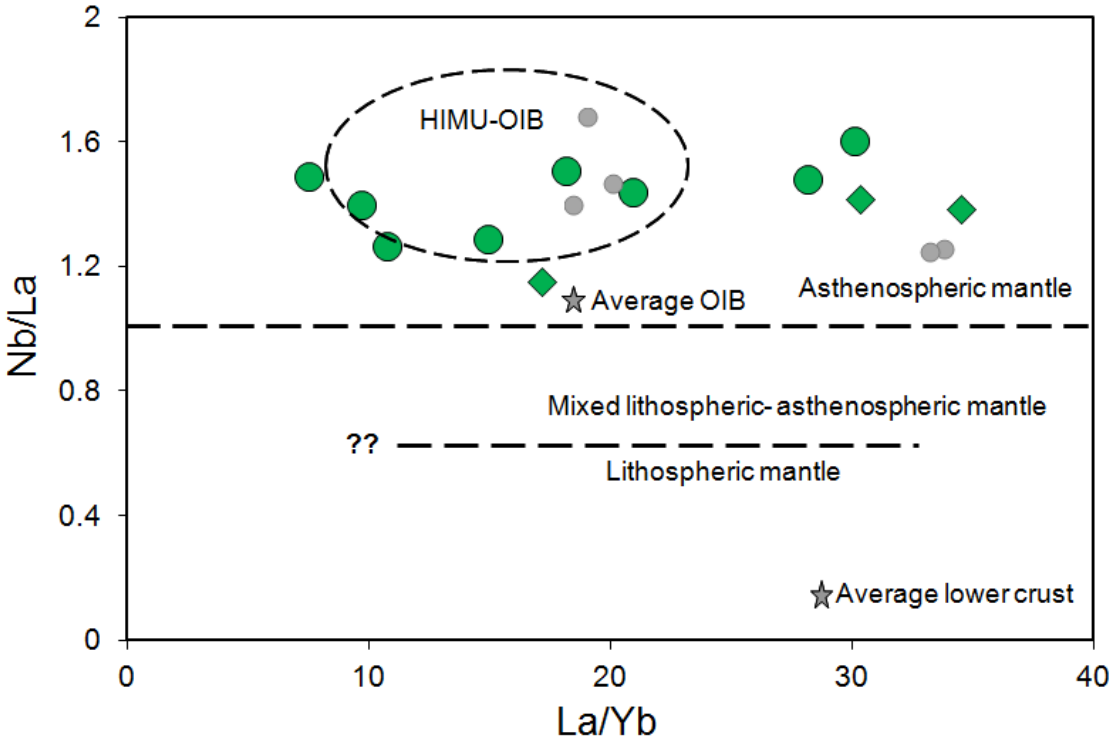

Figure 4.7: Nb/La versus La/Yb variation diagram for basalts of this study (green) from the Garian volcanic province. The same symbols are used in Figure 4.1. The field of HIUM-OIB and the dashed lines separating the fields are from Abdel-Rahman (2002). Average lower crust is from Chen and Arculus, 1995.

Spinel lherzolite xenoliths from the GVP display a range of Sr and Nd isotope compositions (Figure 3.20) from values that are typical of depleted ($^{87}Sr/^{86}Sr$ ~ 0.7023, $^{143}Nd/^{144}Nd$ ~ 0.5139) and enriched ($^{87}Sr/^{86}Sr$ = 0.7030, $^{143}Nd/^{144}Nd$ = 0.5130) mantle (Beccaluva et al. 2008). The xenoliths that appear to have undergone the most chemical modification (e.g. E12A, Beccaluva et al. 2008) have the enriched composition. The GVP basalts have small range in $^{87}Sr/^{86}Sr$–$^{143}Nd/^{144}Nd$ (0.70334-0.70398 and 0.51281-0.51295, respectively) that very close to the composition of metasomatised spinel peridotite xenoliths. The absence of isotope signature indicative of depleted mantle implies that basalts have incorporated significant amount of metasomatised lithospheric mantle.

The Rb/Sr versus Ba/Rb diagram (Figure 4.8) provides a way to assess the presence of phlogopite and amphibole in the source region (Lustrino *et al*., 2012). Amphibole has high Ba and low Rb contents, while the phlogopite is enriched in Rb and Ba (Ionov and Hofmann, 1995; Martin et al., 2005). Melts of a phlogopite-bearing source have low Ba/Rb and high Rb/Sr ratios, and the melt of an amphibole-bearing source is characterized by low Rb/Sr and high Ba/Rb (Furman and Graham, 1999). The existence of amphibole and/or phlogopite in the mantle source region is an indication that the source region has been metasomatised as both minerals are typically metasomatic-volatile bearing phases (Furman, 1995). The majority of GVP basalts have high Ba/Rb and low Rb/Sr ratios, suggestive of melting in the presence of amphibole (Figure 4.8).

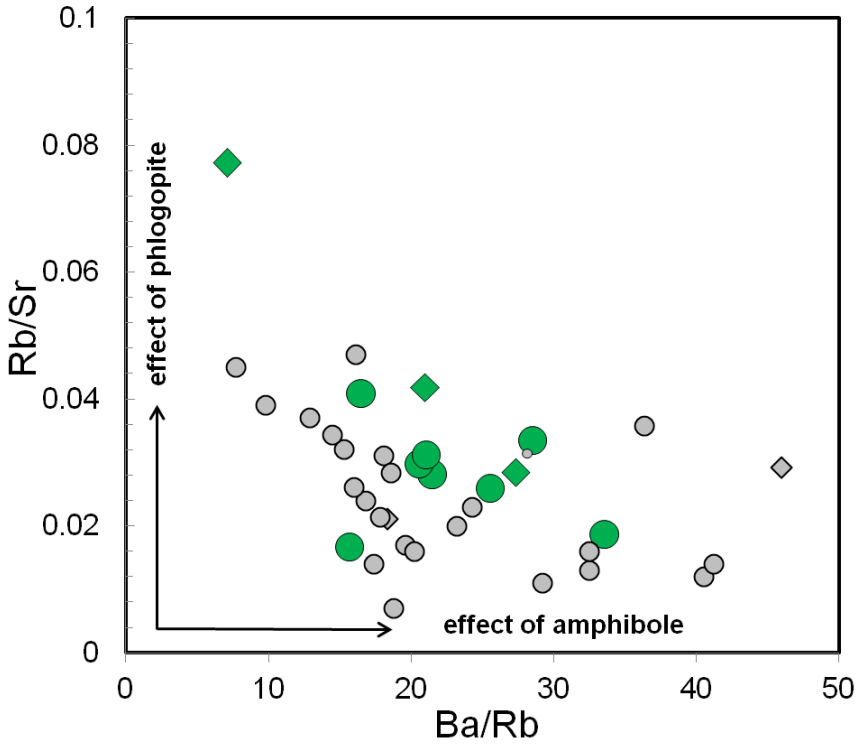

Figure 4.8: Rb/Sr versus Ba/Rb variation diagram for Garian volcanic province basalts from this study (green) and from Busrewil 1974; Hegazy (1999), Aboazom et al. (2006) and Lustrino et al. (2012) (grey). The same symbols are used in Figure 4.4.

The presence of amphibole (Figure 4.8) in this mantle source suggests that the amphibole occurred at depth of asthenosphere melting (e.g. Melluso and Morra, 2000; le Roex et al., 2001; Melluso et al., 2007). Amphibole is constant

just about 2.5-3.5 GPa (~90-110 km depth; Green et al., 2010; Pilet et al., 2010). This observation suggests that the mantle source of the Garian basalts is located at the base of the lithospheric mantle, where the amphibole is established.

The primitive-mantle normalized trace element patterns (Figure 3.19) show relatively smooth patterns with similar bell-shaped trend. These are typical of ocean island basalts (OIB) and E-MORB, both of which have the typical enrichments in LILE (e.g. Ba and Sr) relative to HFSE (e.g. Nb, Zr and Y) and HREE (e.g. Th, Hf and Lu) controlled by different degree of partial melting (Pearce, 1982; Wilson, 1989). The deficiency of Ti in basalt rocks is reflected in larger negative Ti anomalies in metasomatised lherzolites from GVP (Beccaluva *et al*. 2008). These trace element and isotope data suggest that these rocks were derived from low degrees of partial melting of spinel lherzolite that was metasomatized by fluids and further underwent a degree of fractional crystallization before being extruded at the surface.

The similar conclusion of the low Rb/Sr ratios was readed by Hegazy (1999) who concluded that the Cenozoic basalts of Libya have generally Rb/Sr < 1, as generated from asthenenospheric source. Beccaluva *et al*. (2008) suggested that the prevalent HIMU fingerprint and trace element modelling (negative Ti anomalies) of Garian basaltic rocks and associated mantle lherzolite xenliths are linked to a common sub-lithospheric metasomatic agent across the Garian region. Lustrino et al. (2012) indicated that the mantle source of the Garian basalts can be located at the base of the lithospheric mantle, where the amphibole is established.

4.6 Summary

The GVP basalts originate as melts of the asthenosphere mantle. The alkali basalts were produced by different degree of partial melting, between 2 and 10%, while the transitional basalts cluster around 12% melting of mantle sources in the spinel/garnet facies. There is mineralogical (secondary mineral such as clinopyroxene olivine and feldspar as reaction rims around

orthopyroxene in spinel lherzolites in the GVP basalts, Beccaluva *et al*., 2008) and geochemical evidence (e.g., deficiency of Ti anomalies) for the incorporation of metasomatised lithosphere in the melts. Fractional crystallisation is the dominant differentiation process and controlled the major element differentiation trends of Cenozoic basalts at 1100°C to 1300°C, equivalent to depths of 20-40 km. There is no significant evidence for crustal contamination of the GVP basalts except the sample G5, on the basis of Sr and Nd isotopes it appears to be significantly less than 10%.

In conclusion, most peridotite xenoliths from the Garian volcanic province district record metasomatic enrichment that overprinted a previously depleted mantle lithosphere (Beccaluva *et al*., 2008), as well as other volcanic occurrences in the North Africa and south Europe.

According to framework delineated above, mineralogical and geochemical evidence (presence of amphibole, enriched in LREE relative to HREE and high Nb/La) all indicate that magma generation should have occurred within the asthenosphere at the spinel-garnet transition occurs at about 70-90 km depth below average continental geotherms. Based on Ellam (1992) formula, Melting begins at about 120 km and continues to depth of 80 km for alkaline and transitional basalts, respectively. Alkaline volcanism of the Garian district generated from low melting degrees (between 2 and 10%) of mantle sources in the spinel/garnet facies represent prevalent HIMU fingerprint on HIMU-metasomatised mantle sources. The presence of an HIMU signature can be likely interpreted to be related to passive asthenospheric mantle uprising and decompression melting linked to tensional stresses in the lithosphere during Cenozoic reactivation and rifting of the Pan–African basement. This can be considered a far-field foreland reaction of the Africa–Europe collisional system since the Eocene. Seismic tomography of the North African plate confirms a variable lithospheric thickness in the Saharan area due to local asthenospheric upwelling (Ayadi *et al*., 2000). They were followed by dominant differentiation process of fractional crystallisation at 1100°C to 1300°C, equivalent to depths of 20-40 km in the most upper mantle.

Chapter Five

Petrography, geochemistry, geochronology and petrogenesis of the phonolitic rocks

5.1 Introduction

The first identification and study of the mineralogy and petrology of phonolites from Garian volcanic province was made by Von Wervecke (1880). This was extended by Lipparini (1940) who reported most of the trachytic phonolite and alkaline trachyte occurrences between Garian and Mizda. Detailed studies of petrography and geochemistry were done by Piccoli and Spadae (1964), Gray (1971), Almond *et al*. (1974), Busrewil (1974), Bausch (1978) and Aboazom *et al*. (2006), and K/Ar age determinations were reported in other studies (Mobil Oil Company, 1967; Piccoli, 1971) (Table 2.1 and Figure 2.9). In the most recent study of the GVP phonolites, Lustrino *et al*. (2012) distinguished two types based on petrography, mineralogy and geochemistry that he termed type-1 and 2. Type-2 phonolites are the dominant rock type, with type-1 phonolites being restricted to the Kaf El Tekut intrusion.

In this chapter I present the results of a new study of the GVP phonolitic rocks based on petrography, major and trace elements, rare earth elements, Sr-Nd isotope compositions and $^{40}Ar/^{39}Ar$ ages. Four phonolite samples (G8, G10, G11, and G12) were collected in March 2010. One phonolite sample (G81B) was taken from the University of Manchester collection that was originally sampled by Dr Mabruk Busrewil in 1971 (Busrewil, 1974). The location of all samples is shown on Figure 3.1, and details are reported in Table 5.1. Field photographs of samples are shown in Figures A1.2 and A1.3. Detailed descriptions of hand specimens are presented in Appendix A. The details of sample preparation and analytical procedures are given in Appendices A to D. All samples are type-2 phonolites of Lustrino *et al*. (2012) classification.

The main objective of this work is to determine the origin of the phonolites, specifically to constrain the role of crystal fractionation and crustal assimilation, and determine how they fit into the regional volcanic history.

Other phonolite volcanic rocks occurred at Jabal Al Hasawinah (~1,000 km^2) west central Libya. They appear as dikes and cones. They are organized as two different directions following the main fault trends, NW-SE (and NE-SW to ENE-WSW. The difficult terrain and inaccessibility of most parts of Jabal Al Hasawinah have discouraged any detailed study of the phonolites. However, reports by Busrewil and Oun (1991) have given brief information (geochemistry and geochronology study) about the phonolite field. The phonolites are strongly undersaturated (55-60% SiO_2), with 16-35% normative nepheline and 13-17% total alkalis. They show low contents of Rb, Zr (650-1600 ppm) and Nb (150-360 ppm) compared to the phonolites of this study. The K/Ar age of phonolite from Jabal Al Hasawinah was determined to be 23.2 - 15.7 Ma (Jurak, 1978). However, I have not sampled and studied these rocks for the difficult terrain and inaccessibility to them.

5.2 Petrography

5.2.1 Thin-sections

The phonolites are moderately porphyritic with sanidine and anorthoclase being the dominant phenocryst phases. They are up to several millimetres in size, and make up 10-20% of the rock (Figure 5.1A). Both types of feldspar have patchy extinction and exhibit a small degree of alteration to sericite. Small rectangular nepheline phenocrysts (up to 1 mm) occur in all samples (Figure 5.1B). They commonly contain small aegirine and needle-like apatite inclusions. Biotite is also generally present, often in clusters of small phenocrysts and sometimes occurs as large altered phenocrysts up to 3 mm (Figure 5.1C). They never exceed 5% by volume of the rock. Green aegirine-augite is found as pleochroic grains that are up to 0.1 mm. Small grains of Fe oxides and euhedral sphene are present in all rocks (Figure 5.1D).

The groundmass is mainly composed of laths and microlites of alkali feldspar, sanidine, and nepheline, needles of aegirine-augite as well as biotite, sphene, interstitial glass and Fe-Ti oxides. They typically display a trachytic texture. The samples studied here are petrographically similar to those studied earlier (Piccoli, 1970; Almond *et al*., 1974; Busrewil, 1974; Hegazy, 1999; Aboazom *et al*., 2006; Lustrino *et al*., 2012).

5.3 Whole rock geochemistry

5.3.1 Major elements

The rocks are between 56.8 and 60.3 wt% SiO_2 and have total alkali concentrations ranging from 14.2 to 15.4 wt% (Table C.1, Appendix C). They plot in the phonolite field in TAS classification of Le Bas *et al*. (1986) (Figure 3.13) and are compositionally similar to the GVP phonolites reported by previous studies (Almond *et al*., 1974; Busrewil, 1974; Hegazy, 1999; Aboazom *et al*., 2006; Lustrino *et al*., 2012). No trachytic rocks were sampled in this study.

The CIPW norms (Table C.2) show that all the phonolites are SiO_2-undersaturated with a wide range in normative nepheline content (15.1 - 28.4 wt %). All phonolites are silicic peralkaline, i.e. molar $(Na_2O + K_2O)/Al_2O_3 > 1.0$ with the presence of normative acmite (aegirine) and in most cases sodium metasilicate which may be modally represented by an aegirine-rich groundmass and aenigmatite. The major elements exhibit scatter in Harker-type diagrams, and overlap earlier measurements of GVP phonolites (Figure 5.2). They have lower MgO, Fe_2O_3 and CaO concentrations than the basalts, and are significantly enriched in Al_2O_3, Na_2O and K_2O. This is consistent with loss of olivine ± clinopyroxene ± Fe-Ti oxides during fractional crystallisation. Al_2O_3 (21.2 - 18.7 wt%) and Na_2O (10.4 - 7.6 wt%) concentrations decrease with increasing SiO_2 suggesting control by feldspar loss. The low P_2O_5 content (Figure 5.2) indicates apatite loss.

Table 5.1: Details of phonolite samples from Garian Volcanic Province studied here.

Sample	Rock type	Rock	Location	Latitude-longitude	Origin
G8	Phonolite	Plug	35 km NE of Garian	32°12'44.28''N 13°23'6.42''E	February 2010
G10	Phonolite	Laccolith	Kaf Abu Ghannush 2 km NW of Garian	32°11'28.36''N 13°00'0.42''E	February 2010
G11	Phonolite	Plug	Kaf Bu Rshadah 4.5 km NW of Garian	32°12'10.3''N 12°59'10.32''E	February 2010
G12	Phonolite	Plug	Kaf Tunat 8 km NW of Garian	32°13'24.06''N 12°57'58.8''E	February 2010
G81B	Phonolite	Plug	Kaf Mantrus ~12 km W of Garian	32°12'48''N 12°53'55.17''E	Manchester University collection

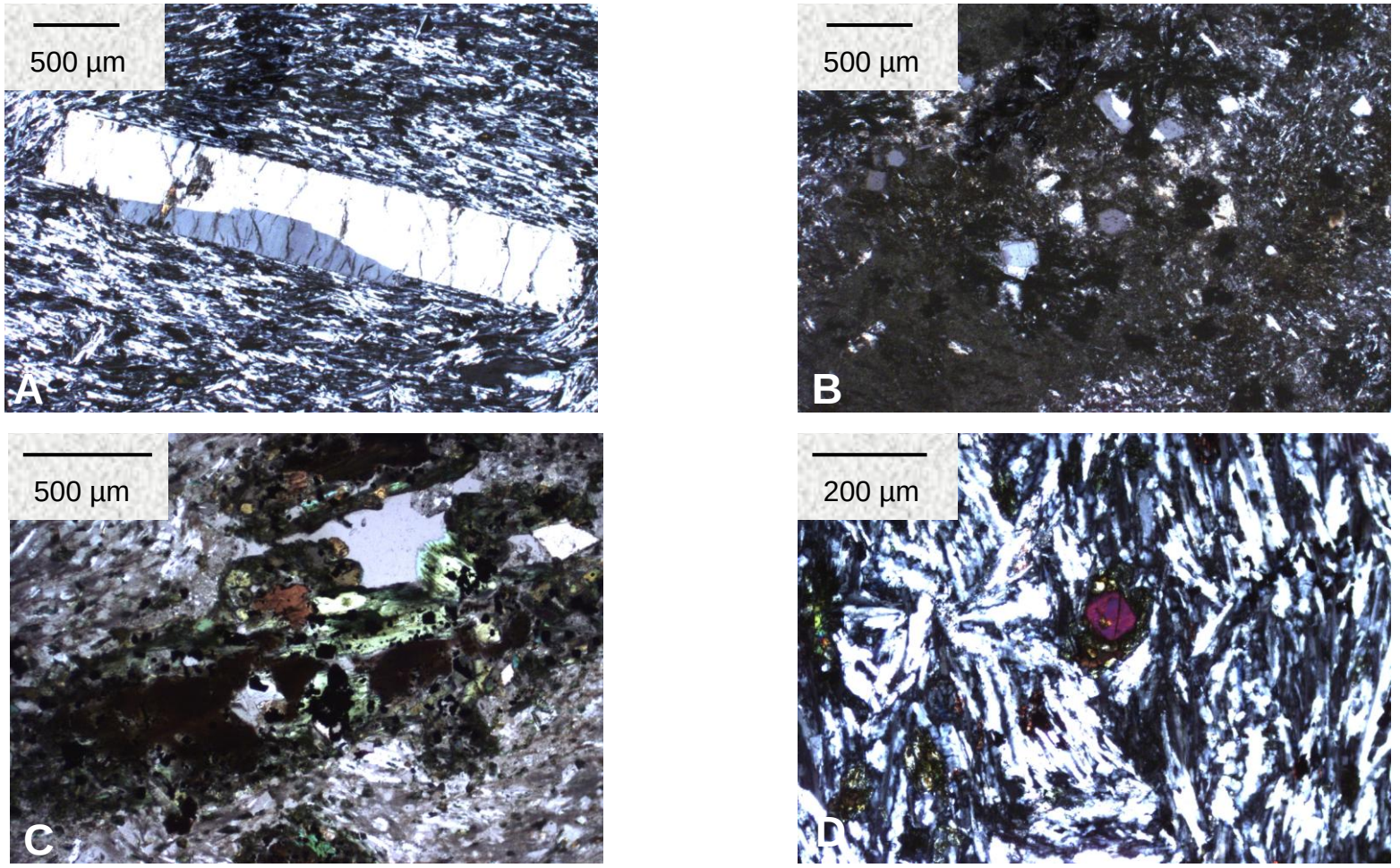

Figure 5.1: Photomicrograph, under crossed polarised of phonolite from GVP. (A) Large sanidine phenocryst set in fine-grained of alkali feldspars (trachytic texture) (G10). (B) Small rectangular nepheline phenocrysts (G8). (C) Large resorbed and altered biotite crystal (G12). (D) Very small crystal of sphene set in fine-grained of alkali feldspars (trachytic texture) (G10).

5.3.2 Trace elements

Phonolite trace element data are presented in Table C.5. They are strongly depleted in compatible elements compared to the basalts. Low Ba (37.6-4.1 ppm) and Sr (54.9-4.8 ppm) indicate that feldspars have been lossed by fractional crystallisation from the phonolite magmas.

Incompatible element (e.g., Rb, Zr and Nb) concentrations are high relative to the basalts. The Zr content of phonolitic magmas can be used as an indicator of fractionation, with more evolved compositions having higher Zr concentrations (Allegre *et al*., 1977). Zr concentrations range from 1010.7 to 2728.5 ppm. These compositions are significantly higher than the Type-1 phonolites (Lustrino *et al*., 2012) except two samples from Kaf Abu Ghannush (G10) and Kaf Tunat (G12) are closer to the type-1 field. On the other hand, they are compatible with the range of previous measurements of Type-2 phonolites (Lustrino *et al*., 2012) and other phonolites from GVP (Aboazom *et al*., 2006), though sample G8 is significantly higher than the highest measured previously (1957 ppm). The Zr concentrations in Garian phonolites are significantly higher than the highest measured in other rift-related phonolites from Massif Central, France (Dautria *et al*., 2004); Central European Volcanic Province, Germany (Jung *et al*., 2013); Atakor (Hoggar), Algeria (Dupuy *et al*., 1993); northern Kenya rift, Kabeto *et al.,* 2001 and Darfur volcanic province, Sudan (Lucassen *et al*., 2012).

Several trace elements are plotted against Zr in Figure 5.3 along with the data from Aboazom *et al*. (2006) and Lustrino *et al*. (2012). In general, the incompatible elements have strong positive correlations with Zr (Figure 5.3) supporting the role of extensive fractional crystallisation of mafic minerals in the generation of the phonolites. The type-1 phonolites are significantly less enriched in incompatible trace elements than the type-2 phonolites (Figure 5.3 and Lustrino *et al*., 2012). Two of the samples of this study (G10 and G12) plot in, or very close to, the range of type-1 phonolitic rocks. The REE (e.g., Yb and La) behave similarly to Nb and Rb but are slightly depleted in the most evolved phonolite (G8) (Figure 5.3). This probably reflects the loss of a REE-bearing mineral (Sazhinite, $Na_3LaSi_6O_{15}(H_2O)_2$) from the melt during crystallisation.

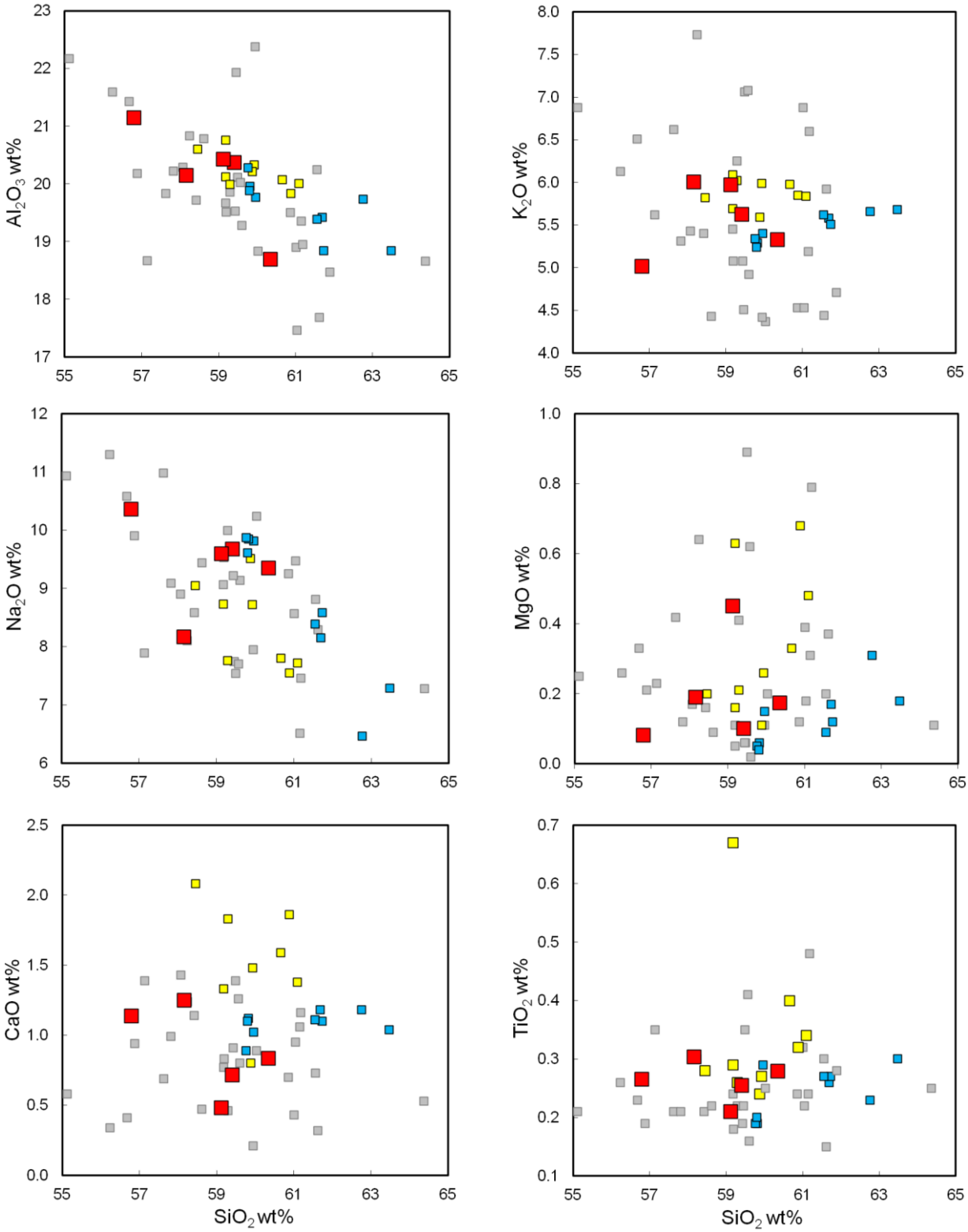

Figure 5.2 Major element oxides of GVP phonolites plotted against SiO_2 wt%. Red squares: this study; small grey squares: previous studies (Almond *et al*., 1974; Hegazy, 1999; Aboazom *et al*., 2006). Type-1 and type-2 phonolites (Lustrino *et al*., 2012) are yellow and blue squares.

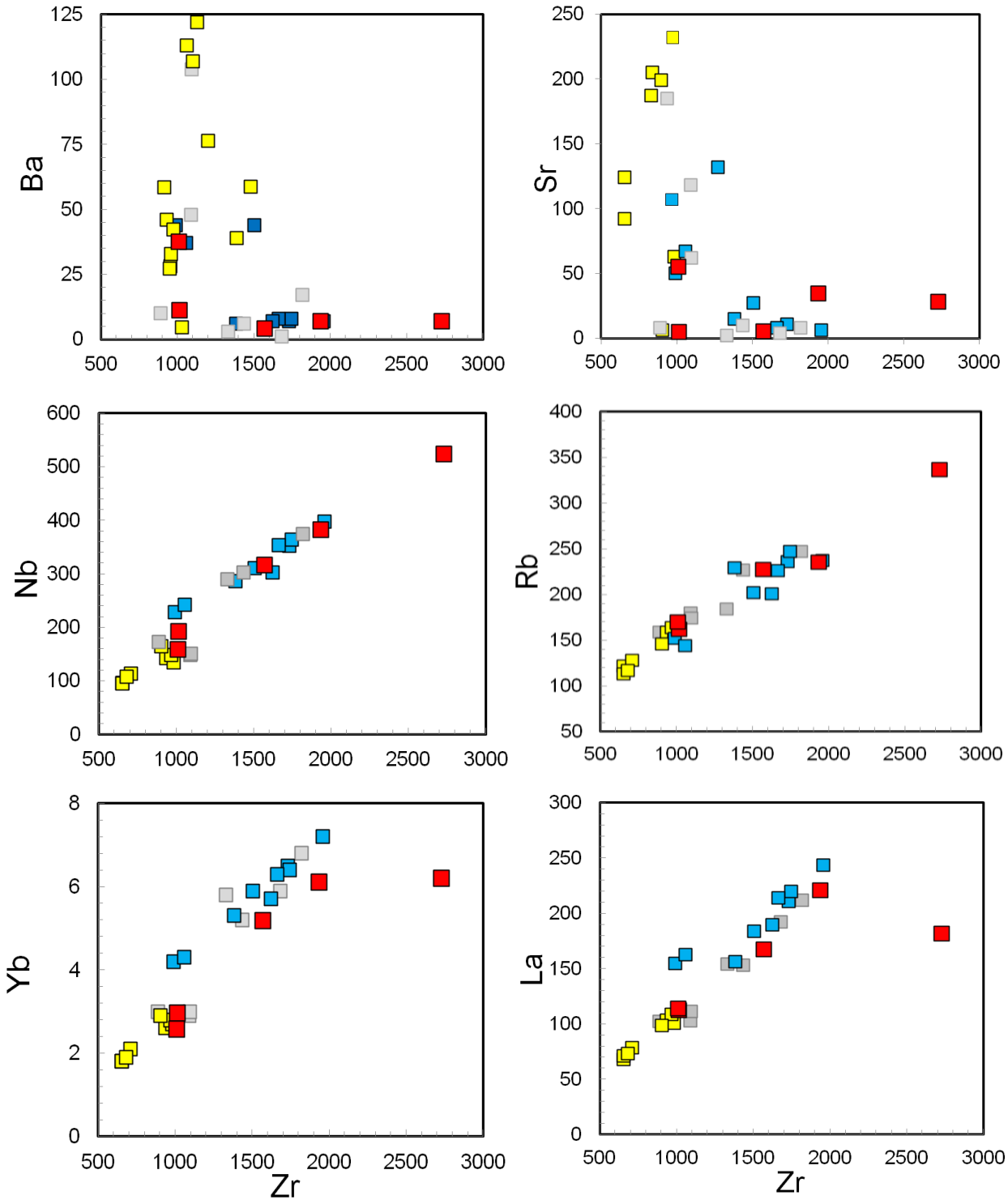

Figure 5.3 Plot of trace elements of GVP phonolites versus Zr (ppm) as differentiation index. Red squares: This study. Literature data from Aboazom *et al*. (2006) (grey) Lustrino *et al*. (2012) (yellow and blue: Type-1 and Type-2 trachytes and phonolites, respectively). Symbols are the same as used in Figure 5.2.

5.3.3 Rare earth elements

Chondrite-normalized REE patterns of all phonolites are plotted in Figure 5.4 and the data is presented in Table C.8. All samples have similar REE patterns; steep LREE [$(La/Sm)_n$ = 20.45-13.55] and spoon-shaped HREE patterns [$(Gd/Yb)_n$ = 1.27-0.77]. REE concentrations range from 320 to 620 times the chondrite value. As noted for incompatible trace elements, the type-1 phonolites are significantly less enriched in REE than the type-2 phonolites (Lustrino *et al*., 2012). Three of the five samples plot in range of type-2 phonolites while the Kaf Abu Ghannush (G10) and Kaf Tunat (G12) samples have relatively low REE concentrations and patterns that overlap the type-1 phonolites. All samples have small negative Eu anomalies. The phonolites of this study have similar REE patterns of Meidob phonolites (Darfur volcanic province, Sudan, Lucassen *et al*., 2012) and Atakor (Hoggar), Algeria (Dupuy *et al*., 1993), but with slightly less enriched in HREE. While, the phonolites of Central European Volcanic Province, Germany (Jung *et al*., 2013) have REE patterns similar to type-1 phonolites. Figure 5.4 of Chondrite-normalized REE patterns with negative Eu anomaly indicating that they are clearly compatible with the Type-2 phonolite of Lustrino *et al*. (2012) classification.

The spoon-shaped REE patterns (Figure 5.4) are typical of phonolites, indicating fractionation of amphibole ± aegirine-augite ± sphene ± apatite (Mahood and Stimac, 1990). The strong negative Eu-anomalies are likely results from fractionation of feldspar.

5.3.4 Sr and Nd isotopes

The Sr and Nd isotopic composition of the 5 phonolites are presented in Table C.9 and plotted in Figure 5.5. $^{87}Sr/^{86}Sr$ (0.71134-0.77947) are significantly more radiogenic than the GVP basalts (0.70319-0.70563, see section 3.3.4) and two type-1 GVP phonolites (0.70327-0.7038) reported by Lustrino *et al*. (2012). Phonolites have $^{143}Nd/^{144}Nd$ (0.51281-0.51292) overlap the range of GVP basalts and the type-1 phonolites (Figure 5.5). The GVP phonolites are different from phonolitic rocks from Massif Central, France (Dautria *et al*., 2004); Central European Volcanic Province, Germany (Jung *et al*., 2013); Atakor (Hoggar), Algeria (Dupuy *et al*., 1993)

and Darfur volcanic province, Sudan (Lucassen *et al*., 2012) mainly by having less radiogenic $^{87}Sr/^{86}Sr$ values (Figure 5.5).

The isotopic variation of the GVP phonolites clearly reflects assimilation of crustal material during fractionation. The details of crustal contamination are discussed in section 5.5.3.

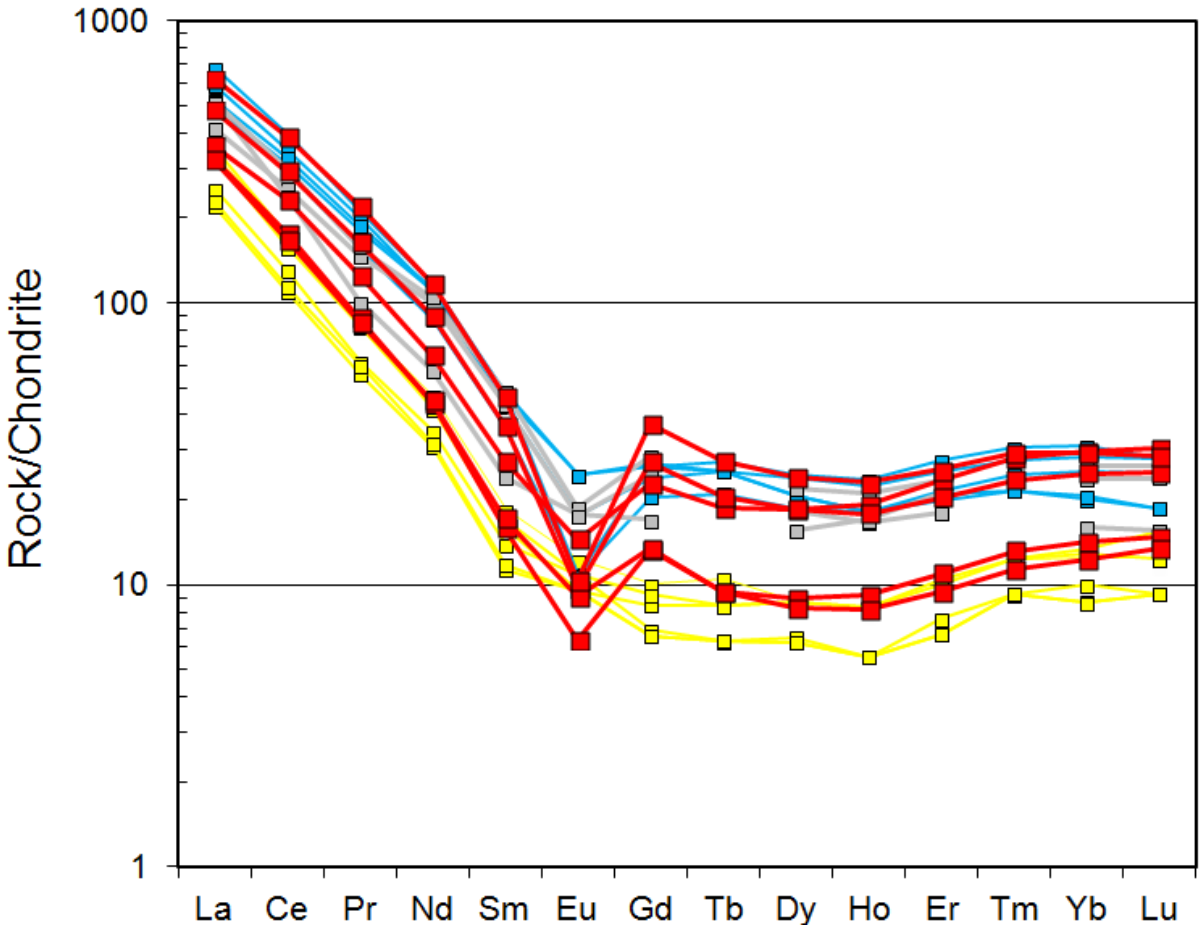

Figure 5.4: Chondrite-normalized REE patterns of phonolite rocks from the Garian volcanic province are shown as red squares. Type-1 and type-2 phonolites (Lustrino *et al*. 2012) are yellow and blue squares respectively. Jabal Al Hasawinah phonolites are grey squares.

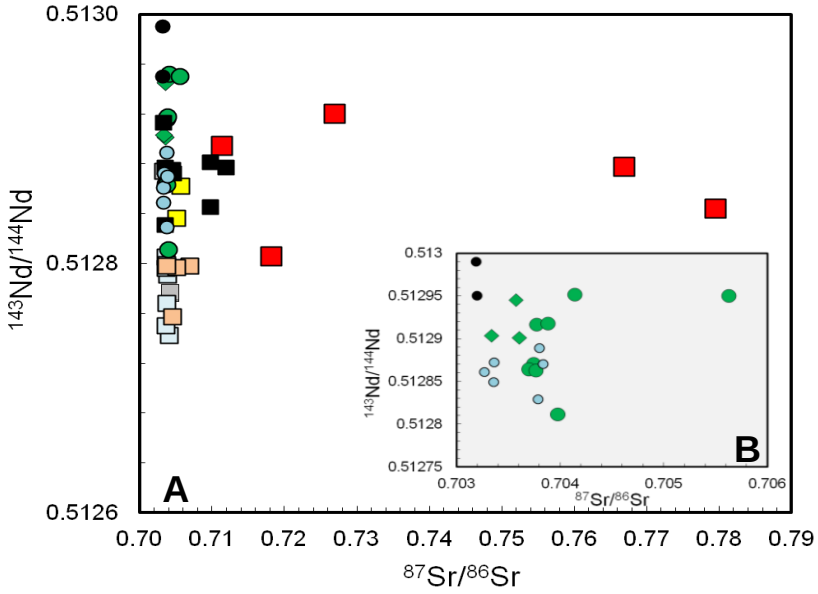

Figure 5.5: (A) $^{143}Nd/^{144}Nd$ vs. $^{87}Sr/^{86}Sr$ for phonolites from the Garian volcanic province (red squares). Type-1 phonolites from GVP (Lustrino *et al*., 2012) are plotted as yellow squares. Phonolites from Massif Central, France (black squares) (Dautria *et al*., 2004); European Volcanic Province, Germany (brown squares) (Jung *et al*., 2013); Atakor (Hoggar), Algeria (grey squares) (Dupuy *et al*., 1993) and Darfur volcanic province, Sudan (light blue squares) (Lucassen *et al*., 2012). GVP basalts of this study are green circles and diamonds. Small symbols are previous studies of Beccaluva *et al*. (2008) (black circles) and Lustrino *et al*. (2012) (blue circles). (B) Magnification of $^{143}Nd/^{144}Nd$ vs. $^{87}Sr/^{86}Sr$ plot showing the GVP basalts.

5.4 $^{40}Ar/^{39}Ar$ geochronology

5.4.1 Introduction

$^{40}Ar/^{39}Ar$ age determinations were made by laser step-heating approach of sanidine separates from the four phonolite collected in 2009 (G8, G10, G11, and G12). The measurements were made at the Ar/Ar laboratory at SUERC. The data tables and sample preparation and analysis procedures are presented in Appendix D. The $^{40}Ar/^{39}Ar$ data are reported in probability distribution diagrams in Figures 5.6 to 5.9. The lower panels show the apparent age (x-axis) plotted versus the summation of the normal distribution of each individual analysis. The upper two panels display data from single-crystal analyses showing the percent radiogenic (non-atmospheric) ^{40}Ar. The probability distribution diagram is useful for displaying single-crystal laser-fusion

data in order to assess the distribution of the population. Individual analyses which fall outside a distinct population are easily identified. $^{40}Ar/^{39}Ar$ ages are calculated relative to the optimisation model of Renne *et al*. (2010, 2011). Summary statistics are provided in Table 5.3. All uncertainties are 1σ.

5.4.2 $^{40}Ar/^{39}Ar$ age determinations

5.4.2.1 Phonolite plug from Kaf Bu Rshadah (G11)

23 of the 26 laser fusion ages of single sanidine crystals define a statistically coherent population. Three analyses are distinctly older, and may represent a xenocryst. The weighted mean age is 8.186 ± 0.011 Ma (MSWD = 0.80). All analyses have consistently high radiogenic yields ($^{40}Ar^*$ ≥ 95 %) indicating a chemically homogeneous population of unaltered crystals. The isochron age (8.220 ± 0.030 Ma) is indistinguishable for the 23 analyses used to calculate the age. The $^{40}Ar/^{36}Ar$ intercept of 270 ± 20 (Figure 5.6 and Table 5.3) is slightly lower than the atmospheric value of 298.56 ± 0.31 (Lee *et al*., 2006) ruling out excess ^{40}Ar. The absolute age relative to Renne *et al*. (2011) is 8.267 ± 0.012 Ma.

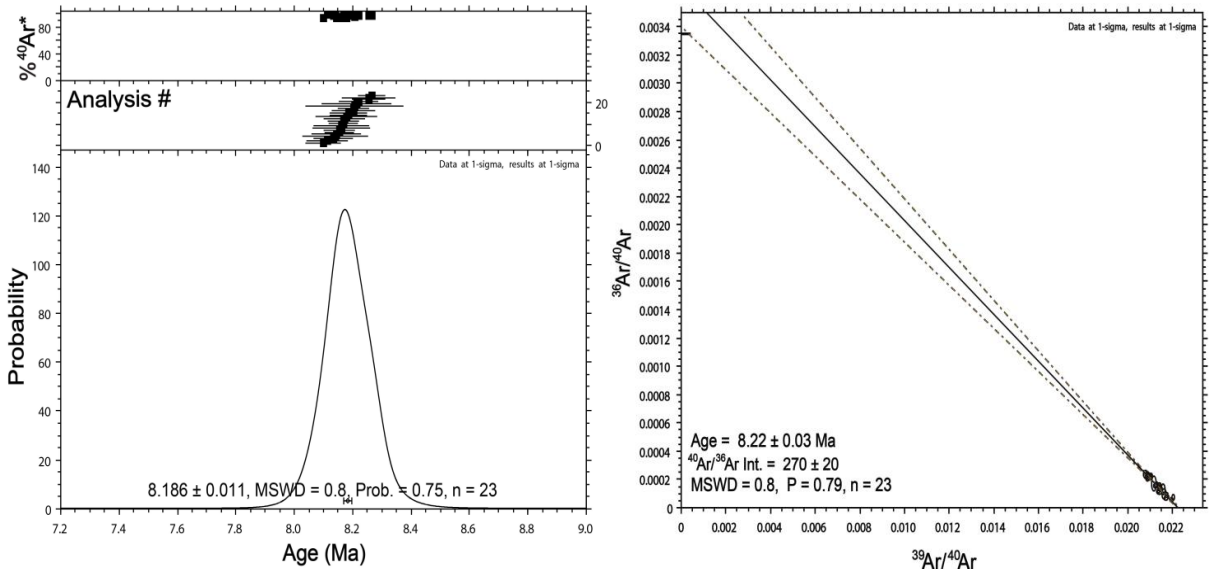

Figure 5.6: Ideogram (left) and inverse isochron plot (right) showing (laser fusion) from G11 and $^{40}Ar/^{39}Ar$ ages of sanidine.

5.4.2.2 Phonolite plug from from Kaf Tunat (G12)

17 of the 25 laser fusion ages of single sanidine crystals define a statistically coherent two population (sanidine and plagioclase crystals, due to its comparatively low K/Ca ratio and $^{39}Ar_K$ yield (Table D1.13). This may indicate some alteration and loss of radiogenic argon from the younger age crystals and the older ages may represent a xenocryst. The weighted-mean age for this sample is 8.171 ± 0.011 Ma (MSWD = 0.80) with systematic regular decrease of $^{40}Ar^*$. The inverse isochron age (8.130 ± 0.030 Ma) is indistinguishable from the mean age with lower MSWD (0.70). The $^{40}Ar/^{36}Ar$ intercept of 307 ± 5 (Figure 5.7 and Table 5.3) is higher than the atmospheric value of 298.56 ± 0.31 (Lee *et al*., 2006) suggest that a small amount of excess argon is present (see inverse isochron diagram). The absolute age relative to Renne *et al*. (2011) is 8.252 ± 0.014.

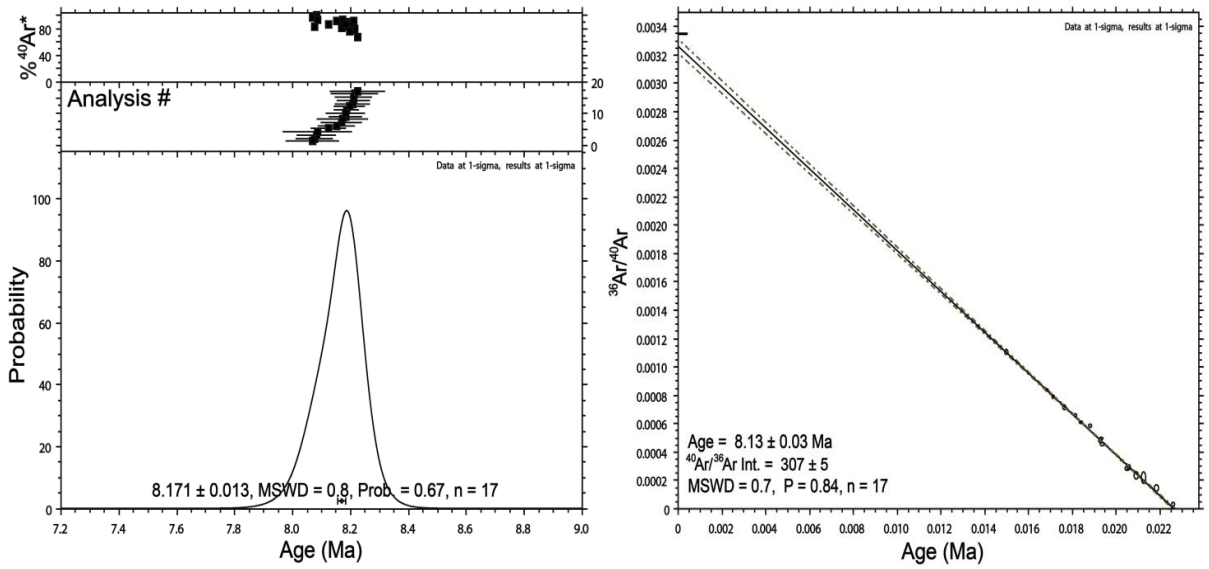

Figure 5.7: Ideogram (left) and inverse isochron plot (right) showing (laser fusion) from G12 and $^{40}Ar/^{39}Ar$ ages of sanidine.

5.4.2.3 Phonolite plug from 35 km northeast of Garian (G8)

This sample produced data similar to that of G11 and similar interpretations apply. 20 of the 35 laser fusion ages of single sanidine crystals define a statistically coherent data set. The 15 outliers are younger and older. This may indicate some alteration and loss of radiogenic argon from the younger age crystals and the older ages may represent a xenocryst. The mean age for this sample is 8.135 ± 0.015 Ma (MSWD = 0.80). The inverse isochron age of 8.160 ± 0.030 Ma is indistinguishable from the weighted mean age. Data plotted on an isotope correlation plot (Figure 5.8 and Table 5.3) define an isochron with initial trapped component of 276 ± 19 is slightly lower than the atmospheric value of 298.56 ± 0.31 (Lee *et al*., 2006) ruling out excess ^{40}Ar. and gives an absolute age of 8.216 ± 0.016 Ma.

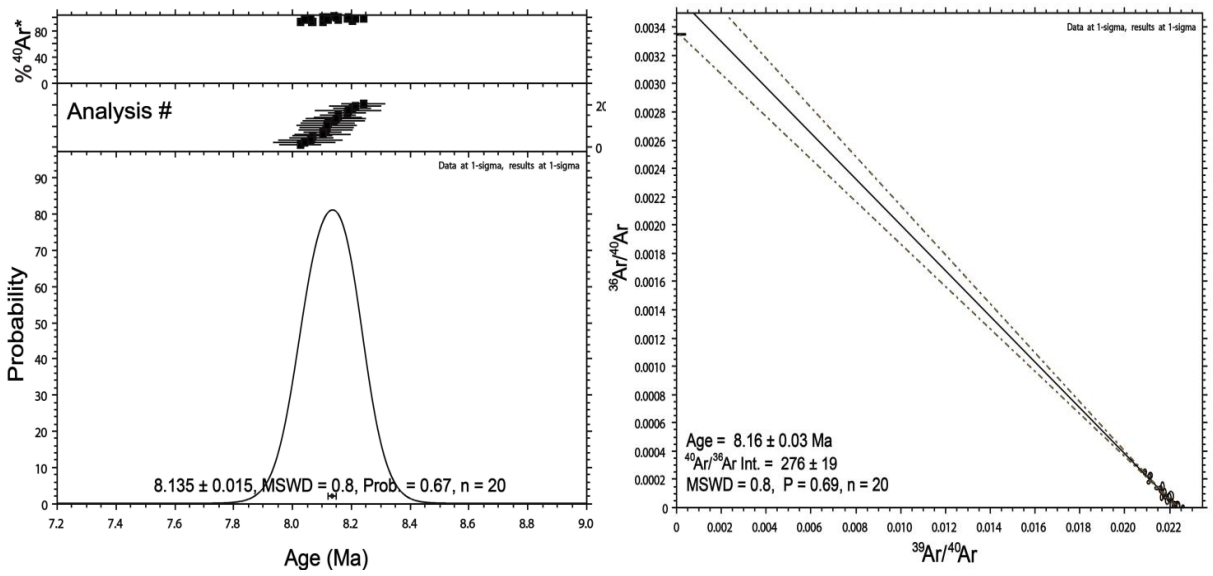

Figure 5.8: Ideogram (left) and inverse isochron plot (right) showing (laser fusion) from G8 and $^{40}Ar/^{39}Ar$ ages of sanidine.

5.4.2.4 Phonolite laccolith from Kaf Abu Ghannush (G10)

This sample produced data similar to that of G8, and similar interpretations apply. 26 of the 27 laser fusion ages of single sanidine crystals define a statistically coherent population. One analysis is distinctly older, and may represent a xenocryst. The mean age for this sample is 8.107 ± 0.009 Ma (MSWD = 1.10). The inverse isochron age of 8.100 ± 0.020 Ma is overlap to the mean age. The $^{40}Ar/^{36}Ar$ intercept is 296 ± 7 is indistinguishable from air. The absolute age relative to Renne *et al*. (2011) is 8.187 ± 0.010 Ma.

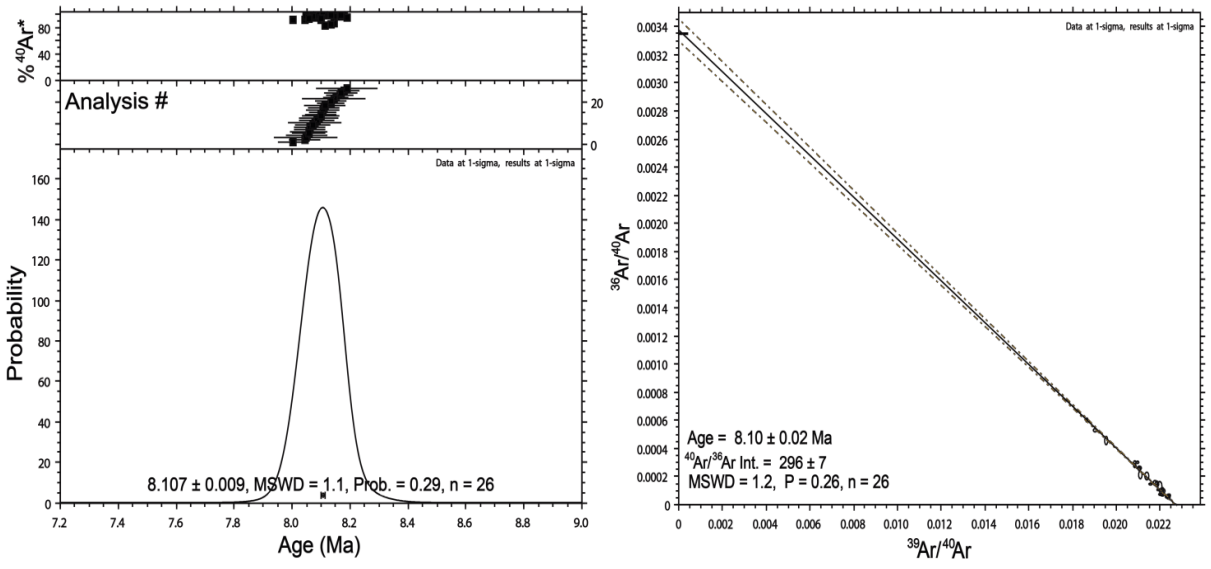

Figure 5.9: Ideogram (left) and inverse isochron plot (right) showing (laser fusion) from G10 and $^{40}Ar/^{39}Ar$ ages of sanidine.

Table 5.2: $^{40}Ar/^{39}Ar$ data of the phonolites from Garian Volcanic Province.

Decay constants of Steiger & Jager (1977), Fish Canyon sanidine at 28.02 ± 0.16 Ma (Renne *et al*., 1998), atmospheric argon isotope ratios of Lee *et al*. (2006) and Mark *et al*. (2011b) (298.56 ± 0.31).										Optimisation model (Renne *et al*., 2010, 2011) - full external precision (standard age, decay constant).	
ID	Sample type	Ideogram age (Ma)	± 1σ	MSWD	Isochron age (Ma)	± 1σ	$^{40}Ar/^{36}Ar$	± 1σ	MSWD	Age (Ma)	± 1σ
G11	Phonolites	8.186 (*n* = 23)	0.011	0.800	8.22 (*n* = 23)	0.030	270	20.000	0.800	8.267	0.012
G12	Phonolites	8.171 (*n* = 17)	0.013	0.800	8.13 (*n* = 17)	0.030	307	5.000	0.700	8.252	0.014
G8	Phonolites	8.135 (*n* = 20)	0.015	0.800	8.16 (*n* = 20)	0.030	276	19.000	0.800	8.216	0.016
G10	Phonolites	8.107 (n = 26)	0.009	1.100	8.10 (n = 26)	0.020	296	7.000	1.200	8.187	0.010

5.4.3 Implications of the geochronology

The weighted mean Ar/Ar ages of the 4 phonolite intrusions are virtually indistinguishable thus they define a single age population (8.267 ± 0.012 to 8.187 ± 0.10 Ma) This age is significantly younger, and more precise, than the range of whole rock K-Ar ages determined in earlier studies (37.2 ± 0.7 Ma, Mobil Oil Company, 1967 and 40.7 ± 1.4 to 37.7 ± 1.3 Ma, Piccoli, 1971) (summarised in Table 2.1, Figure 3.31).

The old K-Ar ages probably reflect the presence of excess Ar in the sanidine phenocrysts (McDougall *et al*., 1969) or the presence of xenocrysts. Lippolt *et al*. (1990) demonstrated the presence of excess Ar in Quaternary phonolitic rocks from the eastern Eifel.

There is no evidence of a significant pulse of basaltic magmatism that coincides with the phonolite intrusions. The new phonolite ages are significantly older than the oldest basaltic lavas dated in this study (5.44 ± 0.04 to 2.67 ± 0.01 Ma), and the mafic intrusive are older than the phonolites. The apparent absence of phonolite and trachyte eruptions associated with the dated intrusive indicates that the region has been affected by erosion that may have removed all flows (evidence for that the presence of plutonic at the surface, G10B syenogabbro plug, Ras al Moher). This would have removed evidence of basalt flows have ages more than 5 Ma.

The K/Ar age of phonolite from Jabal Al Hasawinah was determined as 23.2 - 15.7 Ma (Jurak, 1978). The older K-Ar ages can not be compared to the new ages of Garian phonolites because may affected by presence of excess ^{40}Ar.

5.5 Petrogenesis of the GVP phonolites

5.5.1 Introduction

The prevailing model for the production of phonolite magmas is based on fractional crystallisation of basanite-like melts in complex assimilation and

fractional crystallisation processes in the lithosphere, mainly within the crust (e.g., Baker *et al*., 1977; Wilson *et al*., 1995; Panter *et al*., 1997; Gourgaud and Vincent, 2004). Low degrees of re-melting of mafic rocks in the lithosphere may generate a small proportion of the phonolite and is probably related to small magma volumes (e.g., Bohrson and Reid, 1997; Kaszuba and Wendlandt, 2000; Legendre *et al*., 2005).

In the most recent study, Lustrino *et al*. (2012) showed that both phonolite types are the result of extensive fractional crystallisation of plagioclase and alkali feldspar. Type-1 trachytes and phonolites typically contain phenocrysts of alkali feldspar, clinopyroxene, amphibole, magnetite, and titanite. They are characterised by a smooth, spoon-shaped REE pattern without negative Eu anomalies. They are formed by the removal of clinopyroxene, plagioclase, alkali feldspar, amphibole, magnetite and titanite starting from benmoreitic magmas, found in the same outcrops. Type-1 trachytes and phonolites occur only at the Kaf El Tekut dome, and are similar to pantelleritic volcanic rocks from, for example, Pantelleria, Sicily Channel, and Boseti, Ethiopia (Avanzinelli *et al*., 2004; Ronga *et al*., 2010). Type-2 trachytes and phonolites contain sanidine, anorthoclase and small rectangular nepheline and biotite phenocrysts. They are characterised by a negative Eu anomaly (Eu/Eu* = 0.67-0.25), have higher concentrations of HFSE (Nb, Ta, Zr and Hf), REE and Ti than the type-1 phonolites. They have likely resulted from extensive fractional crystallisation of mafic alkaline magmas without the removal of titanite.

The processes that produced the GVP phonolites will be explored in the next sections. Variation results from fractional crystallisation of closely similar parental liquids and other process such as crustal contamination will tested by using the isotope data in conjunction with trace element to provide additional constraints on the nature of the likely AFC process that affected the phonolites.

5.5.2 Fractional crystallisation

The two phonolite types of Lustrino *et al*. (2012) are clearly distinct in La-Zr and Yb-Zr plots (Figure 5.3). Three of the samples studied here are compositionally indistinguishable from the type-2 phonolites, while the Kaf Abu Ghannush (G10) and Kaf Tunat (G12) samples appear to be intermediate in composition, often closer to the type-1 field. A similar story is apparent from the chondrite-normalized REE patterns (Figure 5.4).

The two phonolite types can be distinguished on the basis of Eu anomalies: phonolites of type-1 show no Eu anomaly or small positive Eu anomalies suggesting the presence of cumulus feldspar, while type-2 phonolites have significant negative Eu anomalies (Eu/Eu* = 0.67-0.25). Figure 5.10A displays the positive correlation between the Ba concentration and Eu/Eu*, while the 5.10B shows the negative correlation between the Yb concentration and Eu/Eu*. The two types of phonolites roughly fall along alkali feldspar-plagioclase fractionation vectors but type-1 phonolites with limited fractionation trend compared to type-2 phonolites. The strong negative Eu anomalies of the samples in this study demonstrate all are clearly related to type-2 phonolite.

Figure 5.11A shows that the $(Dy/Yb)_n$ of basalts and phonolites are not correlated with indicators of magmatic differentiation. The basalt $(Dy/Yb)_n$ (1.5-2) is significantly higher than the phonolites (0.5-1), with a significant gap in the $(Dy/Yb)_n$ between basaltic and phonolite samples. The fractionation of minor amphibole from the basaltic rocks could have caused this fractionation (e.g., Lucassen *et al*., 2012), but amphibole phenocrysts are not observed in the thin-sections. It was likely important during an intermediate state of the magmatic fractionation, which is not documented in the rocks, because of the compositions gap between mafic and phonolitic rocks (Figure 3.13). Amphibole formation, which is also indicated by the depletion of MREE in the phonolite rocks as seen in the $(Dy/Yb)_n$, may have resulted in the formation of amphibole-rich cumulate rocks in the crust.

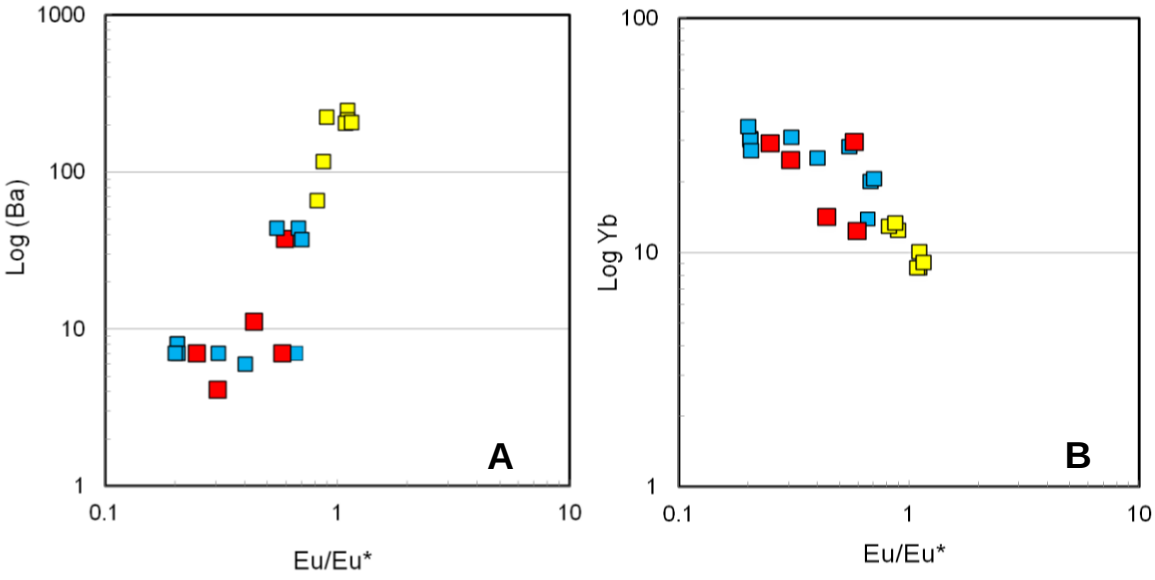

Figure 5.10: (A) Plot of Log Ba versus Log Eu/Eu*. (B) Plot of Logarithm Yb versus Logarithm Eu/Eu*. Red squares: This study. Data from Lustrino *et al*. (2012) (yellow and blue: type-1 and type-2 phonolites respectively). $(Eu/Eu^*)_n$ = Eu/[(Sm + Gd) × 0.5].

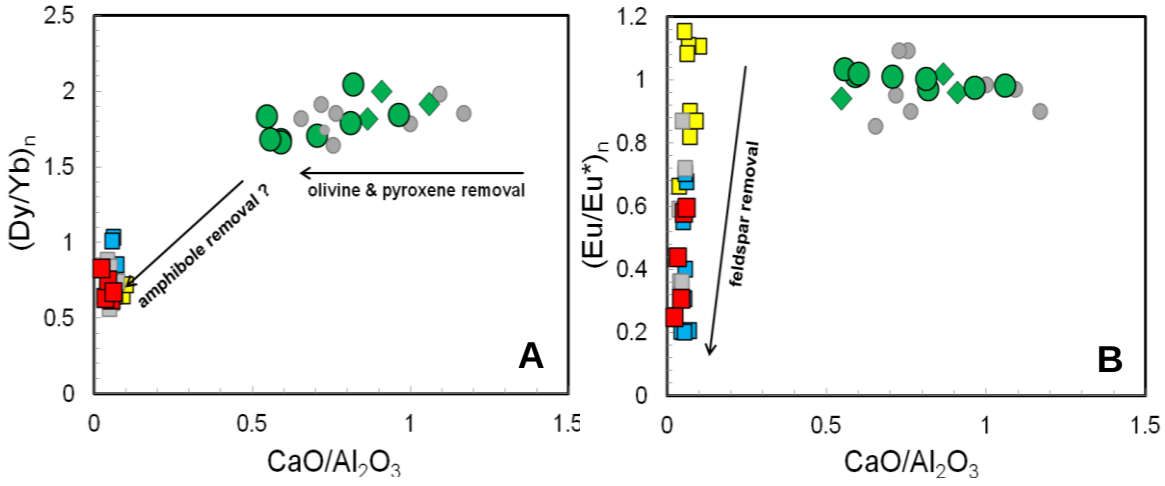

Figure 5.11: Relationship between CaO/Al_2O_3 and $(Dy/Yb)_n$ (A) and $(Eu/Eu^*)_n$ (B) of the basalt and phonolite samples from Garian volcanic province. Green circles: Basalt flow; diamonds: intrusions or dykes. Grey: previous studies (Aboazom *et al*., 2006; Lustrino *et al*., 2012). Red squares: This study. Literature data from Aboazom *et al*. (2006) (grey) Lustrino *et al*. (2012) (yellow and blue: Type-1 and Type-2 trachytes and phonolites, respectively).

Figure 5.11B show that the basaltic rocks do not indicate important plagioclase fractionation, that is $(Eu/Eu^*)_n$ is around 1. Crystal fractionation initially was dominated by removal of olivine and pyroxene as long as CaO/Al_2O_3 ratio was above 0.5. The $(Eu/Eu^*)_n$ phonolites decreases sharply at low CaO/Al_2O_3 (Figure 5.11B) indicating the onset of feldspar fractionation. This observation indicate that the two types of phonolites are generated by plagioclase fractionation dominate and fractionation of amphibole.

5.5.2.1 Quantitative observations

In order to quantify the extent that crystal fractionation has affected the phonolitic rocks from the parent basalt and to try to evaluate the role of this process in the differentiation of this magma, I model the fractional crystallisation (Figure 5.12) by using logarithms of Sr and Rb concentrations. Lines are drawn for mafic and alkali feldspar minerals using D_{sr} varies between 0.8 (pyroxene) and 1.5 - 7.0 (plagioclase and alkali feldspar) and D_{Rb} = 0.1 (mafic and alkali feldspar minerals). Uses the most evolved basalt G1 as starting composition (Sr = 910.8 ppm, Rb = 70.3 ppm).

The amount of fractional crystallisation of a mineral phase or assemblage necessary to generate the observed melt composition can be modelled using the Rayleigh law, which describes the case where crystals are removed from the melt instantly after crystallisation (e.g., Rollinson, 1993). Rayleigh/fractional crystallisation are described by:

$$C_l/C_0 = F^{(D-1)}$$

Where C_0 is the concentration of an element in the initial magma, C_l is the concentration of the same element in the remaining melt, F is the remaining melt fraction and D is the partition coefficient between the crystallizing mineral and the magmatic liquid. This is rewritten as:

$$C_l = \left(F^{(D-1)}\right) * C_0$$

This gives the concentration on an element of known D in the remaining liquid after a certain amount (1-F) of the fractional crystallisation of a given mineral or mineral assemblage.

The results demonstrate that the GVP phonolites are dominantly the result of crystallisation of plagioclase and alkali feldspar. The samples studied here require that between 50% to 83% crystallisation of the more evolved basanitic liquid in order to reproduce the phonolite chemistry, which required high bulk distribution coefficient for Sr (2 to 7) and low bulk distribution coefficient for Rb (0.1). The results are compatible with evolved high-alkali lavas from the northern Kenya rift (Kabeto *et al*., 2001), by using fractional models assumed D_{sr} to vary between 0.8 and 5 and degree of fractionation between 45% - 80%.

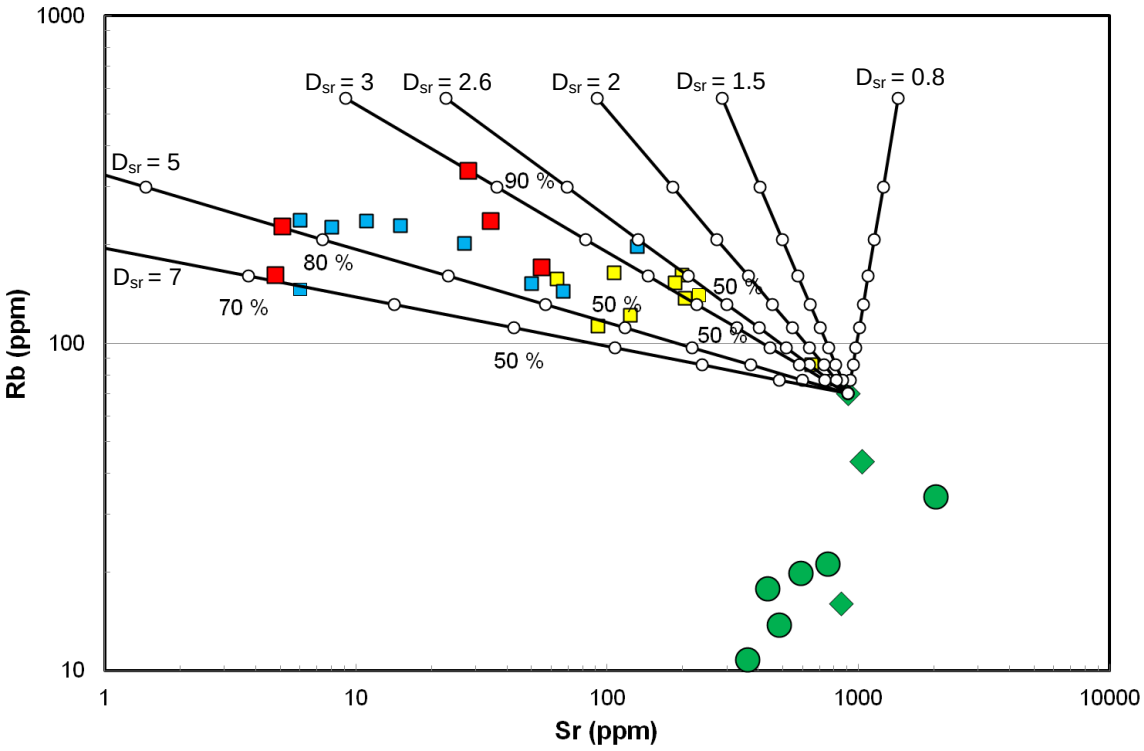

Figure 5.12: Fractional crystallisation (solid line with small circles) model calculated assuming the most evolved basalt G1 as starting composition (Sr = 910.8 ppm, Rb = 70.3 ppm). D_{sr} varies between 0.8 and 7.0 and D_{Rb} = 0.1. Red squares: phonolites of this study. Type-1 and type-2 phonolites (Lustrino *et al*., 2012) are yellow and blue squares.

5.5.3 Assimilation fractional crystallisation

The high radiogenic $^{87}Sr/^{86}Sr$ of the phonolites of this study with slight variation of $^{143}Nd/^{144}Nd$ ratios is a clear indication that crustal contamination (Figures 5.13 and 5.14).

In this section I concentrate on the evidence from Sr isotope systematic. AFC calculations were carried out using basalt G15B ($^{87}Sr/^{86}Sr$ = 0.70370 and Sr = 363.4; Table C.9, Appendix C) as starting basaltic compositions and using equations from DePaolo's (1981) (Figure 5.13).

Figure 5.13 shows the $^{87}Sr/^{86}Sr$ is plotted against Sr concentration, and shows clearly the effect of mixing. A general increase in $^{87}Sr/^{86}Sr$ can be observed with decreasing Sr content, suggesting that, if assimilation of crustal material occurred, the system has been buffered for Sr isotopes in the more Sr-rich samples. The model shows that the all data fit the mixing curve indicating that they are controlled by bulk mixing process.

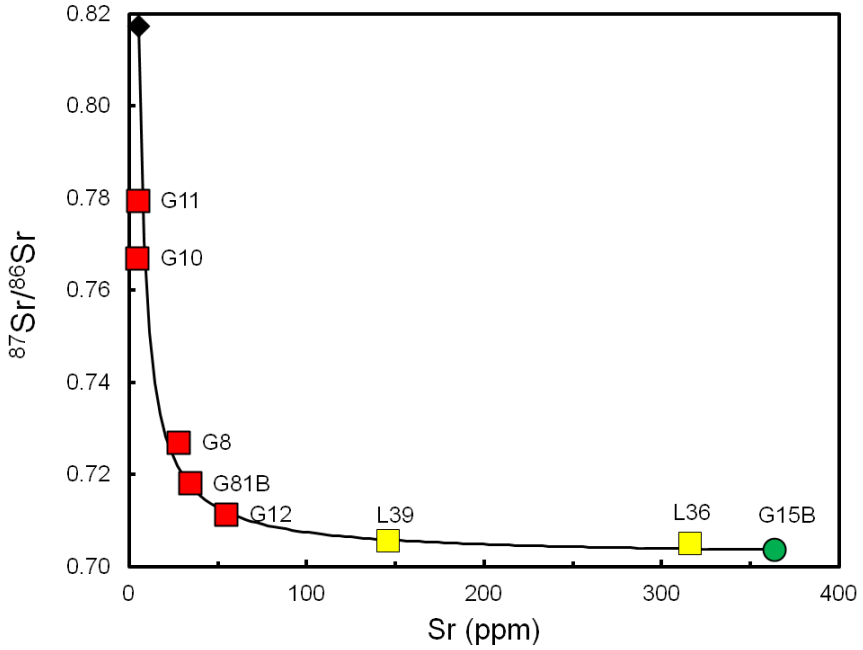

Figure 5.13: Plot of $^{87}Sr/^{86}Sr$ against Sr concentration of GVP phonolites from this study (red squares) and type-1 phonolites (yellow squares) from Lustrino *et al*. (2012). The model curve is calculated for mixing between upper crust (defined by 550 Ma of 2-mica granite from the Tibesti Massif (black diamond) ($^{87}Sr/^{86}Sr$ = 0.81736, Sr = 5.25 ppm; Suayah *et al*., 2006) and G15B basalt (green circle) (Table C.9, Appendix C).

The two phonolite type-1 (strongly porphyritic rocks) samples (L36 and L39, Kaf Tukut) from Lustrino *et al*. (2012) show variable Sr contents, but with low variation in the $^{87}Sr/^{86}Sr$ ratios (Figure 5.13) can be explained with cumulus of plagioclase and/or pyroxene in these rocks. This characteristics of isotopic composition may be taken as representing the isotopic composition of their parental melt source, regardless of whether crustal contamination took place or not.

In contrast, the samples from Abu Ghannush (G10) and Bu Rshadah (G11) show lowest Sr contents, and highest $^{87}Sr/^{86}Sr$ ratios. This may be confirmed that the lowest Sr contents may be useful in pinpointing relatively large amounts of crustal contamination. This observation of Sr-isotope contrast between the phonolite rocks of this study and Lustrino *et al*. (2012) samples could be taken as evidence of the differences between those two types of phonolite.

5.5.3.1 Model of assimilation-fractional crystallisation

The GVP phonolites are characterised by unusually radiogenic $^{87}Sr/^{86}Sr$ ratios (0.71133 to 0.77947) despite having almost constant $^{143}Nd/^{144}Nd$ ratios. The GVP phonolites have high radiogenic $^{87}Sr/^{86}Sr$ ratios compared to other rift-related phonolites from Massif Central, France (0.70335 to 0.71192) (Dautria *et al*., 2004); Central European Volcanic Province, Germany (0.703757 to 0.706972) (Jung *et al*., 2013); Atakor (Hoggar), Algeria (0.703293 to 0.712715) (Dupuy *et al*., 1993); northern Kenya rift (0.70323 to 0.71547), Kabeto *et al.,* 2001 and Darfur volcanic province (Meidob) (0.70364 to 0.70581), Sudan (Lucassen *et al*., 2012).

The GVP phonolites have low Sr concentrations (4.8-54.9 ppm) relative to the GVP basalts, and significantly negative Eu anomlies (Figure 5.4 and 5.10), suggesting loss of a high proportion of plagioclase during fractional crystallisation (section 5.3.4 and 5.5.2). Low Sr concentration melts are prone to crustal contamination, the more evolved the residual liquid the more prone to contamination it is.

In Figure 5.14 I model the effect of AFC of phonolite with three different crust end-members by using the same conditions was to deal with basaltic magma. Here the AFC modal of DePaolo (1980) along with the bulk mixing equations of Langmuir *et al*. (1978) will be used to assess the contribution of crustal contamination to the Garian phonolites.

The bulking mixing (thick line, Figure 5.14) was calculation following Langmuir *et al*. (1978) by using the same method I have done in section 4.2.2, chapter four. While the AFC modals (thin line) are calculated by lowering the Sr/Nd ratio to the least phonolite rock has Sr/Nd ratio (0.1, G11) (Lucassen *et al*., 2008), combine with different mantle end-members as heterogeneous source region.

Figure 5.14 also shows the bulking mixing between basalts that span the range of GVP and the crustal end-members identified above. Sample G32B ($^{143}Nd/^{144}Nd$ = 0.512811) is from this study (Table C.9, Appendix C), and A2 ($^{143}Nd/^{144}Nd$ = 0.51299) is from Beccaluva *et al*. (2008). The curvature of the mixing lines is defined by Sr and Nd concentrations of the end-members (calculations following Langmuir *et al*., 1978). Bulk mixing trends are unable to account for the variation observed in isotopic data of phonolite rocks (Finger 5.14A).

Only the upper crust 2-mica Granite end-member with extremely high $^{87}Sr/^{86}Sr$ (0.81736) provides AFC trends for all the phonolites that have starting compositions that are within the range measured in the GVP basalts (Figure 5.14B). In this model the phonolites have assimilated between 2 and 45 % granite. The phonolite sample with the highest $^{87}Sr/^{86}Sr$, sample G11, requires the highest (~45 %) degree of crustal contamination.

The low $^{87}Sr/^{86}Sr$, low $^{143}Nd/^{144}Nd$ sample of upper crustal end-member can account for the isotopic composition of the three phonolites with the lowest $^{87}Sr/^{86}Sr$ but cannot explain the isotope composition of the two high $^{87}Sr/^{86}Sr$ samples (Figure 5.14B). The data cannot be forced to lie on a simple AFC-derived evolution line with the low $^{87}Sr/^{86}Sr$, low $^{143}Nd/^{144}Nd$ lower crust

material. Clearly this demonstrates that the composition of the contaminant lies within the upper crust, likely acquired by entrainment and assimilation of wall rock in the upper crust.

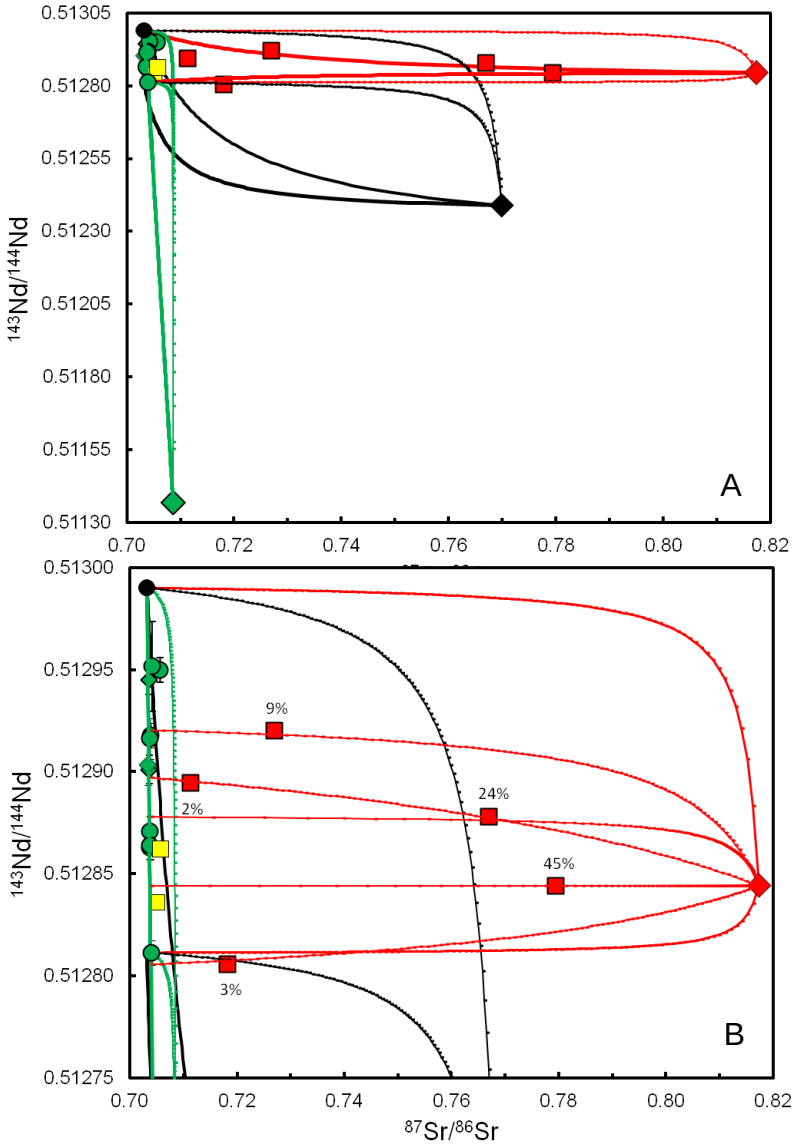

Figure 5.14: (A) AFC (thin line) and bulk mixing (thick line) calculations illustrating the possible effects on $^{143}Nd/^{144}Nd$ vs. $^{87}Sr/^{86}Sr$ isotopic composition for phonolites of GVP (red squares). Also shown are determinations of phonolites from GVP (yellow squares) (Lustrino *et al.*, 2012). North African crustal compositions: upper crust samples (red and black diamond) Suayah *et al*. (2006) and lower crust samples (green diamond) from Davidson and Wilson (1989). (B) Magnification of $^{143}Nd/^{144}Nd$ vs. $^{87}Sr/^{86}Sr$ isotopic composition shows the AFC curves.

5.5.4 The genesis of phonolites

The typical model for phonolite genesis is based on fractional crystallisation of basanite, in variably complex assimilation and fractional crystallisation processes (AFC) in the lithosphere, mainly within the crust. Low degrees of re-melting of mafic rocks in the lithosphere may generate a small proportion of the phonolite and is probably related to large magma volumes. However, as fractionation of basalts produces a continuum of compositions, the problem of the absence or scarcity of intermediate rocks (Daly Gap) requires an explanation (why the volcanism formed phonolites, not lots of basalts?).

The phonolites of this study (type-2 of Lustrino *et al*., 2012, classification) show significant enrichment in incompatible elements (e.g., Zr and Nb) and negative Eu anomalies with high radiogenic $^{87}Sr/^{86}Sr$ ratios compared to other rift-related phonolites (from Europe and Africa) and type-1 phonolites. These Characteristics indicate that they are generated by extensive fractional crystallisation (50-83%) of plagioclase and alkali feldspars (similar to northern Kenya phonolites) combined with an unusual style of assimilation (2-45%) of old upper crust typical of Pan-African shield. While the other rift-related phonolites from Massif Central, France are generated by assimilation of lower crust with rates comprised between 3.3 and 4.2%, Central European Volcanic Province, Germany rocks have undergone assimilation of 40% after 55-65% fractional crystallisation.

Low degrees of re-melting of mafic rocks in the lithosphere as the possible source for the phonolitic magma can be tested by Rb-Sr batch melting calculations (Shaw, 1970). However, Kabeto *et al*. (2001) showed that partial melting of the assumed under-plated mafic magma cannot generate liquids with extreme Sr-depletion, even if very high D_{Sr} (up to 20) are assumed.

These phonolites could be formed and erupted associated with the classical models of magma chambers (Turner & Campbell, 1986) which suggest that crystallisation along walls generates lighter, silica-rich liquids, which migrate toward the top of the reservoir; here they accumulate and possibly undergo

further evolution. While the mafic magma staying at the bottom of the chamber is subjected to continuous stirring and mixing with newly injected mafic melts, which prevent evolution toward phonolitic compositions. The upper phonolitic layer acts as a density barrier with respect to the underlying mafic magma, which is prohibited from reaching the surface. As a result, phonolitic magmas have been shortly erupted controlled by geotectonic sitting which happened before or in the same time of the eruption, whereas the mafic magmas are tapped sporadically, possibly only when the upper part of the reservoir is completely emptied.

The type-2 phonolites appear to have formed during a single short period (8.3 to 8.17 Ma). This timing of phonolite formation implies a geologically-short event may have controlled their production. On the basis of combination of structural survey and remotely sensed image analysis, Capitanio *et al*. (2011) concluded that Tripolitania area (from the Jebel-Al Khums region to Jebel As Sawda, southern Hun Graben) underwent reactivation of normal faults during NE-SW directed extension in early Pliocene. This was due to the opening of the Sicily Channel rift zone (Capitanio *et al*., 2011). Volcanism in the Strait of Sicily started at about 9 Ma (Beccaluva *et al*., 1981), in this period, the volcanism of Garian area and its orientation (field investigation) are compatible with the opening of the Sicily Channel rift zone (Capitanio *et al*., 2011).

Chapter Six

Geochronology of Libyan Cenozoic volcanic provinces (Jabal al Hasawinah, Jabal as Sawda and Al Haruj al Aswad)

6.1 Introduction

In order to understand the temporal history of Cenozoic volcanism in Libya $^{40}Ar/^{39}Ar$ age determinations have been made on basaltic lavas and dykes from the main volcanic provinces (Jabal al Hasawinah (6 samples), Jabal as Sawda (7 samples) and Al Haruj al Aswad (16 samples)). The civil war in Libya restricted my ability to obtain original geological maps that were produced by the Libyan Industrial Research Centre from many sources (e.g., Industrial Research Centre, Tripoli and Sebha University). The location of all samples is reported in Tables E1, E7 and E13 in Appendix E.

Previous age determinations of these volcanic fields were largely done using the K/Ar method; Jabal Al Hasawinah volcanic field (Jurak, 1978); Jabal as Sawda volcanism (Schult and Soffel, 1973, Ade-Hall *et al*., 1975, Busrewil and Esson, 1991) Jabal Al Haruj (Ade-Hall *et al*., 1974, Vesely, 1985, Peregi *et al*., 2003, Cvetkovic *et al.* 2010). This study provides a more comprehensive assessment of the eruption history of the Libyan Cenozoic volcanic provinces in order to better understanding the regional volcanic history. The sample selection aimed to cover the greatest spatial extent whilst also attempting the largest possible temporal variation according to the previous age determinations combined with used some available geological maps and satellite images. Detailed descriptions of locations and hand specimens are presented in Appendix E.

In this chapter I compare the chemistry of basalts from the Garian province with other Libyan Cenozoic volcanic provinces, in order to recognize similarities and differences, which may serve as genetic fingerprints. The geochemical data collected in the present study will also shed some light on

the process of differentiation which controlled the variation of chemistry of these rocks. In addition, based on detailed descriptions of the $^{40}Ar/^{39}Ar$ age determinations, I will also constrain the time of volcanism.

6.2 Geochemistry

Major and trace element concentrations were determined by X-ray fluorescence at the Edinburgh University. Rare earth element concentrations were determined on all samples by inductively coupled plasma mass spectrometry (ICP-MS). The details of the analytical procedures and data are given in Appendix C.

6.2.1 Major and trace elements

The basaltic rocks of Al Haruj, Jabal al Hasawinah and Jabal as Sawda have large variation of SiO_2 (39.4 - 52.7 wt %), and plot in the alkaline fields on a TAS diagram (Figure 6.1, Table C11, Appendix C). Most samples plot in tephrite-basanite fields and generally overlap the range of basalts from the GVP. They appear to form a continuous range. The new analyses generally overlap the range reported by previous studies (Jabal Al Haruj province, Busrewil, (1993), Aboazom *et al*. (2006), Cvetkovic *et al*. (2010) and Nixon, (2011); Jabal Al Hasawinah province, Busrewil and Oun, (1991); Jabal As Sawda province, Woller and Fediuk, (1980) Garian province, Piccoli, (1970), Almond *et al*. (1974), Busrewil, (1974), Hegazy, (1999), Aboazom *et al*. (2006); Lustrino *et al*. (2012)).

In Harker-type SiO_2 variation diagrams (Figure 6.2) all basalts overlap and the new data also overlap previous studies. The Jabal as Sawda basalts are characterized by lower range of MgO (6.3 to 10.8 wt %) compared to the other field (2.0 to 16.0 wt %). There is a generally positive correlation between SiO_2 and Al_2O_3, and negative correlations with MgO and CaO indicating that, like the GVP basalts, the major element variation of the other Libyan Cenozoic basalts is controlled by fractional crystallisation.

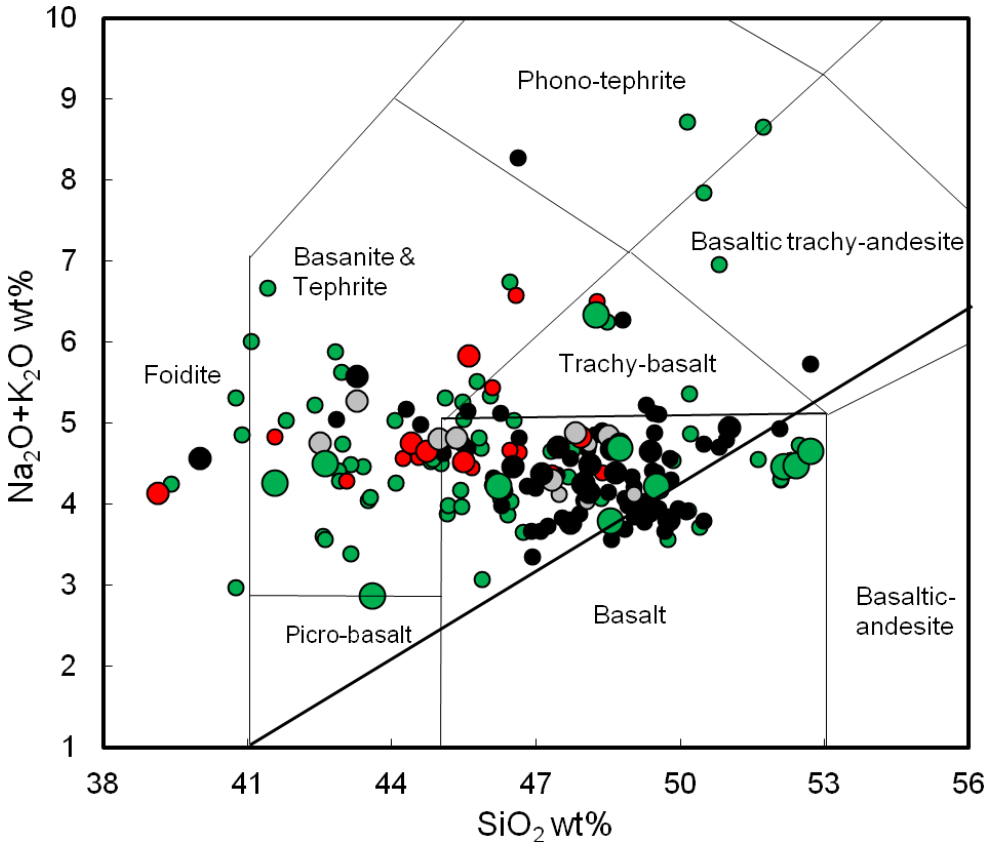

Figure 6.1: Total alkalis plotted against SiO_2 for basalts from the Libyan volcanic provinces. Large red circles: Jabal Al Hasawinah, small red circles: published data (Busrewil and Oun, 1991). Large grey circles: Jabal As Sawda and small grey circles: published data (Woller and Fediuk, 1980). Large black circles: Jabal Al Haruj and small black circles: published data (Busrewil, 1993; Aboazom *et al*., 2006; Cvetkovic *et al*., 2010, Nixon, 2011). Large green circles: Garian basalts (this study) and small green circles: published data (Piccoli, 1970; Almond *et al*., 1974; Busrewil, 1974; Hegazy, 1999, Aboazom *et al*., 2006; Lustrino *et al*., 2012). The subdivision of alkaline (above) and tholeiitic field (below) is distinguished by the heavy line (after Irvine and Baragar, 1971).

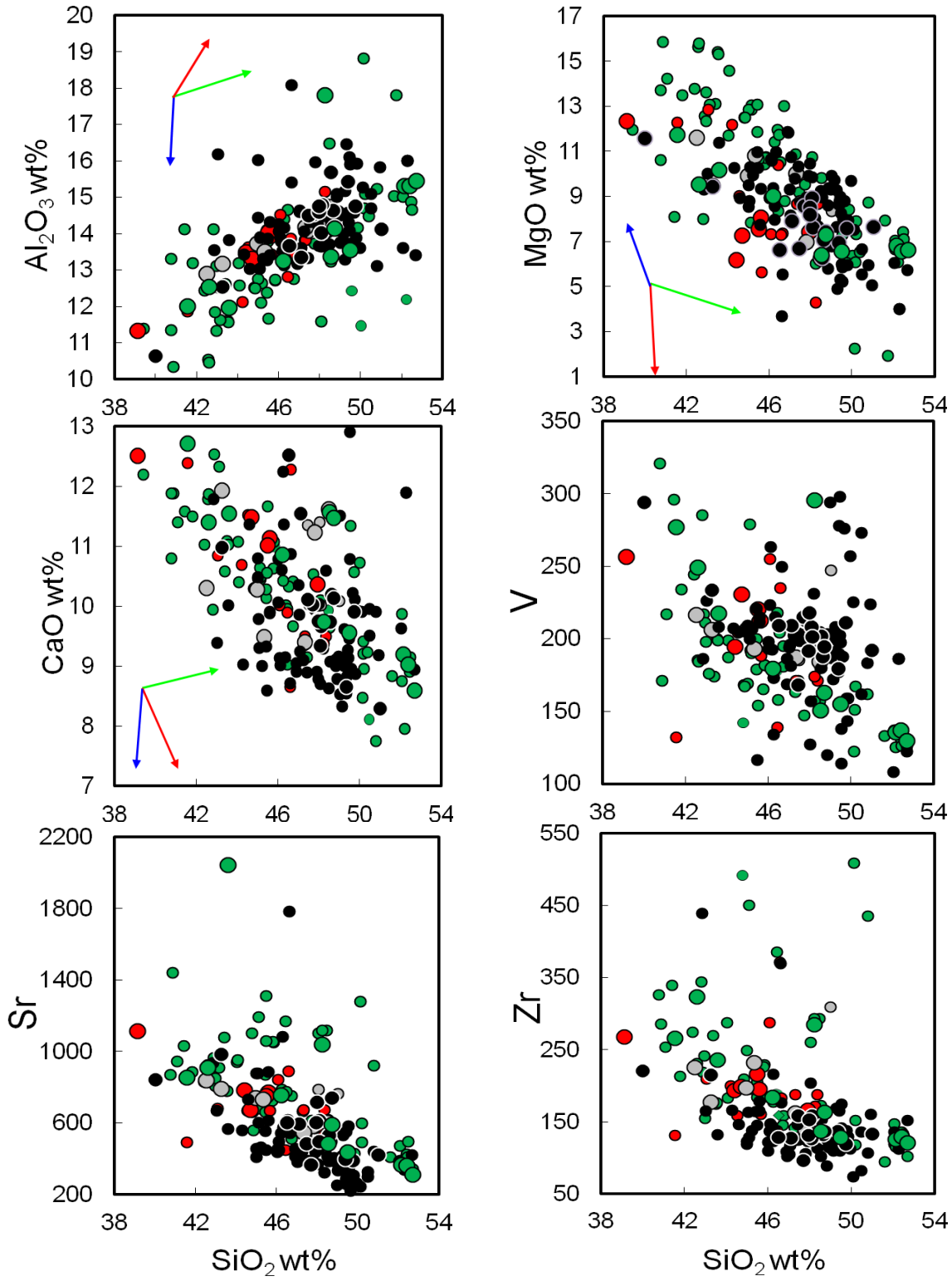

Figure 6.2: Harker diagrams of major and trace (ppm) element abundances plotted against SiO_2 wt% for basaltic rocks from the Libyan volcanic provinces. The same symbols are used in Figure 6.1.

In trace element variation diagrams (Figures 6.2, Tables C11-C14, Appendix C) the Al Haruj basalts have consistently larger variation in concentrations than the basalt rocks from Jabal al Hasawinah and Jabal as Sawda. The new measurements overlap the range of previous measurements of Libyan basalts, and in many cases form continuous trends. Compatible (e.g., V) and incompatible elements (e.g., Sr and Zr) show negative correlations with SiO_2, consistent with the crystal fractionation trends identified from the variation in the major element concentrations.

6.2.2 Rare earth elements

Chondrite-normalized rare earth element patterns are shown in Figure 6.3 and Tables C15-C17. Basalts from all fields generally show light rare earth element enrichment relative to the middle and heavy rare earth elements with no significant Eu anomaly. The patterns overlap those of GVP basalts. The REE content of the Garian basalt rocks have a huge range from 7 to 40 and 11 to 240 times the value of chondrite (Figure 6.3 A and B), whereas the other Libyan basalts rocks range within Garian ranges except one sample from Jabal As Sawda has highest range from 10 to 400 times chondrite values. Basalts from Jabal Al Haruj show slight depletion in HREE compared to other fields.

Figure 6.3B show that the comparison between Garian basalts of this study and Al Haruj basalts from Nixon, (2011) and Abdel-Karim *et al*. (2013). The patterns of the Figure 6.3B indicate that the Al Haruj basalts overlap within the Garian value but with lower range of REE concentrations from 6 to 33 and 9 to 97 times the value of chondrite.

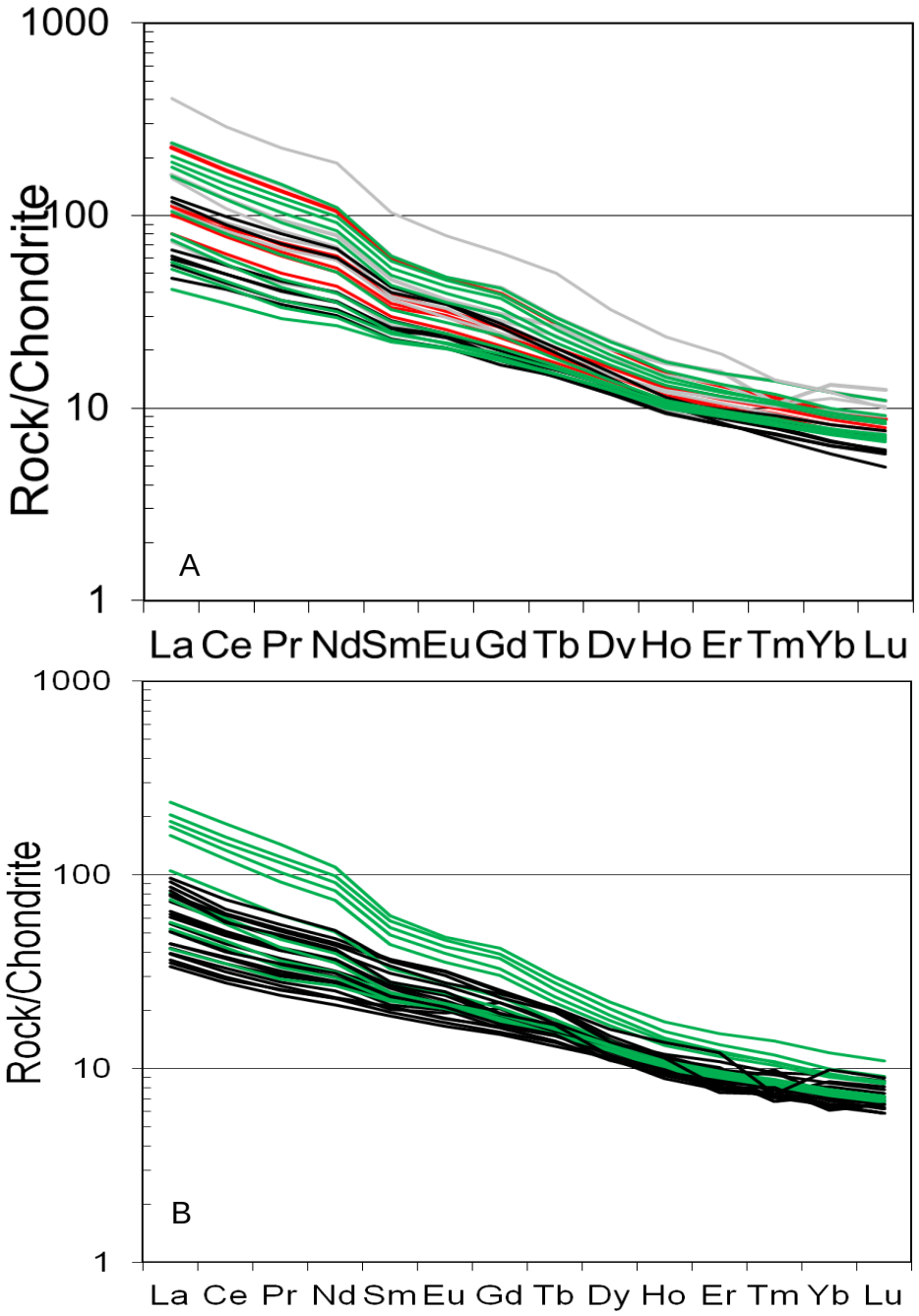

Figure 6.3: Chondrite-normalized REE patterns for basalt rocks from Cenozoic volcanic provinces of Libya. (A) Shows all data from this study. Green lines: Garian; red lines: Jabal Al Hasawinah; grey lines: Jabal As Sawda and black lines: Jabal Al Haruj. (B) Shows the Garian basalts compared to Al Haruj basalts from Cvetkovic *et al*., 2010, Nixon, 2011 and Abdel-Karim *et al*., 2013. Chondrite values are from Nakamura (1974).

6.2.3 Implications of the basalt geochemistry

The geochemistry can be used to make some general observations about the magmatic differentiation history and source of the Cenozoic basaltic volcanism of Libya. The results are summarised as follows:

1. The major, trace and rare earth element variations suggest that fractional crystallization was a key process in the evolution of the basaltic magmas.

2. The overlap of major, trace and rare earth elements in basalts from all fields, and Sr-Nd isotopes of GVP and Jabal Al Haruj basalts (Figure 7.5 in chapter 7), indicates that they are probably derived from a similar mantle source.

3. The enrichment in LREE relative to HREE indicates the equilibration of the basaltic melts with shallow mantle in the spinel-garnet facies transition (i.e. < 80–90 km) (Nickel, 1986; Adam and Green, 2006).

4. The overlap of basaltic rocks from Garian and Al Haruj province (see Figure 7.5 in chapter 7) with metasomatised mantle xenoliths from Garian (Beccaluva *et al*., 2008), suggests that the asthenosphere melts have incorporated metasomatised mantle lithosphere.

6.3 Geochronology

Samples of basalt groundmass were separated and subjected to incremental heating $^{40}Ar/^{39}Ar$ age determinations. The results for the 26 samples are shown in Tables 6.1, 6.2 and 6.3, and plotted as the cumulative percent of ^{39}Ar released (x axis) against apparent age (y axis) for each step. K/Ca ratios were calculated for each increment from the measured $^{39}Ar/^{37}Ar$ ratios. The $^{40}Ar/^{39}Ar$ data are reported as plateau ages, inverse isochron and integrated ages.

6.4 $^{40}Ar/^{39}Ar$ dating of Jabal al Hasawinah volcanism

The Jabal al Hasawinah volcanic province is the smallest (~1,000 km^2) and least studied Cenozoic volcanic field in west central Libya (Figure 1.1). A volcanic field comprises flows, dikes and cones of phonolite, trachyte and basalt (Busrewil and Oun, 1991). The difficult terrain and inaccessibility of some parts of Jabal al Hasawinah have discouraged any detailed study of the volcanism. Based on field observations, the basaltic rocks can be divided into basaltic cones, lava flows and dikes. Two samples of phonolites have been dated using the K/Ar method with the results of 15.7 and 23.2 Ma and one basalt cone in the Wadi ash Shdidah gave an age of 24.9 ± 1.0 Ma (Jurak, 1978).

The locations and rock descriptions of five basalt samples used in this study (two plugs and three lavas) are discussed in more details within section E1.1, Figure E1 and Table E1, Appendix E. The difficult terrain and inaccessibility of some parts of Jabal al Hasawinah forced us to sample the rocks from an availability of outcrops at south, north and west of the central volcanism. The total age span of Jabal al Hasawinah volcanism have been estimated according to the available geological map (Jurak, 1978) and satellite images (Figure E1) which covered an area about 120 km from south to north included two intrusive plugs and three basaltic lavas.

$^{40}Ar/^{39}Ar$ age determinations were made on the purified groundmass separates from five samples. Sample preparation and analysis procedures are described in Appendix F along with the data tables. $^{40}Ar/^{39}Ar$ ages are calculated relative to the optimisation model of Renne *et al*. (2010, 2011). Summary statistics are provided in Table 6.1. All uncertainties are 1σ. The $^{40}Ar/^{39}Ar$ step-heating analytical results are summarised in Tables F2 to F6.

6.4.1 H7 intrusive plug

The plateau age of 19.811 ± 0.030 Ma (1σ, internal precision) is determined from 85 % of the ^{39}Ar released (steps 3 to 9 from 10 age steps). K/Ca decreases with temperature, the last steps correspond to the degassing of K-poor, Ca-rich mineral phases (plagioclase and/or pyroxene). This sample gives an integrated age (20.000 ± 0.200 Ma) that is indistinguishable from the plateau age. The older ages presented in this sample resemble with ^{39}Ar recoil-induced old apparent ages obtained at lowest temperatures. The inverse isochron yields an age (19.890 ± 0.060 Ma) that overlaps with the plateau and integrated age. The initial ^{40}Ar/^{36}Ar of 293 ± 3 is statistically lower than the atmospheric value (298.56 ± 0.31) (Lee *et al*., 2006 and Mark *et al*., 2011b) (Figure 6.4 and Table 6.2). The absolute age relative to Renne *et al*. (2010, 2011) is 20.007 ± 0.033 Ma.

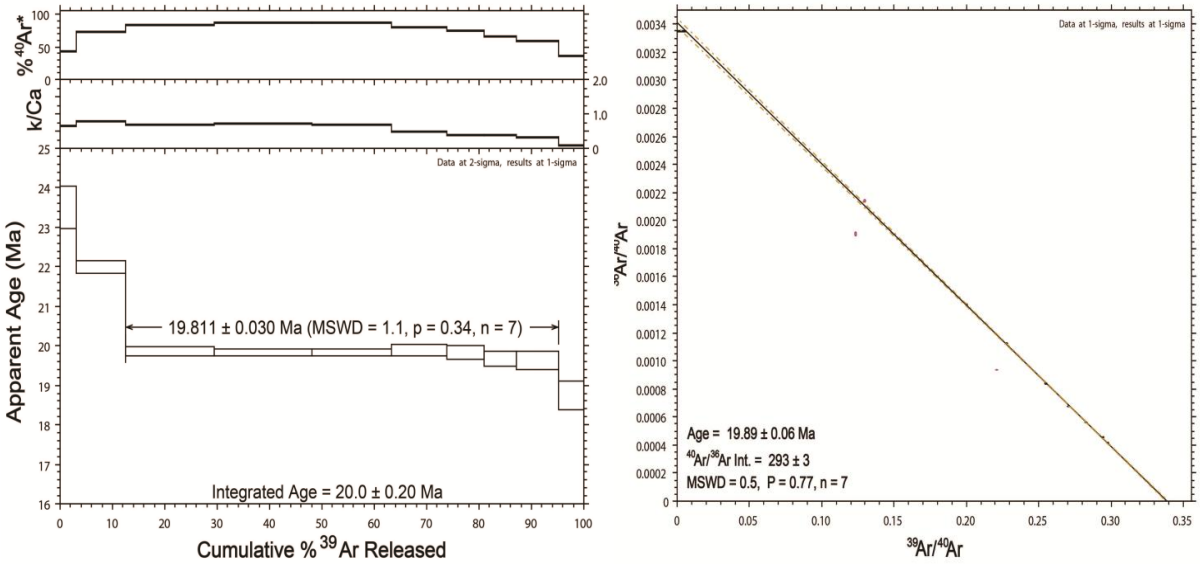

Figure 6.4: ^{40}Ar/^{39}Ar age spectra (left) and inverse isochron plot (right) for basaltic intrusive (sample H7).

6.4.2 H1 intrusive plug

The plateau age of 15.246 ± 0.110 Ma (steps 2 to 11 from 11 age steps) has MSWD of 1.10 for 96 % of the ^{39}Ar released. The change of K/Ca with temperature and shape of the $^{40}Ar/^{39}Ar$ profile are similar to H7. This sample gives an integrated age (15.340 ± 0.150 Ma) that is indistinguishable from the plateau age. The isochron age (15.340 ± 0.120 Ma) overlap with the plateau and integrated age. The initial $^{40}Ar/^{36}Ar$ is 290 ± 4 (Figure 6.5 and Table 6.2) is lower than the atmospheric value of 298.56 ± 0.31 (Lee *et al*., 2006 and Mark *et al*., 2011b). The recalculated age relative to Renne *et al*. (2010, 2011) is 15.397 ± 0.111 Ma.

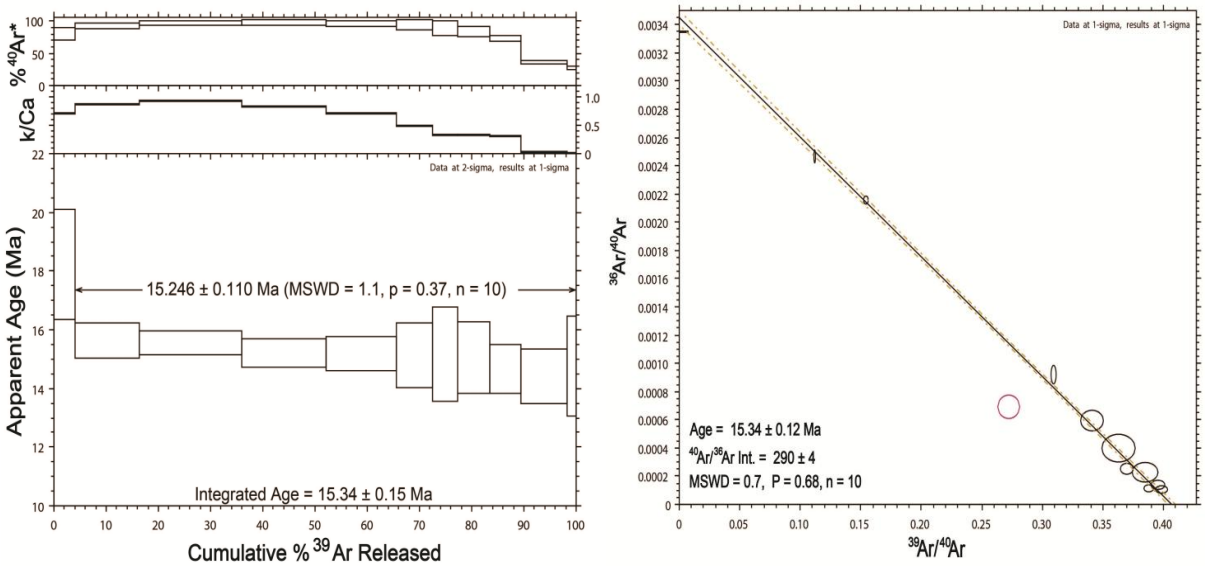

Figure 6.5: $^{40}Ar/^{39}Ar$ age spectra (left) and inverse isochron plot (right) for basaltic intrusive (sample H1).

6.4.3 H9 basaltic lava

This sample produced data similar to that of H7 and similar interpretations apply. This sample yields a plateau age of 16.251 ± 0.019 Ma (MSWD = 0.30) for 90 % of the ^{39}Ar released (steps 3 to 12 from 12 age steps) with ^{40}Ar*. The change of K/Ca with temperature and shape of the ^{40}Ar/^{39}Ar profile are similar to H7. The integrated age of 16.350 ± 0.120 Ma overlaps with the plateau age. The inverse isochron yields an age (16.260 ± 0.040 Ma) that is indistinguishable from the plateau and integrated age. The initial ^{40}Ar/^{36}Ar = 298 ± 1 is equivalent to modern day atmosphere (298.56 ± 0.31) indicating that excess ^{40}Ar is not a significant factor in the age of this sample. The low MSWD of 0.20 and p of 0.99 for this sample may indicate overestimated analytical uncertainties (Figure 6.6 and Table 6.2). The absolute age relative to Renne *et al*. (2010, 2011) is 16.411 ± 0.022 Ma.

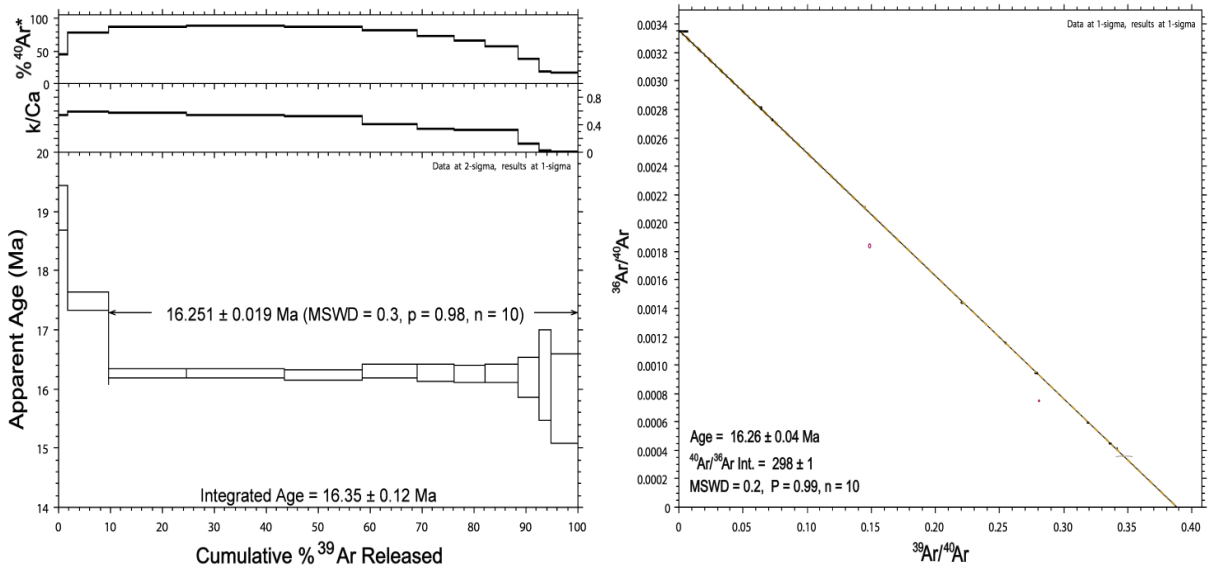

Figure 6.6: ^{40}Ar/^{39}Ar age spectra (left) and inverse isochron plot (right) for basaltic lava (sample H9).

6.4.4 H2 basaltic lava

This sample yields a plateau age of 15.132 ± 0.016 (1σ, internal precision) with MSWD of 1.50 for 82 % of the ^{39}Ar released (steps 3 to 8 from 11 age steps). The integrated age of 15.140 ± 0.140 Ma overlaps with the plateau age. Slightly younger ages occur in the higher temperature fractions (step 9 to 11) may be caused by recoil of ^{39}Ar. The inverse isochron yields an age (15.170 ± 0.040 Ma) with low MSWD of 0.50 that is indistinguishable from the plateau and integrated age. The ^{40}Ar/^{36}Ar intercept of 291 ± 3 is statistically lower than the atmospheric value (298.56 ± 0.31) (Figure 6.7 and Table 6.2). All ages overlap and recalculated relative to Renne *et al*. (2010, 2011) is 15.282 ± 0.019 Ma.

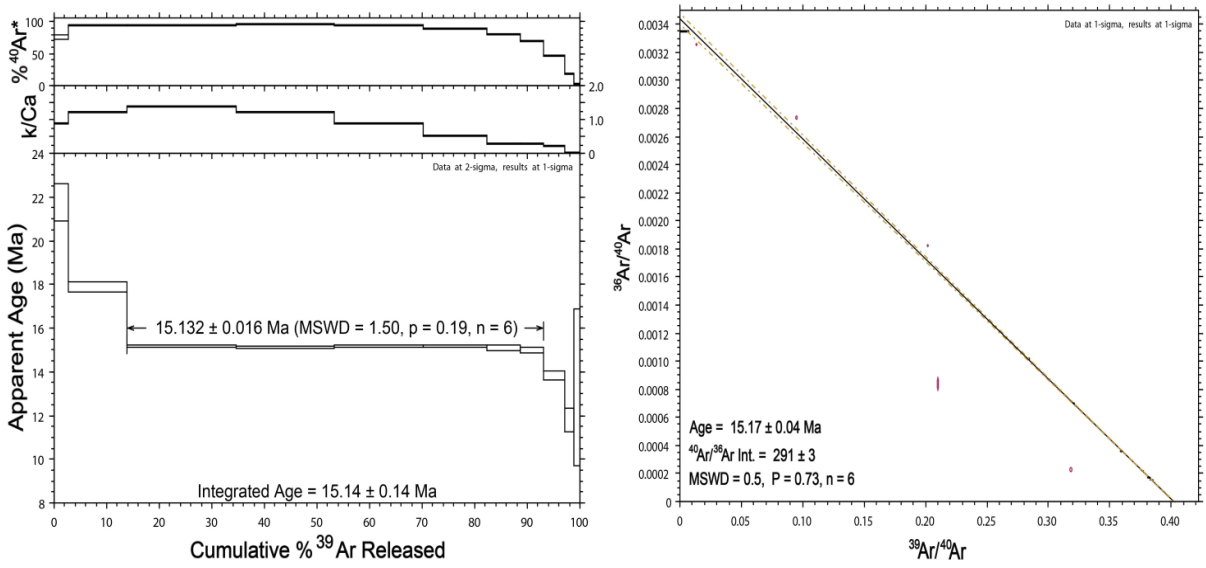

Figure 6.7: ^{40}Ar/^{39}Ar age spectra (left) and inverse isochron plot (right) for basaltic shield lava (sample H2).

6.4.5 H3 basaltic lava

This sample produced data similar to that of H7 and similar interpretations apply. The plateau age of 10.78 ± 0.01 Ma (1σ, internal precision) is determined from 83 % of the ^{39}Ar released (steps 2 to 8 from 10 age steps). The change of K/Ca with temperature and shape of the $^{40}Ar/^{39}Ar$ profile are similar to H7. This sample gives an integrated age (10.780 ± 0.050 Ma) that is indistinguishable from the plateau age. The inverse isochron yields an age (10.800 ± 0.030 Ma) that overlaps with the plateau and integrated age. It has an initial $^{40}Ar/^{36}Ar$ of 296 ± 3 that is statistically equivalent to the atmospheric value and indicates that excess ^{40}Ar is not a significant factor in the age of this sample (Figure 6.8 and Table 6.2). The absolute age relative to Renne *et al*. (2010, 2011) is 10.890 ± 0.013 Ma.

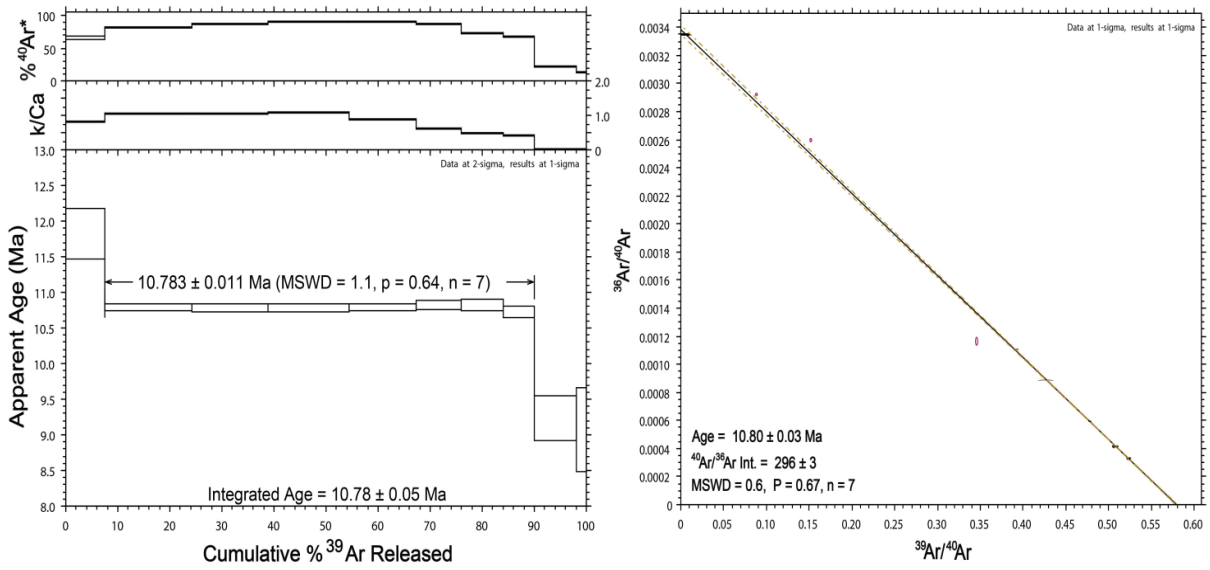

Figure 6.8: $^{40}Ar/^{39}Ar$ age spectra (left) and inverse isochron plot (right) basaltic lava (sample H3).

Table 6.1: $^{40}Ar/^{39}Ar$ data of the basalts from Jabal al Hasawinah Volcanic Province.

Decay constants of Steiger & Jager (1977), Fish Canyon sanidine at 28.02 ± 0.16 Ma (Renne *et al*., 1998), atmospheric argon isotope ratios of Lee *et al*. (2006) and Mark *et al*. (2011b) (298.56 ± 0.31).													Optimisation model (Renne *et al*., 2010, 2011) - full external precision (standard age, decay constant).	
ID	Sample Type	Location	Mass (mg)	Plateau age (Ma)	1σ	^{39}Ar (%)	MSWD	Isochron age (Ma)	1σ	$^{40}Ar/^{36}Ar$	1σ	MSWD	Age (Ma)	1σ
H7	Plug	144 km NE of Sebha	253	19.811 (*n* = 7)	0.030	85	1.100	19.890 (*n* = 7)	0.060	293	3.000	0.500	20.007	0.033
H1	Plug	245 km N of Sebha	263	15.246 (*n* = 10)	0.110	96	1.100	15.340 (*n* = 10)	0.120	290	4.000	0.700	15.397	0.111
H9	Lava	126 km N of Sebha	250	16.251 (*n* = 10)	0.019	90	0.300	16.260 (*n* = 10)	0.040	298	1.000	0.200	16.411	0.022
H2	Lava	235 km N of Sebha	251	15.132 (*n* = 6)	0.016	82	1.500	15.170 (*n* = 6)	0.040	291	3.000	0.500	15.282	0.019
H3	Lava	207 km NE of Sebha	247	10.783 (*n* = 7)	0.011	83	1.100	10.800 (*n* = 10)	0.030	296	3.000	0.600	10.890	0.013

6.4.6 Comparison with previous studies

Total fusion K/Ar dating of one basalt sample from Wadi ash Shdidah Jabal Al Hasawinah volcanic field yielded an age of 24.9 ± 1.0 Ma (Jurak, 1978). In general, the new basalt $^{40}Ar/^{39}Ar$ ages are younger than this age.

The intrusive rocks record the oldest ages determined here. Basalt plugs H7 and H1 (144 and 245 km northeast of Sebha) are 20.01 ± 0.03 Ma and 15.40 ± 0.11 Ma respectively. These ages confirm that the intrusive rocks of Jabal Al Hasawinah and Garian volcanic provinces (28.19 ± 0.05 Ma to 10.57 ± 0.02) overlap and erupted at the same time. The basaltic lavas of Jabal Al Hasawinah (16.41 ± 0.02 to 10.89 ± 0.01 Ma) associated and overlap with the old intrusive rocks (20.01 ± 0.03 Ma and 15.40 ± 0.11 Ma) (Figure 6.30 and Table 6.1) indicate that this region has not been affected by erosion.

According to the available geological map (Jurak, 1978) and satellite images (Figure E1, Appendix E) the basalts sampled for this study based on geological history which covered an area about 120 km from south to north included two intrusive plugs and three basaltic lavas suggest that there is no younger age than these rocks. The new ages suggest that the lavas were erupted over a period of approximately 6 million years between 16.4 and 10.9 Ma (Figure 6.30). The absence of flows which appear to be significantly younger than the sampled flows (Figure E1) suggest that volcanic activity of the Jabal Al Hasawinah province ceased approximately 10 million years ago.

6.5 $^{40}Ar/^{39}Ar$ dating of Jabal as Sawda volcanism

The Jabal as Sawda volcanic province is located about 550 km southeast of Tripoli in central Libya (Figure 1.1). Basaltic flood lavas cover an area about 6000 km^2 but the distribution of outliers and significant dissection of the plateau indicate that the original area of volcanic rocks was probably at least 10,000 km^2

(Busrewil and Esson, 1991). Woller and Fediuk (1980) conclude that the plateau lavas are predominantly alkali olivine basalts with occasional olivine tholeiites and basanites, where the shield volcanoes and cones consist entirely of alkali olivine basalt. The basalts of Jabal as Sawda volcanic field have K-Ar ages in the range 15.4 ± 2.1 to 8.7 ± 1.2 Ma (Schult and Soffel 1973: Ade-Hall *et al*., 1975; Busrewil and Esson, 1991).

The location and description of the five samples that were used in this study (one small intrusive plug and four basaltic lavas) are discussed in more detail in section E1.2, Figure E2 and Table E7. The difficult terrain and inaccessibility of central part of the Jabal as Sawda volcanic province meant I could sample only one rock from the centre, the others sampled from available outcrops at the south and north parts of the province. Sampling the Jabal as Sawda volcanism was guided by the available geological map (Woller, 1978) and satellite images (Figure E2, Appendix E).

$^{40}Ar/^{39}Ar$ age determinations were made on the purified groundmass separates from five samples. Sample preparation and analysis procedures are described in Appendix F along with the data tables. $^{40}Ar/^{39}Ar$ ages are calculated relative to the optimisation model of Renne *et al*. (2010, 2011). Summary statistics are provided in Table 6.2. $^{40}Ar/^{39}Ar$ results are presented at 68% confidence level (1σ) which summarised in Tables E8 to E12.

6.5.1 S9 intrusive plug

The plateau age of 22.723 ± 0.019 Ma (1σ, internal precision) is determined from 68 % of the ^{39}Ar released (steps 3 to 9 from 13 age steps). ^{40}Ar* and K/Ca decrease with temperature, the last four steps correspond to the degassing of K-poor, Ca-rich mineral phases (plagioclase and/or pyroxene). This sample gives an integrated age (22.670 ± 0.140 Ma) that is indistinguishable from the plateau age. The inverse isochron yields an age (22.790 ± 0.080 Ma) that overlaps with the plateau and integrated age. It has an initial ^{40}Ar/^{36}Ar of 292 ± 6 that is statistically equivalent to the atmospheric value (Lee *et al*., 2006 and Mark *et al*., 2011b) indicating that excess ^{40}Ar is not an important factor in the age of this sample (Figure 6.9 and Table 6.3). The absolute age relative to Renne *et al*. (2010, 2011) is 22.948 ± 0.024 Ma.

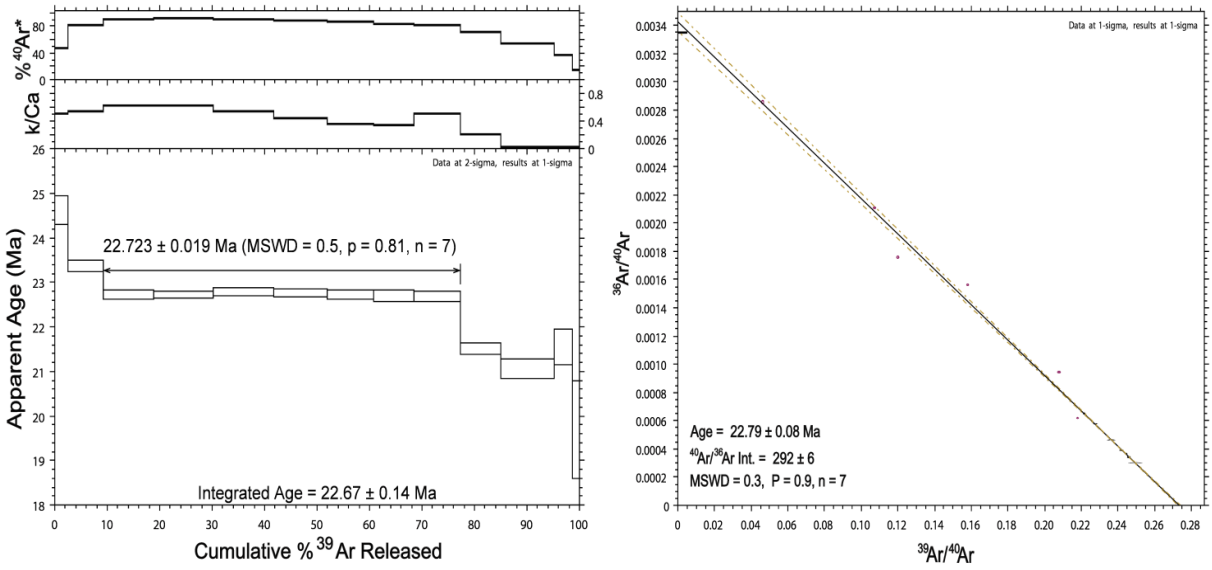

Figure 6.9: ^{40}Ar/^{39}Ar age spectra (left) and inverse isochron plot (right) for basaltic plug (sample S9).

6.5.2 S3 basaltic lava

This sample yields a plateau age of 13.915 ± 0.015 Ma which determined from 86 % of the ^{39}Ar released (steps 3 to 9 from 9 age steps). The integrated age (14.050 ± 0.130 Ma is indistinguishable from the plateau age. The change of K/Ca with temperature and shape of the $^{40}Ar/^{39}Ar$ profile are similar to S9. The inverse isochron yields an age (13.940 ± 0.050 Ma) that overlaps with the plateau and integrated age. It has an initial $^{40}Ar/^{36}Ar$ of 294 ± 7 that is statistically equivalent to the atmospheric value with MSWD of 0.90 and p of 0.49 indicating that excess ^{40}Ar is not the important factor in the age of this sample (Figure 6.10 and Table 6.3). The absolute age relative to Renne *et al*. (2010, 2011) is 14.053 ± 0.018 Ma.

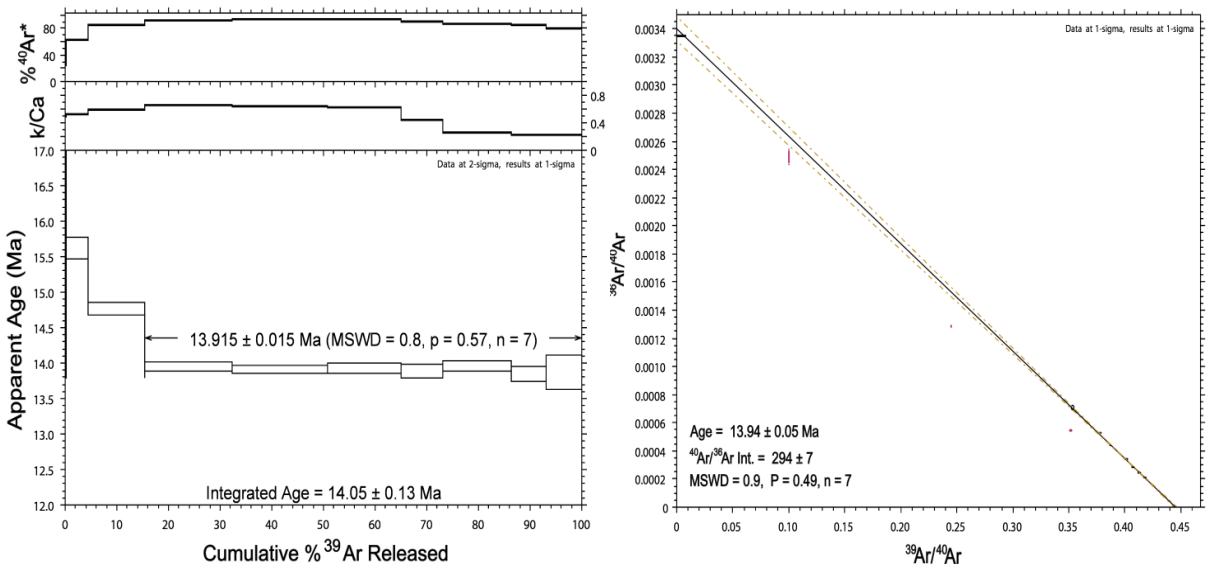

Figure 6.10: $^{40}Ar/^{39}Ar$ age spectra (left) and inverse isochron plot (right) for basaltic lava (sample S3).

6.5.3 S7 Shield lava

The plateau age of 13.818 ± 0.011 Ma is determined from 80 % of the ^{39}Ar released (steps 3 to 8 from 10 age steps). The change of K/Ca with temperature and shape of the $^{40}Ar/^{39}Ar$ profile are similar to S9. This sample gives an integrated age (13.870 ± 0.160 Ma) that is indistinguishable from the plateau age. The inverse isochron yields an age (13.840 ± 0.060 Ma) that overlaps with the plateau and integrated age. It has an initial $^{40}Ar/^{36}Ar$ of 292 ± 11 statistically equivalent to the atmospheric value, with MSWD = 1.00 and p = 0.41 (Figure 6.11 and Table 6.3). The absolute age relative to Renne *et al*. (2010, 2011) is 13.955 ± 0.014 Ma.

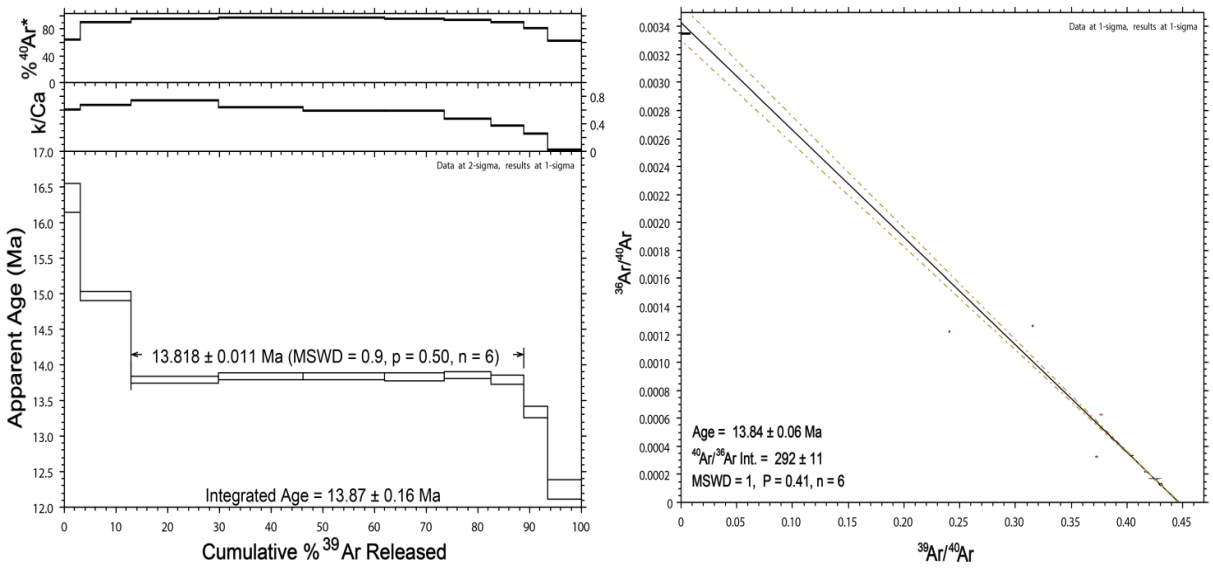

Figure 6.11: $^{40}Ar/^{39}Ar$ age spectra (left) and inverse isochron plot (right) basaltic shield lava (sample S7).

6.5.4 S1 basaltic lava

This sample produced data similar to that of S7 and similar interpretations apply. The plateau age (12.840 ± 0.011 Ma) is determined from 89 % of the ^{39}Ar released (1σ, internal precision) with low MSWD of 0.50 (step 3 to 13 from 11 age steps). It has a integrated age indistinguishable from the plateau age of 12.860 ± 0.060 Ma by revealing that the slightly older ages occur in the lower temperature fractions (step 1 and 2) and the younger age occurs in the last steps of high temperature (step 12 and 13). The inverse isochron yields an age overlaps with the plateau and integrated age of 12.840 ± 0.030 Ma, and an initial $^{40}Ar/^{36}Ar$ of 299 ± 2 statistically equivalent to the atmospheric value (Figure 6.12 and Table 6.3). The absolute age relative to Renne *et al*. (2010, 2011) is 12.967 ± 0.011 Ma.

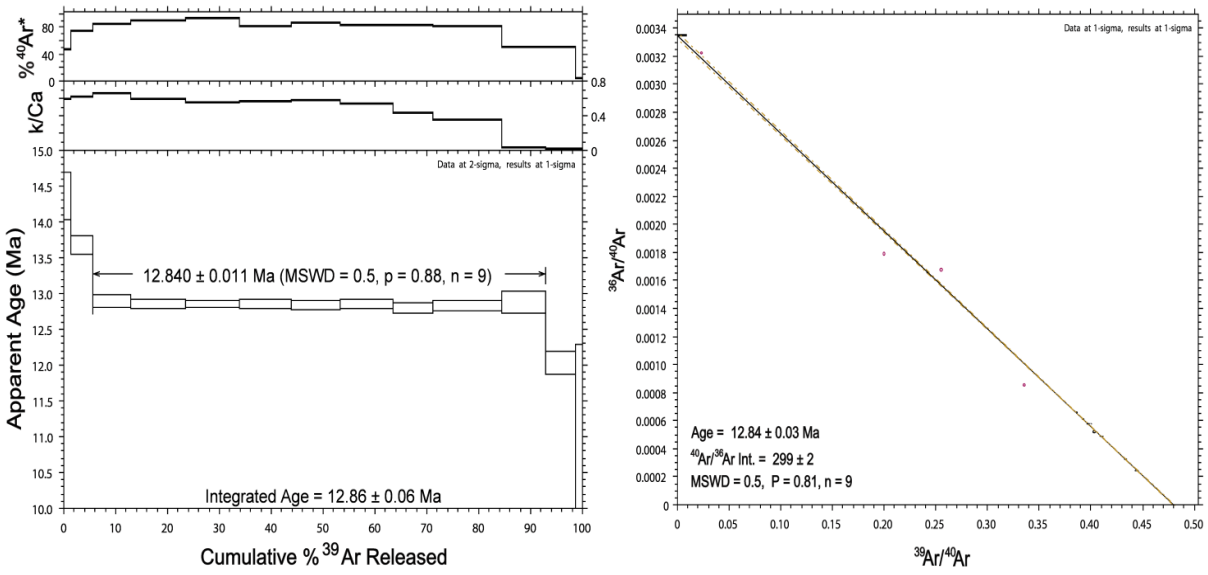

Figure 6.12: $^{40}Ar/^{39}Ar$ age spectra (left) and inverse isochron plot (right) for basaltic lava (sample S1).

6.5.5 S10B basaltic lava

This sample yields statistically plateau age of 11.984 ± 0.012 Ma (1σ, internal precision) for 83 % of the ^{39}Ar released at the first 7 steps (from 11 age steps) with regularly decrease of K/Ca ratios and $^{40}Ar^*$. The inverse isochron ages are comparable with the plateau age of 11.980 ± 0.030 Ma. The initial $^{40}Ar/^{36}Ar$ of 298 ± 2 is statistically indistinguishable from the atmospheric value. MSWD of 0.50 and p of 0.75 indicating that define initial trapped components of atmospheric composition. Further the inverse isochron age and plateau age overlap and show the data to be precise. This age (11.930 ± 0.060 Ma) is similar to the integrated age of (Figure 6.13 and Table 6.3). The recalculated age relative to Renne *et al*. (2010, 2011) is 12.103 ± 0.014 Ma.

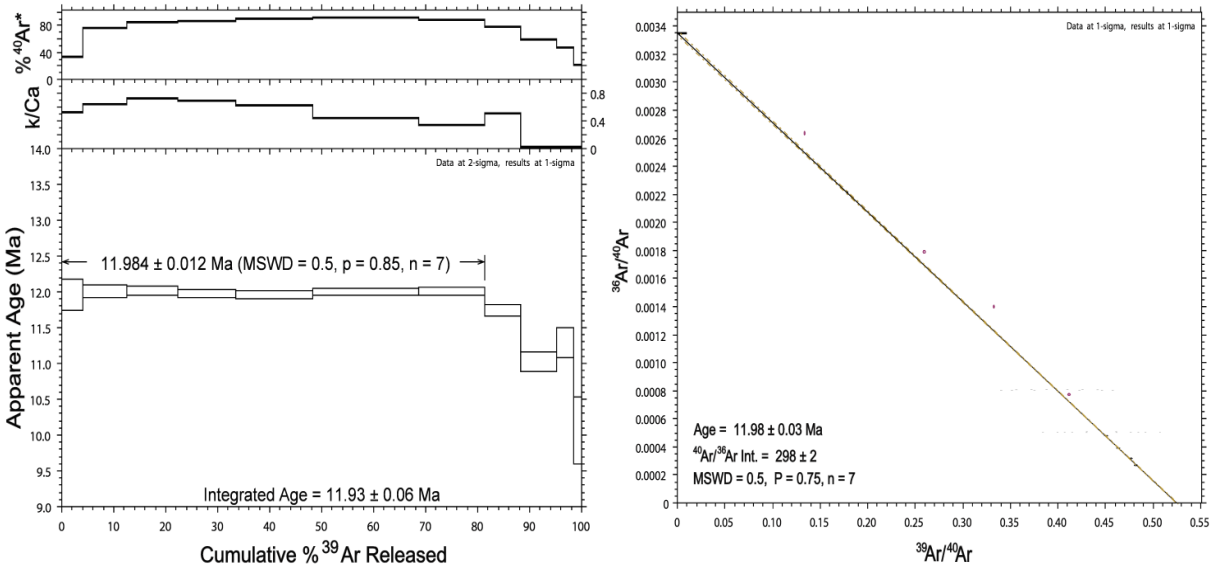

Figure 6.13: $^{40}Ar/^{39}Ar$ age spectra (left) and inverse isochron plot (right) for basaltic lava (sample S10B).

Table 6.2: $^{40}Ar/^{39}Ar$ data of the basalts from Jabal as Sawda Volcanic Province.

Decay constants of Steiger & Jager (1977), Fish Canyon sanidine at 28.02 ± 0.16 Ma (Renne *et al*., 1998), atmospheric argon isotope ratios of Lee *et al*. (2006) and Mark *et al*. (2011b) (298.56 ± 0.31).													Optimisation model (Renne *et al*., 2010, 2011) - full external precision (standard age, decay constant)	
ID	Sample type	Location	Mass (mg)	Plateau age (Ma)	1σ	^{39}Ar (%)	MSWD	Isochron age (Ma)	1σ	$^{40}Ar/^{36}Ar$	1σ	MSWD	Age (Ma)	1σ
S9	Plug	84 km W of Sawknah	254	22.723 (*n* = 7)	0.019	68	0.500	22.790 (*n* = 7)	0.080	292	6.000	0.300	22.948	0.014
S3	Lava	57 km S of Sawknah	252	13.915 (*n* = 7)	0.015	86	0.800	13.940 (*n* = 7)	0.050	294	7.000	0.900	14.053	0.018
S7	Shield lava	46 km SW of Sawknah	246	13.818 (*n* = 6)	0.011	80	0.900	13.840 (*n* = 6)	0.060	292	11.000	1.000	13.955	0.014
S1	Lava	62.5 km SW of Sawknah	250	12.840 (*n* = 9)	0.011	89	0.500	12.840 (*n* = 9)	0.030	299	2.000	0.500	12.967	0.011
S10B	Lava	34 km SW of Sawknah	252	11.984 (*n* = 7)	0.012	83	0.500	11.980 (*n* = 7)	0.030	298	2.000	0.500	12.103	0.014

6.5.6 Comparison with previous studies

The new age of basalt plug (S9), 22.95 ± 0.02 Ma, is the oldest age determined here. This confirms that the intrusive rocks of Jabal as Sawda are comparable in age to the intrusive rocks of Jabal al Hasawinah and Garian volcanic provinces.

The basaltic lavas of Jabal as Sawda yield ages of 14.05 ± 0.02 to 12.10 ± 0.01 Ma (Figure 6.30 and Table 6.2). This compares to previous basalts age determinations (K-Ar) in the range 15.4 ± 2.1 to 8.7 ± 1.2 Ma (Schult and Soffel 197; Ade-Hall *et al*., 1975; Busrewil and Esson, 1991). Basalts of this age are not preserved in the Garian volcanic province, despite the fact that there are intrusive rocks of this age. The preservation of old basalts in the region suggests that it has not been affected by erosion to the same extent.

According to the available geological map (Woller, 1978) and satellite images (Figure E2, Appendix E) the basalt sample S10B, 12.10 ± 0.01 Ma appear to be the youngest basaltic flows in Jabal as Sawda. This suggests that the Jabal as Sawda basalts were erupted over a duration about 2 million years (14.05 ± 0.02 to 12.10 ± 0.01). This compares to a longer period (~7 Ma) according to previous K/Ar studies (15.4 ± 2.1 to 8.7 ± 1.2 Ma) (Figure 6.30). It also implies that the volcanism in the region ceased approximately 12 million years ago.

6.6 $^{40}Ar/^{39}Ar$ dating of Jabal Al Haruj al Aswad volcanism

The Jabal Al Haruj volcanic province in central Libya is the largest of the four main Cenozoic volcanic provinces in Libya. The basaltic volcanism of the province was separated into six distinct time phases by Klitzsch, (1967). The divisions of flows were based upon the morphology of lavas in field and geological map of 1:250,000 scales. B1 and B2 (the oldest generations have been levelled by erosion and have smooth and accessible surfaces), B3 and B4 (the middle generations have kept their original flow relief but the surface of the

flows are weathered), B5 and B6 (the youngest generations have ropy lava and rough, unweathered surfaces). These phases were further subdivided into mappable sub-phases (Busrewil and Suwesi, 1993). The size of the area covered by flows, and the absence of pyroclastic material make the Jabal Al Haruj al Aswad province a typical example of the plateau basalt-type of effusion. More details are presented in section E1.3, Figure E3 and Table E13, Appendix E.

In this study I have dated one dyke, three intrusives and thirteen basaltic lava flows. Three basalts are from phase 1 (oldest), two from phase 2, three from phase 3; three from phase 4 and one from phase 5. The location and descriptions of these samples which are discussed in more details within section E1.3, Figure E3 and Table E13. The total age span of Jabal Al Haruj volcanism have been estimated according to the available geological map (Vesely, 1985; Busrewil and Suwesi, 1993) and satellite images (Figure E3) which covered an area about 235 km^2 from the most southern part to the most northern part of the volcanism included all phases except the youngest phase 6 which exposure at northwest of Jabal Al Haruj volcanism near Al Fuqaha village.

The age of the volcanic province has previously been determined by combined paleomagnetic, K/Ar whole-rock and cosmogenic ^{3}He exposure age dating methods, giving ages between 11.8 ± 0.41 Ma and 2,300 years (Ade-Hall *et al*. 1974, Vesely 1985, Busrewil and Suwesi 1993, Peregi *et al.* 2003, Cvetkovic *et al*. 2010, and Nixon 2011). Those ages were compared with the new ages of this study to understand the temporal history of Cenozoic volcanism in Libya.

^{40}Ar/^{39}Ar age determinations were made on the purified groundmass separates. Sample preparation and analysis procedures are described in Appendix E along with the data tables. ^{40}Ar/^{39}Ar ages are calculated relative to the optimisation model of Renne *et al*. (2010, 2011). Summary statistics are provided in Table 6.2. All uncertainties are 1σ. The ^{40}Ar/^{39}Ar step-heating analytical results are summarised in Tables E14 to E29.

6.6.1 HS12A intrusive plug

This sample yields plateau age of 13.472 ± 0.010 Ma (1σ, internal precision) which determined from 91 % of the ^{39}Ar released (the last 10 steps from 12 age steps) with MSWD of 1.40. This sample gives an integrated age (13.450 ± 0.040 Ma) that is indistinguishable from the plateau age. However, slightly younger ages occur in the lower temperature fraction (steps 1 and 2) affected by ^{39}Ar recoil during irradiation, with loss of ^{39}Ar clearly shown by decreasing ages at low temperature. The isochron yields an age (13.490 ± 0.040 Ma) that overlaps with the plateau and integrated age. It has an initial ^{40}Ar/^{36}Ar of 296 ± 3 that is statistically equivalent to the atmospheric value (298.56 ± 0.31) (Lee *et al*., 2006 and Mark *et al*., 2011b) with MSWD of 1.50 and p of 0.14 (Figure 6.14 and Table 6.4). The absolute age relative to Renne *et al*. (2010, 2011) is 13.605 ± 0.013 Ma.

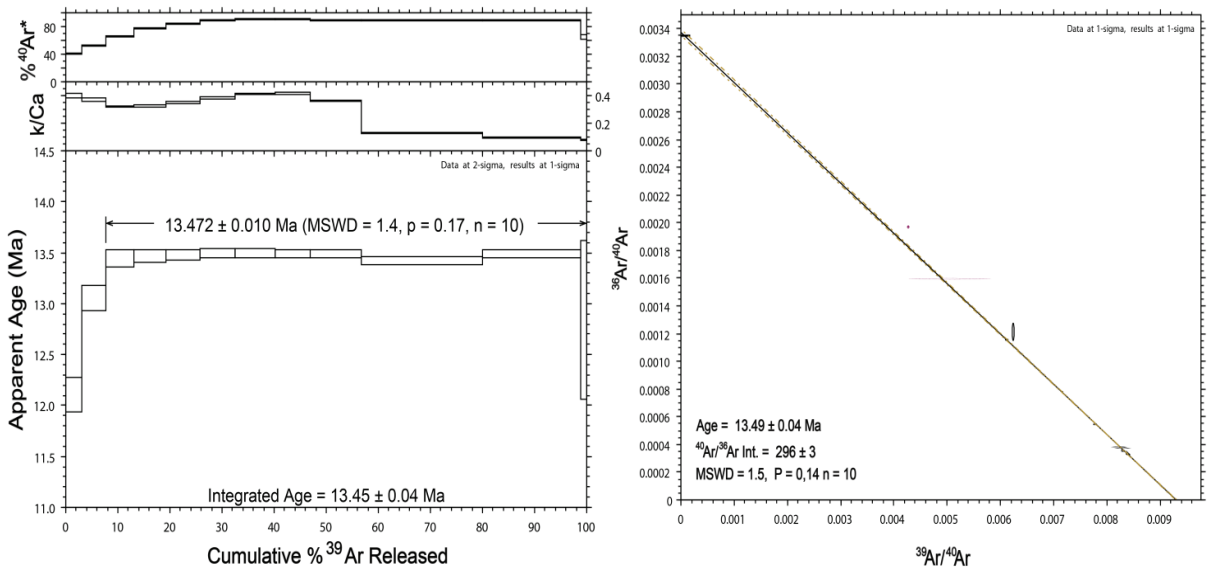

Figure 6.14: ^{40}Ar/^{39}Ar age spectra (left) and inverse isochron plot (right) for basaltic plug (sample HS12A).

6.6.2 HS14 intrusive plug

This sample yields plateau age of 9.559 ± 0.011 Ma (1σ, internal precision) which is determined from 79% of the ^{39}Ar released (steps 6 to 10 from 11 age steps) with MSWD of 1.10. This sample gives an integrated age (9.680 ± 0.090 Ma) that is indistinguishable from the plateau age. The older ages presented in this sample resemble with ^{39}Ar recoil-induced old apparent ages obtained at lowest temperatures. The inverse isochron yields an age (9.570 ± 0.030 Ma) that overlaps with the plateau and integrated age. It has an initial ^{40}Ar/^{36}Ar ratio of 297 ± 1 that is similar to the atmospheric value (Figure 6.15 and Table 6.4). The recalculated age relative to Renne *et al*. (2010, 2011) is 9.654 ± 0.013 Ma.

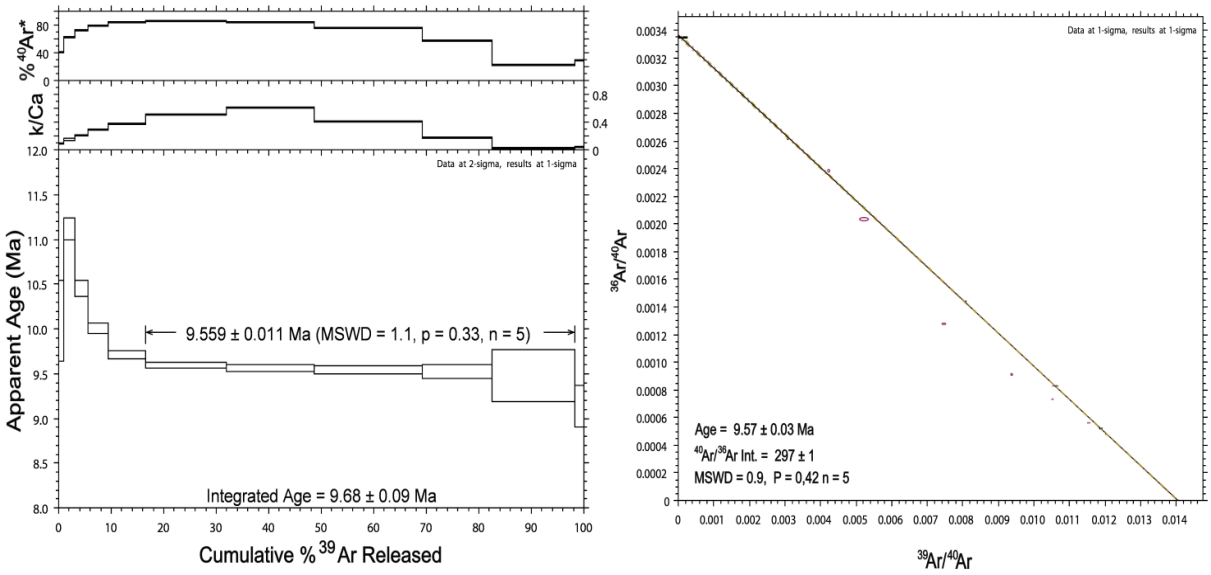

Figure 6.15: ^{40}Ar/^{39}Ar age spectra (left) and inverse isochron plot (right) for basaltic plug (sample HS14).

6.6.3 HS18 intrusive plug

The plateau age of 8.665 ± 0.010 Ma recorded from all steps (1σ, internal precision) is comparable to the inverse isochron of 8.680 ± 0.020 Ma. The $^{40}Ar/^{36}Ar$ ratio at of 297 ± 1 is statistically indistinguishable from the atmospheric value, with low MSWD of 0.50 and p of 0.87 indicating generally good correspondence between expected errors and estimated errors. Further the inverse isochron analysis is indistinguishable from plateau ages and showing the data to be robust. These ages are comparable with the integrated age of 8.660 ± 0.010 Ma, comprising step ages with the same systematically decreasing of K/Ca ratios and $^{40}Ar^*$ (Figure 6.16 and Table 6.4). The recalculated age relative to Renne *et al*. (2010, 2011) is 8.751 ± 0.011 Ma.

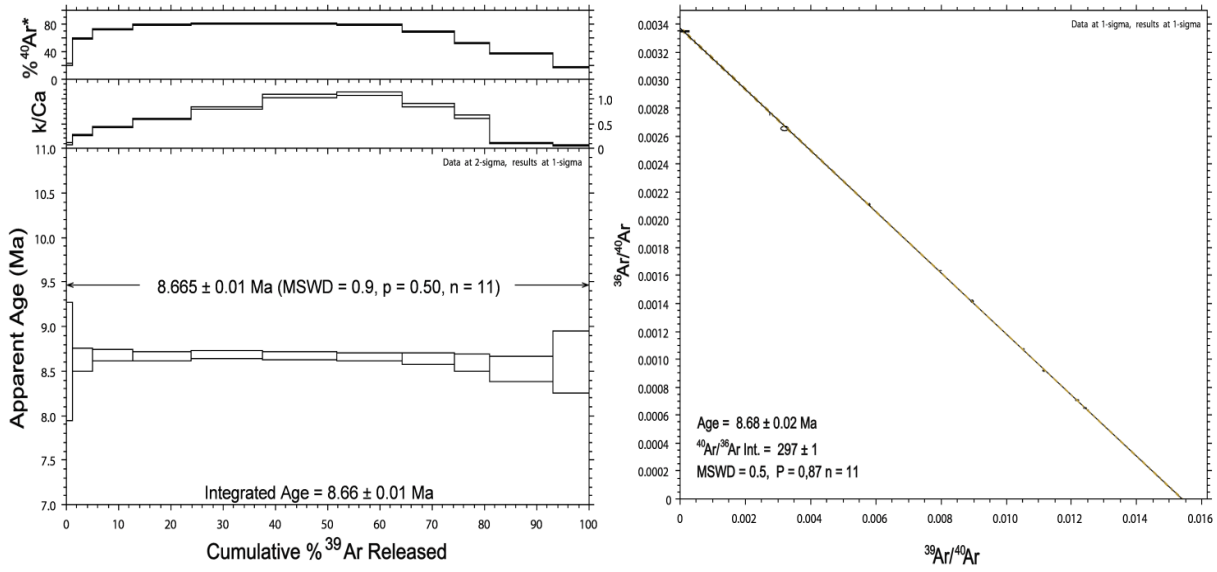

Figure 6.16: $^{40}Ar/^{39}Ar$ age spectra (left) and inverse isochron plot (right) for basaltic shield lava (sample HS18).

6.6.4 HS22 dyke

This sample produced data similar to that of three samples above with similar interpretations apply. The statistically robust age use plateau age 5.370 ± 0.011 Ma is from all steps. It is indistinguishable from the inverse isochron of 5.410 ± 0.040 Ma. The $^{40}Ar/^{36}Ar$ of 279 ± 14 statistically is lower than the atmospheric value (298.56 ± 0.31), with low MSWD of 0.40. Further the inverse isochron and plateau ages overlap with integrated age of 5.370 ± 0.010 Ma (Figure 6.17 and Table 6.4). This sample gives age yield by high constant of $^{40}Ar^*$, and increasing of K/Ca within the first four steps than decreases within the high temperatures The recalculated age relative to Renne *et al*. (2010, 2011) is 5.424 ± 0.015 Ma.

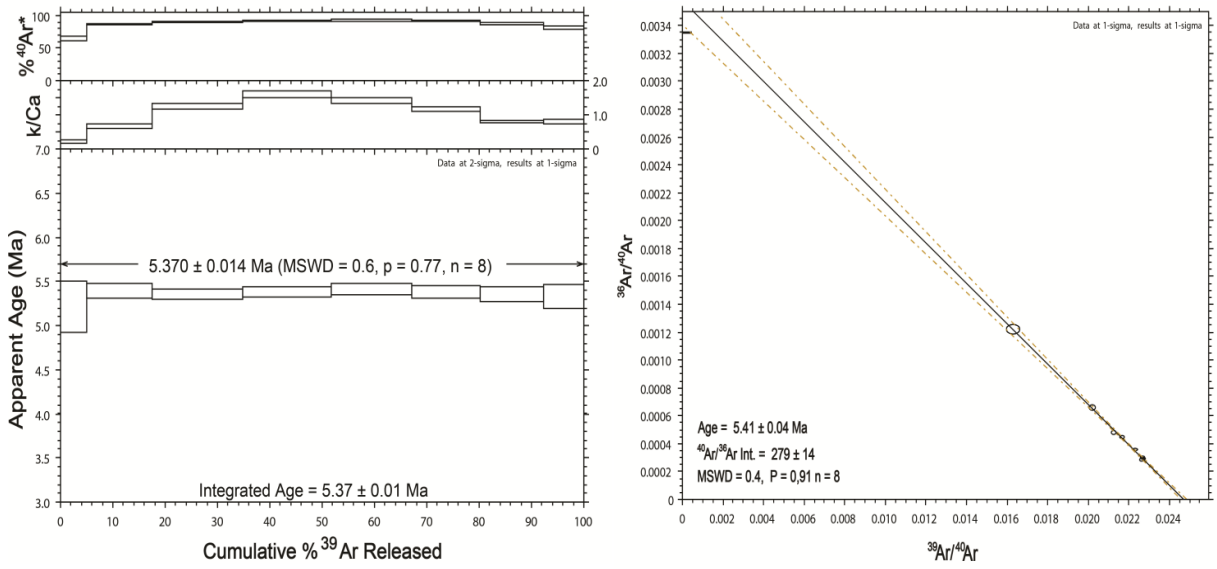

Figure 6.17: $^{40}Ar/^{39}Ar$ age spectra (left) and inverse isochron plot (right) for basaltic dyke (sample HS22).

6.6.5 HS24 basaltic lava (phase 1)

This sample produced data similar to that of HS18 and similar interpretations apply. The plateau age of 6.265 ± 0.011 Ma recorded from all steps (1σ, internal precision) is comparable to the inverse isochron of 6.280 ± 0.010 Ma. The $^{40}Ar/^{36}Ar$ ratio at of 296 ± 1 is statistically indistinguishable from the atmospheric value, with low MSWD of 1.00 and p of 0.45. Further the inverse isochron analysis is indistinguishable from plateau ages and showing the data to be robust. These ages are comparable with the integrated age of 6.270 ± 0.010 Ma. The change of $^{40}Ar^*$ and K/Ca with temperature profile are similar to HS22 but with slightly lower in $^{40}Ar^*$ and K/Ca (Figure 6.18 and Table 6.4). The recalculated age relative to Renne *et al*. (2010, 2011) is 6.327 ± 0.012 Ma.

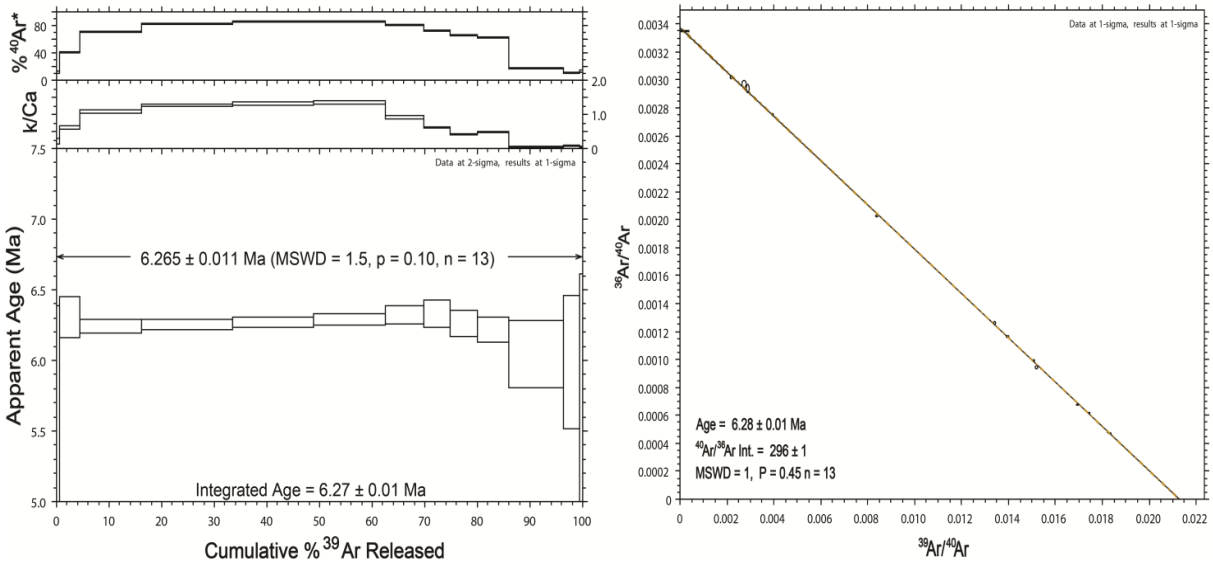

Figure 6.18: $^{40}Ar/^{39}Ar$ age spectra (left) and inverse isochron plot (right) for basaltic lava (sample HS24).

6.6.6 HS23 basaltic lava (phase 1)

This sample produced data similar to that of HS18 and HS24, and similar interpretations apply. The statistically robust age use plateau age 5.997 ± 0.005 Ma is from all steps. It is indistinguishable from the inverse isochron of 6.020 ± 0.030 Ma. The $^{40}Ar/^{36}Ar$ of 296 ± 1 with low MSWD of 0.10 (indicate overestimated analytical uncertainties) is slightly lower than the atmospheric air (298.56 ± 0.31), ruling out excess ^{40}Ar. Further the inverse isochron and plateau ages overlap with integrated age of 5.990 ± 0.010 Ma and showing the data to be robust (Figure 6.19 and Table 6.4). This ages comprising with the same change of $^{40}Ar^*$ and K/Ca with temperature profile are similar to HS22. The recalculated age relative to Renne *et al*. (2010, 2011) is 6.057 ± 0.006 Ma.

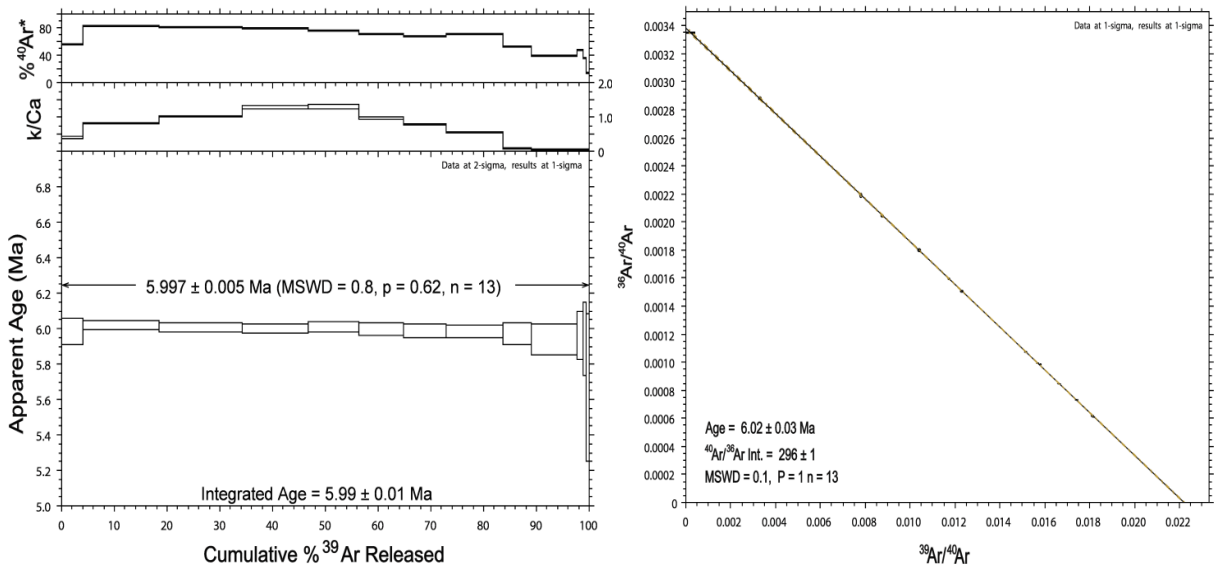

Figure 6.19: $^{40}Ar/^{39}Ar$ age spectra (left) and inverse isochron plot (right) for basaltic lava (sample HS23).

6.6.7 HS4A basaltic lava (phase 1)

This sample produced data similar to that of four samples above with similar interpretations apply. The statistically robust age use plateau age 4.392 ± 0.005 Ma is from all steps. It is indistinguishable from the inverse isochron of 4.390 ± 0.020 Ma. The $^{40}Ar/^{36}Ar$ of 298 ± 1 statistically close to the atmospheric value, with MSWD of 1.50 and p of 0.14 indicating that define initial trapped components of atmospheric composition. These ages are comparable with their integrated age of 4.390 ± 0.010 Ma, This ages comprising with the same change of $^{40}Ar^*$ and K/Ca with temperature profile are similar to HS23 (Figure 6.20 and Table 6.4). The recalculated age relative to Renne *et al*. (2010, 2011) is 4.436 ± 0.006 Ma.

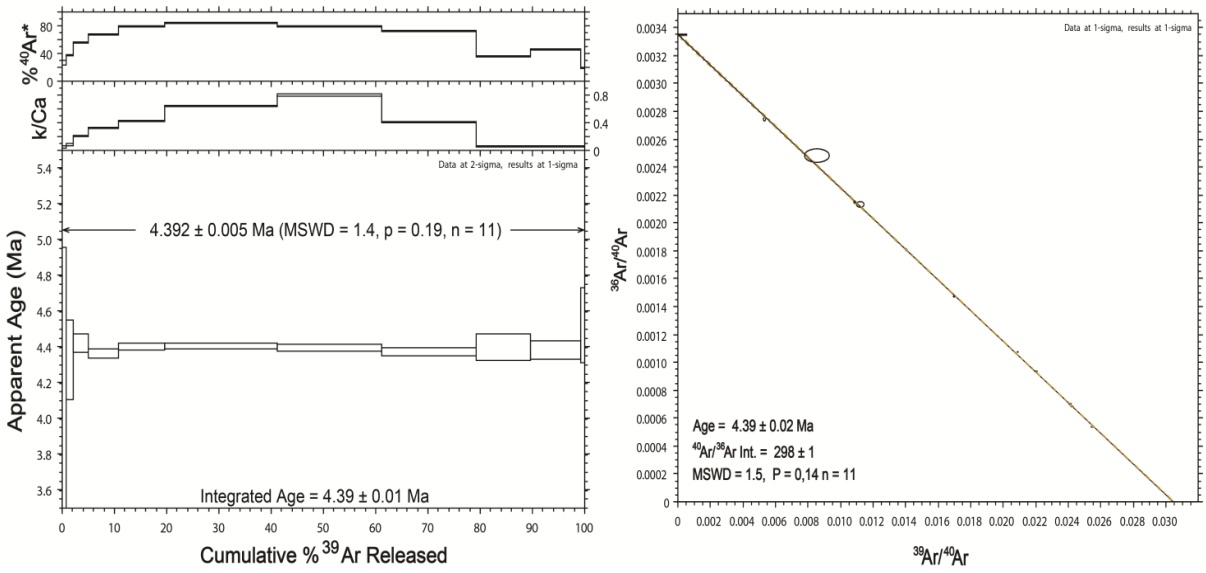

Figure 6.20: $^{40}Ar/^{39}Ar$ age spectra (left) and inverse isochron plot (right) for basaltic lava (sample HS4A).

6.6.8 HS1 basaltic lava (phase 2)

This sample yields plateau age of 2.406 ± 0.008 Ma (1σ, internal precision) which determined from 84 % of the ^{39}Ar released (the last 9 steps from 11 age steps) with MSWD of 1.50. This sample gives an integrated age (2.400 ± 0.020 Ma) that is indistinguishable from the plateau age. However, slightly younger ages occur in the lower temperature fraction (steps 1 to 3) affected by ^{39}Ar recoil during irradiation, with loss of ^{39}Ar clearly shown by decreasing ages at low temperature. The inverse isochron yields an age (2.410 ± 0.020 Ma) that overlaps with the plateau and integrated age. It has an initial ^{40}Ar/^{36}Ar ratio of 298 ± 1 that is statistically equivalent to the atmospheric value with MSWD of 1.50 and p of 0.13 indicating that excess ^{40}Ar is not the important factor in the age of this sample (Figure 6.21 and Table 6.4). The recalculated age relative to Renne *et al*. (2010, 2011) is 2.430 ± 0.008 Ma.

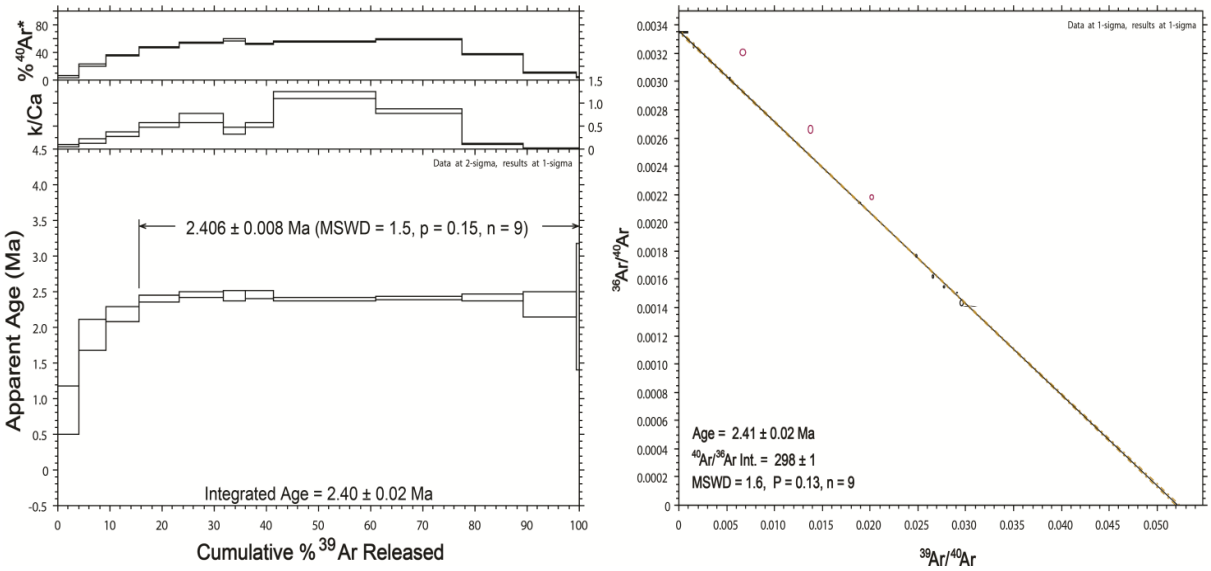

Figure 6.21: ^{40}Ar/^{39}Ar age spectra (left) and inverse isochron plot (right) for basaltic lava (sample HS1).

6.6.9 HS6 basaltic lava (phase 2)

This sample produced data similar to that of HS1 described above with similar interpretations apply. This sample yields plateau age of 1.983 ± 0.011 Ma (1σ, internal precision) which determined from 90 % of the ^{39}Ar released (the last 7 steps from 11 age steps) with MSWD of 1.90. This sample gives an integrated age (1.960 ± 0.030 Ma) that is indistinguishable from the plateau age. However, slightly younger ages occur in the lower temperature fraction (steps 1 to 4). The inverse isochron yields an age (2.010 ± 0.020 Ma) that overlaps with the plateau and integrated age. It has an initial $^{40}Ar/^{36}Ar$ ratio of 296 ± 1 that is statistically slightly lower to the atmospheric value with MSWD of 1.80 and p of 0.11 indicating that excess ^{40}Ar is not the important factor in the age of this sample (Figure 6.22 and Table 6.4). The recalculated age relative to Renne *et al*. (2010, 2011) is 2.003 ± 0.011 Ma.

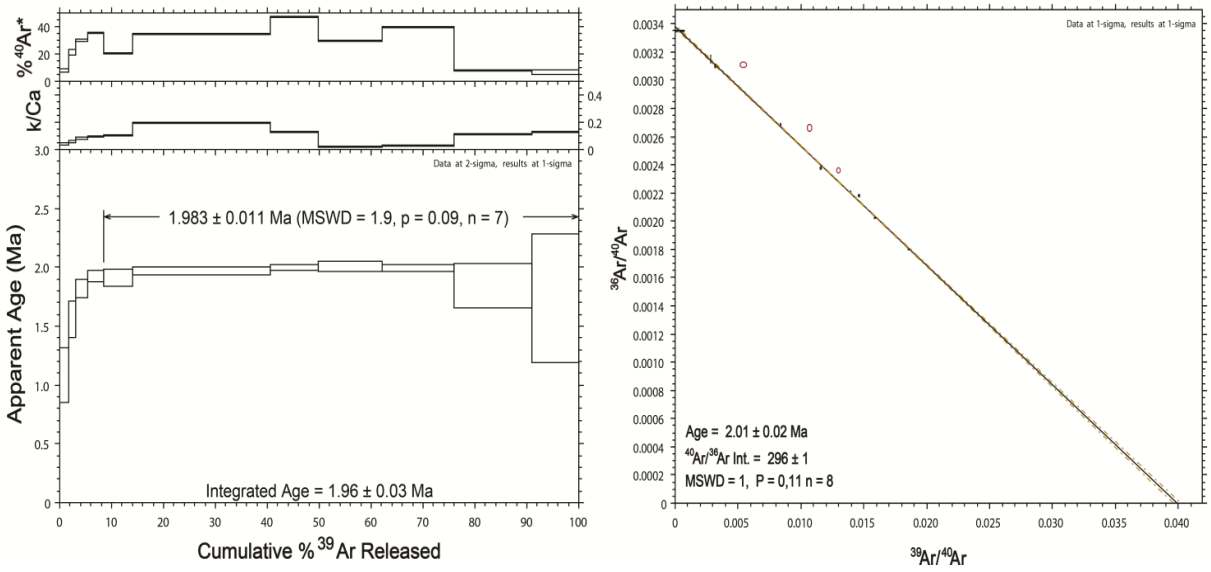

Figure 6.22: $^{40}Ar/^{39}Ar$ age spectra (left) and inverse isochron plot (right) for basaltic lava (sample HS6).

6.6.10 HS10 basaltic lava (phase 3)

The statistically robust age plateau age 1.257 ± 0.004 Ma is from all steps (1σ, internal precision). It is indistinguishable from the inverse isochron of 1.270 ± 0.010 Ma. The $^{40}Ar/^{36}Ar$ of 296 ± 2 statistically closes to the atmospheric value (298.56 ± 0.31) (Lee *et al*., 2006 and Mark *et al*., 2011b) with low MSWD of 0.40 and p of 0.97 indicating overestimated analytical uncertainties. These ages are comparable with their integrated age of 1.260 ± 0.010 Ma. This ages comprising with the same change of $^{40}Ar^*$ and K/Ca with temperature profile are similar to HS22 (Figure 6.23 and Table 6.4). The recalculated age relative to Renne *et al*. (2010, 2011) is 1.270 ± 0.004 Ma.

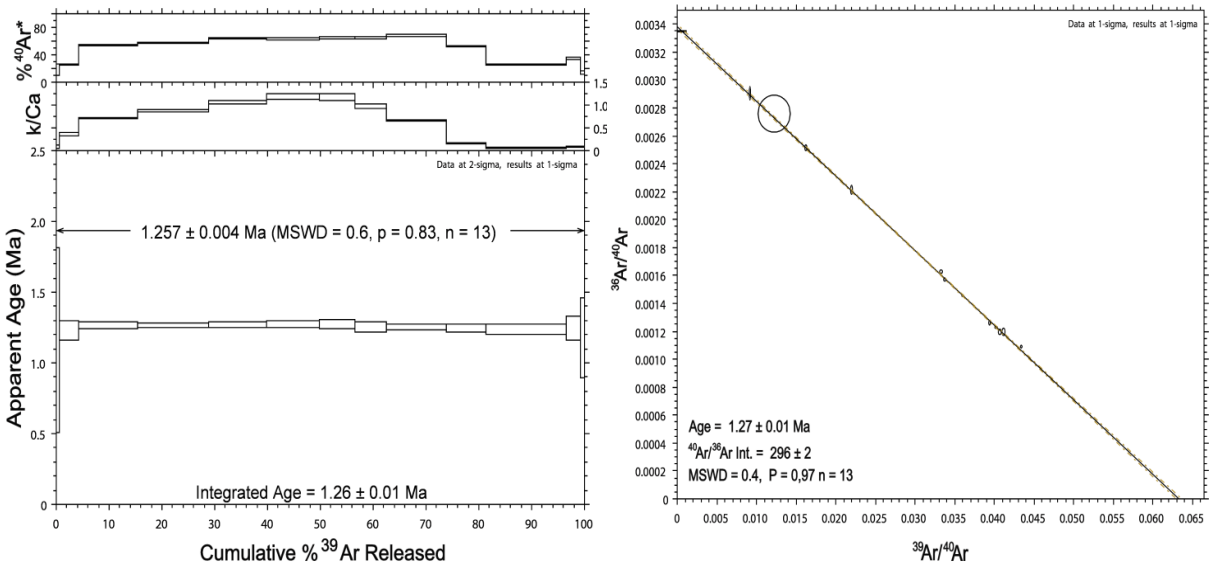

Figure 6.23: $^{40}Ar/^{39}Ar$ age spectra (left) and inverse isochron plot (right) for basaltic lava (sample HS10).

6.6.11 HS19 basaltic lava (phase 3)

This sample produced data similar to most samples yield plateau age from all steps with similar interpretations apply. The statistically robust age use plateau age 0.987 ± 0.003 Ma is from all steps (1σ, internal precision). It is indistinguishable from the inverse isochron of 0.990 ± 0.010 Ma. The $^{40}Ar/^{36}Ar$ of 298 ± 2 statistically closed to the atmospheric value (298.56 ± 0.31) (Lee *et al*., 2006 and Mark *et al*., 2011b) with MSWD of 0.90 and p of 0.50 indicating that the excess of ^{40}Ar is ruling out. These ages are comparable with their integrated age of 0.990 ± 0.010 Ma. K/Ca increase with temperature until the last 4 steps which correspond to the degassing of K-poor, Ca-rich mineral phases (plagioclase and/or pyroxene) (Figure 6.24 and Table 6.4). The recalculated age relative to Renne *et al*. (2010, 2011) is 0.997 ± 0.003 Ma.

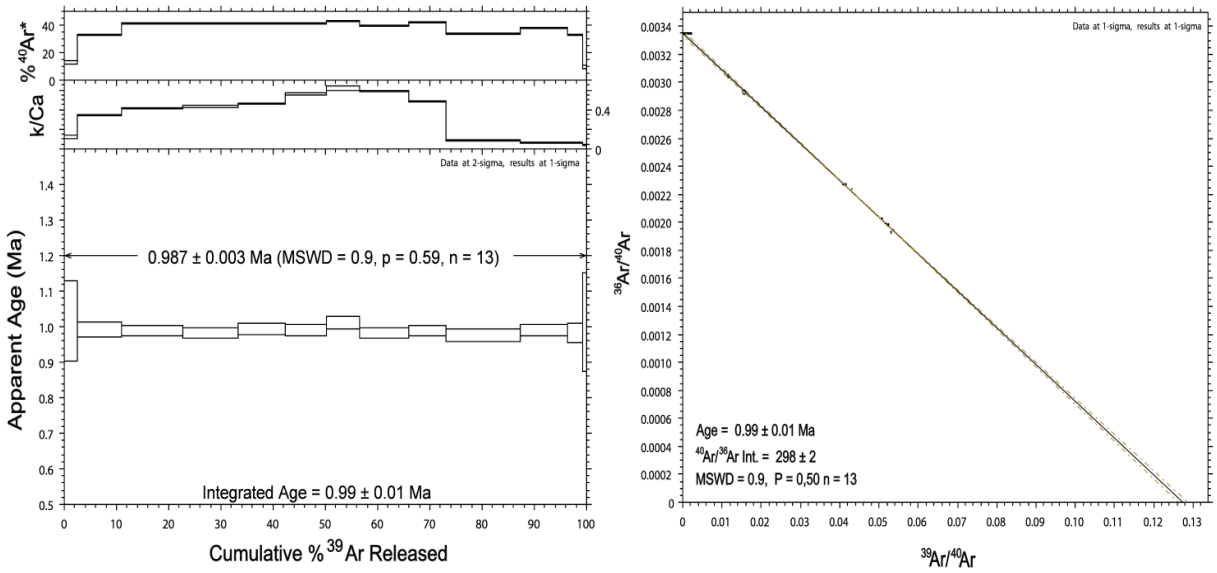

Figure 6.24: $^{40}Ar/^{39}Ar$ age spectra (left) and inverse isochron plot (right) for basaltic lava (sample HS19).

6.6.12 HS20 basaltic lava (phase 3)

This sample produced Ar/Ar data similar to that of HS1 and HS6 described above with similar interpretations. This sample yields plateau age of 0.951 ± 0.003 Ma (1σ, internal precision) which determined from 82 % of the ^{39}Ar released (the last 9 steps from 12 age steps) with MSWD of 1.10. This sample gives an integrated age (0.950 ± 0.010 Ma) that is indistinguishable from the plateau age. However, slightly younger ages occur in the lower temperature fraction (steps 1 to 3) affected by ^{39}Ar recoil. The inverse isochron yields an age (0.950 ± 0.010 Ma) that overlaps with the plateau and integrated age. It has an initial ^{40}Ar/^{36}Ar ratio of 297 ± 2 that is statistically equivalent to the atmospheric value with MSWD of 1.90 and p of 0.06 attesting to a slight excess of scatter exceeding analytical uncertainties (Figure 6.25 and Table 6.4). The recalculated age relative to Renne *et al*. (2010, 2011) is 0.960 ± 0.003 Ma.

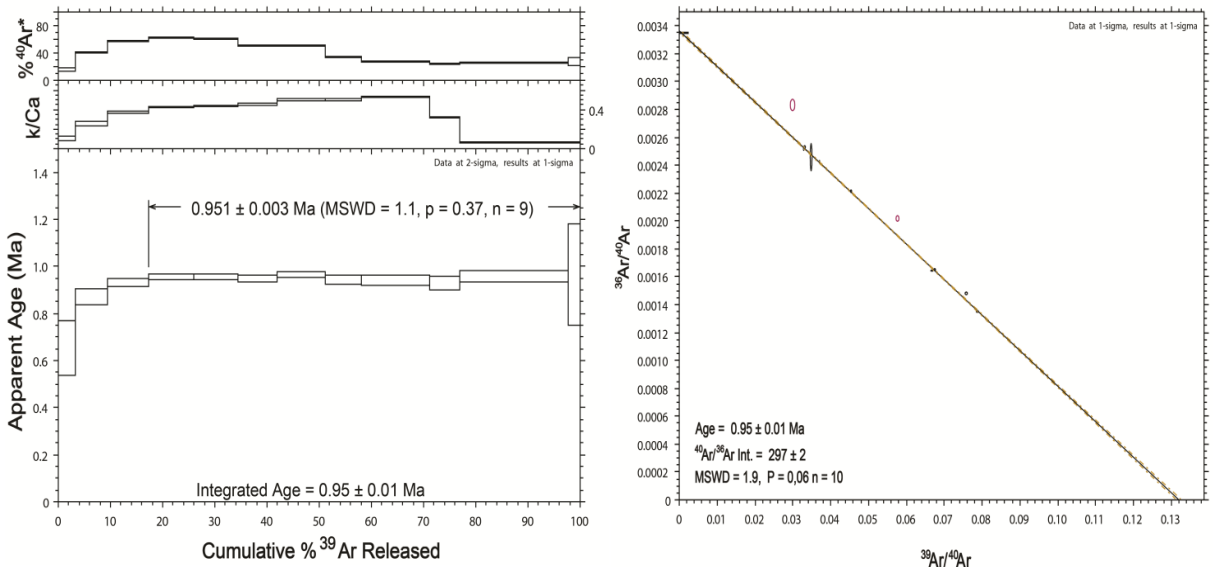

Figure 6.25: ^{40}Ar/^{39}Ar age spectra (left) and inverse isochron plot (right) for basaltic lava (sample HS20).

6.6.13 HS16 basaltic lava (phase 4)

This sample produced data similar to most samples yield plateau age from all steps with similar interpretations apply. The statistically robust age use plateau age 0.931 ± 0.003 Ma is from all steps (1σ, internal precision). It is indistinguishable from the inverse isochron of 0.940 ± 0.010 Ma. The $^{40}Ar/^{36}Ar$ of 296 ± 1 is slightly lower than the atmospheric value (298.56 ± 0.31) (Lee *et al*., 2006 and Mark *et al*., 2011b), with MSWD of 0.60 and p of 0.85 indicating that the excess of ^{40}Ar is ruling out. These ages are comparable with their integrated age of 0.930 ± 0.010 Ma. K/Ca decrease with temperature, the last 3-4 steps correspond to the degassing of K-poor, Ca-rich mineral phases (plagioclase and/or pyroxene) (Figure 6.26 and Table 6.4). The recalculated age relative to Renne *et al*. (2010, 2011) is 0.940 ± 0.003 Ma.

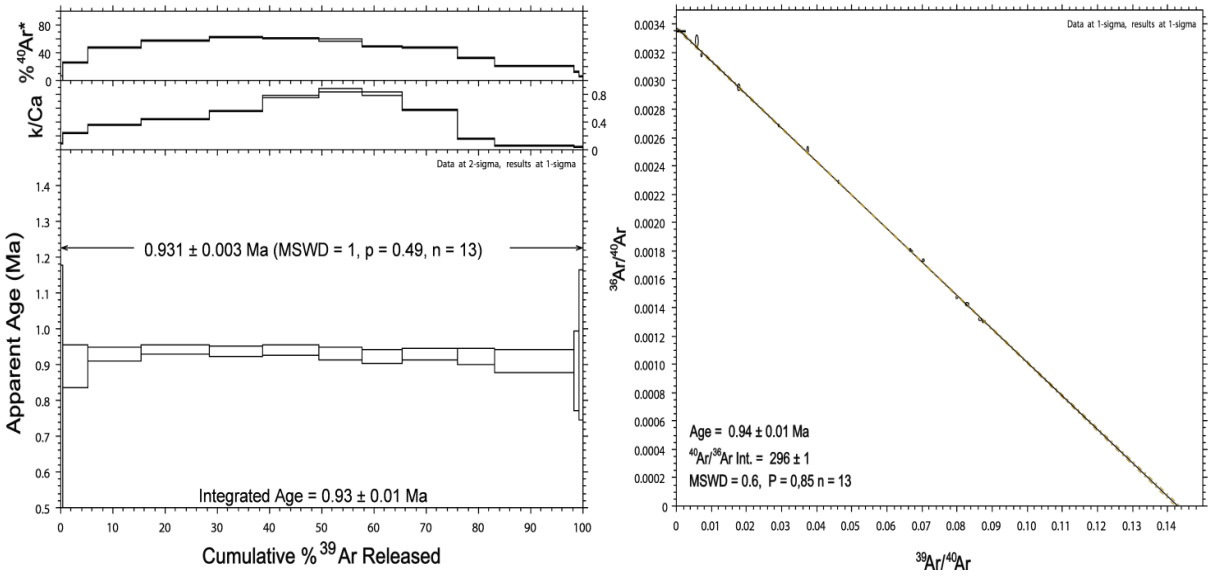

Figure 6.26: $^{40}Ar/^{39}Ar$ age spectra (left) and inverse isochron plot (right) for basaltic lava (sample HS16).

6.6.14 HS3 basaltic lava (phase 4)

This sample produced data similar to that of HS16 described above with similar interpretations apply. This sample produced data similar to most samples yield plateau age from all steps with similar interpretations apply. The statistically robust age use plateau age 0.605 ± 0.007 Ma is from all steps (1σ, internal precision). It is indistinguishable from the inverse isochron of 0.640 ± 0.020 Ma. The $^{40}Ar/^{36}Ar$ of 296 ± 1 is slightly lower than the atmospheric value (298.56 ± 0.31) (Lee *et al*., 2006 and Mark *et al*., 2011b) with low MSWD = 0.10 and p = 1.00 indicating overestimated analytical uncertainties. These ages are comparable with their integrated age of 0.610 ± 0.010 Ma. K/Ca decrease normally with temperature (Figure 6.27 and Table 6.4). The recalculated age relative to Renne *et al*. (2010, 2011) is 0.611 ± 0.007 Ma.

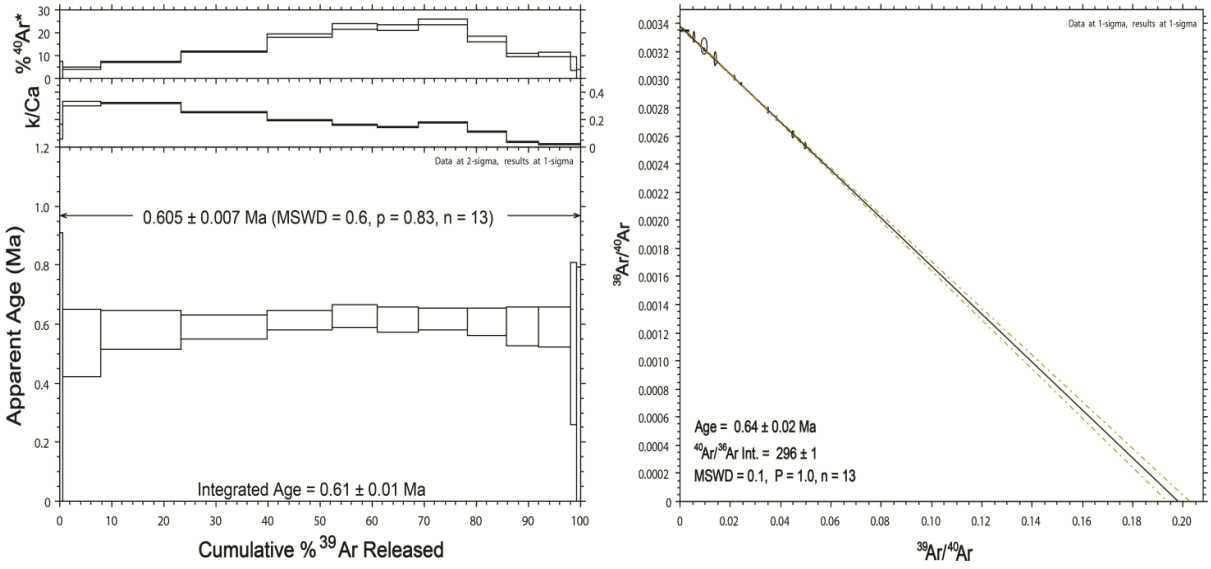

Figure 6.27: $^{40}Ar/^{39}Ar$ age spectra (left) and inverse isochron plot (right) for basaltic lava (sample HS3).

6.6.15 HS21 basaltic lava (phase 4)

This sample produced data similar to most samples yield plateau age from all steps with similar interpretations apply. The statistically robust age use plateau age 0.113 ± 0.005 Ma is from all steps (1σ, internal precision). It is indistinguishable from the inverse isochron of 0.110 ± 0.010 Ma. The $^{40}Ar/^{36}Ar$ of 300 ± 2 is statistically equivalent to the atmospheric value (298.56 ± 0.31) (Lee *et al*., 2006 and Mark *et al*., 2011b) with MSWD of 0.80 and p of 0.66 indicate that excess ^{40}Ar is not a significant factor in the age of this sample. These ages are comparable with their integrated age of 0.110 ± 0.010 Ma. The K/Ca increase with low temperature then decrease within middle to high temperature, the last 3 steps correspond to the degassing of K-poor, Ca-rich mineral phases (plagioclase and/or pyroxene) (Figure 6.29 and Table 6.4). The data points plot near the y-axis indicate the low radiogenic. The calculated age relative to Renne et al. (2010, 2011) is 0.115 ± 0.005 Ma.

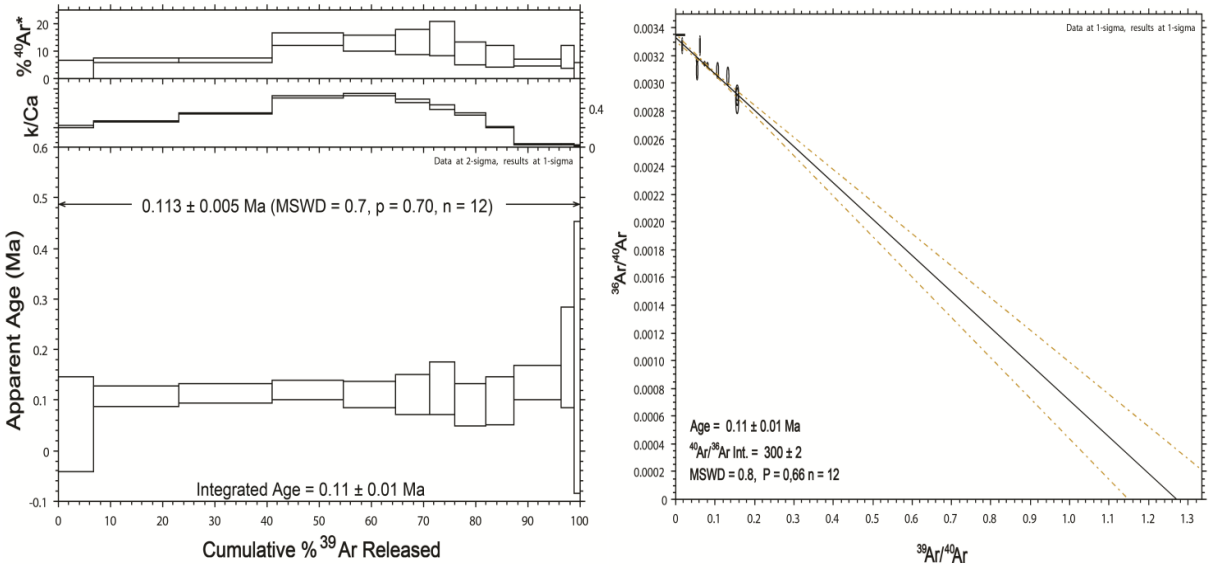

Figure 6.28: $^{40}Ar/^{39}Ar$ age spectra (left) and inverse isochron plot (right) for basaltic lava (sample HS21).

6.6.16 HS11 basaltic lava (phase 5)

This sample yields statistically plateau age of 0.473 ± 0.002 Ma (1σ, internal precision) which determined from 94 % of the ^{39}Ar released (all steps except the last step from 9 age steps) with MSWD of 1.3. The inverse isochron age (0.480 ± 0.010 Ma) is comparable with the plateau age. The initial $^{40}Ar/^{36}Ar$ ratio of 295 ± 1 is slightly lower than the atmospheric value (298.56 ± 0.31) with MSWD of 1.30 and p of 0.28. Further the inverse isochron age and plateau age is overlap and showing the data to be precise. These ages are similar to their integrated age of 0.470 ± 0.010 Ma (Figure 6.28 and Table 6.4). The recalculated age relative to Renne *et al*. (2010, 2011) is 0.478 ± 0.002 Ma.

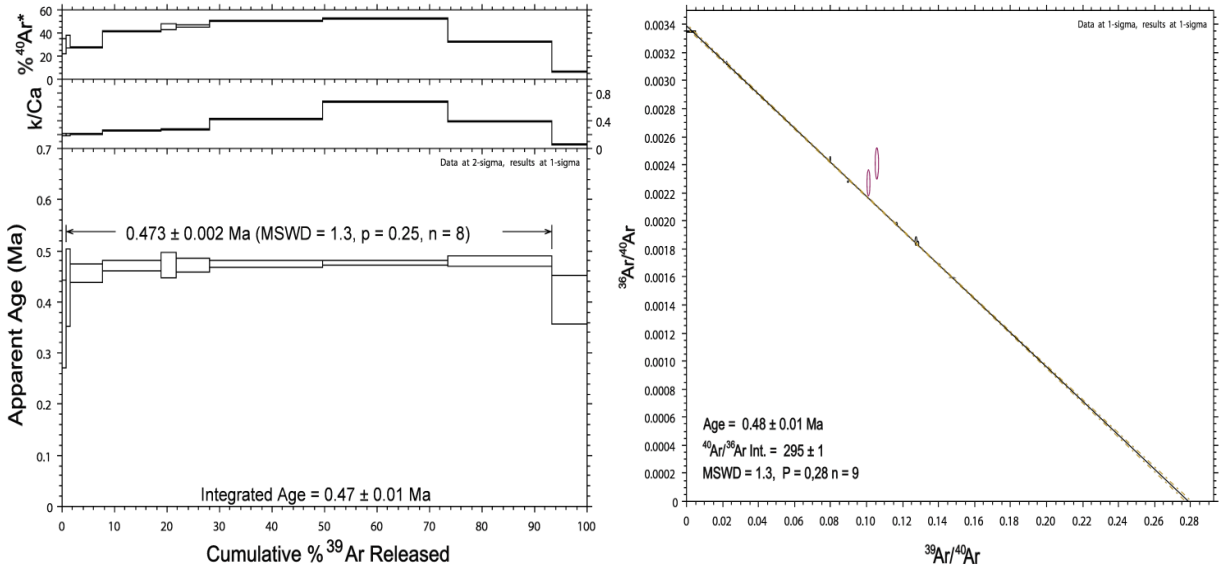

Figure 6.29: $^{40}Ar/^{39}Ar$ age spectra (left) and inverse isochron plot (right) for basaltic lava (sample HS11).

Table 6.3: $^{40}Ar/^{39}Ar$ data of the basalts from Jabal Al Haruj Aswad volcanic province.

Decay constants of Steiger & Jager (1977), Fish Canyon sanidine at 28.02 ± 0.16 Ma (Renne *et al*., 1998), atmospheric argon isotope ratios of Lee *et al*. (2006) and Mark *et al*. (2011b) (298.56 ± 0.31).													Optimisation model (Renne *et al*., 2010, 2011) - full external precision (standard age, decay constant)	
ID	Sample type	Location	Mass (mg)	Plateau age (Ma)	1σ	^{39}Ar (%)	MSWD	Isochron age (Ma)	1σ	$^{40}Ar/^{36}Ar$	1σ	MSWD	Age (Ma)	1σ
HS12 A	Plug	112 km south of Zalla	493	13.472 (*n* = 10)	0.010	91	1.400	13.490 (*n* = 10)	0.040	296	3.000	1.500	13.605	0.013
HS14	Plug	99 km south of Zalla	492	9.559 (*n* = 5)	0.011	79	1.100	9.570 (*n* = 5)	0.030	297	1.000	0.900	9.654	0.013
HS18	Plug	80 km south of Zalla	501	8.665 (*n* = 11)	0.010	100	0.900	8.680 (*n* = 11)	0.020	297	1.000	0.500	8.751	0.011
HS22	Dyke	39 km south of Zalla	493	5.370 (*n* = 8)	0.011	100	0.600	5.410 (*n* = 8)	0.040	279	14.00	0.400	5.424	0.015
HS24	Lava	35 km south of Zalla (phase 1)	492	6.265 (*n* = 13)	0.011	100	1.500	6.280 (*n* = 13)	0.010	296	1.000	1.000	6.327	0.012

HS23	Lava	37 km south of Zalla (phase 1)	497	5.997 (*n* = 13)	0.005	100	0.800	6.020 (*n* = 13)	0.030	296	1.000	0.100	6.057	0.006
HS4A	Lava	240 km south of Zalla (phase 1)	492	4.392 (*n* = 11)	0.005	100	1.400	4.390 (*n* = 11)	0.020	298	1.000	1.500	4.436	0.006
HS1	Lava	270 km south of Zalla (phase 2)	501	2.406 (*n* = 9)	0.008	84	1.500	2.410 (*n* = 9)	0.020	298	1.000	1.600	2.430	0.008
HS6	Lava	230 km south of Zalla (phase 2)	490	1.983 (*n* = 7)	0.011	90	1.900	2.010 (*n* = 8)	0.020	296	1.000	1.800	2.003	0.011
HS10	Lava	172 km south of Zalla (phase 3)	496	1.257 (*n* = 13)	0.004	100	0.600	1.270 (*n* = 13)	0.010	296	2.000	0.400	1.270	0.004
HS19	Lava	55 km south of Zalla (phase 3)	499	0.987 (*n* = 13)	0.003	100	0.900	0.990 (*n* = 13)	0.010	298	2.000	0.900	0.997	0.003

HS20	Lava	48 km south of Zalla (phase 3)	503	0.951 (*n* = 10)	0.003	82	1.100	0.950 (*n* = 10)	0.010	297	2.000	1.900	0.960	0.003
HS16	Lava	88 km south of Zalla (phase 4)	500	0.931 (*n* = 13)	0.003	100	1.000	0.940 (*n* = 13)	0.010	296	1.000	0.600	0.940	0.003
HS3	Lava	245 km south of Zalla (phase 4)	506	0.605 (*n* = 13)	0.007	100	0.600	0.640 (*n* = 13)	0.020	296	1.000	0.100	0.611	0.007
HS21	Lava	40 km south of Zalla (phase 4)	503	0.113 (*n* = 12)	0.005	100	0.700	0.110 (*n* = 12)	0.010	300	2.000	0.800	0.115	0.005
HS11	Lava	166 km south of Zalla (phase 5)	500	0.473 (*n* = 8)	0.002	94	1.300	0.480 (*n* = 8)	0.010	295	1.000	1.300	0.478	0.002

6.6.17 Comparison with previous studies

The first K/Ar age dates for the Al Haruj volcanic province were presented by Ade-Hall et al. (1974). They conducted a combined palaeomagnetic and age dating study of basaltic rocks from north eastern part of the volcanic field. Using K/Ar dating, they found the volcanic activity extended back at least to 6.0 ± 0.2 Ma (phase B1 of Klitzsch, 1968) and the youngest volcanic phase (B5 of Klitzsch, 1968) was found to be 0.41 ± 0.20 Ma and majority of the volcanism is believed to be less than 2.2 million years ago. Vesely (1985) determined ages of 7.96 ± 0.40 to 6.69 ± 0.33 Ma for two basaltic rocks of phase 1 (BF1 and BF0) which covers the northern part of Al Haruj close to Zallah village. Peregi et al. (2003) have used K/Ar method to account the ages of Al Haruj al Aswad basalts to be range from 5.27 to 0.10 Ma which covered all six phases that was compatible with the stratigraphic ages given by Busweril and Suwesi (1993) to produce a map of the southern Al Haruj volcanic province. In a more recent study done by Cvetkovic et al. (2010), K/Ar analyses of whole-rock samples from the eastern part of the Al Haruj province range from 11.8 ± 0.4 to 0.51 ± 0.26 Ma. Nixon (2011) determined cosmogenic ^{3}He exposure ages of 2.31 ± 0.81 ka from an uneroded flow from phase 6.

Interestingly, the new ages of the intrusive rocks record the oldest ages, similar to other Libyan Cenozoic volcanic provinces. A basalt plug (HS12A) from 112 km south of Zalla is 13.61 ± 0.01 Ma.

The new ages from the five different phases of Al Haruj al Aswad volcanic province, are shown in Table 6.5. The ^{40}Ar/^{36}Ar ages generally show stratigraphic consistency. Based on the new ages, geological map, satellite images (Figure E3, Appendix E) and petrographic studies, it can be seen that the Al Haruj basalts formed during different phases which developed from 6.33 ± 0.01 to 0.12 ± 0.01. Each phase is represented by several generations of basaltic lava flows

but in some places the youngest lava overlies the oldest lavas (the estimated volume of lava erupted has decreased with time).

The new Ar/Ar ages generally overlap the K/Ar ages of previous works (Table 6.4). The consistency can be directly tested because two samples (HS23 and HS24) are from the same flows as dated by Vesely (1985) and have ages of 7.96 ± 0.40 and 6.69 ± 0.33 Ma, BF1 and BF0, respectively. The new $^{40}Ar/^{39}Ar$ ages (6.33 ± 0.01 Ma and 6.06 ± 0.01 Ma respectively) are slightly younger than Vesely (1985) ages with better precision. This is typical of $^{40}Ar/^{36}Ar$ ages versus K/Ar ages.

According to previous studies and the new $^{40}Ar/^{39}Ar$ ages, the Al Haruj basalts were erupted after 6.3 Ma, with the majority occurring in the last 2 million years (Figure 6.30). Based on the unavailability of good geological map, I used Nixon, 2011 as a reference to an estimate volume of lava. Nixon, 2011 concluded that the estimated volume of lava erupted has decreased with time. For example Phase 1 appears to have covered the majority of the volcanic province before being masked by deposition of younger flows, possibly covering an area of 45,000 km^2, while the phase 4 is estimated at approximately 75 km^3 and the phase 6 at approximately 10 km^3. The southern part of Al Haruj is dominated by volcanic phase 1 and does not show any younger lava flows suggesting the volcanic centre of the Al Haruj has shifted northwards with time (according to the available geological map of Vesely (1985) and Busweril and Suwesii (1993) and the discussed of Nixon (2011). The large eruptive volume of phase 1 (6.33 ± 0.01 - 4.44 ± 0.01) was probably produced in a relatively short time period (~2-3 Ma) that is equal to combine of all other phases (2.43 ± 0.01 - 0.48 ± 0.01) eruptive volume (phases 2 to 5) at the same period of time.

Table 6.4: The new ages of the Al Haruj volcanic phases compared to previous studies.

Volcanic Phase	Ade-Hall *et al*. (1974)	Vesely (1985)	Peregi *et al.* (2003)	Nixon (2011)	This study
Method	K/Ar (Ma)	K/Ar (Ma)	K/Ar (Ma)	^{3}He exposure (Ma)	^{40}Ar/^{39}Ar (Ma)
Phase 1	6.0 ± 0.2 - 2.0 ± 0.2	7.96 ± 0.40 - 6.69 ± 0.33	5.27 - 2.73		6.33 ± 0.01 - 4.44 ± 0.01
Phase 2	1.2 ± 0.2		2.24 - 1.46		2.43 ± 0.01 - 2.00 ± 0.01
Phase 3			1.77 - 1.12		1.27 ± 0.01 - 0.96 ± 0.01
Phase 4			1.22 - 0.34		0.94 ± 0.01 - 0.12 ± 0.01
Phase 5	0.41 ± 0.2		0.78 - 0.15		0.48 ± 0.01
Phase 6			0.50 - 0.10	0.0023 ± 0.00081	

6.7 Implications of the basalt geochronology

High precision $^{40}Ar/^{39}Ar$ age determinations of the basalts from Libyan Cenozoic volcanic provinces reveal:

(1) The intrusive rocks (dykes and plugs) associated with all the Libyan Cenozoic volcanic provinces record the oldest ages. The intrusive rocks from Garian are from 28.2 to 10.8 Ma; Jabal al Hasawinah from 20.0 to 15.4 Ma; Jabal as Sawda 22.9 Ma and Al Haruj al Aswad from 13.6 to 8.8 Ma. Across much of the region the basaltic volcanism appears to have initiated simultaneously in the early to mid-Miocene and could have been controlled by the same tectonic process.

(2) The youngest basalt lavas of the Libyan Cenozoic volcanic provinces, Garian, Jabal Al Hasawinah and Jabal as Sawda, imply that the volcanism in these regions ceased approximately 3, 11 and 12 million years ago, respectively. The young age of Al Haruj volcanic province (< 10 ka) should be considered as an active volcanic region. The new ages determinations confirm the stratigraphic ages given by Klitzsch (1968).

(3) The presence of basaltic lavas of the same age as intrusives in the Jabal Al Hasawinah, Jabal as Sawda and Jabal Al Haruj provinces indicates that these regions have not been affected by erosion or subsequent basalt volcanism.

(4) The basaltic lavas of the Garian volcanic province (5.44 ± 0.04 to 2.67 ± 0.01 Ma) were erupted broadly contemporaneously with the volcanism of Al Haruj al Aswad (6.33 ± 0.01 to 0.12 ± 0.01 Ma). Basaltic lavas of the Jabal al Hasawinah (15.28 ± 0.02 to 10.89 ± 0.01) and Jabal as Sawda (14.05 ± 0.02 to 12.10 ± 0.01 Ma) provinces appear to have been erupted on a short period, at the same time, but much earlier than the latest phase of eruptions to the north and south. It therefore appears volcanism in Libya has been episodic during the Cenozoic and does not define a temporal trend.

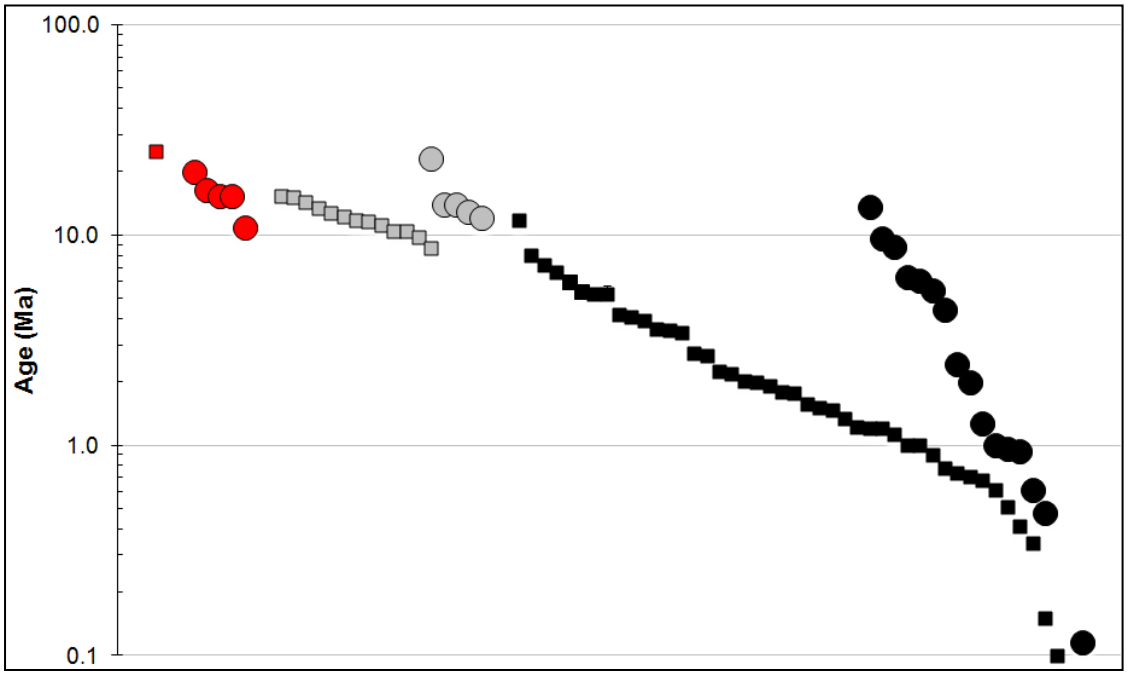

Figure 6.30: Comparison of new $^{40}Ar/^{39}Ar$ ages (circles) to published K-Ar determinations (squares) of the Cenozoic volcanic provinces of Libya; Al Hasawinah volcanic field (red color), Jurak (1978); Jabal as Sawda volcanic field (grey color), Schult and Soffel (1973), Ade-Hall *et al*. (1975) Busrewil and Esson (1991); Al Haruj volcanic field (black color), Ade-Hall *et al*. (1974), Vesely (1985), Peregi *et al*. (2003) and Cvetkovic *et al*. (2010).

Chapter Seven

Geodynamic setting of the Cenozoic volcanism of Libya

7.1 Introduction

I have undertaken the first detailed study of the geochemistry and geochronology of all the major Cenozoic volcanic provinces of Libya. In order to understand the tectonic setting and the origin of the Libyan volcanism, this study was extended to review the geochemical, geochronological data, geophysical and tectonic framework of the central Mediterranean, Sicily Channel (Etna, Pantelleria and Linosa volcanic islands) and North Africa volcanism (Hoggar, Darfur and Tibesti volcanic fields) to determine the possible relationship between them. The aim of this chapter is to try to decipher the geodynamic setting of the Libyan Cenozoic volcanism using geochemical and geochronological data with geophysical observations.

7.2 Regional Cenozoic volcanism

The majority of Cenozoic basaltic volcanic provinces of south Europe and north Africa have produced alkalic to transitional basalts (basalts, tephrite-basanite and trachybasalt fields) (Civetta *et al.*, 1998; Gourgaud and Vincent, 2004; Azzouni-Sekkal *et al*., 2007; Lucassen, 2008; Nixon, 2011; Mollo *et al*.., 2013). These are compositionally similar to the Cenozoic basalts from Libya reported in Chapter 6.

Chondrite-normalized rare earth element patterns of Cenozoic basalts from Libya, north Africa and south Europe show light rare earth element enrichments relative to the middle and heavy rare earth elements (Figure 7.1A and B). This is evidence that the basaltic melts originate from similar mantle depths around the spinel-garnet transition (80–90 km) (Nickel, 1986; Adam and Green, 2006).

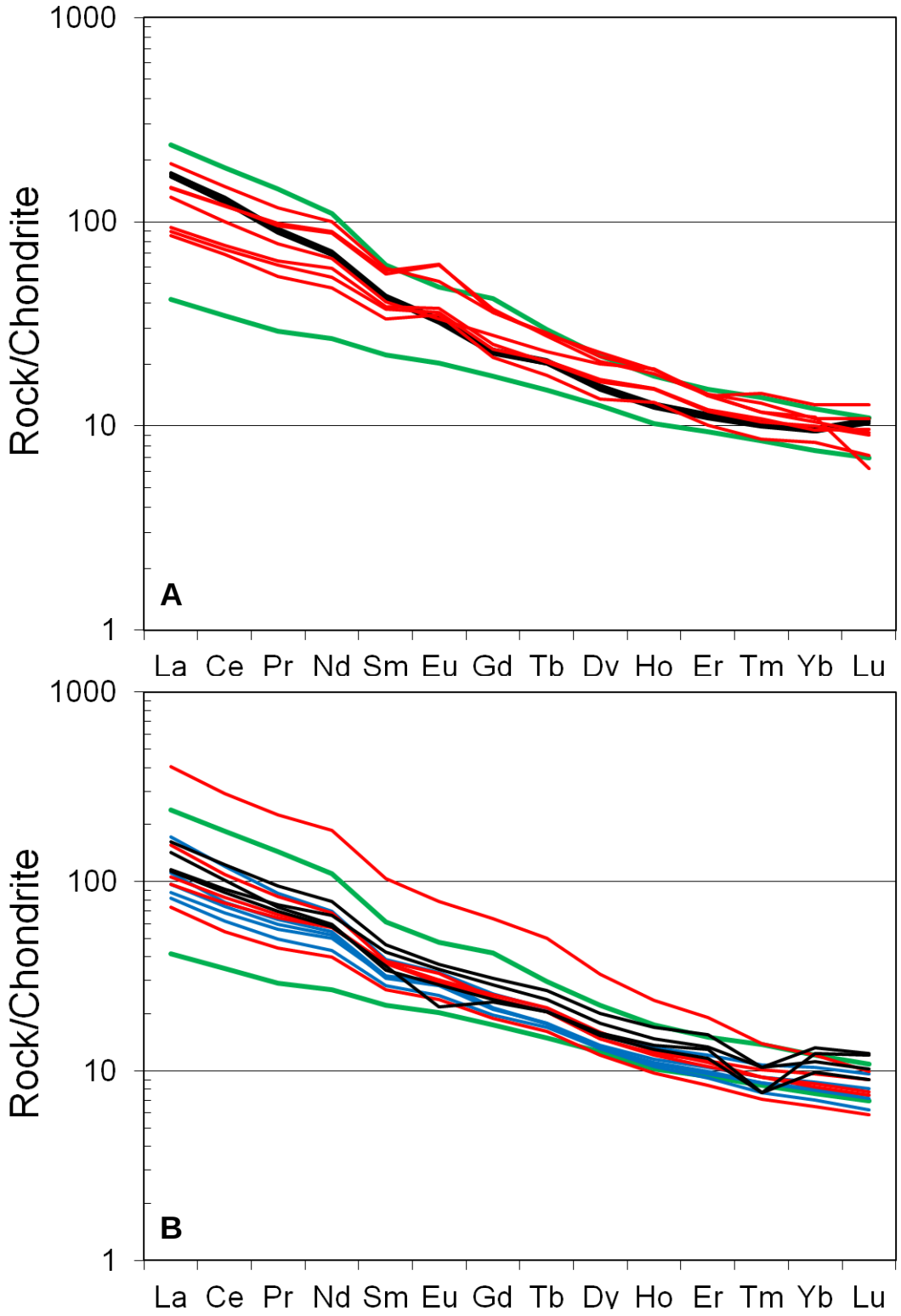

Figure 7.1: Chondrite-normalized REE patterns for basalt rocks from the Garian volcanic province (green line) with (A) south European volcanic rocks: Mt. Etna (black line); Pantelleria (red line) and (B) north Africa volcanic rocks: Darfur (blue line); Hoggar (red line) and Tibesti (black line). Chondrite values are from Nakamura (1974).

The Garian basalts have $^{87}Sr/^{86}Sr$ and $^{143}Nd/^{144}Nd$ compositions that overlap the fields of Cenozoic volcanic rocks from south Europe: (e.g. Etna: Viccaro and Cristofolini (2008), Tonarini *et al*., (2001); Pantelleria: Esperaqa and Crisci (1995)) and North African (Al Haruj; Nixon (2011), Cameroon Line; Lee *et al*., (1994)) (Figure 7.2). The data tend to define mixtures between the HIMU mantle component of Zindler and Hart (1986) and a variety of more enriched mantle compositions, with little involvement of evolved depleted mantle.

While the melts originate in asthenosphere (section 4.5), the HIMU Sr and Nd isotope composition can be traced to metasomatised lithospheric spinel peridotite xenoliths that are found in basalts from Garian, Hoggar, Elba and Veneto volcanic province (e.g. Beccaluva *et al*. 2001, 2008, 2009). The widespread nature of this mantle signature in the Cenozoic basalts of southern Europe has been recognised previously (termed the Common Mantle Reservoir by Lustrino and Wilson (2007)). This study indicates that post-Miocene basalts of north Africa have also acquired the signature and implies the enrichment of the lithosphere is widespread.

7.3 Geodynamics of Cenozoic volcanism in Libya

The Cenozoic volcanism in Europe and north Africa is associated with most prominent low-velocity mantle anomalies, which can be interpreted as zones of higher temperature (e.g. Al-Hajri et al. 2009). Rare earth element inversion modelling of alkali and tholeiitic basalts from Jabal Al Haruj produced mantle temperatures of ~1460-1480°, and led Nixon (2011) to propose that the Cenozoic basalt volcanism of Libya is related to an upwelling mantle plume. Based on the apparent decrease in the previously measured age of basaltic rocks from NNW to SSE, Fouad (1990) and Hegazy (1999) proposed that the volcanism was related to the movement of the African plate over a fixed hot-spot in the mantle.

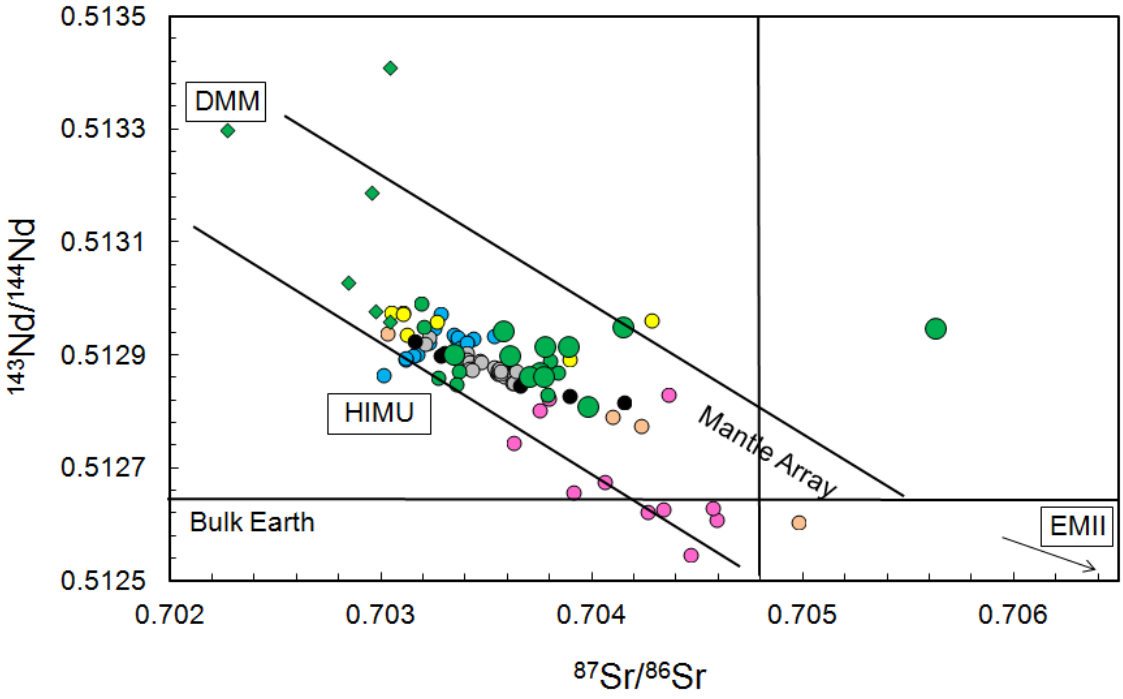

Figure 7.2: $^{143}Nd/^{144}Nd$ vs. $^{87}Sr/^{86}Sr$ composition of the basalts from the Garian volcanic province along with data from South European and North African volcanic provinces. Mantle end-member compositions from Zindler & Hart (1986); DMM = depleted mantle, EMII = enriched mantle type 2 and HIMU = mantle with high U/Pb ratio. Large green circles: Garian basalts of this study. Small green circles: Previous studies of Beccaluva et al., 2008, Lustrino et al., 2012 and the small green diamonds, xenoliths, Beccaluva et al., 2008. Al Haruj basalts (Nixon, 2011, black); Southern Europe: Etna (Viccaro & Cristofolini, 2008; Tonarini et al., 2001, grey); Pantelleria (Esperaqa & Crisci 1995, yellow); Northern Africa: Hoggar (Aït-Hamou et al., 2000, pink); Darfur (Franz et al., 1999, light brown) and Cameroon line (Lee et al., 1994, blue).

However, the new high precision chronology of Cenozoic volcanic provinces of Libya tends to rule out typical hotspot volcanism. There is no simple age progression. Instead the most recent basalt volcanism is in the north (Garian ~2 Ma) and south (Al Haruj 2.3 ka), while the last basalt eruptions in the central part are considerably older (10-20 Ma)

A deep origin for the upwelling mantle is difficult to reconcile with existing $^{3}He/^{4}He$ ratios of the Cenozoic volcanism of North Africa. $^{3}He/^{4}He$ ratios measured in olivine xenoliths from Garian and Hoggar (5.3 - 6.5 R_a) (Beccaluva *et al*. 2008, 2009) and olivine phenocrysts from basalts from Al Haruj (4.4 - 6.2 R_a) (Nixon, 2011) are, in all cases, lower than typical values of mid-ocean ridge basalts (8 ± 1 R_a), and considerably lower than recorded in the nearest mantle plume (Oligocene flood basalts, Ethiopia, ~21 R_a).

The Cenozoic Libyan volcanic fields are located at the intersection of major tectonic lineaments: the N-S or NW-SE structures being Pan-African Paleozoic, and the NE-SW faults Mesozoic (Chapter 2). This holds also for the volcanic provinces of Hoggar and Tibesti (Liégeois *et al*., 2005). Seismic tomography of the North African plate confirms a variable lithospheric thickness in the Saharan area due to local asthenospheric upwelling (Ayadi et al., 2000), but seems to rule out the existence of deep mantle plumes (Davaille et al., 2005; Sebai et al., 2006). The proximity of the Cenozoic volcanism of Libya to extension of the Sirt basin and Sicily Channel implies that melt generation is related to crustal thinning in response to plate reorganisation during and after Alpine collision.

The main structural and tectonic features of NW Africa have been studied by many geologists (e.g. Conant and Goudarzi, 1967; Klitzsch, 1970; 1971; Desio, 1971; El Hinnawy and Cheshitev, 1975; Goudarzi, 1980; Vail, 1991 and Capitanio *et al*., 2011). Klitzsch (1970; 1971) indicated that the basins in NW Africa developed as a result of diagonally-intersecting normal faults (uplifts) throughout the Phanerozoic. These uplifts represent a weak suture zone of Pan-African origin that was later reactivated during the Early Caledonian tectonic phase. Consequently, this appears to be the source of an often repeated idea that the uplift is part of a E-W trending Nafusah uplift (Saadi *et al*., 2008; 2009).

The main tectonic trend of the Garian area formed as a NW–SE trending anticline whose axial trace lies west of Garian. A number of NW-SE major

fault zones (Coastal fault zone, Al Aziziah fault zone and Wadi Ghan fault zone) are parallel to the main fold which is formed as the positions for volcanic intrusion and extrusion. These zones are controlled by two main trends, NW-SE and E-W. The component faults show dip-slip normal motion with the amount of throw varying from a few metres to some hundred metres. The origin of the faults was interpreted to be linked to African–European collision and to reactivation of the Jeffara uplift of Hercynian age (Lipparini, 1940; Desio *et al*., 1963; Christie, 1966, Anketell and Ghellali, 1991).

The most recent study of Abadi *et al*. (2008) for the subsidence of the Hun Graben and Sirt Basin indicated that the E-W to SE-NW faulting was most active in the Lower Cretaceous but continued sporadically in parts of the basin until Upper Cretaceous. During Upper Cretaceous and continuing into the Tertiary several rifting phases are identified with subsidence and normal faulting in a NW-SE orientation. Therefore, it is believed that the main NW trending of Hun Graben system faults and their associated folds correspond with the Jabal Nafusah fault system (Alfandi, 2012).

Capitanio *et al*. (2011) used structural survey and remotely sensed image analysis to describe a tectonic model for the Tripolitania area (Northwest of Libya). They found evidence of Pliocene deformation along a belt stretching from the Jebel-Al Khums region to Jebel As Sawda, southern Hun Graben, where volcanism and reactivation of normal faults suggest a NE-directed extension.

The age of the deformation and its orientation are compatible with the opening of the Sicily Channel rift zone, representing the southernmost culmination of a belt that propagates from the convergent margin for more than 1400 km (Figure 7.3). Seismotectonics and GPS analysis show that this regime is still active, indicative of an important role in the tectonics of the Mediterranean (Capitanio *et al*., 2011).

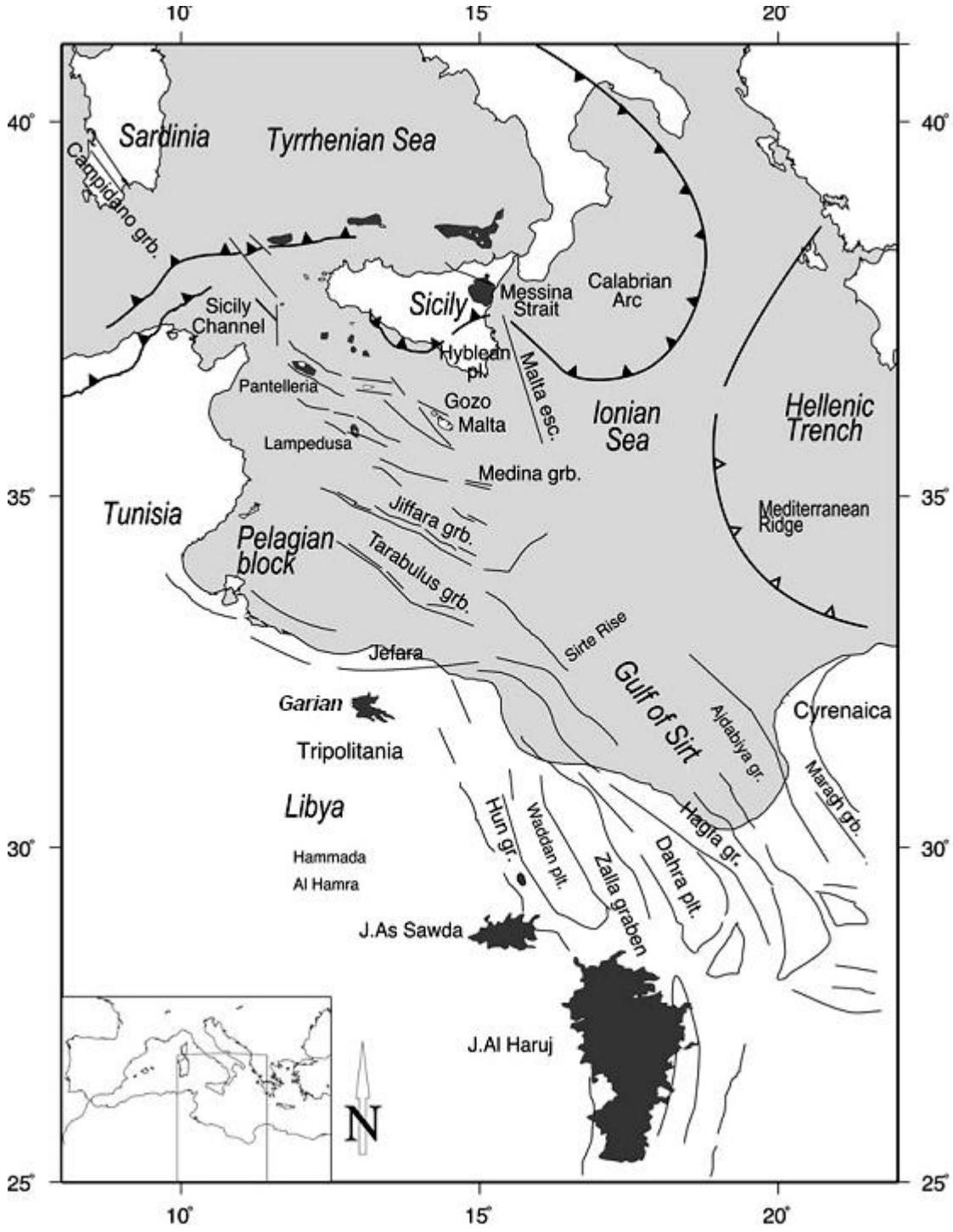

Figure 7.3: Tectonic map of Central Mediterranean Sea and Tripolitania–Sirt Basin, Libya. Dark grey areas show volcanism, thin lines major lineaments, thick lines collisional fronts, black triangles the Maghreb–Appenninic front and hollow triangles the Hellenic trench (after Anketell, 1992).

7.4 Implications

The Libyan, Hoggar and Tibesti volcanic fields are similarly controlled, because they are located at the intersection of major tectonic lineaments: the N-S or NW-SE being Pan-African and Palaeozoic in age and the NE-SW Mesozoic in age (Liégeois *et al*., 2005). All the West African Cenozoic volcanic provinces formed in the same period (related to the new $^{40}Ar/^{39}Ar$ data, from ~30 Ma to the Quaternary), i.e., since the initiation of the Europe-Africa collision. Also, the alignments of volcanic fields do not delineate any spatial age progression. Magmatism occurs repeatedly in a single place, as observed for the whole Phanerozoic.

The compatibility of geophysical and geochemical data, the sources and the timing of overlap of volcanic activity of Libya, Sicily Channel (Etna, Pantelleria and Linosa) and North Africa (Hoggar, Darfur and Tibesti) share a common source and indicate that they could be controlled by the same tectonic setting and cause of volcanism. Reviewing the constraints of geochemical, geophysical data and tectonic framework, I believe that these cannot be explained by the mantle plume.

Beccaluva *et al*. (2007, 2008) concluded that the convection in the upper mantle and lithosphere/asthenosphere interactions mainly along lithospheric discontinuities such as craton/mobile belt borders, as proposed by the edge-driven convection model (King & Anderson, 1995; 1998), could be one of the possibility geodynamic scenarios for the mantle evolution of the Hoggar swell and the Cenozoic volcanic districts of the Saharan belt.

Several studies argued that the plume and small-scale convection system is responsible for the formation of the North Western African volcanic fields. Spatial distribution of the splitting parameters in the study area does not support the small-scale mantle convection hypothesis nor the mantle plume, related to structural control of volcanisms, geochamical and geophysical data as the following:

The depths of melt segregation of the basaltic magma in the Garian volcanic province (this study) is at about 120 km deep and continues to depths of 80 km for alkaline and transitional basalts, respectively. This result is similar to the most primitive mafic magmas in the Hoggar which vary from about 110 km in Tahalra to about 65-40 km in Atakor, with intermediate values of about 75-40 km (Taharaq), 80 km (Tazrouq), and about 100 km (Serouenout). These calculated depths are shallower than the LATEA metacraton (corresponding to the Laouni, Azrou-n-Fad, Tefedest and Egere-Aleksod terrans) lithospheric thickness of 160 km (Azzouni-Sekkal *et al*., 2007). These apparently contradictory results can be reconciled if we consider the possibility that magmatism was triggered by lithospheric delamination along linear shear zones, allowing the ascent and decompression partial melting of the asthenospheric mantle. The extent of asthenospheric ascent was more or less significant according to the magmatic period and the location of the igneous activity.

The relatively low $^{3}He/^{4}He$ of the Garian xenoliths (5.3–6.5 $R_{a,}$ Beccaluva *et al*., 2008) indicates that this component originates within the upper mantle and is unrelated to the deep-seated mantle plume source of the Ethiopian–Yemen plateau basalts (up to 20 R_a).

North Western African maps (Figure 7.4) showing lithospheric structures were generated using the 3D shear wave velocity tomography model which is based on surface wave diffraction data. The data processing techniques are described by Ritzwoller et al. (2002) and Shapiro and Ritzwoller (2002).

Figure 7.4 of the North Western African volcanic fields correlate with lithospheric structure and indicates that three groups could be distinguished: (1) The Maghreb provinces, like the Atlas Mountains, follow the northern boundary of the cratonic lithosphere, especially to the west, where there is evidence for transcurrent movements (Piqué et al., 1998b). If low velocities in the tomographic images correspond to higher temperature, there is a link with a warmer mantle down to a depth of 150 km.

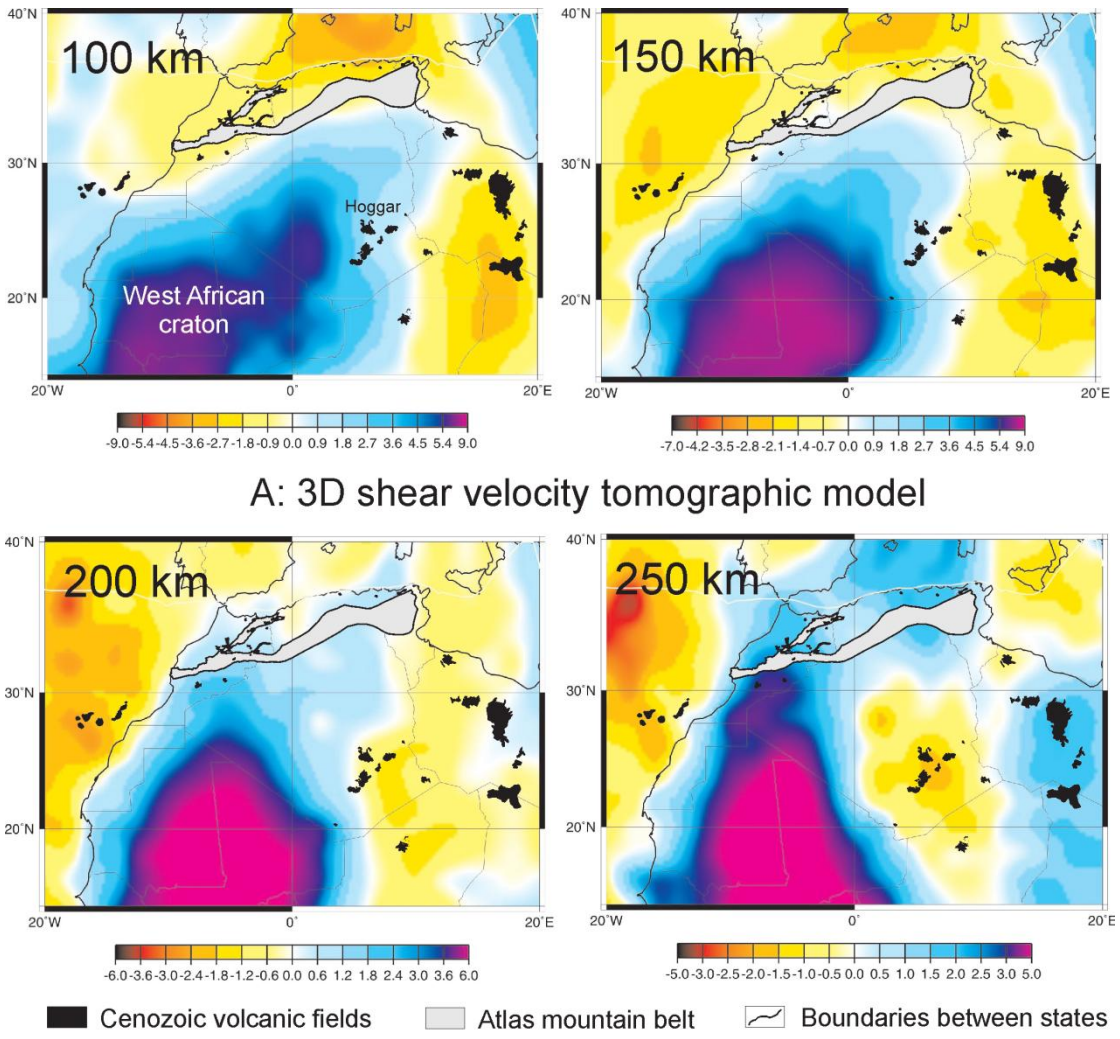

Figure 7.4: North western African maps showing the 3D shear wave velocity tomographic model based on surface wave diffraction tomography map generated from the model of N. Shapiro. Surface wave diffraction tomography and data processing are described in Ritzwoller et al. (2002) and Shapiro and Ritzwoller (2002). Colour scale shows the shear velocity as a percentage of perturbation relative to the reference velocity values, which are 4.483 km/s, 4.473 km/s, 4.494 km/s, and 4.562 km/s for depths of 100 km, 150 km, 200 km, and 250 km, respectively.

(2) The Tibesti and Libyan volcanic fields are also located over a warmer mantle area at shallow depth (100 and 150 km), particularly the Tibesti, whereas at greater depth (250 km) the mantle is colder (as suggested by higher velocities) than the mean. (3) The Hoggar field is located on the eastern shoulder of the West African cratonic mantle, which extends down to 200 km, and a low-velocity seismic mantle exists at a depth of 250 km. The cross-sections and maps of the seismic structure indicate that the entire mantle pass through the Hoggar area. When we look at north western Africa as a whole, it is apparent that there is a correlation between low seismic velocities and Cenozoic volcanic fields down to a depth of 150 km but no deeper. This is in agreement with the melting depth of the source of such magmas, and would imply that deeper mantle velocity variations (e.g., those suggested at 250 km below Hoggar) have no direct influence on the volcanism.

As discussed above, I agree with the suggestion that the surface location of the volcanism is influenced by Paleozoic and Mesozoic brittle faults (e.g., reactivation of the Precambrian Tuareg shield during Alpine convergence and West African Cenozoic volcanism on the Hoggar swell and volcanism, Liégeois et al., 2005). These events produced the first eruption in Garian province during the early Oligocene. This volcanism is now completely eroded away leaving only dykes and intrusions. Later eruption of Garian volcanism and their reactivation was effected by normal faults suggesting a NE-directed extension which is compatible with the opening of the Sicily Channel rift zone during the Pliocene.

7.5 Future work

Questions were raised by this study that should be taken into account within future research if the Cenozoic volcanic history of the region is to be understood. The only volcanic province that has been mapped in detail is Jabal Al Haruj. The new chronology of that province can be used to measure the rate of basalt volcanism (section 6.6.17). It is not sure that the new Ar/Ar

ages presented in Chapter 6 for the other volcanic fields reflects the real duration of basaltic eruptions because there are no detailed maps for volcanic stratigraphy.

While further isotopic analyses of Cenozoic basalts (e.g. Pb, He) will provide better constraints on the source, the volcanic fields of Jabal al Hasawinah and Jabal as Sawda should be highlighted. They are considerably older than Garian and Jabal Al Haruj provinces and measuring the radiogenic (Sr, Nd and Pb) isotope and trace element composition of basalts from these volcanic provinces will identify whether the source of the basaltic magmas has changed with time. This would help in clarifying the relationship between the basaltic volcanism and the tectonic activity (e.g. Capitano et al. 2011). Also it will allow comparison with other regionally important volcanic fields, e.g Hoggar, Algeria, which shows a compositional change with time that is interpreted as a change in the melt regime (Aït-Hamou et al., 2000).

REFERENCES

Abadi, A. M., Van Wees, J. D., Van Dijk, P. M., Cloetingh, S. A. P. L., 2008. Tectonics and subsidence evolution of the Sirt Basin, Libya. AAPG Bulletin, 92, 993-1027.

Abdel-Karim, A., El-Nuri M. R., Mohamed, R. E., 2013. Multiphase Alkaline Basalts of Central Al-Haruj Al-Abyad of Libya: Petrological and Geochemical Aspects. Journal of Geological Research, 1-12.

Abdel-Rahman, A. F. M., 2002. Mesozoic volcanism in the Middle East: geochemical, isotopic and petrogenetic evolution of extension-related alkali basalts from central Lebanon. Geological Magazine, 139, 621-640.

Aboazom, A. S., Asran, A. S. H., Abdel Ghani, M. S., Farahat, E. S., 2006. Geologic and geochemical constraints on the origin of some Tertiary alkaline rift volcanics, the Gharyan area, northwestern Libya. Assiut University Journal of Geology, 35, 1.

Adam, J., Green, T. H., 2006. Trace element partitioning between mica- and amphibole-bearing garnet lherzolite and hydrous basanitic melt: 1. Experimental results and the investigation of controls on partitioning behaviour. Contributions to Mineralogy and Petrology, 152, 1, 1-17.

Adam, J., Green, T. H., 2011. Trace element partitioning between mica- and amphibole-bearing garnet lherzolite and hydrous basanitic melt: 2. Tasmanian Cainozoic basalts and the origins of intraplate basaltic magmas. Contributions to Mineralogy and Petrology, 161, 6, 883-899.

Ade-Hall, J. M., Gerstein, S., Gerstein, R. E., Reynolds, P. H., Dagley, P., Musset, A. E., Hubbard, T. B., 1975. Geophysical studies of North African Cenozoic volcanic areas: Garian, Libya. Canadian Journal of Earth Science, 12, 8, 1264-1271.

Ade-Hall, J. M., Reynolds, P. H., Dagley, P., Musset, A. E., Hubbard, T. P., Klizch, 1974. Geophysical studies of North African Cenozoic volcanic areas: Haruj Asswad, Libya. Canadian Journal of Earth Science, 12, 8, 998-1006.

Ahmad, T., Mukherjee, P. K., Trivedi, J. R., 1999. Geochemistry of Precambrian mafic magmatic rocks of the Western Himalaya, India; petrogenetic and tectonic implications. Chemical Geology, 160, 103-119.

Aït-Hamou, F., Dautria J. M., Cantagrel J. M., Dostal J., Briqueu L., 2000. Nouvelles données géochronologiques et isotopiques sur le volcanisme cénozoïque de l'Ahaggar (Sahara algérien): des arguments en faveur d'un panache. Comptes Rendus de l'Académie des Sciences de Paris, 330, 829-836.

Al Festawi, Y. A., 2001. The structural, palegeographical and hydrocarbon systems analysis of the Ghadamis and Murzuq Basins, West Libya, with emphasis on their relation to the intervening Al Qarqaf Arch. M.Sc thesis, International Institute for Aerospace Survey and Earth Sciences Tripoli, Libya.

Alfandi, E., 2012. Early Mesozoic stratigraphy, sedimentology and structure of the Gharian area, north-western Libya. PhD thesis, Plymouth University.

Allegre, C. J., Treuil, M., Minster, J. F., Minster, J. L., Albarede, F., 1977. Systematic use of trace elements in igneous processes. I. Fractional crystallization processes in volcanic suites. Contributions to Mineralogy and Petrology, 60, 57-65.

Almond, D. C., Busrewil, M. T., Wadsworth, W. J., 1974. The Gharian tertiary volcanic province of Tripoltania, Libya. Geological Journal, 9, 17-28.

Anketell, J. M., 1992. History of the Sirt Basin and its relationship to the Sabratah Basin and Cirenaica Platform. In: Salem, M., Hammuda, O. S. &

Eliagoubi, B. A. (eds) The Geology of Sirte Basin. Elsevier, Amsterdam, 57-88.

Anketell, J. M., Chellali, S. M., 1991. A Palaeogeographic map of the Pre-Tertiary surface in the region of the Jafarrah Plain and its implication to the structural history of northern Libya. In: Salem, M. J., Sbeta, A. M., Bakbak, M. R. (eds.) The Geology of Libya Academic Press, London,VI, 381-2406.

Artini, E., 1914. Sulla diffusion delle rocce a nefeline nella Libia. Rend. R. Accad. Lincei, 23, 25-27.

Asran, A. S. H., Aboazom, A. S., Abdel Ghani, M. S., Farahat, E. S., 2004. CRZ Al- Haruj tertiary basalts, Libya: petrological and geochemical approach. In: Proceeding of the 6th International Conference on the Geology of the Arab world (GAW6).

Avanzinelli, R., Bindi, L., Menchetti, S., Conticelli, S., 2004. Crystallisation and genesis of peralkaline magmas from Pantelleria, Italy: an integrated petrological and crystalchemical study. Lithos, 73, 41-69.

Avanzinelli, R., Braschi, E., Marchionni, S., Bind, L., 2014. Mantle melting in within-plate continental settings: Sr-Nd-Pb and U-series isotope constraints in alkali basalts from the Sicily Channel (Pantelleria and Linosa Islands, Southern Italy). Lithos, 188, 1,113-129.

Avanzinelli, R., Sapienza, G. T., Conticelli, S., 2012. The Cretaceous to paleogene within plate magmatism of Pachno-Capo Passero (southeastern Sicily) and Adria (La Queglia and Pietre Nere, southern Italy): geochemical and isotopic evidence against a plume related origin of circum-Mediterranean magmas. European Journal of Mineralogy, 24, 73-96.

Ayadi, A., Dorbath, C., Lesquer, A., Bezzeghoud, M., 2000. Crustal and upper mantle velocity structure of the Hoggar swell (Central Sahara, Algeria). Physical. Earth Planet. Inter, 118, 111-123.

Azzouni-Sekkal, A., Bonin, B., Benhallou, A., Yahiaoui, R., Paul Liegeois, J., 2007. Cenozoic alkaline volcanism of the Atakor massif, Hoggar, Algeria. Geological Society of America, 418, 321-340.

Baker J. A., Menzies M. A., Thirlwall M. F., Macpherson, C. G., 1997. Petrogenesis of Quaternary intraplate volcanism, Sana'a,Yemen: implications for plume-lithosphere interaction and polybaric melt hybridization. Journal of Petrology, 38, 1359-1390.

Baker, B. H., Goles, G. G., Leeman, W. P., Linstrom, M. M., 1977. Geochemistry and petrogenesis of a basalt-benmoreite-trachyte suite from the southern part of the Gregory Rift, Kenya. Contributions to Mineralogy and Petrology, 64, 303-332.

Barberi, F., Santacroce, R., Varet, J., 1982. Chemical aspects of rift magmatism. In: Palmason, G. (Ed), Continental and Oceanic Rifts, Geodynamic Series, 8. American Geophysical Union, Washington, DC, 223-258.

Barberi, F., Innocenti, F., Ferrara, G., Keller, J., Villari, L., 1974. Evolution of Eolian Arc volcanism (Southern Tyrrhenian Sea). Earth and Planetary Science Letters, 21, 269-276.

Bardintzeff J. M., Deniel, C., Guillou, H., Platevoet, B., Te´louk, P., Oun, K. M., 2012. Miocene to recent alkaline volcanism between Al Haruj and Waw an Namous (southern Libya). International Journal Earth Science, 101, 1047-1063.

Bausch, W. M., 1978. The Central Part of the Jebel Nefusa Volcano (Libya) Survey map, age relationship and preliminary results. Geologische Rundschau, 67, 389-400.

Beattie, P., 1993. Olivine-melt and orthopyroxene-melt equilibria. Contributions to Mineralogy and Petrology, 115, 103-111.

Beccaluva, L., Azzouni-Sekkal, A., Benhallou, A., Bianchini, G., Ellam, R. M., Marzola, M., Siena, F., Stuart F. M., 2007. Intracratonic asthenosphere upwelling and lithosphere rejuvenation beneath the Hoggar swell (Algeria): Evidence from HIMU metasomatised lherzolite mantle xenoliths, Earth Planet. Science. Letter., 260, 482-494.

Beccaluva, L., Bianchini, G., Ellam, R. M., Marzola, M., Oun, K. M., Siena, F., Stuart, F. M., 2008. The role of HIMU metasomatic components in the African lithospheric mantle: petrological evidence from the Gharyan lherzolite xenoliths, NW Libya. In M. Coltorti, M. Grégoire (Eds.) *Mantle metasomatism in intra-plate and suprasubduction settings,* Geological Society, Special Publication, 293, 253-277.

Beccaluva, L., Bianchini, G., Natali, C., Siena, F., 2009. Continental flood basalts and mantle plumes: a case study of the Northern Ethiopian Plateau. Journal of Petrology, 50, 1377-1403.

Beccaluva, L., Bianchini, G., Natali, C., Siena, F., 2011. Geodynamic control on orogenic and anorogenic magmatic phases in Sardinia and Southern Spain: Inferences for the Cenozoic evolution of the western Mediterranean. Lithos, 123, 218-224.

Beccaluva, L., Colantoni, P., Di Girolamo, P., Savelli, C., 1981. Upper-Miocene submarine volcanism in the Strait of Sicily (Banco senza Nome). Bulletin Volcanologique 44, 3, 573-581.

Ben-Avraham, Z., Nur, A., Cello, G., 1987. Active transcurrent fault system along the North African passive margin. Tectonophysics, 141, 249-260.

Bianchini, G., Beccaluva, L., Siena, F., 2008. Post-collisional and intraplate Cenozoic magmatism in the rifted Apennines/Adriatic domain. Lithos, 101, 125-140.

Boccaletti, M., Cello, G., Tortorici, L., 1987. Transtensional tectonics in the Sicily Channel. Journal of Structural Geology, 9, 869-876.

Bohrson, W. A., Reid, M. R., 1997. Genesis of silicic peralkaline volcanic rocks in an oceanic island setting by crustal melting and open-system processes: Socorro Island, Mexico. Journal of Petrology, 38, 1137-1166.

Bordet, P., Freulon, J. M., Lefrance, J. P., 1955. Phonolite à eudialite du Jebel Fazzan. Bulletin de la Société géologique de France. Mineral. Cristallographie, 78, 7-9, 425-431.

Bottinga, Y., Weill, D., 1972. The viscosity of magmatic silicate liquids: a model for calculation. American Journal of Sciences, 272, 438-475.

Bowen, N. L., 1928. The Evolution of the Igneous Rocks. New York: Dover.

Bradshaw, T. K., Smith, E. I., 1994. Polygenetic Quaternary volcanism in Crater Flat, Nevada: Journal of Volcanology and Geothermal Research, 63, 165-182.

Brey, G., Staudigel, H., Spettel, B., 1979. Neogene primare Basalte in Deutschland, Spurenelement-und Isotopengeochemie. Fortschr. Mineral, 57, 172-176.

Browne, S., Fairhead, J., 1983. Gravity study of the Central African Rift System: A model of continental disruption 1. The Ngaoundere and Abu Gabra rifts, Tectonophysics, 94 (1-4), 187-203.

Busrewil, M. T., 1974. The petrology and geochemistry of tertiary volcanic rocks from Ghirian area, Tripolitania, Libya. PhD thesis. Manchester University.

Busrewil, M. T., Esson, J., 1991. Chronology and composition of the igneous rocks of Jabal as Sawda. In: Salem, M. J; Busrewil, M. T.; Ben Ashour, A. M. (Eds.). The Geology of Libya, VII, 2599-2604.

Busrewil, M. T., Oun, K. M., 1991. Geochemistry of the Tertiary alkaline rocks of Jabal al Hasawinah, west central Libya. In: Salem, M. J.; Busrewil, M. T; Ben Ashour, A. M. (Eds.). The Geology of Libya, VII, 2587-2598.

Busrewil, M. T., Suwesi, S. K., 1993. Geologic Map of Libya 1:250000, Sheet: Al Haruj Al Aswad NG (33-4). Explanatory Booklet. Industrial Research Centre, Tripoli, 95 p.

Busrewil, M. T., Wadsworth, W. J., 1980. Preliminary chemical data on the volcanic rocks of Al Haruj area, central Libya. In: Salem, M. J., Busrewil, M. T. (Eds.). The Geology of Libya, 3, 1077-1080.

Capitanio, F. A., Faccenna, C., Funiciello, R., Salvini, F., 2011. Recent tectonics of Tripolitania, Libya: and intraplate record of Mediterranean subduction. Geological Society of London Special Publication, 357, 319-328.

Carpenter, R. L., Edgar, A. D., Thibault, Y., 2002. Origin of sieve-textured in clinopyroxene and spinel from mantle xenoliths, Hessian Depression, Germany. Mineral Petrology. 74, 149-162.

Carroll, M. R. Toplis, M. J., 1995. An experimental study of the influence of oxygen fugacity on Fe-Ti oxide stability, phase relations, and mineral-melt equilibria in ferro-basaltic systems. Journal of Petrology, 36, 1137-1170.

Catalano, S., De Guidi, G., Lanzafame, G., Monaco, C., Tortorici, L., 2009. Late quaternary deformation on the island on Pantelleria: new constraints for the recent tectonic evolution of the Sicily Channel rift (southern Italy). Journal of Geodynamics, 48, 75-82.

Cello, G., 1987. Structure and deformation processes in the Strait of Sicily “rift zone”. Tectonophysics, 141, 237-247.

Cello, G., Crisci, M., Marabini, S., Tortorici, L., 1985. Transtensive tectonics in the Strait of Sicily: structural and volcanological evidence from the Island of Pantelleria. Tectonophysics, 4, 311-322.

Chen, W., Arculus, R. J., 1995. Geochemical and isotopic characteristics of lower crustal xenoliths, San Francisco Volcanic Field, Arizona, USA. Lithos, 36, 203-225.

Christie, A. M., 1966. Geology of the Gharian Area, Tripolitania, Libya. Geological section, Bull. No. 5, Ministry of Industry, Libya/2, 60 p.

Civetta, L., D'Antonio, M., Orsi, G., Tilton, G.R., 1998. The geochemistry of volcanic rocks from Pantelleria island, Sicily channel: petrogenesis and characteristics of the mantle source region. Journal of Petrology, 39, 1453-1491.

Civile, D., Lodolo, E., Accettella, D., Geletti, R., Ben-Avraham, Z., Deponte, M., Facchin, L., Ramella, R., Romeo, R., 2010. The Pantelleria graben (Sicily Channel, Central Mediterranean): An example of intraplate ‘passive’ rift. Tectonophysics, 490, 3-4, 173-183.

Conant, L. E., Goudarzi, G. H., 1967. Stratigraphic and tectonic framework of Libya, Bulletin American Association of Petroleum, Geologist, 51, 719-730.

Corti G, Cuffaro M, Doglioni C, Innocenti F, Manetti P., 2006. Coexisting geodynamic processes in the Sicily Channel. Geological Society of America, special paper, 409, 83-96.

Cvetkovic, M., Toljic, N., Ammar, L., Rundic., Trish, K. B., 2010. “Petrogenesis of the eastern part of theAlHaruj basalts (Libya),”Journal of African Earth Sciences, 58, 1, 37-50.

Dalloni, M., 1931. Une mission scientifique au Tibesti. Comptes Rendus de l'Académie des Sciences, 193, 720-722.

Danyushevsky, L., Plechov, P., 2008. Petrolog3: Integrated software for modelling crystallisation processes, Geochemistry,Geophysics, Geosystems.

Dautria, J. M., Liotard, J. M., Briot, D., 2004. Particularités de la contamination crustale des phonolites : exemple du Velay oriental (Massif central). Comptes Rendus de Geosciences, 336, 971-981.

Davaille, A., Stutzmann, E., Silveira, G., Besse, J., Courtillot, V., 2005. Convective patterns under the Indo-Atlantic « box ». Earth Planet. Science. Letter, 239, 233-252.

Davidson, J. P., Wilson, I. R., 1989. Evolution of an alkali basalt-trachyte suite from Jebel Marra volcano, Sudan, through assimilation and fractional crystallization. Earth and Planetary Science Letters, 95, 141-160.

Deer, W. A., Howie, R. A., Zussman, J., 1966. An Introduction to the Rock Forming Minerals: New York (Longman).

DePaolo, D. J., 1981. Trace element and isotopic effects of combined wallrock assimilation and fractional crystallisation. Earth and Planetary Science Letters, 53, 189-202.

DePaolo, D. J., Daley, E. E., 2000. Neodymium isotopes in basalts of the southwest basin and range and lithospheric thinning during continental extension. Chemical Geology, 169, 157-185.

Desio, A., 1971. Outlines and problems in the geomorphological evolution of Libya from the Tertiary to the present day. In: Gray, C. (ed.) In: Symposium on the Geology of Libya. Tripoli: University of Libya, 11-36.

Desio, A., Ronchetti, C. R., Pozzi, R., Clerici, F., Invernizzi, G., Pisoni, C., Vigano, P. L., 1963. Stratigraphic studies in the Tripolitanian Jabel, Libya. Rivista italiana di paleontologia e stratigraphia, Milano, 9, 1-26.

Dupuy, C., Chikhaoui, M., Dostal, J., 1993. Trace element and isotopic geochemistry of Cenozoic alkali basaltic lavas from the Atakor (Central Sahara). Geochemical Journal, 27, 131-145.

El Hinnawy, M., Cheshitev, G., 1975. Geologic Map of Libya 1:250000, Sheet: Tarabulus (NH 33-13). Explanatory Booklet. Industrial Research Centre, Tripoli.

Ellam, R. M., 1992. Lithospheric thickness as a control on basalt geochemistry. Geology, 20, 153-156.

Embey-Isztin. A., Dobosi. G., 2007. Composition of olivines in the young alkali basalts and their peridotite xenoliths from the Pannonian Basin. Annales Historico-Naturales Musei Nationalis Hungarici, 99, 5-22.

Esperanqa, S., Crisci, G. M., 1995. The island of Pantelleria: a case for the development of DMM–HIMU isotopic compositions in a long-lived extensional setting. Earth and Planetary Science Letters, 136, 167-182.

Farahat, E. S., Abdel Ghani, M. S., Aboazom, A. S., Asran, A. S. H., 2006. Mineral chemistry of Al-Haruj low-volcanicity rift basalts, Libya: implications for Petrogenetic and geotectonic evolution. Journal of African Earth Science, 45, 198-212.

Fishwick, S., 2010. Surface wave tomography: imaging of the lithosphere asthenosphere boundary beneath central and southern Africa. Lithos, 120, 63-73.

Fodor, R. V., Dobosi, G., Sial, A. N., 1995. Zoned clinopyroxenes in alkalic basalt: clues to fractionation and magma-mixing histories for seemingly primitive magmas. Chemie der Erde Geochemistry, 55,133-148.

Fouad, K., 1990. Correlation of Satellite Geoid Features and Hot-Spot Activity with the Tectonic Framework of Libya, in Salen & Busreuil (ED.). The Geology of Libya. VI, 2451-2459, Academic.

Franz, G., Pudlo, D., Urlacher, G., HauBmann, U. Boven, A., Wemmer, K. 1994. The Darfur Dome, western Sudan: the product of a subcontinental mantle plume. Geologische Rundschau, 83, 3, 614-623.

Franz, G., Steiner, G., Volker, F., Pudlo, D., Hammerschmidt, K., 1999. Plume related alkaline magmatism in central Africa - the Meidob Hills (W Sudan). Chemical Geology, 157, 27-47.

Freulon, J. M., Lefrance, J. P., 1954. Structure et stratigraphie du Nord Fazzan, Libya. International Geological Conference, Algiers, 1952, 14, 223-225.

Frey, F. A., Green, D. H., Roy, S. D., 1978. Integrated models of basalt petrogenesis: a study of quartz tholeiites to olivine melilitites from South eastern Australia utilizing geochemical and experimental petrological data: Journal of Petrology, 19, 463-513.

Frizon de Lamotte, D., Saint Bezar, B., Bracène, R., 2000. The two main steps of the Atlas building and geodynamics of the Western Mediterranean. Tectonics, 19, 4, 740-761.

Furman, T., 1995. Melting of metasomatized subcontinental lithosphere: undersaturated mafic lavas from Rungwe, Tanzania. Contributions to Mineralogy and Petrology, 122, 97-115.

Furman, T., Graham, D., 1999. Erosion of lithospheric mantle beneath the East African Rift system: geochemical evidence from the Kivu volcanic province. Lithos, 48, 237-262.

Gast, P. W., 1960. Limitations on the composition of the upper mantle. Journal of geophysical research 65, 1287.

Goudarzi G. H., 1980. Structure-Libya. In: Salem, M. J., Busrewil, M. T (eds) The geology of Libya, III. Academic Press, London, 879-892.

Goudarzi, G. H., 1964. Geologic map of the Kingdom of Libya: U.S. Geological Survey Miscellaneous Investigations Series Map I-350-A, scale 1:2,000,000 (also published in 1977 by Industrial Research Centre, Tripoli, Libya).

Goudarzi, G. H., 1970. Geology and Mineral Resources of Libya-A Reconnaissance. U.S. Geological Survey Professional Paper 660, 104 p., Washington.

Gourgaud A., Vincent, P. M., 2004. Petrology of two continental alkaline intraplate series at Emi Koussi volcano, Tibesti, Chad. Journal of Volcanology and Geothermal Research, 129, 261-290.

Gray, C, 1971. Structure and origin of the Gharian Domes. In: GRAY, C. (ed.) In: Sympoisum on the Geology of Libya. Faculty of Science, University of Libya, 307-319.

Green, D. H., Hibberson, W. O., Kovacs, I., Rosenthal, A., 2010. Water and its influence on the lithosphere-asthenosphere boundary. Nature, 467, 448-452.

Grove, T. L., Kinzler, R. J., Bryan, W. B., 1992. Fractionation of mid-ocean ridge basalt (MORB), in Mantle flow and generation at mid-ocean ridges. American Geophysical Union, 71, 281-310.

Guiraud, R., Maurin, J. C., 1992. Early Cretaceous Rifts of Western and Central Africa: an overview. In: Ziegler, P.A. (Ed.), Tectonophys, 213, 153-168.

Gumati, Y. D., Nairn, E. M. 1991. Tectonic subsidence of the Sirte basin, Libya. Petrolum geology, 14, 93-102.

Hart, S. R., J., Blusztajn, W. E., LeMasurier. Rex, D. C., 1997. Hobbs Coast Cenozoic volcanism: Implications for the West Antarctic rift system, Chemical Geology, 139, 223-248.

Hegazy, A. H., 1999**.** Tertiary volcanics in Libya: evidence for the direction and rate of the African plate motion. In: Proceeding of the 4th International Conference on Geochemistry. Alexandria University, Egypt, 401-419.

Hirose, K., Kushiro, I., 1993. Partial melting of dry peridotites at high pressures: determinations of compositions of melts segregated from peridotite

using aggregates of diamond. Earth and Planetary Science Letters, 114, 477-489.

Horneman, F., 1802. The journal of Frederick Horneman´s travels: from Cairo to Mourzouk, the capital of the kingdom of Fezzan, in Africa, in the years 1797-1788. Nicol, London (Reprint: Darf, London, 188 pages and 3 maps, 1985).

Huppert, H. E., Sparks, R. S. J., 1985. Cooling and contamination of mafic and ultramafic magmas during ascent through the continental crust. Earth and Planetary Science Letters, 74, 371-386.

Illies, J. H. 1981. Graben formation: the Maltese Islands, a case history. Tectonophysics, 73, 151-168.

Ionov, D. A., Hofmann, A. W., 1995. Nb-Ta rich mantle amphiboles and micas: implications for subductionrelated metasomatic trace element fractionations. Earth and Planetary Science Letter, 131, 3-4, 341-356.

Irvine T. N., Bargar W. R. A., 1971. A guide to the chemical classification of the common volcanic rocks. Canadian Journal of Earth Sciences, 8, 523-545.

Jongsma, D., Van Hinte, J. E., Woodside, J. M., 1985. Geologic structure and neotectonics of the North African continental margin south of Sicily. Marine and Petroleum Geology, 2, 156-179.

Jung, S., Masberg, P., 1998. Major and trace element systematics and isotope geochemistry of Cenozoic mafic volcanic rocks from the Vogelsberg (central Germany): Constraints on the origin of continental alkaline and tholeiitic basalts and their mantle sources. Journal of Volcanology and Geothermal Research, 86, 151-177.

Jung, S., Mezger, K., Hauff, F., Pack, A., Hoernes, S., 2013. Petrogenesis of rift-related tephrites, phonolites and trachytes (Central European Volcanic Province, Rhön, FRG): constraints from Sr, Nd, Pb and O isotopes. Chemical Geology, 354, 203-215.

Jurak, L., 1978. Geologic Map of Libya 1:250000, Sheet: Jabal Al Hasawnah (NH 33-14). Explanatory Booklet. Industrial Research Centre, Tripoli, 74-100.

Kabeto, K., Sawada, Y., Wakatsuki, T., 2001. Different evolution trends in alkaline evolved lavas from the northern Kenya Rift. Journal of African Earth Science, 32, 419-433.

Kaszuba, J. P., Wendlandt, R. F., 2000. Effect of carbon dioxide on dehydration melting reactions and melt compositions in the lower crust and the origin of alkaline rocks. Journal of Petrology, 41, 363–386.

Kay, R. W., Gast, P. W., 1973. The rare earth content and origin of alkali rich basalts. The Journal of Geology, 81, 653-682.

Kerr, A. C., 1994. Lithospheric thinning during the evolution of continental large igneous provinces: A case study from the North Atlantic Tertiary province. Geology, 22, 1027-1030.

Kilinc, A., Carmichael, I. S. E., Rivers, M., Sack, R. O., 1983. The Ferric-Ferrous Ratio of Natural Silicate Liquids Equilibrated in Air, Contributions to Mineralogy and Petrology, 83, 136-140.

King, S. D., Anderson, D. L., 1995. An alternative mechanism of flood basalt formation, Earth and Planetary Science Letters, 136 269-279.

King, S. D., Anderson, D. L., 1998. Edge-driven convection: Earth and Planetary Science Letters,160, 289-296.

Klitzsch, E., 1968. Der Basalt vulkanismus des Djebel Haroudj Ost fezzan/ Libyen, Geologische Rundschau, 57, 2, 585-601.

Klitzsch, E., 1968. Outline of the geology of Libya. In: (ed. Barr, F.T.) Pesl 10th Annual Field Conference Guide, Geology and Archaeology of Northern Cyrenica, Libya, 71-78.

Klitzsch, E., 1970. Die struckturgeschichte der zentral-Sahara: Neue Erkenntnisse zum Bau und zur Palaeographie eines Tafellandes. Geol.Rundsch, 59, 2, 459-527.

Klitzsch, E., 1971. The structural developments of parts of North Africa since Cambrian time: 1st Symposium on the geology of Libya, (ed. C. Gray) Faculty of Science, University of Libya, Tripoli, 253-262.

Koppers, A. A. P., Staudigel, H., Wijbrans, J. R., 2000. Dating crystalline groundmass separates of altered Cretaceous seamount basalts by the $^{40}Ar/^{39}Ar$ incremental heating technique. Chemical Geology, 166, 139-158.

Koulakov I., Kaban, M. K., Tesauro, M., Cloetingh, S., 2009a. P and S velocity anomalies in the upper mantle beneath Europe from tomographic inversion of ISC data, Geophysical Journal International, 179, 1, 345-366.

Kushiro, I., 2001. Partial melting experiments on peridotite and origin of mid-ocean ridge basalts. Annual Review of Earth and Planetary Sciences, 29, 71-107.

Lange, R. A., Carmichael, I. S., 1987. Densities of Na_2O-K_2O-CaO-MgO-FeO-Fe_2O_3-Al_2O_3-TiO_2-SiO_2 liquids: New measurements and derived partial molar properties. Geochimica et Cosmochimica Acta, 51, 2931-2946.

Langmuir, C. H., Klein, E. M., Plank, T., 1992. Petrological systematics of mid-ocean ridge basalts: constraints on melt generation beneath ocean ridge. American Geophysical Union Geophysical Monograph Series, 71, 81-180.

Langmuir, C. H., Vocke, R. D., Hansan, G. N., Hart, S. R., 1978. A general mixing equation with applications to Icelandic basalts. Earth and Planetary Science Letters, 37, 380-392.

Lanphere, M. A., Dalrymple, G. B., 1976. Identification of excess ^{40}Ar by the $^{40}Ar/^{39}Ar$ age spectrum technique. Earth and Planetary Science Letters, 32, 2, 141-148.

Le Bas, M. J., Le Maitre, R. W., Streckeisen, A., Zanettin, B., 1986. A chemical classification of volcanic rocks based on the Total Alkali–Silica diagram. Journal of Petrology, 27, 745-750.

le Roex, A. P., Späth, A., Zartman, R. E., 2001. Lithospheric thickness beneath the southern Kenya Rift: implications from basalt geochemistry. Contributions to Mineralogy and Petrology, 142, 89-106.

Lee, D. C, Halliday, A. N., Fitton, J. G., Poli, G., 1994. Isotopic variations with distance and time in the volcanic islands of the Cameroon line: evidence for a mantle plume origin. Earth and Planetary Science Letters, 123, 119-138.

Lee, J. Y., Marti, K., Severinghaus, J. P., Kawamura, K., Yoo, H. S., Lee, J. B., Kim, J. S. 2006. A redetermination of the isotopic abundances of atmospheric Ar. Geochimica et Cosmochimica Acta, 70, 4507-4512.

Legendre, C., Maury, R. C., Savanier, D., Cotten, J., Chauvel, C., Hemond, C., Bollinger, C., Guille, G., Blais, S., Rossi, Ph., 2005. The origin of intermediate and evolved lavas in the Marquesas archipelago : an example from Nuku Hiva island (French Polynesia). Journal of Volcanologycal and Geothermal Research, 143, 293-317.

Liégeois, J. P., Benhallou, A., Azzouni-Sekkal, A., Yahiaouni, R., Bonin, B., 2005, The Hoggar swell and volcanism: Reactivation of the Precambrian Tuareg shield during Alpine convergence and West African Cenozoic volcanism, in Foulger, G. R., Natland, J. H., Presnall, D. C., Anderson, D. L., eds., Plates, plumes, and paradigms: Geological Society of America Special Paper, 388, 379-400.

Lipparini, T., 1940. Tettonica e geomorfologia della Tripolitania. Bollettino della Societa Geologica Italiana. Roma, 59, 222-301.

Lippolt, H. J., Troesch, M., Hess, J. C. 1990. Excess argon and dating of Quaternary Eifel volcanism, IV. Common argon with high and lower-than-atmospheric $^{40}Ar/^{36}Ar$ ratios in phonolitic rocks, East Eifel F.R.G. Earth and Planetary Science Letters, 101, 19-33.

Lodolo, E., Civile, D.. Zanolla, C., Geletti, R., 2012. Magnetic signature of the Sicily Channel volcanism. Marine Geophysical Research, 33, 1, 33-44.

Lucassen, F., Franz, G., Romer, R. L., Bulski, P., 2008. Late Cenozoic xenoliths as a guide to the chemical-isotopic composition and thermal state of the upper mantle under northern Africa. European Journal of Mineralogy, 20, 1079-1096.

Lucassen, F., Pudlo, D., Franz, G., Romer, R. L., Dulski, P., 2012. Cenozoic intra-plate magmatism in the Darfur volcanic province: mantle source, phonolite-trachyte genesis and relation to other volcanic provinces in NE Africa. International Journal of Earth Sciences, 102, 1,183-205.

Lustrino, M., 2011. What ‘anorogenic’ igneous rocks can tell us about the chemical composition of the upper mantle. Case studies from the circum-Mediterranean area. Geological Magazine, 148, 304-316.

Lustrino, M., Carminati, E., 2007. Phantom plumes in Europe and the circum-Mediterranean region. In: G.R. Foulger and D.M. Jurdy (Eds.) The origins of melting anomalies: Plumes, Plates and Planetary Processes. Geological Society of America Special Paper, 430, 723-746.

Lustrino, M., Cucciniello, C., Melluso, L., Tassinari, C. C. G., Gennaro, R., Serracino, M., 2012. Petrogenesis of Cenozoic volcanic rocks in the NW sector of the Gharyan volcanic field, Libya. Lithos, 155, 218-235.

Lustrino, M., Duggen, S., Rosenberg, C. L., 2011. The Central-Western Mediterranean: Anomalous igneous activity in an anomalous collisional tectonic setting. Earth Science Reviews, 104, 1-40.

Lustrino, M., Fedele, L., Melluso, L., Morra, V., Ronga, F., Geldmacher, G., Duggen, S., Agostini, S., Cucciniello, C., Franciosi, L., Meisel, T., 2013. Origin and evolution of Cenozoic magmatism of Sardinia (Italy). Acombined isotopic (Sr-Nd-Pb-O-Hf-Os) and petrological view. Lithos, 180-181, 138-158.

Lustrino, M., Wilson, M., 2007. The circum-Mediterranean an orogenic Cenozoic igneous province. Earth Science Reviews, 81, 1-65.

Lyubetskaya, T., Korenaga, J., 2007. Chemical composition of the Earth primitive mantle and its variance: 1. Method and results. Journal. Geophysics. Research, 112.

Mahood, G. A., Stimac, J. A., 1990. Trace-element partitioning in pantellerites and trachytes. Geochim. Cosmochim Acta, 54, 2257-2276.

Mark, D. F., Stuart, F. M., de Podesta, M., 2011b. New high-precision measurements of the isotopic composition of atmospheric argon. Geochimica et Cosmochimica Acta, 75, 7494-7501.

Martin, H., Smithies, R. H., Rapp, R., Moyen, J. F., Champion, D., 2005. An overview of adakite, tonalite-trondhjemite-granodiorite (TTG) and sanukitoid: relationships and some implications for crustal evolution. Lithos, 79, 1-24.

McDonough, W. F., 1990. Constraints on the composition of the continental lithospheric mantle. Earth and Planetary Science Letters, 101, 1-18.

McDougall, I., Polach H. A., Stipp J. J., 1969. Excess radiogenic argon in young sub-aerial basalts from the Auckland volcanic field, New Zealand. Geochimica et cosmochimica acta, 33, 1485-1520.

Meinhold, G., Morton, A. C., Fanning, C. M., Frei, D., Howard, J. P., Phillips, R. J., Strogen, D., Whitham, A. G., 2011. Evidence from detrital zircons for recycling of Mesoproterozoic and Neoproterozoic crust recorded in Paleozoic and Mesozoic sandstones of southern Libya. Earth and Planetary Science Letters, 312, 1-2, 164-175.

Melluso, L., Morra, V., 2000. Petrogenesis of late Cenozoic mafic alkaline rocks of the Nosy Be archipelago (northern Madagascar): relationships with the Comorean magmatism. Journal of Volcanology and Geothermal Research, 56, 129-142.

Melluso, L., Morra, V., Riziky, H., Veloson, J., Lustrino, M., Del Gatto, L., Modeste, V., 2007. Petrogenesis of a basanite-tephrite-phonolite volcanic suite in the Bobaomby (Cap d'Ambre) peninsula, northern Madagascar. Journal of African Earth Sciences, 49, 29-42.

Miller, V. C., 1971. A Preliminary Investigation of the Geomorphology of the Jebel Nefusa. Symposium. On the Geology of Libya, University. Of Libya, Tripoli, 365-385.

Miller, V. C., Zanetti, A., Thöni, M., Konzett, J., Klötzli, U., 2012. Petrogenesis of Mafic and silica-rich glasses in mantle xenoliths from Wau-en-Namus,

Libya: Textural and geochemical evidence for peridotite-melt reactions. Lithos, 128-131, 11-26.

Mjelde, R., Wessel, P., Dietmar Müller, R., 2010. Global pulsations of intraplate magmatism through the Cenozoic. Lithosphere, 2, 361-376.

Mobil Research Department, Dallas Texas, U.S.A., 1967.

Mollo, S., Scarlato, P., Lanzafame, G., Ferlito, C., 2013. Deciphering lava flow post eruption differentiation processes by means of geochemical and isotopic variations: A case study from Mt. Etna volcano. Lithos, 162-163, 115-127.

Morimoto, N., 1988. Nomenclature of pyroxenes. Fortschritte der Mineralogie, 66, 237-252.

Nakamura, N., 1974. Determination of REE, Ba, Fe, Mg, Na and K in carbonaceous and ordinary chondrites. Geochim Cosmochim Acta 38: 757-775.

Nickel, K. G., 1986. Phase equilibria in the system SiO_2–MgO–Al_2O_3–CaO–Cr_2O_3 (SMACCr) and their bearing on spinel/garnet lherzolite relationships. Neues Jahrbuch für Mineralogie Abhandlungen, 155, 259-287.

Nielsen, R. L., 1985. EQUIL: A program for the modeling of low-pressure differentiation processes in natural mafic magma bodies, Computer. Geosciences, 11, 531-546.

Nixon, S., 2011. Intra-plate magmatism of the Al Haruj Volcanic Field, Libya. Unpublished PhD thesis. Cambridge University.

Panter, K. S., Kyle, P. R., Smellie J. L., 1997. Petrogenesis of a Phonolite-Trachyte succession at Mount Sidley, Marie Byrd Land, Antartica. Journal of Petrology, 38, 1225-1253.

Pearce, J. A., 1980. Geochemical evidence for the genesis and eruption setting of lavas from Tethyan ophiolites. proceedings of the International Ophiolite Symposium, Cyprus, 261-272.

Pearce, J. A., 1982, Trace element characteristics of lavas from destructive plate boundaries, in Thorpe, R.S., ed., Andesites. Wylie and Sons, 525-548.

Pearce, J. A., 1983. Role of sub-continental lithosphere in magma genesis at destructive plate margins. In: Hawkesworth C.J., Norry M.J (Eds.): Continental basalts and mantle xenoliths. Nantwich, Shiva, 230-249.

Pearce, J. A., Norry, M., 1979. Petrogenetic implications of Ti, Zr, Y and Nb variations in volcanic rocks. Contributions to Mineralogy and Petrology, 69, 33-47.

Peccerillo, A., 2005. Plio-Quaternary volcanism in Italy. Petrology, geochemistry, geodynamics. Springer, Berlin Heidelberg New York, 365.

Peregi, Z., Less, G. Y., Konrad, G. Y., 2003. Explanation booklet, Geological map of Libya, 1:250.000. Sheet, AlHaruj Al Abyad NG 33-8, Industrial Research Center, Tripoli, Libya.

Peterman, Z. E., Hedge, C. E., Tourtelot, H. A. 1970. isotopic composition of strontium in seawater throughout Phanerozoic time. Geochimica et Cosmochimica Acta, 34, 104-120.

Piccoli, G., 1960. Osservazioni geologiche sui fenomeni errutivi della Tripolitania Settentrionale. Bollettino della Societa Geologica Italiana. Roma, 8, 79, 165-195.

Piccoli, G., 1970. Outlines of volcanism in northern Tripolitania (Libya). Bollettino della Societa Geologica Italiana, 89, 449-461.

Piccoli, G., 1971. Outlines of volcanism in northern Tripolitania. In symposium of the Geology of Libya (Ed.C.Grag) Faculty of Science, University of Libya, 323.

Piccoli, G., Spadea, P., 1964. Richerche geologiche e petrografic sul vulcanusmodella Tripolitania Settentrionale, Mem. 1st. Geological Mineral. University of Padova, 24, 1-70.

Pilet, S., Ulmer, P., Villiger, S., 2010. Liquid line of descent of a basanitic liquid at 1·5 GPa: constraints on the formation of metasomatic veins. Contributions to Mineralogy and Petrology, 159, 621-643.

Piqué, A., Aït Brahim, L., El Azzouzi, M'H., Maury, R.C., Bellon, H., Semroud, B., and Laville, E., 1998b, The Maghreb indenter: Structural and chemical data: Comptes Rendus de l'Académie des Sciences, Paris, 326, 575-581.

Pizzi, G., Sartori, L., 1984. Groundwater management by means of a quasi-three-dimensional finite element flow model. Challengs in A frican hydrology and water resources (Procceding of the Harare Symposium), 144, 175-191.

Priestley, K., McKenzie, D., 2006. The thermal structure of the lithosphere from shear wave velocities. Earth and Planetary Science Letters, 244, 285-301.

Putirka, K. D., Perfit, M., Ryerson, F. J., Jackson, M. G., 2007. Ambient and excess mantle temperatures, olivine thermometry, and active vs. passive upwelling: Chemical Geology, 241, 177-206.

Renne P. R., Swisher C. C., Deino A. L., Karner D. B., Owens T. L., DePaolo D. J., 1998. Intercalibration of standards, absolute ages and uncertainties in $^{40}Ar/^{39}Ar$ dating. Chemical Geology, 145, 117-152.

Renne, P. R., Balco, G., Ludwig, K. R., Mundil, R., Min, K., 2011. Response to the comment by W. H. Schwarz et al. on ''Joint determination of ^{40}K decay constants and $^{40}Ar/^{40}K$ for the Fish Canyon sanidine standard, and improved accuracy for $^{40}Ar/^{39}Ar$ geochronology by Renne et al., 2010''. Geochimica et Cosmochimica Acta, 75, 5097-5100.

Renne, P. R., Cassata, W. S., Morgan, L. E., 2009. The isotopic composition of atmospheric argon and $^{40}Ar/^{39}Ar$ geochronology: Time for a change? Quaternary Geochronology, 4, 288-298.

Renne, P. R., Mundil, R., Balco, G., Min, K., Ludwig, K. R., 2010. Joint determination of ^{40}K decay constants and $^{40}Ar^*/^{40}K$ for the Fish Canyon sanidine standard and improved accuracy for $^{40}Ar/^{39}Ar$ geochronology: Geochimica et Cosmochimica Acta, 74, 5349-5367.

Reuther, C. D., 1990. Strike-slip generated rifting and recent tectonic stresses on the African foreland (Central Mediterranean Region), Ann. Tectonicae, 4, 120-130.

Reuther, C. D., Eisbacher, G. H., 1985. Pantelleria Rift-crustal extension in a convergent intraplate setting, Geologische Rundschau, 74, 3, 585-597.

Ritzwoller, M. H., Shapiro, N. M., Barmin, M. P., Levshin, A. L., 2002. Global surface wave diffraction tomography. Journal Geophysical Research. 107, 23-35.

Roeder P. L., Emslie R. F., 1970. Olivine liquid equilibrium. Contributions to Mineralogy and Petrology, 29, 275-289.

Rognon, P., Levy, A., Ballais, J .L., Coude-Gaussen, G. et Riser, J., 1983. Essai d'interpretation des coupes du Quaternaire recent de l'O. el Akarit (Sud-Tunisien). Geologie méditerranéenne, 10, 2, 71- 92.

Rollinson, H., 1993. Using geochemical data: Evaluation, presentation, interpretation. Harlow, England: Addison Wesley Longman.

Ronga, F., Lustrino, M., Marzoli, A., Melluso, L., 2010. Petrogenesis of a basalt-comendite-pantellerite rock suite: the Boseti volcanic complex (Main Ethiopian Rift). Mineralogy and Petrology, 98, 227-243.

Rossi, G., Tranne, C. A., Calanchi, N., Lanti, E., 1996. Geology, stratigraphy and volcanological evolution of the island of Linosa (Sicily Channel), Acta Vulcanologica, 8, 73-90.

Rudnick, R., Gao, S., 2003. The composition of the continental crust. In: Rudnick RL (ed) The crust, 3. Oxford, Elsevier, 1-64.

Saadi, N. M., Aboud, E., Saibi, H., Watanabe, K., 2008. Integrating data from remote sensing and gravity for geological investigation in the Tarhunah area, Northwest Libya. International Journal of Digital Earth, 1, 347-366.

Saadi, N. M., Aboud, E., Watanabe, K., 2009. Integration of DEM, ETM+, Geologic, and Magnetic Data for Geological Investigations in the Jifara Plain, Libya. Geoscience and Remote Sensing, IEEE Transactions on, 47, 3389-3398.

Said, F. M., 1974. Sedimentary History of the Paleozoic of the Rocks of the Ghadamis Basin, Libya. Unpublished M.Sc. Thesis, University of South Carolina, 39p.

Sarah E. Rilling., 2009. Geochronological and geochemical assessment of Cenozoic volcanism from the Terror rift region of the west Antarctic rift system. PhD thesis, University of Michigan.

Schult, A., Soffel, H., 1973. Palaeomagnatism of Tertiary basalts from Libya. Geophysical Journal of Astron Society, 323, 373-380.

Sebai, A., Stutzmann, E., Montagner, J. P., Sicilia, D., 2006. Anisotropic structure of the African upper mantle from Rayleigh and Love wave tomography. Physical. Earth Planet. Inter, 155, 48-62.

Shapiro, N. M., Ritzwoller, M. H., 2002. Monte Carlo inversion for a global shear velocity model of the crust and upper mantle, Journal Geophysical Research, 151, 88-105.

Shaw, D. M., 1970. Trace element fractionation during anatexis. Geochimica et Cosmochimica Acta, 34, 237-243.
Simkin, T., Smith, J. V., 1970. Minor-element distribution in olivine. Journal of Geology, 78, 304-325.

Smith, D., Riter, J. C. A., Mertzman, S. A., 1999. Water-rock interactions, orthopyroxene growth, and Si-enrichment in the mantle: Evidence in xenoliths from the Colorado Plateau, southwestern United States: Earth and Planetary Science Letters, 165, 45-51.

Steiger, R. H., Jäger, E., 1977, Subcommission on geochronology: convention on the use of decay constants in geo- and cosmo-chronology: Earth and Planetary Science Letters, 6, 359-362.

Suayah, I. B., Miller, J. S., Miller, B. V., Bayer, T. M., Rogers, J. J. W., 2006. Tectonic significance of late Neoproterozoic granites from the Tibesti massif in southern Libya inferred from Sr and Nd isotopes and U-Pb zircon data. Journal of African Earth Sciences, 44, 561-570.

Sun, S., Hanson, G. N., 1975. Origin of Ross Island basanitoids and limitations upon the heterogeneity of mantle sources for alkali basalts and nephelinites: Contributions to Mineralogy and Petrology, 52, 77-106.

Sun, S., McDonough, W. F., 1989. Chemical and isotopic systematics of oceanic basalts: implications for mantle composition and processes, In: Saunders, A.D., Norry, M.J., Eds.., Magmatism in the Ocean Basins, the Geological Society, Special Publications , 42, Blackwell, London, 313-345.

Swezey C. S., 2009. Cenozoic stratigraphy of the Sahara, Northern Africa. Journal of African Earth Sciences, 53, 89-121.

Takahashi, E and Kushiro, I., 1983. Melting of a dry peridotite at high pressures and basalt magma genesis, American Mineralogist, 68, 859-879.

Tawadros, T., 2001. Geology of Egypt and Libya. , Balkema, Rotterdam, 461p.

Taylor, H. P., 1980. The effects of assimilation of country rocks by magmas on $^{18}O/^{16}O$ and $^{87}Sr/^{86}Sr$ systematics in igneous rocks. Earth Planet. Earth and Planetary Science Letters, 47, 243-254.

Taylor, S. R., McLennan, S. M., 1985. The Continental Crust: its Composition and Evolution, Blackwell, London, 312p.

Thirlwall M. F., Upton B. G. J., Jenkins C. 1994. Interaction between continental lithosphere and the Iceland plume: Sr-Nd-Pb isotope geochemistry of Tertiary basalts, NE Greenland. Journal of Petrology, 35, 839 -879.

Turner, J. S., Campbell, I. H., 1986. Convection and mixing in magma chambers. Earth Science Reviews, 23, 255-352.

Ulmer, P., 1989: The dependence of Fe^{2+}- Mg cation partitioning between olivine and basaltic liquid on pressure, temperature and composition. An

experimental study to 3 kbars. Contributions to Mineralogy and Petrology, 101, 261-273.

Vail, J. R., 1991. The Precambrian tectonic structure of North Africa. In: Salem, M. J., Sbeta, A. M., Bakbak, M. Rda. (eds.). Third symposium on the Geology of Libya, 6, 2259-2268. Tripoli, Libya.

Vesely, J., 1985. Geologic Map of Libya 1:250000, Sheet: Zallah (NH 33-16). Explanatory Booklet. Industrial Research Centre, Tripoli, 125 p.

Viccaro M., Cristofolini R., 2008. Nature of mantle heterogeneity and its role in the short-term geochemical and volcanological evolution of Mt. Etna (Italy). Lithos, 105, 272-288.

Von Wervecke, L., 1880. Mineralogisch - Petrographische Mittelungen. II. Phonolte von Msid Garian. Jb. Min. Geolg. Pal. 2, 275-281.

Watson, E. B., 1982. Basalt contamination by continental crust: some experiments and models. Contributions to Mineralogy and Petrology, 80, 73-87.

Weaver, B. L., 1991. The origin of ocean island basalt end-member compositions: trace element and isotopic constraints. Earth Planet. Scipical Letter. 104, 381-397.

Willbold, M., Stracke, A, 2006. Trace element composition of mantle end-members: Implications for recycling of oceanic and upper and lower continental crust. Geochemistry, Geophysics, Geosystems, 7, 4, 1-30.

Wilson, M., 1989. Igneous Petrogenesis. A global tectonic approach. Oxford, Chapman and Hall.

Wilson, M., Bianchini, G., 1999. Tertiary-Quaternary magmatism within the Mediterranean and surrounding regions: In Durand, B., Jolivet, L., Horvath, F. and Séranne, M. (Eds.) The Mediterranean Basins: Tertiary extension within the Alpine Orogen, Geological Society of London Special Publication, 156, 141-168.

Wilson, M., Downes, H., 2006. Tertiary-Quaternary intra-plate magmatism in Europe and its relationship to mantle dynamics. In: Stephenson, R. A., Gee, D. (eds) European Lithosphere Dynamics. Geological Society, London, Memoirs, 32, 147-166.

Wilson, M., Downes, H., Cebria, J. M., 1995. Contrasting fractionation trends in coexisting continental alkaline magma series; Cantal, Massif Central, France. Journal of Petrology, 36, 1729-1753.

Winnock, E., 1981. Structure du Bloc Pelagien. In: Wezel, F.C. (Ed.), Sedimentary Basin of Mediterranean Margins. Tecnoprint, Bologna, 445-464.

Woller, F., 1978. Geologic Map of Libya 1:250000, Sheet: AL WASHKAH (NH 33-15). Explanatory Booklet. Industrial Research Centre, Tripoli.

Woller, F., Fediuk, F., 1980. Volcanic rocks of Jabal as Sawda. In: Salem, M.J., Busrewil, M.T. (Eds.). The Geology of Libya, 3, 1081-1093.

Zaccagna, D., 1919. Itinerari geologici della Tripolitania occidentale con appendice paleontologica. Mem. Descr. Carta Geol. Ital. Roma, XVIII, 126.

Zindler, A., Hart, S.R., 1986. Chemical geodynamics. Annual Review of Earth and Planetary Sciences, 14, 493-571.

APPENDIX A

Sample location and description

A1 Introduction

The 2010 Garian samples included four LVC basalts, four phonolites and two sample of plateau basalt. Sample selection is based on geological history and an availability of outcrops. Great care was taken to collect the freshest possible samples in the field (Table 3.1 and Figure A1.1 and A1.2).

The civil war in Libya, which started in February 2011, forced us to cancel subsequent field trips that were important to collect more samples from plateau lavas and make some mapping to understand the relationship between the different types of rock and the geological history and their distribution. In June 2011, I was given access to six samples (four plateau lavas, one LVC and one phonolite) from the Manchester University collection (Table 3.1 and Figure A1.3) that were originally sampled by Busrewil (1974).

A2 Plateau Basalts and related rocks

The lava sequence rarely comprises more than four or five individual flows, reaching a maximum total thickness of about 40 m. in the more peripheral parts of the lava field, only one or two flows are present, but they are nevertheless surprisingly persistent and dominate wide areas of plateau country. There is no obvious petrological variation among the plateau lavas, and they are characterized by the absence of ultra-basic xenoliths (Busrewil, 1991). In many places the base of the lavas is not exposed, but elsewhere they are seen to rest unconformably on the sedimentary rocks (Upper Cretaceous age), particularly along the wadis. The existence of a prominent wadi system before the eruption of the plateau lavas is indicated by the long sinuous outcrops extending from the main volcanic region, particularly

towards Beni Walid in the south-east and northwards in the vicinity of the present drainage system of Wadi Ghan (Christie, 1955).

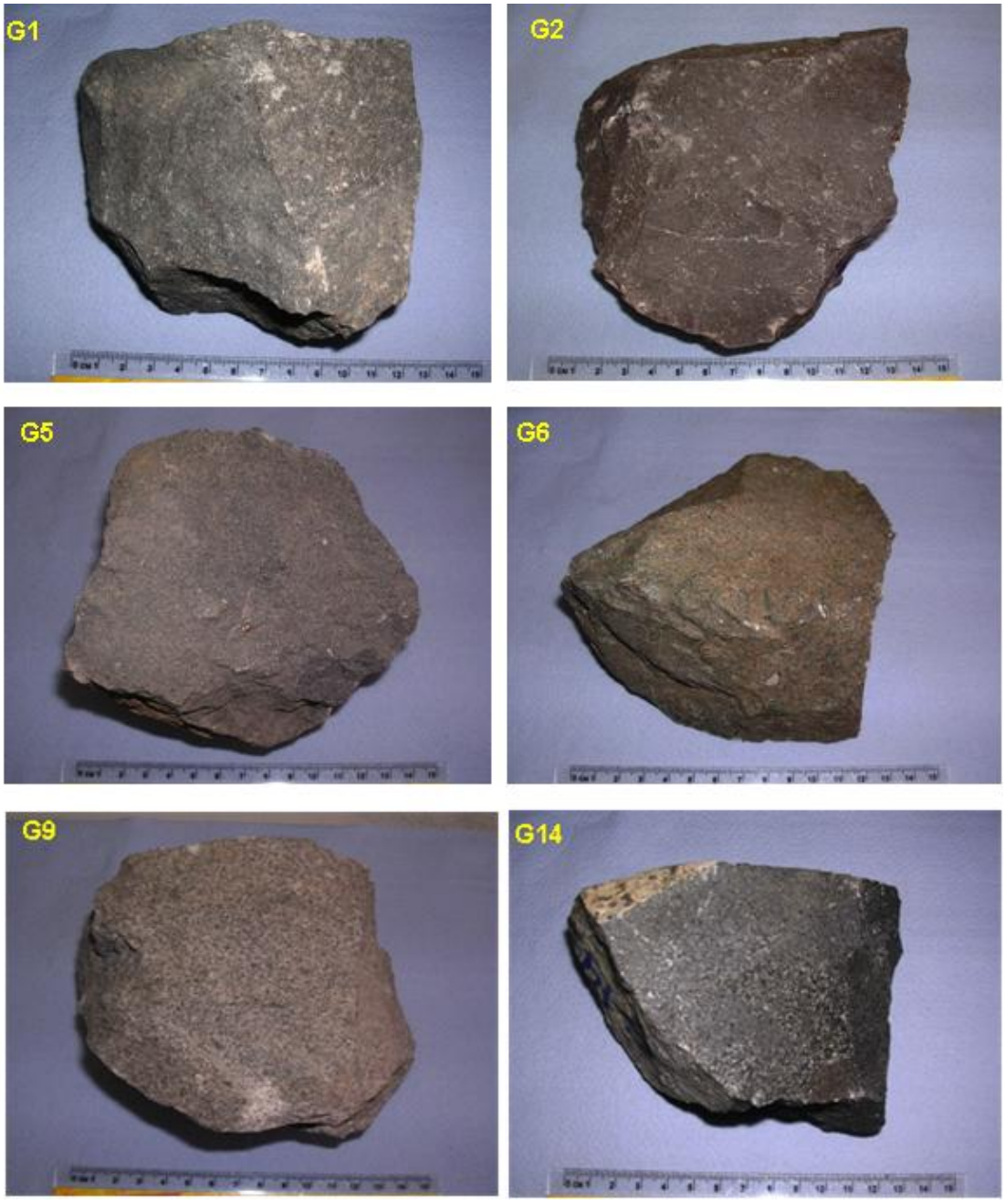

Figure A1.1 Basaltic samples from Garian volcanic province collected during field season of February to March 2010.

Figure A1.2 Phonolitic samples from Garian volcanic province collected during field season of February to March 2010.

Figure A1.3 Samples from the Manchester University collection that were originally sampled by Busrewil (1974).

A2.1 Sample G9 (North Wadi al Waar)

This rock sampled from middle part of flow outcrop occurs in the small Wadi related to Wadi Ghan and about 26 km northeast of Garian Town. This flow occurs of limited in length (~ 6 meters) (Figure A1.4). This rock, in hand specimen, is light gray in color. It is coarse grained (Figure A1.1).

A2.2 Sample G8B

This rock sampled from flow near the east side Wadi Qidmu ~61 km southeast of Garian Town. This rock, in hand specimen, is light gray in color. It is coarse grained (Figure A1.3).

A2.3 Sample G14 (Kabdet El Gamal)

This rock sampled from a dyke-like body intruded into the sedimentary sequences. Formally, it occurs such as camel liver. This rock, in hand specimen, is dark green to gray (Figure A1.3), massive and locally exhibit amygdaloidal structures and doleritic texture. Moreover, it is displays strongly jointed in different direction (Figure A1.5).

A2.4 Sample G15B (Wadi Hashem)

This rock sampled from the lower flow in Wadi Hashem (west side) ~71 km southeast of Garian Town. This rock, in hand specimen, is light gray in color. It is medium to fine grained (Figure A1.3).

A2.5 Sample G32B (South Wadi al Waar)

This rock sampled from the lower part of Wadi al Waar ~26 km northeast of Garian Town. This rock, in hand specimen, is dark gray in color. It is very fine grained (Figure A1.3).

Figure A1.4 Show the outcrop of samples no G9 in occur in small Wadi related to Wadi Ghan

Figure A1.5 Show close view of the Kabdet El Gamal (G14) display the different direction jointed.

A2.6 Sample G116B (Wadi Ghan)

This rock sampled from a top of a flow Wadi Ghan ~12.5 km northeast of Garian Town. This rock, in hand specimen, is very dark gray in color. It is medium to fine grained (Figure A1.3).

A3 Late Basalts and related rocks

More detailed investigation of the most prominent and accessible centres indicate that many of these structures have been considerably modified by erosion, and they often seem to represent intra-volcanic structures (volcanic conduits and related minor intrusions), mantled by rock waste, rather than the original constructional edifice. The lavas were evidently very mobile, and pyroclastic deposits are scarce. Scoria cones are locally present at a few meters, suggesting that they are fairly young. In some areas, only intrusive rocks are found, in the form of dykes, pipes, plugs and small dome-shaped masses that probably did not reach the surface in the liquid state, but have been exposed by erosion.

A3.1 Sample G1

This rock sampled from middle part of intrusive small circular outcrop occurs north of Mizdah and about 33 km south of Garian Town (along Mizdah – Garian road). This intrusive occur as a dyke of limited in length (a few tens of meters) and display the horizontal jointed (Figure A1.6). This rock, in hand specimen, is very dark gray in color, compact and occasionally contains vesicles. It is medium to fine grained (Figure A1.1).

A3.2 Samples G2

This rock sampled from lower part of small cone near Elsalhat Village about 19 km Southeast of Garian Town. This outcrop very limited in length (~ 10

meters) and up to 100 m in diameter (Figure A1.7). This rock is massive, dark black in color and medium to fine grained (Figure A1.1).

A3.3 Samples G5

This rock sampled from middle part of small cone outcropped by the road near Elsalhat Village about 31.5 km East of Garian Town (Figure A1.89). This outcrop limited in length (~ 5 meters) and up to 60 m in diameter. This rock is weakly, dark gray in color and contains vesicles. It is fine to micro grained (Figure A1.1).

A3.4 Samples G6

This rock sampled from lower part of small cone outcropped by the road about 35 km northeast of Garian Town (Figure A1.9). This outcrop limited in length (~ 5 meters) and up to 35 m in diameter. This rock is dark gray in color and occasionally contains jointing. It is medium to fine grained (Figure A1.1).

A3.5 Sample G10B (Ra's al Muhar)

This volcanic centre forms a prominent hill above the general level of the plateau lavas. It piles of basalt fragments overlying more massive basalt outcrops. The main outcrops display vertical columnar jointing, but are not clear whether they represent pounded lava flows or sub-volcanic intrusions. In addition there occurs a sub-vertical sheet (approximately 100 m by 50 m) of coarse-grained, light coloured syenogabbro to the north of the summit. This locally contains blocks of the basaltic material which in invades (Figure A1.1).

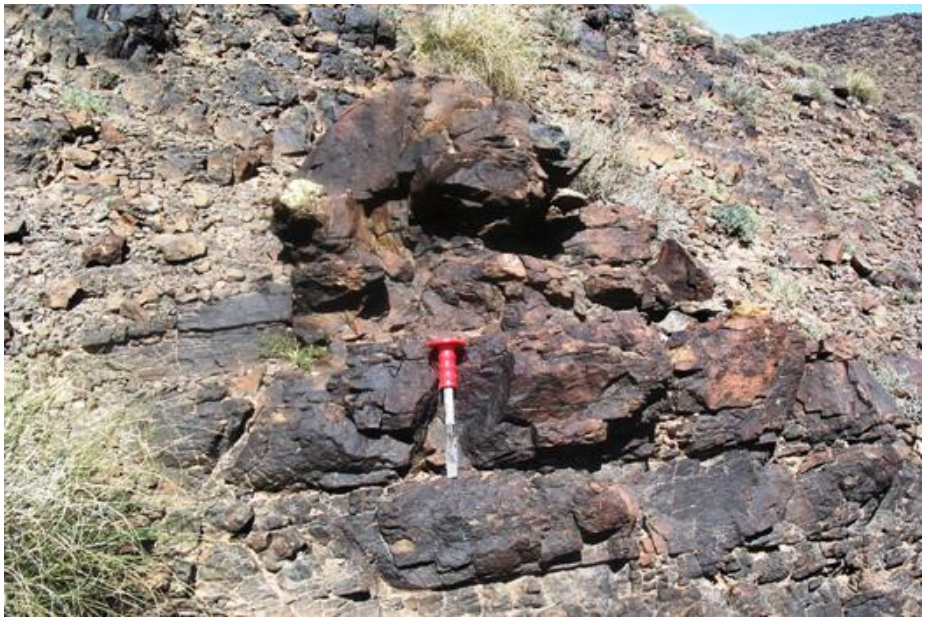

Figure A1.6 Show close view of the Kabdet El Gamal (G14) display the horizontal jointed.

Figure A1.7 Show the outcrop of samples no G2 in occur in small cons near Elsalhat Village about 19 km Southeast of Garian Town**.**

Figure A1.8 Show the outcrop of samples no G5 in occur in small cons near Elsalhat Village about 31.5 km East of Garian Town**.**

Figure A1.9 Show close view of the outcrop of samples no G6 near Elsalhat Village about 35 km East of Garian Town**.**

A4 Phonolites

The phonolites are scattered in an approximately east-west belt along the northern edge of plateau lava field, where they from prominent conical hills. The relative accessibility of these bodies, particularly those exposed near the Town of Garian has meant that they have been studied in more detail than most of the other parts of the area. Piccoli and Spadea (1964) briefly described their field relation to the country rocks, while Gray (1971) has discussed their structural setting. Occurrences of Trachytes, phonolites and alkali trachytes between Mizdah and Garian were reported by Lipparini (1940). Further reconnaissance of this region reveals no traces of such exposures.

The phonolites from dome-shaped intrusions and they display a variety of contact relationships with the associated Mesozoic sediments. In some cases they are clearly intrusive laccoliths, with the overlying sediments strongly arched over the dome shaped intrusion, while the underlying sediments are relatively undisturbed. In other example, the phonolites are strikingly discordant with generally steep contacts against almost horizontal sediments, and with sill-like apophyses locally. The overall impression is of masses of viscous phonolitic magma rising diapirically through the sediments, with varying degrees of success, some appear to solidify at depth in transgressive mode, while others from dome beneath their roof of county rocks. A brief description of the selected phonolites is summarised here.

A4.1 Sample G8 (closed to Suq al Jumah)

This occurs as small plug very limited in length (~ ten meters) (Figure A1.10a and b). It is occurring at 35 km northeast of Garian Town. This consists mainly of phonolitic with a few phenocrysts of sanidine. This rock is massive, dark black in color and coarse to medium grained (Figure A1.2).

A4.2 Sample G10 (Kaf Abu Ghannush)

It is a discordant mass of irregular shape, displaying a variety of contact relationships. The mass itself is cut approximately in the centre by two phonolitic sheets of dykes (> 642 m above sea level). The setting of the mass is best explained as a stock or laccoliths intrude into the Mesozoic sedimentary rocks. The main mass could be differentiated from the outer margin which grades inward into trachyte, phonolitic trachyte porphyritic phonolite and phonolite porphyry. Their structure is complex and has been investigated in some detail by Gray (1971). It is occurring at 2 km northwest of Garian Town. This rock is massive, dark grey in color and coarse to medium grained (Figure A1.2).

A4.3 Sample G11 (Kaf Tekut)

This is apparently the most straightforward phonolitic intrusion, as the country rock is generally domed all around it. The intrusion, now has the appearance of a crater, breached on its east side and it is not entirely regular in shape, as the phonolites bulge out beneath a skin of sediments, when it reaches lower levels on the south and south-west side. Near this bulge occur the patchy outcrops of basaltic breccias (Wadi Qurdu) (Figure A1.11). The outer part of the dome is apparently a thick skin of porphyritic phonolite (about 30 m thick), shows a progressive chilling of the groundmass towards the margin, and exhibits a very prominent columnar jointing perpendicular to the margin. It is occurring at 8 km northwest of Garian Town. It is occurring at 4.5 km northwest of Garian Town. This rock is massive, dark brown in color and coarse to medium grained (Figure A1.2).

Inside this jointed skin is a zone of smooth rounded outcrops of coarser (groundmass) phonolites, but equally porphyritic, and inside this is inferred to be the heavily altered zone responsible for the eroded (crater like) cores of the intrusive. It seem highly likely that the highest and most central part of the original dome-shaped plug would be the most susceptible to hydrothermal modifications, because the late stage fluids would all tend to concentration

here, beneath the viscous impervious skin. Indeed this may have helped the body rise dioptrically through the sediments.

A4.4 Sample G12 (Kaf Abu Rashadah)

It is occur as two circular plugs on the western flank of Abu Rashadah dome (Figure A1.12a and b). Generally, it has a moderate relief, brownish grey to greyish green weathered surface, four to six sided columnar joints, and predominance of flow structure and porphyritic texture. The first plug that close to major road composed mainly of trachyte along the margin that grades inward into phonolitic trachyte It is occurring at 4.5 km northwest of Garian Town. The second plug occurs to the south of the first one and varied from the margin inward into trachyte, phonolitic trachyte and eventually porphyritic phonolite with increasing the contents of sanidine and nepheline as parallel orientation phenocrysts. It is occurring at 2 km northwest of Garian Town. This rock is massive, very dark grey in color and medium grained (Figure A1.2).

A4.5 Sample G81B (Kaf Mantrus)

It is prominent hill with an impression of more resistant marginal facies (given summit peaks at 512 m above sea level) with steep jointing; this is also probably an intrusive dome. It is very difficult to assess the field relationships between the phonolitic mass (Kaf Mantrus) and the country rocks, as the sedimentary rocks are weathered all around, particularly north and north-west of the phonolitic mass where the Jefara lowland emerges. It is occurring at 12 km west of Garian Town. Piccoli (1971) interpreted the morphological setting of Kaf Mantrus as a doming protrusion or plug of highly viscous lavas up to 400 m in diameter (Figure A1.13). This plug consists mainly of trachyte which grades inward into phonolitic trachyte with a few phenocrysts. It is occurring at about 12 km west of Garian Town. This rock is massive, black in color and medium grained (Figure A1.3).

Figure A1.10a Show the outcrop of samples G8 in occur in small plug near Suq al Jumah Village and about 35 km East of Garian Town.

Figure A1.10b Show close view of the sampled outcrop of samples G8.

Figure A1.12a Show the outcrop of Kaf Abu Rashadah in occur in small plug near Suq al Jumah Village and about 35 km East of Garian Town.

Figure A1.12b Show close views of the sampled outcrop of Kaf Abu Rashadah.

Figure A1.13 Show the Kaf Mantrus phonolitic plug intrude the Mesozoic sediments in west of Garian Town.

APPENDIX B

Electron Microprobe Analysis

A element mineral phase compositions were determined using a Cameca SX-100 electron microbe at University of Edinburgh. Analyses were made in wavelength dispersive mode. The six thin sections were polished and carbon coated. Operating conditions were 15 keV and 10 nA for major elements and 15 keV and 100 nA for minor elements. Peak count times were 30 second for major and 20 second for minor elements with background count times being half that of the peak for elements. Standards used for calibration before each session were Si and Ca on Diopside, Fe on hematite, Mg on Periclase, Al on Corundum, Na on Jadeite, K on K-feldspar, Ti on Rutile, Ni on Nimetal, Mn on Mn metal, Cr on Cr metal, Sr on Celest and Ba on Benitoite. The precision can be calculated from counting statistics. Precision estimates for each type of mineral analysis are given in Tables B1 to B6.

Mineral	Olivine	Clinopyroxene	Plagioclase	Spinel
Mg	0.91	0.36	0.01	0.32
Si	0.37	0.45	0.47	0.08
Fe	0.55	0.37	0.03	0.39
Ca	0.01	0.36	0.24	0.01
Ni	0.03	0.03		0.03
Mn	0.03	0.03	0.02	0.03
Cr	0.02	0.04		0.33
Ti	0.01	0.03	0.01	0.11
Al	0.01	0.03	0.35	0.33
Na		0.03	0.13	
K		0.01	0.03	
Sr			0.03	
Ba			0.06	

Table B.1: Precision estimates for Electron Microprobe Analysis.

Table B1.a: Electron microprobe analyses of euhedral olivine from the sample G2.

	SiO_2	MgO	CaO	FeO	Al_2O_3	Na_2O	K_2O	MnO	NiO	Cr_2O_3	TiO_2	P_2O_5	Total
core	39.53	40.89	0.26	18.84	0.03	0.00	0.00	0.26	0.19	0.02	0.01	0.04	100.08
rim	37.97	29.77	0.67	29.58	0.74	0.06	0.02	0.26	0.16	0.02	0.02	0.04	99.31
core	39.37	41.44	0.25	18.16	0.03	0.01	0.00	0.21	0.21	0.02	0.01	0.03	99.74
rim	42.91	22.89	9.92	21.32	1.08	0.17	0.00	0.30	0.05	0.17	0.51	0.02	99.36
core	39.52	41.43	0.25	18.68	0.03	0.01	0.00	0.23	0.20	0.03	0.02	0.04	100.42
rim	36.26	27.91	1.90	32.06	0.69	0.04	0.00	0.32	0.12	0.00	0.02	0.05	99.37
core	39.52	41.45	0.25	18.65	0.03	0.00	0.00	0.24	0.19	0.03	0.01	0.02	100.39
rim	37.43	27.04	1.64	31.49	0.86	0.08	0.07	0.22	0.17	0.02	0.03	0.05	99.10
core	39.06	32.37	0.63	27.59	0.72	0.07	0.01	0.26	0.13	0.02	0.05	0.06	100.97
rim	36.56	27.93	1.62	31.53	0.65	0.05	0.01	0.28	0.11	0.01	0.03	0.04	98.85
core	38.97	40.27	0.25	19.20	0.03	0.02	0.00	0.24	0.19	0.02	0.01	0.03	99.23
rim	36.58	30.02	0.36	32.23	0.01	0.01	0.01	0.40	0.06	0.01	0.04	0.04	99.77
core	38.93	40.74	0.27	18.98	0.03	0.00	0.00	0.23	0.17	0.02	0.01	0.02	99.39
rim	36.25	28.74	0.32	33.63	0.02	0.00	0.01	0.40	0.06	-0.01	0.04	0.05	99.53
core	39.15	41.58	0.24	17.94	0.03	0.01	0.00	0.21	0.21	0.03	0.02	0.03	99.46
rim	35.41	25.19	1.78	35.70	0.84	0.05	0.02	0.21	0.12	0.01	0.08	0.08	99.47
core	38.96	41.17	0.25	18.63	0.03	-0.02	0.01	0.23	0.15	0.02	0.01	0.02	99.47
rim	38.24	41.32	0.28	18.40	0.03	0.01	0.01	0.22	0.20	0.03	0.01	0.04	98.78
core	39.34	40.99	0.26	18.55	0.02	0.00	0.00	0.22	0.16	0.02	0.01	0.01	99.59
rim	35.90	31.62	0.63	30.28	0.39	0.04	0.01	0.32	0.11	0.01	0.04	0.05	99.40

Table B1.b: Electron microprobe analyses of groundmass olivine from the sample G2.

	SiO_2	MgO	CaO	FeO	Al_2O_3	Na_2O	K_2O	MnO	NiO	Cr_2O_3	TiO_2	P_2O_5	Total
core	39.42	40.98	0.27	18.61	0.03	0.02	0.00	0.22	0.23	0.01	0.02	0.06	99.88
rim	38.85	39.17	0.26	21.04	0.03	0.02	0.00	0.41	0.17	0.01	0.02	0.04	100.02
core	39.23	40.78	0.26	18.61	0.06	0.03	0.00	0.26	0.18	0.03	0.03	0.04	99.51
core	39.15	38.66	0.27	20.95	0.03	0.02	0.00	0.21	0.27	0.04	0.02	0.01	99.60
rim	37.58	38.41	0.47	22.83	0.27	0.02	0.01	0.70	0.13	0.00	0.03	0.04	100.49
core	38.28	39.03	0.27	21.00	0.03	0.01	0.00	0.37	0.18	0.03	0.02	0.03	99.24
core	38.52	40.14	0.35	19.48	0.04	0.01	0.00	0.34	0.20	0.04	0.03	0.03	99.18
core	38.50	37.57	0.25	23.06	0.03	0.02	0.00	0.42	0.15	0.02	0.02	0.04	100.10
core	38.45	37.99	0.52	21.12	0.66	0.04	0.02	0.24	0.20	0.02	0.03	0.04	99.34
rim	36.04	33.10	0.69	29.13	0.10	0.08	0.05	0.49	0.08	0.00	0.10	0.05	99.92
core	38.43	36.23	0.30	23.06	0.04	0.00	0.00	0.34	0.13	0.02	0.03	0.03	98.62

Table B1.c: Electron microprobe analyses of resorbed olivine from the sample G2.

	SiO_2	MgO	CaO	FeO	Al_2O_3	Na_2O	K2O	MnO	NiO	Cr_2O_3	TiO_2	P_2O_5	Total
core	40.71	47.21	0.04	11.09	0.01	0.01	0.00	0.17	0.34	0.01	0.01	0.00	99.60
core	37.97	39.88	0.06	20.85	0.01	0.05	0.00	0.34	0.26	0.01	0.01	0.02	99.46
rim	37.42	37.96	0.03	22.41	0.18	0.32	0.01	0.25	0.34	0.01	0.06	0.03	99.02
core	38.53	40.51	0.05	20.25	0.04	0.01	0.01	0.27	0.18	0.03	0.02	0.03	99.93
rim	40.02	44.88	0.37	14.15	0.06	0.02	0.00	0.27	0.24	0.00	0.03	0.03	100.07
core	40.59	46.47	0.07	11.38	0.01	0.01	0.01	0.15	0.32	0.00	0.00	0.02	99.03
core	38.54	39.61	0.08	20.85	0.04	0.04	0.01	0.34	0.17	0.01	0.00	0.02	99.71
rim	39.40	44.50	0.13	15.17	0.04	0.00	0.02	0.25	0.24	0.01	0.04	0.03	99.83

core	40.61	47.52	0.04	10.63	0.02	0.01	0.00	0.18	0.35	0.01	0.00	0.01	99.38
rim	39.97	39.52	0.48	18.62	0.14	0.42	0.04	0.16	0.02	0.00	0.23	0.03	99.63
core	39.88	44.03	0.07	15.45	0.01	0.02	0.00	0.17	0.14	0.00	0.00	0.04	99.81
rim	39.66	37.18	0.29	21.89	0.03	0.01	0.00	0.37	0.16	0.03	0.02	0.03	99.67
core	40.49	47.96	0.06	10.63	0.01	0.03	0.01	0.19	0.32	0.01	0.00	0.03	99.74
rim	37.38	37.88	0.07	22.96	0.19	0.04	0.05	0.22	0.28	0.01	0.05	0.05	99.18
core	42.21	47.27	0.04	10.06	0.00	0.02	0.00	0.18	0.11	0.02	0.00	0.00	99.91
rim	40.99	44.87	0.29	12.92	0.02	0.01	0.00	0.29	0.23	0.03	0.00	0.03	99.68
core	41.41	47.37	0.06	10.61	0.01	0.00	0.00	0.17	0.31	0.01	0.00	0.00	99.95
rim	38.46	36.44	0.05	23.86	0.03	0.03	0.03	0.32	0.36	0.03	0.03	0.04	99.68

Table B1.d: Electron microprobe analyses of clinopyroxene from the sample G2.

	SiO_2	MgO	CaO	FeO	Al_2O_3	Na_2O	K_2O	MnO	NiO	Cr_2O_3	TiO_2	P_2O_5	Total
core	52.01	17.45	17.59	7.14	3.11	0.41	0.01	0.16	0.04	0.67	0.73	0.01	99.31
core	51.57	17.09	17.79	7.19	3.16	0.43	0.00	0.16	0.04	0.72	0.74	0.02	98.9
core	52.98	18.01	17.54	7.07	1.95	0.36	0.01	0.18	0.05	0.44	0.50	0.01	99.1
core	53.35	17.88	17.94	6.82	1.98	0.37	0.00	0.17	0.05	0.45	0.52	0.01	99.53
rim	51.94	15.34	18.90	9.65	1.38	0.28	0.01	0.20	0.01	0.02	0.99	0.01	98.72
core	52.44	16.52	19.84	6.39	2.34	0.35	0.00	0.14	0.05	0.74	0.69	0.01	99.51
core	49.11	7.540	13.81	8.04	11.49	0.14	0.02	0.14	0.02	0.28	0.92	0.02	91.52
rim	52.70	16.10	19.08	8.71	1.39	0.29	0.00	0.18	0.01	0.06	0.89	0.01	99.42
core	53.11	17.80	18.29	6.79	1.94	0.37	0.00	0.15	0.04	0.51	0.52	0.00	99.52
core	49.70	14.200	18.31	8.24	6.63	0.9	0.11	0.09	0.03	0.42	0.50	0.01	99.32
core	51.34	15.40	19.52	7.91	2.66	0.92	0.00	0.16	0.01	0.32	1.22	0.02	99.78
core	52.41	15.76	17.27	11.12	1.22	0.678	0.00	0.25	0.03	0.01	0.92	0.01	99.96

core	50.47	13.51	19.40	11.01	2.26	1.38	0.00	0.21	0.01	0.01	1.66	0.02	99.94
core	52.12	16.16	19.21	7.67	1.87	0.31	0.00	0.18	0.01	0.37	0.85	0.01	98.75
core	51.33	16.39	19.26	6.68	3.35	0.48	0.00	0.14	0.03	0.68	0.80	0.02	99.16
rim	50.48	12.87	19.44	11.89	2.10	0.45	0.01	0.23	0.01	-0.01	1.65	0.03	99.15
core	49.48	14.82	20.14	7.33	4.99	1.31	0.00	0.14	0.03	0.22	1.54	0.02	100
rim	52.17	15.86	19.88	8.86	1.58	0.31	0.00	0.19	0.02	0.06	0.93	0.01	99.86
core	51.19	15.81	21.14	6.53	2.71	0.34	0.01	0.14	0.03	0.68	0.89	0.01	99.48
rim	49.84	14.51	21.55	8.66	1.69	0.31	0.01	0.17	0.02	0.03	0.91	0.02	97.72
core	51.52	16.29	20.31	6.45	3.29	0.44	0.01	0.13	0.04	0.65	0.76	0.00	99.87
rim	51.55	14.59	18.81	11.12	1.40	0.30	0.00	0.24	0.01	0.01	1.09	0.01	99.12

Table B1.f: Electron microprobe analyses of plagioclase from the sample G2.

	SiO_2	MgO	CaO	FeO	Al_2O_3	Na_2O	K_2O	MnO	NiO	Cr_2O_3	TiO_2	P_2O_5	Total
core	53.44	0.19	11.76	0.49	27.50	4.77	0.21	0.00	0.01	0	0.1	0.01	98.47
rim	57.88	0.06	8.14	0.69	24.29	6.79	0.55	-0.01	-0.01	0.01	0.18	0.03	98.6
core	55.61	0.13	10.41	0.53	26.39	5.57	0.30	0.01	-0.01	-0.01	0.13	0.02	99.1
core	53.68	0.15	11.42	0.57	27.27	4.98	0.25	0.00	-0.01	0.00	0.11	0.01	98.42
core	54.58	0.17	11.97	0.50	27.96	4.84	0.22	0.00	0.00	0.00	0.11	0.00	100.5
rim	54.76	0.14	11.48	0.52	28.39	5.03	0.26	-0.01	0.00	0.00	0.11	0.00	100.8
core	54.58	0.15	11.67	0.51	28.05	5.02	0.22	-0.01	0.00	0.00	0.11	0.00	100.4
rim	54.15	0.15	11.72	0.56	28.71	4.75	0.23	-0.02	0.00	0.00	0.11	0.00	100.5
rim	56.97	0.10	9.51	0.73	26.43	6.09	0.40	0.00	0.00	0.00	0.15	0.00	100.5
core	55.00	0.18	11.42	0.50	27.56	5.11	0.24	0.01	0.00	0.00	0.10	0.00	100.2
rim	54.62	0.18	11.2	0.54	27.18	5.04	0.25	0.01	0.00	0.00	0.12	0.00	99.25
rim	57.13	0.09	9.34	0.59	25.97	6.27	0.46	0.01	0.00	0.00	0.15	0.00	100.20

core	54.47	0.17	11.89	0.53	27.92	4.85	0.22	0.00	0.00	0.00	0.10	0.00	100.30
core	54.27	0.15	11.76	0.47	28.06	4.88	0.25	-0.01	0.00	0.00	0.11	0.00	100.10
rim	57.26	0.09	9.33	0.58	25.49	6.23	0.43	-0.01	0.00	0.00	0.16	0.00	99.67
core	54.65	0.16	11.36	0.48	27.18	5.02	0.23	0.00	0.00	0.00	0.11	0.02	99.21
rim	55.29	0.05	10.42	0.57	26.47	5.32	0.35	0.00	0.01	0.02	0.13	0.01	98.63
core	53.85	0.14	11.53	0.45	27.34	4.94	0.23	0.01	0.01	0.00	0.10	0.01	98.60
rim	56.68	0.08	9.20	0.48	25.42	6.17	0.42	0.01	0.00	0.00	0.13	0.01	98.60
core	53.57	0.16	11.81	0.50	27.56	4.78	0.21	-0.01	-0.01	0.00	0.10	0.02	98.70
rim	59.39	0.07	7.00	0.58	23.48	7.14	0.72	0.00	0.01	0.00	0.12	0.03	98.54
core	54.24	0.10	11.52	0.49	27.53	4.88	0.25	0.01	-0.01	0.00	0.10	0.01	99.13
rim	54.11	0.11	11.32	0.64	27.32	4.91	0.28	0.00	0.00	0.00	0.11	0.02	98.83
core	54.22	0.13	11.40	0.44	27.14	5.13	0.23	0.00	0.00	0.00	0.11	0.02	98.83
rim	57.77	0.09	8.352	0.56	24.82	6.60	0.51	0.00	0.00	0.00	0.15	0.02	98.86
core	53.92	0.15	11.74	0.51	27.58	4.75	0.23	0.01	0.00	-0.01	0.10	0.01	99.01
rim	57.55	0.07	8.22	0.70	24.81	6.48	0.58	0.00	0.00	-0.01	0.16	0.03	98.60
core	53.88	0.16	11.80	0.47	27.37	4.85	0.21	0.01	0.00	0.01	0.10	0.01	98.86
core	54.22	0.16	11.43	0.39	27.09	5.01	0.23	0.00	0.00	0.00	0.11	0.01	98.67
rim	55.78	0.11	10.30	0.61	26.10	5.66	0.32	-0.01	0.00	-0.01	0.13	0.02	98.97

Table B2.a: Electron microprobe analyses of euhedral olivine from the sample G5.

	SiO_2	MgO	CaO	FeO	Al_2O_3	Na_2O	K_2O	MnO	NiO	Cr_2O_3	TiO_2	P_2O_5	Total
core	38.70	39.25	0.27	20.63	0.04	0.00	0.00	0.37	0.15	0.02	0.02	0.03	99.48
rim	37.75	28.88	0.34	29.77	1.58	0.26	0.03	0.45	0.01	0.01	0.07	0.04	99.18
core	38.94	39.78	0.26	19.81	0.03	0.03	0.02	0.33	0.21	0.03	0.02	0.04	99.50
rim	37.93	28.94	0.79	28.87	1.77	0.04	0.02	0.76	0.13	0.01	0.03	0.04	99.31

core	38.90	41.22	0.24	17.81	0.04	0.09	0.00	0.28	0.12	0.02	0.02	0.03	98.80
rim	34.60	24.40	6.04	29.61	1.69	0.09	0.02	0.50	0.07	0.00	0.31	2.81	100.14
core	39.41	41.69	0.20	17.22	0.06	0.03	0.00	0.22	0.21	0.01	0.02	0.06	99.13
rim	37.96	35.65	0.46	23.77	0.20	0.02	0.00	0.51	0.12	0.00	0.04	0.04	98.76
core	39.69	43.24	0.24	15.13	0.06	0.02	0.00	0.21	0.17	0.01	0.04	0.04	98.85
rim	37.53	36.03	0.52	24.91	0.11	0.02	0.01	0.48	0.11	0.02	0.03	0.03	99.79
core	40.25	43.61	0.39	14.92	1.09	0.03	0.01	0.16	0.23	0.04	0.02	0.03	100.76
rim	33.45	34.23	0.92	29.09	1.82	0.05	0.02	0.42	0.09	0.02	0.06	0.06	100.24
core	40.37	32.29	1.37	22.20	1.39	0.28	0.02	0.37	0.12	0.06	1.07	0.02	99.56
rim	36.96	30.93	0.91	28.84	0.88	0.11	0.01	0.48	0.08	0.01	0.05	0.02	99.28
core	38.79	39.84	0.07	19.95	0.01	0.05	0.00	0.43	0.28	-0.01	0.01	0.02	99.45
rim	39.02	37.88	0.37	21.75	0.06	0.02	0.00	0.37	0.14	0.00	0.03	0.03	99.66

Table B2.b: Electron microprobe analyses of groundmass olivine from the sample G5.

	SiO_2	MgO	CaO	FeO	Al_2O_3	Na_2O	K_2O	MnO	NiO	Cr_2O_3	TiO_2	P_2O_5	Total
core	39.24	40.93	0.24	18.61	0.03	0.02	0.00	0.32	0.23	0.03	0.02	0.06	99.74
rim	38.42	38.69	0.26	22.04	0.03	0.02	0.00	0.41	0.17	0.01	0.02	0.04	100.12
core	38.57	38.31	0.30	22.06	0.04	0.00	0.00	0.43	0.15	0.02	0.03	0.04	99.96
core	39.11	41.78	0.27	17.61	0.08	0.03	0.00	0.26	0.18	0.03	0.02	0.02	99.40
core	40.40	44.66	0.24	13.95	0.03	0.02	0.00	0.20	0.25	0.03	0.01	0.02	99.79
rim	37.77	36.41	0.57	24.97	0.27	0.02	0.01	0.71	0.13	0.00	0.03	0.04	100.93
core	39.07	42.99	0.32	15.96	0.67	0.03	0.01	0.23	0.24	0.04	0.03	0.04	99.62
rim	36.42	35.58	0.77	24.7	1.56	0.07	0.03	0.56	0.08	0.00	0.09	0.04	99.92
core	38.28	39.03	0.27	21.00	0.03	0.01	0.00	0.37	0.18	0.03	0.02	0.03	99.24
rim	36.05	32.21	0.77	27.27	0.96	0.01	0.02	1.19	0.09	0.02	0.06	0.07	98.70
core	38.50	37.57	0.25	23.06	0.03	0.02	0.00	0.43	0.15	0.02	0.02	0.04	100.10
rim	35.76	29.37	0.92	30.72	1.82	0.06	0.02	0.5	0.06	0.01	0.15	0.11	99.50
core	38.68	38.30	0.24	21.51	0.03	0.02	0.00	0.38	0.18	0.04	0.02	0.02	99.42

core	35.08	34.75	0.89	26.85	1.00	0.04	0.01	0.55	0.13	0.02	0.10	0.02	99.46
core	38.75	39.14	0.27	20.60	0.03	0.01	0.00	0.38	0.20	0.04	0.03	0.04	99.48
rim	32.51	20.24	0.98	32.62	1.06	0.04	0.02	0.61	0.07	0.01	0.06	0.06	88.27

Table B2.c: Electron microprobe analyses of resorbed olivine from the sample G5.

	SiO_2	MgO	CaO	FeO	Al_2O_3	Na_2O	K_2O	MnO	NiO	Cr_2O_3	TiO_2	P_2O_5	Total
core	40.79	46.71	0.06	11.74	0.01	0.03	0.00	0.22	0.33	0.01	0.00	0.04	99.93
rim	39.41	40.04	0.30	19.03	0.32	0.01	0.02	0.35	0.21	0.04	0.02	0.02	99.75
core	40.69	46.17	0.06	11.71	0.01	0.00	0.01	0.18	0.32	0.01	0.00	0.03	99.21
rim	40.64	46.64	0.05	11.84	0.01	0.01	0.00	0.22	0.35	0.01	0.00	0.02	99.79
core	41.01	48.10	0.04	10.19	0.01	0.01	0.00	0.14	0.37	0.01	0.01	0.00	99.90
core	38.93	41.51	0.25	18.25	0.04	0.01	0.01	0.27	0.18	0.03	0.02	0.03	99.53
rim	39.02	37.88	0.37	21.75	0.06	0.02	0.00	0.37	0.14	0.00	0.03	0.03	99.66
core	38.79	39.84	0.07	19.95	0.01	0.05	0.00	0.43	0.28	-0.01	0.01	0.02	99.45
rim	36.92	36.96	0.03	21.01	0.48	0.32	0.01	0.34	0.04	0.01	1.86	1.41	99.39
core	40.49	47.74	0.10	9.80	0.10	0.10	0.01	0.14	0.37	0.00	0.00	0.02	98.87
core	40.40	47.61	0.08	9.85	0.04	0.04	0.01	0.14	0.37	0.01	0.00	0.02	98.56
rim	38.90	43.70	0.43	15.17	0.14	0.00	0.02	0.45	0.14	0.01	0.03	0.03	99.01
core	40.73	47.12	0.04	11.33	0.02	0.01	0.00	0.18	0.35	0.01	0.00	0.01	99.79
core	40.16	44.31	0.05	15.09	0.01	0.03	0.01	0.22	0.26	0.01	0.00	0.01	100.14
rim	37.73	36.49	0.37	23.66	0.05	0.01	0.00	0.47	0.13	0.02	0.03	0.03	99.01
core	39.68	44.33	0.07	14.65	0.01	0.02	0.00	0.27	0.34	0.00	0.00	0.04	99.40
rim	38.66	38.18	0.29	21.68	0.03	0.01	0.00	0.41	0.16	0.03	0.02	0.03	99.49
core	40.99	47.46	0.06	10.23	0.01	0.03	0.01	0.19	0.32	0.01	0.00	0.03	99.34
rim	35.58	32.18	0.07	30.96	0.21	0.04	0.05	0.42	0.08	0.01	0.09	0.07	99.77
core	41.18	48.17	0.04	10.36	0.00	0.02	0.00	0.18	0.38	0.02	0.00	0.00	100.36

rim	40.49	45.87	0.10	12.92	0.02	0.01	0.00	0.19	0.32	0.02	0.00	0.01	99.94
core	40.91	48.07	0.06	10.41	0.01	0.00	0.00	0.17	0.31	0.01	0.00	0.00	99.96
rim	36.76	35.99	1.00	23.06	1.53	0.03	0.03	0.32	0.16	0.03	0.03	0.04	98.99

Table B2.d: Electron microprobe analyses of clinopyroxene from the sample G5.

	SiO_2	MgO	CaO	FeO	Al_2O_3	Na_2O	K_2O	MnO	NiO	Cr_2O_3	TiO_2	P_2O_5	Total
core	50.71	12.12	11.45	4.79	18.02	3.16	0.26	0.10	0.06	0.02	0.12	0.07	100.87
core	47.09	14.72	14.61	2.70	16.56	1.91	0.81	0.06	0.00	0.11	1.12	0.02	99.71
core	51.62	15.98	19.12	5.39	4.63	0.80	0.00	0.09	0.02	0.17	1.16	0.02	99.00
core	45.01	3.39	6.62	7.53	23.71	3.53	1.71	0.05	0.02	0.02	0.44	0.01	92.03
rim	48.90	11.91	15.04	7.57	12.32	1.50	0.00	0.11	0.02	0.18	2.89	0.07	100.49
rim	44.99	6.58	17.67	4.03	14.8	2.41	0.74	0.09	0.00	0.02	1.40	2.21	94.93
core	50.44	14.48	20.11	5.38	4.44	1.32	0.01	0.09	0.03	0.77	1.33	0.01	98.31
core	49.93	13.96	20.41	5.60	5.46	1.42	0.02	0.10	0.02	0.55	1.42	0.03	99.92
core	45.86	11.65	21.89	8.99	7.24	1.67	0.01	0.15	0.02	0.04	2.86	0.05	99.42
core	45.78	4.74	13.75	2.49	16.01	4.29	0.97	0.12	0.03	0.01	1.42	0.03	89.63
rim	44.99	9.58	18.67	4.03	14.8	2.41	0.74	0.09	0.00	0.02	1.40	2.21	98.93
core	48.71	11.88	20.84	8.63	6.35	1.62	0.02	0.17	0.00	0.06	1.35	0.02	99.65
rim	46.42	10.45	14.96	6.82	17.72	1.47	0.13	0.03	0.00	0.01	0.51	1.08	99.60
core	50.58	14.61	21.17	5.22	4.88	0.73	0.02	0.13	0.02	0.91	1.79	0.03	100.10
rim	47.44	11.72	10.01	1.27	26.66	2.16	0.55	0.01	0.01	0.00	0.19	0.05	100.05
core	52.12	12.65	17.75	7.17	6.96	1.20	0.88	0.14	0.03	0.05	0.90	0.01	99.84
rim	46.52	11.78	22.45	7.17	7.39	0.55	0.01	0.11	0.02	0.18	3.14	0.03	99.34
core	45.68	11.49	21.26	7.68	7.35	2.34	0.00	0.15	0.02	0.16	2.85	0.06	99.04
rim	44.00	10.95	22.27	7.50	8.88	0.77	0.01	0.14	0.01	0.2	3.99	0.02	98.73
core	49.83	13.19	22.34	5.94	4.38	1.10	0.00	0.09	0.02	0.53	1.62	0.01	99.05

rim	46.18	11.99	14.62	3.27	19.85	1.25	1.22	0.08	0.01	0.01	0.71	0.60	99.80
core	53.07	12.53	21.19	6.57	3.38	1.94	0.01	0.19	-0.01	0.01	0.38	0.01	99.27
rim	51.81	12.66	22.08	6.55	4.12	1.56	0.01	0.15	0.01	0.38	0.90	0.01	100.26

Table B3.a: Electron microprobe analyses of euhedral olivine from the sample G8B.

	SiO_2	MgO	CaO	FeO	Al_2O_3	Na_2O	K_2O	MnO	NiO	Cr_2O_3	TiO_2	P_2O_5	Total
core	39.57	43.49	0.28	15.36	0.05	0.01	0.00	0.20	0.20	0.02	0.01	0.04	99.23
rim	36.13	23.72	0.97	36.77	0.83	0.04	0.03	0.33	0.08	0.01	0.03	0.03	98.97
core	37.32	33.25	0.36	28.56	0.02	0.02	0.00	0.37	0.11	0.01	0.03	0.04	100.10
rim	37.14	32.02	0.39	29.39	0.02	0.01	0.00	0.41	0.10	0.00	0.03	0.05	99.57
core	36.26	29.82	0.25	32.98	0.01	0.02	0.00	0.41	0.11	0.01	0.03	0.02	99.92
rim	37.81	31.99	0.32	28.52	0.02	0.02	0.00	0.53	0.10	0.01	0.03	0.04	99.39
core	38.15	30.28	0.25	30.36	0.02	0.01	0.00	0.47	0.10	0.01	0.02	0.03	99.70
rim	36.93	22.29	0.91	38.00	0.51	0.04	0.03	0.39	0.07	0.01	0.31	0.05	99.54
core	39.93	41.66	0.29	17.17	0.05	0.01	0.01	0.26	0.16	0.03	0.01	0.04	99.62
rim	37.92	29.12	0.84	30.91	0.56	0.02	0.01	0.23	0.13	0.00	0.03	0.05	99.82
core	53.27	17.64	19.61	7.98	0.91	0.09	0.37	0.00	0.01	0.00	0.10	0.02	100.00
rim	49.17	16.52	17.81	14.68	0.52	0.02	0.01	0.31	0.13	0.02	0.01	0.04	99.24

Table B3.b: Electron microprobe analyses of groundmass olivine from the sample G8B.

	SiO_2	MgO	CaO	FeO	Al_2O_3	Na_2O	K_2O	MnO	NiO	Cr_2O_3	TiO_2	P_2O_5	Total
core	34.74	22.26	0.25	41.88	0.01	0.01	0.00	0.54	0.04	0.00	0.07	0.06	99.86
rim	35.44	19.87	0.28	43.24	0.07	0.01	0.01	0.46	0.04	0.00	0.09	0.04	99.55
core	34.74	22.53	0.26	41.40	0.00	0.00	0.00	0.61	0.04	0.01	0.06	0.07	99.72

rim	35.37	20.87	0.24	42.45	0.01	0.01	0.01	0.62	0.05	0.00	0.05	0.05	99.73
core	52.38	18.38	19.97	7.68	0.91	0.09	0.37	0.00	0.01	0.00	0.10	0.02	99.91
rim	53.60	16.67	17.46	9.87	0.96	0.02	0.38	0.03	0.01	0.01	0.21	0.01	99.23
core	35.13	21.89	0.25	41.54	0.03	0.01	0.00	0.35	0.06	0.00	0.06	0.05	99.37
rim	35.70	19.67	0.31	42.67	0.04	0.04	0.01	0.58	0.05	0.01	0.11	0.10	99.29
core	51.54	13.53	19.52	12.74	1.14	0.37	0.01	0.29	0.01	0.01	0.84	0.02	100.00
rim	51.93	13.36	18.46	13.61	1.10	0.38	0.01	0.29	0.02	0.01	0.85	0.00	100.00
core	35.18	24.63	0.41	38.75	0.01	0.01	0.00	0.56	0.06	0.00	0.03	0.05	99.68
core	37.31	33.03	0.36	28.57	0.02	0.00	0.00	0.40	0.09	0.01	0.02	0.04	99.85
core	39.02	44.61	0.25	14.52	0.03	0.01	0.00	0.18	0.21	0.03	0.01	0.03	98.91
core	36.85	27.05	0.88	27.42	1.08	0.03	0.05	0.29	0.12	0.00	0.03	0.03	93.83

Table B3.c: Electron microprobe analyses of clinopyroxene from the sample G8B.

	SiO_2	MgO	CaO	FeO	Al_2O_3	Na_2O	K_2O	MnO	NiO	Cr_2O_3	TiO_2	P_2O_5	Total
core	51.34	15.40	20.14	6.27	3.57	1.11	0.00	0.12	0.02	0.35	1.03	0.02	99.36
core	51.05	15.05	20.68	6.52	3.72	1.17	0.00	0.13	0.02	0.24	1.30	0.02	99.80
core	51.13	16.18	20.44	6.43	3.01	0.41	0.00	0.12	0.03	0.43	0.78	0.01	98.97
rim	52.10	16.40	21.57	5.69	2.63	0.40	0.00	0.11	0.03	0.29	0.68	0.01	99.90
core	50.79	15.48	20.98	6.52	3.70	1.13	0.00	0.14	0.03	0.26	0.91	0.02	99.80
rim	50.29	13.83	21.74	8.77	2.76	0.48	0.00	0.16	0.02	0.03	1.78	0.01	99.87
core	51.58	15.90	20.40	6.08	3.48	0.46	0.00	0.13	0.04	0.44	0.87	0.02	99.39
rim	49.80	14.22	21.05	6.76	3.79	0.37	0.00	0.13	0.01	0.28	1.47	0.01	97.90
core	52.18	16.02	20.10	7.01	2.08	0.78	0.00	0.16	0.02	0.21	0.94	0.01	99.51
core	50.16	13.94	21.28	8.38	2.40	1.12	0.00	0.16	0.00	0.02	1.54	0.02	99.01
core	50.24	14.13	21.19	8.52	2.03	1.25	0.01	0.18	0.01	0.01	1.44	0.01	99.03
core	52.27	15.32	20.33	7.10	2.09	0.94	0.00	0.16	0.02	0.22	1.00	0.02	99.46

core	52.01	16.11	20.35	7.12	2.10	0.31	0.00	0.15	0.01	0.24	0.97	0.01	99.38

Table B3.d: Electron microprobe analyses of plagioclase from the sample G8B.

	SiO_2	MgO	CaO	FeO	Al_2O_3	Na_2O	K_2O	MnO	NiO	Cr_2O_3	TiO_2	P_2O_5	Total
core	54.41	0.06	11.32	0.52	28.46	5.17	0.32	-0.01	0.00	0.00	0.12	0.00	100.54
rim	65.51	0.00	1.69	0.30	20.32	7.45	6.18	0.00	0.00	0.00	0.14	0.00	101.64
core	53.24	0.10	12.15	0.49	28.45	4.64	0.28	0.01	0.00	0.00	0.10	0.00	99.67
rim	53.91	0.08	11.79	0.56	28.97	4.67	0.26	0.00	0.00	0.00	0.10	0.00	100.51
core	53.57	0.10	11.91	0.48	28.40	4.82	0.31	0.00	0.00	0.00	0.11	0.00	99.85
rim	59.12	0.03	7.18	0.42	25.19	7.20	0.56	-0.01	0.00	0.00	0.11	0.00	100.02
core	54.84	0.08	10.65	0.47	27.65	5.44	0.39	0.00	0.00	0.00	0.13	0.00	99.83
rim	53.37	0.07	12.25	0.52	29.40	4.59	0.29	0.00	0.00	0.00	0.09	0.00	100.77

Table B4.a: Electron microprobe analyses of euhedral olivine from the sample G9.

	SiO_2	MgO	CaO	FeO	Al_2O_3	Na_2O	K_2O	MnO	NiO	Cr_2O_3	TiO_2	P_2O_5	Total
core	35.66	27.10	0.24	36.30	0.02	0.01	0.01	0.47	0.10	0.00	0.02	0.02	99.95
rim	41.08	20.45	0.21	35.56	0.85	0.07	0.26	0.46	0.01	0.00	0.16	0.03	99.14
core	34.25	21.60	0.26	41.85	0.02	0.03	0.01	0.60	0.06	0.00	0.03	0.04	98.74
rim	34.09	21.65	0.27	41.06	0.04	0.00	0.01	0.60	0.05	0.00	0.07	0.03	97.86
core	35.26	25.82	0.26	36.98	0.01	-0.02	0.00	0.51	0.07	0.01	0.03	0.04	99.00
rim	35.41	24.29	0.27	38.52	0.02	0.02	0.00	0.53	0.08	-0.01	0.03	0.04	99.22
core	38.68	38.76	0.23	20.68	0.02	0.01	0.00	0.26	0.18	0.03	0.01	0.02	98.89
rim	33.51	19.71	0.71	35.90	0.45	0.04	0.01	0.26	0.11	0.02	0.03	0.04	90.79
core	36.65	30.28	0.25	31.95	0.02	0.01	0.00	0.37	0.11	0.00	0.02	0.01	99.67

rim	35.53	24.79	0.91	36.77	0.51	0.03	0.02	0.39	0.04	0.01	0.31	0.05	99.36
core	34.36	21.63	0.29	42.13	0.01	0.00	0.00	0.60	0.06	0.00	0.02	0.07	99.16
rim	33.74	20.27	0.24	42.43	0.05	0.02	0.01	0.58	0.04	0.00	0.09	0.22	97.70
core	38.03	38.06	0.29	21.17	0.03	0.00	0.01	0.26	0.16	0.03	0.01	0.01	98.05
rim	33.62	20.12	0.84	35.41	0.56	0.02	0.01	0.23	0.13	0.00	0.03	0.05	91.03
rim	36.74	26.35	0.46	32.49	0.14	0.01	0.00	0.37	0.09	0.01	0.04	0.02	96.70
core	45.57	20.04	0.61	30.98	0.91	0.39	0.37	0.00	0.01	0.00	0.10	0.02	99.00
rim	34.17	21.52	0.81	32.68	0.52	0.02	0.01	0.31	0.13	0.02	0.01	0.04	90.25
rim	36.23	28.68	0.27	33.20	0.03	0.00	0.00	0.41	0.11	0.03	0.02	0.01	99.00

Table B3.b: Electron microprobe analyses of groundmass olivine from the sample G9.

	SiO_2	MgO	CaO	FeO	Al_2O_3	Na_2O	K_2O	MnO	NiO	Cr_2O_3	TiO_2	P_2O_5	Total
core	34.67	21.99	0.27	42.07	0.01	0.00	0.00	0.59	0.05	0.01	0.04	0.03	99.73
rim	32.29	17.35	0.32	44.90	0.18	0.04	0.04	0.58	0.02	0.00	0.23	0.07	96.03
core	34.21	20.46	0.25	43.88	0.01	0.01	0.00	0.64	0.04	0.00	0.07	0.06	99.63
rim	34.44	19.40	0.28	42.17	0.07	-0.01	0.01	0.56	0.04	0.00	0.09	0.04	97.10
core	37.14	31.42	0.26	29.62	0.02	0.02	0.01	0.37	0.13	0.01	0.02	0.04	99.05
core	35.89	26.97	0.41	35.21	0.12	-0.02	0.00	0.46	0.08	0.01	0.05	0.03	99.21
core	34.74	20.83	0.26	42.40	0.00	0.00	0.00	0.61	0.04	-0.01	0.04	0.07	98.99
rim	34.37	20.80	0.24	42.75	0.01	-0.01	0.01	0.62	0.05	0.00	0.05	0.05	98.95
core	34.54	21.73	0.28	41.60	0.02	0.03	0.00	0.61	0.05	0.00	0.05	0.07	98.98
rim	32.30	20.81	0.26	44.87	0.18	0.05	0.08	0.56	0.04	0.00	0.27	0.08	99.50
core	41.58	25.38	0.47	31.98	0.17	0.03	0.00	0.28	0.02	0.04	0.01	0.03	99.99
rim	43.60	22.67	0.46	32.87	0.28	0.02	0.08	0.03	0.01	0.01	0.02	0.01	100.06
core	35.12	23.75	0.26	39.57	0.01	0.01	0.01	0.51	0.07	0.01	0.04	0.06	99.42
rim	34.62	23.42	0.25	39.87	0.01	0.01	0.00	0.51	0.06	0.00	0.05	0.05	98.85

core	34.03	21.39	0.25	41.74	0.03	0.01	0.00	0.55	0.06	0.00	0.06	0.05	98.18
rim	34.70	19.37	0.31	44.07	0.14	0.04	0.01	0.58	0.05	0.01	0.11	0.1	99.49
core	45.41	24.57	0.85	27.76	0.28	0.03	0.00	0.60	0.03	0.34	0.07	0.02	99.96
rim	46.77	22.22	0.67	28.23	0.29	0.02	0.00	0.59	0.01	0.34	0.08	0.01	99.23
core	46.54	22.53	0.12	30.24	0.28	0.01	0.01	0.69	0.01	0.01	0.08	0.02	100.54
rim	46.33	22.36	0.16	30.31	0.28	0.01	0.01	0.59	0.02	0.01	0.05	0.00	100.13
core	46.49	22.35	0.41	29.36	0.27	0.01	0.00	0.51	0.02	0.04	0.07	0.02	99.55
rim	46.90	22.15	0.34	29.40	0.27	0.04	0.00	0.53	0.02	0.04	0.07	0.02	99.78

Table B4.c: Electron microprobe analyses of resorbed olivine from the sample G9.

	SiO_2	MgO	CaO	FeO	Al_2O_3	Na_2O	K_2O	MnO	NiO	Cr_2O_3	TiO_2	P_2O_5	Total
core	40.92	44.76	0.25	12.95	0.04	0.02	0.00	0.17	0.27	0.07	0.02	0.04	99.51
rim	39.87	44.21	0.29	14.87	0.04	0.02	0.00	0.19	0.22	0.03	0.02	0.04	99.80
core	39.82	45.86	0.19	13.01	0.05	0.03	0.00	0.18	0.22	0.03	0.02	0.06	99.47
rim	39.98	44.44	0.21	14.76	0.04	0.02	0.00	0.22	0.16	0.02	0.05	0.03	99.93
core	40.35	45.87	0.26	12.53	0.04	0.02	0.00	0.20	0.24	0.07	0.02	0.02	99.62
core	40.63	45.78	0.25	12.67	0.04	0.01	0.00	0.17	0.25	0.05	0.03	0.02	99.90
core	40.87	46.00	0.19	12.26	0.03	0.01	0.00	0.16	0.35	0.01	0.01	0.02	99.91
core	41.41	46.45	0.07	11.21	0.03	0.02	0.01	0.14	0.38	0.01	0.01	0.03	99.77

Table B4.d: Electron microprobe analyses of clinopyroxene from the sample G9.

	SiO_2	MgO	CaO	FeO	Al_2O_3	Na_2O	K_2O	MnO	NiO	Cr_2O_3	TiO_2	P_2O_5	Total
core	52.02	15.03	19.07	10.10	1.50	0.89	0.01	0.2	0.00	0.08	0.95	0.01	99.87
rim	52.10	11.08	16.80	14.70	2.02	0.78	0.24	0.27	0.01	0.01	1.12	0.02	99.14
core	51.87	16.11	19.82	6.99	2.71	0.38	0.00	0.16	0.04	0.78	0.62	0.01	99.49
rim	51.4	15.95	20.23	8.48	2.00	0.36	0.01	0.19	0.03	0.24	0.94	0.02	99.83

core	51.77	15.97	19.62	7.52	2.67	0.34	0.00	0.16	0.03	0.39	0.87	0.02	99.35
rim	51.00	14.87	18.85	9.83	2.42	0.34	0.02	0.19	0.01	0.38	0.71	0.02	98.65
core	51.65	15.03	20.38	7.92	2.05	0.33	0.01	0.17	0.03	0.56	0.89	0.01	99.04
rim	50.52	15.12	20.14	9.16	1.95	0.35	0.00	0.17	0.01	0.47	0.87	0.01	98.77
core	51.90	15.28	19.89	7.88	2.51	0.34	0.00	0.16	0.02	0.51	0.77	0.01	99.27
rim	50.20	13.92	19.51	11.72	1.73	0.45	0.00	0.26	0.03	0.32	1.02	0.02	99.17
core	51.54	15.20	20.67	7.68	2.08	0.36	0.00	0.16	0.03	0.58	0.89	0.01	99.19
rim	51.26	16.05	20.66	6.15	2.93	0.43	0.01	0.12	0.03	0.99	0.65	0.01	99.30
core	51.76	16.02	20.38	6.10	2.87	0.38	0.00	0.14	0.03	0.98	0.64	0.01	99.31
rim	49.92	15.61	20.05	9.44	1.90	0.47	0.01	0.18	0.03	0.71	0.88	0.02	99.22

Table B4.f: Electron microprobe analyses of plagioclase from the sample G9.

	SiO_2	MgO	CaO	FeO	Al_2O_3	Na_2O	K_2O	MnO	NiO	Cr_2O_3	TiO_2	P_2O_5	Total
core	53.13	0.12	11.99	0.87	28.07	4.93	0.26	0.00	0.00	-0.01	0.09	0.00	99.44
rim	59.80	0.04	6.24	0.61	25.27	7.83	1.00	-0.01	0.01	0.00	0.08	0.00	100.86
core	54.43	0.13	11.51	0.59	26.99	5.17	0.31	0.01	0.00	-0.01	0.11	0.01	99.25
rim	54.98	0.05	10.45	0.59	26.67	5.87	0.34	-0.01	0.00	0.01	0.11	0.01	99.06
core	54.48	0.14	10.96	0.58	27.58	5.16	0.33	-0.01	0.00	0.00	0.10	0.02	99.35
rim	57.49	0.05	8.91	0.57	24.81	6.62	0.48	-0.01	-0.01	0.00	0.12	0.02	99.05
core	55.15	0.08	10.90	0.55	27.20	5.22	0.29	0.01	0.01	0.00	0.10	0.01	99.53
rim	56.31	0.14	10.39	0.71	26.81	5.84	0.34	0.00	0.00	-0.01	0.12	0.01	100.66
core	54.46	0.09	11.21	0.60	27.73	4.96	0.30	0.00	-0.01	0.01	0.09	0.01	99.43
rim	54.76	0.07	11.20	0.63	27.40	4.94	0.29	0.01	0.00	0.01	0.10	0.02	99.43
core	54.51	0.08	11.72	0.64	28.30	4.87	0.28	0.01	0.00	0.00	0.09	0.00	100.64
rim	61.50	0.04	5.83	0.61	23.27	7.83	1.00	-0.01	0.00	0.00	0.12	0.00	100.33
core	58.98	0.07	8.13	0.58	25.36	6.69	0.54	0.00	0.00	0.00	0.13	0.00	100.60

rim	75.54	0.04	0.13	0.53	13.20	5.72	4.31	0.00	0.00	0.00	0.28	0.00	99.77
core	54.94	0.11	11.34	0.62	27.80	5.08	0.27	0.00	0.00	0.00	0.10	0.00	100.39
rim	67.28	0.01	1.06	0.77	19.22	8.48	3.76	-0.01	0.00	0.00	0.10	0.00	100.75
core	55.58	0.14	10.44	0.62	26.70	5.73	0.30	0.00	0.00	0.00	0.09	0.00	99.60
rim	67.06	0.13	2.83	0.66	19.12	8.15	2.46	0.01	0.00	0.00	0.04	0.00	100.48
core	54.72	0.08	10.89	0.66	26.87	5.60	0.31	0.00	0.00	0.00	0.09	0.00	99.22
rim	67.10	0.01	0.66	0.44	19.18	7.70	5.33	0.02	0.00	0.00	0.05	0.00	100.51
core	55.30	0.10	10.29	0.60	27.13	5.48	0.27	0.00	0.00	0.00	0.09	0.00	99.27
rim	55.53	0.09	10.63	0.83	27.75	5.61	0.31	0.00	0.00	0.00	0.12	0.00	100.99
core	55.08	0.04	10.79	0.67	27.86	5.24	0.31	-0.01	0.00	0.00	0.1	0.00	100.21
rim	55.24	0.04	9.72	0.65	26.65	6.36	0.44	0.01	0.00	0.00	0.12	0.00	99.33
core	55.03	0.04	11.16	0.81	28.18	5.14	0.31	-0.01	0.00	0.00	0.11	0.00	100.92
rim	53.44	0.11	15.08	1.17	26.06	2.97	0.09	0.17	0.00	0.00	1.01	0.00	100.08
core	55.71	0.06	14.09	0.65	25.01	4.37	0.29	0.00	0.00	0.00	0.1	0.00	100.29
rim	54.52	0.06	11.08	0.90	27.66	5.25	0.30	0.01	0.00	0.00	0.11	0.00	100.01
core	54.72	0.09	11.34	0.65	27.84	5.25	0.30	-0.01	0.00	0.00	0.11	0.00	100.41
rim	54.57	0.05	10.99	0.67	28.09	5.15	0.33	0.01	0.00	0.00	0.11	0.00	100.09

Table B5.a: Electron microprobe analyses of euhedral olivine from the sample G10B.

	SiO_2	MgO	CaO	FeO	Al_2O_3	Na_2O	K_2O	MnO	NiO	Cr_2O_3	TiO_2	P_2O_5	Total
core	36.83	37.72	0.33	23.80	0.05	0.02	0.00	0.52	0.12	0.01	0.05	0.02	99.47
rim	37.48	36.30	0.38	24.40	0.07	0.02	0.01	0.55	0.12	0.00	0.05	0.04	99.42
core	37.15	36.37	0.26	24.83	0.05	0.02	0.02	0.54	0.11	0.00	0.03	0.03	99.41
core	37.43	37.33	0.24	23.54	0.04	0.01	0.02	0.51	0.12	0.01	0.06	0.03	99.34
core	38.37	38.35	0.25	22.13	0.03	0.02	0.00	0.53	0.09	0.01	0.05	0.04	99.87
core	38.34	38.46	0.24	22.25	0.02	0.02	0.01	0.51	0.08	0.01	0.06	0.04	100.04

rim	38.14	38.54	0.21	22.13	0.03	0.03	0.02	0.52	0.09	0.02	0.04	0.05	99.82
core	40.16	40.09	0.18	18.02	0.02	0.00	0.00	0.16	0.30	0.00	0.04	0.03	99.00
rim	40.14	42.76	0.18	16.20	0.02	0.01	0.00	0.14	0.25	0.00	0.05	0.01	99.76
core	39.25	46.23	0.11	13.53	0.27	0.03	0.01	0.14	0.25	0.00	0.08	0.04	99.94
rim	39.45	38.23	0.11	20.30	0.27	0.02	0.03	0.24	0.15	0.00	0.40	0.03	99.23
rim	38.35	38.23	0.22	21.73	0.22	0.01	0.00	0.20	0.13	0.02	0.45	0.03	99.59

Table B5.b: Electron microprobe analyses of resorbed olivine from the sample G10B.

	SiO_2	MgO	CaO	FeO	Al_2O_3	Na_2O	K_2O	MnO	NiO	Cr_2O_3	TiO_2	P_2O_5	Total
core	43.64	46.63	0.06	9.55	0.03	0.01	0.01	0.14	0.33	0.00	0.00	0.00	100.40
rim	41.64	49.13	0.06	8.35	0.06	0.00	0.01	0.12	0.26	0.00	0.01	0.00	99.64
core	39.13	44.24	0.09	15.34	0.04	0.00	0.01	0.23	0.35	0.01	0.03	0.00	99.47
core	40.38	50.04	0.04	8.33	0.01	0.01	0.01	0.35	0.31	0.01	0.07	0.01	99.57
rim	39.87	50.05	0.06	9.42	0.05	0.00	0.01	0.11	0.40	0.01	0.01	0.00	99.99

Table B5.c: Electron microprobe analyses of clinopyroxene from the sample G10B.

	SiO_2	MgO	CaO	FeO	Al_2O_3	Na_2O	K_2O	MnO	NiO	Cr_2O_3	TiO_2	P_2O_5	Total
core	41.38	10.36	22.04	8.78	9.36	2.16	0.00	0.11	0.02	0.00	5.14	0.03	99.36
rim	44.88	11.68	22.05	7.97	7.78	0.72	0.00	0.13	0.00	0.00	3.88	0.04	99.13
core	45.55	11.81	22.73	7.38	6.50	1.90	0.00	0.15	0.00	0.00	3.25	0.02	99.29
rim	48.98	11.70	22.29	8.06	4.75	0.95	0.01	0.21	0.02	-0.01	2.28	0.03	99.25
core	42.26	11.72	22.12	8.03	9.56	2.00	0.00	0.12	0.01	0.00	4.18	0.04	100.05
rim	45.80	11.50	22.68	7.59	6.96	0.69	0.00	0.11	0.03	0.01	3.50	0.03	98.89
core	44.93	11.59	22.72	7.36	7.18	1.86	0.00	0.14	0.01	0.00	3.69	0.03	99.52
rim	48.73	12.76	22.91	7.11	4.24	0.63	0.00	0.16	0.01	0.00	2.22	0.02	98.78
core	43.40	11.02	22.38	8.25	8.32	2.00	0.00	0.12	0.03	0.01	4.21	0.05	99.80

rim	46.89	11.86	22.72	7.39	6.23	0.73	0.00	0.15	0.00	0.01	3.31	0.02	99.32
core	49.41	11.99	22.83	7.20	4.25	1.73	0.00	0.16	0.00	0.00	2.24	0.01	99.83
rim	45.71	11.17	22.51	7.95	6.68	0.79	0.00	0.17	0.00	0.00	3.93	0.02	98.92
core	45.18	11.10	22.61	7.55	7.37	1.90	0.00	0.14	0.01	0.00	3.80	0.02	99.70
core	44.01	10.28	22.11	8.20	8.20	1.91	0.00	0.13	0.02	0.00	4.36	0.04	99.25
rim	46.88	12.30	22.52	7.44	6.34	0.69	0.01	0.12	0.01	0.00	3.23	0.02	99.54
core	43.88	10.97	21.25	8.11	8.41	1.97	0.00	0.11	0.01	0.00	4.37	0.05	99.13
rim	46.61	11.58	22.58	7.77	6.46	0.79	0.01	0.17	0.01	0.01	3.57	0.02	99.57

Table B5.d: Electron microprobe analyses of plagioclase from the sample G10B.

	SiO_2	MgO	CaO	FeO	Al_2O_3	Na_2O	K_2O	MnO	NiO	Cr_2O_3	TiO_2	P_2O_5	Total
core	65.39	0.00	0.73	0.14	19.72	5.83	8.53	0.01	0.00	0.00	0.10	0.00	100.61
rim	62.67	0.04	2.30	0.15	18.97	5.56	9.74	0.02	0.00	0.00	0.07	0.00	99.50
core	54.90	0.03	11.91	0.29	26.49	5.11	0.39	0.00	0.00	0.00	0.09	0.00	99.21
rim	54.49	0.00	8.78	0.33	24.67	7.18	3.71	0.00	0.00	0.00	-0.11	0.00	99.07
core	61.68	0.56	4.29	0.36	20.24	5.78	4.19	1.01	0.00	0.00	0.07	0.00	98.57
rim	55.70	3.42	8.10	1.06	23.78	5.37	1.49	0.02	0.00	0.00	0.12	0.00	99.07
core	54.41	0.05	12.14	0.47	29.24	4.54	0.20	0.00	0.00	0.00	0.14	0.00	101.19
rim	55.92	0.03	10.56	0.40	28.39	5.22	0.27	0.00	0.00	0.00	0.11	0.00	100.90
core	57.53	0.04	10.78	0.57	25.74	4.31	0.19	0.00	0.00	0.00	0.14	0.00	99.71
rim	57.69	2.83	8.18	0.96	24.86	3.81	0.24	0.02	0.00	0.00	0.15	0.00	99.14
core	55.24	0.02	11.05	0.38	28.18	5.21	0.25	-0.01	0.00	0.00	0.12	0.00	100.45
rim	54.64	0.01	10.75	0.23	26.28	6.85	0.39	-0.02	0.00	0.00	0.06	0.00	99.19
core	65.92	-0.01	0.32	0.16	18.58	5.30	9.03	0.00	0.01	0.00	0.10	0.00	99.42
core	53.75	0.04	11.7	0.35	28.27	4.75	0.29	-0.01	0.00	0.00	0.13	0.01	99.27
rim	54.87	0.01	10.66	0.26	27.58	5.47	0.34	0.00	0.00	0.00	0.11	0.02	99.33
core	58.68	-0.01	7.97	0.17	24.59	7.23	0.70	-0.01	0.00	-0.01	0.02	0.00	99.37

rim	65.66	-0.02	1.37	0.17	19.50	7.44	6.13	0.00	0.00	0.00	0.09	0.01	100.37
core	65.70	-0.02	0.44	0.11	18.66	5.77	8.57	0.01	0.01	0.00	0.09	0.01	99.37
rim	66.27	-0.03	0.33	0.22	18.72	5.81	8.49	-0.01	0.01	-0.01	0.06	0.01	99.92
core	65.62	0.00	0.35	0.16	18.72	6.01	8.17	0.00	-0.01	0.01	0.09	0.00	99.13
rim	65.41	0.07	0.90	0.19	18.87	5.78	7.95	-0.01	-0.01	0.01	0.09	0.02	99.27
core	65.65	0.01	0.46	0.12	18.72	5.61	8.62	0.00	0.00	0.00	0.14	0.02	99.35
rim	64.64	0.11	1.40	0.21	18.95	7.17	6.67	0.1	0.00	-0.01	0.12	0.02	99.39
core	50.63	0.04	0.08	0.37	29.91	17.05	2.10	-0.01	0.00	0.00	0.06	0.02	100.28
rim	48.42	0.41	1.06	0.70	30.12	17.27	1.49	0.01	-0.03	0.01	0.06	0.10	99.62
core	49.64	0.04	0.06	0.35	29.76	17.06	2.33	0.00	-0.01	0.00	0.05	0.01	99.30
rim	49.33	0.04	0.09	0.34	30.3	17.05	2.66	0.01	-0.01	0.00	0.04	0.01	99.88
core	50.38	0.04	0.04	0.33	30.42	17.03	2.39	0.00	0.01	-0.01	0.07	0.01	100.73
rim	49.87	0.05	0.12	0.42	28.28	17.92	2.68	-0.01	0.00	0.01	0.06	0.02	99.43
core	66.18	0.01	0.44	0.16	18.82	6.26	7.68	0.01	-0.01	0.00	0.14	0.01	99.71
rim	65.74	0.01	0.40	0.14	18.60	5.18	9.22	-0.01	0.00	0.01	0.14	0.01	99.45

Table B6.a: Electron microprobe analyses of resorbed olivine from the sample G14.

	SiO_2	MgO	CaO	FeO	Al_2O_3	Na_2O	K_2O	MnO	NiO	Cr_2O_3	TiO_2	P_2O_5	Total
core	40.43	46.02	0.17	12.25	0.04	0.03	0.00	0.16	0.32	0.04	0.02	0.04	99.52
rim	40.42	45.42	0.26	12.5	0.04	0.02	0.01	0.18	0.22	0.05	0.02	0.03	99.18
core	39.92	45.96	0.21	12.77	0.04	0.02	0.00	0.17	0.27	0.05	0.02	0.04	99.47
rim	39.87	45.21	0.29	13.51	0.04	0.02	0.00	0.19	0.22	0.03	0.02	0.04	99.45
core	40.36	45.80	0.20	12.58	0.04	0.02	0.00	0.16	0.28	0.05	0.01	0.02	99.53
rim	40.58	44.90	0.27	13.47	0.03	0.02	0.00	0.21	0.22	0.03	0.02	0.02	99.77
core	39.57	45.57	0.17	13.21	0.05	0.04	0.00	0.18	0.22	0.03	0.02	0.07	99.11
rim	39.98	44.80	0.41	13.96	0.04	0.01	0.00	0.22	0.16	0.02	0.05	0.03	99.67

core	39.75	45.91	0.14	12.92	0.03	0.01	0.01	0.19	0.36	0.02	0.02	0.03	99.37
rim	40.46	45.23	0.27	12.96	0.04	0.00	0.00	0.20	0.21	0.04	0.03	0.04	99.49
core	40.19	45.62	0.23	12.44	0.04	0.02	0.00	0.18	0.24	0.07	0.02	0.02	99.06
core	40.33	45.85	0.23	12.27	0.04	0.01	0.00	0.17	0.25	0.05	0.03	0.02	99.25
core	40.57	46.13	0.09	12.26	0.03	0.01	0.00	0.16	0.35	0.01	0.01	0.02	99.65
core	41.01	47.45	0.07	10.41	0.03	0.02	0.01	0.14	0.38	0.01	0.01	0.03	99.56

Table B6.b: Electron microprobe analyses of clinopyroxene from the sample G14.

	SiO_2	MgO	CaO	FeO	Al_2O_3	Na_2O	K_2O	MnO	NiO	Cr_2O_3	TiO_2	P_2O_5	Total
core	50.86	15.37	22.58	4.36	3.45	0.5	0.00	0.08	0.03	0.64	1.19	0.01	99.06
core	50.04	14.74	22.72	4.60	4.36	0.52	0.00	0.09	0.03	0.50	1.47	0.02	99.10
core	49.33	11.86	23.41	6.70	5.63	1.1	0.00	0.09	0.00	0.01	3.12	0.04	99.30
rim	41.75	9.64	23.02	7.83	11.07	0.56	0.00	0.09	0.00	0.00	5.80	0.02	99.80
core	50.06	15.20	22.72	4.94	3.87	0.48	0.00	0.08	0.02	0.59	1.31	0.02	99.28
rim	41.50	10.08	23.20	7.56	10.4	0.56	0.01	0.07	0.01	0.01	5.67	0.06	99.12
core	49.00	14.20	22.76	4.48	5.45	0.69	0.24	0.10	0.02	1.01	1.46	0.01	99.42
rim	46.99	12.71	23.67	6.48	5.71	0.40	0.01	0.09	0.00	0.03	3.06	0.04	99.19
core	48.86	13.85	21.69	4.85	6.61	0.93	0.00	0.07	0.04	1.36	1.91	0.01	100.2
rim	44.71	11.48	21.66	8.57	8.44	0.65	0.02	0.19	0.00	0.01	3.99	0.24	99.96
core	50.84	15.24	21.97	4.33	3.76	0.62	0.01	0.09	0.03	0.83	1.10	0.00	98.81
rim	43.49	10.00	22.29	7.04	10.44	0.63	0.02	0.12	0.01	-0.01	5.34	0.03	99.42
core	43.25	11.15	22.10	7.18	10.01	1.32	0.01	0.09	0.02	0.04	4.29	0.04	99.51
core	50.24	15.85	22.16	4.40	3.94	0.51	0.01	0.10	0.03	0.58	1.34	0.00	99.17
rim	42.88	9.97	21.47	7.69	10.84	0.56	0.06	0.09	0.01	-0.01	5.53	0.05	99.17
core	48.94	13.18	21.54	5.25	7.25	0.77	0.00	0.08	0.01	0.62	2.28	0.01	99.94
rim	45.66	11.64	22.72	6.65	7.88	0.52	0.00	0.09	0.01	0.17	3.68	0.04	99.06
core	48.39	15.38	22.39	4.64	5.01	1.54	0.01	0.10	0.00	0.54	1.61	0.01	99.62

rim	42.68	12.49	22.65	7.14	9.38	0.62	0.03	0.14	-0.01	0.00	4.21	0.06	99.40
core	46.95	14.43	21.59	6.62	6.71	0.67	0.00	0.07	0.02	1.19	1.93	0.01	100.19
rim	45.51	12.49	22.65	7.26	7.65	0.47	0.01	0.13	0.01	0.00	3.44	0.05	99.67
core	48.48	13.49	22.62	5.87	4.96	1.09	0.01	0.09	0.01	0.2	2.42	0.03	99.28
core	48.72	13.49	22.86	5.88	4.91	1.00	0.01	0.10	0.03	0.16	2.42	0.03	99.26
core	48.31	13.21	22.44	6.50	5.46	1.12	0.00	0.11	0.02	0.00	2.82	0.03	100.01
core	47.54	13.53	21.66	6.62	5.94	1.07	0.01	0.11	0.01	0.00	3.01	0.02	99.53
core	47.89	13.30	22.23	6.59	5.80	1.45	0.01	0.11	0.01	0.07	2.70	0.04	100.19
core	48.35	13.76	22.55	6.29	4.53	1.09	0.00	0.10	0.02	0.22	2.61	0.03	99.53
core	47.58	13.26	22.65	6.37	5.40	1.08	0.00	0.12	0.01	0.07	2.79	0.04	99.57
core	48.47	13.93	22.52	5.97	4.92	1.09	0.00	0.07	0.01	0.35	2.15	0.01	99.50
core	47.53	13.18	22.56	6.55	5.48	1.10	0.00	0.11	0.01	0.07	2.94	0.04	99.57
core	46.91	12.98	22.73	7.23	5.78	1.12	0.00	0.12	0.02	0.01	3.04	0.05	100.00

APPENDIX C

X-ray fluorescence analysis (XRF) Major and trace element analysis

Major and trace element composition of all samples were determination by X-ray fluorescence (XRF) at University of Edinburgh in March and August 2011. Approximately 10g of powder was prepared in carbide or agate grinding apparatus.

Major element concentrations were measured on 40 mm-diameter fused glass discs. Approximately 1 g of sample powder was mixed with a borate flux using a 5:1 (flux sample) dilution and fused in Pt-5%Au crucibles at 1100°C. Trace element concentrations were measured on pressed powder pellets. Several drops of binder were added to 8g of powder to make a 40 mm-diameter pellet by using automatic pressure at 10 to 30 ton (Hannah *et al*., 2002).

Table C.1: XRF analyses (major element) for the basaltic and phonolitic rocks of Garian volcanic province.

Sample name	SiO_2	Al_2O_3	Fe_2O_3	MgO	CaO	Na_2O	K2O	TiO_2	MnO	P_2O_5	LOI	Total
G1	42.61	12.53	13.13	9.52	11.40	3.33	1.180	3.352	0.174	0.926	1.67	99.82
G2	41.57	12.00	11.35	11.74	12.72	3.42	0.837	3.193	0.184	0.867	1.76	99.64
G5	43.60	11.97	12.70	10.16	11.54	2.11	0.758	2.444	0.178	0.804	3.55	99.81
G6	46.22	13.25	12.74	9.03	10.86	3.03	1.185	2.234	0.170	0.605	0.60	99.93
G10B	48.25	17.81	5.10	6.00	9.74	3.27	3.070	2.190	0.120	1.040	0.00	96.59
G8B	48.73	14.14	2.99	7.3	11.47	3.39	1.310	2.110	0.170	0.520	0.00	92.13
G9	49.50	13.54	11.16	6.56	9.56	3.33	0.896	1.490	0.144	0.379	2.97	99.90
G14	48.55	13.37	11.04	6.41	11.57	3.46	0.827	1.935	0.141	0.393	2.05	99.74
G15B	52.41	15.31	2.92	6.56	9.03	3.88	0.600	1.770	0.150	0.270	0.00	92.90
G32B	52.71	15.45	2.95	6.63	8.60	4.17	0.490	1.730	0.150	0.250	0.00	93.13
G116B	52.16	15.30	1.73	6.82	9.20	4.00	0.470	1.670	0.150	0.310	0.00	91.81
G8	56.80	21.15	3.52	0.08	1.14	10.36	5.015	0.265	0.434	0.022	0.98	99.76
G10	59.41	20.37	2.76	0.10	0.72	9.68	5.627	0.255	0.178	0.025	0.85	99.97
G11	60.35	18.69	2.98	0.16	0.84	9.35	5.332	0.279	0.220	0.033	1.34	99.59
G12	58.16	20.15	3.10	0.19	1.25	8.17	6.006	0.304	0.191	0.045	2.51	100.08
G81B	59.49	20.11	1.81	0.89	1.39	7.54	7.060	0.350	0.140	0.150	0.00	98.93

Table C.2: CIPW norm calculation shows the basaltic and phonolites of Garian volcanic composition.

Sample	Plateau Basaltic and related rocks						Late Basaltic and related rocks					Phonolites				
	G8B	G9	G14	G15B	G32B	G116B	G1	G2	G5	G6	G10B	G8	G10	G11	G12	G81B
Quartz	0.00	1.52	0.00	0.00	0.00	0.00	0.00	0.00	0.00	0.00	0.00	0.00	0.00	0.00	0.00	0.00
Anorthite	18.20	18.00	17.2	21.3	20.7	21.1	14.50	13.6	19.6	17.80	23.50	0.00	0.00	0.00	0.00	0.00
Albite	21.00	28.20	27.4	32.8	35.3	33.9	14.00	5.18	17.9	23.70	17.50	25.40	30.6	36.10	32.10	28.2
Na_2SiO_3	0.00	0.00	0.00	0.00	0.00	0.00	0.00	0.00	0.00	0.00	0.00	0.00	0.44	1.24	0.00	0.00
Acmite	0.00	0.00	0.00	0.00	0.00	0.00	0.00	0.00	0.00	0.00	0.00	8.18	7.99	8.62	1.24	1.88
Diopside	28.60	21.00	29.3	17.6	17.00	18.4	24.50	31.30	25.8	21.30	14.00	3.40	2.94	3.46	5.10	4.73
Hypersthene	5.30	6.78	0.00	10.4	8.67	4.97	0.00	0.00	0.00	0.00	0.00	0.00	0.00	0.00	0.00	0.00
Orthoclase	9.40	7.93	7.52	6.16	5.51	5.39	9.59	7.58	7.10	9.59	20.80	32.20	35.9	34.10	38.10	44.30
Olivine	5.50	0.00	1.67	3.97	5.50	10.4	8.65	10.30	9.13	8.83	5.93	0.00	0.15	0.79	0.06	0.45
Perovskite	0.00	0.00	0.00	0.00	0.00	0.00	2.21	1.75	0.00	2.33	0.00	0.00	0.00	0.00	0.00	0.00
Nepheline	3.24	0.00	0.00	0.00	0.00	0.00	7.70	12.9	0.00	1.06	5.53	28.40	21.9	15.10	19.10	18.10
Apatite	1.20	0.81	0.90	0.63	0.35	0.72	2.15	2.02	1.85	1.39	2.40	0.05	0.07	0.07	0.12	0.35
Ilmenite	4.00	3.40	3.68	3.36	3.11	3.17	3.86	4.10	4.63	1.63	4.16	0.50	0.47	0.53	0.55	0.66
Magnetite	4.33	4.84	1.44	4.23	4.28	2.51	0.00	0.00	4.96	0.00	5.03	1.00	0.00	0.00	3.85	1.68
Hematite	0.00	7.82	10.10	0.00	0.00	0.00	13.20	11.4	9.28	12.7	1.62	0.00	0.00	0.00	0.00	0.00
TOTAL	100.5	100.3	100.2	100.5	100.4	100.6	100	100.1	100.2	100.3	100.5	99.4	100.5	100	100.4	100.4

Table C.3: XRF analyses (trace element) for the late basalts rocks of Garian volcanic province.

Sample No	G1	G2	G5	G6	G10B
Zn	113.8	106.5	115.2	101.5	100.3
Cu	48.6	43.3	51.1	50.0	161.4
Ni	827.6	319.7	776.9	185	43.3
Cr	390.5	257.2	524.9	288.8	n.d.
V	248.9	150.4	217.4	179.3	295.6
Ba	499.2	377.5	534.0	455.3	911
Sc	20.8	16.7	22.5	20.8	5.7
La	60.0	26.3	53.4	37.9	87.3
Ce	121.5	50.6	102.7	74.5	159.9
Nd	57.3	24.5	47.5	33.4	67.3
U	1.7	0.5	0.9	0.9	1.8
Th	6.2	3.3	6.0	3.8	9.5
Pb	4.3	2.1	3.5	2.5	3.6
Nb	84.7	30.2	79.1	57.2	120.5
Zr	323.1	136.7	235.4	184.2	285.1
Y	29.1	21.7	26.3	24.7	37.9
Sr	910.8	485.4	2042.3	754.0	1039.0
Rb	70.3	13.8	34.0	21.2	43.4

Table C.4: XRF analyses (trace element) for the plateau basalt rocks of Garian volcanic province.

Sample No	G8B	G9	G14	G15B	G32B	G116B
Zn	104.3	106.5	97.5	99.0	107.5	109.6
Cu	43.6	48.1	57.3	41.2	35.2	45.1
Ni	126.2	882.3	827.7	108.9	82.3	122.0
Cr	213.2	390.8	721.1	211.6	140	207.9
V	162.8	155.0	277.0	136.8	129.7	135.4
Ba	565.0	293.5	536.8	222.2	204.2	242.7
Sc	20.1	18.9	26.5	19.8	21.0	20.6
La	34.0	22.6	58.6	15.7	11.9	16.6
Ce	65.2	47.5	111.4	36.1	28.9	37.1
Nd	29.9	22.5	52.1	18.7	15.4	18.1
U	0.7	0.4	1.8	0.6	0.2	0.6
Th	4.3	3.1	7.2	0.7	1.5	1.6
Pb	2.8	2.8	3.5	2.6	1.7	2.2
Nb	48.9	29.1	94.0	21.9	17.7	21
Zr	163.7	128.9	266.0	129.6	120.6	126.1
Y	23.0	21.1	28.8	21.3	21.2	21.6
Sr	591.7	435.5	855.0	363.4	311	367.1
Rb	19.8	17.8	16.0	10.8	7.9	9.5

Table C.5: XRF analyses (trace element) for the phonolite rocks of Garian volcanic province.

Sample No	G8	G10	G11	G12	G81B
Zn	324.8	119.5	148.2	138.6	208.8
Cu	3.8	6.2	2.9	9.9	1.9
Ni	2.5	0.1	978.2	0.1	4.5
Cr	n.d.	n.d.	202.7	n.d.	n.d.
V	1.1	1.8	0.9	8.0	-4.1
Ba	7.0	11.1	4.1	37.6	7.0
Sc	n.d.	n.d.	n.d.	n.d.	n.d.
La	181.5	112.3	167.5	114.1	221.0
Ce	303.6	156.6	260.3	155.9	337.6
Nd	64.3	29.9	59.8	30.0	78.0
U	22.8	9.7	14.6	6.4	14.8
Th	65.7	30.8	47.9	30.0	50.8
Pb	31.3	18.2	23.7	17.2	25.4
Nb	523.9	192.6	316.8	158.8	382.5
Zr	2728.5	1015.7	1570.7	1010.7	1935.5
Y	64.8	24.4	46.1	21.8	58.1
Sr	28.0	4.8	5.1	54.9	34.5
Rb	336.4	161.8	227.5	170.0	235.5

Inductively coupled plasma mass spectrometry (ICP-MS) rare earth element (REE) analysis

The rare earth elements (REE) concentrations of 16 samples were determined by Inductive Coupled Plasma Mass Spectrometry (ICP-MS). The samples were prepared for ICP-MS analysis by HF dissolution at the SUERC. Approximately 100 mg of powdered rock samples and reference materials were weighed into 15 ml flat bottom Teflon (PFA) screw cap vials for dissolution. 5 ml of HF and 2 ml of HNO_3 were added and the closed vials were left on a hotplate at 160°C for 12 hours. After subsequent evaporation to dryness 5 ml of HNO_3 were added, again leaving the capped vials for 12 hours on a hotplate at 160°C, before dry down. The third step consisted of adding 5 ml of HCl, closing the vial, gently swirling it and then evaporating to dryness straight away, and was repeated once. The samples were picked up in 2.5 ml of (16 mol) HNO3, transferred to volumetric flasks and diluted to 100 ml with deionised H_2O and decanted into polythene bottles for storage (Olive *et al*., 2001).

Table C.6: ICP-MS analyses for the late basalt rocks of Garian volcanic province.

Sample No	G1	G2	G5	G6	G10B
Th	6.18	2.92	5.98	4.23	7.51
U	1.75	0.77	1.73	1.05	2.20
Hf	6.79	3.52	5.09	4.97	5.61
Ta	4.29	1.46	3.84	2.79	
Pb	5.21	3.29	5.11	3.49	3.10
La	58.51	24.98	49.49	63.14	73.73
Ce	117.92	48.57	97.39	127.54	148.95
Pr	14.11	5.67	11.26	15.21	17.62
Nd	54.83	23.70	44.29	59.41	66.00
Sm	10.43	5.48	8.51	11.32	11.97
Eu	3.14	1.80	2.61	3.40	3.51
Gd	9.56	5.32	7.83	10.14	10.90
Tb	1.22	0.78	1.04	1.31	1.41
Dy	6.09	4.28	5.39	6.58	7.13
Ho	1.03	0.76	0.94	1.12	1.25
Er	2.59	1.98	2.42	2.81	3.17
Tm	0.35	0.27	0.34	0.38	0.45
Yb	1.98	1.53	1.90	2.09	2.53
Lu	0.27	0.22	0.27	0.29	0.35

Table C.7: ICP-MS analyses for the plateau basalt rocks of Garian volcanic province.

Sample No	G8B	G9	G14	G15B	G32B	G116B
Th	3.77	3.08	6.56	1.88	1.35	1.66
U	0.94	0.90	1.96	0.55	0.31	0.46
Hf	4.39	3.42	5.73	3.19	3.24	2.81
Ta		1.44	4.53			
Pb	2.57	3.62	6.37	1.92	2.86	1.72
La	32.51	23.20	55.13	17.70	12.90	16.30
Ce	65.29	45.23	108.12	36.99	28.12	34.28
Pr	7.61	5.17	12.65	4.42	3.54	4.07
Nd	30.62	21.19	49.74	19.04	16.13	17.66
Sm	6.38	4.84	9.59	4.73	4.33	4.43
Eu	2.05	1.58	2.90	1.60	1.50	1.51
Gd	6.11	4.74	8.49	4.92	4.54	4.63
Tb	0.85	0.71	1.12	0.76	0.71	0.71
Dy	4.48	3.98	5.74	4.20	4.05	4.02
Ho	0.79	0.72	1.00	0.77	0.74	0.73
Er	2.04	1.89	2.52	2.02	1.97	1.91
Tm	0.28	0.26	0.35	0.28	0.27	0.27
Yb	1.63	1.51	1.95	1.62	1.58	1.55
Lu	0.23	0.22	0.28	0.23	0.22	0.23

Table C.8: ICP-MS analyses for the phonolite rocks of Garian volcanic province.

Sample No	G8	G10	G11	G12	G81B
Th	47.60	29.85	45.90	28.55	43.76
U	21.12	8.84	13.55	6.01	12.97
Hf	37.42	16.96	28.83	17.30	29.95
Ta	10.24	5.61	12.06	4.82	
Pb	39.69	24.86	30.18	22.97	24.45
La	111.81	100.46	149.07	99.11	192.75
Ce	188.62	142.22	235.98	135.08	314.29
Pr	15.31	10.74	19.95	10.42	26.81
Nd	39.07	26.39	53.78	26.99	70.36
Sm	5.35	3.09	7.12	3.34	9.10
Eu	1.06	0.47	0.71	0.66	0.76
Gd	5.88	3.43	7.05	3.50	9.65
Tb	0.89	0.45	0.97	0.45	1.30
Dy	5.94	2.87	5.97	2.67	7.80
Ho	1.37	0.66	1.28	0.58	1.65
Er	4.89	2.31	4.28	1.98	5.37
Tm	0.91	0.43	0.76	0.37	0.95
Yb	6.20	2.96	5.18	2.57	6.11
Lu	0.98	0.48	0.81	0.43	0.92

Sr and Nd isotope chemistry procedures (Thermal Ionisation Mass Spectrometry)

At the laboratory approximately 200 mg of whole-rock powder was dissolved in 30 ml Teflon beakers in concentrated HF-HNO_3, followed by the chemical separation of Sr and Nd was performed using routine action-exchange column techniques after repeated digestion by HF-HNO_3 mixtures in closed Teflon beakers. Once separated, the elements in each isotopic system were loaded by standard procedures onto metal filaments to be used in the solid source thermal ionization mass spectrometer (TIMS). Sr and Nd isotopic compositions were determined on a VG sector-54 mass spectrometer at SUERC for 12 samples from Garian volcanic rocks using Thermal Ionization Mass Spectrometer (TIMS). The samples analysis was taken up in 2 µl 1 M QD HCl for loading. Half of the sample drop onto the Ta filament with 0.5 µl 1 M phosphoric acid (H_3PO_4) at a current of ~0.8 A and dried up to a current of ~2.0 A.

The samples were analysed at a stable beam intensity of ~1.5 pA with filament current of ~1.5 pA. Sr isotopes were measured in dynamic mode with on line corrections for interferences, mass fractionation and error calculations built into the VG software. A dynamic $^{87}Sr/^{86}Sr$ value was obtained from a maximum of ratios with rejection of 10%. International standard NBS 987 ($^{87}Sr/^{86}Sr$ ~0.71248, Jochum *et al*., 2008) was used to monitor analytical precision and accuracy. Repeat analyses of NBS during the run gave a mean of $^{87}Sr/^{86}Sr$ 0.710267 ± 0.000012 (2σ, n= 7) and precision and accuracy within ± 0.002%. the mean error for the samples analysed was ± 0.000012 (2σ, n= 13) a maximum error of 0.000025 (2σ).

Table C.9: Sr/Nd isotope data for selected samples from the Garian Volcanic Province.

Rock Type	Plateau Basaltic and related rocks					
sample	G8B	G9	G14	G15B	G32B	G116B
$^{87}Sr/^{86}Sr$	0.703881	0.703765	0.703340	0.703698	0.703977	0.703773
2σ	0.000014	0.000011	0.000011	0.000013	0.000014	0.000014
$^{143}Nd/^{144}Nd$	0.512918	0.512863	0.512903	0.512864	0.512811	0.512916
2σ	0.000006	0.000006	0.000010	0.000007	0.000006	0.000010
Rock Type	Late Basaltic and related rocks					
sample	G1	G2	G5	G6	G10B	
$^{87}Sr/^{86}Sr$	0.703576	0.703745	0.705625	0.704141	0.703608	
2σ	0.000012	0.000012	0.000013	0.000013	0.000013	
$^{143}Nd/^{144}Nd$	0.512945	0.512871	0.512950	0.512952	0.512901	
2σ	0.000007	0.000007	0.000006	0.000022	0.000007	
Rock Type	Phonolites					
sample	G8	G10	G11	G12	G81B	
$^{87}Sr/^{86}Sr$	0.726982	0.766966	0.779474	0.711335	0.718132	
2σ	0.000013	0.000013	0.000016	0.000012	0.000011	
$^{143}Nd/^{144}Nd$	0.512920	0.512878	0.512844	0.512894	0.512806	
2σ	0.000009	0.000011	0.000007	0.000007	0.000008	

Table C.10: North African crustal compositions.

	Upper crust					Lower crust			
Rock type	Bayuda Granite	Biotite-hornblende Granite	2-mica Granite	Granitic-basement	Leucocratic-gneiss	Kas Granite	Granitic-basement	kas Granite	Biotite-gnesiss
Location	Bayuda	Tibesti Massif	Tibesti Massif	Darfur (X36)	Darfur (X139)	Darfur	Darfur (X37)	Darfur (137)	Darfur (X135)
Reference	Lucassen *et al*. (2008)	Suayah *et al.* (2006)	Suayah *et al.* (2006)	Davidson & Wilson (1989)	Davidson & Wilson (1989)	Lucassen *et al*. (2008)	Davidson & Wilson (1989)	Davidson & Wilson (1989)	Davidson & Wilson (1989)
Sr		94.17	53.25	69	220	779	678	814	350
$^{87}Sr/^{86}Sr$	0.72650	0.76988	0.81736	0.76447	0.72706	0.70930	0.70863	0.70902	0.73063
Nd		28.1	13.84	18.5	21.38	53.29	34.19	29.94	17.36
$^{143}Nd/^{144}Nd$	0.51205	0.51238	0.51296	0.51139	0.51205	0.51120	0.51136	0.51127	0.51074

Table C.11: XRF analyses (major element) for the basaltic rocks of Libyan Cenozoic volcanic provinces.

Sample name	SiO_2	Al_2O_3	Fe_2O_3	MgO	CaO	Na_2O	K2O	TiO_2	MnO	P_2O_5	LOI	Total
Basalt rocks of Jabal Al Hasawinah volcanic province												
H1	47.94	14.39	11.01	7.41	10.36	3.65	1.188	2.191	0.149	0.506	0.77	99.56
H2	44.41	13.48	11.33	6.19	13.02	3.36	1.396	2.270	0.153	0.567	3.52	99.70
H3	45.61	13.95	11.45	8.06	11.13	4.27	1.559	2.419	0.159	0.705	0.85	100.16
H6	39.13	11.34	13.67	12.33	12.51	3.30	0.841	3.078	0.192	1.395	1.55	99.33
H7	44.72	13.31	13.12	7.26	11.49	3.33	1.331	2.907	0.178	0.747	1.43	99.82
H9	45.50	14.04	12.43	7.55	11.02	3.14	1.387	2.692	0.153	0.692	1.18	99.87
Basalt rocks of Jabal As Sawda volcanic province												
S1	48.50	14.74	10.94	6.25	11.62	3.76	1.094	2.054	0.149	0.436	0.01	99.55
S3	47.82	14.54	10.69	6.98	11.23	3.73	1.159	2.111	0.146	0.454	1.09	99.95
S5	43.28	13.17	11.72	9.45	11.93	3.80	1.474	2.246	0.164	0.664	1.44	99.34
S7	44.98	13.73	11.83	9.92	10.28	3.62	1.185	2.419	0.164	0.676	1.02	99.82
S8	42.52	12.90	12.77	11.62	10.30	3.41	1.352	2.446	0.189	0.763	1.17	99.44
S9	45.34	13.51	12.34	10.81	9.48	3.77	1.053	2.322	0.173	0.680	0.65	100.13
S10B	47.33	14.18	11.81	10.01	9.40	3.16	1.140	2.102	0.162	0.451	0.52	100.27
Basalt rocks of Jabal Al Haruj volcanic province												
HS1	40.01	10.64	13.79	11.57	13.73	3.78	0.786	2.724	0.193	0.647	1.89	99.76
HS3	49.76	14.76	11.81	7.58	9.91	3.23	0.583	1.762	0.153	0.260	-0.15	99.66
HS4A	48.65	14.63	11.78	7.07	10.19	3.42	0.965	1.986	0.152	0.296	0.6	99.74
HS6	47.71	14.53	13.07	8.58	10.03	3.25	0.523	1.847	0.167	0.224	-0.22	99.71
HS10	48.57	15.68	12.70	6.26	9.74	3.73	0.951	2.250	0.167	0.379	1.19	99.79
HS11	49.38	15.43	12.45	6.93	8.65	3.64	1.014	1.988	0.156	0.324	-0.45	99.51
HS12A	47.46	14.50	12.36	6.67	10.11	3.72	0.987	2.504	0.156	0.397	0.15	99.01
HS14	48.09	14.03	12.48	8.92	9.33	3.30	0.851	1.858	0.157	0.301	0.61	99.93

Table C.11: XRF analyses (major element) for the basaltic rocks of Libyan Cenozoic volcanic provinces.

Sample name	SiO_2	Al_2O_3	Fe_2O_3	MgO	CaO	Na_2O	K2O	TiO_2	MnO	P_2O_5	LOI	Total
Basalt rocks of Jabal Al Haruj volcanic province												
HS16	51.03	14.13	11.46	7.63	8.29	3.66	1.292	2.261	0.140	0.508	-0.26	100.14
HS18	47.12	13.34	11.29	7.90	11.55	3.31	1.072	2.296	0.146	0.360	1.44	99.82
HS19	48.12	14.80	12.45	7.61	9.66	3.48	1.007	1.986	0.163	0.335	-0.04	99.57
HS20	47.99	14.59	12.15	8.50	9.78	3.28	0.986	1.958	0.164	0.328	0.06	99.79
HS21	47.97	14.75	12.45	8.18	9.75	3.43	0.823	1.900	0.159	0.310	-0.19	99.53
HS22	43.27	12.54	13.51	9.42	10.98	4.25	1.336	2.909	0.176	0.738	0.46	99.59
HS23	48.73	14.18	11.79	7.41	10.14	3.48	1.259	2.321	0.154	0.420	0.13	100.01
HS24	46.53	13.67	10.78	6.61	12.52	3.35	1.117	2.230	0.142	0.377	2.32	99.65

Table C.12: XRF analyses (trace element) for the basalt rocks of Jabal Al Hasawinah volcanic province.

Sample No	H1	H2	H3	H6	H7	H9
Zn	99.7	95.2	100.4	101.3	110.2	94.1
Cu	45	52	50.2	65.3	22.8	47.7
Ni	1708.3	174.8	1428.2	256.1	1228	166.5
Cr	729.2	321.4	603.7	412.1	604.2	290
V	202.2	194.6	212.3	256.6	230.6	220.2
Ba	321.8	1512.2	449.2	579	420.5	416.5
Sc	20.3	17.9	20.1	20.8	22.1	22.5
La	22.6	33.1	33.4	71.7	28.2	34.8
Ce	52.7	59.7	68.5	138.4	71.5	72.7
Nd	26.7	28.5	31.8	62.5	39	36.6
U	1.2	0.9	1.1	2.4	0.9	1.2
Th	2.7	3.6	4.3	7.3	1.6	3.7
Pb	2	2.4	2.7	4.3	1.5	2.2
Nb	40.1	49.9	62	94.1	53.1	56.5
Zr	166.3	193.1	195.4	267.8	198.9	216
Y	22.7	24	24.4	31.9	26.3	27.3
Sr	581.7	785.2	772.6	1115.1	674.7	752
Rb	20.9	26.1	26.2	31	19.6	24.8

Table C.13: XRF analyses (trace element) for the basalt rocks of Jabal As Sawda volcanic province.

Sample No	S1	S3	S5	S7	S8	S9	S10B
Zn	93	95.6	100.4	100.4	106	108.3	90.1
Cu	54.3	58.7	65.3	53.2	49.2	54.9	60.2
Ni	111.7	1616.1	223.5	1122	294.5	1161.3	194.2
Cr	256.5	673.6	424.1	545.9	342.6	653.2	265.2
V	184.2	199.9	206.3	206	216.6	192.9	187.1
Ba	665.7	360.1	1243.4	393.9	471.2	360.6	293.9
Sc	19	21.7	19.6	20.3	20.1	20.2	20.6
La	20.1	21.8	32.8	33.1	43.8	36.3	21.4
Ce	41.2	45.4	63.6	68.1	83.2	77.8	48.4
Nd	19.4	23.6	27.4	32.4	39.5	34.4	23.6
U	0.8	0.4	1.4	0.7	1.6	1.3	1
Th	3	2.9	3.8	4.1	4.8	4.3	3.3
Pb	1.8	1.5	3.1	2.5	2.6	2.6	2.1
Nb	36	39.5	58.6	59.7	70	61.2	39.6
Zr	138.7	138.7	177.4	197.2	225.8	232	162.5
Y	20.9	19.9	23.2	24.1	26.2	24.3	23
Sr	603.3	581.6	792.8	740.5	839	731.4	546.6
Rb	19.2	19.5	27.9	14	31.2	9.7	20.5

Table C.14: XRF analyses (trace element) for the basalt rocks of Jabal Al Haruj volcanic province.

Sample No	HS1	HS3	HS4A	HS6	HS10	HS11	HS12A	HS14
Zn	109.2	106.6	95.8	104.5	99.5	105.2	102.8	105.4
Cu	80	63.6	103.3	57.8	35.7	46.1	48.3	53.5
Ni	302.7	2307	162.4	1888.2	50	1624.6	418.5	1427.6
Cr	509.6	847.3	259.6	725.3	87.3	582.5	208.8	534.9
V	294	211.2	187.7	214.9	201.6	179.3	168.1	208
Ba	447	209.3	591.1	115.2	292	192.1	426.6	650.8
Sc	21.4	24.4	17.3	24.9	19	18.8	15.8	18.7
La	39.6	9.9	14	8.6	16	16.8	18.5	15.8
Ce	81.4	29.6	34	25.4	40.1	39.6	43.9	38.1
Nd	41.5	17.9	18.1	14.8	21.7	21.5	25.3	19.4
U	1.8	0	0.4	0.4	0.4	0.5	1	0.4
Th	4.3	0.8	1.3	n.d.	1.5	1.4	3.6	1.7
Pb	2.7	1.9	2.1	1.7	2.3	2.2	3	1.4
Nb	64	18.5	21.4	16.8	32.4	20.8	30.3	31
Zr	220.4	119.3	132.1	96.5	153.2	137	158.3	126.5
Y	23.5	21.2	22.3	19.9	22.9	23.6	21.9	20
Sr	841.5	387.8	496	366.9	531.6	396	485.9	614.3
Rb	8	9.7	16.3	6.8	13	15.1	21.5	15.5

Table C.14: XRF analyses (trace element) for the basalt rocks of Jabal Al Haruj volcanic province.

Sample No	HS16	HS18	HS19	HS20	HS21	HS22	HS23	HS24
Zn	98	98.7	99	102.4	100.2	119.7	96	95.2
Cu	86.2	42.2	61.4	54.2	94.2	67	54.2	50.1
Ni	223.4	1774.5	128.3	1665.1	199.3	1414	142.4	1374.7
Cr	336.3	718.4	286.8	705.1	298.6	536.5	234.5	580.7
V	192.1	209.1	201.1	217.8	191.5	233.3	194.6	209
Ba	200.6	596.6	255.7	671.6	245.9	344.5	444.4	246.1
Sc	19.6	18.1	20.2	23.7	18.7	16.8	17.3	18.8
La	13.9	14.9	25.1	14.6	14.1	36.7	18.1	15.4
Ce	39.4	35.3	41.8	36.4	33.7	76.9	41.1	37.1
Nd	19.8	20	21.9	19.1	18.4	37	22.7	22.8
U	0.2	0.7	1	0.5	0.3	1.8	0.4	0.2
Th	1.4	1.7	1.7	1.6	1.2	4.3	2	1.5
Pb	2.1	2.2	2.4	2.2	2	3.2	2.1	2
Nb	23.1	30.6	25.8	25.1	22.4	69	34.8	31
Zr	132.8	127.4	158.7	153.1	131.3	214.6	137.2	128.2
Y	20.9	18.8	24.4	23.1	21.3	21.5	19.9	19
Sr	421.5	594.5	495.2	717.1	604	982.4	741.3	603.7
Rb	15.7	18.9	17.1	15.6	11.8	16.3	21.4	19

Table C.15: ICP-MS analyses for the basalt rocks of Jabal Al Hasawinah volcanic province.

Sample No	H1	H2	H3	H6	H7	H9
Th	3.04	4.07	7.55	2.59	4.37	3.75
U	0.97	1.20	2.27	0.74	1.32	1.12
Hf	3.92	4.40	5.84	4.74	4.34	4.61
Ta	1.94	2.51	4.63	3.04	2.82	2.78
Pb	2.93	3.98	5.16	2.28	3.25	3.57
La	24.80	31.32	69.95	30.95	34.46	35.10
Ce	50.94	62.88	138.87	69.39	67.03	71.53
Pr	6.15	7.51	16.32	8.85	7.85	8.59
Nd	25.90	30.67	62.99	37.04	32.03	35.30
Sm	5.79	6.53	11.64	7.65	6.84	7.44
Eu	1.87	2.19	3.44	2.37	2.22	2.34
Gd	5.46	6.03	10.09	6.85	6.26	6.74
Tb	0.81	0.87	1.31	0.97	0.90	0.97
Dy	4.43	4.76	6.51	5.20	4.77	5.26
Ho	0.78	0.84	1.10	0.91	0.83	0.93
Er	2.05	2.19	2.73	2.33	2.12	2.41
Tm	0.28	0.30	0.37	0.32	0.29	0.33
Yb	1.59	1.72	2.03	1.81	1.62	1.89
Lu	0.22	0.25	0.28	0.26	0.23	0.27

Table C.16: ICP-MS analyses for the basalt rocks of Jabal As Sawda volcanic province.

Sample No	S1	S3	S5	S7	S8	S9	S10B
Th	2.59	2.60	4.09	3.91	5.12	4.24	2.86
U	0.85	0.74	1.24	1.19	1.55	1.33	0.89
Hf	3.49	3.36	3.97	4.38	4.79	4.93	3.77
Ta	1.75	1.87	2.73	2.89	3.30	3.07	1.96
Pb	2.59	2.16	4.44	5.15	3.40	4.87	2.86
La	21.01	21.46	32.89	32.86	41.37	35.88	22.67
Ce	42.50	43.29	64.00	65.31	80.01	71.55	46.34
Pr	5.13	5.23	7.55	7.81	9.37	8.46	5.60
Nd	21.76	22.18	30.73	32.02	37.37	34.08	23.42
Sm	5.10	5.12	6.47	6.84	7.59	7.03	5.34
Eu	1.77	1.73	2.15	2.19	2.36	2.21	1.75
Gd	4.78	4.81	5.87	6.11	6.76	6.23	5.00
Tb	0.73	0.72	0.84	0.88	0.96	0.88	0.76
Dy	4.03	3.95	4.49	4.70	5.09	4.70	4.31
Ho	0.72	0.70	0.78	0.81	0.89	0.82	0.78
Er	1.85	1.80	1.98	2.06	2.27	2.07	2.06
Tm	0.26	0.25	0.27	0.28	0.31	0.28	0.29
Yb	1.44	1.38	1.53	1.55	1.74	1.59	1.64
Lu	0.20	0.19	0.21	0.22	0.24	0.23	0.24

Table C.17: ICP-MS analyses for the basalt rocks of Jabal Al Haruj volcanic province.

Sample No	HS1	HS4A	HS10	HS12A	HS14	HS22	HS23
Th	4.68	2.10	2.09	2.80	2.11	4.52	5.40
U	1.27	0.70	0.58	1.00	0.66	1.41	1.50
Hf	5.25	3.33	3.80	3.80	3.10	4.68	3.32
Ta	3.30	1.21	1.65	1.69	1.48	3.31	1.71
Pb	5.60	3.82	3.38	3.68	2.19	3.89	2.85
La	38.46	14.67	18.52	20.57	17.16	36.51	19.00
Ce	79.62	33.47	40.23	44.85	35.79	72.59	39.98
Pr	9.77	4.20	5.01	5.59	4.43	8.72	4.91
Nd	40.32	18.20	21.53	23.82	19.57	35.93	21.31
Sm	8.31	4.46	5.03	5.56	4.82	7.76	5.13
Eu	2.58	1.52	1.70	1.78	1.78	2.55	1.77
Gd	7.10	4.32	4.79	5.11	4.55	6.75	4.73
Tb	0.97	0.70	0.74	0.77	0.69	0.92	0.72
Dy	4.94	4.07	4.23	4.18	3.80	4.59	3.91
Ho	0.82	0.74	0.78	0.73	0.68	0.75	0.68
Er	2.00	1.98	2.08	1.85	1.72	1.76	1.72
Tm	0.26	0.28	0.29	0.25	0.24	0.23	0.24
Yb	1.41	1.58	1.71	1.39	1.34	1.20	1.33
Lu	0.19	0.23	0.25	0.20	0.19	0.16	0.19

APPENDIX D

$^{40}Ar/^{39}Ar$ geochronology

Radiogenic dating systems are based on the constant decay of a parent isotope and the accumulation of a stable daughter isotope. The calculated age reflects radiogenic ingrowth following the closure of the system to the incorporation or loss of either the parent or daughter species. The $^{40}Ar/^{39}Ar$ dating technique is, like the K-Ar system, based on the decay of the radiogenic parent species ^{40}K to its daughter ^{40}Ar.

^{40}K has a half-life of 1.25 billion years, 89.5% decaying to ^{40}Ca by electron (β^-) emission, and 10.5% decaying to ^{40}Ar predominantly by orbital electron capture. As both daughter products are stable, the ratios of both $^{40}Ca/^{40}K$ and $^{40}Ar/^{40}K$ could theoretically be used to obtain dates. However, ^{40}Ca is an abundant element in nature and distinguishing ^{40}Ca produced by decay of ^{40}K from naturally present ^{40}Ca is only possible in the oldest, potassium-rich rocks. In contrast, ^{40}Ar is only ever present in trace amounts and dating based on the production of ^{40}Ar from ^{40}K can be applied to geological problems.

$^{40}Ar/^{39}Ar$ geochronology is one of the most valuable tools for determining the timing of geologic events. It is a modified version of the K-Ar dating technique using the natural radioactive decay of ^{40}K to ^{40}Ar. The $^{40}Ar/^{39}Ar$ technique involves fast neutron irradiation, in a nuclear reactor, of very small samples to convert another isotope of potassium, ^{39}K to ^{39}Ar. Heating the samples, via furnaces or lasers, releases the Ar gas into an ultra-high vacuum extraction line where unwanted gases are removed by hot and cold Zr-Al getter pumps. Subsequent isotopic analysis by a noble gas mass spectrometer measures the ratio of the proxy-parent ($^{39}Ar_K$) and radiogenic daughter (^{40}Ar) isotopes to determine a series of ages for each sample.

The $^{40}Ar/^{39}Ar$ dating method can provide information on age complexities in samples using age spectra (cumulative % ^{39}Ar released at each temperature

step versus apparent age box plots), $^{36}Ar/^{40}Ar$ versus $^{39}Ar/^{40}Ar$ isotope correlation plots, chemical information from K/Ca ratios produced as a bi-product of neutron irradiation, and also identify the presence of excess Ar.

In recent years the introduction of laser techniques for single spot and laser heating analysis has widened the range of applications for Ar-Ar dating and the introduction of more sophisticated models for stepwise heating continue to provide ever more detailed thermal histories from K-feldspars. This technique has gained importance because they avoid the vacuum breakdown problems exhibited during conventional furnace step heating techniques and because they involve lower background values.

Some of the advantages of the $^{40}Ar/^{39}Ar$ method over the conventional K-Ar technique, McDougall and Harrison (1988) are:

1. Samples do not have to be splitted for separate K and Ar analyses; the parent/daughter abundance is obtained from the same sample aliquot analysed. This allows accurate ages determination for minerals with low potassium contents such as pyroxene or plagioclase, and very small samples, such as single crystals and groundmass.

2. The sample does not need to be completely fused, but rather can be incrementally heated. The $^{40}Ar/^{39}Ar$ ratio (age) can be measured for each fraction of argon released and this allows for the generation of an age spectrum.

3. Argon isotope data from incremental heating with carefully controlled temperature and time can be used to determine closure temperature for argon system of that particular mineral.

4. The error in $^{40}Ar/^{39}Ar$ dates are commonly less than the usual 2-3% error associated with K-Ar dates. The precision of age is determined by the uncertainty in age of standard used to calibrate the neutron flux (usually 1% or

less). The precision of relative dates for samples irradiated in the same sample container is limited by uncertainty in flux determination and analytical precision of the mass spectrometer (0.1 to 0.2%).

5. By utilizing laser ablation technique, separate mineral grains or grains in thin section can be analysed. This allows accurate determination of ages of microgram to milligram quantities of minerals sample that is difficult to separate or in-situ analysis is desirable.

6. Incremental heating of individual mineral grains with a laser is more rapid and straightforward compared to conventional furnace extraction systems.

D1 Research Methodology

I have performed $^{40}Ar/^{39}Ar$ dating of 15 samples of Garian province (11 basalts and 4 phonolites), 16 basalts from Al Haruj volcanic province, 5 basalts from As Sawda volcanic province and 5 basalts from Al Hasawinah volcanic province. $^{40}Ar/^{39}Ar$ age determinations (Tables D1.1 to D1.41) were made on the groundmass of basaltic samples and on the sanidine separates from the phonolite samples at the Ar/Ar laboratory at SUERC. The plateau diagrams plot the data at 95% confidence level (2σ) and the result at 68% confidence level (1σ) while the isochrons data and results are presented at 68% confidence level (1σ).

The samples were crushed and sieved to different grain size fractions in the range < 1mm, and washed under tap water. The fractions 125-250 μm were used for $^{40}Ar/^{39}Ar$ dating. Magnetic separation was required to remove any olivine and pyroxene phenocrysts from the groundmass; isodynamic Frantz magnetic separator was used. The phenocryst-free fraction was leached in 10% HNO_3 acid in ultrasonic cleaning and washed in de-ionized water. This process was repeated more than six times until the water remained clear. Small aggregates of groundmass, free of phenocrysts (e.g., olivine, pyroxene) and xenocrysts (e.g., contamination by xenolithic material) were hand-picked under a binocular microscope. Between 230 and 500 mg of groundmass for

each sample was parcelled into small Cu packets, placed within Al discs, and stacked in a flame sealed glass vial for irradiation.

The basalt samples were step-heated using a resistively heated double-vacuum furnace over a temperature range from 500 to 1750 °C. Isotope data were collected using a GVI ARGUS multi collector mass spectrometer which has a measured sensitivity of 7×10^{-14} mol/volt (Mark *et al*., 2009). Samples were heated for 5 min prior to 10 min cleanup. Extracted gases were cleaned using 3 GP50 SAES getters (two operated at 450 °C and one at room temperature) and a cold finger maintained at - 95 °C using an acetone-solid CO_2 slush trap. The extraction, clean up and data collection processes are entirely automated. Experiments were conducted over 7 h periods with hot furnace blanks (500-1750 °C) collected prior to every sample run.

Due to its high potassium concentration in the phonolites Garian sanidine, I dated four samples by laser step-heating methods. The phonolite samples were crushed and sanidine was handpicked under a binocular microscope to ensure a pure separate. After leaching in dilute HF acid and rinsing in deionised water and methanol, the grains were parcelled into Cu packets and positioned within an Al holder for irradiation. International standard referenced against the Fish Canyon sanidine age (FCs) (28.02 ± 0.16 Ma) of Renne *et al*. (1998), was loaded adjacent to the samples of unknown age. Single grains (up to 500 µm) of sanidine were loaded into a Cu planchette in an ultra-high vacuum laser cell with a doubly pumped ZnSe window. Using a CO_2 laser, the sanidine crystals were degassed at low temperature and subsequently fused. Radiogenic ^{40}Ar ($^{40}Ar^*$) yields were thus improved from 70-80% to typically greater than 90%; no ^{39}Ar was liberated. The Ar isotope data were corrected for backgrounds, mass discrimination, and reactor-produced nuclides and processed using standard data reduction protocols (e.g., Mark *et al*., 2011a). The atmospheric argon ratios of Lee *et al*. (2006) which have been independently verified by Mark *et al*. (2011b) were employed. The Ideogram diagrams and isochrons data and results plot the data at 68% confidence level (1σ).

The decay constants of Steiger and Jäger (1977) were used as an intermediary step in the calculation of the $^{40}Ar/^{39}Ar$ ages. Ages relative to the optimisation model of Renne *et al*. (2010, 2011). Recently, Renne et al. (2010, 2011) published an optimisation model that utilised constraints from ^{40}K activity, K-Ar isotopic data, and pairs of ^{238}U-^{206}Pb and $^{40}Ar/^{39}Ar$ data as inputs for estimating the partial decay constants of ^{40}K and $^{40}Ar^*/^{40}K$ ratio for Fish Canyon sanidine (FCs) age of 28.02 ± 0.16 Ma, 1σ, Renne et al., 1998). This calibration reduced systematic uncertainties (i.e., accuracy) in the $^{40}Ar/^{39}Ar$ system from c. 2.5% to < 0.25%. Fish Canyon sanidine (FCs) is a widely used secondary standard whose age (or more correctly, $^{40}Ar^*/^{40}K$) has been determined by reference to several different primary standards.

Plateau criteria: For $^{40}Ar/^{39}Ar$ analyses a plateau segment consists of 3 or more contiguous gas fractions having analytically indistinguishable ages (i.e. all plateau steps overlap in age at ± 1σ analytical error, 68% confidence level) and comprising a significant portion of the total gas released (typically >50%). The uncertainties in plateau ages reflect multiplication by the MSWD and were obtained by standard weighting of errors for individual steps according the variance. Total gas (integrated) ages are calculated by weighting by the amount of ^{39}Ar released, whereas plateau ages are weighted by the inverse of the variance McDougall and Harrison (1999).

Plateau uncertainty: The standard error on the mean (SEM) was determined for all samples that displayed a Gaussian (normal) distribution with a mean square weighted deviation (MSWD) < 1. The SEM $MSWD^{0.5}$ used for samples that displayed a Gaussian (normal) distribution with a MSWD>1. It has been pointed out by Roddick (1978) that in instances where the MSWD > 1, the calculated error in the plateau should be multiplied by $(MSWD)^{0.5}$. I will follow this procedure only when the plateau is statistically acceptable (p > 0.05). In cases where MSWD is very large (e.g., > 10), such multiplication of the plateau age error, would make the age “less precise” and may be thought to be functionally usable. However, if p < 0.05, the probability of the steps defining a proper plateau are unacceptable. Estimating its age with a less precise “number” is to be avoided.

The MSWD is essentially the ratio of the measurement error and the observed scatter about the regression line through the points on the isochron plot. A value of 1.0 indicates that the scatter about the regression line is accounted for by the measurements errors. A value less than one suggest that the errors for the individual measurements may be over estimated.

Inverse isochron criteria: MSWD of contiguous steps, 0.05 probability cut off, minimum ^{39}Ar 60%, minimum number of contiguous steps 3. Argon data can be plotted on isotope correlation diagrams to help assess the isotopic composition of Ar trapped at the time of argon closure, thereby testing the assumption that trapped argon isotopes have the composition of modern atmosphere which is implicit in age spectra. To construct an "inverse isochron" the ^{36}Ar/^{40}Ar ratio is plotted versus the ^{39}Ar/^{40}Ar ratio. A best fit line can be calculated for the data array which yields the value for the trapped argon (Y-axis intercept) and the ^{40}Ar*/^{39}Ar$_K$ value (age) from the X-axis intercept. Isochron analysis is most useful for step-heated or total fusion data which have a significant spread in radiogenic yield. In addition to the MSWD value, we use the χ^2 test and determined the probability of occurrence (p) as statistical tools for evaluating the reliability of the inverse isochron age information. If $p < 0.05$, excess scatter of data points relative to the expected scatter is demonstrated. If $p > 0.05$, the probability that the deviation from the expected result is due to chance only is 5% or more, which is generally considered as acceptable (for details see Baksi, 1999 and 2006).

Additional parameters for each heating step are often plotted versus the cumulative %^{39}Ar$_K$ released. These auxiliary parameters can aid age spectra interpretation and may include radiogenic yield (percent of ^{40}Ar which is not atmospheric), K/Ca (determined from measured K-derived ^{39}Ar and Ca-derived ^{37}Ar) Incremental heating analysis is often effective at revealing complex argon systematics related to excess argon, alteration, contamination, ^{39}Ar recoil, argon loss, etc. Often low-temperature heating steps have low radiogenic yields and apparent ages with relatively high errors due mainly to loosely held, non-radiogenic argon residing on grain surfaces or along grain

boundaries. Alteration may yield dates that are too young, and ^{39}Ar recoil loss may result in dates for very small grains that are too old.

Excess argon ($^{40}Ar_E$) is that component of ^{40}Ar, apart from atmospheric ^{40}Ar, incorporated into samples by processes other than by in site radioactive decay of ^{40}K (McDougall and Harrison, 1999). Early reports of excess argon covered the whole range of minerals and (e.g., Damon and Kulp 1958) and most importantly, fluid inclusions within quartz and fluorite (Rama et al. 1965). More recently, excess argon has come to mean parent-less radiogenic argon incorporated into a mineral during crystallisation, introduced into the mineral lattice by subsequent diffusion or occluded within fluid or melt inclusions within the mineral. One feature of stepped heating samples containing excess argon is the saddle or 'U' shaped Ar–Ar stepped heating release spectrum (e.g., McDougall and Harrison, 1999), commonly associated with low potassium rocks and minerals such as plagioclase, amphibole and clinopyroxene.

The step heating technique has been quite successful in discriminating against low concentrations of homogeneously distributed excess argon (e.g., Renne et al. 1997) which can be plotted on an isochron diagram (e.g., Roddick 1978).

Recoil effects may cause the loss and redistribution of the $^{39}Ar_K$ and $^{37}Ar_{Ca}$ when the fine-grained altered groundmass basaltic samples are irradiated [e.g., Roddick and Koppers et al., 2000]. This can be detected by discordance between the preirradiation and postirradiation K/Ca ratios [Koppers et al., 2000]. For example, if the bulk K/Ca ratios measured during $^{40}Ar/^{39}Ar$ analyses is lower than the K/Ca ratios measured before irradiation, the groundmass samples have lost $^{39}Ar_K$ preferentially over $^{37}Ar_{Ca}$ during sample irradiation and bake-out. Therefore, the discordance in K/Ca ratios could be a useful measure of $^{39}Ar_K$ recoil in groundmass alteration minerals. ^{39}Ar recoil loss during the neutron irradiation to produce ^{39}Ar from ^{39}K. As a result of this process, a portion of the ^{39}Ar produced during the irradiation procedure will be lost from grain margins. While the effects on large grains will be negligible, recoil ^{39}Ar losses from fine-grained, clay-size particles may be significant,

resulting in anomalously old apparent ages. Argon loss, on the other hand, causes data points to move towards higher $^{39}Ar/^{40}Ar$ values because ^{39}Ar, which is produced in the nuclear reactor from ^{39}K, is not affected by Ar loss from the mineral. Hence, Ar loss will lead to younger apparent ages. If the Ar loss is complete, the timing of this event or the end of the Ar loss episode can be determined. However, if the Ar loss is incomplete, the inverse isochron age is geologically meaningless and will yield values between the initial age and the age when the Ar loss stopped (Kuiper, 2002).

NOTES:

Phonolite Samples were irradiated for 1.917 hours in the Cd-lined facility of the OSU TRIGA reactor. Sanidine from the Fish Canyon Tuff was used as the neutron fluence monitor with a reference age of 28.021 ± 0.023 Ma (Kuiper *et al*., 2008).

Nucleogenic production ratios:

$(^{36}Ar/^{37}Ar)_{Ca}$	2.65	± 0.2	$\times 10^{-4}$
$(^{39}Ar/^{37}Ar)_{Ca}$	6.95	± 0.9	$\times 10^{-4}$
$(^{38}Ar/^{37}Ar)_{Ca}$	0.196	± 0.08	$\times 10^{-4}$
$(^{40}Ar/^{39}Ar)_{K}$	7.3	± 9.2	$\times 10^{-4}$
$(^{38}Ar/^{39}Ar)_{K}$	1.22		$\times 10^{-2}$
$(^{36}Ar/^{38}Ar)_{Cl}$	2.63	± 0.02	$\times 10^{2}$
$^{37}Ar/^{39}Ar$ to Ca/K	1.96		

Isotopic constants and decay rates:

$\lambda(^{40}K)$ /yr	5.81	± 0.04	$\times 10^{-11}$
$\lambda\ (^{40}K)$ /yr	4.962	± 0.00043	$\times 10^{-10}$
$\lambda\ (^{37}Ar)$ /yr	1.975		$\times 10^{-2}$
$\lambda\ ^{39}Ar$ /d	7.068		$\times 10^{-6}$
$\lambda\ ^{36}Cl$ /d	6.308		$\times 10^{-9}$
$(^{40}Ar/^{36}Ar)_{Atm}$	295.5	± 0.5	
$(^{40}Ar/^{38}Ar)_{Atm}$	1575	± 2	
$^{40}K/K_{Total}$	0.01167		

Lab ID	Watts	Relative Isotopic Abundances										Derived Results								
												^{39}Ar Mol ¥ 10^{-14}	^{39}Ar % of total	% $(^{36}Ar)_{Ca}$			% $^{40}Ar^{*}$			w/±*J* ±1σ
G14																				
28 EK61		^{40}Ar	±1σ	^{39}Ar	±1σ	^{38}Ar	±1σ	^{37}Ar	±1σ	^{36}Ar	±1σ				Ca/K	±1σ		Age (Ma)	±1σ	
50174-4	8.0	188	0.08	16.9	0.02	0.36	0.01	2.61	0.01	0.35	0.002	0.01	7.4	1.1	1.68	0.006	45.2	30.7	0.26	0.27
50174-5	9.0	208	0.1	35.2	0.03	0.52	0.01	2.38	0.01	0.17	0.002	0.02	15.5	2.1	0.74	0.003	76.6	27.8	0.10	0.12
50174-6	10.0	207	0.11	36	0.03	0.47	0.01	2.03	0.01	0.14	0.001	0.03	16.0	2.1	0.61	0.003	80.1	28.0	0.09	0.10
50174-7	11.0	153	0.08	25.3	0.02	0.36	0.01	1.64	0.01	0.13	0.001	0.02	11.1	1.9	0.71	0.004	75.5	27.9	0.10	0.12
50174-8	12.0	122	0.06	17.9	0.02	0.26	0.01	2.01	0.01	0.14	0.002	0.01	7.9	2.2	1.22	0.006	67.2	28.1	0.18	0.19
50174-9	13.0	94.5	0.05	11.7	0.01	0.17	0.01	1.45	0.01	0.14	0.001	0.01	5.1	1.5	1.35	0.008	56.1	28.0	0.22	0.23
50174-10	14.0	120	0.06	14.6	0.02	0.23	0.00	2.34	0.01	0.19	0.002	0.01	6.4	1.8	1.75	0.007	54.5	27.5	0.26	0.26
50174-11	15.0	119	0.06	11.5	0.01	0.21	0.01	3.53	0.01	0.23	0.001	0.01	5.1	2.2	3.35	0.009	43.4	27.7	0.27	0.28
50174-12	17.0	189	0.1	19.2	0.02	0.41	0.01	28.2	0.02	0.38	0.001	0.01	8.4	10.8	16.1	0.024	46.0	28.0	0.21	0.22
50174-13	19.0	263	0.13	27.2	0.03	0.58	0.01	123	0.01	0.65	0.001	0.02	11.9	27.8	49.4	0.066	46.5	28.0	0.20	0.20
50174-14	25.0	186	0.08	11.8	0.01	0.26	0.01	164	0.13	0.73	0.002	0.01	5.2	33.1	152	0.201	21.4	21.7	0.50	0.50

Lab ID	Watts	Inverse Isochron Data					*J* (X 10^{-3}) ± 1σ = 3.43 ± 0.007
						^{36}Ar/^{39}Ar Er.Corr.	
G14							
28 EK61		^{36}Ar/^{40}Ar	±1σ	^{39}Ar/^{40}Ar	±1σ		
50174-4	8.0	0.002	0.64	0.09	0.14	0.50	
50174-5	9.0	0.002	1.01	0.17	0.14	0.32	
50174-6	10.0	0.002	0.96	0.18	0.14	0.33	
50174-7	11.0	0.002	0.90	0.17	0.14	0.36	
50174-8	12.0	0.001	1.19	0.15	0.14	0.26	
50174-9	13.0	0.002	0.96	0.12	0.15	0.33	
50174-10	14.0	0.002	1.06	0.12	0.15	0.30	
50174-11	15.0	0.002	0.70	0.10	0.15	0.45	
50174-12	17.0	0.002	0.56	0.10	0.16	0.57	
50174-13	19.0	0.002	0.53	0.10	0.15	0.63	
50174-14	25.0	0.003	0.61	0.06	0.14	0.54	

Table D1.1: ^{40}Ar/^{39}Ar step-heating analytical results for *G14 dolerite dyke, Kabdet El Gamel,* in Garian volcanic province.

Lab ID	Watts	Relative Isotopic Abundances										Derived Results									
G32												^{39}Ar Mol ¥ 10^{-14}	^{39}Ar % of total	% (^{36}Ar)$_{Ca}$			% ^{40}Ar*			w/±*J* ±1σ
65 EK63		^{40}Ar	±1σ	^{39}Ar	±1σ	^{38}Ar	±1σ	^{37}Ar	±1σ	^{36}Ar	±1σ				Ca/K	±1σ		Age (Ma)	±1σ	
61190-4	8.0	303	1.77	19.4	0.25	0.7	0.07	0.42	0.05	0.96	0.010	0.01	7.4	1.1	1.68	0.005	45.2	30.7	0.26	0.27
61190-5	9.0	2769	1.33	302	0.11	6	0.01	3.97	0.01	8.35	0.007	0.02	15.5	2.1	0.73	0.003	76.6	27.8	0.10	0.12
61190-6	10.0	2778	1.33	377	0.14	7.06	0.01	10	0.01	8.2	0.008	0.03	16.0	2.1	0.61	0.003	80.1	28.0	0.09	0.10
61190-7	11.0	1702	1.3	316	0.11	5.34	0.01	21.5	0.01	4.87	0.007	0.02	11.1	1.9	0.71	0.004	75.5	27.9	0.10	0.12
61190-8	12.0	894	1.3	269	0.12	3.93	0.01	36.6	0.02	2.49	0.007	0.01	7.9	2.2	1.22	0.006	67.2	28.1	0.18	0.19
61190-9	13.0	554	1.31	238	0.1	3.19	0.00	43.6	0.02	1.55	0.007	0.01	5.1	1.5	1.35	0.008	56.1	28.0	0.22	0.23
61190-10	14.0	374	1.3	174	0.07	2.29	0.00	35.8	0.01	1.08	0.007	0.01	6.4	1.8	1.75	0.007	54.5	27.5	0.26	0.26
61190-11	15.0	277	1.3	115	0.05	1.54	0.00	26.1	0.01	0.84	0.007	0.01	5.1	2.2	3.35	0.009	43.4	27.7	0.27	0.28
61190-12	17.0	341	1.3	97	0.04	1.43	0.00	23	0.01	1.09	0.007	0.01	8.4	10.8	16.1	0.024	46.0	28.0	0.21	0.22
61190-13	19.0	392	1.3	64	0.03	1.17	0.00	16.5	0.01	1.31	0.007	0.02	11.9	27.8	49.4	0.066	46.5	28.0	0.20	0.20
61190-14	25.0	1306	1.35	92	0.04	2.72	0.00	200	0.08	6.29	0.008	0.01	5.2	33.1	152	0.201	21.4	21.7	0.50	0.50
61190-15	30.0	249	1.3	37	0.02	0.65	0.00	42	0.02	1.17	0.007	0.01	5.2	33.1	152	0.201	21.4	21.7	0.50	0.50

Lab ID	Watts	Inverse Isochron Data				
G32						^{36}Ar/^{39}Ar Er.Corr.
65 EK63		^{36}Ar/^{40}Ar	±1σ	^{39}Ar/^{40}Ar	±1σ	
61190-4	8.0	0.002	0.64	0.09	0.14	0.50
61190-5	9.0	0.001	1.01	0.17	0.14	0.32
61190-6	10.0	0.001	0.96	0.18	0.14	0.33
61190-7	11.0	0.001	0.90	0.17	0.14	0.36
61190-8	12.0	0.001	1.19	0.15	0.14	0.27
61190-9	13.0	0.002	0.96	0.12	0.15	0.33
61190-10	14.0	0.002	1.06	0.12	0.15	0.30
61190-11	15.0	0.002	0.70	0.10	0.15	0.45
61190-12	17.0	0.002	0.56	0.10	0.16	0.57
61190-13	19.0	0.002	0.53	0.10	0.15	0.63
61190-14	25.0	0.03	0.61	0.06	0.14	0.54
61190-15	30.0	0.003	0.61	0.06	0.14	0.54

J (X 10^{-3}) ± 1σ = 3.040 ± 0.003

Table D1.2: ^{40}Ar/^{39}Ar step-heating analytical results for *G32B tholeiitic olivine basalt, Wadi Al Waar,* in Garian volcanic province.

Lab ID	Watts	Relative Isotopic Abundances										Derived Results								
G8B												^{39}Ar Mol ¥ 10^{-14}	^{39}Ar % of total	% $(^{36}Ar)_{Ca}$			% $^{40}Ar^{*}$			w/±*J* ±1σ
61 EK63		^{40}Ar	±1σ	^{39}Ar	±1σ	^{38}Ar	±1σ	^{37}Ar	±1σ	^{36}Ar	±1σ				Ca/K	±1σ		Age (Ma)	±1σ	
61197-5	9.0	123.2	1.4	60.2	0.05	0.87	0.01	1.47	0.01	0.25	0.007	0.04	1.2	5.5	1.696	0.007	42.8	4.80	0.23	0.23
61197-6	10.0	280.9	1.3	248	0.08	3.11	0.00	5.12	0	0.26	0.007	0.17	4.9	18.2	1.428	0.001	77.1	4.78	0.06	0.06
61197-7	11.0	637.2	1.3	663	0.25	8	0.01	9.63	0.01	0.32	0.007	0.46	13.2	28.1	1.007	0.001	89.2	4.69	0.02	0.02
61197-8	12.0	896.9	1.3	954	0	14.4	0.01	14.8	0.01	0.39	0.007	0.67	18.9	35.1	1.074	0.001	91.5	4.71	0.02	0.02
61197-9	13.0	907.7	1.3	954	0	15.4	0.01	19	0.01	0.47	0.007	0.67	18.9	38.1	1.382	0.001	90.5	4.72	0.02	0.02
61197-10	14.0	602.3	1.3	614	0.24	7.49	0.01	14.3	0.01	0.38	0.007	0.43	12.2	35.0	1.611	0.001	87.7	4.71	0.02	0.02
61197-11	15.0	294.8	1.3	283	0.11	3.47	0.00	10.7	0.01	0.28	0.007	0.20	5.6	36.3	2.634	0.002	82.1	4.68	0.05	0.05
61197-12	17.0	432	1.3	400	0.17	4.93	0.01	22.4	0.01	0.53	0.007	0.28	7.9	39.7	3.89	0.003	77.9	4.61	0.04	0.04
61197-13	19.0	393.3	1.3	322	0.13	4.09	0.00	39.7	0.01	0.78	0.007	0.23	6.4	47.9	8.572	0.006	69.2	4.64	0.05	0.05
61197-14	25.0	667.8	1.3	350	0.21	4.72	0.00	307	0.17	4.15	0.008	0.25	7.0	69.8	61.05	0.058	44.0	4.7	0.13	0.13
61197-15	30.0	189.2	1.3	107	0.05	1.4	0.00	66.8	0.03	0.96	0.007	0.08	2.1	65.5	43.31	0.033	47.6	4.68	0.16	0.16
61197-16	40.0	187.7	1.3	58.5	0.03	0.82	0.00	36.7	0.02	0.81	0.007	0.04	1.2	42.7	43.58	0.037	26.4	4.70	0.26	0.26
61197-17	50.0	187.8	1.3	21.0	0.02	0.37	0.00	15.7	0.01	0.73	0.007	0.01	0.4	20.4	51.9	0.056	8.1	4.04	0.70	0.70

Lab ID	Watts	Inverse Isochron Data					*J* (X 10^{-3}) ± 1σ = 3.040 ± 0.003
G8B						^{36}Ar/^{39}Ar Er.Corr.	
61 EK63		^{36}Ar/^{40}Ar	±1σ	^{39}Ar/^{40}Ar	±1σ		
61197-5	9.0	0.001	3.24	0.49	1.12	0.35	
61197-6	10.0	0.001	3.30	0.89	0.48	0.16	
61197-7	11.0	0.000	3.12	1.04	0.23	0.12	
61197-8	12.0	0.000	2.79	1.07	0.18	0.13	
61197-9	13.0	0.000	2.49	1.05	0.18	0.14	
61197-10	14.0	0.000	2.86	1.02	0.24	0.13	
61197-11	15.0	0.001	3.99	0.96	0.45	0.13	
61197-12	17.0	0.001	2.30	0.93	0.32	0.19	
61197-13	19.0	0.001	1.83	0.82	0.35	0.25	
61197-14	25.0	0.002	0.91	0.51	0.23	0.46	
61197-15	30.0	0.002	2.33	0.56	0.69	0.32	
61197-16	40.0	0.003	1.73	0.31	0.70	0.43	
61197-17	50.0	0.003	1.48	0.11	0.70	0.50	

Table D1.3: ^{40}Ar/^{39}Ar step-heating analytical results for *G8B olivine basalt from Wadi Qidmu*, in Garian volcanic province.

Lab ID	Watts	Relative Isotopic Abundances										Derived Results								
G15B												^{39}Ar Mol ¥ 10^{-14}	^{39}Ar % of total	% $(^{36}Ar)_{Ca}$			% $^{40}Ar^{*}$			w/±*J* ±1σ
64 EK63		^{40}Ar	±1σ	^{39}Ar	±1σ	^{38}Ar	±1σ	^{37}Ar	±1σ	^{36}Ar	±1σ				Ca/K	±1σ		Age (Ma)	±1σ	
61180-5	9.0	1228	1.3	221	0.09	3.88	0.00	3.98	0	3.59	0.041	0.16	6.1	1.2	1.382	0.002	13.8	4.21	0.32	0.32
61180-6	10.0	1448	1.4	495	0.2	6.93	0.01	11.2	0	3.61	0.007	0.35	13.5	3.2	1.741	0.001	28.1	4.50	0.06	0.06
61180-7	11.0	1249	1.4	592	0.24	7.67	0.01	22.1	0.01	2.79	0.007	0.42	16.2	8.3	2.878	0.002	38.8	4.49	0.04	0.04
61180-8	12.0	854.7	1.3	477	0.18	6.14	0.01	31.1	0.01	1.89	0.007	0.33	13.1	17.2	5.025	0.004	45.2	4.44	0.04	0.04
61180-9	13.0	700.4	1.3	376	0.15	4.98	0.00	38.1	0.01	1.73	0.007	0.26	10.3	23.0	7.812	0.006	43.2	4.42	0.05	0.05
61180-10	14.0	501.1	1.3	245	0.1	3.37	0.00	30.9	0.01	1.35	0.007	0.17	6.7	23.8	9.695	0.007	38.6	4.33	0.07	0.07
61180-11	15.0	494.5	1.3	198	0.08	2.86	0.00	24.8	0.01	1.4	0.007	0.14	5.4	18.5	9.638	0.007	31.1	4.27	0.08	0.08
61180-12	17.0	1774	1.4	394	0.15	6.54	0.01	28.7	0.01	5.2	0.008	0.28	10.8	5.8	5.619	0.004	17.5	4.34	0.10	0.10
61180-13	19.0	1804	1.4	223	0.09	4.28	0.00	29.5	0.01	5.77	0.008	0.16	6.1	5.4	10.24	0.008	9.6	4.29	0.18	0.18
61180-14	25.0	3587	1.7	339	0.13	7.11	0.01	182	0.07	12.9	0.009	0.24	9.3	14.8	41.47	0.030	8.8	5.16	0.25	0.25
61180-15	30.0	444.8	1.3	51.3	0.02	0.98	0.00	31.6	0.01	1.65	0.007	0.04	1.4	20.0	47.54	0.035	11.4	5.51	0.34	0.34
61180-16	40.0	281.6	1.3	24.6	0.01	0.52	0.00	14.6	0.01	1.02	0.007	0.02	0.7	15.0	45.97	0.041	8.2	5.24	0.62	0.62
61180-17	50.0	266.3	1.3	17.6	0.01	0.41	0.00	12.6	0.01	0.98	0.007	0.01	0.5	13.5	55.41	0.056	5.4	4.57	0.87	0.87

Lab ID	Watts	Inverse Isochron Data					*J* (X 10^{-3}) ± 1σ = 3.040 ± 0.003
G15B						^{36}Ar/^{39}Ar Er.Corr.	
64 EK63		^{36}Ar/^{40}Ar	±1σ	^{39}Ar/^{40}Ar	±1σ		
61180-5	9.0	0.003	1.22	0.18	0.15	0.27	
61180-6	10.0	0.002	0.46	0.34	0.14	0.72	
61180-7	11.0	0.002	0.51	0.47	0.15	0.67	
61180-8	12.0	0.002	0.64	0.56	0.19	0.55	
61180-9	13.0	0.002	0.71	0.54	0.21	0.52	
61180-10	14.0	0.002	0.86	0.49	0.28	0.47	
61180-11	15.0	0.002	0.81	0.40	0.28	0.51	
61180-12	17.0	0.003	0.44	0.22	0.13	0.75	
61180-13	19.0	0.003	0.44	0.12	0.13	0.76	
61180-14	25.0	0.003	0.43	0.09	0.11	0.78	
61180-15	30.0	0.003	0.74	0.11	0.31	0.57	
61180-16	40.0	0.003	1.03	0.09	0.47	0.53	
61180-17	50.0	0.003	1.06	0.07	0.50	0.53	

Table D1.4: ^{40}Ar/^{39}Ar step-heating analytical results for *G15B porphyritic tholeiitic basalt, Wadi Hashem,* in Garian volcanic province.

Lab ID	Watts	Relative Isotopic Abundances										Derived Results								
G116B												^{39}Ar Mol ¥ 10^{-14}	^{39}Ar % of total	% $(^{36}Ar)_{Ca}$			% $^{40}Ar^{*}$			w/±*J* ±1σ
66 EK63		^{40}Ar	±1σ	^{39}Ar	±1σ	^{38}Ar	±1σ	^{37}Ar	±1σ	^{36}Ar	±1σ				Ca/K	±1σ		Age (Ma)	±1σ	
61166-5	9.0	1997	1.3	166	0.07	3.86	0.01	2.2	0.01	6.4	0.008	0.12	5.5	0.4	1.149	0.003	4.6	3.04	0.27	0.27
61166-6	10.0	4169	1.8	485	0.19	9.85	0.01	9.3	0.01	12.9	0.008	0.34	16.1	0.8	1.661	0.002	8.1	3.82	0.18	0.18
61166-7	11.0	3153	1.6	564	0.23	9.82	0.01	25.4	0.01	9.29	0.009	0.40	18.7	3.2	3.897	0.003	14.8	4.55	0.11	0.11
61166-8	12.0	1420	1.4	413	0.17	6.25	0.00	38.3	0.01	4.01	0.007	0.29	13.7	11.2	8.051	0.006	25.2	4.76	0.07	0.07
61166-9	13.0	256.9	1.3	90.1	0.04	1.31	0.00	9.92	0.01	0.71	0.007	0.06	3.0	16.4	9.553	0.008	30.7	4.82	0.16	0.16
61166-10	14.0	230.6	1.3	113	0.05	1.55	0.00	15.3	0.01	0.63	0.007	0.08	3.7	28.2	11.70	0.010	41.0	4.60	0.13	0.13
61166-11	15.0	265.6	1.3	160	0.07	2.11	0.00	24.3	0.01	0.75	0.007	0.11	5.3	38.2	13.23	0.011	48.0	4.39	0.09	0.09
61166-12	17.0	384.3	1.3	250	0.11	3.28	0.00	39.3	0.02	1.1	0.007	0.17	8.3	42.1	13.69	0.011	50.6	4.29	0.07	0.07
61166-13	19.0	566.5	1.3	263	0.11	3.83	0.00	35.8	0.01	1.67	0.007	0.18	8.7	25.2	11.80	0.009	34.3	4.06	0.07	0.07
61166-14	25.0	1413	0.4	272	0.11	5.03	0.00	106	0.04	5.34	0.003	0.19	9.0	23.4	34.05	0.025	13.6	3.92	0.13	0.13
61166-15	30.0	859.6	0.2	171	0.07	3.05	0.00	132	0.05	3.99	0.003	0.12	5.7	39.0	67.28	0.048	15.5	4.37	0.17	0.17
61166-16	40.0	362.2	0.1	55.9	0.03	1.01	0.00	37.9	0.02	1.53	0.002	0.04	1.9	29.2	58.82	0.049	10.8	3.92	0.19	0.19
61166-17	50.0	189.2	0.1	18.3	0.01	0.38	0.00	12.3	0.01	0.74	0.002	0.01	0.6	19.6	58.37	0.065	6.3	3.67	0.30	0.30

Lab ID	Watts	Inverse Isochron Data					*J* (X 10^{-3}) ± 1σ = 3.041 ± 0.009
G116B						^{36}Ar/^{39}Ar Er.Corr	
66 EK63		^{36}Ar/^{40}Ar	±1σ	^{39}Ar/^{40}Ar	±1σ		
61166-5	9.0	0.003	0.42	0.08326	0.13	0.7681	
61166-6	10.0	0.003	0.41	0.11640	0.12	0.7879	
61166-7	11.0	0.003	0.42	0.17902	0.12	0.7757	
61166-8	12.0	0.003	0.47	0.29031	0.14	0.7167	
61166-9	13.0	0.002	1.35	0.35010	0.51	0.4312	
61166-10	14.0	0.002	1.68	0.48917	0.57	0.3753	
61166-11	15.0	0.001	1.68	0.59951	0.50	0.3396	
61166-12	17.0	0.002	1.25	0.64724	0.35	0.3663	
61166-13	19.0	0.002	0.75	0.46385	0.25	0.5265	
61166-14	25.0	0.003	0.44	0.19015	0.11	0.7758	
61166-15	30.0	0.003	0.48	0.19455	0.11	0.7554	
61166-16	40.0	0.003	0.48	0.15148	0.11	0.7064	
61166-17	50.0	0.003	0.51	0.09468	0.13	0.6499	

Table D1.5: ^{40}Ar/^{39}Ar step-heating analytical results for *G116B tholeiitic olivine basalt, Wadi Ghan,* in Garian volcanic province.

Lab ID	Watts	Relative Isotopic Abundances										Derived Results								
G9												^{39}Ar Mol ¥ 10^{-14}	^{39}Ar % of total	% (^{36}Ar)$_{Ca}$			% ^{40}Ar*			w/±*J* ±1σ
60 EK63		^{40}Ar	±1σ	^{39}Ar	±1σ	^{38}Ar	±1σ	^{37}Ar	±1σ	^{36}Ar	±1σ				Ca/K	±1σ		Age (Ma)	±1σ	
61178-5	9.0	177.3	1.3	70.6	0.03	1.11	0.00	1.77	0	0.5	0.007	0.05	1.4	3.4	1.743	0.004	19.3	2.65	0.2	0.20
61178-6	10.0	305.3	1.3	218	0.09	2.77	0.00	6.95	0	0.74	0.007	0.15	4.4	8.9	2.219	0.002	34.1	2.62	0.07	0.07
61178-7	11.0	476.2	1.3	667	0.27	7.74	0.00	24.5	0.01	0.75	0.007	0.47	13.4	30.7	2.560	0.002	67.3	2.63	0.02	0.02
61178-8	12.0	611.2	1.3	961	0.35	11.2	0.01	41	0.01	0.85	0.007	0.67	19.3	45.4	2.978	0.002	77.2	2.69	0.02	0.02
61178-9	13.0	579.3	1.3	880	0.36	10.5	0.01	33.6	0.01	0.84	0.007	0.62	17.7	37.9	2.661	0.002	73.1	2.64	0.02	0.02
61178-10	14.0	513.1	1.3	739	0.29	8.92	0.01	26.8	0.01	0.79	0.007	0.52	14.9	32.2	2.533	0.002	68.9	2.62	0.02	0.02
61178-11	15.0	400.9	1.3	497	0.2	6.09	0.00	20.8	0.01	0.74	0.007	0.35	10.0	26.4	2.922	0.002	59.2	2.62	0.03	0.03
61178-12	17.0	548.4	1.3	476	0.19	6.09	0.01	21.2	0.01	1.28	0.007	0.33	9.6	15.6	3.110	0.002	41.1	2.60	0.03	0.03
61178-13	19.0	807.9	1.3	310	0.12	4.38	0.00	21.9	0.01	2.42	0.007	0.22	6.2	8.5	4.933	0.004	18.0	2.58	0.07	0.07
61178-14	25.0	1540	1.4	131	0.05	2.76	0.00	149	0.06	6.35	0.008	0.09	2.6	22.2	79.79	0.059	4.2	2.80	0.34	0.34
61178-17	50.0	250.2	1.3	17.4	0.01	0.39	0.00	17.6	0.01	0.98	0.007	0.01	0.3	17.0	70.78	0.068	2.7	2.19	0.88	0.88

Lab ID	Watts	Inverse Isochron Data				^{36}Ar/^{39}Ar Er.Corr.
G9						
60 EK63		^{36}Ar/^{40}Ar	±1σ	^{39}Ar/^{40}Ar	±1σ	
61178-5	9.0	0.003	1.71	0.39861	0.74	0.4565
61178-6	10.0	0.002	1.20	0.71590	0.44	0.4319
61178-7	11.0	0.001	1.46	1.40231	0.29	0.2827
61178-8	12.0	0.001	1.64	1.57383	0.24	0.2325
61178-9	13.0	0.001	1.46	1.52188	0.25	0.2645
61178-10	14.0	0.001	1.41	1.44276	0.27	0.2848
61178-11	15.0	0.001	1.39	1.24151	0.34	0.3203
61178-12	17.0	0.002	0.81	0.86780	0.26	0.4863
61178-13	19.0	0.003	0.55	0.38319	0.19	0.6539
61178-14	25.0	0.003	0.47	0.08263	0.14	0.7407
61178-17	50.0	0.003	1.10	0.06776	0.53	0.5407

J (X 10^{-3}) ± 1σ = 3.040 ± 0.003

Table D1.6: ^{40}Ar/^{39}Ar step-heating analytical results for *G9 tholeiitic olivine basalt, Wadi Ghan,* in Garian volcanic province.

Lab ID	Watts	Relative Isotopic Abundances										Derived Results								
												^{39}Ar Mol ¥ 10^{-14}	^{39}Ar % of total	% $(^{36}Ar)_{Ca}$			% $^{40}Ar^{*}$			w/±*J* ±1σ
G10B																				
62 EK63		^{40}Ar	±1σ	^{39}Ar	±1σ	^{38}Ar	±1σ	^{37}Ar	±1σ	^{36}Ar	±1σ				Ca/K	±1σ		Age (Ma)	±1σ	
61176-5	9.0	1922	1.4	551	0.22	7.17	0.01	2.11	0	3.35	0.007	0.39	5.4	0.7	0.307	0.000	48.3	9.23	0.055	0.06
61176-6	10.0	1320	1.35	747	0.3	8.93	0.01	3.55	0	0.27	0.007	0.52	7.3	14.2	0.381	0.001	94.7	9.16	0.022	0.02
61176-7	11.0	3175	2.56	954	0.00	25.8	1.6	10.2	0.19	0.3	0.038	0.67	9.3	36.6	0.854	0.016	98.2	17.9	0.069	0.07
61176-8	12.0	6444	2.3	954	0.00	46.2	0.03	16.6	0.01	0.27	0.008	0.67	9.3	67.6	1.393	0.001	99.7	36.6	0.041	0.06
61176-9	13.0	7465	2.56	953	0.00	53.5	0.02	15	0.01	0.19	0.007	0.67	9.3	83.9	1.258	0.001	99.9	42.4	0.046	0.06
61176-10	14.0	6058	1.98	954	0.00	43.5	0.08	8.32	0.01	0.13	0.008	0.67	9.3	68.6	0.699	0.001	99.8	34.5	0.039	0.05
61176-11	15.0	4111	2.47	954	0.00	32.3	1.5	4.05	0.17	0.15	0.035	0.67	9.3	28.8	0.341	0.014	99.3	23.3	0.065	0.07
61176-12	17.0	3611	2.56	954	0.00	28.7	1.6	3.53	0.18	0.22	0.037	0.67	9.3	17.2	0.297	0.015	98.5	20.4	0.068	0.07
61176-13	19.0	2446	1.64	954	0.00	17.7	0.4	2.45	0.05	0.2	0.012	0.67	9.3	13.3	0.206	0.004	97.9	13.7	0.027	0.03
61176-14	25.0	3470	2.56	954	0.00	27.1	1.6	3.84	0.19	0.65	0.038	0.67	9.3	6.4	0.323	0.016	94.8	18.8	0.07	0.07
61176-15	30.0	1191	1.34	659	0.27	7.93	0.01	2.26	0	0.33	0.007	0.46	6.4	7.5	0.275	0.000	92.5	9.14	0.024	0.03
61176-16	40.0	1188	1.34	661	0.27	7.93	0.01	2.69	0	0.3	0.007	0.46	6.5	9.7	0.327	0.000	93.2	9.15	0.024	0.03

Lab ID	Watts	Inverse Isochron Data					*J* (X 10^{-3}) ± 1σ = 3.040 ± 0.003
						^{36}Ar/^{39}Ar Er.Corr.	
G10B							
62 EK63		^{36}Ar/^{40}Ar	±1σ	^{39}Ar/^{40}Ar	±1σ		
61176-5	9.0	0.002	0.46	0.28699	0.13	0.7037	
61176-6	10.0	0.000	3.08	0.56658	0.15	0.1074	
61176-7	11.0	0.000	20.2	0.30075	0.13	0.0161	
61176-8	12.0	0.000	10.2	0.14811	0.11	0.0313	
61176-9	13.0	0.000	40	0.12784	0.11	0.0080	
61176-10	14.0	0.000	25.7	0.15759	0.11	0.0124	
61176-11	15.0	0.000	34	0.23231	0.12	0.0095	
61176-12	17.0	0.000	20.6	0.26449	0.12	0.0158	
61176-13	19.0	0.000	6.80	0.39053	0.12	0.0477	
61176-14	25.0	0.000	6.22	0.27527	0.12	0.0523	
61176-15	30.0	0.000	2.36	0.55448	0.16	0.1416	
61176-16	40.0	0.000	2.62	0.55781	0.16	0.1276	

Table D1.7: ^{40}Ar/^{39}Ar step-heating analytical results *G10B syenogabbro plug, Ras al Moher,* in Garian volcanic province.

Lab ID	Watts	Relative Isotopic Abundances										Derived Results								
G1												^{39}Ar Mol ¥ 10^{-14}	^{39}Ar % of total	% $(^{36}Ar)_{Ca}$			% $^{40}Ar^{*}$			w/±*J* ±1σ
32 EK61		^{40}Ar	±1σ	^{39}Ar	±1σ	^{38}Ar	±1σ	^{37}Ar	±1σ	^{36}Ar	±1σ				Ca/K	±1σ		Age (Ma)	±1σ	
50168-4	8.0	60.14	0.02	10.1	0.01	0.16	0.00	2.09	0.01	0.15	0.002	0.01	3.0	2.2	2.344	0.010	28.0	10.4	0.369	0.37
50168-5	9.0	95.08	0.02	40.7	0.04	0.51	0.00	8.38	0.01	0.1	0.001	0.03	11.9	12.5	2.336	0.004	71.8	10.5	0.046	0.05
50168-6	10.0	145.3	0.07	71.3	0.07	0.89	0.00	14.2	0.02	0.1	0.002	0.05	20.8	20.7	2.258	0.003	82.9	10.5	0.045	0.05
50168-7	11.0	162.3	0.09	80.4	0.08	1.02	0.00	13.3	0.02	0.11	0.002	0.06	23.5	18.7	1.871	0.003	83.7	10.5	0.043	0.05
50168-8	12.0	131.4	0.06	63.0	0.06	0.78	0.00	8.48	0.01	0.1	0.001	0.04	18.4	13.1	1.530	0.003	80.4	10.4	0.04	0.05
50168-9	13.0	83.77	0.04	32.4	0.03	0.41	0.00	5.27	0.01	0.11	0.002	0.02	9.5	7.5	1.850	0.004	64.3	10.4	0.093	0.10
50168-10	14.0	62.65	0.03	16.4	0.01	0.22	0.00	2.11	0.01	0.12	0.001	0.01	4.8	2.7	1.462	0.006	43.9	10.5	0.128	0.13
50168-11	15.0	55.91	0.03	8.27	0.01	0.13	0.00	0.88	0.01	0.15	0.001	0.01	2.4	0.9	1.212	0.012	20.5	8.64	0.307	0.31
50168-12	17.0	84.44	0.04	9.09	0.01	0.16	0.00	1.82	0.01	0.25	0.001	0.01	2.7	1.1	2.280	0.011	14.1	8.17	0.292	0.29
50168-13	19.0	102	0.04	10.6	0.01	0.21	0.00	40	0.03	0.36	0.001	0.01	3.1	16.9	42.88	0.055	12.0	7.33	0.305	0.31

Lab ID	Watts	Inverse Isochron Data				^{36}Ar/^{39}Ar Er.Corr.
G1						
32 EK61		^{36}Ar/^{40}Ar	±1σ	^{39}Ar/^{40}Ar	±1σ	
50168-4	8.0	0.002	1.37	0.16842	0.14	0.2288
50168-5	9.0	0.001	0.97	0.42933	0.14	0.3278
50168-6	10.0	0.001	1.86	0.49251	0.14	0.1716
50168-7	11.0	0.001	1.86	0.49767	0.15	0.1716
50168-8	12.0	0.001	1.35	0.48102	0.14	0.2365
50168-9	13.0	0.001	1.56	0.38762	0.14	0.2036
50168-10	14.0	0.002	0.92	0.26217	0.14	0.3447
50168-11	15.0	0.003	0.90	0.14807	0.16	0.3496
50168-12	17.0	0.003	0.57	0.10777	0.15	0.5525
50168-13	19.0	0.003	0.56	0.10261	0.13	0.5786

J (X 10^{-3}) ± 1σ = 3.466 ± 0.007

Table D1.8: ^{40}Ar/^{39}Ar step-heating analytical results *G1 basanite from 33 km south of Garian,* in Garian volcanic province.

Lab ID	Watts	Relative Isotopic Abundances										Derived Results								
G5												^{39}Ar Mol ¥ 10^{-14}	^{39}Ar % of total	% $(^{36}Ar)_{Ca}$			% $^{40}Ar^{*}$			w/±*J* ±1σ
34 EK61		^{40}Ar	±1σ	^{39}Ar	±1σ	^{38}Ar	±1σ	^{37}Ar	±1σ	^{36}Ar	±1σ				Ca/K	±1σ		Age (Ma)	±1σ	
50166-5	9.0	36.08	0.02	11.1	0.01	0.15	0.00	3.36	0.01	0.1	0.001	0.01	3.5	3.0	1.966	0.005	21.3	4.26	0.243	0.24
50166-6	10.0	47.93	0.04	38.8	0.05	0.45	0.00	9.29	0.01	0.08	0.001	0.03	12.2	10.5	1.563	0.003	56.2	4.28	0.056	0.06
50166-7	11.0	63.81	0.03	66.4	0.05	0.78	0.00	13.9	0.01	0.07	0.001	0.05	20.9	17.5	1.364	0.002	72.9	4.31	0.029	0.03
50166-8	12.0	51.71	0.02	57.2	0.05	0.69	0.00	12.5	0.01	0.05	0.002	0.04	18.0	21.8	1.428	0.002	77.0	4.28	0.059	0.06
50166-9	13.0	56.19	0.02	57.4	0.03	0.7	0.00	16.6	0.01	0.07	0.001	0.04	18.1	20.9	1.893	0.002	70.4	4.24	0.033	0.03
50166-10	14.0	49.13	0.04	45.2	0.04	0.56	0.00	17.2	0.02	0.08	0.002	0.03	14.2	19.9	2.482	0.004	62.7	4.20	0.068	0.07
50166-11	15.0	36.71	0.02	25.1	0.02	0.33	0.00	15.2	0.02	0.08	0.001	0.02	7.9	17.0	3.974	0.006	46.5	4.21	0.092	0.09
50166-12	17.0	40.47	0.02	16.0	0.01	0.22	0.00	15.9	0.02	0.11	0.001	0.01	5.0	12.4	6.490	0.009	26.9	4.23	0.16	0.16

Lab ID	Watts	Inverse Isochron Data					*J* (X 10^{-3}) ± 1σ = 3.441 ± 0.007
G5				.		^{36}Ar/^{39}Ar Er.Corr	
34 EK61		^{36}Ar/^{40}Ar	±1σ	^{39}Ar/^{40}Ar	±1σ		
50166-5	9.0	0.003	1.53	0.30962	0.15	0.2069	
50166-6	10.0	0.002	1.63	0.81495	0.18	0.1972	
50166-7	11.0	0.001	1.72	1.04991	0.14	0.1861	
50166-8	12.0	0.001	4.58	1.11741	0.14	0.0700	
50166-9	13.0	0.001	1.79	1.03055	0.12	0.1802	
50166-10	14.0	0.001	2.66	0.92649	0.16	0.1214	
50166-11	15.0	0.002	1.89	0.68664	0.14	0.1691	
50166-12	17.0	0.003	1.38	0.39571	0.14	0.2304	

Table D1.9: ^{40}Ar/^{39}Ar step-heating analytical results for *G5 basanite lava from 31.5 km east of Garian,* in Garian volcanic province.

Lab ID	Watts	Relative Isotopic Abundances										Derived Results								
G6												^{39}Ar Mol ¥ 10^{-14}	^{39}Ar % of total	% $(^{36}Ar)_{Ca}$			% $^{40}Ar^{*}$			w/±*J* ±1σ
61 EK61		^{40}Ar	±1σ	^{39}Ar	±1σ	^{38}Ar	±1σ	^{37}Ar	±1σ	^{36}Ar	±1σ				Ca/K	±1σ		Age (Ma)	±1σ	
50223-4	8.0	58.62	0.03	7.51	0.01	0.13	0.00	0.67	0.01	0.18	0.002	0.01	1.0	1.0	1.700	0.021	8.6	4.17	0.479	0.48
50223-5	9.0	47.91	0.03	33.5	0.03	0.41	0.00	2.73	0.01	0.09	0.001	0.02	4.7	7.7	1.541	0.005	47.3	4.17	0.081	0.08
50223-6	10.0	103.7	0.03	118	0.1	1.38	0.00	6.99	0.01	0.1	0.002	0.08	16.5	18.6	1.122	0.002	77.3	4.17	0.026	0.03
50223-7	11.0	133.4	0.04	171	0.15	2.05	0.00	7.77	0.01	0.08	0.002	0.12	23.9	25.6	0.860	0.002	87.0	4.15	0.022	0.02
50223-8	12.0	113.6	0.04	146	0.13	1.78	0.00	6.77	0.01	0.07	0.001	0.10	20.3	24.4	0.884	0.002	85.8	4.11	0.016	0.02
50223-9	13.0	74.2	0.02	92.7	0.09	1.13	0.00	6.38	0.01	0.06	0.002	0.06	13.0	28.9	1.307	0.002	83.7	4.11	0.033	0.03
50223-10	14.0	35.97	0.01	42.4	0.04	0.52	0.00	5.29	0.01	0.04	0.002	0.03	5.9	36.9	2.369	0.005	80.6	4.20	0.066	0.07
50223-11	15.0	27.02	0.01	30.1	0.03	0.38	0.00	5.39	0.01	0.04	0.002	0.02	4.2	38.8	3.405	0.007	75.7	4.18	0.093	0.09
50223-12	17.0	47.94	0.01	44.8	0.04	0.58	0.00	9.26	0.01	0.09	0.001	0.03	6.3	26.3	3.927	0.006	58.2	3.84	0.052	0.05
50223-13	19.0	122.5	0.05	29.8	0.03	0.46	0.00	121	0.09	0.68	0.002	0.02	4.2	45.7	77.06	0.097	10.1	2.62	0.16	0.16

Lab ID	Watts	Inverse Isochron Data				^{36}Ar/^{39}Ar Er.Corr.
G6						
61 EK61		^{36}Ar/^{40}Ar	±1σ	^{39}Ar/^{40}Ar	±1σ	
50223-4	8.0	0.003	1.08	0.12835	0.15	0.2922
50223-5	9.0	0.002	1.72	0.70412	0.15	0.1863
50223-6	10.0	0.001	1.97	1.14999	0.13	0.1620
50223-7	11.0	0.000	3.33	1.29952	0.14	0.0961
50223-8	12.0	0.001	2.10	1.29481	0.14	0.1528
50223-9	13.0	0.001	4.02	1.26314	0.14	0.0794
50223-10	14.0	0.001	6.50	1.18974	0.14	0.0489
50223-11	15.0	0.001	6.91	1.12277	0.14	0.0463
50223-12	17.0	0.001	1.86	0.94168	0.13	0.1723
50223-13	19.0	0.003	0.67	0.23780	0.14	0.5048

J (X 10^{-3}) ± 1σ = 3.436 ± 0.007

Table D1.10: ^{40}Ar/^{39}Ar step-heating analytical results *G6 alkali olivine basalt from 35 km northeast of Garian,* in Garian volcanic province.

Lab ID	Watts	Relative Isotopic Abundances										Derived Results								
G2												^{39}Ar Mol ¥ 10^{-14}	^{39}Ar % of total	% $(^{36}Ar)_{Ca}$			% $^{40}Ar^{*}$			w/±*J* ±1σ
30 EK61		^{40}Ar	±1σ	^{39}Ar	±1σ	^{38}Ar	±1σ	^{37}Ar	±1σ	^{36}Ar	±1σ				Ca/K	±1σ		Age (Ma)	±1σ	
50171-4	8.0	64.79	0.02	38.8	0.04	0.56	0.01	6.07	0.01	0.14	0.001	0.03	6.5	6.7	1.882	0.004	36.5	3.68	0.07	0.07
50171-5	9.0	109.3	0.04	121	0.1	1.48	0.01	31.7	0.03	0.16	0.001	0.08	20.1	31.5	3.159	0.004	69.2	3.77	0.02	0.03
50171-6	10.0	118.4	0.05	145	0.12	1.76	0.01	39	0.03	0.16	0.002	0.10	24.2	40.9	3.238	0.004	76.7	3.77	0.02	0.02
50171-7	11.0	89.47	0.04	106	0.09	1.31	0.01	18.2	0.02	0.11	0.001	0.07	17.6	28.1	2.076	0.003	74.5	3.79	0.02	0.02
50171-8	12.0	62.16	0.02	68.5	0.06	0.89	0.01	8.71	0.01	0.08	0.002	0.05	11.4	17.9	1.531	0.003	68.5	3.74	0.05	0.05
50171-9	13.0	57.34	0.02	56.0	0.05	0.78	0.01	6.62	0.01	0.08	0.001	0.04	9.3	12.7	1.423	0.003	61.4	3.78	0.04	0.05
50171-10	14.0	53.97	0.02	43.5	0.04	0.62	0.01	7.05	0.01	0.1	0.002	0.03	7.3	11.4	1.951	0.003	50.5	3.77	0.07	0.07
50171-11	15.0	43.63	0.02	21.2	0.02	0.31	0.01	8.03	0.01	0.12	0.002	0.01	3.5	11.1	4.565	0.008	28.1	3.51	0.19	0.19

Lab ID	Watts	Inverse Isochron Data					*J* (X 10^{-3}) ± 1σ = 3.361 ± 0.007
G2						^{36}Ar/^{39}Ar Er.Corr.	
30 EK61		^{36}Ar/^{40}Ar	±1σ	^{39}Ar/^{40}Ar	±1σ		
50171-4	8.0	0.0021	1.10	0.60147	0.14	0.2884	
50171-5	9.0	0.0010	1.33	1.11374	0.14	0.2425	
50171-6	10.0	0.0008	1.82	1.23524	0.14	0.1778	
50171-7	11.0	0.0009	1.32	1.19313	0.14	0.2449	
50171-8	12.0	0.0011	2.65	1.11191	0.14	0.1202	
50171-9	13.0	0.0013	1.82	0.98448	0.14	0.1756	
50171-10	14.0	0.0017	1.74	0.81227	0.14	0.1829	
50171-11	15.0	0.0024	2.14	0.48704	0.14	0.1474	

Table D1.11: ^{40}Ar/^{39}Ar step-heating analytical results for *G2 basanite lava from 19 km southeast of Garian,* in Garian volcanic province.

Lab ID	Relative Isotopic Abundances										Derived Results							Inverse Isochron Data				
G11											^{39}Ar Mol ¥ 10^{-14}			$\%^{40}Ar^{*}$			w/±*J* ±1σ					$^{36}Ar/^{39}Ar$ Er. Corr.
26 EK62	^{40}Ar	±1σ	^{39}Ar	±1σ	^{38}Ar	±1σ	^{37}Ar	±1σ	^{36}Ar	±1σ		Ca/K	±1σ		Age (Ma)	±1σ		$^{36}Ar/^{40}Ar$	±1σ	$^{39}Ar/^{40}Ar$	±1σ	
50441-3	103.7	0.07	2.16	0.004	0.03	0.002	0.004	0.002	0.02	0.001	0.00	0.144	0.069	93.1	8.156	0.040	0.04	0.00023	5.84	0.02086	0.21	0.0525
50441-4	89.54	0.05	1.94	0.003	0.03	0.002	0.003	0.002	0.01	0.001	0.00	0.125	0.077	97.2	8.170	0.038	0.04	0.00009	14.35	0.02175	0.21	0.0213
50441-5	65.44	0.04	1.4	0.004	0.02	0.002	0.004	0.001	0.01	0.001	0.00	0.203	0.051	95.8	8.176	0.059	0.06	0.00014	15.32	0.02143	0.27	0.0188
50441-6	91.32	0.05	1.95	0.005	0.02	0.001	0.004	0.002	0.01	0.001	0.00	0.134	0.073	96.7	8.269	0.035	0.04	0.00011	9.54	0.02137	0.26	0.0307
50441-7	104	0.06	2.23	0.004	0.03	0.002	0.004	0.001	0.01	0.002	0.00	0.114	0.045	96.1	8.172	0.043	0.04	0.00013	11.86	0.02150	0.20	0.0257
50441-8	28.9	0.01	0.61	0.003	0.01	0.002	0.007	0.002	0.01	0.002	0.00	0.836	0.175	95.1	8.210	0.156	0.16	0.00016	35.69	0.02117	0.47	0.0066
50441-9	60.17	0.03	1.26	0.004	0.02	0.002	0.001	0.002	0.01	0.002	0.00	0.051	0.097	93.3	8.163	0.086	0.09	0.00022	14.16	0.02090	0.30	0.0199
50441-10	33.28	0.01	0.72	0.002	0.01	0.002	0.005	0.001	0.00	0.001	0.00	0.469	0.093	96.2	8.143	0.102	0.10	0.00013	30.54	0.02159	0.34	0.0088
50441-11	31.86	0.01	0.69	0.002	0.01	0.002	0.004	0.002	0.00	0.001	0.00	0.396	0.166	97.2	8.216	0.107	0.11	0.00009	43.99	0.02163	0.36	0.0060
50441-12	80.88	0.04	1.7	0.004	0.03	0.001	0.003	0.002	0.02	0.001	0.00	0.116	0.074	93.3	8.102	0.049	0.05	0.00023	7.68	0.02104	0.24	0.0384
50441-14	72.02	0.04	1.56	0.004	0.02	0.001	0.002	0.002	0.00	0.001	0.00	0.099	0.080	98.2	8.259	0.045	0.05	0.00006	24.82	0.02173	0.27	0.0116
50441-15	83.74	0.04	1.78	0.005	0.02	0.001	0.004	0.002	0.01	0.001	0.00	0.178	0.075	95.0	8.158	0.041	0.04	0.00017	7.86	0.02129	0.29	0.0362
50441-16	49.29	0.02	1.03	0.003	0.01	0.002	0.003	0.002	0.01	0.001	0.00	0.216	0.129	93.5	8.147	0.074	0.07	0.00022	12.10	0.02098	0.34	0.0223
50441-17	58.72	0.02	1.26	0.003	0.01	0.001	0.003	0.001	0.01	0.001	0.00	0.178	0.069	95.4	8.135	0.056	0.06	0.00015	13.22	0.02143	0.25	0.0221
50441-18	64.03	0.03	1.39	0.004	0.02	0.002	0.002	0.001	0.01	0.001	0.00	0.096	0.079	97.7	8.207	0.041	0.04	0.00008	17.80	0.02177	0.29	0.0159
50441-19	70.97	0.03	1.51	0.003	0.03	0.002	0.003	0.001	0.01	0.001	0.00	0.136	0.068	95.6	8.224	0.055	0.06	0.00015	13.44	0.02125	0.25	0.0217
50441-20	57.1	0.03	1.22	0.003	0.02	0.001	0.002	0.001	0.01	0.001	0.00	0.117	0.084	95.6	8.187	0.054	0.05	0.00015	12.99	0.02134	0.28	0.0220
50441-21	38.22	0.01	0.79	0.003	0.01	0.002	0.006	0.002	0.01	0.001	0.00	0.543	0.168	93.0	8.166	0.081	0.08	0.00023	12.28	0.02082	0.34	0.0218
50441-22	50.98	0.02	1.12	0.002	0.01	0.002	0.002	0.002	0.00	0.001	0.00	0.121	0.154	98.5	8.189	0.051	0.05	0.00005	37.03	0.02198	0.24	0.0079
50441-23	70.35	0.02	1.55	0.004	0.02	0.002	0.003	0.002	0.01	0.002	0.00	0.128	0.082	97.9	8.117	0.057	0.06	0.00007	29.62	0.02204	0.25	0.0098
50441-24	58.59	0.03	1.25	0.003	0.02	0.002	0.004	0.002	0.01	0.001	0.00	0.271	0.101	95.6	8.207	0.062	0.06	0.00015	14.96	0.02129	0.29	0.0190
50441-25	37.4	0.01	0.8	0.004	0.02	0.002	0.003	0.002	0.00	0.001	0.00	0.252	0.177	96.8	8.259	0.080	0.08	0.00011	25.24	0.02143	0.51	0.0090
50441-26	39.01	0.02	0.81	0.003	0.01	0.002	0.004	0.002	0.01	0.001	0.00	0.425	0.145	93.5	8.182	0.091	0.09	0.00022	15.29	0.02089	0.34	0.0177

Table D1.12: $^{40}Ar/^{39}Ar$ laser step-heating analytical results for *Phonolite plug from Kaf Bu Rshadah (G11)*, in Garian volcanic province.

Lab ID	Relative Isotopic Abundances										Derived Results							Inverse Isochron Data				
G12											^{39}Ar Mol ¥ 10^{-14}			%^{40}Ar*			w/±*J* ±1σ					^{36}Ar/^{39}Ar Er. Corr.
27 EK62	^{40}Ar	±1σ	^{39}Ar	±1σ	^{38}Ar	±1σ	^{37}Ar	±1σ	^{36}Ar	±1σ		Ca/K	±1σ		Age (Ma)	±1σ		^{36}Ar/^{40}Ar	±1σ	^{39}Ar/^{40}Ar	±1σ	
50442-1	104.3	0.08	2.11	0.004	0.03	0.002	0.006	0.002	0.04	0.001	0.00	0.215	0.061	90.0	8.187	0.033	0.03	0.00033	2.87	0.02024	0.22	0.1070
50442-2	106.4	0.08	1.96	0.004	0.03	0.002	0.005	0.002	0.07	0.001	0.00	0.201	0.069	81.9	8.185	0.044	0.05	0.00061	2.10	0.01842	0.24	0.1429
50442-3	125	0.09	2.35	0.005	0.05	0.002	0.010	0.002	0.07	0.002	0.00	0.323	0.066	82.7	8.077	0.051	0.05	0.00058	2.76	0.01884	0.23	0.1096
50442-4	131.8	0.09	2.26	0.005	0.05	0.002	0.003	0.002	0.10	0.002	0.00	0.098	0.063	76.5	8.213	0.045	0.05	0.00079	1.51	0.01714	0.24	0.1993
50442-7	98.87	0.05	1.92	0.004	0.03	0.002	0.001	0.002	0.05	0.001	0.00	0.043	0.082	86.5	8.211	0.047	0.05	0.00045	3.20	0.01939	0.25	0.0920
50442-8	76.53	0.04	1.35	0.003	0.03	0.001	0.010	0.002	0.06	0.002	0.00	0.561	0.106	78.8	8.214	0.070	0.07	0.00071	2.98	0.01765	0.25	0.0986
50442-11	93.6	0.06	1.70	0.004	0.03	0.001	0.006	0.002	0.06	0.002	0.00	0.300	0.092	80.5	8.170	0.060	0.06	0.00065	2.81	0.01815	0.24	0.1060
50442-13	67.07	0.03	1.40	0.004	0.02	0.002	0.004	0.002	0.02	0.002	0.00	0.206	0.097	93.0	8.174	0.077	0.08	0.00023	12.05	0.02095	0.27	0.0238
50442-14	141.1	0.07	2.38	0.004	0.05	0.002	0.003	0.002	0.12	0.002	0.00	0.114	0.075	75.1	8.198	0.044	0.04	0.00083	1.42	0.01686	0.20	0.2152
50442-15	90.41	0.06	1.75	0.005	0.03	0.002	0.004	0.002	0.04	0.001	0.00	0.168	0.082	85.4	8.127	0.047	0.05	0.00049	2.83	0.01934	0.29	0.1014
50442-16	101.6	0.08	1.96	0.004	0.03	0.001	0.004	0.002	0.05	0.002	0.00	0.154	0.080	85.8	8.185	0.055	0.06	0.00048	3.74	0.01930	0.23	0.0809
50442-17	86.3	0.05	1.78	0.003	0.03	0.002	0.010	0.002	0.03	0.002	0.00	0.431	0.092	91.3	8.153	0.051	0.05	0.00029	6.00	0.02061	0.22	0.0501
50442-18	63.84	0.03	1.44	0.004	0.02	0.001	0.004	0.002	0.00	0.001	0.00	0.242	0.091	99.3	8.084	0.055	0.06	0.00002	84.01	0.02261	0.27	0.0034
50442-21	69.09	0.04	1.42	0.004	0.02	0.002	0.002	0.002	0.02	0.001	0.00	0.095	0.097	91.6	8.214	0.051	0.05	0.00028	5.93	0.02053	0.28	0.0484
50442-22	48.5	0.03	1.06	0.004	0.01	0.002	0.001	0.002	0.01	0.001	0.00	0.102	0.129	95.8	8.070	0.079	0.08	0.00014	20.87	0.02186	0.35	0.0128
50442-24	75.11	0.04	1.13	0.003	0.03	0.001	0.003	0.002	0.08	0.002	0.00	0.232	0.122	67.1	8.225	0.085	0.08	0.00110	1.98	0.01501	0.28	0.1446
50442-25	44.15	0.02	0.94	0.003	0.01	0.002	0.001	0.002	0.01	0.002	0.00	0.067	0.198	93.5	8.088	0.109	0.11	0.00022	18.53	0.02127	0.36	0.0143

Table D1.13: ^{40}Ar/^{39}Ar laser step-heating analytical results for *Phonolite plug from Kaf Tunat (G12),* in Garian volcanic province.

Lab ID	Relative Isotopic Abundances										Derived Results							Inverse Isochron Data				
G8											^{39}Ar Mol ¥ 10^{-14}			$\%^{40}Ar^{*}$			w/±*J* ±1σ					$^{36}Ar/^{39}Ar$ Er. Corr.
23 EK62	^{40}Ar	±1σ	^{39}Ar	±1σ	^{38}Ar	±1σ	^{37}Ar	±1σ	^{36}Ar	±1σ		Ca/K	±1σ		Age (Ma)	±1σ		$^{36}Ar/^{40}Ar$	±1σ	$^{39}Ar/^{40}Ar$	±1σ	
50434-3	65.69	0.03	1.39	0.003	0.02	0.002	0.002	0.002	0.02	0.001	0.00	0.222	0.160	93.2	8.029	0.059	0.06	0.00023	9.40	0.02118	0.26	0.0309
50434-4	54.76	0.03	1.20	0.003	0.01	0.002	0.005	0.001	0.00	0.002	0.00	0.536	0.165	97.9	8.114	0.081	0.08	0.00007	44.90	0.02201	0.27	0.0064
50434-6	56.93	0.03	1.27	0.003	0.02	0.002	0.002	0.002	0.00	0.002	0.00	0.214	0.185	99.6	8.156	0.071	0.07	0.00001	190.58	0.02227	0.30	0.0015
50434-7	92.2	0.07	1.98	0.004	0.02	0.002	0.003	0.001	0.01	0.002	0.00	0.207	0.089	96.1	8.158	0.048	0.05	0.00013	12.85	0.02148	0.26	0.0231
50434-10	51.95	0.03	1.16	0.003	0.02	0.002	0.006	0.001	0.00	0.002	0.00	0.677	0.152	99.6	8.118	0.081	0.08	0.00001	269.24	0.02239	0.31	0.0010
50434-13	83.02	0.05	1.75	0.003	0.03	0.002	0.002	0.001	0.01	0.001	0.00	0.171	0.101	94.9	8.207	0.050	0.05	0.00017	10.36	0.02108	0.22	0.0292
50434-17	91.75	0.05	1.92	0.004	0.03	0.002	0.004	0.002	0.02	0.002	0.00	0.255	0.123	92.9	8.106	0.051	0.05	0.00024	7.57	0.02090	0.25	0.0391
50434-18	47.85	0.03	1.08	0.002	0.01	0.002	0.000	0.002	0.00	0.002	0.00	0.000	0.207	101	8.104	0.085	0.09	0.00000	0.00	0.02262	0.24	0.0014
50434-19	68.3	0.04	1.43	0.003	0.02	0.002	0.003	0.002	0.01	0.001	0.00	0.242	0.157	92.5	8.068	0.060	0.06	0.00025	8.69	0.02092	0.23	0.0343
50434-21	44.69	0.02	1.01	0.002	0.01	0.002	0.003	0.002	0.00	0.002	0.00	0.331	0.246	101	8.144	0.091	0.09	0.00000	0.00	0.02259	0.25	0.0022
50434-22	61.51	0.04	1.35	0.003	0.02	0.002	0.000	0.002	0.00	0.002	0.00	0.022	0.203	98.7	8.215	0.077	0.08	0.00004	67.58	0.02191	0.27	0.0043
50434-24	72.63	0.04	1.57	0.003	0.02	0.002	0.005	0.001	0.01	0.002	0.00	0.460	0.112	97.9	8.244	0.063	0.06	0.00007	33.16	0.02165	0.23	0.0090
50434-25	56.42	0.03	1.22	0.003	0.01	0.001	0.004	0.002	0.01	0.002	0.00	0.438	0.224	96.2	8.124	0.078	0.08	0.00013	23.14	0.02161	0.30	0.0122
50434-26	41.94	0.02	0.94	0.003	0.01	0.002	0.008	0.001	0.00	0.001	0.00	1.188	0.213	100	8.149	0.090	0.09	0.00000	0.00	0.02239	0.33	0.0001
50434-27	44.03	0.02	0.97	0.003	0.01	0.001	0.004	0.002	0.00	0.002	0.00	0.536	0.268	97.7	8.063	0.096	0.10	0.00008	48.64	0.02210	0.33	0.0056
50434-28	43.72	0.02	0.95	0.003	0.01	0.001	0.004	0.002	0.01	0.002	0.00	0.600	0.249	95.7	8.044	0.093	0.09	0.00015	24.59	0.02169	0.32	0.0113
50434-31	51.77	0.02	1.13	0.003	0.01	0.001	0.001	0.002	0.01	0.002	0.00	0.133	0.199	97.0	8.120	0.087	0.09	0.00010	33.10	0.02178	0.29	0.0085
50434-33	46.92	0.02	1.04	0.002	0.01	0.002	0.006	0.002	0.00	0.002	0.00	0.731	0.228	99.3	8.191	0.102	0.10	0.00002	185.96	0.02212	0.26	0.0016
50434-34	75.11	0.04	1.13	0.003	0.03	0.001	0.003	0.002	0.08	0.002	0.00	0.232	0.122	67.1	8.225	0.085	0.08	0.00110	1.98	0.01501	0.28	0.1446
50434-35	44.15	0.02	0.94	0.003	0.01	0.002	0.001	0.002	0.01	0.002	0.00	0.067	0.198	93.5	8.088	0.109	0.11	0.00022	18.53	0.02127	0.36	0.0143

Table D1.14: $^{40}Ar/^{39}Ar$ laser step-heating analytical results *Phonolite plug from 35 km northeast of Garian (G8),* in Garian volcanic province.

Lab ID	Relative Isotopic Abundances										Derived Results							Inverse Isochron Data				
G10											^{39}Ar Mol ¥ 10^{-14}			%^{40}Ar*			w/±*J* ±1σ					^{36}Ar/^{39}Ar Er. Corr.
25 EK62	^{40}Ar	±1σ	^{39}Ar	±1σ	^{38}Ar	±1σ	^{37}Ar	±1σ	^{36}Ar	±1σ		Ca/K	±1σ		Age (Ma)	±1σ		^{36}Ar/^{40}Ar	±1σ	^{39}Ar/^{40}Ar	±1σ	
50436-1	131	0.08	2.87	0.004	0.04	0.002	0.008	0.002	0.01	0.001	0.00	0.181	0.051	97.0	8.154	0.030	0.03	0.00010	10.22	0.02190	0.17	0.0307
50436-2	119.3	0.09	2.49	0.004	0.04	0.002	0.005	0.002	0.04	0.002	0.00	0.133	0.048	91.1	8.047	0.040	0.04	0.00030	4.59	0.02085	0.20	0.0674
50436-3	106.5	0.08	2.36	0.004	0.04	0.002	2.000	0.002	0.01	0.002	0.00	0.001	0.059	97.1	8.063	0.042	0.04	0.00010	15.64	0.02217	0.22	0.0196
50436-4	122.5	0.09	2.60	0.004	0.04	0.001	0.007	0.002	0.02	0.001	0.00	0.175	0.048	95.8	8.169	0.033	0.03	0.00014	7.80	0.02159	0.20	0.0398
50436-5	98.55	0.06	2.20	0.004	0.03	0.002	0.002	0.002	0.01	0.002	0.00	0.051	0.057	98.5	8.111	0.043	0.04	0.00005	30.25	0.02235	0.23	0.0099
50436-6	117.4	0.08	2.46	0.005	0.04	0.002	0.004	0.002	0.04	0.002	0.00	0.117	0.056	91.2	8.004	0.040	0.04	0.00030	4.43	0.02098	0.24	0.0677
50436-7	100.3	0.06	2.09	0.003	0.03	0.002	0.006	0.002	0.03	0.001	0.00	0.200	0.057	91.8	8.103	0.042	0.04	0.00027	5.24	0.02086	0.20	0.0585
50436-8	103.2	0.07	2.25	0.005	0.03	0.002	0.003	0.002	0.02	0.002	0.00	0.081	0.062	95.5	8.060	0.053	0.05	0.00015	12.75	0.02181	0.25	0.0234
50436-9	116.1	0.08	2.56	0.005	0.03	0.002	0.003	0.001	0.01	0.002	0.00	0.083	0.039	97.3	8.109	0.043	0.04	0.00009	17.46	0.02210	0.22	0.0175
50436-10	93.75	0.05	2.10	0.004	0.03	0.002	0.003	0.002	0.01	0.001	0.00	0.111	0.054	98.2	8.063	0.041	0.04	0.00006	25.48	0.02243	0.21	0.0120
50436-12	69.99	0.04	1.54	0.004	0.02	0.002	0.003	0.002	0.01	0.001	0.00	0.153	0.075	97.1	8.096	0.056	0.06	0.00010	21.36	0.02209	0.27	0.0136
50436-13	107.8	0.07	2.41	0.005	0.03	0.002	0.005	0.002	0.01	0.001	0.00	0.129	0.053	98.7	8.108	0.036	0.04	0.00004	28.18	0.02241	0.22	0.0107
50436-14	75.23	0.04	1.64	0.004	0.03	0.001	0.004	0.002	0.01	0.002	0.00	0.180	0.086	95.7	8.054	0.059	0.06	0.00014	14.97	0.02188	0.27	0.0192
50436-15	102.6	0.07	2.26	0.005	0.03	0.001	0.006	0.001	0.01	0.001	0.00	0.180	0.043	98.0	8.182	0.040	0.04	0.00007	21.15	0.02206	0.24	0.0142
50436-16	49.45	0.03	1.06	0.002	0.02	0.002	0.004	0.001	0.01	0.002	0.00	0.251	0.091	94.0	8.080	0.082	0.08	0.00020	15.52	0.02143	0.23	0.0192
50436-17	54.7	0.03	1.07	0.003	0.01	0.002	0.001	0.002	0.03	0.002	0.00	0.081	0.132	86.5	8.147	0.096	0.10	0.00045	7.33	0.01955	0.26	0.0395
50436-18	77.9	0.05	1.74	0.002	0.02	0.002	0.002	0.001	0.00	0.001	0.00	0.069	0.052	98.3	8.090	0.045	0.05	0.00006	31.34	0.02239	0.18	0.0099
50436-19	44.46	0.02	0.98	0.003	0.01	0.002	0.003	0.002	0.01	0.002	0.00	0.248	0.140	96.2	8.051	0.096	0.10	0.00013	28.71	0.02200	0.37	0.0091
50436-20	89.18	0.05	1.97	0.004	0.02	0.002	0.004	0.002	0.01	0.002	0.00	0.158	0.060	97.0	8.073	0.051	0.05	0.00010	18.89	0.02212	0.22	0.0159
50436-21	85.53	0.05	1.89	0.002	0.03	0.001	0.002	0.001	0.01	0.001	0.00	0.072	0.049	97.8	8.135	0.036	0.04	0.00007	18.27	0.02215	0.17	0.0171
50436-22	81.16	0.04	1.79	0.003	0.02	0.002	0.006	0.002	0.01	0.001	0.00	0.237	0.069	98.0	8.170	0.045	0.05	0.00007	25.35	0.02210	0.22	0.0118
50436-23	69.91	0.04	1.47	0.003	0.02	0.002	0.000	0.002	0.02	0.001	0.00	0.015	0.111	92.3	8.060	0.047	0.05	0.00026	6.38	0.02109	0.24	0.0465
50436-24	113.3	0.09	2.16	0.005	0.03	0.002	0.004	0.002	0.06	0.001	0.00	0.120	0.067	84.2	8.136	0.042	0.04	0.00053	2.29	0.01906	0.24	0.1315
50436-25	103.6	0.06	2.18	0.003	0.03	0.002	0.004	0.002	0.03	0.002	0.00	0.128	0.054	92.7	8.102	0.051	0.05	0.00025	7.50	0.02106	0.19	0.0412
50436-26	77.37	0.04	1.44	0.002	0.03	0.002	0.006	0.001	0.05	0.002	0.00	0.277	0.060	82.2	8.114	0.061	0.06	0.00060	3.35	0.01866	0.20	0.0909
50436-27	42.46	0.02	0.90	0.003	0.01	0.002	0.005	0.002	0.01	0.001	0.00	0.356	0.153	93.9	8.193	0.093	0.09	0.00020	16.59	0.02110	0.34	0.0164

Table D1.15: ^{40}Ar/^{39}Ar laser step-heating analytical results for *Phonolite laccolith from Kaf Abu Ghannush (G10),* in Garian volcanic province.

APPENDIX E

Libyan Cenozoic volcanic provinces (Jabal al Hasawinah, Jabal as Sawda and Al Haruj al Aswad)

E1 Sample location and description

In 2010 I have collected 29 basalt samples from Libyan Cenozoic volcanism (Jabal al Hasawinah (6 samples), Jabal as Sawda (7 samples) and Al Haruj al Aswad (16 samples)). Sample selection is based on geological history and an availability of outcrops. Great care was taken to collect the freshest possible samples in the field (Tables E.1, E.2 and E.3).

E1.1 Jabal al Hasawinah province

The Jabal al Hasawinah province is the smallest (~1000 km^2) and least studied Cenozoic volcanism in west central Libya. A volcanic field comprises tholodids, dikes and cones of phonolite, trachyte and basalt (Busrewil and Oun, 1991). The difficult terrain and inaccessibility of some parts of Jabal al Hasawinah have discouraged any detailed study of volcanics. Morphologically, the basaltic rocks can be divided into basaltic cones, lava flows and dikes, based on field observations. The dikes radially dissect the cores of the two domes, while the cones are scattered over the area showing no distinct relationship to the updoming. The location of all samples is reported in Figure E1 and Table E1.

E1.1.1 Sample H1 (245 km north of Sebha)

This rock sampled from middle part of plug (Figure E1.1) large circular outcrop occurs at about 245 km north of Sebha closed to the Sebha-Hun Road. This cone occurs as a plug of limited in length (a few hundreds of meters) and display the horizontal jointed. This rock, in hand specimen, is very dark gray in color, compact and occasionally contains vesicles. It is medium to fine grained.

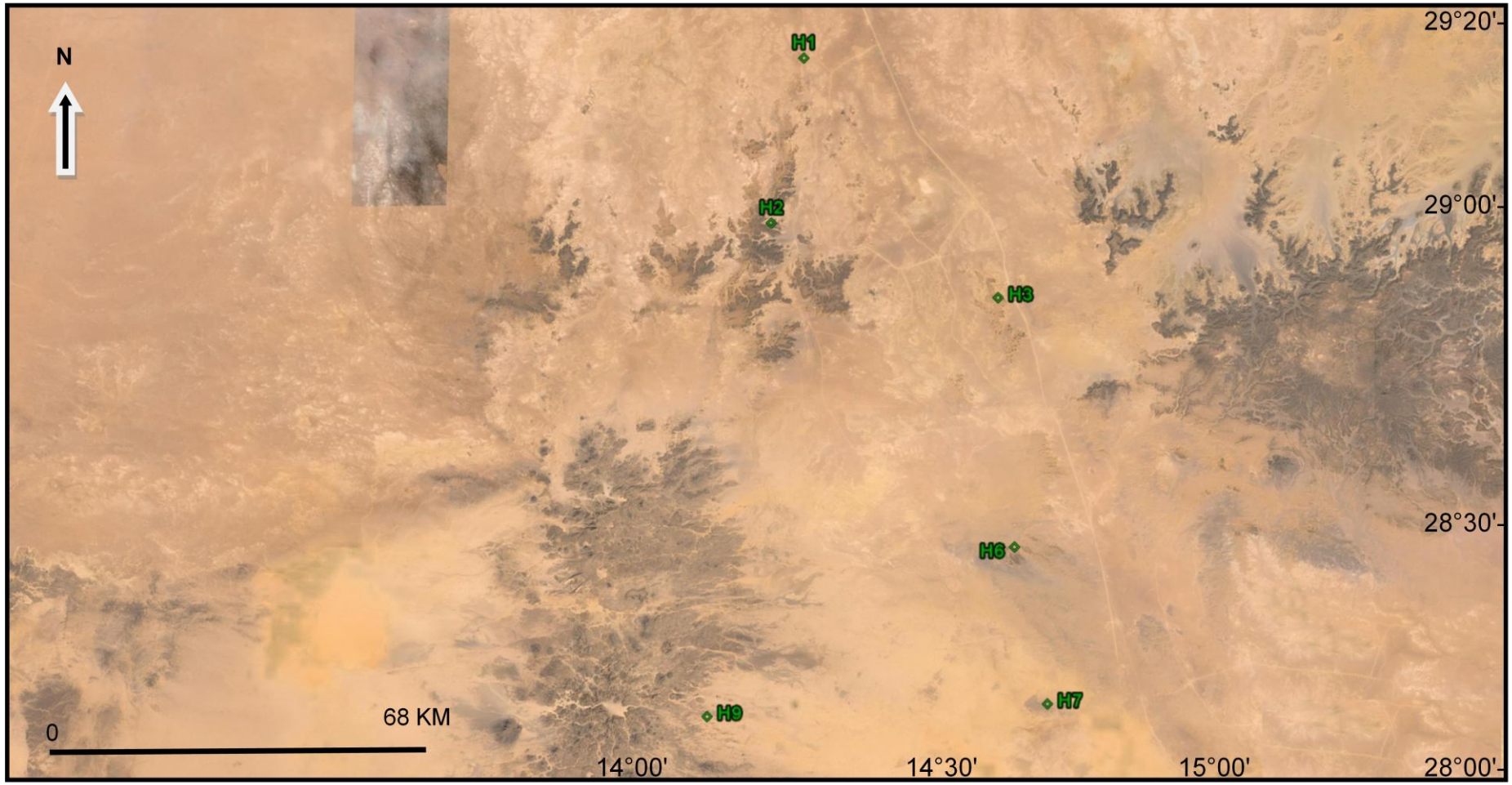

Figure E1: satellite image (Google Earth Pro4) for the area covering the Jabal al Hasawinah and west part of Jabal as Sawda volcanic provinces showing the location of six samples used in this study.

Figure E1.1 show the outcrop of samples H1 in occur in large plug 245 km north of Sebha closed to the Sebha-Hun Road.

E1.1.2 Sample H2 (235 km north of Sebha)

This rock sampled from upper part of lava flow (235 km N of Sebha) closed to the Sebha-Hun Road. This outcrop is vast in length (Figure E1.2). This rock is massive, dark black in color and medium to fine grained.

Figure E1.2 show the outcrop of samples no H2 in occur in length lava, 235 km north of Sebha, closed to the Sebha-Hun Road**.**

E1.1.3 Sample H3 (207 km northeast of Sebha)

This rock sampled from middle part of flow outcrop occurs in the small Wadi 207 km northeast of Sebha. This flow occurs of limited in length (~ 6 meters). This rock, in hand specimen, is dark gray in color. It is coarse grained.

E1.1.4 Sample H6 (164 km northeast of Sebha)

This rock sampled from lower part of lava flow (164 km northeast of Sebha) closed to the Sebha-Hun Road. This outcrop is vast in length. This rock is massive, dark black in color and fine grained.

E1.1.5 Sample H7 (144 km northeast of Sebha)

This rock sampled from middle part of small plug outcrop occurs at about 144 km northeast of Sebha. This plug occurs in limited length of about a few tens of meters (Figure E1.3). The hand specimen is black in color. It is medium grained.

E1.1.6 Sample H9 (126 km northwest of Sebha)

This rock sampled from middle part of lava flow (126 km northwest of Sebha) closed to the main part of Jabal al Hasawinah volcanism. This outcrop is vast in length. This rock is dark gray in color, compact and occasionally contains vesicles. It is medium-fine grained.

Figure E1.3 show the outcrop of samples H7 in occurs in small plug at 144 km north of Sebha closed to the Sebha-Hun Road.

Table E1: Details of basalt samples from Jabal al Hasawinah volcanic province.

Sample	Rock type	Rock	Location	Latitude and longitude
H1	Alkali basalt	plug	245 km north of Sebha	29°13'105"N 14°17'547"E
H2	Basanite	lava	215 km north of Sebha	28°57'244"N 14°14'135"E
H3	Basanite	lava	200 km northeast of Sebha	28°50'300"N 14°39'240"E
H6	Basanite	lava	158 km northeast of Sebha	28°26'465"N 14°41'492"E
H7	Basanite	plug	130 km northeast of Sebha	28°11'430"N 14°45'000"E
H9	Basanite	lava	129 km northwest of Sebha	28°09'866"N 14°07'654"E

Lab ID	Watts	Relative Isotopic Abundances										Derived Results								
H7												^{39}Ar Mol ¥ 10^{-14}	^{39}Ar % of total	% (^{36}Ar)$_{Ca}$			% ^{40}Ar*			w/±*J* ±1σ
59 EK61		^{40}Ar	±1σ	^{39}Ar	±1σ	^{38}Ar	±1σ	^{37}Ar	±1σ	^{36}Ar	±1σ				Ca/K	±1σ		Age (Ma)	±1σ	
50226-4	8.0	127.7	0.05	15.8	0.02	0.29	0.00	2.11	0.01	0.25	0.002	0.01	3.2	1.3	1.545	0.007	43.2	23.5	0.262	0.27
50226-5	9.0	215.4	0.10	47.6	0.04	0.64	0.00	5.28	0.01	0.21	0.001	0.03	9.5	4.0	1.286	0.003	72.2	22.0	0.079	0.09
50226-6	10.0	300.1	0.15	84.7	0.07	1.04	0.00	11.0	0.01	0.18	0.001	0.06	16.9	9.3	1.500	0.002	83.3	19.9	0.053	0.07
50226-7	11.0	311.5	0.15	92.6	0.08	1.14	0.00	11.0	0.01	0.15	0.002	0.06	18.5	11.8	1.376	0.002	87.6	19.8	0.049	0.06
50226-8	12.0	259.5	0.13	76.3	0.06	0.95	0.00	9.80	0.01	0.13	0.001	0.05	15.2	11.7	1.488	0.002	86.6	19.8	0.046	0.06
50226-9	13.0	194.7	0.09	52.7	0.04	0.67	0.00	9.15	0.01	0.14	0.001	0.04	10.5	9.9	2.011	0.003	80.0	19.9	0.067	0.08
50226-10	14.0	142.3	0.07	36.3	0.03	0.47	0.00	7.95	0.01	0.13	0.001	0.03	7.2	9.5	2.539	0.004	75.1	19.8	0.084	0.09
50226-11	15.0	135.7	0.06	30.9	0.03	0.42	0.00	6.95	0.01	0.16	0.001	0.02	6.2	6.7	2.605	0.005	66.6	19.7	0.095	0.10
50226-12	17.0	200.8	0.10	40.2	0.04	0.56	0.00	11.0	0.01	0.3	0.002	0.03	8.0	5.8	3.163	0.005	58.3	19.6	0.113	0.12
50226-13	19.0	179.8	0.10	23.5	0.02	0.38	0.00	30.0	0.03	0.43	0.001	0.02	4.7	10.9	14.82	0.020	36.2	18.7	0.184	0.19

Lab ID	Watts	Inverse Isochron Data				^{36}Ar/^{39}Ar Er.Corr.
H7						
59 EK61		^{36}Ar/^{40}Ar	±1σ	^{39}Ar/^{40}Ar	±1σ	
50226-4	8.0	0.002	0.81	0.12376	0.15	0.3897
50226-5	9.0	0.001	0.73	0.22122	0.14	0.4393
50226-6	10.0	0.001	0.93	0.28298	0.14	0.3421
50226-7	11.0	0.000	1.24	0.29802	0.14	0.2575
50226-8	12.0	0.001	0.96	0.2471	0.14	0.3343
50226-9	13.0	0.001	1.08	0.27124	0.14	0.2950
50226-10	14.0	0.001	1.10	0.25541	0.14	0.2907
50226-11	15.0	0.001	0.83	0.22817	0.14	0.3813
50226-12	17.0	0.001	0.70	0.20037	0.15	0.4530
50226-13	19.0	0.002	0.51	0.13012	0.14	0.6426

J (X 10^{-3}) ± 1σ = 3.750 ± 0.008

Table E2: ^{40}Ar/^{39}Ar step-heating analytical results for *H7 basalt plug from 144 km northeast of Sebha,* in Jabal al Hasawinah .

Lab ID	Watts	Relative Isotopic Abundances										Derived Results								
H9												^{39}Ar Mol ¥ 10^{-14}	^{39}Ar % of total	% $(^{36}Ar)_{Ca}$			% $^{40}Ar^{*}$		w/±*J* ±1σ
24 EK61		^{40}Ar	±1σ	^{39}Ar	±1σ	^{38}Ar	±1σ	^{37}Ar	±1σ	^{36}Ar	±1σ				Ca/K	±1σ		Age (Ma)	±1σ	
50179-4	8.0	84.11	0.01	12.5	0.01	0.23	0.01	2.07	0.01	0.16	0.001	0.01	1.9	2.0	1.835	0.008	45.1	19.1	0.188	0.19
50179-5	9.0	185.9	0.23	52.1	0.04	0.75	0.01	7.96	0.01	0.15	0.002	0.04	7.8	7.9	1.700	0.003	77.8	17.5	0.075	0.08
50179-6	10.0	296.3	0.16	99.5	0.09	1.24	0.01	15.7	0.01	0.16	0.001	0.07	15.0	15.2	1.760	0.002	86.7	16.3	0.041	0.05
50179-7	11.0	360.8	0.2	125	0.11	1.55	0.01	21.0	0.02	0.16	0.002	0.09	18.8	19.9	1.870	0.003	89.5	16.3	0.039	0.05
50179-8	12.0	293.9	0.15	100	0.09	1.26	0.01	17.0	0.02	0.15	0.002	0.07	15.0	17.5	1.893	0.003	87.7	16.2	0.044	0.05
50179-9	13.0	220.5	0.11	70.2	0.06	0.9	0.01	15.2	0.01	0.15	0.002	0.05	10.6	15.0	2.410	0.003	82.4	16.3	0.054	0.06
50179-10	14.0	171.1	0.08	47.7	0.04	0.63	0.01	12.7	0.01	0.18	0.001	0.03	7.2	10.6	2.958	0.004	72.0	16.3	0.072	0.08
50179-11	15.0	154.9	0.08	39.4	0.04	0.53	0.01	10.6	0.01	0.19	0.001	0.03	5.9	8.2	3.010	0.005	65.5	16.2	0.069	0.08
50179-12	17.0	191.3	0.09	42.3	0.04	0.6	0.01	11.5	0.01	0.29	0.001	0.03	6.4	5.9	3.039	0.004	57.0	16.3	0.081	0.09
50179-13	19.0	188.4	0.1	27.4	0.02	0.44	0.01	20.5	0.02	0.43	0.002	0.02	4.1	7.2	8.358	0.011	37.2	16.2	0.17	0.17
50179-15	30.0	205.2	0.1	15.3	0.01	0.29	0.01	64.9	0.05	0.66	0.002	0.01	2.3	14.9	47.44	0.059	18.8	16.2	0.383	0.38
50179-14	25.0	511.7	0.27	33.8	0.03	0.72	0.01	206	0.17	1.75	0.002	0.02	5.1	17.7	67.96	0.085	16.2	15.8	0.381	0.38

Lab ID	Watts	Inverse Isochron Data				^{36}Ar/^{39}Ar Er.Corr.
H9						
24 EK61		^{36}Ar/^{40}Ar	±1σ	^{39}Ar/^{40}Ar	±1σ	
50179-4	8.0	0.002	0.76	0.14931	0.13	0.4127
50179-5	9.0	0.001	1.23	0.28079	0.17	0.2731
50179-6	10.0	0.001	1.14	0.33671	0.14	0.2796
50179-7	11.0	0.000	1.41	0.34768	0.14	0.2277
50179-8	12.0	0.000	1.47	0.34137	0.14	0.2165
50179-9	13.0	0.001	1.23	0.31926	0.14	0.2591
50179-10	14.0	0.001	0.97	0.27924	0.14	0.3294
50179-11	15.0	0.001	0.64	0.25474	0.14	0.4978
50179-12	17.0	0.001	0.54	0.22146	0.14	0.5986
50179-13	19.0	0.002	0.58	0.14509	0.14	0.5568
50179-15	30.0	0.003	0.53	0.07328	0.14	0.6123
50179-14	25.0	0.003	0.45	0.06459	0.14	0.7402

J (X 10^{-3}) ± 1σ = 3.510 ± 0.007

Table E3: ^{40}Ar/^{39}Ar step-heating analytical results for *H9 basalt lava from 126 km north of Sebha,* in Jabal al Hasawinah.

Lab ID	Watts	Relative Isotopic Abundances										Derived Results								
H1												^{39}Ar Mol ¥ 10^{-14}	^{39}Ar % of total	% $(^{36}Ar)_{Ca}$			% $^{40}Ar^{*}$			w/±*J* ±1σ
46 EK61		^{40}Ar	±1σ	^{39}Ar	±1σ	^{38}Ar	±1σ	^{37}Ar	±1σ	^{36}Ar	±1σ				Ca/K	±1σ		Age (Ma)	±1σ	
50184-5	9.0	163.7	5.28	44.5	0.04	0.62	0.01	9.71	0.01	0.12	0.014	0.03	4.1	7.0	1.396	0.003	79.5	18.2	0.937	0.94
50184-6	10.0	361.0	5.00	133	0.11	1.66	0.01	24.2	0.02	0.11	0.014	0.09	12.3	18.7	1.161	0.002	92.5	15.6	0.305	0.31
50184-7	11.0	551.1	5.28	213	0.17	2.59	0.01	35.7	0.03	0.09	0.014	0.15	19.7	33.2	1.071	0.001	96.6	15.5	0.197	0.20
50184-8	12.0	438.4	5.28	174	0.14	2.13	0.01	32.6	0.03	0.07	0.014	0.12	16.1	39.2	1.197	0.002	97.0	15.2	0.241	0.24
50184-9	13.0	367.3	5.28	145	0.11	1.78	0.01	31.9	0.03	0.08	0.014	0.10	13.4	36.3	1.410	0.002	96.1	15.2	0.289	0.29
50184-10	14.0	198.6	5.29	76.3	0.07	0.97	0.01	24.5	0.02	0.07	0.014	0.05	7.0	32.1	2.058	0.003	93.3	15.1	0.549	0.55
50184-11	15.0	142.6	5.30	51.7	0.04	0.7	0.01	24.3	0.02	0.08	0.014	0.04	4.8	27.1	3.017	0.004	88.2	15.2	0.809	0.81
50184-12	17.0	196.4	5.00	67.0	0.05	0.9	0.01	31.6	0.03	0.14	0.014	0.05	6.2	19.0	3.022	0.004	82.3	15.0	0.605	0.61
50184-13	19.0	210.2	1.00	65.0	0.05	0.89	0.01	32.6	0.03	0.22	0.014	0.05	6.0	12.8	3.221	0.004	72.6	14.6	0.415	0.42
50184-14	25.0	608.2	5.40	95.3	0.07	1.62	0.01	635	0.46	1.86	0.014	0.07	8.8	29.6	42.73	0.050	35.7	14.4	0.469	0.47
50184-15	30.0	151.6	0.06	17.4	0.01	0.31	0.00	153	0.12	0.51	0.008	0.01	1.6	26.3	56.77	0.070	26.6	14.8	0.851	0.85

Lab ID	Watts	Inverse Isochron Data					*J* (X 10^{-3}) ± 1σ = 3.469 ± 0.007
						^{36}Ar/^{39}Ar Er.Corr.	
H1							
46 EK61		^{36}Ar/^{40}Ar	±1σ	^{39}Ar/^{40}Ar	±1σ		
50184-5	9.0	0.001	13	0.27253	3.21	0.2482	
50184-6	10.0	0.000	15.7	0.36998	1.39	0.0895	
50184-7	11.0	0.000	22.8	0.38823	0.96	0.0435	
50184-8	12.0	0.000	32.3	0.39871	1.21	0.0380	
50184-9	13.0	0.000	29.1	0.39565	1.44	0.0500	
50184-10	14.0	0.000	31.7	0.38537	2.65	0.0840	
50184-11	15.0	0.000	25.2	0.36333	3.70	0.1470	
50184-12	17.0	0.001	12.4	0.34177	2.54	0.2056	
50184-13	19.0	0.001	7.34	0.30988	0.49	0.0756	
50184-14	25.0	0.002	1.46	0.15478	0.89	0.6341	
50184-15	30.0	0.003	2.09	0.11243	0.13	0.1512	

Table E4: ^{40}Ar/^{39}Ar step-heating analytical results for *H1 basalt plug from 245 km north of Sebha,* in Jabal al Hasawinah.

Lab ID	Watts	Relative Isotopic Abundances										Derived Results								
												^{39}Ar Mol ¥ 10^{-14}	^{39}Ar % of total	% $(^{36}Ar)_{Ca}$			% $^{40}Ar^{*}$			w/±*J* ±1σ
H2																				
26 EK61		^{40}Ar	±1σ	^{39}Ar	±1σ	^{38}Ar	±1σ	^{37}Ar	±1σ	^{36}Ar	±1σ				Ca/K	±1σ		Age (Ma)	±1σ	
50176-4	8.0	134.3	0.04	28.2	0.02	0.36	0.00	2.72	0.01	0.12	0.007	0.02	2.8	3.7	1.139	0.004	75.0	21.7	0.420	0.42
50176-5	9.0	349.4	0.19	111	0.10	1.27	0.00	7.71	0.01	0.09	0.007	0.08	11.1	13.7	0.819	0.001	93.4	17.9	0.120	0.12
50176-6	10.0	548.4	0.32	209	0.18	2.42	0.00	12.8	0.01	0.11	0.001	0.15	20.9	18.5	0.723	0.001	95.1	15.2	0.027	0.04
50176-7	11.0	486.1	0.24	186	0.15	2.23	0.00	13.1	0.01	0.1	0.001	0.13	18.6	21.9	0.831	0.001	95.4	15.1	0.026	0.04
50176-8	12.0	452.1	0.24	170	0.15	2.07	0.00	16.3	0.02	0.12	0.001	0.12	17.0	20.9	1.133	0.002	93.5	15.1	0.029	0.04
50176-9	13.0	338.4	0.17	121	0.10	1.51	0.00	20.1	0.02	0.15	0.001	0.09	12.1	21.0	1.958	0.003	89.3	15.1	0.030	0.04
50176-10	14.0	195	0.10	62.4	0.06	0.79	0.00	17.9	0.02	0.16	0.002	0.04	6.2	17.5	3.398	0.005	79.3	15.1	0.056	0.06
50176-11	15.0	159.2	0.07	45.2	0.04	0.60	0.00	14.3	0.01	0.18	0.002	0.03	4.5	12.4	3.731	0.005	69.8	15.0	0.075	0.08
50176-12	17.0	194.5	0.09	39.2	0.03	0.59	0.00	16.5	0.01	0.38	0.001	0.03	3.9	6.9	4.963	0.007	45.7	13.8	0.102	0.11
50176-13	19.0	193.1	0.10	18.7	0.02	0.37	0.00	69.9	0.06	0.64	0.001	0.01	1.9	17.4	44.23	0.059	18.4	11.8	0.271	0.27
50176-14	25.0	661.8	0.04	10.1	0.01	0.51	0.00	242	0.20	2.54	0.000	0.01	1.0	15.2	284.1	0.339	3.0	13.3	1.801	1.80

Lab ID	Watts	Inverse Isochron Data					*J* (X 10^{-3}) ± 1σ = 3.389 ± 0.007
				.		^{36}Ar/^{39}Ar Er.Corr	
H2							
26 EK61		^{36}Ar/^{40}Ar	±1σ	^{39}Ar/^{40}Ar	±1σ		
50176-4	8.0	0.001	5.81	0.21013	0.13	0.0544	
50176-5	9.0	0.000	9.21	0.31876	0.14	0.0345	
50176-6	10.0	0.000	1.51	0.38241	0.14	0.2126	
50176-7	11.0	0.000	1.67	0.38476	0.14	0.1919	
50176-8	12.0	0.000	1.49	0.37666	0.14	0.2142	
50176-9	13.0	0.000	0.85	0.35981	0.14	0.3785	
50176-10	14.0	0.001	1.19	0.32067	0.14	0.2687	
50176-11	15.0	0.001	1.02	0.28429	0.13	0.3126	
50176-12	17.0	0.002	0.55	0.20184	0.14	0.5814	
50176-13	19.0	0.003	0.50	0.09542	0.14	0.6532	
50176-14	25.0	0.003	0.42	0.01381	0.11	0.7592	

Table E5: ^{40}Ar/^{39}Ar step-heating analytical results for *H2 lava from 235 km north of Sebha,* in Jabal al Hasawinah.

Lab ID	Watts	Relative Isotopic Abundances										Derived Results								
H3												^{39}Ar Mol ¥ 10^{-14}	^{39}Ar % of total	% (^{36}Ar)$_{Ca}$			% ^{40}Ar*			w/±*J* ±1σ
57 EK61		^{40}Ar	±1σ	^{39}Ar	±1σ	^{38}Ar	±1σ	^{37}Ar	±1σ	^{36}Ar	±1σ				Ca/K	±1σ		Age (Ma)	±1σ	
50228-6	10.0	231.7	0.11	80.1	0.06	1.14	0.00	13.5	0.01	0.28	0.008	0.06	7.6	4.7	1.216	0.002	65.4	11.8	0.179	0.18
50228-7	11.0	365.5	0.19	174	0.15	2.23	0.00	23.2	0.02	0.24	0.001	0.12	16.6	9.5	0.960	0.001	82.4	10.8	0.026	0.03
50228-8	12.0	301.6	0.15	153	0.12	1.92	0.00	20.3	0.02	0.14	0.002	0.11	14.6	13.9	0.955	0.001	87.8	10.8	0.027	0.03
50228-9	13.0	314.7	0.17	164	0.14	2.05	0.00	21.3	0.02	0.12	0.002	0.11	15.7	16.8	0.937	0.001	90.2	10.8	0.029	0.04
50228-10	14.0	256.7	0.12	134	0.11	1.67	0.00	20.9	0.02	0.10	0.001	0.09	12.8	19.7	1.123	0.001	90.4	10.8	0.026	0.03
50228-11	15.0	178.9	0.08	90.4	0.07	1.15	0.00	20.2	0.02	0.09	0.001	0.06	8.6	21.0	1.615	0.002	87.6	10.8	0.032	0.04
50228-12	17.0	199.5	0.09	84.9	0.07	1.13	0.00	24.8	0.02	0.20	0.001	0.06	8.1	12.1	2.111	0.002	73.8	10.8	0.042	0.05
50228-13	19.0	159.3	0.08	62.4	0.05	0.84	0.00	20.3	0.02	0.19	0.001	0.04	6.0	10.2	2.349	0.003	67.2	10.7	0.042	0.05
50228-14	25.0	551.8	0.27	85.9	0.07	1.52	0.00	741	0.61	2.15	0.002	0.06	8.2	33.5	62.35	0.079	22.5	9.23	0.159	0.16
50228-15	30.0	201.1	0.08	18.5	0.02	0.39	0.00	212	0.16	0.79	0.001	0.01	1.8	26.1	83.08	0.101	12.9	9.07	0.293	0.29

Lab ID	Watts	Inverse Isochron Data				^{36}Ar/^{39}Ar Er.Corr
H3				.		
57 EK61		^{36}Ar/^{40}Ar	±1σ	^{39}Ar/^{40}Ar	±1σ	
50228-6	10.0	0.001	2.83	0.34655	0.14	0.1125
50228-7	11.0	0.001	0.62	0.47844	0.14	0.5173
50228-8	12.0	0.000	1.30	0.51034	0.14	0.2472
50228-9	13.0	0.000	1.90	0.52415	0.14	0.1681
50228-10	14.0	0.000	1.63	0.52445	0.14	0.1960
50228-11	15.0	0.000	1.68	0.50718	0.14	0.1905
50228-12	17.0	0.001	0.90	0.42706	0.14	0.3548
50228-13	19.0	0.001	0.62	0.39248	0.14	0.5176
50228-14	25.0	0.003	0.47	0.15270	0.14	0.7402
50228-15	30.0	0.003	0.47	0.08937	0.13	0.7233

J (X 10^{-3}) ± 1σ = 3.475 ± 0.007

Table E6: ^{40}Ar/^{39}Ar step-heating analytical results for *H3 basalt lava from 207 km northeast of Sebha,* in Jabal al Hasawinah.

E1.2 Jabal as Sawda province

Jabal as Sawda basaltic province is one of extrusive rocks in central Libya, about 550 km southeast of Tripoli. At the present time basaltic flood lavas cover an area about 6000 km^2 but the distribution of outliers and significant dissection of the plateau indicate that the original area of volcanic rocks was probably at least 10.000 km^2 (Busrewil and Esson, 1991). Woller and Fediuk (1980) conclude that the plateau lavas are predominantly alkali olivine basalts with occasional olivine tholeiites and basanites, where the shield volcanoes and cones consist entirely of alkali olivine basalt. The location of all samples is reported in Figure E2 and Table E7.

E1.2.1 Sample S1and S3 (62.5 and 57 km southwest of Sawknah, respectively)

These rocks (S1and S3) sampled from upper part of lava flow (62.5 and 57 km southwest of Sawknah, respectively), south part of Jabal as Sawda volcanism. These outcrops are vast in length and dark black in color. It is medium-fine grained.

E1.2.2 Sample S5 (49 km southwest of Sawknah)

This rock sampled from lower part of lava flow (49 km southwest of Sawknah) closed to central of Jabal as Sawda basaltic province. This outcrop is vast in length (Figure E1.4). This rock is massive, dark black in color and medium to fine grained.

E1.2.3 Sample S7 (46 km southwest of Sawknah)

This rock sampled from lower part of shield lava (46 km southwest of Sawknah) closed to central of Jabal as Sawda basaltic province. This outcrop is largest shield volcano called Qarat Tiziqyarah (about 11 km in diameter) (Figure E1.5). This rock is massive, light gray in color and fine grained.

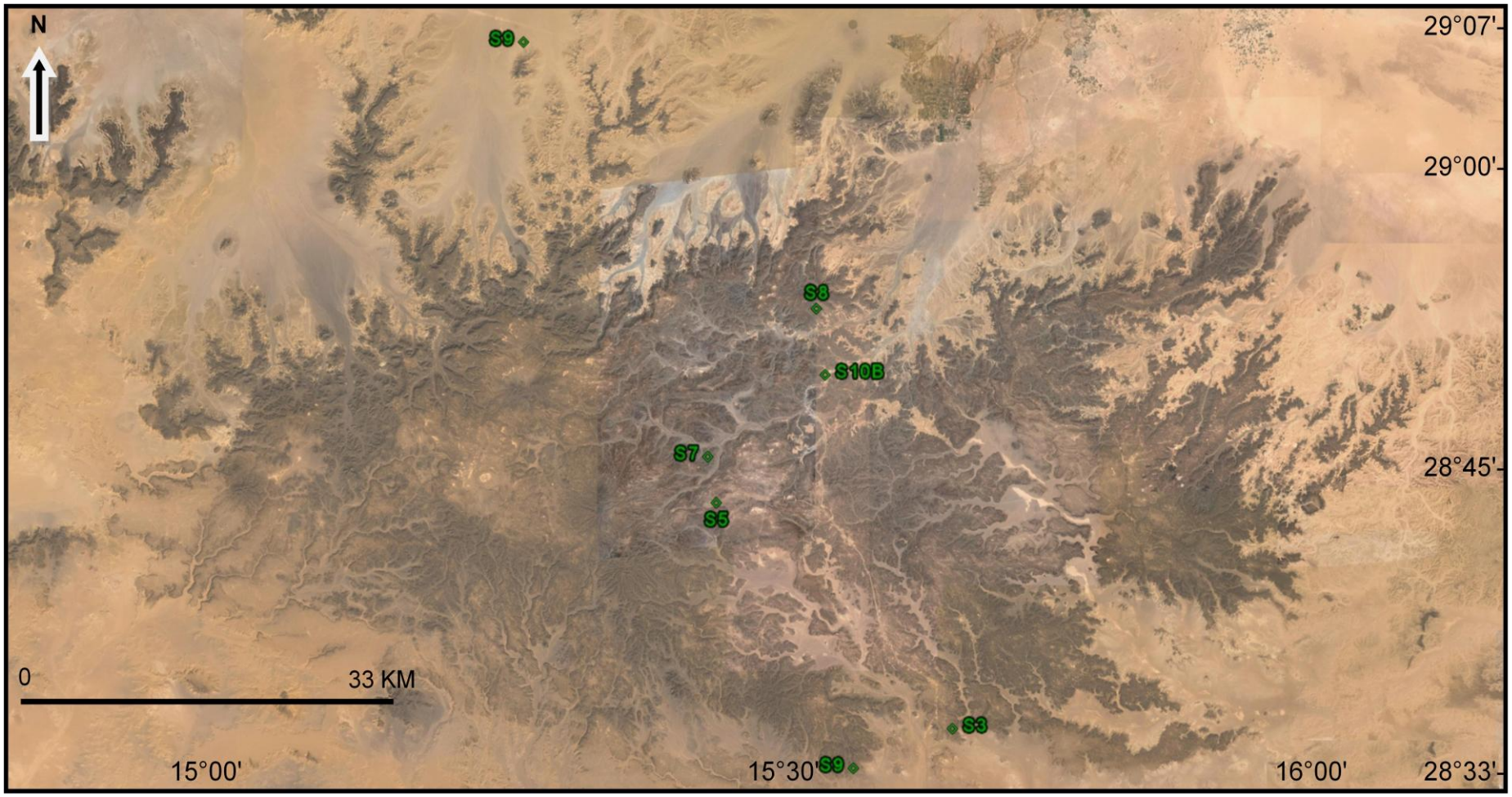

Figure E2: satellite image (Google Earth Pro4) for the area covering the Jabal as Sawda volcanic provinces showing the location of seven samples used in this study.

Figure E1.4 show the outcrop of samples S5 in occurs in huge lava at 49 km southwest of Sawknah, closed to central of Jabal as Sawda basaltic province.

Figure E1.5 show the largest shield volcano (Qarat Tiziqyarah) (sample no S7) occurs at 46 km southwest of Sawknah, closed to central of Jabal as Sawda basaltic province.

E1.2.4 Sample S8 (32 km southwest of Sawknah)

This rock sampled from lower part of lava flow (32 km southwest of Sawknah) northeast of Jabal as Sawda basaltic province. This outcrop is limited in length. This rock is massive, dark black in color and medium to fine grained.

E1.2.5 Sample S9 (84 km west of Sawknah)

This rock sampled from most upper part of the plug (84 km west of Sawknah) which to centered in the most north of Jabal as Sawda basaltic province. This outcrop occurs as stock-like body, about one km in diameter (Figure E1.6). This rock, in hand specimen, is dark green to gray, massive and locally exhibit amygdaloidal structures and doleritic texture. Moreover, it is displays strongly jointed in different direction (Figure E1.7).

Figure E1.6 show the outcrop of samples S9 which occur in large plug at about 84 km west of Sawknah (centered in the most north of Jabal as Sawda basaltic province).

Figure E1.7 show close view of the plug and outcrop of sample no. S9 display the different direction jointed.

E1.2.6 Sample S10 (34 km west of Sawknah)

This rock sampled from lower part of lava flow (34 km west of Sawknah), northeast part of Jabal as Sawda volcanism. These outcrops are limited in length and dark black in color, compact and occasionally contain vesicles. It is fine grained.

Table E7 Details of basalt samples from Jabal as Sawda volcanic province.

Sample	Rock type	Rock	Location	Latitude and longitude
S1	Alkali olivine basalt	lava	62.5 km southwest of Sawknah	28°31'040"N 15°35'582"E
S3	Alkali olivine basalt	lava	57 km south of Sawknah	28°33'500"N 15°38'828"E
S5	Basanite	lava	49 km southwest of Sawknah	28°43'680"N 15°27'392"E
S7	Basanite	shield lava	46 km southwest of Sawknah	28°45'615"N 15°27'595"E
S8	Basanite	lava	32 km southwest of Sawknah	28°52'510"N 15°32'745"E
S9	Basanite	plug	84 km west of Sawknah	29°04'615"N 15°17'010"E
S10B	Alkali olivine basalt	lava	34 km southwest of Sawknah	28°49'500"N 15°33'250"E

Lab ID	Watts	Relative Isotopic Abundances										Derived Results								
S9												^{39}Ar Mol ¥ 10^{-14}	^{39}Ar % of total	%(^{36}Ar)$_{Ca}$			% ^{40}Ar*			w/±*J* ±1σ
44 EK61		^{40}Ar	±1σ	^{39}Ar	±1σ	^{38}Ar	±1σ	^{37}Ar	±1σ	^{36}Ar	±1σ				Ca/K	±1σ		Age (Ma)	±1σ	
50187-4	8.0	224.9	0.12	27.0	0.02	0.42	0.01	5.08	0.01	0.4	0.001	0.02	2.6	1.8	2.007	0.004	47.5	24.6	0.16	0.17
50187-5	9.0	327.1	0.15	71.2	0.06	0.92	0.01	12.3	0.01	0.22	0.001	0.05	6.8	8.1	1.842	0.003	81.8	23.4	0.06	0.08
50187-6	10.0	409	0.22	99.8	0.08	1.22	0.01	15.2	0.02	0.17	0.002	0.07	9.5	12.8	1.626	0.002	89.1	22.7	0.05	0.07
50187-7	11.0	478.7	0.27	119	0.10	1.45	0.01	18.0	0.01	0.17	0.001	0.08	11.4	15.4	1.614	0.002	91.1	22.7	0.042	0.06
50187-8	12.0	490.4	0.23	121	0.10	1.48	0.01	20.6	0.02	0.19	0.001	0.08	11.5	15.3	1.827	0.002	90.0	22.8	0.044	0.06
50187-9	13.0	441.9	0.24	107	0.09	1.33	0.01	22.6	0.02	0.20	0.001	0.07	10.2	16.0	2.262	0.003	88.4	22.8	0.045	0.06
50187-10	14.0	393.4	0.19	93.0	0.08	1.16	0.01	24.6	0.02	0.22	0.001	0.07	8.9	16.5	2.836	0.004	86.3	22.7	0.052	0.07
50187-11	15.0	351.2	0.19	80.0	0.07	1.01	0.01	22.1	0.02	0.23	0.002	0.06	7.6	13.7	2.970	0.004	82.9	22.7	0.062	0.08
50187-12	17.0	419.8	0.23	92.9	0.08	1.21	0.01	17.4	0.02	0.30	0.002	0.07	8.9	8.4	2.004	0.003	80.6	22.7	0.061	0.08
50187-13	19.0	391.3	0.2	81.5	0.07	1.12	0.01	37.2	0.03	0.42	0.001	0.06	7.8	12.7	4.893	0.006	71.8	21.5	0.067	0.08
50187-14	25.0	661.5	0.29	106	0.08	1.64	0.01	476	0.36	1.72	0.002	0.07	10.1	40.0	48.09	0.057	53.4	21.1	0.115	0.12
50187-15	30.0	339.7	0.16	37.1	0.03	0.64	0.01	171	0.13	0.96	0.002	0.03	3.5	25.7	49.38	0.062	37.2	21.5	0.201	0.21
50187-16	40.0	259.1	0.15	12.3	0.01	0.31	0.01	61.9	0.05	0.83	0.002	0.01	1.2	10.8	53.91	0.070	14.7	19.7	0.55	0.55

Lab ID	Watts	Inverse Isochron Data					*J* (X 10^{-3}) ± 1σ = 3.471 ± 0.007
S9						^{36}Ar/^{39}Ar Er.Corr.	
44 EK61		^{36}Ar/^{40}Ar	±1σ	^{39}Ar/^{40}Ar	±1σ		
50187-4	8.0	0.002	0.51	0.12032	0.14	0.6296	
50187-5	9.0	0.002	0.77	0.21817	0.14	0.4143	
50187-6	10.0	0.000	1.09	0.24451	0.14	0.2931	
50187-7	11.0	0.000	0.76	0.24996	0.14	0.4256	
50187-8	12.0	0.000	0.90	0.24632	0.14	0.3581	
50187-9	13.0	0.000	0.66	0.24222	0.14	0.4930	
50187-10	14.0	0.001	0.88	0.23669	0.14	0.3631	
50187-11	15.0	0.001	0.95	0.22782	0.14	0.3391	
50187-12	17.0	0.001	0.72	0.22163	0.14	0.4462	
50187-13	19.0	0.001	0.53	0.20834	0.14	0.6136	
50187-14	25.0	0.002	0.51	0.15830	0.13	0.6897	
50187-15	30.0	0.002	0.50	0.10770	0.14	0.6720	
50187-16	40.0	0.003	0.47	0.04672	0.15	0.6903	

Table E8: ^{40}Ar/^{39}Ar step-heating analytical results *S9 basalt plug from 84 km west of Sawknah,* in Jabal as Sawda.

Lab ID	Watts	Relative Isotopic Abundances										Derived Results								
S3												^{39}Ar Mol ¥ 10^{-14}	^{39}Ar % of total	% $(^{36}Ar)_{Ca}$			% $^{40}Ar^{*}$			w/±*J* ±1σ
38 EK61		^{40}Ar	±1σ	^{39}Ar	±1σ	^{38}Ar	±1σ	^{37}Ar	±1σ	^{36}Ar	±1σ				Ca/K	±1σ		Age (Ma)	±1σ	
50195-4	8.0	27.13	0.01	2.72	0.00	0.06	0.00	0.77	0.01	0.07	0.002	0.00	0.3	1.1	2.068	0.023	25.7	15.9	1.037	1.04
50195-5	9.0	141	0.07	34.5	0.03	0.53	0.00	8.93	0.01	0.19	0.001	0.02	4.3	4.7	1.904	0.003	61.7	15.6	0.077	0.08
50195-6	10.0	251	0.12	88.1	0.07	1.21	0.00	20.3	0.02	0.16	0.002	0.06	10.9	12.9	1.694	0.002	83.8	14.8	0.044	0.05
50195-7	11.0	334.2	0.17	136	0.11	1.74	0.00	28.1	0.02	0.12	0.002	0.10	16.8	22.8	1.522	0.002	91.5	13.9	0.033	0.04
50195-8	12.0	356.1	0.19	148	0.13	1.86	0.00	31.1	0.03	0.11	0.002	0.10	18.4	29.4	1.543	0.002	93.8	13.9	0.030	0.04
50195-9	13.0	278.3	0.12	115	0.09	1.44	0.00	24.9	0.02	0.09	0.002	0.08	14.2	26.9	1.596	0.002	92.8	13.9	0.034	0.04
50195-10	14.0	161.7	0.08	64.8	0.05	0.84	0.00	20.2	0.02	0.07	0.001	0.05	8.0	26.9	2.294	0.003	89.9	13.9	0.047	0.05
50195-11	15.0	279	0.13	108	0.09	1.43	0.00	55.5	0.04	0.18	0.001	0.08	13.4	31.4	3.791	0.005	87.1	14.00	0.035	0.04
50195-12	17.0	143.8	0.08	54.3	0.05	0.73	0.00	32.8	0.03	0.11	0.001	0.04	6.7	30.3	4.455	0.006	84.4	13.8	0.050	0.06
50195-13	19.0	155.4	0.08	54.9	0.04	0.74	0.00	33.4	0.03	0.14	0.004	0.04	6.8	23.4	4.477	0.006	79.1	13.9	0.122	0.13

Lab ID	Watts	Inverse Isochron Data				
				.		^{36}Ar/^{39}Ar Er.Corr
S3						
38 EK61		^{36}Ar/^{40}Ar	±1σ	^{39}Ar/^{40}Ar	±1σ	
50195-4	8.0	0.003	2.26	0.10034	0.17	0.1365
50195-5	9.0	0.001	0.66	0.24495	0.14	0.4832
50195-6	10.0	0.001	1.18	0.35220	0.14	0.2711
50195-7	11.0	0.000	1.85	0.40740	0.14	0.1725
50195-8	12.0	0.000	2.20	0.41836	0.14	0.1450
50195-9	13.0	0.000	2.43	0.41352	0.13	0.1314
50195-10	14.0	0.000	2.61	0.40201	0.14	0.1220
50195-11	15.0	0.000	1.17	0.38730	0.14	0.2755
50195-12	17.0	0.001	1.66	0.37835	0.14	0.1927
50195-13	19.0	0.001	3.25	0.35398	0.14	0.0980

J (X 10^{-3}) ± 1σ = 3.447 ± 0.007

Table E9: ^{40}Ar/^{39}Ar step-heating analytical results *S3 basalt lava from 57 km south of Sawknah,* in Jabal as Sawda.

Lab ID	Watts	Relative Isotopic Abundances										Derived Results								
S7												^{39}Ar Mol ¥ 10^{-14}	^{39}Ar % of total	% $(^{36}Ar)_{Ca}$			% $^{40}Ar^{*}$			w/±*J* ±1σ
41 EK61		^{40}Ar	±1σ	^{39}Ar	±1σ	^{38}Ar	±1σ	^{37}Ar	±1σ	^{36}Ar	±1σ				Ca/K	±1σ		Age (Ma)	±1σ	
50191-5	9.0	1820	0.09	43.7	0.04	0.73	0.01	10.9	0.01	0.23	0.002	0.03	3.2	4.2	1.657	0.002	63.7	16.3	0.10	0.11
50191-6	10.0	359.3	0.18	134	0.11	1.99	0.01	29.8	0.02	0.14	0.002	0.09	9.8	18.7	1.485	0.002	90.3	15.0	0.04	0.05
50191-7	11.0	541.6	0.31	230	0.19	3.07	0.01	46.7	0.04	0.13	0.002	0.16	16.9	31.6	1.354	0.002	95.0	13.8	0.03	0.04
50191-8	12.0	522.3	0.25	224	0.18	2.8	0.01	52.2	0.04	0.11	0.001	0.16	16.5	43.5	1.551	0.002	96.5	13.8	0.02	0.04
50191-9	13.0	495.6	0.25	213	0.17	2.63	0.01	53.7	0.04	0.11	0.002	0.15	15.6	44.4	1.682	0.002	96.3	13.8	0.03	0.04
50191-10	14.0	375.3	0.24	159	0.15	2.01	0.01	40.6	0.04	0.10	0.001	0.11	11.7	38.4	1.697	0.003	95.3	13.8	0.03	0.04
50191-11	15.0	291.4	0.14	121	0.10	1.57	0.01	38.5	0.03	0.10	0.001	0.08	8.9	35.2	2.121	0.003	93.5	13.9	0.03	0.04
50191-12	17.0	2200	0.10	88.7	0.07	1.23	0.01	35.3	0.03	0.10	0.001	0.06	6.5	30.6	2.653	0.003	90.2	13.8	0.04	0.04
50191-13	19.0	167.5	0.08	63.1	0.05	0.88	0.01	35.8	0.03	0.14	0.001	0.04	4.6	23.6	3.786	0.005	81.4	13.3	0.04	0.05
50191-14	25.0	270.7	0.09	86.6	0.07	1.27	0.01	656	0.49	0.93	0.002	0.06	6.4	63.5	50.54	0.063	62.5	12.2	0.07	0.07

Lab ID	Watts	Inverse Isochron Data					*J* (X 10^{-3}) ± 1σ = 3.432 ± 0.007
S7						^{36}Ar/^{39}Ar Er.Corr.	
41 EK61		^{36}Ar/^{40}Ar	±1σ	^{39}Ar/^{40}Ar	±1σ		
50191-5	9.0	0.001	0.99	0.24086	0.14	0.3201	
50191-6	10.0	0.000	1.53	0.37297	0.14	0.2091	
50191-7	11.0	0.000	1.71	0.42567	0.14	0.1878	
50191-8	12.0	0.000	2.03	0.43119	0.14	0.1584	
50191-9	13.0	0.000	2.69	0.43057	0.14	0.1189	
50191-10	14.0	0.000	2.44	0.42617	0.15	0.1317	
50191-11	15.0	0.000	1.28	0.41696	0.14	0.2521	
50191-12	17.0	0.000	1.73	0.40445	0.13	0.1850	
50191-13	19.0	0.001	1.06	0.37735	0.14	0.3045	
50191-14	25.0	0.001	0.83	0.31549	0.13	0.4215	

Table E10: ^{40}Ar/^{39}Ar step-heating analytical results for *S7 shield lava from 46 km southwest of Sawknah,* in Jabal as Sawda.

Lab ID	Watts	Relative Isotopic Abundances										Derived Results								
S1												^{39}Ar Mol ¥ 10^{-14}	^{39}Ar % of total	%(^{36}Ar)$_{Ca}$			% ^{40}Ar*			w/±*J* ±1σ
40 EK61		^{40}Ar	±1σ	^{39}Ar	±1σ	^{38}Ar	±1σ	^{37}Ar	±1σ	^{36}Ar	±1σ				Ca/K	±1σ		Age (Ma)	±1σ	
50192-5	9.0	83.97	0.04	16.8	0.02	0.28	0.01	2.80	0.01	0.15	0.001	0.01	1.5	2.5	1.679	0.006	46.7	14.4	0.164	0.17
50192-6	10.0	138.4	0.06	46.4	0.04	0.65	0.01	7.51	0.01	0.13	0.001	0.03	4.1	8.0	1.632	0.003	74.5	13.7	0.063	0.07
50192-7	11.0	208.4	0.11	83.9	0.07	1.09	0.00	12.5	0.01	0.13	0.002	0.06	7.4	13.6	1.507	0.002	84.5	12.9	0.044	0.05
50192-8	12.0	274.9	0.13	118	0.10	1.48	0.01	19.9	0.02	0.11	0.001	0.08	10.5	23.6	1.691	0.002	90.5	12.9	0.03	0.04
50192-9	13.0	265.4	0.13	118	0.10	1.45	0.01	21.1	0.02	0.09	0.001	0.08	10.4	31.0	1.813	0.002	92.8	12.9	0.026	0.04
50192-10	14.0	289.6	0.14	113	0.10	1.43	0.00	20.0	0.02	0.20	0.001	0.08	10.0	13.5	1.786	0.002	81.9	12.9	0.034	0.04
50192-11	15.0	256.4	0.11	105	0.08	1.31	0.01	18.1	0.02	0.15	0.001	0.07	9.3	16.6	1.740	0.002	85.6	12.8	0.033	0.04
50192-12	17.0	292.8	0.12	116	0.09	1.45	0.01	21.4	0.02	0.20	0.001	0.08	10.3	14.8	1.867	0.002	82.8	12.9	0.031	0.04
50192-13	19.0	219.8	0.10	87.5	0.07	1.10	0.01	20.0	0.02	0.15	0.001	0.06	7.7	17.9	2.312	0.003	82.9	12.8	0.037	0.04
50192-14	25.0	385.7	0.16	149	0.12	1.89	0.01	42.4	0.03	0.31	0.002	0.10	13.1	18.6	2.887	0.004	80.4	12.8	0.037	0.05
50192-15	30.0	394.2	0.14	96.2	0.07	1.35	0.01	330	0.24	1.10	0.002	0.07	8.5	40.8	34.69	0.040	50.5	12.9	0.079	0.08
50192-16	40.0	251.3	0.12	65.0	0.06	0.89	0.01	265	0.22	0.78	0.001	0.05	5.8	46.3	41.29	0.054	49.9	12.0	0.081	0.08
50192-17	50.0	606.2	0.33	14.7	0.01	0.55	0.01	56.4	0.05	2.03	0.002	0.01	1.3	3.8	38.77	0.047	4.0	10.2	1.037	1.04

Lab ID	Watts	Inverse Isochron Data					*J* (X 10^{-3}) ± 1σ = 3.422 ± 0.007
S1						^{36}Ar/^{39}Ar Er.Corr.	
40 EK61		^{36}Ar/^{40}Ar	±1σ	^{39}Ar/^{40}Ar	±1σ		
50192-5	9.0	0.001	0.96	0.20041	0.14	0.3302	
50192-6	10.0	0.001	1.18	0.33593	0.14	0.2699	
50192-7	11.0	0.001	1.54	0.40382	0.14	0.2075	
50192-8	12.0	0.000	1.55	0.43388	0.14	0.2066	
50192-9	13.0	0.000	1.54	0.44501	0.14	0.2088	
50192-10	14.0	0.001	0.80	0.39262	0.14	0.4004	
50192-11	15.0	0.001	1.06	0.41070	0.13	0.3026	
50192-12	17.0	0.001	0.73	0.39713	0.13	0.4426	
50192-13	19.0	0.001	1.05	0.39957	0.13	0.3063	
50192-14	25.0	0.001	0.87	0.38621	0.14	0.3718	
50192-15	30.0	0.002	0.53	0.24183	0.13	0.6727	
50192-16	40.0	0.002	0.58	0.25594	0.14	0.6080	
50192-17	50.0	0.003	0.42	0.02401	0.14	0.7713	

Table E11: ^{40}Ar/^{39}Ar step-heating analytical results for *S1 basalt lava from 62.5 km southwest of Sawknah,* in Jabal as Sawda.

Lab ID	Watts	Relative Isotopic Abundances										Derived Results								
S10B												^{39}Ar Mol ¥ 10^{-14}	^{39}Ar % of total	% $(^{36}Ar)_{Ca}$			% $^{40}Ar^{*}$			w/±*J* ±1σ
36 EK61		^{40}Ar	±1σ	^{39}Ar	±1σ	^{38}Ar	±1σ	^{37}Ar	±1σ	^{36}Ar	±1σ				Ca/K	±1σ		Age (Ma)	±1σ	
50163-5	9.0	276.5	0.15	49.4	0.04	0.86	0.01	9.03	0.01	0.62	0.001	0.03	4.2	2.0	1.888	0.003	34.0	12.0	0.112	0.11
50163-6	10.0	250.5	0.13	99.7	0.09	1.43	0.01	15.3	0.01	0.22	0.002	0.07	8.4	9.6	1.580	0.002	76.2	12.0	0.045	0.05
50163-7	11.0	262.2	0.12	116	0.1	1.52	0.01	15.5	0.02	0.15	0.001	0.08	9.8	14.2	1.373	0.002	85.1	12.0	0.035	0.04
50163-8	12.0	296.0	0.16	133	0.11	1.69	0.01	18.6	0.02	0.17	0.001	0.09	11.2	15.6	1.448	0.002	85.8	12.0	0.031	0.04
50163-10	14.0	367.4	0.20	175	0.15	2.20	0.01	27.3	0.02	0.15	0.001	0.12	14.7	25.0	1.619	0.002	90.7	12.0	0.025	0.03
50163-11	15.0	503.0	0.26	242	0.22	3.09	0.01	52.4	0.04	0.21	0.001	0.17	20.4	35.2	2.244	0.003	92.0	12.0	0.023	0.03
50163-12	17.0	324.7	0.15	150	0.12	1.98	0.01	43.0	0.03	0.19	0.001	0.11	12.7	32.5	2.970	0.004	88.5	12.0	0.026	0.04
50163-13	19.0	200.0	0.09	82.2	0.07	1.10	0.01	15.7	0.01	0.18	0.001	0.06	6.9	12.5	1.979	0.003	76.9	11.7	0.041	0.05
50163-14	25.0	242.4	0.085	81.3	0.06	1.12	0.01	278	0.21	0.73	0.002	0.06	6.9	53.5	35.44	0.042	58.2	11.0	0.068	0.07
50163-15	30.0	147.3	0.051	38.8	0.03	0.54	0.01	168	0.12	0.50	0.002	0.03	3.3	47.2	44.90	0.055	46.7	11.3	0.105	0.11
50163-16	40.0	127.4	0.064	17.3	0.02	0.28	0.01	69.4	0.06	0.43	0.002	0.01	1.5	22.5	41.68	0.054	21.4	10.1	0.237	0.24

Lab ID	Watts	Inverse Isochron Data					*J* (X 10^{-3}) ± 1σ = 3.492 ± 0.007
S10B						^{36}Ar/^{39}Ar Er.Corr.	
36 EK61		^{36}Ar/^{40}Ar	±1σ	^{39}Ar/^{40}Ar	±1σ		
50163-5	9.0	0.002	0.43	0.17874	0.14	0.7524	
50163-6	10.0	0.001	0.99	0.39941	0.14	0.3216	
50163-7	11.0	0.001	1.30	0.44597	0.14	0.2458	
50163-8	12.0	0.001	1.08	0.45086	0.14	0.2963	
50163-10	14.0	0.000	1.22	0.47714	0.14	0.2641	
50163-11	15.0	0.000	1.00	0.48255	0.14	0.3238	
50163-12	17.0	0.000	0.99	0.46368	0.14	0.3283	
50163-13	19.0	0.001	0.94	0.41227	0.14	0.3395	
50163-14	25.0	0.001	0.75	0.33267	0.13	0.4630	
50163-15	30.0	0.002	0.76	0.26036	0.13	0.4448	
50163-16	40.0	0.003	0.62	0.13390	0.14	0.5235	

Table E12: ^{40}Ar/^{39}Ar step-heating analytical results for *S10B basalt lava from 34 km southwest of Sawknah,* in Jabal as Sawda.

E1.3 Jabal Al Haruj al Aswad province

Al Haruj (Jabal Al Haruj al Aswad) area of central Libya is the largest of four Tertiary - Recent Volcanic provinces in Libya. The location of all samples is reported in Figure E3 and Table E13.

The lava flows of the Jabal Al Haruj al Aswad area have been classified into six major phases by Klitzsch, (1967). Four of the major phases have been subdivided into more mappable sub-phases by Busrewil and Suwesi (1993). The great size of the area covered by flows, the quiet character of the eruptions and the absence of pyroclastic materials make Al Haruj al Aswad a typical example of the plateau basalt type of effusion. The phase's description by Busrewil and Suwesi (1993) and Nixon (2011) as following:

Phase 1 dominates the northwest and southern part of Al Haruj volcanic province. Although it is areally extensive showing a wide distribution over low surface relief with limited thickness (1-3 meter) and covering an area of 40.000 km^2, suggesting the lavas had a low viscosity. It is can be subdivided into three mappable units namely, 1.1, 1.2 and 1.3. A brief description of each unit is as follows.

Unit 1.1 represent the oldest exposed lava flows. In the field, the lava flows are massive, light colour, impassable by car, have a limited geographic extent and crop out in a few small scattered localities in north-north east part of the Al Haruj area, have smooth surfaces with low surface relief. The rocks are fine to medium grained olivine basalts (Figure E1.8).

Unit 1.2 is one of the old subdued topography, with expanses of featureless lavas showing a pale grey tone on air photos. The volume and original extent of this sub-phase are unknown and it can be said that its wide distribution over a surface of low relief is mainly the result of spreading from a ridge of fluid lava over the feeders. The open texture of the basalts of this phase and geographic extent of the lava field suggest that the lavas must have been very fluid.

The constructional surfaces of the lava flows Unit 1.3 occur as sub-phase make conspicuous topographic features readily observed in the field and on aerial photographs. The surfaces of these lava flows do not show any constructional feature similar to those of sub-phase 1.2 except when partly overlain by elongate flows with convex-upward flow-surface profile extending from extrusive sources, which may often comprise of phase four lava fields and to a less extent shield volcanoes. Columnar jointing is common in the elongate superimposed flows. Land slides are frequent along basalt cliffs especially where wadis undercut the base of the slopes was observed in Wadi al Khayeb (28° 00′ N-17° 54′ 40″ E).

Three olivine basalt samples from Phase 1 were collected different locations, HS4A from ~240 km south of Zalla Village (the far south of Al Haruj province). While two samples (HS23 and HS24) (Figure E1.9) are from the far north of Al Haruj province (~37 and 35 km south of Zalla, respectively).

The lava flows of Phase 2 have thick skin, broken into blocks approximately 0.3 - 0.5 m in diameter. It is fairly smooth angular to sub-angular blocks similar to those of sub-phase 1.1 in the field, the lava flows are inaccessible, except along existing tracks and have a low gradient and relatively low surface relief. Compared with the surrounding lava flows, they have lighter colour and appeared to have been originated in a summit. The basalts are fine grained, vesicular (10-20%) and are olivine phyric with rare 2 mm long plagioclase laths.

Two alkaline basalt samples from Phase 2 (Figure E1.10) were collected, HS1 from ~270 km south of Zalla Village (the far south of Al Haruj province) and HS6 from 230 km south of Zalla Village.

The constructional surfaces of the lava flows (Phase 3) make conspicuous topographic features readily observed in the field and on aerial photographs.

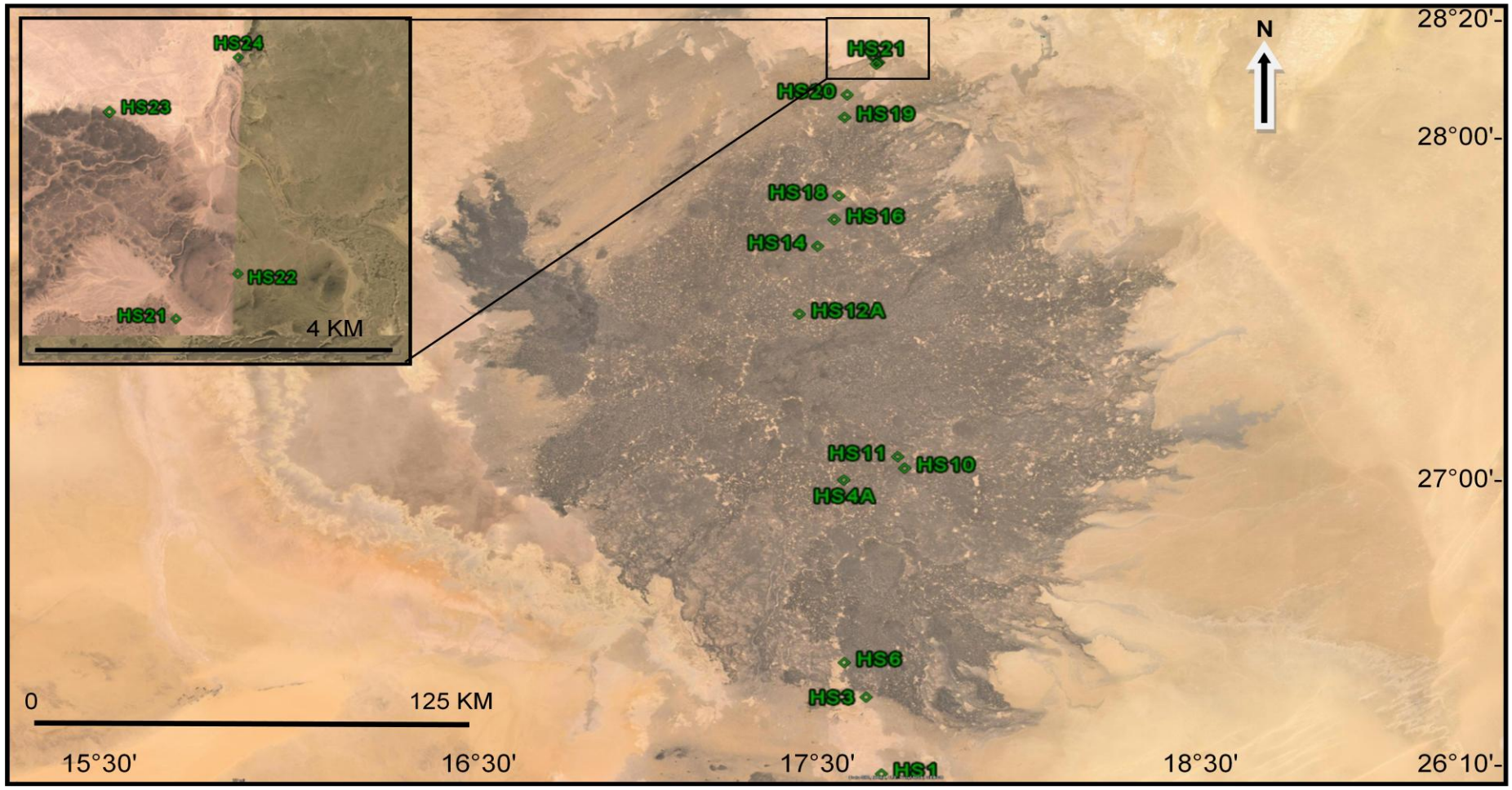

Figure E3: satellite image (Google Earth Pro4) for the area covering the Al Haruj al Aswad volcanic provinces showing the location of sixteen samples used in this study.

Figure E1.8 show the hand specimen of sample HS23 (phase 1) which occurs in huge lava at the far north of Al Haruj province at about 37 km south of Zalla Village.

Figure E1.9 show the outcrop of phase 1 and sample HS23 in occurs in huge lava at about 37 km south of Zalla Village.

The most distinctive criterion of this phase is the presence of numerous baltas (known by Busweril and Suwesi, 1993) (shallow depressions or accretionary mantles). The baltas, developed on basalt flows, consist of a bowl-shaped depression with a maximum diameter of about 200 metres. Accessibility within this phase is fair and gets more difficult as flows become progressively younger.

Figure E1.10 show the outcrop of phase 2 and sample HS1 in occurs at about 270 km south of Zalla Village, the far south of Al Haruj province.

The size and number of baltas and drainage intensity increase with age, and based on that criterion and on accessibility, this phase has been classified into three mappable units (3.1, 3.2 and 3.3). The lava flows are composed of fine grained vesicular olivine basalts. Olivine phenocrysts are 1-2 mm in size and have a green glassy appearance.

Three alkali olivine basalt samples from Phase 3 were collected different locations, HS10 from ~172 km south of Zalla Village, center of Al Haruj province. While two samples (HS19 and HS20) from the far north of Al Haruj province (~55 and 48 km south of Zalla, respectively).

Flows of the phase 4 are distinguished by their irregular morphology and the preservation of relief surface features. The surface is cut by numerous semicircular and elongate open fissures showing concentration in E-W and NE-SW directions particularly north of Qarat al Awdad and SW of Quwayrat ar Rijel respectively. The phase has an areal extent of approximately 15.000 km^2, including where it has been partly buried by phases 5 and 6 amounting to an erupted volume of approximately 75 km^3. This phase has been divided into three mappable units (4.1, 4.2 and 4.3) based on drainage intensity, accessibility and tonal difference. The lava is fine to medium grained vesicular olivine (5-15%) basalts. Olivine phenocrysts were fresh, green and glassy.

Three tholeiitic olivine basalt samples from Phase 4 (Figure E1.11) were collected from different locations, HS3 from ~245 km south of Zalla Village (the far south of Al Haruj province). While two samples (HS16 and HS21) from the north and far north of Al Haruj province (~88 and 40 km south of Zalla, respectively).

Figure E1.11 show the outcrop of phase 4 and sample no Hs16 in occur in length lava, from the north part of Al Haruj province, at about 88 km south from Zalla Village.

The lava flow of the phase 5 is the second youngest phase of volcanism in the Al Haruj and is very distinctive in the field. It is strike in NE-SW and NW-SE directions and has spread over wide areas (Figure E1.12). In the field, the phase has an areal extent of approximately 3.000 km^2; including where it has been partly buried by phase 6 amounting to an erupted volume of approximately 37.5 km^3. There are three major periods of eruptive activity within this phase. This can be observed in the west of Qarat Umm ash Shtayrat and NW of Qarat Shulaymat aj Jidari. The individual lava flows are about 3 - 5 metres thick and the surface structures developed are mainly of the pahoehoe type. This phase is mostly drained internally and the presence of very well preserved pahoehoe surfaces indicates the very recent age of this phase. The rock type is fresh fine grained olivine (7-10%) basalt.

One olivine basalt sample from Phase 5 (Figure E1.12) was collected, HS11 from ~166 km south of Zalla Village, center of Al Haruj province.

Figure E1.12 show the lava of phase 5 occurs within length Wadi, from center of Al Haruj province.

The lava flows of the phase 6 are the youngest eruptive products of the Al Haruj volcanic field. It is found in close proximity to Phase 5. These flows are 4 - 15 meters thick, display many of the superficial flows features that are characteristic of pahoehoe flows formed on moderate gradients, such as linear ridges, lava coils and blisters and lobate to digitate flows margins. The lava field strike NW and although it is thought here that fissure eruption was the dominant type, this phase has been divided into two mappable units (6.1 and 6.2). Sub-phase 6.1 covers an area of approximately 1800 km^2 amounting to a volume of 18 km^3. Sub-phase 6.2 is smaller covering 995 km^2, given an amounting to an erupted volume of approximately 10 km^3. The lavas are composed of medium grained vesicular olivine phyric (10-15%) basalts which have a crystalline doleritic appearance. Olivine phenocrysts are fresh, green and glassy. No samples were collected from this phase.

The volcanic field of Al Haruj al Aswad area contains approximately seventy basaltic cones and shield volcanoes and many associated lava flows of tertiary age. The volcanoes have been broadly classified here into volcanic cones and shield volcanoes.

Volcanic cones are characterised by the presence of steep sides all round. They are distinguished in the field by their small size relative to the shield volcanoes, high angle of repose (30°- 40°) and the fragmentary nature of the top of material ejected. They are also characterised by the presence at the top of the volcanic cones of small flat-bottomed depressions, more or les circular in plan vary few cones have subsided below the level of the surrounding plateau and the depressions are commonly occupied by a thin layer of sand and silt.

Three olivine basalt samples from volcanic cones were collected from different locations, HS12A from ~112 km south of Zalla Village(lower part of cone), north center of Al Haruj province. While two samples (HS14 and HS18) are from north of Al Haruj province (~99 and 80 km south of Zalla Village, respectively).

A number of large volcanoes (shield volcanoes) (base diameter up to 8 km) are built chiefly of overlapping basaltic lava flows. They are fairly old volcanoes that are marked by the presence of radial drainage systems and low profiles with slopes around 5 to 15 degrees. In most of these shield volcanoes, there is a clear evidence of the presence of two periods of major eruptive activity separated by a dormant phase during which erosion was very well developed. The first phase represents the bulk of the shield volcanoes while the latter phase is presented by a small dark coloured cone on the peak of the shield volcanoes. It is thought here that during the early stage, most eruptions issued from central conduits, while at letter stages, discharge of lava and sometimes pyroclastic materials took place increasingly from radial fissures down the flanks, and from closely spaced and sometimes coalescing explosion pits or scoria cones, Busrewil and Suwesi (1993).

In few localities on Al Haruj area doleritic dike-like masses have intruded pre-existing volcanic cones. Shallow erosion of the western slopes of Quwayrat ar Rijel cones have exposed parts of two small separate bodies, with slabby and platy jointing that gives the dolerites a distinctive lighter colour when viewed from a distance. They are a few tens of meters wide and about 50 m apart and may represent extended off-shoots from a larger dike.

One doleritic dyke sample (HS22) was collected from ~39 km south of Zalla, the far north of Al Haruj province.

Table E13 Details of basalt samples from Al Haruj al Aswad volcanic province.

Sample	Rock type	Rock	Location	Latitude and longitude
HS 1	Alkaline basalt	lava	~270 km south of Zalla Village(phase 2), the far south of Al Haruj province	26°08'689''N17°38'962''E
HS 3	Tholeiite olivine basalt	lava	~245 km south of Zalla Village(phase 4), the far south of Al Haruj province	26°22'200''N 17°36'680''E
HS 4A	Olivine basalt	lava	~240 km south of Zalla Village(phase 1), the far south of Al Haruj province	26°24'222''N17°33'689''E
HS 6	Alkaline basalt	lava	~230 km south of Zalla Village(phase 2), south of Al Haruj province	26°28'310''N17°33'182''E
HS 10	Alkali olivine basalt	lava	~172 km south of Zalla Village(phase 3), center of Al Haruj province	27°02'127''N17°43'820''E
HS 11	Olivine basalt	lava	~166 km south of Zalla Village(phase 5), center of Al Haruj province	27°04'157''N17°42'707''E
HS 12A	Olivine basalt	plug	~112 km south of Zalla Village, north center of Al Haruj province	27°29'270''N17°26'813''E
HS 14	Olivine basalt	plug	~99 km south of Zalla Village, north of Al Haruj province	27°41'065''N17°30'065''E
HS 16	Tholeiite olivine basalt	lava	~88 km south of Zalla Village(phase 4), north of Al Haruj province	27°45'682''N17°32'905''E
HS 18	Olivine basalt	plug	~80 km south of Zalla Village, north of Al Haruj province	27°49'824''N17°33'750''E
HS 19	Alkali olivine basalt	lava	~55 km south of Zalla Village(phase 3), the far north of Al Haruj province	28°03'540''N17°34'968''E

HS 20	Alkali olivine basalt	lava	~48 km south of Zalla Village(phase 3), the far north of Al Haruj province	28°07'500''N17°35'485''E
HS 21	Alkali olivine basalt	lava	~40 km south of Zalla Village(phase 4), the far north of Al Haruj province	28°12'795''N17°40'465''E
HS 22	Dolerite	dyke	~39 km south of Zalla Village, the far north of Al Haruj province	28°13'079''N17°40'862''E
HS 23	Olivine basalt	lava	~37 km south of Zalla Village(phase 1), the far north of Al Haruj province	28°14'088''N17°39'999''E
HS 24	Olivine basalt	lava	~35 km south of Zalla Village(phase 1), the far north of Al Haruj province	28°14'438''N17°40'840''E

Lab ID	Watts	Relative Isotopic Abundances										Derived Results								
HS12A												^{39}Ar Mol ¥ 10^{-14}	^{39}Ar % of total	% $(^{36}Ar)_{Ca}$			% $^{40}Ar^{*}$			w/±*J* ±1σ
23 EK63		^{40}Ar	±1σ	^{39}Ar	±1σ	^{38}Ar	±1σ	^{37}Ar	±1σ	^{36}Ar	±1σ				Ca/K	±1σ		Age (Ma)	±1σ	
61103-6	10.0	1131	0.15	4.84	0.00	0.49	0.00	0.08	0.00	2.23	0.002	0.00	3.20	0.10	2.528	0.0531	41.2	12.10	0.08	0.09
61103-7	11.0	1407	0.46	7.11	0.01	0.52	0.00	0.13	0.00	2.24	0.002	0.00	4.70	0.10	2.737	0.0403	52.6	13.05	0.06	0.07
61103-8	12.0	1291	0.39	7.92	0.01	0.37	0.00	0.17	0.00	1.49	0.002	0.01	5.20	0.20	3.180	0.0306	65.7	13.44	0.04	0.06
61103-9	13.0	1310	0.41	9.38	0.01	0.29	0.00	0.19	0.00	1.02	0.002	0.01	6.20	0.40	3.117	0.0259	76.8	13.46	0.03	0.05
61103-10	14.0	1293	0.39	10.1	0.01	0.24	0.00	0.19	0.00	0.71	0.002	0.01	6.60	0.60	2.876	0.0331	83.7	13.47	0.03	0.05
61103-11	15.0	1238	0.36	10.2	0.01	0.20	0.00	0.18	0.00	0.47	0.002	0.01	6.70	0.80	2.634	0.0297	88.6	13.49	0.02	0.05
61103-12	17.0	1395	0.39	11.7	0.01	0.21	0.00	0.19	0.00	0.46	0.002	0.01	7.70	0.80	2.456	0.0182	90.3	13.49	0.02	0.05
61103-13	19.0	1199	0.32	10.1	0.01	0.18	0.00	0.16	0.00	0.39	0.001	0.01	6.60	0.90	2.448	0.0255	90.5	13.48	0.02	0.05
61103-14	25.0	1808	0.54	15.1	0.01	0.28	0.00	0.27	0.00	0.64	0.001	0.01	9.90	0.90	2.764	0.0142	89.6	13.48	0.02	0.05
61103-15	30.0	4226	1.3	35.2	0.02	0.72	0.00	1.77	0.00	1.61	0.002	0.02	23.2	2.20	7.611	0.0115	88.9	13.41	0.02	0.05
61103-16	40.0	3427	1.00	28.6	0.01	0.59	0.00	2.04	0.00	1.27	0.001	0.02	18.8	3.30	10.82	0.0144	89.3	13.48	0.02	0.05
61103-17	50.0	277.4	0.09	1.74	0.00	0.09	0.00	0.15	0.00	0.34	0.018	0.00	1.10	0.90	12.66	0.1326	63.9	12.83	0.39	0.39

Lab ID	Watts	Inverse Isochron Data				^{36}Ar/^{39}Ar Er.Corr.	*J* (X 10^{-3}) ± 1σ = 0.070 ± 0.000
HS12A							
23 EK63		^{36}Ar/^{40}Ar	±1σ	^{39}Ar/^{40}Ar	±1σ		
61103-6	10.0	0.002	0.41	0.00428	0.14	0.7684	
61103-7	11.0	0.0012	0.41	0.00506	0.13	0.7680	
61103-8	12.0	0.001	0.41	0.00614	0.13	0.7674	
61103-9	13.0	0.001	0.43	0.00716	0.13	0.7361	
61103-10	14.0	0.001	0.46	0.00780	0.12	0.6891	
61103-11	15.0	0.000	0.59	0.00824	0.12	0.5445	
61103-12	17.0	0.000	0.58	0.00840	0.11	0.5494	
61103-13	19.0	0.000	0.45	0.00842	0.11	0.7156	
61103-14	25.0	0.000	0.46	0.00834	0.12	0.6939	
61103-15	30.0	0.000	0.42	0.00831	0.11	0.7625	
61103-16	40.0	0.000	0.42	0.00831	0.11	0.7645	
61103-17	50.0	0.0012	5.38	0.00625	0.20	0.0560	

Table E14: ^{40}Ar/^{39}Ar step-heating analytical results for *HS12A basalt plug (27.29.270N17.26.813E),* in Al Haruj al Aswad.

Lab ID	Watts	Relative Isotopic Abundances										Derived Results								
HS14												^{39}Ar Mol ¥ 10^{-14}	^{39}Ar % of total	% $(^{36}Ar)_{Ca}$			% $^{40}Ar^{*}$			w/±*J* ±1σ
24 EK63		^{40}Ar	±1σ	^{39}Ar	±1σ	^{38}Ar	±1σ	^{37}Ar	±1σ	^{36}Ar	±1σ				Ca/K	±1σ		Age (Ma)	±1σ	
61081-7	11.0	196.2	0.25	1.03	0.02	0.14	0.01	0.08	0.01	0.40	0.002	0.00	1.00	0.40	12.43	0.838	39.3	10.1	0.229	0.23
61081-8	12.0	291.4	0.10	2.19	0.01	0.13	0.00	0.10	0.00	0.37	0.001	0.00	2.10	0.60	7.072	0.228	61.9	11.1	0.061	0.07
61081-9	13.0	266.0	0.03	2.50	0.00	0.10	0.00	0.08	0.00	0.24	0.002	0.00	2.50	0.70	5.133	0.135	72.8	10.4	0.045	0.05
61081-10	14.0	376.5	0.10	3.96	0.00	0.12	0.00	0.09	0.00	0.28	0.002	0.00	3.90	0.70	3.559	0.073	78.2	10.0	0.029	0.04
61081-11	15.0	631.4	0.16	7.29	0.00	0.15	0.00	0.13	0.00	0.35	0.002	0.01	7.20	0.80	2.753	0.037	83.4	9.71	0.022	0.04
61081-12	17.0	1289	0.39	15.5	0.01	0.29	0.00	0.20	0.00	0.62	0.001	0.01	15.2	0.70	2.014	0.020	85.8	9.58	0.017	0.03
61081-13	19.0	1434	0.41	17.1	0.01	0.33	0.00	0.18	0.00	0.74	0.001	0.01	16.8	0.50	1.658	0.013	84.6	9.56	0.018	0.03
61081-14	25.0	1983	0.57	21.1	0.01	0.54	0.00	0.33	0.00	1.65	0.002	0.01	20.7	0.40	2.509	0.013	75.3	9.54	0.023	0.04
61081-15	30.0	1656	0.47	13.4	0.01	0.61	0.00	0.49	0.00	2.38	0.002	0.01	13.2	0.40	5.848	0.019	57.2	9.52	0.039	0.05
61081-16	40.0	5119	1.60	16.0	0.01	2.70	0.00	3.55	0.00	13.5	0.005	0.01	15.7	0.60	35.62	0.030	21.8	9.47	0.147	0.15
61081-17	50.0	405.6	0.11	1.74	0.00	0.21	0.00	0.28	0.00	0.97	0.002	0.00	1.70	0.60	26.29	0.168	28.9	9.13	0.115	0.12

Lab ID	Watts	Inverse Isochron Data					*J* (X 10^{-3}) ± 1σ = 0.075 ± 0.000
HS14						^{36}Ar/^{39}Ar Er.Corr.	
24 EK63		^{36}Ar/^{40}Ar	±1σ	^{39}Ar/^{40}Ar	±1σ		
61081-7	11.0	0.002	0.71	0.00524	1.94	0.1220	
61081-8	12.0	0.001	0.55	0.00749	0.37	0.4753	
61081-9	13.0	0.001	0.88	0.00938	0.22	0.3359	
61081-10	14.0	0.001	0.71	0.01052	0.15	0.4407	
61081-11	15.0	0.001	0.75	0.01156	0.12	0.4257	
61081-12	17.0	0.001	0.46	0.01204	0.12	0.7024	
61081-13	19.0	0.001	0.44	0.01190	0.11	0.7203	
61081-14	25.0	0.001	0.42	0.01062	0.11	0.7584	
61081-15	30.0	0.001	0.41	0.00808	0.12	0.7844	
61081-16	40.0	0.002	0.40	0.00309	0.11	0.7889	
61081-17	50.0	0.002	0.47	0.00425	0.25	0.6213	

Table E15: ^{40}Ar/^{39}Ar step-heating analytical results for *HS14 basalt plug (27.39.065N17.29.065E),* in Al Haruj al Aswad.

Lab ID	Watts	Relative Isotopic Abundances										Derived Results								
HS18												^{39}Ar Mol ¥ 10^{-14}	^{39}Ar % of total	% $(^{36}Ar)_{Ca}$			% $^{40}Ar^{*}$			w/±*J* ±1σ
19 EK63		^{40}Ar	±1σ	^{39}Ar	±1σ	^{38}Ar	±1σ	^{37}Ar	±1σ	^{36}Ar	±1σ				Ca/K	±1σ		Age (Ma)	±1σ	
61097-5	9.0	657.2	2.16	2.13	0.06	0.60	0.02	0.20	0.02	1.75	0.006	0.00	1.2	0.2	12.26	1.350	20.8	8.60	0.330	0.33
61097-6	10.0	799.2	2.11	7.16	0.01	0.71	0.01	0.21	0.01	1.13	0.006	0.01	3.9	0.3	3.790	0.098	57.8	8.61	0.065	0.07
61097-7	11.0	1276	1.84	14.3	0.01	0.38	0.01	0.26	0.00	1.18	0.006	0.01	7.8	0.4	2.372	0.030	72.6	8.68	0.033	0.03
61097-8	12.0	1680	1.86	20.4	0.01	0.45	0.01	0.26	0.00	1.19	0.006	0.01	11.1	0.4	1.708	0.021	78.9	8.66	0.025	0.03
61097-9	13.0	2014	1.89	25.2	0.01	0.51	0.01	0.24	0.00	1.27	0.006	0.02	13.7	0.3	1.257	0.018	81.3	8.68	0.022	0.02
61097-10	14.0	2087	1.90	25.9	0.01	0.54	0.01	0.19	0.00	1.35	0.006	0.02	14.1	0.2	0.947	0.018	80.7	8.67	0.022	0.02
61097-11	15.0	1897	1.89	23.1	0.01	0.50	0.01	0.16	0.00	1.33	0.006	0.02	12.6	0.2	0.914	0.016	79.0	8.65	0.023	0.02
61097-12	17.0	1727	1.87	18.2	0.01	0.55	0.01	0.16	0.00	1.85	0.006	0.01	9.9	0.2	1.169	0.022	68.1	8.63	0.031	0.03
61097-13	19.0	1569	1.86	12.5	0.01	0.61	0.01	0.15	0.00	2.56	0.006	0.01	6.8	0.1	1.588	0.031	51.4	8.58	0.050	0.05
61097-14	25.0	3829	2.16	22.3	0.01	1.75	0.01	1.62	0.00	8.10	0.007	0.02	12.2	0.4	9.605	0.018	37.1	8.52	0.069	0.07
61097-15	30.0	4487	2.28	12.4	0.01	2.45	0.01	1.92	0.00	12.4	0.008	0.01	6.8	0.3	20.45	0.039	17.7	8.59	0.172	0.17

Lab ID	Watts	Inverse Isochron Data					*J* ($X 10^{-3}$) ± 1σ = 0.074 ± 0.000
HS18						^{36}Ar/^{39}Ar Er.Corr.	
19 EK63		^{36}Ar/^{40}Ar	±1σ	^{39}Ar/^{40}Ar	±1σ		
61097-5	9.0	0.003	0.63	0.00323	2.79	0.1476	
61097-6	10.0	0.001	0.74	0.00896	0.33	0.5178	
61097-7	11.0	0.001	0.66	0.01118	0.19	0.5180	
61097-8	12.0	0.001	0.65	0.01217	0.16	0.5162	
61097-9	13.0	0.001	0.63	0.01250	0.15	0.5259	
61097-10	14.0	0.001	0.60	0.01245	0.14	0.5457	
61097-11	15.0	0.001	0.60	0.01220	0.15	0.5521	
61097-12	17.0	0.001	0.52	0.01054	0.16	0.6382	
61097-13	19.0	0.002	0.48	0.00799	0.16	0.7003	
61097-14	25.0	0.002	0.41	0.00582	0.12	0.7821	
61097-15	30.0	0.003	0.41	0.00275	0.13	0.7850	

Table E17: ^{40}Ar/^{39}Ar step-heating analytical results for *HS18 plug (27.49.824N17.33.750E),* in Al Haruj al Aswad.

Lab ID	Watts	Relative Isotopic Abundances										Derived Results								
HS23												^{39}Ar Mol ¥ 10^{-14}	^{39}Ar % of total	% $(^{36}Ar)_{Ca}$			% $^{40}Ar^{*}$			w/±*J* ±1σ
13 EK63		^{40}Ar	±1σ	^{39}Ar	±1σ	^{38}Ar	±1σ	^{37}Ar	±1σ	^{36}Ar	±1σ				Ca/K	±1σ		Age (Ma)	±1σ	
61089-5	9.00	726.6	0.49	8.95	0.03	0.37	0.01	0.26	0.01	1.10	0.003	0.01	4.2	0.3	2.649	0.107	55.1	5.98	0.037	0.05
61089-6	10.0	1690	0.59	30.7	0.02	0.55	0.00	0.43	0.01	1.03	0.003	0.02	14.4	0.5	1.274	0.015	81.8	6.01	0.013	0.03
61089-7	11.0	1858	0.52	33.7	0.02	0.61	0.00	0.37	0.00	1.15	0.003	0.02	15.8	0.4	1.005	0.012	81.5	6.01	0.012	0.03
61089-8	12.0	1516	0.45	26.4	0.01	0.51	0.00	0.22	0.01	1.10	0.003	0.02	12.4	0.3	0.782	0.016	78.3	6.00	0.014	0.03
61089-9	13.0	1231	0.43	20.5	0.01	0.44	0.00	0.17	0.01	1.04	0.003	0.01	9.6	0.2	0.776	0.020	74.9	6.01	0.016	0.03
61089-10	14.0	1142	0.43	17.9	0.01	0.42	0.00	0.21	0.00	1.13	0.003	0.01	8.4	0.2	1.057	0.022	70.4	6.00	0.018	0.03
61089-11	15.0	1140	0.45	17.3	0.01	0.43	0.00	0.24	0.00	1.23	0.003	0.01	8.1	0.2	1.297	0.023	68.0	5.99	0.019	0.04
61089-12	17.0	1471	0.53	23.3	0.01	0.54	0.00	0.46	0.00	1.44	0.003	0.02	10.9	0.4	1.808	0.017	70.8	5.98	0.017	0.03
61089-13	19.0	970.8	0.46	11.4	0.01	0.43	0.00	1.39	0.00	1.56	0.003	0.01	5.4	1.1	11.19	0.036	52.4	5.97	0.030	0.04
61089-14	25.0	2080	0.75	18.4	0.01	1.02	0.00	5.22	0.01	4.31	0.003	0.01	8.6	1.5	26.08	0.036	39.0	5.94	0.044	0.05
61089-15	30.0	211.2	0.4	2.22	0.01	0.10	0.00	0.54	0.00	0.39	0.003	0.00	1.0	1.7	22.30	0.200	46.5	5.96	0.068	0.07
61089-16	40.0	194.0	0.41	1.53	0.01	0.10	0.00	0.41	0.01	0.43	0.003	0.00	0.7	1.2	24.93	0.298	34.7	5.94	0.102	0.11
61089-17	50.0	256.0	0.41	0.86	0.01	0.15	0.00	0.25	0.00	0.74	0.003	0.00	0.4	0.4	26.93	0.496	14.1	5.67	0.208	0.21

Lab ID	Watts	Inverse Isochron Data				^{36}Ar/^{39}Ar Er.Corr.	*J* (X 10^{-3}) ± 1σ = 0.074 ± 0.000
HS23							
13 EK63		^{36}Ar/^{40}Ar	±1σ	^{39}Ar/^{40}Ar	±1σ		
61089-5	9.00	0.002	0.51	0.01232	0.38	0.5170	
61089-6	10.0	0.001	0.50	0.01819	0.12	0.6402	
61089-7	11.0	0.001	0.46	0.01815	0.12	0.6892	
61089-8	12.0	0.001	0.48	0.01746	0.12	0.6589	
61089-9	13.0	0.001	0.50	0.01667	0.12	0.6418	
61089-10	14.0	0.001	0.47	0.01571	0.13	0.6764	
61089-11	15.0	0.001	0.47	0.01518	0.12	0.6820	
61089-12	17.0	0.001	0.46	0.01582	0.12	0.6942	
61089-13	19.0	0.002	0.44	0.01174	0.13	0.7207	
61089-14	25.0	0.002	0.41	0.00879	0.13	0.7760	
61089-15	30.0	0.002	0.86	0.01042	0.39	0.3626	
61089-16	40.0	0.002	0.83	0.00781	0.45	0.3659	

Table E18: ^{40}Ar/^{39}Ar step-heating analytical results for *HS23 basalt lava (phase 1) (28.14.088N17.39.999E),* in Al Haruj al Aswad.

Lab ID	Watts	Relative Isotopic Abundances										Derived Results								
HS24												^{39}Ar Mol ¥ 10^{-14}	^{39}Ar % of total	% $(^{36}Ar)_{Ca}$			% $^{40}Ar^{*}$			w/±*J* ±1σ
18 EK63		^{40}Ar	±1σ	^{39}Ar	±1σ	^{38}Ar	±1σ	^{37}Ar	±1σ	^{36}Ar	±1σ				Ca/K	±1σ		Age (Ma)	±1σ	
61087-4	8.0	384.2	1.31	1.06	0.03	0.26	0.01	0.04	0.01	1.14	0.009	0.00	0.60	0.10	4.835	0.869	11.4	5.52	0.431	0.43
61087-5	9.0	819.8	1.31	6.90	0.01	0.4	0.00	0.09	0.00	1.66	0.009	0.00	4.00	0.10	1.680	0.056	39.7	6.30	0.072	0.07
61087-6	10.0	1339	1.35	20.2	0.01	0.48	0.00	0.15	0.00	1.33	0.009	0.01	11.7	0.20	0.936	0.018	70.4	6.24	0.026	0.03
61087-7	11.0	1723	1.39	30.0	0.01	0.54	0.00	0.19	0.00	1.06	0.009	0.02	17.3	0.30	0.801	0.010	81.6	6.25	0.018	0.02
61087-8	12.0	1455	1.36	26.7	0.01	0.44	0.00	0.16	0.00	0.69	0.009	0.02	15.4	0.40	0.761	0.014	86.0	6.26	0.018	0.02
61087-9	13.0	1295	1.38	23.6	0.02	0.38	0.00	0.14	0.00	0.62	0.009	0.02	13.6	0.40	0.748	0.015	85.8	6.29	0.020	0.02
61087-10	14.0	748.1	1.32	12.7	0.01	0.24	0.00	0.11	0.00	0.50	0.009	0.01	7.30	0.40	1.102	0.027	80.1	6.32	0.033	0.03
61087-11	15.0	567.1	1.31	8.61	0.01	0.2	0.00	0.11	0.00	0.53	0.009	0.01	5.00	0.40	1.685	0.036	71.9	6.33	0.048	0.05
61087-12	17.0	650.8	1.31	9.10	0.01	0.24	0.00	0.17	0.00	0.76	0.009	0.01	5.30	0.40	2.454	0.040	65.5	6.26	0.047	0.05
61087-13	19.0	764.2	1.32	10.3	0.01	0.3	0.00	0.17	0.00	0.96	0.009	0.01	5.90	0.30	2.100	0.028	62.4	6.21	0.044	0.04
61087-14	25.0	4489	1.91	18.0	0.01	2.51	0.00	3.14	0.00	12.4	0.010	0.01	10.4	0.40	22.63	0.025	18.0	6.04	0.120	0.12
61087-15	30.0	2387	1.45	5.29	0.01	1.4	0.00	0.59	0.00	7.22	0.009	0.00	3.10	0.10	14.47	0.072	9.90	5.99	0.237	0.24
61087-16	40.0	302.1	1.30	0.89	0.01	0.18	0.00	0.14	0.00	0.89	0.009	0.00	0.50	0.30	20.11	0.373	12.4	5.67	0.469	0.47

Lab ID	Watts	Inverse Isochron Data					*J* (X 10^{-3}) ± 1σ = 0.074 ± 0.000
HS24						^{36}Ar/^{39}Ar Er.Corr.	
18 EK63		^{36}Ar/^{40}Ar	±1σ	^{39}Ar/^{40}Ar	±1σ		
61087-4	8.0	0.003	0.93	0.00275	2.53	0.1140	
61087-5	9.0	0.002	0.68	0.00842	0.23	0.5064	
61087-6	10.0	0.001	0.77	0.01509	0.15	0.4278	
61087-7	11.0	0.001	0.92	0.01745	0.13	0.3561	
61087-8	12.0	0.001	1.33	0.01835	0.14	0.2474	
61087-9	13.0	0.001	1.45	0.01824	0.16	0.2271	
61087-10	14.0	0.001	1.77	0.01694	0.22	0.1997	
61087-11	15.0	0.001	1.68	0.01520	0.27	0.2265	
61087-12	17.0	0.001	1.24	0.01399	0.24	0.2938	
61087-13	19.0	0.001	1.01	0.01343	0.22	0.3494	
61087-14	25.0	0.003	0.41	0.00397	0.12	0.7785	
61087-15	30.0	0.003	0.42	0.00221	0.17	0.7420	
61087-16	40.0	0.003	1.14	0.00292	0.84	0.3085	

Table E16: ^{40}Ar/^{39}Ar step-heating analytical results for *HS24 basalt lava (phase 1) (28.14.438N17.40.840E),* in Al Haruj al Aswad.

Lab ID	Watts	Relative Isotopic Abundances										Derived Results								
												^{39}Ar Mol ¥ 10^{-14}	^{39}Ar % of total	% $(^{36}Ar)_{Ca}$			% $^{40}Ar^{*}$			w/±*J* ±1σ
HS22																				
17 EK63		^{40}Ar	±1σ	^{39}Ar	±1σ	^{38}Ar	±1σ	^{37}Ar	±1σ	^{36}Ar	±1σ				Ca/K	±1σ		Age (Ma)	±1σ	
61075-5	9.0	308.4	3.61	5.04	0.07	0.35	0.03	0.21	0.03	0.38	0.010	0.00	5.10	1.0	5.317	0.654	63.6	5.21	0.143	0.14
61075-6	10.0	576.7	2.54	12.3	0.02	0.27	0.01	0.15	0.01	0.28	0.009	0.01	12.5	0.9	1.539	0.074	85.7	5.39	0.041	0.04
61075-7	11.0	760.4	2.51	17.0	0.01	0.25	0.01	0.11	0.0	0.27	0.009	0.01	17.3	0.7	0.814	0.026	89.4	5.35	0.029	0.03
61075-8	12.0	734.6	2.51	16.7	0.01	0.24	0.00	0.08	0.00	0.21	0.009	0.01	17.0	0.7	0.631	0.021	91.4	5.38	0.030	0.03
61075-9	13.0	669.8	2.51	15.2	0.01	0.21	0.00	0.09	0.00	0.19	0.009	0.01	15.4	0.8	0.713	0.023	91.6	5.41	0.033	0.04
61075-10	14.0	570.3	2.51	12.9	0.01	0.18	0.00	0.09	0.00	0.17	0.009	0.01	13.1	0.9	0.874	0.025	91.2	5.37	0.038	0.04
61075-11	15.0	547.1	2.51	11.9	0.01	0.18	0.00	0.12	0.00	0.24	0.009	0.01	12.0	0.8	1.255	0.027	86.8	5.35	0.042	0.04
61075-12	17.0	371.7	2.50	7.51	0.01	0.13	0.00	0.08	0.00	0.24	0.009	0.01	7.60	0.5	1.270	0.048	80.5	5.32	0.065	0.07

Lab ID	Watts	Inverse Isochron Data					*J* (X 10^{-3}) ± 1σ = 0.074 ± 0.000
						^{36}Ar/^{39}Ar Er.Corr.	
HS22							
17 EK63		^{36}Ar/^{40}Ar	±1σ	^{39}Ar/^{40}Ar	±1σ		
61075-5	9.0	0.001	2.85	0.01633	1.83	0.2792	
61075-6	10.0	0.001	3.19	0.02127	0.48	0.1599	
61075-7	11.0	0.000	3.23	0.02235	0.35	0.1366	
61075-8	12.0	0.000	4.12	0.02274	0.36	0.1094	
61075-9	13.0	0.000	4.59	0.02264	0.39	0.1032	
61075-10	14.0	0.000	5.17	0.02269	0.46	0.1008	
61075-11	15.0	0.000	3.68	0.02168	0.47	0.1457	
61075-12	17.0	0.001	3.66	0.02021	0.69	0.1951	

Table E19: ^{40}Ar/^{39}Ar step-heating analytical results for *HS22 basalt dyke (28.13.079N17.40.862E)*, in Al Haruj al Aswad.

Lab ID	Watts	Relative Isotopic Abundances										Derived Results								
HS4A												^{39}Ar Mol ¥ 10^{-14}	^{39}Ar % of total	% (^{36}Ar)$_{Ca}$			% ^{40}Ar*			w/±*J* ±1σ
22 EK63		^{40}Ar	±1σ	^{39}Ar	±1σ	^{38}Ar	±1σ	^{37}Ar	±1σ	^{36}Ar	±1σ				Ca/K	±1σ		Age (Ma)	±1σ	
61079-7	11.0	170.0	0.90	1.46	0.13	0.30	0.04	0.25	0.04	0.43	0.009	0.00	0.90	1.20	25.19	4.510	26.0	4.07	0.442	0.44
61079-8	12.0	189.5	0.52	2.14	0.04	0.21	0.02	0.20	0.02	0.41	0.003	0.00	1.30	1.00	13.63	1.265	36.3	4.327	0.111	0.11
61079-9	13.0	290.1	0.23	4.93	0.01	0.19	0.00	0.17	0.00	0.43	0.002	0.00	3.00	0.80	5.121	0.132	56.2	4.421	0.027	0.03
61079-10	14.0	455.9	0.06	9.52	0.01	0.21	0.00	0.21	0.00	0.49	0.001	0.01	5.80	0.80	3.233	0.040	68.1	4.361	0.014	0.02
61079-11	15.0	602.9	0.16	14.6	0.01	0.26	0.00	0.24	0.00	0.41	0.002	0.01	8.80	1.10	2.401	0.025	79.8	4.399	0.010	0.02
61079-12	17.0	1395	0.41	35.5	0.02	0.55	0.00	0.38	0.00	0.76	0.002	0.02	21.5	1.00	1.575	0.006	84.0	4.403	0.008	0.02
61079-13	19.0	1369	0.40	33.0	0.01	0.56	0.00	0.28	0.00	0.95	0.002	0.02	20.0	0.60	1.265	0.009	79.3	4.394	0.010	0.02
61079-14	25.0	1352	0.41	29.8	0.01	0.59	0.00	0.50	0.00	1.27	0.001	0.02	18.0	0.80	2.481	0.009	72.1	4.373	0.012	0.02
61079-15	30.0	1572	0.48	17.2	0.01	0.85	0.00	2.00	0.00	3.42	0.002	0.01	10.4	1.20	17.20	0.020	35.9	4.398	0.037	0.04
61079-16	40.0	1128	0.33	15.9	0.01	0.58	0.00	1.76	0.00	2.07	0.002	0.01	9.60	1.70	16.33	0.020	46.1	4.383	0.026	0.03
61079-17	50.0	183.9	0.06	0.99	0.00	0.11	0.00	0.11	0.00	0.51	0.001	0.00	0.60	0.40	16.30	0.276	18.1	4.521	0.105	0.11

Lab ID	Watts	Inverse Isochron Data				
						^{36}Ar/^{39}Ar Er.Corr.
HS4A						
22 EK63		^{36}Ar/^{40}Ar	±1σ	^{39}Ar/^{40}Ar	±1σ	
61079-7	11.0	0.003	2.13	0.00855	8.92	0.0228
61079-8	12.0	0.002	0.98	0.01124	1.80	0.1278
61079-9	13.0	0.002	0.62	0.01699	0.24	0.4882
61079-10	14.0	0.001	0.48	0.02089	0.13	0.6547
61079-11	15.0	0.001	0.54	0.02425	0.12	0.5829
61079-12	17.0	0.001	0.46	0.02551	0.11	0.7020
61079-13	19.0	0.001	0.45	0.02415	0.11	0.7121
61079-14	25.0	0.001	0.42	0.02206	0.11	0.7721
61079-15	30.0	0.002	0.41	0.01091	0.12	0.7828
61079-16	40.0	0.002	0.41	0.01405	0.12	0.7765
61079-17	50.0	0.003	0.49	0.00537	0.40	0.5200

J (X 10^{-3}) ± 1σ = 0.074 ± 0.000

Table E20: ^{40}Ar/^{39}Ar step-heating analytical results for *HS4A basalt lava (phase 1) (26.24.222N17.33.689E),* in Al Haruj al Aswad.

Lab ID	Watts	Relative Isotopic Abundances										Derived Results								
HS1												^{39}Ar Mol ¥ 10^{-14}	^{39}Ar % of total	% $(^{36}Ar)_{Ca}$			% $^{40}Ar^{*}$			w/±*J* ±1σ
27 EK63		^{40}Ar	±1σ	^{39}Ar	±1σ	^{38}Ar	±1σ	^{37}Ar	±1σ	^{36}Ar	±1σ				Ca/K	±1σ		Age (Ma)	±1σ	
61105-6	10.0	263.1	1.80	1.77	0.07	0.51	0.03	0.16	0.02	0.85	0.004	0.00	4.10	0.40	14.42	2.284	4.40	0.83	0.169	0.17
61105-7	11.0	161.3	1.50	2.23	0.03	0.43	0.01	0.09	0.01	0.43	0.003	0.00	5.20	0.40	6.289	0.882	20.7	1.89	0.107	0.11
61105-8	12.0	134.7	0.64	2.72	0.01	0.17	0.01	0.05	0.01	0.29	0.003	0.00	6.30	0.40	3.190	0.295	35.1	2.18	0.052	0.05
61105-9	13.0	135.6	0.37	3.36	0.01	0.12	0.00	0.04	0.00	0.24	0.001	0.00	7.80	0.40	1.948	0.107	47.3	2.40	0.023	0.02
61105-10	14.0	131.8	0.24	3.65	0.00	0.10	0.00	0.03	0.00	0.20	0.001	0.00	8.50	0.40	1.510	0.126	54.0	2.45	0.020	0.02
61105-11	15.0	62.65	0.09	1.86	0.01	0.05	0.00	0.03	0.00	0.09	0.002	0.00	4.30	0.70	2.586	0.221	57.4	2.44	0.035	0.04
61105-12	17.0	85.52	0.11	2.27	0.00	0.07	0.00	0.03	0.00	0.14	0.002	0.00	5.30	0.40	1.947	0.101	51.8	2.46	0.028	0.03
61105-13	19.0	292.0	0.10	8.49	0.01	0.19	0.00	0.04	0.00	0.44	0.001	0.01	19.7	0.20	0.867	0.029	55.2	2.39	0.012	0.01
61105-14	25.0	234.4	0.07	7.14	0.01	0.16	0.00	0.05	0.00	0.33	0.001	0.01	16.5	0.40	1.227	0.034	58.2	2.40	0.012	0.01
61105-15	30.0	268.7	0.09	5.11	0.01	0.18	0.00	0.27	0.00	0.58	0.002	0.00	11.8	1.10	8.821	0.056	36.3	2.41	0.024	0.03
61105-16	40.0	745.5	0.21	4.36	0.01	0.50	0.00	6.10	0.00	2.39	0.002	0.00	10.1	5.70	229.9	0.358	9.90	2.32	0.090	0.09
61105-17	50.0	121.1	0.07	0.21	0.01	0.09	0.00	0.40	0.00	0.40	0.002	0.00	0.50	2.20	313.6	7.627	2.80	2.28	0.443	0.44

Lab ID	Watts	Inverse Isochron Data				^{36}Ar/^{39}Ar Er.Corr.
HS1						
27 EK63		^{36}Ar/^{40}Ar	±1σ	^{39}Ar/^{40}Ar	±1σ	
61105-6	10.0	0.003	0.90	0.00672	4.06	0.1687
61105-7	11.0	0.003	1.25	0.01382	1.45	0.5256
61105-8	12.0	0.003	1.11	0.02023	0.65	0.4211
61105-9	13.0	0.002	0.67	0.02482	0.35	0.5771
61105-10	14.0	0.002	0.82	0.02774	0.25	0.4279
61105-11	15.0	0.001	1.84	0.02963	0.37	0.1603
61105-12	17.0	0.002	1.17	0.02657	0.26	0.2705
61105-13	19.0	0.002	0.49	0.02910	0.14	0.6473
61105-14	25.0	0.001	0.56	0.03051	0.14	0.5582
61105-15	30.0	0.002	0.52	0.01899	0.15	0.6018
61105-16	40.0	0.003	0.42	0.00538	0.18	0.7275
61105-17	50.0	0.003	0.56	0.00156	2.70	0.1060

J (X 10^{-3}) ± 1σ = 0.070 ± 0.000

Table E21: ^{40}Ar/^{39}Ar step-heating analytical results for *HS1 basalt lava (phase 2) (26.08.689N17.38.962E),* in Al Haruj al Aswad.

Lab ID	Watts	Relative Isotopic Abundances										Derived Results								
HS6												^{39}Ar Mol ¥ 10^{-14}	^{39}Ar % of total	% $(^{36}Ar)_{Ca}$			% $^{40}Ar^{*}$			w/±*J* ±1σ
25 EK63		^{40}Ar	±1σ	^{39}Ar	±1σ	^{38}Ar	±1σ	^{37}Ar	±1σ	^{36}Ar	±1σ				Ca/K	±1σ		Age (Ma)	±1σ	
61099-7	11.0	187.7	0.38	1.03	0.05	0.19	0.02	0.17	0.01	0.59	0.004	0.00	1.80	0.60	26.161	2.466	7.3	1.08	0.118	0.12
61099-8	12.0	77.96	0.21	0.84	0.01	0.07	0.01	0.10	0.01	0.21	0.002	0.00	1.40	1.00	18.77	0.945	20.8	1.56	0.077	0.08
61099-9	13.0	99.46	0.07	1.30	0.01	0.07	0.00	0.10	0.00	0.24	0.002	0.00	2.20	0.90	12.45	0.415	29.5	1.81	0.037	0.04
61099-10	14.0	124.5	0.04	1.82	0.01	0.09	0.00	0.12	0.00	0.27	0.001	0.00	3.10	0.90	10.47	0.141	35.0	1.92	0.024	0.02
61099-11	15.0	395.7	0.30	3.33	0.01	0.25	0.00	0.20	0.00	1.07	0.002	0.00	5.70	0.40	9.588	0.143	19.9	1.91	0.036	0.04
61099-14	25.0	1110	0.11	15.5	0.01	0.65	0.00	0.51	0.00	2.46	0.002	0.01	26.5	0.40	5.233	0.024	34.2	1.97	0.017	0.02
61099-15	30.0	287.8	0.22	5.38	0.01	0.17	0.00	0.27	0.00	0.52	0.001	0.00	9.20	1.10	8.011	0.069	46.5	1.99	0.013	0.01
61099-16	40.0	614.8	0.13	7.24	0.01	0.37	0.00	1.88	0.00	1.50	0.001	0.01	12.4	2.70	40.90	0.061	29.1	2.01	0.022	0.02
61099-17	50.0	502.3	0.16	8.08	0.01	0.30	0.00	1.82	0.00	1.06	0.002	0.01	13.8	3.70	35.63	0.058	39.5	1.99	0.015	0.02
61099-12	17.0	2727	0.93	8.82	0.01	1.69	0.00	0.50	0.00	8.47	0.004	0.01	15.1	0.10	9.014	0.059	7.4	1.84	0.095	0.10
61099-13	19.0	1839	0.25	5.22	0.01	1.15	0.00	0.27	0.00	5.79	0.055	0.00	8.90	0.10	8.047	0.103	6.1	1.73	0.275	0.27

Lab ID	Watts	Inverse Isochron Data				^{36}Ar/^{39}Ar Er.Corr.	*J* (X 10^{-3}) ± 1σ = 0.044 ± 0.000
HS6							
25 EK63		^{36}Ar/^{40}Ar	±1σ	^{39}Ar/^{40}Ar	±1σ		
61099-7	11.0	0.003	0.77	0.00542	4.70	0.0550	
61099-8	12.0	0.003	1.21	0.01070	1.58	0.1146	
61099-9	13.0	0.002	0.80	0.01305	0.53	0.2866	
61099-10	14.0	0.003	0.63	0.01463	0.29	0.4479	
61099-11	15.0	0.003	0.44	0.00839	0.20	0.7111	
61099-14	25.0	0.002	0.41	0.01395	0.12	0.7778	
61099-15	30.0	0.002	0.45	0.01869	0.20	0.6946	
61099-16	40.0	0.002	0.42	0.01162	0.14	0.7599	
61099-17	50.0	0.002	0.44	0.01590	0.15	0.7254	
61099-12	17.0	0.0031	0.41	0.00323	0.17	0.7653	
61099-13	19.0	0.0031	1.03	0.00283	0.16	0.2999	

Table E22: ^{40}Ar/^{39}Ar step-heating analytical results for *HS6 basalt lava (phase 2) (26.28.310N17.33.182E),* in Al Haruj al Aswad.

Lab ID	Watts	Relative Isotopic Abundances										Derived Results								
HS10												^{39}Ar Mol ¥ 10^{-14}	^{39}Ar % of total	% $(^{36}Ar)_{Ca}$			% $^{40}Ar^{*}$			w/±*J* ±1σ
15 EK63		^{40}Ar	±1σ	^{39}Ar	±1σ	^{38}Ar	±1σ	^{37}Ar	±1σ	^{36}Ar	±1σ				Ca/K	±1σ		Age (Ma)	±1σ	
61101-4	8.0	78.59	1.08	0.97	0.16	0.21	0.05	0.15	0.03	0.22	0.010	0.00	0.60	0.90	14.64	3.974	17.6	1.16	0.328	0.33
61101-5	9.0	376.9	0.92	6.13	0.03	0.30	0.01	0.19	0.01	0.95	0.007	0.00	3.70	0.20	2.849	0.140	24.9	1.23	0.033	0.03
61101-6	10.0	554.0	0.91	18.7	0.02	0.39	0.00	0.29	0.00	0.87	0.007	0.01	11.2	0.40	1.423	0.019	53.2	1.26	0.011	0.01
61101-7	11.0	622.7	0.92	22.4	0.01	0.44	0.00	0.28	0.00	0.91	0.007	0.02	13.4	0.40	1.153	0.014	56.6	1.26	0.009	0.01
61101-8	12.0	456.9	0.91	18.4	0.01	0.32	0.00	0.19	0.00	0.56	0.007	0.01	11.0	0.40	0.948	0.018	63.5	1.26	0.010	0.01
61101-9	13.0	422.1	0.91	16.6	0.01	0.29	0.00	0.15	0.00	0.53	0.007	0.01	10.0	0.40	0.850	0.019	62.4	1.27	0.011	0.01
61101-10	14.0	272.1	0.90	11.1	0.01	0.19	0.00	0.10	0.00	0.33	0.007	0.01	6.60	0.40	0.854	0.027	64.5	1.27	0.016	0.02
61101-11	15.0	246.4	0.91	10.1	0.01	0.18	0.00	0.11	0.00	0.30	0.007	0.01	6.10	0.50	1.047	0.030	64.3	1.25	0.018	0.02
61101-12	17.0	431.3	0.91	18.7	0.01	0.31	0.00	0.31	0.00	0.47	0.007	0.01	11.2	0.80	1.534	0.016	67.6	1.25	0.010	0.01
61101-13	19.0	377.1	0.91	12.6	0.01	0.27	0.00	0.89	0.00	0.62	0.007	0.01	7.60	1.80	6.523	0.024	51.6	1.24	0.015	0.02
61101-14	25.0	1511	0.99	25.3	0.01	1.02	0.00	4.17	0.00	3.82	0.007	0.02	15.2	1.40	15.26	0.0180	25.6	1.23	0.017	0.02
61101-15	30.0	197.2	0.90	4.35	0.01	0.14	0.00	0.51	0.00	0.44	0.007	0.00	2.60	1.50	10.89	0.0648	34.0	1.24	0.042	0.04
61101-16	40.0	137.5	0.90	1.27	0.01	0.09	0.00	0.18	0.00	0.40	0.007	0.00	0.80	0.60	13.25	0.2440	13.4	1.17	0.143	0.14

Lab ID	Watts	Inverse Isochron Data					*J* (X 10^{-3}) ± 1σ = 0.044 ± 0.000
						^{36}Ar/^{39}Ar Er.Corr.	
HS10							
15 EK63		^{36}Ar/^{40}Ar	±1σ	^{39}Ar/^{40}Ar	±1σ		
61101-4	8.0	0.003	4.83	0.01223	16.62	0.0252	
61101-5	9.0	0.003	0.85	0.01628	0.54	0.3533	
61101-6	10.0	0.002	0.89	0.03383	0.21	0.3922	
61101-7	11.0	0.002	0.85	0.03601	0.19	0.4057	
61101-8	12.0	0.001	1.27	0.04030	0.23	0.2888	
61101-9	13.0	0.001	1.33	0.03941	0.25	0.2806	
61101-10	14.0	0.001	2.15	0.04075	0.35	0.2065	
61101-11	15.0	0.001	2.32	0.04120	0.39	0.2018	
61101-12	17.0	0.001	1.50	0.04341	0.24	0.2487	
61101-13	19.0	0.002	1.18	0.03338	0.27	0.3274	
61101-14	25.0	0.003	0.45	0.01666	0.13	0.7263	
61101-15	30.0	0.002	1.65	0.02200	0.49	0.3219	
61101-16	40.0	0.003	1.85	0.00918	0.79	0.3393	

Table E23: ^{40}Ar/^{39}Ar step-heating analytical results for HS10 basalt lava *(phase 3)* (27.02.127N17.43.820E), in Al Haruj al Aswad.

Lab ID	Watts	Relative Isotopic Abundances										Derived Results								
HS19												^{39}Ar Mol ¥ 10^{-14}	^{39}Ar % of total	% $(^{36}Ar)_{Ca}$			% $^{40}Ar^{*}$			w/±*J* ±1σ
21 EK63		^{40}Ar	±1σ	^{39}Ar	±1σ	^{38}Ar	±1σ	^{37}Ar	±1σ	^{36}Ar	±1σ				Ca/K	±1σ		Age (Ma)	±1σ	
61109-5	9.0	273.9	0.62	4.33	0.06	0.30	0.02	0.26	0.02	0.81	0.021	0.00	2.60	0.60	8.340	0.653	12.7	1.02	0.057	0.06
61109-6	10.0	337.6	0.09	13.9	0.02	0.33	0.00	0.29	0.00	0.77	0.004	0.01	8.50	0.70	2.937	0.034	32.4	0.99	0.010	0.01
61109-7	11.0	364.2	0.14	19.1	0.02	0.37	0.00	0.34	0.00	0.73	0.002	0.01	11.60	0.90	2.479	0.020	41.0	0.99	0.007	0.01
61109-8	12.0	335.3	0.13	17.6	0.01	0.34	0.00	0.29	0.00	0.67	0.003	0.01	10.70	0.80	2.342	0.019	40.9	0.98	0.008	0.01
61109-9	13.0	286.7	0.09	14.9	0.01	0.29	0.00	0.23	0.00	0.57	0.002	0.01	9.00	0.80	2.169	0.011	40.9	0.99	0.008	0.01
61109-10	14.0	247.5	0.11	12.8	0.01	0.25	0.00	0.16	0.00	0.5	0.001	0.01	7.80	0.60	1.796	0.017	40.6	0.99	0.008	0.01
61109-11	15.0	200.9	0.11	10.7	0.01	0.20	0.00	0.12	0.00	0.39	0.001	0.01	6.50	0.60	1.635	0.026	42.5	1.01	0.009	0.01
61109-12	17.0	303.3	0.09	15.4	0.01	0.31	0.00	0.19	0.00	0.62	0.002	0.01	9.40	0.60	1.716	0.013	39.6	0.98	0.008	0.01
61109-13	19.0	219.7	0.11	11.8	0.01	0.23	0.00	0.18	0.00	0.43	0.002	0.01	7.20	0.80	2.084	0.014	42.1	0.99	0.008	0.01
61109-14	25.0	539.8	0.14	23.4	0.01	0.53	0.00	2.01	0.00	1.24	0.002	0.02	14.2	3.10	12.08	0.013	33.4	0.98	0.009	0.01
61109-15	30.0	304.5	0.08	14.6	0.01	0.31	0.00	1.72	0.00	0.67	0.002	0.01	8.90	4.90	16.50	0.023	37.5	0.99	0.009	0.01
61109-16	40.0	120.7	0.06	5.05	0.01	0.12	0.02	0.26	0.02	0.81	0.021	0.00	3.10	3.80	15.90	0.060	32.4	0.98	0.013	0.01
61109-17	50.0	81.42	0.10	0.95	0.00	0.06	0.00	0.29	0.00	0.77	0.004	0.00	0.60	1.20	22.36	0.241	9.4	1.01	0.070	0.07

Lab ID	Watts	Inverse Isochron Data					*J* (X 10^{-3}) ± 1σ = 0.070 ± 0.000
HS19				.		^{36}Ar/^{39}Ar Er.Corr	
21 EK63		^{36}Ar/^{40}Ar	±1σ	^{39}Ar/^{40}Ar	±1σ		
61109-6	10.0	0.002	0.46	0.04121	0.15	0.6826	
61109-7	11.0	0.002	0.46	0.05239	0.14	0.6897	
61109-8	12.0	0.002	0.47	0.05248	0.13	0.6770	
61109-9	13.0	0.002	0.48	0.05190	0.13	0.6598	
61109-10	14.0	0.002	0.48	0.05168	0.14	0.6588	
61109-11	15.0	0.002	0.62	0.05307	0.15	0.5147	
61109-12	17.0	0.002	0.44	0.05083	0.12	0.7246	
61109-13	19.0	0.002	0.49	0.05370	0.15	0.6425	
61109-14	25.0	0.002	0.42	0.04316	0.11	0.7675	
61109-15	30.0	0.002	0.47	0.04772	0.12	0.6814	
61109-16	40.0	0.002	0.60	0.04165	0.17	0.5210	
61109-17	50.0	0.003	0.70	0.01165	0.47	0.3624	

Table E24: ^{40}Ar/^{39}Ar step-heating analytical results for *HS19 basalt lava (phase 3) (28.03.540N17.34.968E),* in Al Haruj al Aswad.

Lab ID	Watts	Relative Isotopic Abundances										Derived Results								
HS16												^{39}Ar Mol ¥ 10^{-14}	^{39}Ar % of total	% $(^{36}Ar)_{Ca}$			% $^{40}Ar^{*}$			w/±*J* ±1σ
12 EK63		^{40}Ar	±1σ	^{39}Ar	±1σ	^{38}Ar	±1σ	^{37}Ar	±1σ	^{36}Ar	±1σ				Ca/K	±1σ		Age (Ma)	±1σ	
61091-4	8.0	160.2	1.92	0.98	0.02	0.17	0.01	0.12	0.01	0.53	0.005	0.00	0.50	0.30	11.43	0.747	2.30	0.50	0.337	0.34
61091-5	9.0	236.9	1.43	8.89	0.01	0.27	0.01	0.41	0.00	0.60	0.004	0.01	4.80	0.80	4.175	0.043	25.0	0.89	0.029	0.03
61091-6	10.0	284.2	0.86	18.9	0.01	0.33	0.00	0.61	0.00	0.52	0.003	0.01	10.2	1.40	2.884	0.015	46.2	0.93	0.010	0.01
61091-7	11.0	303.5	0.65	24.3	0.01	0.38	0.00	0.62	0.00	0.45	0.003	0.02	13.0	1.70	2.295	0.011	56.1	0.94	0.007	0.01
61091-8	12.0	217.4	0.59	19.1	0.01	0.29	0.00	0.38	0.00	0.29	0.003	0.01	10.2	1.60	1.797	0.014	61.3	0.94	0.007	0.01
61091-9	13.0	231.9	0.54	20.1	0.01	0.30	0.00	0.29	0.00	0.31	0.002	0.01	10.8	1.20	1.321	0.013	60.7	0.94	0.007	0.01
61091-10	14.0	185.0	0.52	15.4	0.01	0.24	0.00	0.20	0.00	0.27	0.002	0.01	8.20	0.90	1.176	0.019	57.6	0.93	0.009	0.01
61091-11	15.0	202.9	0.52	14.3	0.01	0.24	0.00	0.20	0.00	0.35	0.003	0.01	7.70	0.70	1.246	0.015	48.4	0.92	0.010	0.01
61091-12	17.0	292.7	0.45	19.7	0.00	0.34	0.00	0.38	0.00	0.53	0.002	0.01	10.6	0.90	1.764	0.011	46.5	0.93	0.007	0.01
61091-13	19.0	290.0	0.36	13.4	0.00	0.29	0.00	0.97	0.00	0.67	0.002	0.01	7.20	1.80	6.511	0.016	31.8	0.921	0.011	0.01
61091-14	25.0	951.4	0.33	28.1	0.01	0.82	0.00	6.14	0.00	2.63	0.003	0.02	15.1	2.90	19.73	0.018	19.9	0.91	0.016	0.02
61091-15	30.0	112.7	0.30	2.05	0.01	0.09	0.00	0.46	0.00	0.34	0.002	0.00	1.10	1.70	20.45	0.143	11.8	0.88	0.056	0.06
61091-16	40.0	153.3	0.29	1.13	0.01	0.11	0.00	0.35	0.00	0.49	0.002	0.00	0.60	0.90	28.17	0.325	5.20	0.95	0.105	0.11

Lab ID	Watts	Inverse Isochron Data					*J* (X 10^{-3}) ± 1σ = 0.074 ± 0.000
HS16						^{36}Ar/^{39}Ar Er.Corr.	
12 EK63		^{36}Ar/^{40}Ar	±1σ	^{39}Ar/^{40}Ar	±1σ		
61091-4	8.0	0.003	1.55	0.00610	2.46	0.4061	
61091-5	9.0	0.003	0.93	0.03743	0.62	0.7040	
61091-6	10.0	0.002	0.73	0.06667	0.32	0.5853	
61091-7	11.0	0.002	0.76	0.07997	0.24	0.4951	
61091-8	12.0	0.001	1.00	0.08784	0.29	0.4051	
61091-9	13.0	0.001	0.91	0.08674	0.26	0.4225	
61091-10	14.0	0.001	1.04	0.08306	0.30	0.3976	
61091-11	15.0	0.002	0.85	0.07042	0.28	0.4677	
61091-12	17.0	0.002	0.59	0.06722	0.19	0.5908	
61091-13	19.0	0.002	0.51	0.04621	0.16	0.6716	
61091-14	25.0	0.003	0.42	0.02937	0.12	0.7648	
61091-15	30.0	0.003	0.83	0.01804	0.48	0.3969	
61091-16	40.0	0.003	0.59	0.00728	0.75	0.3670	

Table E25: ^{40}Ar/^{39}Ar step-heating analytical results for *HS16 basalt lava (phase 4) (27.45.682N17.32.905E),* in Al Haruj al Aswad.

Lab ID	Watts	Relative Isotopic Abundances										Derived Results								
HS20												^{39}Ar Mol ¥ 10^{-14}	^{39}Ar % of total	% (^{36}Ar)$_{Ca}$			% ^{40}Ar*			w/±*J* ±1σ
26 EK63		^{40}Ar	±1σ	^{39}Ar	±1σ	^{38}Ar	±1σ	^{37}Ar	±1σ	^{36}Ar	±1σ				Ca/K	±1σ		Age (Ma)	±1σ	
61108-6	10.0	165.9	0.70	4.98	0.09	0.31	0.04	0.32	0.03	0.48	0.007	0.00	3.40	1.40	10.17	1.047	15.5	0.65	0.058	0.06
61108-7	11.0	159.1	0.33	9.21	0.03	0.23	0.01	0.23	0.01	0.33	0.004	0.01	6.20	1.50	3.993	0.227	39.9	0.87	0.017	0.02
61108-8	12.0	153.4	0.11	11.7	0.01	0.20	0.00	0.20	0.00	0.23	0.002	0.01	7.90	1.90	2.734	0.052	56.0	0.93	0.008	0.01
61108-9	13.0	156.4	0.03	12.7	0.01	0.20	0.00	0.19	0.00	0.20	0.002	0.01	8.60	2.00	2.381	0.033	61.8	0.96	0.006	0.01
61108-10	14.0	159.3	0.04	12.6	0.01	0.20	0.00	0.18	0.00	0.22	0.001	0.01	8.50	1.80	2.320	0.023	59.8	0.95	0.005	0.01
61108-11	15.0	166.5	0.06	11.3	0.01	0.20	0.00	0.16	0.00	0.28	0.001	0.01	7.60	1.20	2.242	0.026	50.8	0.95	0.006	0.01
61108-12	17.0	202.3	0.08	13.5	0.01	0.23	0.00	0.17	0.00	0.33	0.002	0.01	9.10	1.10	2.033	0.024	51.1	0.96	0.007	0.01
61108-13	19.0	225.0	0.08	10.2	0.01	0.23	0.00	0.13	0.00	0.50	0.002	0.01	6.90	0.60	2.013	0.025	34.0	0.94	0.010	0.01
61108-14	25.0	527.3	0.15	19.5	0.01	0.48	0.00	0.23	0.00	1.28	0.002	0.01	13.2	0.40	1.903	0.016	27.7	0.94	0.011	0.01
61108-15	30.0	260.1	0.08	8.66	0.01	0.24	0.00	0.17	0.00	0.66	0.002	0.01	5.80	0.60	3.201	0.039	24.5	0.93	0.015	0.01
61108-16	40.0	928.2	0.25	30.6	0.02	0.82	0.00	2.80	0.00	2.39	0.002	0.02	20.7	2.60	14.72	0.088	25.0	0.96	0.013	0.01
61108-17	50.0	94.04	0.03	3.31	0.01	0.09	0.00	0.34	0.00	0.24	0.009	0.00	2.20	3.10	16.46	0.121	26.7	0.96	0.108	0.11

Lab ID	Watts	Inverse Isochron Data					*J* (X 10^{-3}) ± 1σ = 0.070 ± 0.000
HS20						^{36}Ar/^{39}Ar Er.Corr.	
26 EK63		^{36}Ar/^{40}Ar	±1σ	^{39}Ar/^{40}Ar	±1σ		
61108-6	10.0	0.003	1.57	0.02996	1.93	0.1068	
61108-7	11.0	0.002	1.24	0.05786	0.38	0.2612	
61108-8	12.0	0.002	1.06	0.07600	0.17	0.3009	
61108-9	13.0	0.001	0.94	0.08154	0.14	0.3329	
61108-10	14.0	0.001	0.73	0.07895	0.14	0.4318	
61108-11	15.0	0.002	0.62	0.06761	0.14	0.5079	
61108-12	17.0	0.002	0.65	0.06691	0.14	0.4827	
61108-13	19.0	0.002	0.52	0.04549	0.14	0.6133	
61108-14	25.0	0.002	0.42	0.03707	0.12	0.7565	
61108-15	30.0	0.003	0.49	0.03330	0.13	0.6503	
61108-16	40.0	0.003	0.41	0.03289	0.12	0.7841	
61108-17	50.0	0.003	4.09	0.03500	0.21	0.0731	

Table E26 ^{40}Ar/^{39}Ar step-heating analytical results for *HS20 basalt lava (phase 3) (28.07.500N17.35.485E),* in Al Haruj al Aswad.

Lab ID	Watts	Relative Isotopic Abundances										Derived Results								
HS3												^{39}Ar Mol ¥ 10^{-14}	^{39}Ar % of total	% $(^{36}Ar)_{Ca}$			% $^{40}Ar^{*}$			w/±*J* ±1σ
14 EK63		^{40}Ar	±1σ	^{39}Ar	±1σ	^{38}Ar	±1σ	^{37}Ar	±1σ	^{36}Ar	±1σ				Ca/K	±1σ		Age (Ma)	±1σ	
61095-4	8.0	58.46	0.40	0.58	0.05	0.09	0.01	0.06	0.01	0.19	0.003	0.00	0.60	0.40	8.974	2.203	3.40	0.43	0.237	0.24
61095-5	9.0	691.5	0.48	6.72	0.02	0.54	0.01	0.24	0.01	2.22	0.004	0.00	7.30	0.10	3.215	0.087	4.10	0.53	0.056	0.06
61095-6	10.0	953.7	0.52	14.3	0.01	0.76	0.00	0.50	0.00	2.98	0.004	0.01	15.4	0.20	3.152	0.024	6.90	0.58	0.034	0.03
61095-7	11.0	623.5	0.51	15.3	0.01	0.55	0.00	0.68	0.00	1.86	0.003	0.01	16.5	0.40	4.006	0.020	11.4	0.59	0.021	0.02
61095-8	12.0	301.0	0.49	11.5	0.01	0.30	0.00	0.65	0.00	0.83	0.004	0.01	12.5	1.00	5.118	0.028	18.6	0.61	0.017	0.02
61095-9	13.0	179.2	0.48	8.11	0.01	0.19	0.00	0.56	0.00	0.47	0.003	0.01	8.80	1.50	6.287	0.042	22.4	0.62	0.019	0.02
61095-10	14.0	158.0	0.48	7.15	0.01	0.17	0.00	0.54	0.00	0.42	0.003	0.01	7.70	1.60	6.859	0.043	22.0	0.61	0.021	0.02
61095-11	15.0	173.9	0.49	8.69	0.01	0.20	0.00	0.55	0.00	0.45	0.003	0.01	9.40	1.50	5.694	0.038	24.4	0.62	0.018	0.02
61095-12	17.0	201.4	0.49	7.07	0.01	0.20	0.00	0.72	0.00	0.57	0.003	0.00	7.70	1.60	9.235	0.045	16.9	0.61	0.024	0.02
61095-13	19.0	257.6	0.49	5.57	0.01	0.23	0.00	1.49	0.00	0.79	0.003	0.00	6.00	2.30	24.26	0.070	10.1	0.59	0.033	0.03
61095-14	25.0	262.1	0.49	5.80	0.01	0.23	0.00	2.57	0.00	0.82	0.004	0.00	6.30	3.90	40.31	0.074	10.2	0.59	0.033	0.03
61095-15	30.0	72.46	0.48	1.05	0.01	0.06	0.00	0.49	0.00	0.23	0.003	0.00	1.10	2.60	41.93	0.362	6.10	0.53	0.138	0.14
61095-16	40.0	102.3	0.48	0.60	0.01	0.07	0.00	0.30	0.00	0.34	0.003	0.00	0.70	1.10	45.78	0.673	1.40	0.29	0.248	0.25

Lab ID	Watts	Inverse Isochron Data					*J* ($X\ 10^{-3}$) ± 1σ = 0.070 ± 0.000
HS3						$^{36}Ar/^{39}Ar$ Er.Corr.	
14 EK63		$^{36}Ar/^{40}Ar$	±1σ	$^{39}Ar/^{40}Ar$	±1σ		
61095-4	8.0	0.003	1.90	0.00992	8.45	0.0389	
61095-5	9.0	0.003	0.45	0.00972	0.32	0.6243	
61095-6	10.0	0.003	0.42	0.01498	0.13	0.7649	
61095-7	11.0	0.003	0.44	0.02451	0.15	0.7341	
61095-8	12.0	0.003	0.60	0.03834	0.21	0.5765	
61095-9	13.0	0.003	0.86	0.04519	0.29	0.4705	
61095-10	14.0	0.003	0.93	0.04519	0.33	0.4549	
61095-11	15.0	0.003	0.90	0.04996	0.31	0.4553	
61095-12	17.0	0.003	0.76	0.03505	0.29	0.5039	
61095-13	19.0	0.003	0.61	0.02144	0.25	0.5780	
61095-14	25.0	0.003	0.63	0.02182	0.24	0.5651	
61095-15	30.0	0.003	1.65	0.01431	0.85	0.3701	
61095-16	40.0	0.003	1.16	0.00581	1.02	0.2894	

Table E27: $^{40}Ar/^{39}Ar$ step-heating analytical results for *HS3 basalt lava (phase 4) (26.22.200N 17.36.680E),* in Al Haruj al Aswad.

Lab ID	Watts	Relative Isotopic Abundances										Derived Results								
HS11												^{39}Ar Mol ¥ 10^{-14}	^{39}Ar % of total	% $(^{36}Ar)_{Ca}$			% $^{40}Ar^{*}$			w/±*J* ±1σ
20 EK63		^{40}Ar	±1σ	^{39}Ar	±1σ	^{38}Ar	±1σ	^{37}Ar	±1σ	^{36}Ar	±1σ				Ca/K	±1σ		Age (Ma)	±1σ	
61077-8	12.0	13.36	0.04	1.42	0.01	0.03	0.00	0.05	0.00	0.03	0.002	0.00	0.80	3.00	5.230	0.172	28.1	0.36	0.043	0.04
61077-9	13.0	15.83	0.03	1.61	0.01	0.03	0.00	0.06	0.00	0.04	0.002	0.00	0.90	3.00	5.139	0.160	32.3	0.43	0.038	0.04
61077-6	10.0	133.3	0.26	10.6	0.00	0.22	0.00	0.36	0.00	0.33	0.002	0.01	6.10	2.10	4.819	0.044	27.1	0.46	0.009	0.01
61077-7	11.0	168.3	0.06	19.7	0.02	0.30	0.00	0.55	0.00	0.34	0.002	0.01	11.2	3.10	3.953	0.014	41.1	0.47	0.005	0.01
61077-10	14.0	37.58	0.07	4.79	0.01	0.08	0.00	0.12	0.00	0.07	0.001	0.00	2.70	3.30	3.694	0.048	44.8	0.47	0.012	0.01
61077-11	15.0	88.43	0.04	11.4	0.01	0.17	0.00	0.29	0.00	0.17	0.002	0.01	6.50	3.30	3.614	0.033	45.3	0.47	0.007	0.01
61077-12	17.0	267.9	0.11	37.7	0.02	0.54	0.00	0.63	0.00	0.46	0.001	0.03	21.5	2.60	2.372	0.008	49.7	0.47	0.003	0.00
61077-13	19.0	282.8	0.10	41.8	0.02	0.59	0.00	0.44	0.00	0.46	0.001	0.03	23.8	1.80	1.492	0.006	52.6	0.48	0.003	0.00
61077-14	25.0	388.1	0.14	34.8	0.02	0.59	0.00	0.63	0.00	0.89	0.002	0.02	19.9	1.40	2.563	0.009	32.1	0.48	0.005	0.01
61077-15	30.0	513.1	0.16	11.6	0.01	0.45	0.00	1.42	0.00	1.63	0.002	0.01	6.60	1.70	17.51	0.028	6.7	0.40	0.024	0.02

Lab ID	Watts	Inverse Isochron Data					*J* (X 10^{-3}) ± 1σ = 0.074 ± 0.000
				.		^{36}Ar/^{39}Ar Er.Corr	
HS11							
20 EK63		^{36}Ar/^{40}Ar	±1σ	^{39}Ar/^{40}Ar	±1σ		
61077-8	12.0	0.002	4.69	0.10604	0.55	0.0657	
61077-9	13.0	0.002	4.20	0.10137	0.46	0.0673	
61077-6	10.0	0.002	0.66	0.07985	0.22	0.5515	
61077-7	11.0	0.002	0.70	0.11694	0.13	0.4521	
61077-10	14.0	0.002	2.07	0.12757	0.33	0.1606	
61077-11	15.0	0.002	1.13	0.12886	0.15	0.2805	
61077-12	17.0	0.002	0.51	0.14072	0.12	0.6282	
61077-13	19.0	0.002	0.48	0.14804	0.12	0.6613	
61077-14	25.0	0.002	0.44	0.08982	0.12	0.7239	
61077-15	30.0	0.003	0.42	0.02240	0.13	0.7600	

Table E28: ^{40}Ar/^{39}Ar step-heating analytical results for *HS11 basalt lava (phase 5) (27.04.157N17.42.707E),* in Al Haruj al Aswad.

Lab ID	Watts	Relative Isotopic Abundances										Derived Results								
HS21												^{39}Ar Mol ¥ 10^{-14}	^{39}Ar % of total	% $(^{36}Ar)_{Ca}$			% $^{40}Ar^{*}$			w/±*J* ±1σ
16 EK63		^{40}Ar	±1σ	^{39}Ar	±1σ	^{38}Ar	±1σ	^{37}Ar	±1σ	^{36}Ar	±1σ				Ca/K	±1σ		Age (Ma)	±1σ	
61093-5	9.0	155.3	0.96	9.65	0.04	0.27	0.01	0.39	0.01	0.51	0.011	0.01	6.80	1.20	4.858	0.153	2.40	0.05	0.047	0.05
61093-6	10.0	285.2	0.76	23.4	0.01	0.45	0.00	0.76	0.00	0.91	0.004	0.02	16.4	1.40	3.891	0.018	6.50	0.11	0.010	0.01
61093-7	11.0	340.6	0.76	25.5	0.02	0.51	0.00	0.63	0.00	1.08	0.004	0.02	17.9	0.90	2.974	0.018	6.30	0.11	0.010	0.01
61093-8	12.0	123.0	0.75	19.4	0.02	0.30	0.00	0.32	0.00	0.36	0.004	0.01	13.6	1.40	1.969	0.021	14.0	0.12	0.010	0.01
61093-9	13.0	90.69	0.75	14.3	0.01	0.21	0.00	0.22	0.00	0.27	0.004	0.01	10.0	1.40	1.877	0.027	12.9	0.11	0.013	0.01
61093-10	14.0	57.72	0.75	9.11	0.02	0.14	0.00	0.16	0.00	0.17	0.004	0.01	6.40	1.50	2.131	0.045	13.0	0.11	0.020	0.02
61093-11	15.0	44.29	0.75	6.95	0.01	0.11	0.00	0.14	0.00	0.13	0.004	0.00	4.90	1.80	2.467	0.065	14.4	0.12	0.026	0.03
61093-12	17.0	63.98	0.75	8.53	0.01	0.14	0.00	0.22	0.00	0.20	0.004	0.01	6.00	1.80	3.038	0.048	9.00	0.09	0.021	0.02
61093-13	19.0	69.77	0.76	7.51	0.01	0.13	0.00	0.31	0.00	0.22	0.004	0.01	5.30	2.30	4.891	0.060	7.90	0.10	0.024	0.02
61093-14	25.0	228.9	0.76	13.1	0.01	0.30	0.00	4.28	0.01	0.79	0.004	0.01	9.20	8.70	39.19	0.062	5.60	0.13	0.017	0.02
61093-15	30.0	64.17	0.75	3.62	0.01	0.08	0.00	1.15	0.00	0.22	0.004	0.00	2.50	8.60	37.87	0.151	7.70	0.18	0.050	0.05
61093-16	40.0	78.50	0.75	1.38	0.01	0.07	0.00	0.51	0.00	0.27	0.004	0.00	1.00	3.10	44.52	0.388	2.40	0.18	0.135	0.13

Lab ID	Watts	Inverse Isochron Data					*J* (X 10^{-3}) ± 1σ = 0.074 ± 0.000
HS21						^{36}Ar/^{39}Ar Er.Corr.	
16 EK63		^{36}Ar/^{40}Ar	±1σ	^{39}Ar/^{40}Ar	±1σ		
61093-5	9.0	0.003	2.21	0.06208	0.72	0.2786	
61093-6	10.0	0.003	0.63	0.08206	0.29	0.6403	
61093-7	11.0	0.003	0.59	0.07477	0.25	0.6435	
61093-8	12.0	0.003	1.31	0.15795	0.62	0.5094	
61093-9	13.0	0.003	1.68	0.15771	0.83	0.5156	
61093-10	14.0	0.003	2.56	0.15790	1.31	0.5138	
61093-11	15.0	0.003	3.43	0.15706	1.69	0.4947	
61093-12	17.0	0.003	2.25	0.13346	1.18	0.5271	
61093-13	19.0	0.003	2.06	0.10764	1.10	0.5321	
61093-14	25.0	0.003	0.72	0.05635	0.35	0.6162	
61093-15	30.0	0.003	2.20	0.05574	1.19	0.5359	
61093-16	40.0	0.003	1.78	0.01738	1.09	0.5010	

Table E29: ^{40}Ar/^{39}Ar step-heating analytical results for *HS21 basalt lava (phase 5) (28.12.795N17.40.465E),* in Al Haruj al Aswad.